Wayne State University

Wayne State University Dissertations

1-1-2014

Redox-Active Trivalent Metallosurfactants With Low Global Symmetry For Molecule-Based Electronics: Spectroscopic, Electrochemical, And Amphiphilic Properties Of New Molecular Materials For Current-Voltage Measurements In M|lb-Monolayer|m Devices

Lanka Dilruksi Wickramasinghe Wickramasinghe Arachchilage
Wayne State University,

Follow this and additional works at: http://digitalcommons.wayne.edu/oa_dissertations

REDOX-ACTIVE TRIVALENT METALLOSURFACTANTS WITH LOW GLOBAL SYMMETRY FOR MOLECULE-BASED ELECTRONICS: SPECTROSCOPIC, ELECTROCHEMICAL, AND AMPHIPHILIC PROPERTIES OF NEW MOLECULAR MATERIALS FOR CURRENT-VOLTAGE MEASUREMENTS IN M|LB-MONOLAYER|M DEVICES

by

LANKA D. W. WICKRAMASINGHE ARACHCHILAGE

DISSERTATION

Submitted to the Graduate School of

Wayne State University,

Detroit, Michigan

in partial fulfillment of the requirements

for the degree of

DOCTOR OF PHILOSOPHY

2014

MAJOR: CHEMISTRY (Inorganic)

Approved by:

_____

Advisor   Date

_____

_____

_____

DEDICATION

I would like to dedicate this thesis to my dearest father Dayananda Wickramasinghe Arachchilage, mother Rupa Wickramasinghe Arachchilage, and my loving husband Dr. Thuduwage Hiran Perera.

ACKNOWLEDGEMENTS

Most importantly, I would like to convey my sincere gratitude to my research advisor Prof. Cláudio N. Verani for his immense support, encouragement, and for the guidance that he provided as I pursued my research career at the Department of Chemistry at Wayne State University. His knowledge, perception, enthusiasm, and motivation for research, inspired me to carry out my research studies diligently in his research laboratory. During the course of my research, he provided me the opportunity to participate in various international and regional conferences. He also introduced me to several talented research collaborators to advance my research project to a more sophisticated level. He has been a very engaging and a helpful mentor, not only during my graduate studies but also during personal difficulties. He understood my competences and weaknesses, and he always provided valuable suggestions to strengthen my personality not only as a researcher, but also as an individual. Once again, I would like to cordially thank Prof. Verani for accepting me into his research group and providing me the opportunity to succeed as a chemical researcher.

I would like to thank my dissertation committee members, Professors Matthew J. Allen, Colin F. Poole, Zhixian Zhou, and Sandro R. P. da Rocha for their valuable support, comments, suggestions, and time that they provided during my Ph.D. study at Wayne State University. Also, I would like to convey my heartfelt thanks to all of my research collaborators, Prof. Zhixian Zhou and Meeghage Madusanka Perera from Department of Physics and Astronomy; Prof. Guangzhao Mao and Li Li from Department of Chemical Engineering and Materials Science; Prof. H. Bernhard Schlegel, Shivnath Mazumder, and Bishnu Thapa from Department of Chemistry; and Prof. Sarah Trimpin and Tarick El-Baba from Department of Chemistry at Wayne State University for their valuable support,

comments, suggestions, and precious time that they provided to improve the quality of my research project. Without their contribution and dedication, the completion of my research project would have not been a success.

My earnest gratitude extends to Dr. Mary Jane Heeg, Dr. Philip D. Martin, and Dr. Richard Staples (MSU) for solving X-ray crystal structures. Also I would like to express my appreciation to Dr. Lew M. Hryhorczuk and Dr. Yuriy Danylyuk for mass spectrometry data; Dr. Bashar Ksebati for training me on NMR instruments; and Dr. Zhi Mei (Mike) for guiding me on the use of gold sputtering machine. I would like to thank Prof. William Martin McClain, Prof. David Coleman, Dr. Patricia B. Coleman, and Prof. Stephanie L. Brock to whom I worked as a graduate teaching assistant during my first two years at Wayne State University.

My gratitude extends to Melissa Barton for helping me with all of the administrative work related to the graduate program. I would like to thank Nestor Ocampo for information technology support. I would also like to thank the administrative staff at Department of Chemistry, including Deborah McCreless, Mary Gorny Wood, Diane Kudla, Bernadette Miesik, Jacqueline Baldyga, Francine Owczarek, Lisa G. Smith, and Erin Bachert. I would like give my earnest acknowledgements to all the science stores staff, including Elizabeth

Ries, Joseph Oravec, Bonnie Cetlinski, Gregory Kish, Lorraine Lewis, and Jason Parizon for their enormous support in chemical and supply purchases.

My heartfelt gratitude extends to all the past and present Verani group members. I am truly fortunate to join the Verani group and without the support and friendly nature of my group members, it would have not been possible to complete my graduate studies with such a joyous feeling. The Verani lab has always felt like a second home to me. The lab and the group members provided me a very pleasant environment to carry out my research work. Therefore I never felt home sick when I was in the lab. Especially, I would like to thank Dr. Rajendra Shakya, Dr. Fernando Xavier, Dr. Ramadevi Shanmugam, Dr. Frank Lesh, and Dr. Marco Allard for their enormous support, valuable discussions, suggestions, and training me on all the lab instruments and techniques. While I was in the lab, I valued their company very much. I would also like to sincerely thank Dr. Ramadevi Shanmugam for being my mentor and a friend when I first joined the Verani group and for training me on the Langmuir-Blodgett method.

I appreciate Dr. Dakshika Wanniarachchi and Dajena Tomco, who joined the Verani group as graduate students with me in year 2008 and ever since we have become good friends. I thank them for all the help and support that they have given me during these years. Also I would like to thank Debashis Basu and Ryan Thomas for their friendship and valuable suggestions that they provided me during these years. Next, I would like to thank Sunalee Gonawala for her friendship and support. I appreciate the time that I spent mentoring her and she is a good friend to me. Then, I would like to extend my thanks to Habib Baydoun, Kenneth Kpogo, Brittany Venglarcik, Danushka Ekanayake, and Pavithra Hetti Achchi for their friendship and support. Especially I am thankful to Habib Baydoun and Kenneth Kpogo

for solving some of the X-ray crystal structure data that I have reported herein. Also I would like to thank Prof. Verani's wife Priscila and their daughter Clara for the hospitability that they provided during group gatherings.

I would also like to extend my gratitude to members in Winter group, Brock group, and Allen group for allowing me to use their instrumentation during my dissertation research. I would like to thank the Sri Lankan Student Association at Wayne State University and all the friends for their friendship and support.

I am really blessed to have loving parents, who always stand behind me and support me in all possible ways. Even though they lived far away from me, they never allowed me to miss them even for a fraction of a second and always cared for me. They provided me a good education and advised me to become a person with noble values. Principally, they guided me to become who I am today and I would like to thank them from the bottom of my heart for all of their support, encouragement, and love. Also I would like to thank my brother Asanka Wickramasinghe Arachchilage, sisters, Chammi Wickramasinghe Arachchilage and Shalini Wickramasinghe Arachchilage for their love, support, and courage that they provided during these years.

Last but not least, I would like to convey my heartiest gratitude to my loving husband Dr. Thuduwage Hiran Perera. He is another person who always stands behind me and encourages me to achieve my dreams. He never let go of my hand even during the most difficult times of life. Thank you very much Hiran for all your love, support, and encouragement.

TABLE OF CONTENTS

LIST OF TABLES

ix

LIST OF FIGURES

xi

xvi

xvii

LIST OF SCHEMES

CHAPTER 1

INTRODUCTION

1.1 General

At present the microelectronic industry has accomplished several different technological advancements, such as speed of data processing and performance. These advancements are made possible due to new fabricating techniques and novel materials. Among these achievements the advancement of silicon-based integrated circuits hold an impressive position.[1,2] A target of the microelectronic industry today is to make faster, cheaper, and smaller electronic devices which can perform more efficiently toward new tasks. Moore's law states that the chip density of an integrated circuit doubles every eighteen to twenty four months.[3] Therefore, the miniaturization process of electrical components will soon become a major obstacle. Major limitations to the decreasing size of computer chips are the leakage of current and the high costs that are inevitable to improve the technology.[4] To overcome the difficulties of the miniaturization process,[5,6,7] new approaches should aim to maximize chip density. In an effort to make efficient microelectronic devices, a large number of approaches have been attempted.[2] The seminar presented by the Nobel Prize winner, Prof. Richard P. Feynman, "There's Plenty of Room at the Bottom," was the foundation for the revolutionary idea of using molecules for information storage. In his talk, he mentioned that technical applications can be governed in small scale. This idea was different from the regular miniaturization of electronic devices, but comprised the idea of building electronics, such as information storage at an atomic or molecular level.[8] Furthermore, he mentioned that the size of computers can be decreased tremendously by considering the phenomenon of possible atomic storage. Even though the use of molecule-based devices is an advanced

alternative, enough effort has not yet been put into this field.[9] The impression of molecular electronics involves the ability of a molecule, a collection of molecules, metallic or semiconductor materials, or carbon nanotubes to execute tasks related to electrical components. When employing the above mentioned materials in electronic devices, there are a few requirements that need to be fulfilled.[2] The foremost requirements are as follows: (i) these molecules should tolerate high temperatures (~ 400 °C) which are used in fabrication methods, (ii) they should be chemically inert with own species to avoid side reactions, (iii) they should show reversible electron transfer processes, (iv) there should be a way to connect different components with each other,[2] and (v) they should be able to organized into stable well-ordered molecular films to avoid the leakage of current.[10] These electrical components will include molecular switches, static elements for data storage, molecular wires, transistors and logic gates, capacitors, and molecular diodes. As an initial attempt, in 1974, Aviram and Ratner[11] proposed the use of single molecules with electron acceptor and donor properties as molecular rectifiers. This new concept involves the design of molecules or collection of molecules which can function as electrical components.[12] Organic molecules can be beneficial in accomplishing the different electrical components due to abundant numbers of synthetic opportunities in fine-tuning the geometric and electronic properties to obtain the desired structures.[13] Hence, inorganic and organic chemists play a major role in improving the technology, materials, and concepts needed to execute these experiments. Nevertheless, synthetic molecules alone will not be able to generate high-tech electronic devices such as computers, however synthetic molecules accompanied with silicon mediated components would be a reliable source. One of the most common methods that have been used to determine the electrical properties of such synthetic molecular

components is the metal|molecule|metal configuration.[14] This chapter will briefly discuss the use of new materials and their derivatives in designing different components such as molecules for information storage, displays, molecular wires, transistors, and molecular rectifiers or diodes that have been developed in the literature. Further, it will discuss different current rectification mechanisms which are shown by molecular rectifiers. Lastly, this chapter will present the research statement and objectives of the dissertation project.

1.2 Molecules for Information Storage

With the pioneering work established over a decade ago by the groups of Lindsey and Bocian, metalloporphyrins are known to be stable at elevated temperatures and over a large number of operating cycles.[15] These are two important conditions required in building robust memory elements with high charge densities that can endure current manufacturing conditions.[16] Metalloporphyrins (**Figure 1.1a**) can form very stable π-cationic species at ambient conditions, these cationic species can be probed at low potential values and can store charge for long periods of time without marked decomposition. The consecutive reduction and oxidation processes of these porphyrin units therefore, can be used to read and write bits of information using '0' and '1' as shown in **Figure 1.1b**.

(a)

Charge-storage molecule

Surface-attachment group

Surface: Au, Si, SiO$_2$, TiN, Ge

(b)

Oxidation		
P	P $\longrightarrow$ **P$^+$** + e$^-$	**P$^+$** $\longrightarrow$ **P^{++}** + e$^-$
Neutral species	Mono-π-cation radical	Di-π-cation radical
00	Write 01	Write 10

Reduction		
P^{++} + e$^-$ $\longrightarrow$ P$^+$	**P$^+$** + e$^-$ $\longrightarrow$ P	**P**
Di-π-cation radical	Mono-π-cation radical	Neutral species
Read 10	Read 01	00
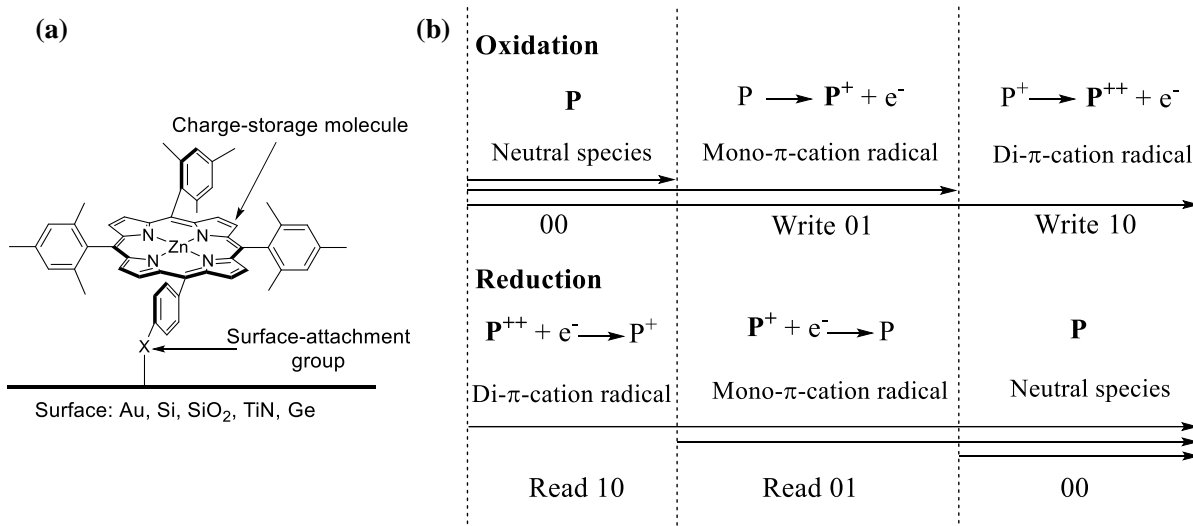
Figure 1.1. (a) A simple memory element with a zinc porphyrin unit and (b) read and write processes in porphyrin (**P**) systems.

The simplest zinc coordinated porphyrin unit can show up to two redox processes and initially it forms the mono-π-cationic species followed by the di-π-cationic species. During the formation of mono-π-cationic species, a bit of information can be recorded and when the π-cationic species is reducing back to its neutral species the bit of information can be released. When using porphyrin-based systems for multibit information storage a minimum of three π-cationic states are required to record all the combinations of '0' and '1'. Therefore, different approaches have been used to increase redox properties of porphyrin systems. The number of redox states of a system can be increased by introducing a collection of redox active molecules into the system or by integrating several redox states into a distinct system.[17] This prerequisite has been achieved easily by incorporating several porphyrin units to result in a dyad. Some of the dyads which can show up to three[18] or four cationic states[19] are shown in **Figure 1.2**.

(a) Ferrocene-porphyrin
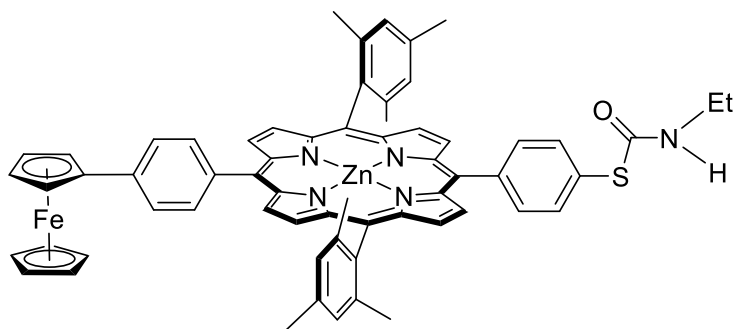
(b) Porphyrin dyad
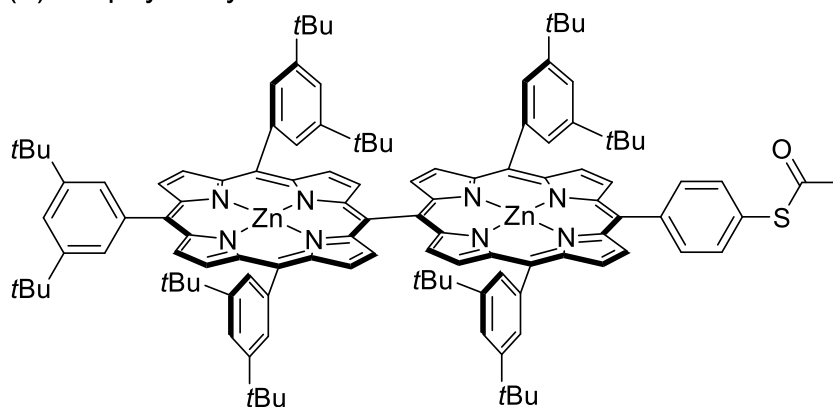
Figure 1.2. Porphyrin dyad structures.

Among these dyads, lanthanide coordinated triple-decker porphyrin structures are well-known.[20,21] These structures can show four cationic states and the lanthanide ions have been used to stack the porphyrin units. The number of cationic states and their potentials can be modulated depending on substituents on the porphyrin unit and the metal ion. Porphyrin units can also be substituted by phthalocyanine units to modify the ligand structure. Eight different cationic states have been obtained by combining two of these triple-decker structures and they tend to occupy large footprints (the area occupied by one molecule) on substrates.[22,23] This feature is not favorable for memory elements, because a large number of

molecules should reside in a minimum space to acquire high charge density.[24] Therefore in memory elements, molecules which can occupy small footprints will be more beneficial.

To attach the porphyrin units onto solid surfaces, a tether has been coupled to the main molecular structure. The tether is composed of two units, namely a surface attachment group and a linker. These tether groups support to bind the molecules onto solid surfaces. Therefore, self-assembly methods have been employed for the fabrication of molecules and different attachment groups have been used depending on the substrates. Phosphonate groups have been used for SiO_2 and WO_2 surfaces,[25] whereas alcohols,[26] thiols,[27] seleniols,[28] and all-carbon[29] attachment groups have been used for Si surfaces. The surface attachment groups also help in positioning the molecule and to make a good electrical contact between the surface and the molecule.[30,31,32] The most common surface tether groups are shown in **Figure 1.3**.

Thiols

—CH₂SAc

SAc

—(CH₂)₁₅SAc

(CH₂)ₙSAc
n = 0-3

n = 0, 1
SAc

Alcohols

—CH₂OH

OH

—OH

—CH₂OH

OH

OH

Phophonates

Carbon

—I

n = 0-3

n = 0, 1

—CH₂Br

—H

Selenols

—CH₂SeAc

—CH₂SeAc

Multipodal Tethers
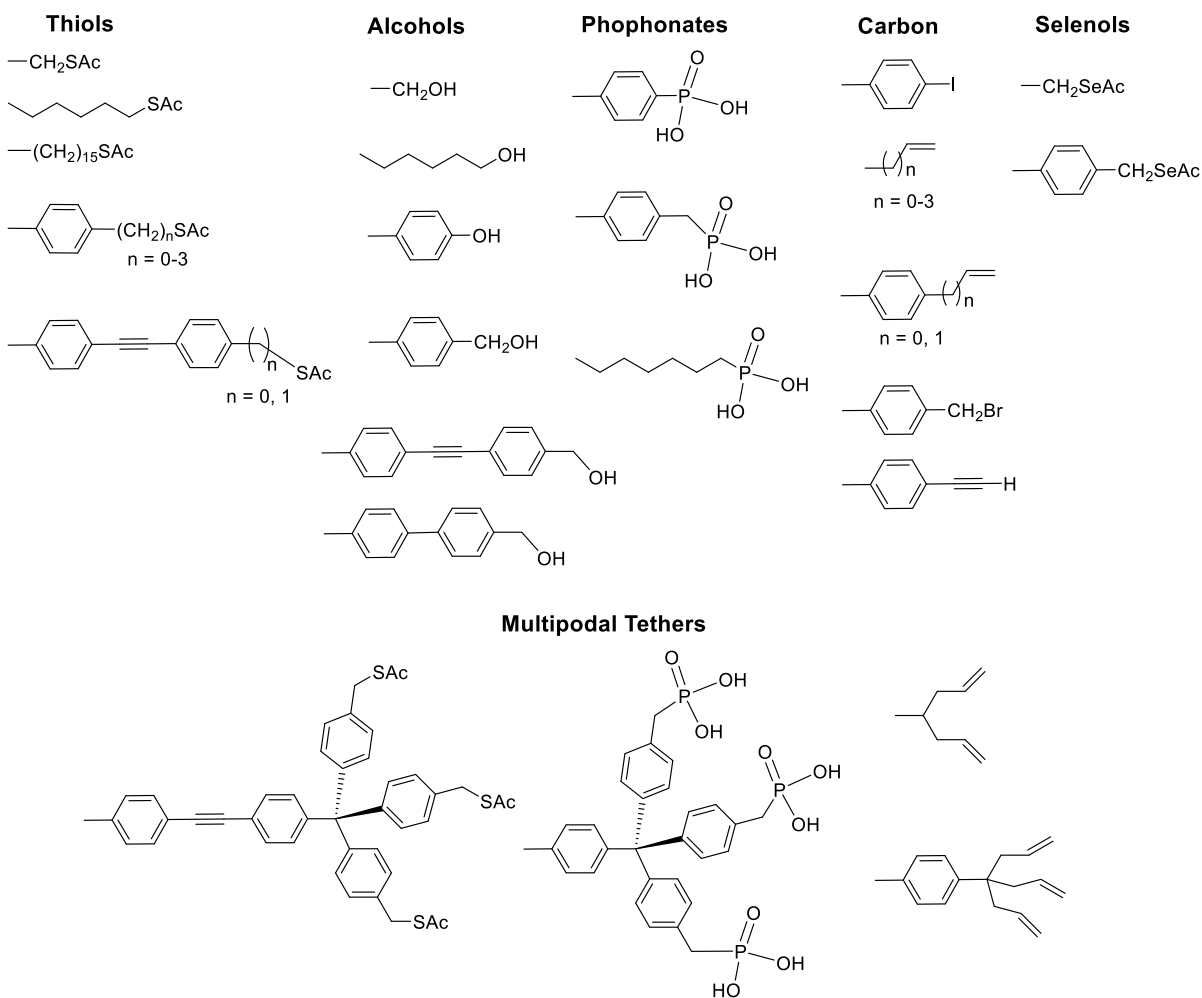
Figure 1.3. Alternative tether groups.

The porphyrin units in molecular devices have demonstrated remarkable features, and according to the experiments they have shown that the π-cationic based redox processes can be cycled up to 1×10^{10} without any decomposition for 27 days.[1] The experiments have been carried out with intentional interruptions to study the stability of the electrical cycling and have demonstrated very robust data.[33] According to this data it was shown that the porphyrin-based structures can be used as dynamic random access memory (DRAM) elements in the engineering process of desktop and laptop computers.

Few other metal complexes have been studied as molecular memory elements, namely ruthenium(II)-terpyridine,[10,34] cobalt(III)-azo,[35] and rhodim(III)-azo[36] incorporated systems (**Figure 1.4**). The devices of these complexes with metal|molecule|metal configurations have shown symmetric current responses (**Figure 1.4d**) in both negative and positive applied bias potentials which are indicative for typical molecular memory elements. Also, these metal complexes are able to operate in two different redox states with high ON/OFF ratios. During these experiments, the read-write cycles have been investigated by applying voltage pulses. These molecular devices further indicate that they are potentially applicable as random-access memory (RAM) and read-only memory (ROM) elements.[36]
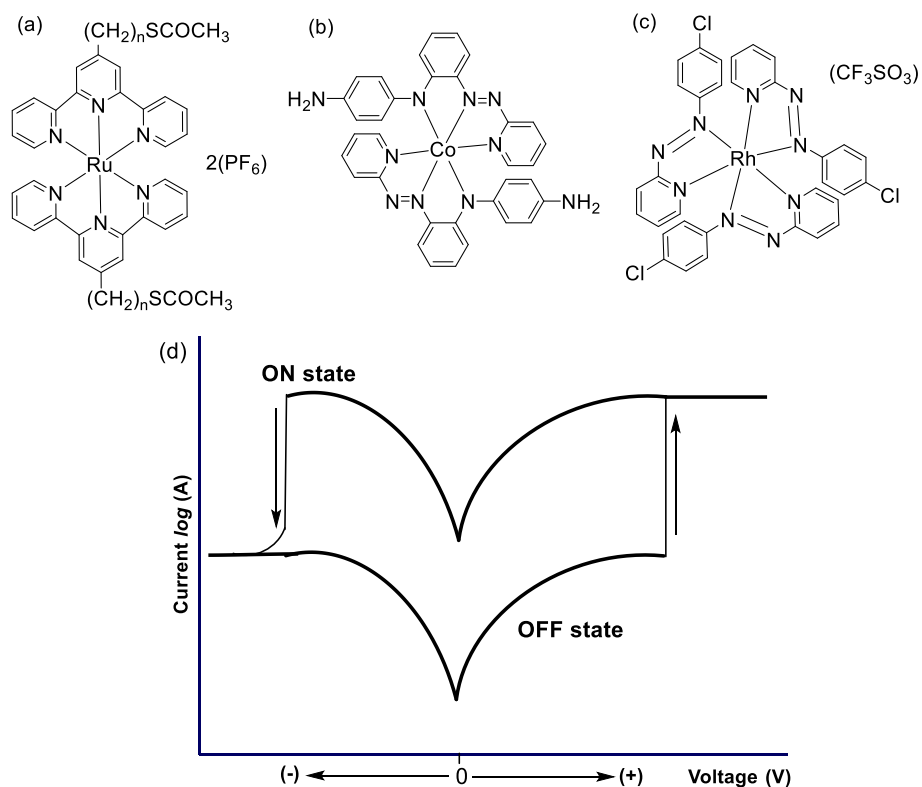
Figure 1.4. Molecular structures of (a) Ru(II), (b) Co(III), and (c) Rh(III) complexes, and (d) a representative current-voltage (I-V) response observed for molecular memory elements.

1.3 Molecules for Display Technology

The original concept of molecule-based electronic field was to use pure organic molecules in devices. Nevertheless, during the last decade there was an increase in interest of using metal complexes due to their promising electronic properties, such as redox and photoluminescence.[37] Also in many of these applications, symmetric and asymmetric metal complexes have been used due to their different electronic, magnetic, and optical properties.[38] For instance, in such applications, mesogens, commonly known as liquid crystals, are of special interest since they can be used in different electronic displays. Liquid crystalline materials can be categorized in to two types, namely, thermotropic and lyotropic. In both of these types the material of interest is between an organized solid and a less organized liquid phase, known as a mesophase.[39] In thermotropic-type of mesogens, the liquid crystalline property can be achieved in accordance with different temperatures. In the lyotropic-type, liquid crystalline properties can be attained with different solution concentrations and solvents. However, in thermotropic- and lyotropic-type the 3D arrangement of molecules are not observed, but they form supramolecular structures with particular patterning in orientation of molecules. Introduction of metal ions can be important, because they can cause different geometries, oxidation states, and spin states. These structure properties are also helpful in reflecting different properties of metallomesogens such as conduction,[40] reflection,[41] luminescence,[42] and display technology.[43] In general, molecular structures, which can arrange into aggregates, such as rod-like cyanobiphenyls and disc-like long chain triphenylene molecules, are known to be used as liquid crystal materials. Some common examples of mesogens are shown in **Figure 1.5**. Surfactants, mostly with linear structures have also been used as mesogens. Initial studies of metallomesogens were

performed with square planar structures [eg. copper(II), nickel(II), palladium(II), and platinum(II) complexes] and linear structures [eg. silver(II) and mercury(II) complexes], since they can be organized into disc-like or rod-like structures.[44] Afterwards, new systems with different metal ions and geometries were studied. Among these, mononuclear octahedral iron, molybdenum, tungsten, and chromium complexes of 1,4,7-triazacyclononane tricarbonyl or trichloro ligands,[45] and lanthanide complexes[46,47] were important bench marks. Multimetallic copper complexes[48,49,50] and iron cluster dendrimers[51] have also been probed as metallomesogens to obtain different redox and magnetic properties.

Anisometric Molecules

Rod-like molecules

Rod-like polymers

$C_6H_{13}O$—CN

Disk-like molecules

OC_6H_{13}

$C_6H_{13}O$

OC_6H_{13}

OC_6H_{13}

$C_6H_{13}O$

OC_6H_{13}

Amphiphilic Molecules

Detergents
Lipids

Block copolymers

$C_{16}H_{33}COO^-K^+$
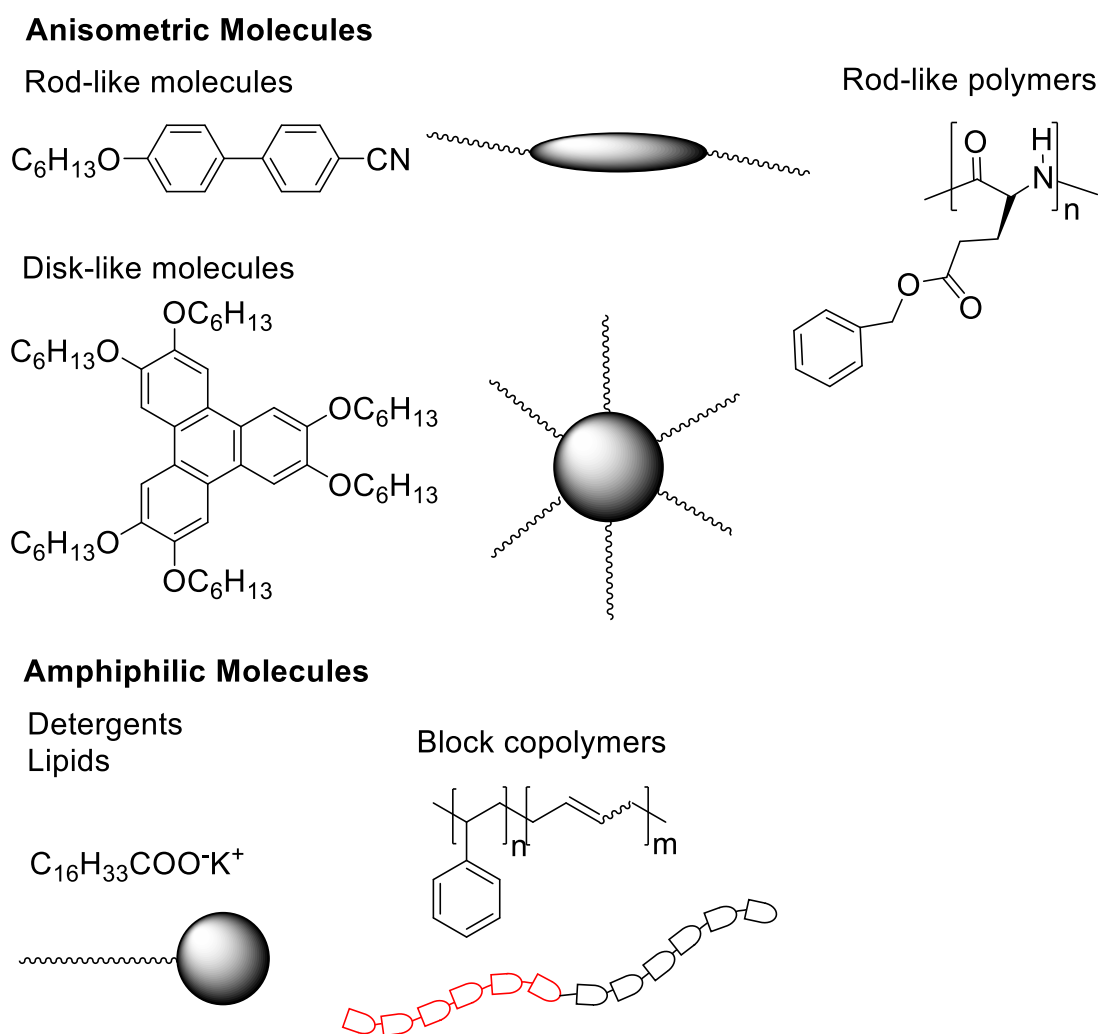
Figure 1.5. General examples of mesogens.

1.4 Molecular Wires

Molecular wires, being one of the most important candidates in molecule-based electronic field, assists the connection of other necessary electrical components together to assure better electrical conductivity between them. The current-voltage (I-V) characteristics of this class of electrical components show symmetrical sigmoidal shape curves to indicate the bidirectional electrical passage between two entities.[52] Different types of highly conjugated aromatic and aliphatic oligomer structures have gained attention in this area.[53] Two types of oligomer structures have been reported, namely, conductors and proconductors. Conductor oligomers can conduct electrical current when they are in the neutral state, while proconductors need external stimuli to conduct current. Therefore, proconductors show conduction properties in presence of dopants or when they become oxidized or reduced. For instance, polythiophenium can act as a conductor while polythiophene poorly conducts current.[54] In reality, for different applications conductors are of greater importance when compared to proconductors. Organic molecules with different structures have been probed vastly as molecular wires. Among these organic molecular wires, cross linked porphyrin units[55,56] are predominant. In porphyrins, the conduction properties can be altered by substituents, linkers, and the degree of conjugation (**Figure 1.6**). Another class of oligomers is the phenylene ethylene structures, and some have shown promising results as molecular wires.[57] To measure the electrical properties of assemblies, the scanning tunneling microscopy method (STM) has been used for the I-V characterization and self-assembly methods have been used to deposit oligomer units. After the formation of the monolayer, atomic force microscopy (AFM) studies have shown aggregate formation on the surface of the gold electrode. Consequently the authors have observed large defected areas in these

films.[58] Therefore, the assessment of conductivity properties of these metal|molecule junctions has been a challenge due to the lack of surface coverage. Surface passivation due to excess organic material deposition on the surface of the gold electrode was found to be another challenge that was faced in these studies.[59]
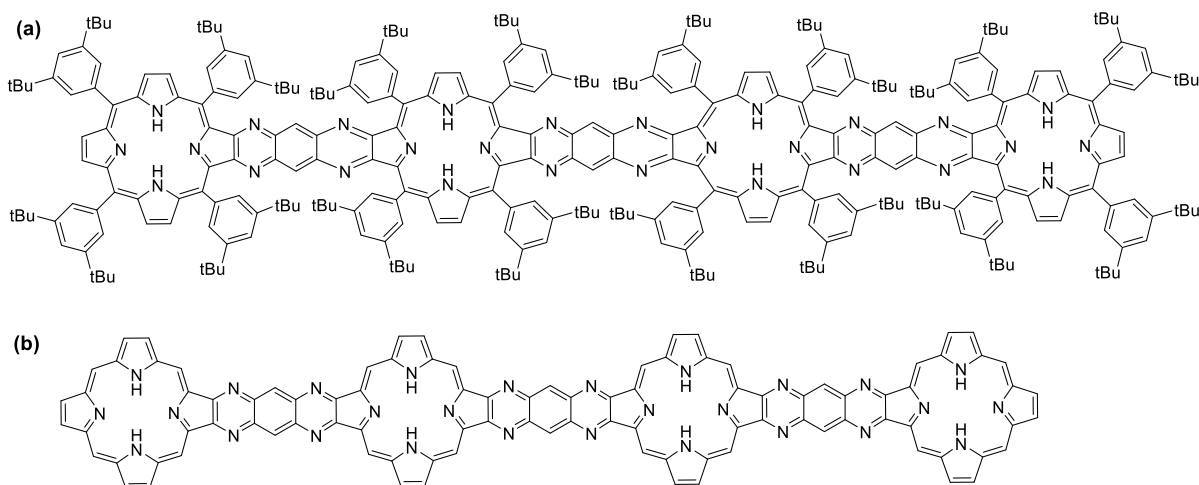
Figure 1.6. Substituted and non-substituted porphyrin oligomers.

Recently, metal-containing molecular wires have gained attention owing to the work of the Gladysz group.[60] Unsaturated carbon chains with rhenium metal centers have shown positive electrical conductivity data only for short carbon units of n = 2-10, but have shown irreversible redox processes when the two metal centers are further apart. These irreversible redox processes indicate a poor electrical communication between the two metal centers.[60] Metal wires, which are in use at present, contain an insulating material around the metal to protect unnecessary short circuits. Therefore, to incorporate this new technology to molecular wires, unsaturated carbon chains with platinum metal terminals which are surrounded with saturated carbon helices have been studied (**Figure 1.7**).[61,62,63] Electrical conductivity properties of these precursors after device fabrication is yet to be studied.
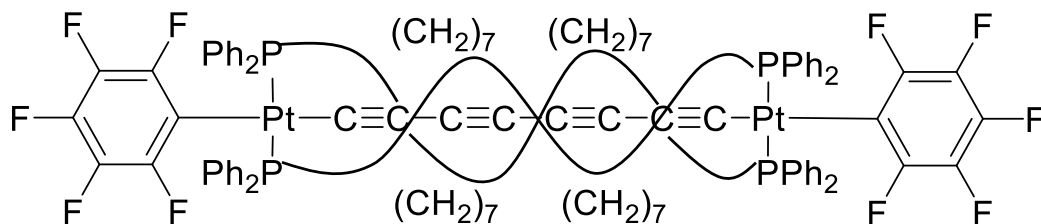
Figure 1.7. Double-helical platinum complex.

In all the above cases, the ultimate goal is to obtain precursors with fast electron transfer rates between two designated entities. So far the obtained precursors show electron transfer due to tunneling effect. Therefore, electron transfer rate decreases with increasing distance between the two designated places. However, further investigations are necessary to improve the current designs and to obtain faster electron transfer rates.

1.5 Transistors and Molecular Switches

Transistors are current amplifiers with three terminals namely, gate, source, and drain. In transistors, the voltage applied to drain-source terminals are different to the voltage measured through gate-source terminals. A representative view of drain current vs. drain-to-source voltage obtained for a semiconductor transistor[64] is shown in **Figure 1.8**. Once, the transistor starts to work, the threshold voltage becomes smaller than the gate-to-source voltage. The transistor can be used as a resistor, when the drain current and drain-to-source voltage follow the Ohms law. This linear active region is known as the triode region. The transistor can be used as a switch, when the transistor starts work between saturated and cut off regions.[64]
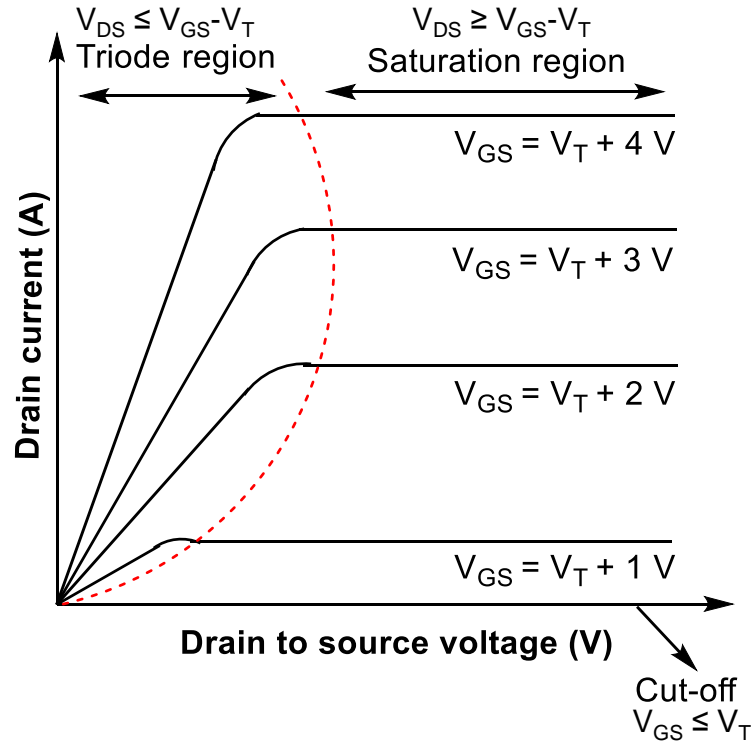
Figure 1.8. A representative plot of a drain current *vs*. drain-to-source voltage obtained for a transistor (V_{DS} = drain-to-source voltage; V_{GS} = gate-to-source voltage; and V_T = threshold voltage).

Molecules which are suitable for transistor-like activity should show a switching mechanism; at times they should suppress the current conduction through the molecule and after exceeding the barrier (threshold voltage), they should facilitate the current response with higher amplitude.[2] Building of such devices with three electrode arrangements is a challenge in molecule-based electronics due to reasons such as the connection of electrodes to molecules with small dimensions, connecting the electrodes with a good separation, and the stability of molecules after cycling for few oxidations and reductions.[65] In the literature, molecular transistors have been developed with carbon nanotubes, single molecules, and quantum dots.[2,66] A field effect transistor was built by Tans *et al.*[67] by installation of a carbon

nanotube between two platinum electrodes as shown in **Figure 1.9**. The current-voltage measurements at different gate voltages were performed at 300 K and the semiconducting behavior of the carbon nanotube was supported by the non-linear I-V characteristic observed at zero applied gate voltage. This device exhibited low conductivity measurements at zero bias voltage with positive applied gate voltages and high conductivity at negative gate voltages. Therefore, this device has unveiled a switching mechanism which can be seen in regular transistors.
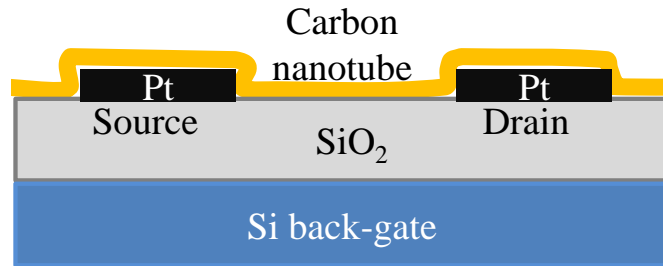
Figure 1.9. Device layout of the carbon nanotube field effect transistor.

Park *et al*. assembled an archetype of a single molecule transistor[68] by self-assembling a cobalt(II)-terpyridine [*Co(II)-terpy*] complex between source (platinum) and drain (gold) electrodes (**Figure 1.10**). During the experiment, they observed a step-wisely increasing I-V plot after the threshold voltage, which denote the Coulomb blockade. Also the measured resistance of the junction varies between 100 MΩ and 1 GΩ. In this device a single molecule connects the two electrodes, and due to its small dimensions, the molecule can block the electron transport passage through the junction. The study has exposed that the Co(II)/Co(III) conversion is necessary for the molecule to act as a transistor. At a certain applied potential only one electron can pass through the junction. Since the length of the alkyl chain which is fused to the *terpy* unit could also govern the coupling between the

molecule and the electrode, it could affect the performance of the electron transfer between them. For the molecule to function as a single molecule transistor, it needs to have an alkyl chain attached to the *terpy*-molecule. In the absence of the alkyl chain, the junction shows rapid increase of tunneling currents, known to be the Kondo effect. The Kondo tunneling effect has been demonstrated with a complex directly attached to electrodes via *terpy* units, showing a high conductance.
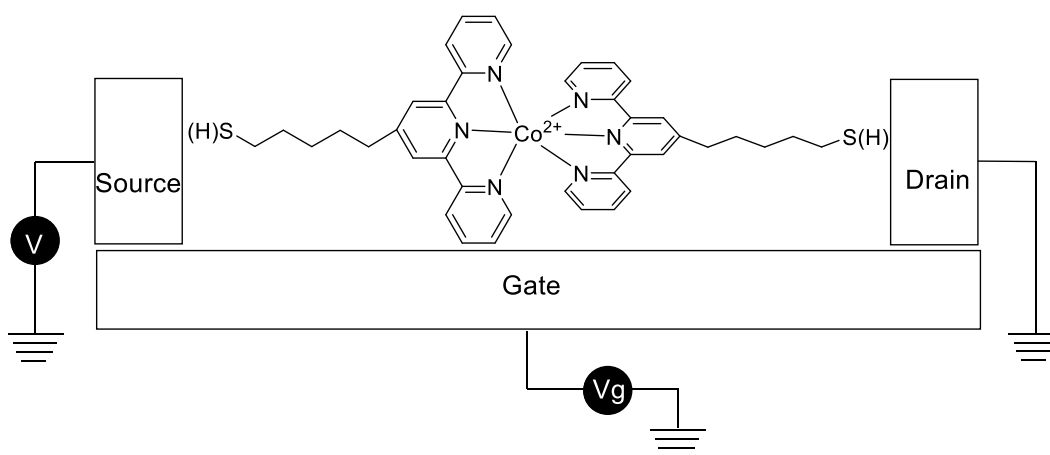
Figure 1.10. Schematic representation of a single molecule transistor.

A similar single molecule transistor was demonstrated using an organic molecule.[69] In that device, a phenylenevinylene oligomer was used to build the transistor, and revealed that the electron-transfer properties are governed by sequential oxidation and reduction redox processes.[69] Quantum dots also have been used to build transistors, since quantum dots can act as unit charges and can show redox activity.[70]

By varying the molecular structure and confirmation the electronic properties can be modulated.[2] Therefore, Joachim *et al*.[71] used the above mentioned strategy to develop a single molecular transistor using a C_{60} molecule. During this study a C_{60} molecule was sandwiched between a STM tip and a substrate, then an external force has been placed on the

C_{60} molecule using the STM tip to result in a distortion on the molecular structure. The distorted C_{60} molecule exhibited a higher current response, which was twice the original current response due to alteration of the highest occupied molecular orbital (HOMO) and lowest unoccupied molecular orbital (LUMO) energy levels. Theoretical studies have also supported the idea of energy level deviation that took place during the distortion of the molecule.[72] To support the same phenomenon, regarding the structure confirmation and electrical properties, a study has been carried out with copper-containing metalloporphyrin units (**Figure 1.11**).[73] The electrical responses have been measured using the scanning tunneling microscopy (STM) method with the copper metalloporphyrin unit being deposited onto a copper substrate at 15 K. During the deposition of the molecule, the orientation of one phenyl group can deviate slightly to give two conformations of the metalloporphyrin unit and those can be identified by STM. These two different conformations also presented dissimilar electrical conductivity properties to denote the switching ability of the molecule. During the current-voltage characterization, they have observed a difference of current response ~ 100 nA between 'ON' and 'OFF' states of the molecule. These investigations have proven that the modulation of chemical and physical properties of molecules can alter the electrical conductivity properties, which lead to the observed switching phenomenon.
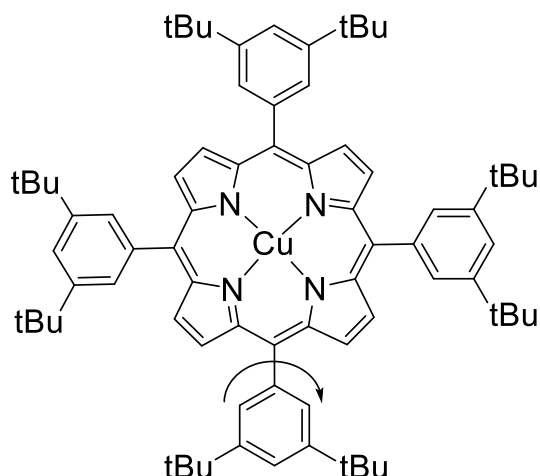
Figure 1.11. Copper coordinated metalloporphyrin.

1.6 Molecular Rectifiers

Rectifiers are another important class of electrical components which governs the direction of the flow of electrical current and they are used to transform the alternating current into direct current. These devices are categorized to be two terminal electrical components. At present the rectifiers, known as diodes, are established with semiconductor materials. In regular semiconductor p-n junctions, the n-component is constructed by doping group IV crystalline materials with low amounts of group V elements. Similarly the p-component is constructed by doping group IV crystalline materials with low amounts of group III elements. Therefore, the n-component is rich in electron density and p-component is electron deficient, and in this regular p-n junction, the n-component act as the "Donor" and p-component act as the "Acceptor".

Rectifiers demonstrate unidirectional flow of electrical current (**Figure 1.12a**), and therefore, the molecular devices which display an asymmetrical flow of electrical current can be considered to be molecular rectifiers. Molecular rectification was originally proposed by

Aviram and Ratner as a *gedanken* experiment anticipating the feasibility of directional flow of electrical current in a molecule.[74] This proposed organic molecule consisted of a donor group (D) attached via an σ bridge to an acceptor group (A) and hence had the structure [D-σ-A] as shown in **Figure 1.12b**. Theoretical calculations carried out on this Aviram and Ratner model showed asymmetrical current responses suggesting that the above mentioned [D-σ-A] molecule is a probable current rectifier. Nevertheless, experimental studies on this molecule were not performed.
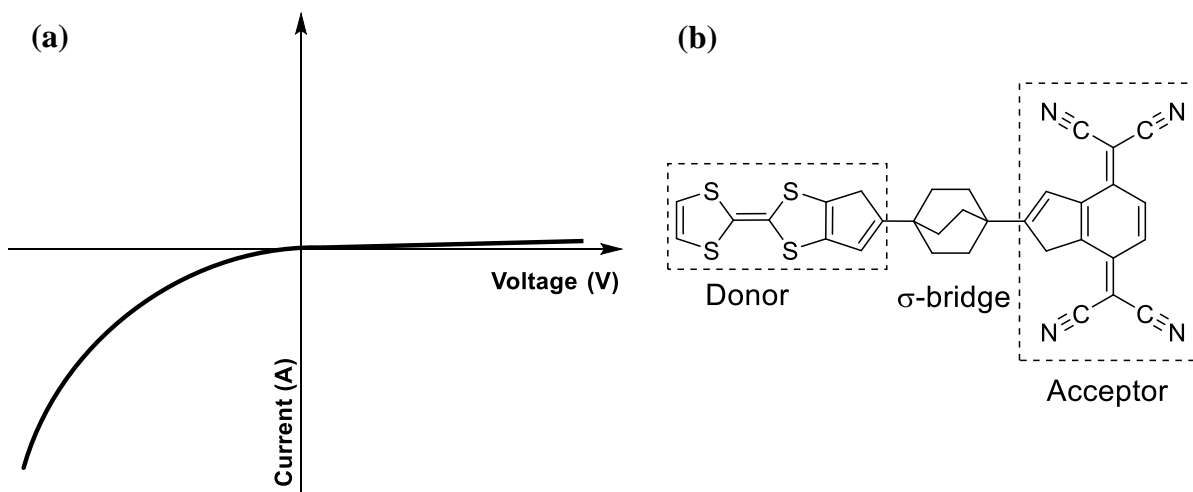
Figure 1.12. (a) A representative asymmetric current-voltage plot and (b) [D-σ-A] molecule proposed by Aviram and Ratner.

In these [D-A] type molecules, overall electron donor and acceptor properties can be modified by introducing electron donating and electron withdrawing substituents into the structure. However, the donor and acceptor moieties of molecules are opposite to that of semiconductor p-n junctions. In a [D-A] molecule, the donor moiety should have a small first ionization potential for it to be a good donor and the acceptor moiety should have a large

electron affinity to be a good acceptor. When considering the molecular orbitals of a [D-A] type molecule, the HOMO energy level corresponds to the ionization potential and the LUMO energy level corresponds to the electron affinity of that molecule.[75] These energies must also be comparable to the Fermi level of the metal electrodes to have conduction between them. In addition, to achieve efficient electron transfer (conduction through the molecule), charge recombination must be avoided. Thus donor and acceptor moieties should be well-separated via σ or π bridge, so that there will be a good charge separation between them. Another parameter that is necessary for the construction of molecular rectifiers is the mobilization of molecules on the surface of an electrode. Therefore, defect-free and closely packed thin films are essential to build effective molecular devices. Few methods have been used in the literature, and among these, the Langmuir-Blodgett and the self-assembly methods are widespread.[76] Initially, Polymeropoulos *et al*.[77] and Sugi *et al*.[78] constructed molecular rectifiers using the LB method, but in these cases the devices were based on LB multilayers and hence showed higher thicknesses of molecular layers between the electrodes. The use of multilayers is disadvantageous in electronic devices, due to the formation of Schottky barriers at the metal|molecule junctions. Similarly, deposition of multilayers will exceed the desired thickness. Therefore, devices with molecular dimensions of 1-3 nm (commonly a monolayer), are better candidates where semiconductor materials fail to function. Later on Sambles *et al*. carried out experiments using $C_{16}H_{33}Q$-π-3CNQ[79,80] molecule to study the molecular rectification using LB monolayers and revealed favorable results. A main advantage of using the LB method is that, by changing substituents on the ligand structure, the film formation ability of molecules at the air/water interface can be modulated. Thin films obtained by the LB method are also known to produce well-ordered

monolayers with high surface coverage,[75] but when designing precursors for the LB method, alkyl groups are introduced to the molecular structure. This is disadvantageous in device fabrication process, since alkyl groups hinder the conduction property of the film. In LB monolayers, the molecules attach to the two metal electrodes via physisorption and have weak van der Waals interactions, thus the orientation of the molecule can change over time. In self-assembled monolayers, physisorption can be experienced in one metal|molecule junction and on the other, there will be covalent bonding between the molecule and the electrode. This helps to create unnecessary dipole moments at the two metal|molecule junctions, which lead to the formation of Schottky barriers. Even though SAM forms rigid monolayers, the surface coverage is poor when compared to LB monolayers. However, after the monolayer deposition using either the LB or the SAM method, the monolayer is sandwiched between two metal electrodes to generate the metal|molecule|metal junction that enables to measure the electrical properties.

There are three mechanisms responsible for molecular current rectification, namely Schottky, gives rise to S-rectifiers, asymmetric, gives rise to A-rectifiers, and unimolecular, gives rise to U-rectifiers. The most common mechanism is the Schottky mechanism, which is based on devices having electrodes with dissimilar work functions (eg. gold and aluminum or titanium and palladium) or due to covalent bonding between the molecule and the electrode which leads to interfacial dipole layers.[81,82,83,84] The work function of a material can be defined as, the energy that is necessary to remove an electron from the electrode and transport it to the infinity under vacuum conditions. Asymmetric and unimolecular mechanisms are influenced by the frontier molecular orbitals of the molecules. Therefore, A- and U-rectifiers are dependent on the molecular properties which are associated to HOMO

and LUMO energies. The metal|molecule|metal devices with M_1 and M_2 electrodes ($M_1 = M_2$ = gold), after applying a bias voltage to one of the electrodes, will tend to lower the energy of the metal Fermi levels of that electrode to resonate with the frontier molecular orbitals of the molecule.

In the asymmetric mechanism, the frontier molecular orbitals distribute unevenly among the metal Fermi levels and the HOMO or LUMO energy level become closer in energy to the metal Fermi levels.[85] In this case, the LUMO molecular orbital of the acceptor moiety, accepts an electron from the Fermi level of M_1 and donates to the Fermi level of M_2 as shown in **Figure 1.13a**. In this example, the LUMO level is comparable in energy to that of the metal Fermi levels and HOMO is much lower in energy. Therefore, the HOMO energy level is not involved in the rectifying mechanism. Molecules with asymmetric structural properties extensively contribute to asymmetric current rectification.

(a) Asymmetric mechanism:
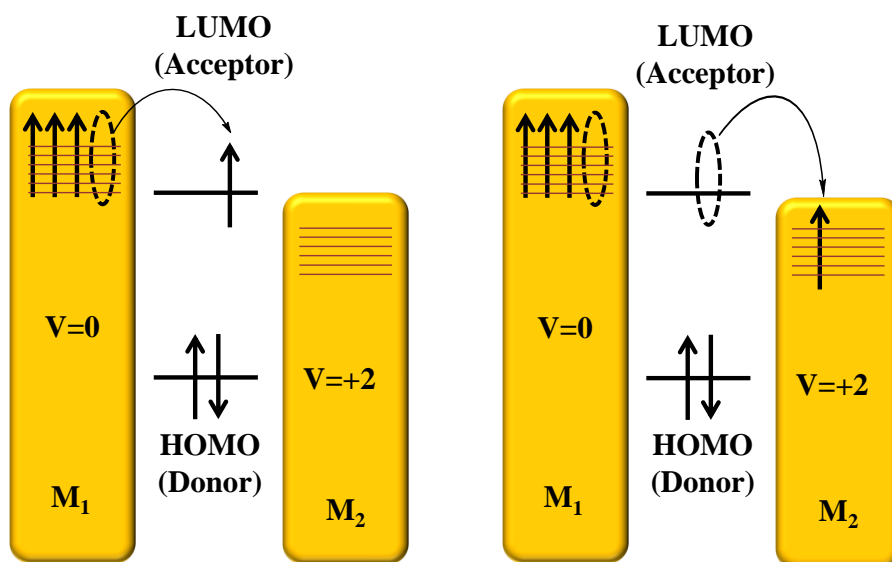
(b) Unimolecular mechanism:
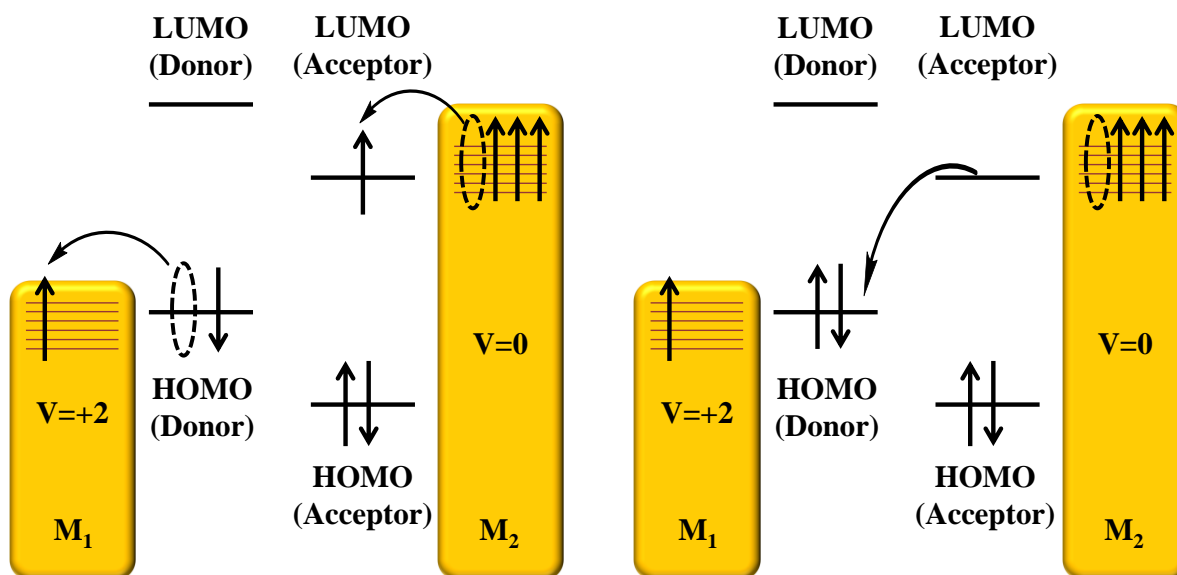
Figure 1.13. Different current rectifying mechanisms; (a) asymmetric mechanism and (b) unimolecular mechanism.

The unimolecular mechanism involves [D-A] type systems with low HOMO-LUMO energy gaps which permit current to tunnel through the molecule. In these, the LUMO of the

acceptor moiety accepts an electron from the electrode M_2 and the HOMO of the donor donates an electron to the electrode M_1 as illustrated in **Figure 1.13b**. Since there are small energy gaps between HOMO and LUMO, the electron in the LUMO of the acceptor moiety can be transferred to the HOMO of the donor moiety to facilitate the upcoming electron transfer. As mentioned earlier, for the above electron transfer to occur, the HOMO and LUMO of donor and acceptor moieties must have comparable energies with metal Fermi levels at applied bias potentials.[86] However, molecules which show pure unimolecular rectification mechanism are extremely rare.

The rectification ratio (RR), which is the ratio between the magnitudes of current at positive and negative bias voltage V, aids when evaluating the current rectification behavior of a particular system. The RR value should be at least ≥ 2 to consider the system as a rectifier, the higher the RR value the better the rectification behavior.[86]

$$RR(V) = |I(V)| \, / \, |I(-V)|$$

The asymmetric and unimolecular mechanisms are difficult to distinguish, since they both involve frontier molecular orbitals of molecules. However, the redox active molecules with low local global symmetry and good film formation properties are advantageous in molecular current rectification. Up-to-date various [D-A] type organic molecules with current rectification have been studied in detail by the Metzger and Ashwell groups.[79,82,86] They have demonstrated a new organic assembly, with the structure of [D-π-A], (**Figure 1.14**) to establish the unimolecular current rectification.[87] This molecule is different from the Aviram and Ratner model, due to the presence of a π bridge between the D and A moieties. This molecule has shown the LB film formation properties due to the

presence of an alkyl chain attached to the quinolinium group. Strong current rectification behavior has been observed for the monolayers and multilayers of this molecule, when sandwiched between aluminum electrodes. Results have shown that the electron transfer takes place from tricyanoquinodimethanide to (n-hexadecyl)quinolinium moiety. However, the devices made out of monolayers have shown a higher rectification ratio when compared to multilayer devices. In multilayer structures a limited electron transfer can be observed owing to excess organic material.
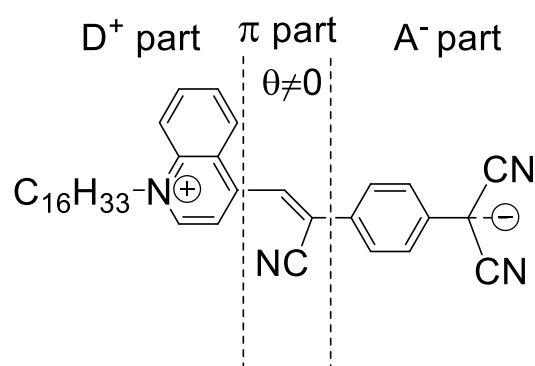
Figure 1.14. [D-π-A] type molecular rectifier introduced by Metzger group.

The proposed mechanism for current rectification suggested that, initially an intervalence charge transfer is taking place to produce the neutral molecule from the zwitterionic form, and then electrons transfer from the electrodes to create the original form of the molecule, which is the [D$^+$-π-A$^-$] zwitterion.[87] This proposed mechanism is opposite to the mechanism observed in the Aviram-Ratner model. In there, first the electrodes transfer the electrons to the acceptor moiety to generate the zwitterionic form from the neutral molecule, and then the intervalence charge transfer takes place to create the neutral state of the molecule. Nonetheless, in all these cases the acceptor moiety accepts electrons from the

www.manaraa.com

first electrode and the donor moiety donates electrons to the second electrode, creating electrons to flow from the acceptor moiety to donor moiety.[2] Some of the [D-A] systems which show unimolecular current rectification are shown in **Figure 1.15**.[75]

X = H, R = n-C$_{16}$H$_{33}$
X = H, R = CH$_3$C(O)S-C$_{14}$H$_{28}$
X = H, R = CH$_3$C(O)S-C$_{16}$H$_{32}$
X = F, R = n-C$_{16}$H$_{33}$
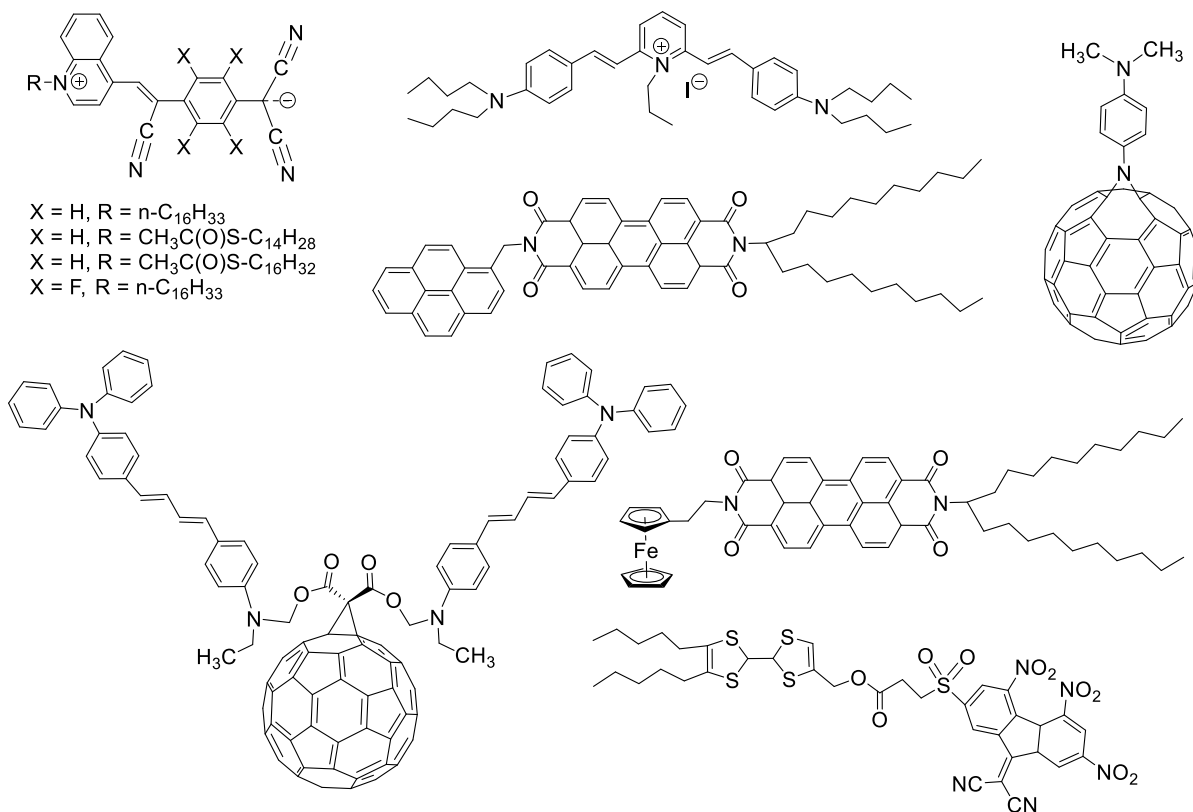
Figure 1.15. Unimolecular rectifiers introduced by Metzger group.

Besides these studies, few other groups have investigated current rectification using macroscopic systems (thick layers of indigo or phenazine and chloranil) and LB multilayer structures (arachidic acid, bis(octadecyl)viologen, and cyanine dye; and palladium phthalocyanine and *N,N'*-bis(di(ethoxy)methyl)perylene-3,4,9,10-tetracarboxyl diimide).[88,89,90,91] The use of coordination metal complexes for current rectification is not well-investigated. Lee *et al*. has reported a molecular current rectifier using a hexacoordinate

[^{Ar}S-bipyRu^{II}(^{F3}acac)$_2$] complex.[92] This ruthenium(II) complex (**Figure 1.16**) has exhibited an efficient electron transfer when compared to the free ligand due to conjugation obtained upon metallation. They have observed asymmetric current responses for the ruthenium(II) complex with rectification ratio being close to 4, but the free ligand has shown symmetric current responses. The DFT calculations carried out on the ruthenium(II) complex have revealed a permanent dipole moment of 11.3 D. Lee *et al*. suggest that the observed current rectification behavior is related to the observed asymmetric nature of the metal complex.
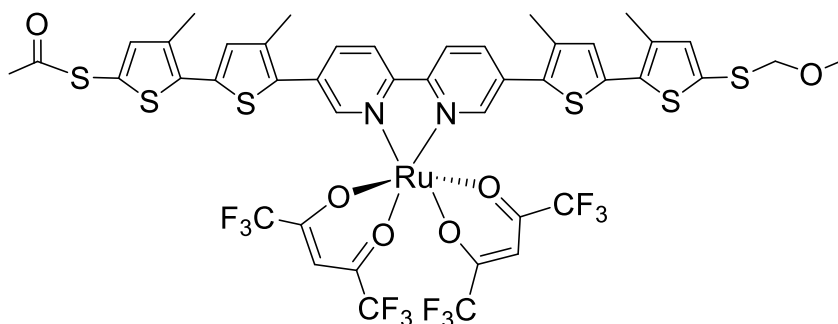
Figure 1.16. The ruthenium(II) complex [^{Ar}S-bipyRu^{II}(^{F3}acac)$_2$].

The discussed data of this section reveals that, mostly organic systems have been investigated as molecular current rectifiers. To the best of my knowledge, the understanding of coordination metal complexes as current rectifiers is less renowned. Therefore, the investigation of metal complexes with asymmetric structures as current rectifiers is expected to uncover a new direction for coordination chemistry.

1.7 Research Statement and Objectives

One of the main research interests in the Verani lab focuses on designing and synthesizing new bioinspired phenolate-containing asymmetric ligands that are redox-active, and their metal complexes to be used towards molecule-based electronics. During the design of these molecules, hydrophobic and hydrophilic substituents have been introduced to the system, to deposit them onto solid surfaces using the Langmuir-Blodgett method. Then, these surface immobilized LB films are intended to be used in metal|molecule|metal devices.

In the dissertation research, my main focus was to develop bioinspired redox non-innocent phenolate-containing asymmetric systems with [N$_2$O$_3$] and [N$_2$O$_2$] coordination environments with different trivalent metal ions such as gallium(III), iron(III), and manganese(III) for device fabrication, and to test them as molecular rectifiers. The asymmetric structures were a topic of special interest during the design of molecules as current rectifiers, because in such systems, the molecular orbitals distribute asymmetrically between the electrodes. These factors help in creating an asymmetrical flow of electrical current. Therefore, my dissertation research focuses on (i) the design and synthesis of new [N$_2$O$_3$]- and [N$_2$O$_2$]-containing surfactant ligands with different substituents attached to the ligand backbone, and the metallosurfactants formed by them; (ii) the investigation of geometric, electronic, redox, and film formation properties of metallosurfactants; (iii) the characterization of Langmuir-Blodgett films including composition, molecular integrity, and surface properties, and (iv) device fabrication based on monolayers of these metallosurfactants and the study of their current-voltage behavior. The specific goals of my research include the following:

➢ **Goal #1**. To investigate the electronic, redox, electron donor/acceptor, and film formation properties of [N₂O₃]-containing gallium(III) and iron(III) metallosurfactants. Results are described in chapter 3.

This research goal focused on the development of new redox-active pentacoordinate gallium(III) and iron(III) metallosurfactants with [N₂O₃] donor sets that are useful in understanding film formation ability at the air/water and air/solid interfaces. The iron(III) and gallium(III) ions were selected for this study to compare the electronic and redox properties of the metallosurfactants. This study also provided additional information regarding the electron-donor and -acceptor moieties of relevant asymmetric molecules with phenolate entities. This investigation helped to understand film formation and redox behavior of pentacoordinate metal complexes as well as the viability of using such systems in molecular rectifiers.

➢ **Goal #2**. To assess the properties of nitro-substituted iron(III) complexes with [N₂O₃] and [N₂O₂] environments. Results are described in chapter 4.

This investigation expanded the synthesis and characterization of new pentacoordinate iron(III) complexes with different substituents and coordination environments such as [N₂O₃] and [N₂O₂] binding sites intended to modulate the redox behavior, as well as, the molecular HOMO-LUMO energies relevant for current rectification. The substituents on the ligand backbone can also influence the surface properties which is important in device fabrication. Further investigations of this study focused on the asymmetrical geometry and, the presence of nitro and *tert*-butyl substituents on iron(III) complexes for stabilizing the radical generation. These iron(III) complexes were also

modeled using theoretical calculations to understand the electronic and redox properties, and to identify the possible donor and acceptor moieties to be tested them for current rectification.

> **Goal #3**. To study the rectification behavior in nanoscale devices based of an asymmetric five-coordinate iron(III)/phenolate complex. Results are described in chapter 5.

The investigation of rectification behavior in nanoscale devices based on asymmetric metal complexes is limited in literature. Chapter 5 discusses the use of an iron(III) metallosurfactant for molecule-based device fabrication. A new asymmetric ligand with [N_2O_3] donor set and its low symmetry pentacoordinate iron(III) complex were synthesized and structurally characterized to address the electronic, redox, and film formation properties. This investigation also included the analysis of surface properties of the LB monolayers and multilayers. Finally, the current-voltage characteristics of the nanoscale devices were tested to identify the current rectification behavior.

> **Goal #4**. To evaluate the behavior of saloph-type iron(III) complexes with [N_2O_2] donor sets in rectifying devices. Results are described in chapter 6.

This study was focused on the design of two new symmetrical tetradentate ligands and their respective trivalent redox-active iron(III) complexes for current rectification. Further studies were performed to investigate whether the asymmetric nature of the metal complex favors the current rectification property in iron(III) systems. The understanding of these results helped to distinguish asymmetric and unimolecular current rectification mechanisms in iron(III) complexes. To understand the current rectification mechanism, two

iron(III) complexes were synthesized and characterized. These two iron(III) complexes had different substituents on the phenolate moiety, but they had similar $[N_2O_2]$-type coordination environments around the metal ion.

➢ **Goal #5**. To investigate the behavior of redox-active manganese complexes with $[N_2O_3]$ and $[N_2O_2]$ coordination environments for thin film formation and current rectification. Results are described in chapter 7.

Investigating the properties of manganese(III) complexes, which are immobilized onto surfaces is less studied in the literature, and is a missing step preventing the further development of electronic applications. This goal was focused on merging redox and film formation properties onto manganese(III) systems. This study investigated manganese complexes with $[N_2O_3]$ and $[N_2O_2]$ donor sets. Different hydrophilic and hydrophobic substituents were used to modulate the chemical and physical properties. Finally, suitable metal complexes were employed in nanoscale devices to measure the current rectification behavior.

REFERENCES

1. Lindsey, J. S.; Bocian, D. F. *Acc. Chem. Res*. **2011**, *44*, 638.

2. Carroll, R. L.; Gorman, C. B. *Angew. Chem. Int. Ed.* **2002**, *41*, 4378.

3. Moore, G. E. *Electronics* **1965**, *38*, 114.

4. Robertson, N.; McGowan, C. A. *Chem. Soc. Rev.* **2003**, *32*, 96.

5. Strukov, D. B.; Snider, G. S.; Stewart, D. R.; Williams, R. S. *Nature* **2008**, *453*, 80.

6. Staikov, G.; Szot, K. *Adv. Mater*. **2009**, *21*, 2632.

7. Bandyopadhyay, A.; Sahu, S.; Higuchi, M. *J. Am. Chem. Soc*. **2011**, *133*, 1168.

8. Feynman, R. P. There is Plenty of Room at the Bottom. In *Miniaturization*; Gilbert, H. D., Ed.; Reinhold: New York, **1961**, p 282.

9. Wassel, R. A.; Gorman, C. B. *Angew. Chem. Int. Ed.* **2004**, *43*, 5120.

10. Lee, J.; Chang, H.; Kim, S.; Bang, G. S.; Lee, H. *Angew. Chem. Int. Ed*. **2009**, *48*, 8501.

11. Aviram, A.; Ratner, M. A. *Chem. Phys. Lett.* **1974**, *29*, 277.

12. Terada, K.; Kanaizuka, K.; Iyer, V. M.; Sannodo, M.; Saito, S.; Kobayashi, K.; Haga, M. *Angew. Chem. Int. Ed.* **2011**, *123*, 6411.

13. Bernasek, S. L. *Angew. Chem. Int. Ed.* **2012**, *51*, 9737.

14. Rigaut, S. *Dalton Trans*. **2013**, *42*, 15859.

15. Roth, K. M.; Dontha, N.; Dabke, R. B.; Gryko, D. T.; Clausen, C.; Lindsey, J. S.; Bocian, D. F.; Kuhr, W. G. *J. Vac. Sci. Technol. B.* **2000**,*18*, 2359.

16. Kuhr, W. G.; Gallo, A. R.; Manning, R. W.; Rhodine, C. W. *MRS Bull.* **2004**, *29*, 838.

17. Li, Q.; Mathur, G.; Gowda, S.; Surthi, S.; Zhao, Q.; Yu, L.; Lindsey, J. S.; Bocian, D. F.; Misra, V. *Adv. Mater.* **2004**, *16*, 133.

18. Gryko,D. T.; Zhao, F.; Yasseri,A. A.; Roth, K. M.; Bocian, D. F.; Kuhr, W. G.; Lindsey, J. S. *J. Org. Chem.* **2000**, *65*, 7356.

19. Clausen, C.; Gryko, D. T.; Yasseri, A. A.; Diers, J. R.; Bocian, D. F.; Kuhr, W. G.; Lindsey, J. S. *J. Org. Chem.* **2000**, *65*, 7371.

20. Gryko, D.; Li, J.; Diers, J. R.; Roth, K. M.; Bocian, D. F.; Kuhr, W. G.; Lindsey, J. S. *J. Mater. Chem.* **2001**, *11*, 1162.

21. Padmaja, K.; Youngblood, W. J.; Wei, L.; Bocian, D. F.; Lindsey, J. S. *Inorg. Chem.* **2006**, *45*, 5479.

22. Schweikart, K.-H.; Malinovskii, V. L.;Diers, J. R.; Yasseri, A. A.; Bocian, D. F.; Kuhr, W. G.; Lindsey, J. S. *J. Mater. Chem.* **2002**, *12*, 808.

23. Lysenko, A. B.;Malinovskii, V. L.; Kisari, P.;Wei, L.; Diers, J. R.; Bocian, D. F.; Lindsey, J. S. *J. Porphyrins Phthalocyanines* **2005**, *9*, 491.

24. Schweikart, K.-H.; Malinovskii, V. L.; Yasseri, A. A.; Li, J.; Lysenko, A. B.; Bocian, D. F.; Lindsey, J. S. *Inorg. Chem*. **2003**, *42*, 7431.

25. Li, Q.; Surthi, S.; Mathur, G.; Gowda, S.; Zhao, Q.; Sorenson, T. A.; Tenent, R. C.; Muthukumaran, K.; Lindsey, J. S.; Misra, V. *Appl. Phys. Lett*. **2004**, *85*, 1829.

26. Li, Q.;Mathur, G.; Homsi,M.; Surthi, S.;Misra, V.;Malinovskii, V.; Schweikart, K.-H.; Yu, L.; Lindsey, J. S.; Liu, Z.; Dabke, R. B.; Yasseri, A.; Bocian, D. F.; Kuhr,W. G. *Appl. Phys. Lett.* **2002**, *81*, 1494.

27. Carcel, C. M.; Laha, J. K.; Loewe, R. S.; Thamyongkit, P.; Schweikart, K.-H.; Misra, V.; Bocian, D. F.; Lindsey, J. S. *J. Org. Chem.* **2004**, *69*, 6739.

28. Zaidi, S. H. H.; Loewe, R. S.; Clark, B. A.; Jacob, M. J.; Lindsey, J. S. *Org. Process Res. Dev*. **2006**, *10*, 304.

29. Anariba, F.; Tiznado, H.; Diers, J. R.; Schmidt, I.; Muresan, A. Z.; Lindsey, J. S.; Zaera, F.; Bocian, D. F. *J. Phys. Chem. C* **2008**, *112*, 9474.

30. Yasseri, A. A.; Syomin, D.; Malinovskii, V. L.; Loewe, R. S.; Lindsey, J. S.; Zaera, F. Bocian, D. F. *J. Am. Chem. Soc.* **2004**, *126*, 11944.

31. Wei, L.; Tiznado, H.; Liu, G.; Padmaja, K.; Lindsey, J. S.; Zaera, F.; Bocian, D. F. *J. Phys. Chem. B* **2005**, *109*, 23963.

32. Jiao, J.; Thamyongkit, P.; Schmidt, I.; Lindsey, J. S.; Bocian, D. F. *J. Phys. Chem. C* **2007**, *111*, 12693.

33. Liu, Z.; Yasseri, A. A.; Lindsey, J. S.; Bocian, D. F. *Science* **2003**, *302*, 1543.

34. Seo, K.; Konchenko, A. V.; Lee, J.; Bang, G. S.; Lee, H. *J. Am. Chem. Soc.* **2008**, *130*, 2553.

35. Bandyopadhyay, A.; Sahu, S.; Higuchi, M. *J. Am. Chem. Soc.* **2011**, *133*, 1168.

36. Paul, N. D.; Rana, U.; Goswami, S.; Mondal, T. K.; Goswami, S.; *J. Am. Chem. Soc.* **2012**, *134*, 6520.

37. Low, P. J. *Dalton Trans.* **2005**, 2821.

38. (a) Binnemans, K. *Molecular Materials* **2010**, 61. (b) Gaspar, A. B.; Seredyuk, M.; Gutlich, P. *Coord. Chem. Rev*. **2009**, *253*, 2399. (c) Decher, G. *Science*, **1997**, *277*, 1232.

39. Tschierske, C. *J. Mater. Chem.* **1998**, *8*, 1485.

40. Woon, K. L.; Aldred, M. P.; Vlachos, P.; Mehl, G. H.; Stirner, T.; Kelly, S.; O'Neill, M. *Chem. Mater.* **2006**, *18*, 2311.

41. Mitov, M.; Dessaud, N. *Nature Mater.* **2006**, *5*, 361.

42. Camerel, F.; Bonardi, L.; Schmutz, M.; Ziessel, R. *J. Am. Chem. Soc.* **2006**, *128*, 4548.

43. (a) Fernández, G. *Nature Materials* **2013**, *12*, 12. (b) Binnemans, K. *Chem. Rev.* **2005**, *105*, 4148. (c) Neve, F. *Adv. Mater.* **1996**, *8*, 277.

44. Binnemans, K.; Gorller-Warland, C. *Chem. Rev.* **2002**, *102*, 2303.

45. (a) Lattermann, G.; Schmidt, S.; Kleppinger, R.; Wendorf, J. H. *Adv. Mater.* **1992**, *4*, 30. (b) Schmidt, S.; Lattermann, G.; Kleppinger, R.; Wendorff, J. H. *Liq. Cryst.* **1994**, *16*, 693. (c) Walf, G. H.; Benda, R.; Litterst, F. J.; Stebani, U.; Schmidt, S.; Lattermann, G. *Chem. Eur. J.* **1998**, *4*, 93.

46. Galyametdinov, Yu.; Athanassopoulou, M. A.; Griesar, K.; Kharitonova, O.; Soto Bustamante, E. A.; Tinchurina, L.; Ovchinnikov, I.; Haase, W. *Chem. Mater.* **1996**, *8*, 922.

47. Binnemans, K.; Galyametdinov, Yu. G.; Van Deun, R.; Bruce, D. W.; Collinson, S. R.; Polishchuk, A. P.; Bikchantaev, I.; Haase, W.; Prosvirin, A. V.; Tinchurina, L.; Litvinov, I.; Gubajdullin, A.; Rakhmatullin, A.; Uytterhoeven, K.; Van Meervelt, L. *J.Am. Chem. Soc.* **2000**, *122*, 4335.

48. Serrano, J. L. Metallomesogens: Synthesis, Properties, and Applications; VCH Verlagsgesellschaft mbH: Weinheim, 1996; p 498.

49. Paschke, R.; Liebsch, S., Tschierske, C.; Oakley, M. A., and Sinn, E. *Inorg. Chem.* **2003**, *42*, 8230.

50. Gatteschi, D.; Sessoli. R. *Angew. Chem. Int. Ed.* **2003**, *42*, 268.

51. Tyson, L.; Chasse; Gorman, C. B. *Langmuir* **2004**, *20*, 8792.

52. Villares, A.; Lydon, D. P.; Low, P. J.; Robinson, B. J.; Ashwell, G. J.; Royo, F. M.; Cea, P. *Chem. Mater.* **2008**, *20,* 258.

53. Aviram, A. *J. Am. Chem. Soc.* **1988**, *110*, 5687.

54. M.llen, K.; Wegner, G. *Electronic Materials: The Oligomer Approach*; Wiley-VCH: Weinheim, 1998.

55. Crossley, M. J.; Burn, P. L. *J. Chem. Soc. Chem. Commun.* **1991**, 1569.

56. Reimers, J. R.; Hall, L. E.; Crossley, M. J.; Hush, N. S. *J. Phys. Chem. A* **1999**, *103*, 4385.

57. (a) Pearson, D. L.; Tour, J. M. *J. Org. Chem.* **1997**, *62*, 1376. (b) Jones, L. Schumm, J. S.; Tour, J. M. *J. Org. Chem.* **1997**, *62*, 1388.

58. (a) Cygan, M. T.; Dunbar, T. D.; Arnold, J. J.; Bumm, L. A.; Shedlock, N. F.; Burgin, T. P.; Jones II, L.; Allara, D. L.; Tour, J. M.; Weiss, P. S. *J. Am. Chem. Soc.* **1998**, *120*, 2721. (b) Bumm, L. A.; Arnold, J. J.; Cygan, M. T.; Dunbar, T. D.; Burgin, T. P.; Jones, L.; Allara, D. L.; Tour, J. M.; Weiss, P. S. *Science* **1996**, *271*, 1705.

59. Doescher, M. S.; Tour, J. M.; Rawlett, A. M.; Myrick, M. L. *J. Phys. Chem. B* **2001**, *105*, 105.

60. Dembinski, R.; Bartik, T.; Bartik, B.; Jaeger, M.; Gladysz, J. A. *J. Am. Chem. Soc.* **2000**, *122*, 810.

61. Stahl, J.; Bohling, J. C.; Bauer, E. B.; Peters, T. B.; Mohr, W.; MartIn-Alvarez, J. M.; Hampel, F.; Gladysz, J. A. *Angew. Chem. Int. Ed*. **2002**, *41*, 1871.

62. Stahl, J.; Mohr, W.; de Quadras, L.; Peters, T. B.; Bohling, J. C.; Martin-Alvarez, J. M.; Owen, G. R.; Hampel, F.; Gladysz, J. A. *J. Am. Chem. Soc*. **2007**, *129*, 8282.

63. de Quadras, L.; Hampel, F.; Gladysz, J. A. *Dalton Trans*. **2006**, 2929.

64. http://www.ni.com/newsletter/50081/en/

65. Joachim, C.; Gimzewski, J. K.; Aviram, A. *Nature* **2000**, *408*, 541.

66. Liang, W.; Shores, M. P.; Bockrath, M.; Long, J. R.; Park, H. *Nature* **2002**, *417*, 725.

67. Tans, S. J.; Verschueren, A. R. M.; Dekker, C. *Nature* **1998**, *393*, 49.

68. Park, J.; Pasupathy, A. N.; Goldsmith, J. I.; Chang, C.; Yaish, Y.; Petta, J. R.; Rinkoski, M.; Sethna, J. P.; Abruña, H. D.; McEuen, P. L.; Ralph, D. C *Nature* **2002**, *417*, 722-725.

69. Kubatkin, S.; Danilov, A.; Hjort, M.; Cornil, J.; Brédas, J.-L.; Stuhr-Hansen, N.; Hedegård, P.; Bjørnholm, T. *Nature* **2003**, *425*, 698.

70. (a) Lent, C. S. *Science* **2000**, *288*, 1597. (b) Hush, N. *Nat. Mater.* **2003**, *2*, 134. (c) Cowburn, R. P.; Welland, M. E. *Science* **2000**, *287*, 1466.

71. Joachim, C.; Gimzewski, J. K. *Chem. Phys. Lett.* **1997**, *265*, 353.

72. Joachim, C.; Gimzewski, J. K.; Schlittler, R. R.; Chavy, C. *Phys. Rev.Lett*. **1995**, *74*, 2102.

73. Moresco, F.; Meyer, G.; Rieder, K. H.; Tang, H.; Gourdon, A.; Joachim, C. *Phys. Rev. Lett.* **2001**, *86*, 672.

74. Aviram, A.; Ratner, M. A. *Chem. Phys. Lett.* **1974**, *29*, 277.

75. Metzger, R. M. *J. Mater. Chem.* **2008**, *18*, 4364.

76. Metzger, R. M. *Acc. Chem. Res*. **1999**, *32*, 950.

77. Polymeropoulos, E. E.; Mobius, D.; Kuhn, H. *Thin Solid Films* **1980**, *68*, 173.

78. Sugi, M.; Sakai, K.; Saito, M.; Kawabata, Y.; Iizima, S. *Thin Solid Films* **1985**, *132*, 69.

79. Martin, A. S.; Sambles, J. R.; Ashwell, G. J. *Phys. Rev. Lett.* **1993**, *70*, 218.

80. Ashwell, G. J.; Sambles, J. R.; Martin, A. S.; Parker, W. G.; Szablewski, M. *J. Chem. Soc., Chem. Commun.* **1990**, 1374.

81. Ashwell, G. J.; Urasinska, B.; Tyrrell, W. D. *Phys. Chem. Chem. Phys.* **2006**, *8*, 3314.

82. Ashwell, G. J.; Mohib, A. *J. Am. Chem. Soc.* **2005**, *127*, 16238.

83. Liu, Y.; Xu, Y.; Zhu, D. *Synth. Met.* **1997**, *90*, 143.

84. Liu, Y.; Xu, Y.; Wu, J.; Zhu, D. *Solid State Commun.* **1995**, *95*, 695.

85. Metzger, R. M. *The Chemical Record* **2004**, *4*, 291.

86. Metzger, R. M. *Chem. Rev*. **2003**, *103*, 3803.

87. Metzger, R. M.; Chen, B.; Hopfner, U.; Lakshmikantham,M. V.; Vuillaume, D.; Kawai, T.; Wu, X.; Tachibana, H.; Hughes, T. V.; Sakurai, H.; Baldwin, J. W.; Hosch, C.; Cava, M. P.; Brehmer, L.; Ashwell, G. J. *J. Am. Chem. Soc.* **1997**, *119*, 10455.

88. Sugi, M.; Sakai, K.; Saito, M.; Kawabata, Y.; Iizima, S. *Thin Solid Films* **1985**, *132*, 69.

89. Fischer, C. M.; Burghard, M.; Roth, S.; v. Klitzing, K. *Europhys. Lett.* **1994**, *28*, 129.

90. Fischer, C. M.; Burghard, M.; Roth, S. *Synth. Met.* **1995**, *71*, 1975.

91. Schmelzer, M.; Burghard, M.; Fischer, C. M.; Roth, S.; Gopel, W. *Synth. Met.* **1995**, *71*, 2087.

92. Lee, Y.; Yuan, S.; Sanchez, A.; Yu, L. *Chem. Commun*. **2008**, 247.

CHAPTER 2

MATERIALS, METHODS, AND INSTRUMENTATION

2.1 Materials

The designed ligands and their respective metal complexes that are described in chapters 3-7 were synthesized by multistep synthetic procedures. Air and moisture-sensitive compounds were handled using standard Schlenk and glove box techniques, where it was necessary. The chemicals that were used to synthesize the ligands and the metal complexes of interest were purchased from Alfa Aesar, Sigma Aldrich, Acros Organics, Fisher Scientific, and Strem Chemicals and were used without further purification. The organic solvents dichloromethane, methanol, and ethanol were purified using standard distillation methods, and calcium hydride was used as the drying agent. The solid substrates (mica, quartz, and gold) that were used to deposit the thin films were purchased from SPI Supplies and Ted Pella, Inc.

2.2 Methods and Instrumentation

The compounds that will be discussed in each of the chapters were thoroughly characterized using a wide range of techniques. The ligands and the metal complexes were characterized using standard techniques, including infrared (IR) spectroscopy, nuclear magnetic resonance (NMR) spectroscopy, mass spectrometry, CHN elemental analysis, melting point, and X-ray diffraction, if possible. The electronic and redox properties of the compounds were analyzed using UV-visible spectroscopy, electron paramagnetic resonance

(EPR) spectroscopy, cyclic voltammetry, and spectroelectrochemistry. The film formation and surface analysis of the thin films were assessed using Langmuir-Blodgett (LB) method, Brewster angle microscopy (BAM), static contact angle measurements, atomic force microscopy (AFM), and infrared reflection absorption spectroscopy (IRRAS). Finally, after device fabrication, conductivity properties were examined by measuring the current-voltage (I-V) characteristics. An overview of each of the above mentioned techniques will be discussed in the following sections.

2.2.1 Infrared (IR) Spectroscopy

Infrared spectroscopy is especially useful in detection of functional groups of compounds depending on the peak position and intensity. For a compound to be identified by IR spectroscopy there should be a change in dipole moment of the molecule. IR radiation contains three main components namely, near-infrared region (NIR) from 14290-4000 cm^{-1}, mid-infrared region from 4000-400 cm^{-1}, and far-infrared region from 700-200 cm^{-1}. Among these usually mid- and far-infrared regions are of special interest to detect organic compounds.[1,2] The spectrum is typically recorded, the wave number in x-axis with the units of cm^{-1} and transmittance or absorbance in y-axis. In the IR spectrum it shows absorption bands related to different stretching and bending vibrations at different regions as shown in **Figure 2.1**. In this research project, the IR spectra were recorded in the region of 4000-400 cm^{-1} using a Bruker Tensor 27 FTIR-spectrophotometer with OPUS 5.0 or 6.5 software versions. The samples were prepared by mixing the compound with dry KBr salt in ~ 1:10 ratio and they were pressed into transparent pellets using high pressures at ambient

conditions. The compound spectrum was collected when compared to a blank KBr sample and 32/64 scans were used to obtain the IR spectra of compounds.
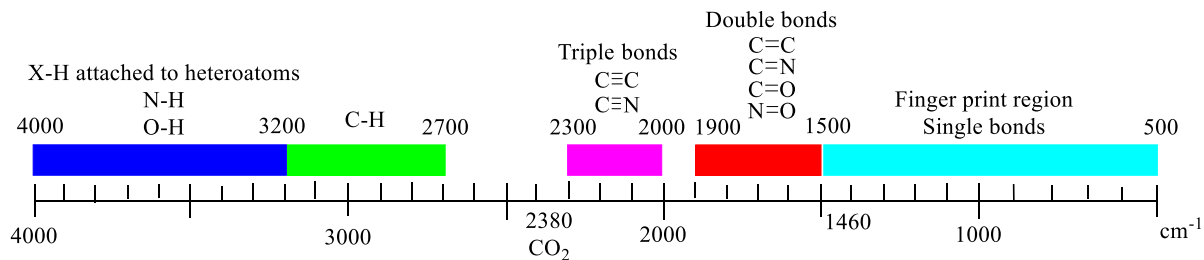
Figure 2.1. An overview of mid- to far-IR spectrum with important absorption regions.

2.2.2 Nuclear Magnetic Resonance (NMR) Spectroscopy

NMR spectroscopy is a widely used analytical method to determine the structure of compounds. In this project, the ^{1}H-NMR spectroscopy was used to characterize different organic building block precursors and ligands based on their peak positions, peak patterning, and peak integration. Since ^{1}H-NMR spectroscopy gives information regarding different number of protons which are present in different environments. ^{1}H-NMR spectra of different compounds were recorded using Varian 300 MHz, 400 MHz, and 500 MHz instruments during the course of this research project.

2.2.3 Mass Spectrometry

Another widely used standard characterization technique in analyzing compounds is Mass spectrometry. This method gives information regarding the molecular weight of the compound based on its mass/charge (m/z) ratio. Electrospray ionization mass spectrometry

(ESI-MS) was mostly used during this research project in analyzing organic precursors, ligands, and metal complexes. In ESI-MS, fragmentation of the molecules has been carried out by bombarding the sample ions with a high energy electron beam creating charged species with different molecular weights. Therefore, ESI-MS gives rise to a spectrum with mass/charge ratio plotted in the x-axis and relative intensity in y-axis.[3] The dissertation research used high resolution ESI/APCI mass spectrometry methods in positive ion mode and was able to obtain dominant peaks mostly for their molecular ion peaks $(M+H^+)$, (M^+), or $(M+Na^+)$. The spectra were measured on a Micromass LCT Premier XE (TOF) high resolution mass spectrometer. High resolution mass spectra values and isotopic distribution patterns were used to assign the chemical compositions of ligands and metal complexes. The standard limit for the difference between exact and accurate masses has been proposed to be smaller than ±5 ppm.[4] Statistical methods can be used to calculate the difference between exact and accurate masses.[5,6] For a given compound the difference between exact and accurate masses should be as small as possible.

The matrix assisted ionization vacuum (MAIV) mass spectrometry data of Langmuir-Blodgett (LB) monolayers for a few of the metal complexes were analyzed in collaboration with Prof. Sarah Trimpin from Department of Chemistry at Wayne State University. MAIV mass spectrometry measurements were performed by Mr. Tarick El-Baba. To measure MAIV mass spectrometry data for LB monolayers, the monolayers were deposited onto glass substrates and then the mass spectrometry measurements were carried out using a Waters IMS-MS SYNAPT-G2 instrument. MAIV measurements were carried out by removing the atmospheric pressure source to gain direct access to the skimmer cone.[7,8] The monolayer films were ionized in combination with 3-nitrobenzonitrole (3-NBN) matrix in

acetonitrile/water mixture and then exposing to the mass spectrometer vacuum. All the monolayer samples were analyzed in comparison to their bulk samples which were measured using the same instrument under similar conditions.

2.2.4 Elemental Analysis

CHN elemental analyses were carried out to measure the purity and the elemental composition of samples. The samples were prepared by drying them in a heated vacuum chamber for ~ 48 hours. The CHN analyses of the samples were performed using Exeter analytical CHN analyzer by Midwest Microlab, Indianapolis, Indiana. During elemental analyses, a known weight of the compound has been burned in presence of excess of dioxygen gas. Then the resulting gases such as water, carbon dioxide, and nitric oxide[9] are collected to calculate the percentages of carbon, hydrogen, and nitrogen that were originally present in the sample. It is important to obtain a full combustion of the sample to when calculating the percentages of the elements during CHN elemental analyses.

2.2.5 X-ray Single Crystal Analysis

X-ray crystallography is important to identify structure, geometry, and coordination environment of the molecule. X-ray crystallography also provides an estimate about the bond distances and angles of the metal complexes. In this thesis, X-ray quality single crystals were obtained by following the slow evaporation method. The X-ray diffraction method was developed by following Bragg's law which states that $n\lambda = 2d \sin\theta$,[10] where λ is the incident

wavelength, n is an integer, d is the distance between two planes of the crystal lattice, and θ is the scattering angle. A schematic representation of the Bragg's law is shown in **Figure 2.2**.
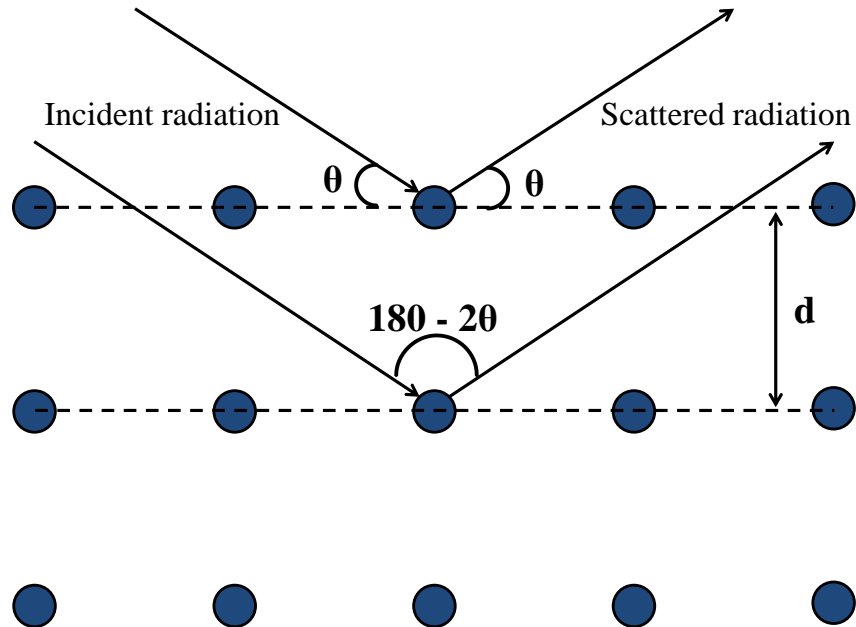
Figure 2.2. A schematic representation of Bragg's law.

X-ray quality crystals were identified by analyzing samples through a microscope, and a good quality single crystals were mounted to a goniometer via a needle like sample holder. Crystals were mounted on Bruker X8 APEX-II Kappa geometry diffractometer, which uses Mo radiation and a graphite monochromator. After illuminating the crystal by an x-ray beam, the scattering pattern was collected by a Bruker CCD (charge coupled device) diffractometer equipped with an Oxford Cryostream low-temperature device and analyzed using APEX-II suite[11] and SHELX-97[12] incorporated with OLEX2 software.[13]

2.2.6 UV-visible Spectroscopy

During UV-visible spectroscopy, molecules of a particular sample absorb the energy of the UV to visible region, and their electrons are excited from the ground state to energetically higher excited states. This phenomenon helps to identify the possible electronic transitions that can happen in a particular sample. The absorbance, A of the sample can be calculated using the Beer-Lambert law which is given by, $A = \varepsilon\, c\, l$. In this equation, ε is the molar absorptivity, c is the concentration of the sample, and l is the path length of the cuvette that is used to carry out the experiment. Therefore, it is important to use the same cuvette for all measurements that belong to the same experiment to use the same path length for comparison. Also, the absorbance is given by, $A = log\, I_o/I$, where I_o and I are the intensities of the incident and transmitted light, respectively. The molar absorptivity of a sample with known concentration can be calculated using a plot of absorbance versus wavelength. UV-visible spectroscopy is used to acquire information regarding the possible charge transfer transitions such as ligand-to-metal (LMCT), metal-to-ligand (MLCT), intervalence (IVCT), intra-ligand (ILCT), and electron transitions that occur between d-d and f-f orbitals. The most frequent electronic transitions involved in organic compounds[14] are shown in **Figure 2.3**.
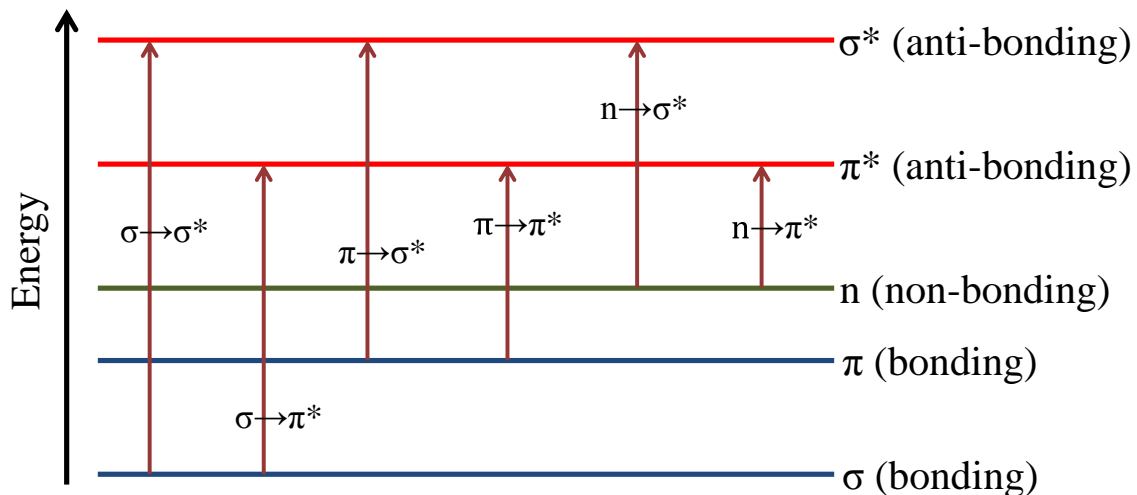
Figure 2.3. The general electronic transitions observed in organic compounds.

The color of a compound depends on wavelengths that are transmitted by chromophores after absorbing certain wavelengths to occur electronic transitions. The near-UV region is considered to be from 200 to 380 nm, and the visible region is considered to be from 380 to 780 nm. A UV-visible spectrophotometer is composed of a light source, mirrors to coordinate the light beam, a diffraction grating, a sample holder, and a detector. A schematic diagram of a UV-visible spectrophotometer[15] is shown in **Figure 2.4**. The UV-visible spectra of solution and solid LB films were measured from 200 to 1100 nm on a Cary 50 spectrophotometer.
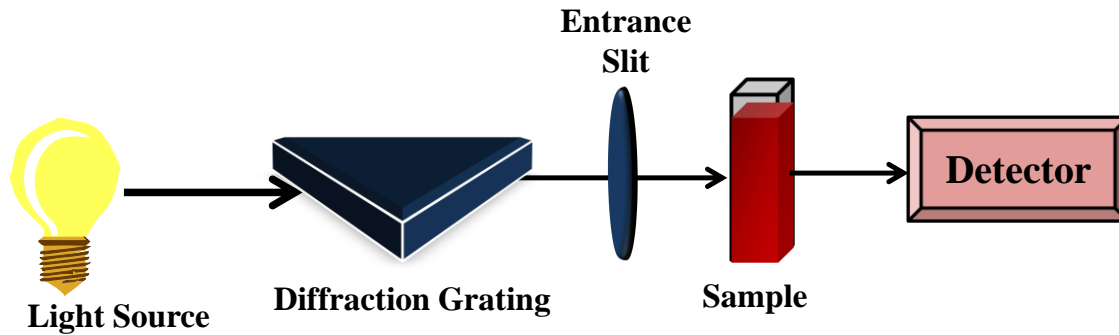
Figure 2.4. Schematic diagram of a UV-visible spectrophotometer.

The measurement of UV-visible spectra of LB films provides additional information about the molecular ordering such as possible chromophore aggregations during the film deposition.[16] There are two types of aggregate formations, namely, H- and J-aggregates. There are three types of chromophore arrangements in dye molecules: ladder-type, staircase-type, and brickwork-type[17] (**Figure 2.5**). Among these, brickwork-type chromophore arrangements give rise to J-aggregates. When comparing the UV-visible spectra observed for solution and well-ordered films, a hypochromic shift of absorption bands indicate the formation of H-aggregates whereas a bathochromic shift of absorption bands indicate the formation of J-aggregates.[18] Therefore, by comparing the solution and the solid-state LB film spectra, information is obtained regarding the possible chromophore arrangements present in the LB film.
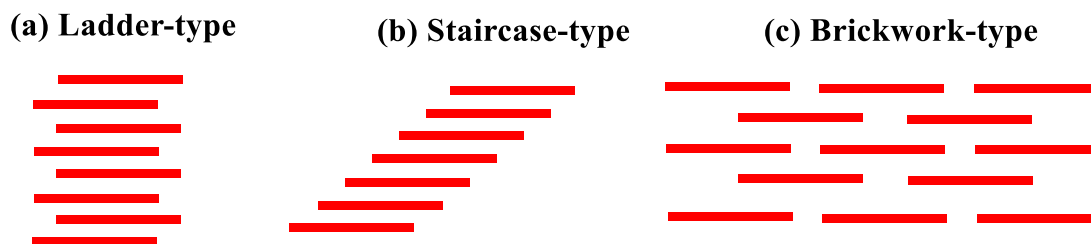
Figure 2.5. Different types of chromophore aggregations.

2.2.7 Cyclic Voltammetry (CV)

Cyclic voltammetry is one of the main techniques that was employed in studying the redox properties of compounds. Cyclic voltammetry measures the electron transfer between electrodes and molecules in solution.[19] The cyclic voltammetry setup (**Figure 2.6**) consists of a cell, which is filled with sample solution and three electrodes, namely, working electrode (glassy-carbon), an auxiliary electrode (Pt-wire), and a reference electrode (Ag/AgCl). During this dissertation research, dry solvents were used to dissolve the sample and the solution was purged with an inert gas to remove dissolved dioxygen from the system.

Reference Electrode - Ag/AgCl

Auxiliary Electrode - Pt

Working Electrode - Glassy Carbon
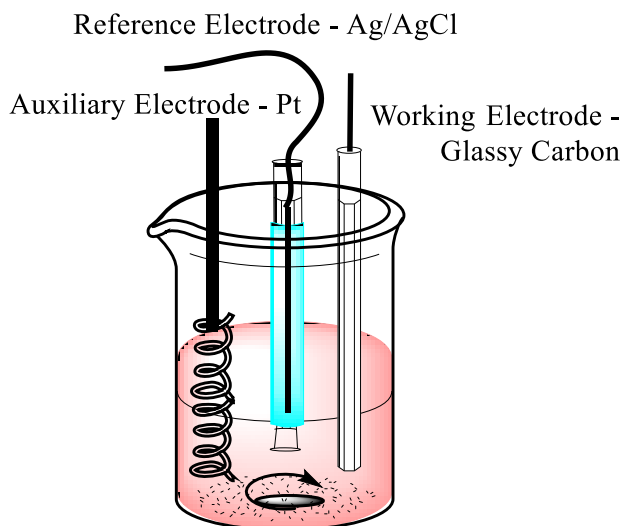
Figure 2.6. Demonstrative view of cyclic voltammetry experimental setup.

The plot obtained between the applied potential and current is referred to as a cyclic voltammogram (**Figure 2.7**) and using this plot one can obtain many parameters such as $E_{\frac{1}{2}}$ [$(E_{pa}+E_{pc})/2$], ΔE, and i_{pa}/i_{pc} values for particular redox active compounds.
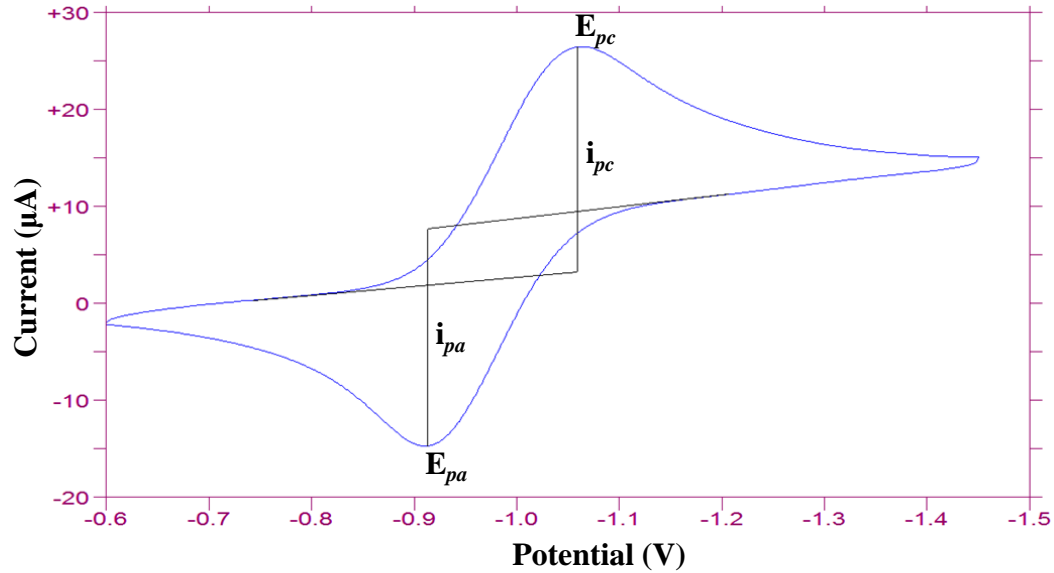
Figure 2.7. An illustration of a cyclic voltammogram.

During an electrochemical process, electrons are transferred from the oxidized species (O) to the reduced species (R) as denoted by **Equation 2.1**.

$$O + ne \underset{K_b}{\overset{K_f}{\rightleftharpoons}} R \quad \text{-----------} \rightarrow \quad \textbf{Equation 2.1}$$
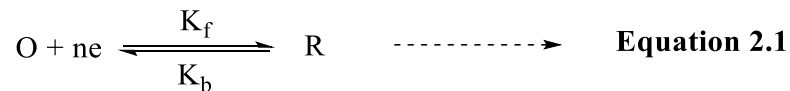
The Nernst equation (**Equation 2.2**) provides the relationship between the cell potential and the concentration of chemical species present in the electrochemical cell. Therefore, with known parameters, an unknown species, such as concentration of oxidized or reduced species, can be calculated.

$$E = E^o + \frac{RT}{nF} \ln \frac{[O]}{[R]} \quad \text{-----------} \rightarrow \quad \textbf{Equation 2.2}$$

In the **Equation 2.2**, E is the electrode potential, E^o is the standard electrode potential, R is the universal gas constant, T is the temperature, n is the number of electrons, F

is the Faraday's constant, [O] is the concentration of the oxidized species, and [R] is the concentration of the reduced species.

The conditions for an electrochemical process to be considered as reversible are as follows,[20]

1. The peak potential difference between cathodic and anodic half processes, $\Delta E = (E_{pc} - E_{pa}) = 0.058$ V for an one electron process

2. The ratio between anodic and cathodic peak currents, $i_{pa}/i_{pc} = 1.0$

3. The peak currents of a redox process, (i_{pa} and i_{pc}) are relative to the square root of the scan rate.

If the ΔE and i_{pa}/i_{pc} values of a redox process are approximate to the above mentioned ideal values, then the electrochemical process is quasi-reversible. In this dissertation research, the electrochemical experiments were carried out at ambient temperature using a BAS 50W voltammetric analyzer. Cyclic voltammograms were recorded at 100 mV/s in dichloromethane, using tetrabutylammonium hexafluorophosphate (TBAPF$_6$) as the supporting electrolyte. All the potential values were recorded versus the Fc$^+$/Fc couple.[21]

2.2.8 Spectroelectrochemistry

Spectroelectrochemical experiments were carried out to distinguish the spectral bands associated with electronic transitions. Spectroelectrochemical experiments were conducted by coupling UV-visible spectroscopy along with cyclic voltammetry. In this dissertation research, the spectroelectrochemistry experiments were carried out as follows: An optically transparent thin layer cell was constructed using indium-tin oxide (ITO) (8-12 Ω/sq) coated glass slides. A flat platinum wire with "U" shape was used as the working electrode and this

was sandwiched between two ITO plates. The optical path of the cell was found to be *ca*. 0.1 mm. Dichloromethane solutions of the compounds were introduced to the cell through capillary action. A pseudo Ag/AgCl electrode and a platinum wire were used as the reference and auxiliary electrodes, respectively. A BAS 50W voltammetric analyzer and a Varian Cary 50 spectrophotometer were used together to collect the data. All the spectroelectrochemistry experiments were carried out under ambient conditions.

2.2.9 Electron Paramagnetic Resonance Spectroscopy (EPR)

EPR spectroscopy detects the unpaired electrons present in paramagnetic compounds. Therefore, this gives information regarding the spin state of a molecule. The basis of the EPR spectroscopy is equivalent to the NMR spectroscopy, but EPR spectroscopy is not widely used when compared to NMR spectroscopy due to the complexity. EPR spectroscopy measures the electron spin, which becomes excited by absorbing microwave radiation, when in an external magnetic field whereas NMR spectroscopy measures the nuclei spin. In EPR spectroscopy, the electrons are considered as charged particles and these charged particles spin around their axis, and generate a magnetic moment (μ_B). Once the paramagnetic sample is located in the presence of a magnetic field, the electrons will start to form parallel and anti-parallel spin states by aligning with the magnetic field. During this process, if a sufficient magnetic field is applied, the electrons will start to transfer between the two states.[22] The energy difference between these two states is given in **Equation 2.3**.

$$\Delta E = h\nu = g\mu_B B_0 \ldots\ldots\ldots\ldots.\textbf{Equation 2.3}$$

(Where, h - Planck's constant, ν - frequency, g - Landé *g*-factor, μ_B - Bohr magneton, and B_0 - magnetic field).

The response obtained between the magnetic field strength versus the absorption is known as the EPR spectrum, and usually the first derivative of the original spectrum is presented. In this dissertation research, few compounds were analyzed by X-band EPR spectroscopy with a Bruker ESP 300 spectrometer at 115 K.

2.2.10 Langmuir-Blodgett (LB) Methods: Isothermal Compression and Brewster Angle Microscopy (BAM)

The Langmuir-Blodgett method is used to analyze the amphiphilic behavior of molecules at the air/subphase interface. The LB method is an inexpensive process that uses to deposit molecules without any structural decomposition. LB films are conformal well-ordered thin films with controlled thicknesses. In addition, the method allows depositing multilayers with approximately same surface coverage. The thickness of the Langmuir film can vary depending on the molecular structure and the packing morphology, but provides a rough estimate on molecular dimensions. To carry out LB experiments, the molecules of interest should show amphiphilic properties. Therefore, the molecules should contain hydrophilic and hydrophobic parts to interact with each other to make a film at the air/water interface. The thin film formed at the interface is known as a Langmuir film and this can be composed of a mono- or multilayered film (mostly monolayer) with a 2D structure. During

the LB experiment, a smooth surface is used to form defect free films at the interface. Therefore, nano-pure water with a resistivity value of 18.2 MΩ•cm^{-1} is used as the subphase, nonetheless at times mercury,[23] glycerol,[24] and other brine solutions[25] (sodium chloride and sodium terephthalate) have been reported. The LB experimental setup is composed of a trough to fill the subphase, two barriers to move across the subphase to compress the Langmuir film, a thermocouple to sense the temperature of the subphase, and a Wilhelmy plate (paper plates of 20 mm × 10 mm) balance to measure the surface pressure. The LB setup is shown in **Figure 2.8**. On the LB trough, a special well has been designed to carry out the dipping experiments.
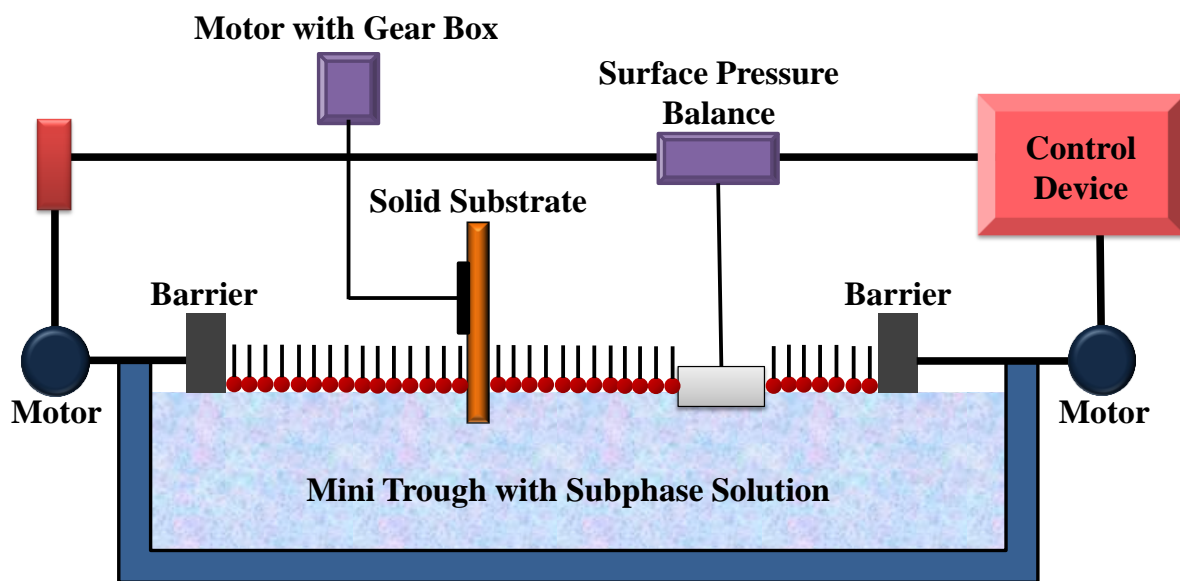
Figure 2.8. A diagram of the LB experimental setup.

During the experiment, the trough is filled with the subphase and a known volume of compound is spread on the subphase surface by dissolving it in a volatile, non-reactive solvent such as chloroform, dichloromethane, or n-hexanes (solution concentration; 1 mg/ml). Usually the experiment is carried out at 23 ± 0.5 °C. After about 20 minutes of waiting time, the experiment starts and the barriers move at a constant, slow speed. During

the compression, surface pressure increases, and plots a graph between average molecular area ($\mathring{A}^2$) versus surface pressure (mN/m). This plot is known as the compression isotherm of the compound, and a representative plot is shown in **Figure 2.9**. Within the time of compression, the molecules will transfer through gaseous 2D → expanded 2D → condensed 2D phases.
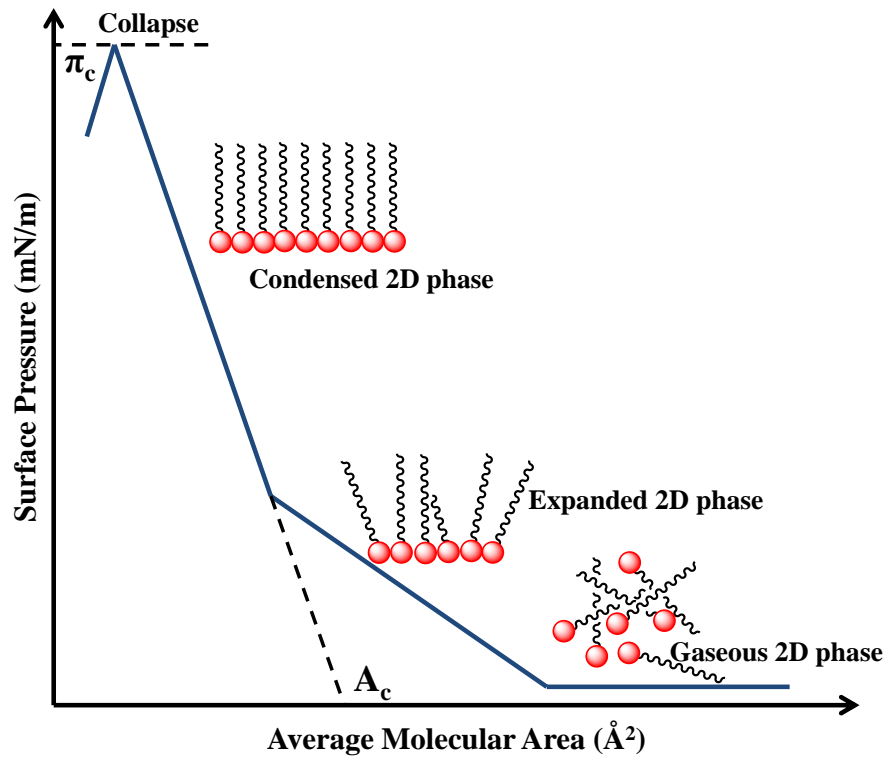
Figure 2.9. Representative view of a LB compression isotherm.

The isotherm plot provides different characteristics that belong to the compound, such as the area where the molecules will start to interact with each other, possible phase transition surface pressures, critical area of the molecule (A_c), and the collapse pressure (π_c). During the compression, the Langmuir film will transfer from a liquid-expanded to a liquid-condensed state, and at the end when the film becomes unstable, it will collapse. The collapse of the film

can happen via either constant pressure or constant area collapse mechanisms.[26,27] Usually the most homogeneous film will be formed at the steepest region of the isotherm plot.

LB method has been vastly used to deposit thin films of organic molecules on to solid substrates. After analyzing the isotherm plot, a stable surface pressure should be identified to deposit the Langmuir film on to a solid substrate. Weak van der Waals forces are used to transfer the 2D Langmuir films on to solid surfaces, and therefore, the hydrophilic and hydrophobic interactions play a major role when depositing the film. These deposited thin films are Langmuir-Blodgett films. When hydrophilic substrates such as, glass, quartz, mica, silicon, and gold are used for the deposition, the up-stroke dipping method is used. Then the hydrophilic parts of the molecule will first attract to the surface. On the other hand, if a hydrophobic substrate such as HOPG is used, then the hydrophobic counterparts will initially attract to the substrate surface. Therefore, a down-stroke dipping method will be most useful. Depending on these up- and down-stroke deposition methods, there can be three main LB film structures, namely X-, Y-, and Z-type (**Figure 2.10**).
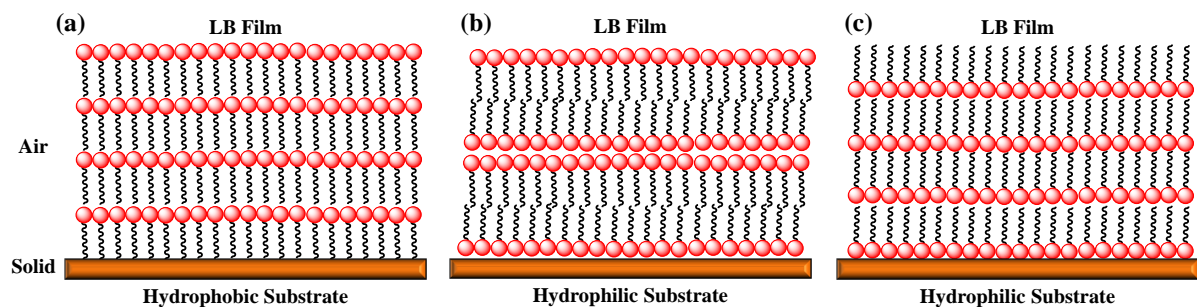
Figure 2.10. Different (a) X-type, (b) Y-type, and (c) Z-type LB multilayer film structures.

Y-type structures originate by following both up and down dipping methods, and they are the most common type (**Figure 2.11**). X- and Z-type structures are generated by following only down- or up-stroke dipping methods, respectively.[28]
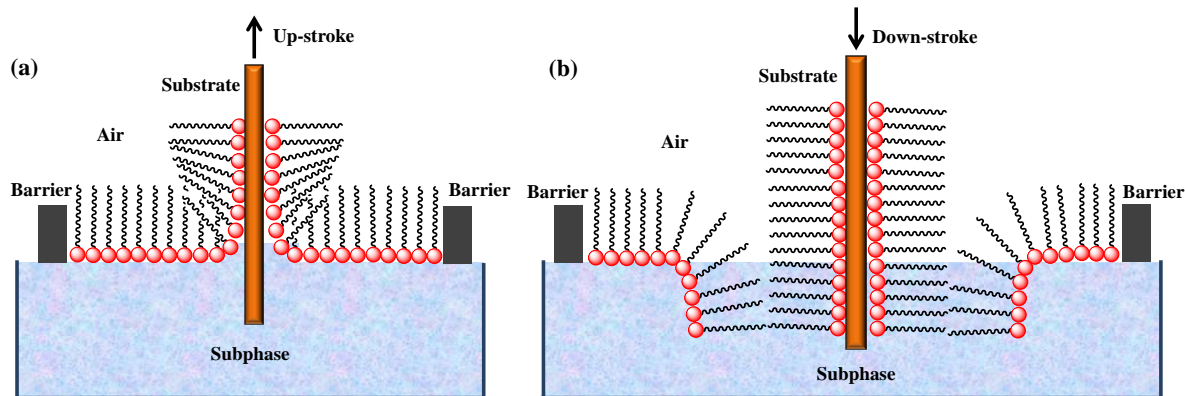
Figure 2.11. The (a) up-stroke and (b) down-stroke LB dipping methods.

An idea about the surface coverage of the substrate can be gained by calculating the transfer ratio [Transfer Ratio (TR) = Area covered on the substrate/Area lost from the Langmuir film].[29] A complete surface coverage is denoted when the TR is close to unity. The desired film thickness can be achieved by repeating the deposition process. Depending on the purpose of film fabrication the substrate material can be changed. Also, it is important to use clean substrates for film fabrication. The glass and quartz substrates can be cleaned with Piranha solution (3:1 concentrated sulfuric acid/30% hydrogen peroxide solution) and gold substrates can be cleaned with absolute ethanol. Then, the substrates can be washed with abundant amounts of deionized water and ultra-pure water. Mica and HOPG substrates can be freshly cleaved before use. Since the LB experiments are very sensitive to contaminants, a clean vibration free laboratory environment is desired. Before starting the experiment, the subphase surface is cleaned by sweeping method upon barrier compression. During the dissertation research, the LB experiments were carried out using an automated KSV 2000

mini trough at 23 ± 0.5 °C and a compression rate of 10 mm/min using Barnstead NANOpure water (18.2 MΩ/cm). Spreading of a known volume of chloroform solutions (1.0 mg/mL) of metal complexes were followed by 20 min equilibrium time before compression. The pressure was measured by the Wilhelmy plate method (paper plates 20 mm × 10 mm).

Mostly, Brewster angle microscopy (BAM) is accompanied with the LB experiment to image the formation of Langmuir films at the air/water interface. The BAM consists of a laser source, an analyzer, and a CCD camera to detect the reflected light as shown in **Figure 2.12**. The digital images that are collected by BAM are known as micrographs. The angle of incidence, where it completely transmits the polarized light without any reflection is known as the Brewster angle.[30] Different Brewster angles are observed for different materials, since they have dissimilar refractive indices. The air/water and air/glass interfaces show Brewster angles of 53 and 56°, respectively. The refractive indices (n) are different for pure water subphase (n = 1.333) and the Langmuir film containing subphase. Therefore, by analyzing the reflected light beam, the structural features belonging to the film can be observed. BAM is used to infer the features belonging to the Langmuir film, such as phase transitions, domain formation, Newton ring formation, collapse, and defects. At the collapse, the BAM images show unique features with linearly structured Newton rings.[31] For the dissertation research, a KSV-Optrel 300 Brewster angle microscope equipped with a He/Ne laser (10 mW, 632.8 nm) and a CCD detector was used to collect the micrographs. The field view of the microscope is 800 × 600 μm and the lateral resolution is 2 μm.
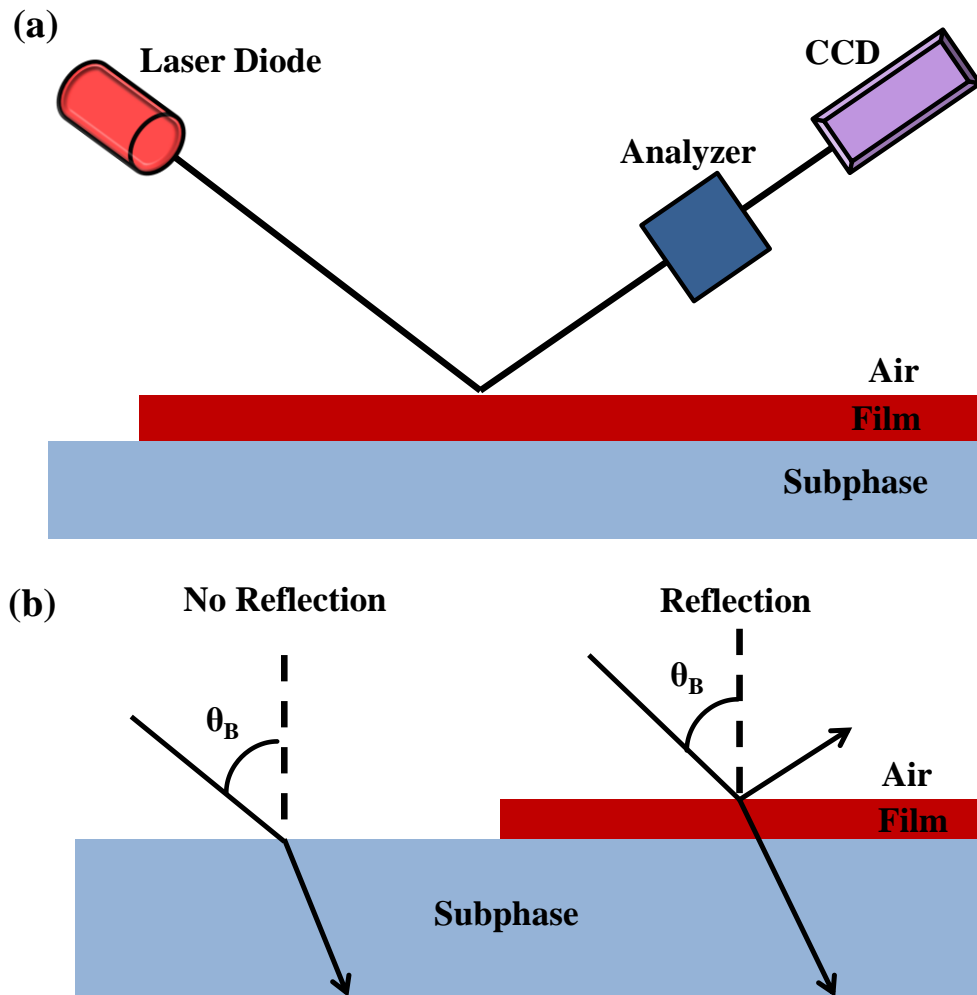
Figure 2.12. (a) The experimental BAM module and (b) an illustration of the Brewster angle at air/subphase interface.

2.2.11 Infrared Reflection Absorption Spectroscopy (IRRAS)

Infrared reflection absorption spectroscopy (grazing angle reflection spectroscopy) is used to assess the molecular patterning, structural information, defects, and the packing topologies of thin films. Different substrates can be used to deposit the molecular films namely, metal plates, silicon wafers, gold coated glass plates, and quartz. Among these, the metal plated substrates are well-suited, because they can reflect light more efficiently when

compared to dielectric substrates.[32] In this method, the signal to noise ratio (S/N) is an important factor that governs the resolution of the obtained IRRAS spectrum. Higher the S/N ratio the better the quality of the spectrum and that is relative to the film thickness.[33] A schematic representation of the IRRA spectrophotometer is shown in **Figure 2.13.** The spectrophotometer consists of an IR light source, a mid infrared range (MIR) polarizer, a ZnSe photoelastic modulator (PEM), and a mercury cadmium telluride detector.
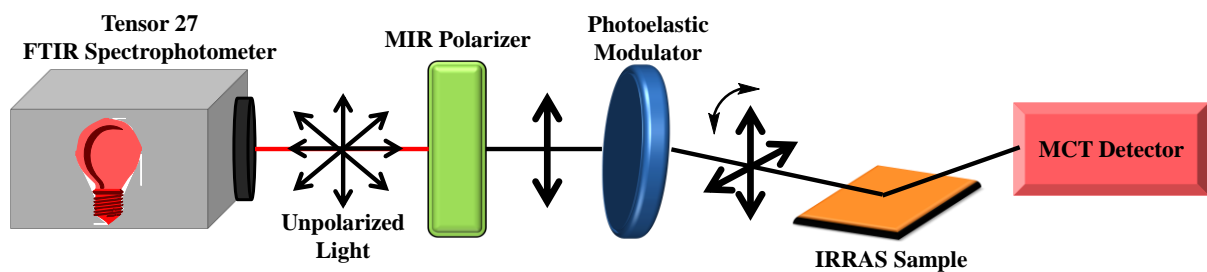
Figure 2.13. A representative view of an IRRA spectrophotometer.

The unpolarized light that is generated from the IR light source converts into polarized light after passing through the MIR polarizer. Inside the spectrophotometer, the ZnSe PEM is situated at an angle of 45° to that of the MIR polarizer. Therefore, the PEM modulates the polarized light between *s*- and *p*-polarization modes. With the aid of computer controlled mirrors, the sample can be irradiated with the *s*- or *p*-polarized light. During this process, the angle of incidence can be varied from 13 to 85°. The reflected light from the sample contains both *s*- and *p*-components of polarized light. However, the detector detects the difference of reflected light ($\Delta R = R_p - R_s$) and provides vibrational information with respect to their transition dipole moments along the substrate surface. The liquid nitrogen-cooled MCT detector generates a high quality IRRAS spectrum with minimized noise level. In this regard, the polarization module is useful to remove the noise generated due to

atmospheric moisture and carbon dioxide. The interaction of incident and reflected light with the thin film is shown in **Figure 2.14**.
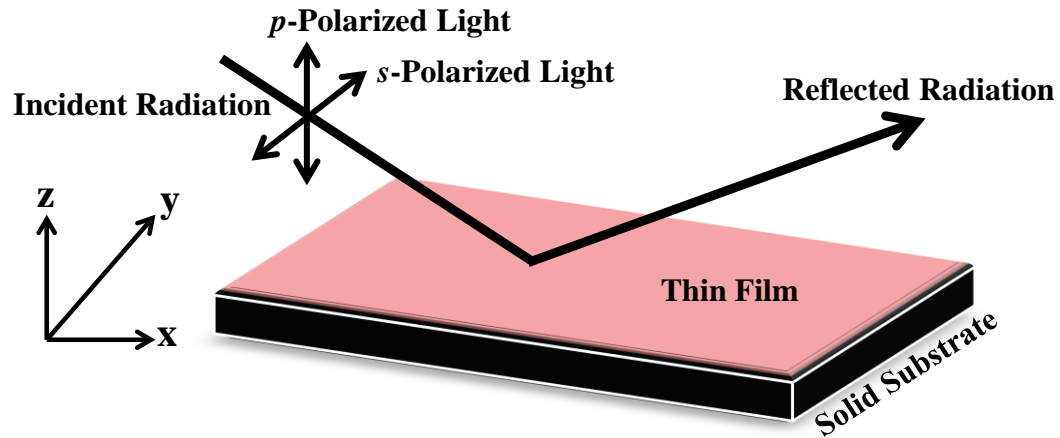
Figure 2.14. The interaction of incident and reflected light with the sample.

In this dissertation research, prior to IRRAS measurements, the LB multilayers (up to 50 layers) of metal complexes were deposited onto thoroughly cleaned glass substrates and they were dried in a desiccator for 24-48 hours to remove the adventitious moisture. Prior to the experiment, the sample chamber was purged with nitrogen gas to remove the interference of carbon dioxide and moisture. Afterward, the sample containing substrates were placed in the sample chamber with an aid of a sample holder. A set of data was collected using a blank sample (a clean glass slide) under similar experimental conditions (with same angle of incidences), to that of the sample. Depending on the data collection mode (transmittance or absorbance), the IRRAS spectrum of the compound can be generated, by dividing or subtracting the sample spectrum and the blank spectrum. A Bruker Tensor 27 infrared spectrophotometer outfitted with an A 513/Q variable-angle accessory was used along with a

liquid nitrogen cooled MCT detector to detect the IRRA spectra. A two minute scanning time was used to obtain the IRRA spectra.

2.2.12 Static Contact Angle Measurements

The static contact angle measurements provide information about the hydrophilicity or the hydrophobicity of a surface covered with a thin film. To carry out the static contact angle measurements, an ultrapure water droplet is placed on the surface of a substrate that is covered with a LB monolayer, and the contact angle is measured using a goniometer. The angle between the surface of the substrate and the tangent drawn between the air/water interface is known as the contact angle. Theoretically, a hydrophilic surface displays a contact angle below 90° and a hydrophobic surface displays a contact angle above 90° (**Figure 2.15**). However, experimentally, the observed contact angle is always compared with the blank (a similar clean substrate). A pure glass substrate shows a contact angle of ~ 8°. Hydrophilic surfaces show surface wetting properties and hydrophobic surfaces do not show surface wetting properties. To obtain reproducible data, the contact angle of the sample was measured at several different places and a 3 µL volume of water was used to create the water droplets. In this dissertation research, the contact angles of a few metal complexes were measured at ambient conditions using a KSV CAM 200 goniometer equipped with a CCD camera.
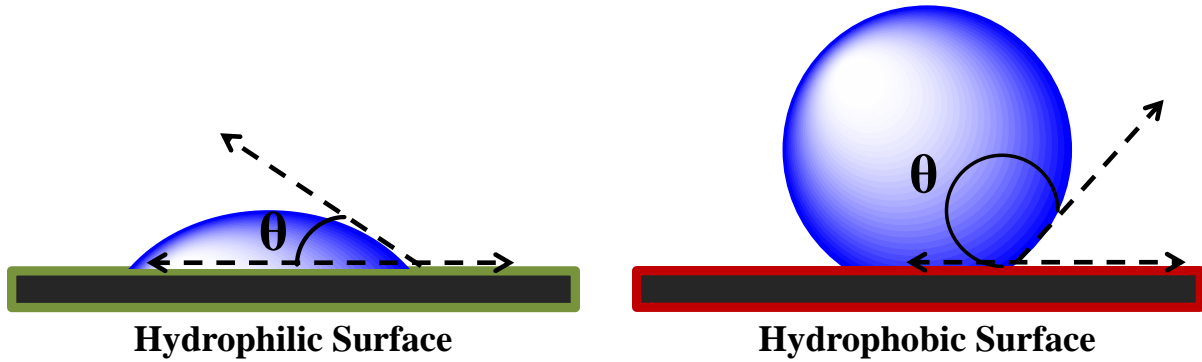
Figure 2.15. The contact angle on hydrophilic and hydrophobic surfaces.

2.2.13 Atomic Force Microscopy (AFM)

Atomic force microscopy is a nanoscopic surface analyzing technique that provides information regarding the surface features of coatings. In AFM, the probe which is connected to the end of a cantilever scans the surface of the sample, by smoothly moving over the sample and creating a data map. This data map can provide information regarding the surface morphology, surface roughness, and thickness of a given thin film. There are three operational modes present in AFM, namely tapping, contact and non-contact modes. The contact mode uses repulsive forces and the non-contact mode uses attractive forces to generate the data map. In the tapping mode, tip makes contact with the surface of the sample for a short period of time, but with a constant frequency. In the dissertation research, AFM was used to analyze the surface properties of LB films. The morphology of mono and multilayer LB films on mica, quartz, and gold were characterized by Dimension 3100 AFM (VEECO). The height, amplitude, and phase images were obtained in the tapping mode at ambient conditions, using silicon probes (nanoScience Instruments, VistaProbes T300) with

resonance frequency of 300 kHz and nominal radius of curvature < 10 nm. Scan rates were varied from 0.5 to 2 Hz depending on the scan size. Integral and proportional gains were approximately 0.4 and 0.8, respectively. Height images have been plane-fit in the fast scan direction with no additional filtering operation. Images were analyzed using the Nanoscope software from Digital Instruments (Version 5.12). Morphology and surface roughness of mono and multilayer LB films were displayed using height images as well as 3D surface plots from 3 to 5 areas with 5×5 or 1×1 μm^2 size on mica substrates. Film thicknesses were determined by measuring the depth of scratches made by a sharp blade at five different locations on the film, using the sectional height analysis command. The AFM measurements and surface analysis were performed in collaboration with Prof. Guangzhao Mao from Department of Chemical Engineering and Materials Science at Wayne State University. The AFM measurements were carried out by Dr. Li Li.

2.2.14 Device Fabrication and Current-Voltage (I-V) Characterization

The main goal of this dissertation research was to investigate the properties of a series of new redox active metallosurfactants, which are suitable to be used in the molecular electronics field. The metal complexes were fabricated into nanoscale devices, and their current-voltage characteristics were measured. The metal|molecule|metal junction is the most well-known architecture that has been reported to study the electrical properties of organic and inorganic materials.[34] To build the metal|molecule|metal junction, the compound has been sandwiched between two symmetric or asymmetric metal electrodes. In the dissertation research, nanoscale devices were fabricated using LB monolayers. A suitable surface

pressure to deposit the LB monolayers was identified by AFM analysis that was carried out prior to device construction. LB film deposited gold coated mica substrates were dried in a desiccator for five days to remove moisture. Devices, which comprised the structure of gold|LB-monolayer|gold (Au|LB-monolayer|Au) were fabricated using the shadow masking[35] method by depositing the top gold electrode using an EffaCoater gold sputter with argon as the carrier gas. In this method, copper TEM grids were used to generate isolated devices on the same gold substrate. At least three assemblies which constitute of an average of 16 devices were measured, to obtain consecutive results. The general assembly layout is shown in **Figure 2.16**. The current-voltage (I-V) characteristics were measured using a Keithley 4200 semiconductor parameter analyzer and a Signatone S-1160 Probe Station at ambient conditions in collaboration with Prof. Zhixian Zhou from Department of Physics and Astronomy at Wayne State University. I-V characteristics were measured by Mr. Meeghage Madusanka Perera.
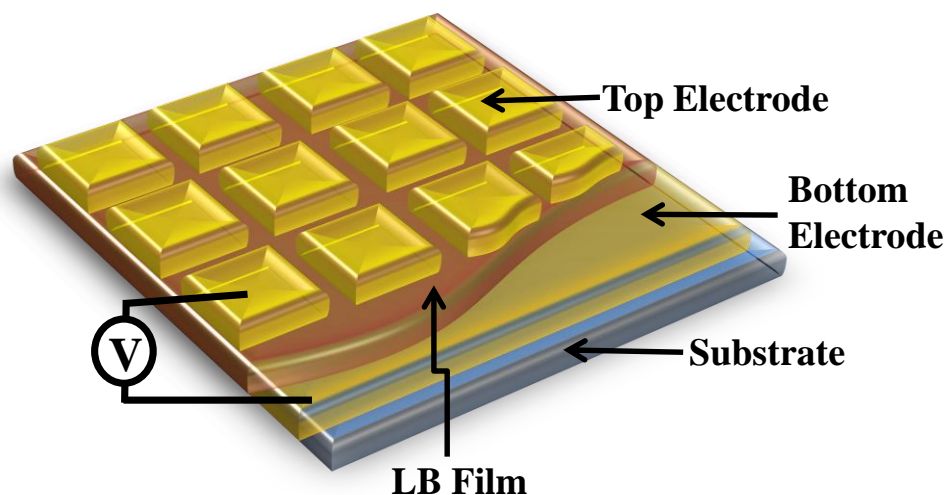
Figure 2.16. The representative assembly layout of Au|LB-monolayer|Au.

2.2.15 Density Functional Theory (DFT) Calculations

DFT calculations were conducted for a few of the iron(III) complexes that were studied during the dissertation research. In these cases, the calculations were performed to understand the electronic transitions in UV-visible spectra and to assign the sequence of redox processes. In addition, the calculations provided information regarding the HOMO-LUMO energies, which were useful in understanding the current rectifying mechanism in iron(III) complexes. The calculations were carried out with the GAUSSIAN program[36] using B3LYP/SDD, 6-31G(d,p) level of theory[37] and SMD solvation (dichloromethane) model. Geometries of all the structure models that were probed during the calculations were minimized with the aid of standard methodologies.[38] These calculations were performed in collaboration with Prof. H. Bernhard Schlegel from Department of Chemistry at Wayne State University. The calculations were carried out by Dr. Shivnath Mazumder and Mr. Bishnu Thapa.

REFERENCES

1. Nakamoto, K. *Infrared and Raman Spectra of Inorganic and Coordination Compounds, Part B: Applications in Coordination, Organometallic and Bioinorganic Chemistry,* 6th ed.; John Wiley & Sons, Inc, Hoboken, New Jersey, 2008; chapter 1, pp 1-275.

2. Silverstein, R. M.; Webster, F. X. *Spectrometric Identification of Organic Compounds,* 6th ed.; John Wiley & Sons, Inc, New York, 1998; chapter 3, pp 71-109.

3. Johnstone, R. A. W.; Rose, M. E. *Mass Spectrometry for Chemists and Biochemists*. 2nd ed.; Cambridge University Press, 1996.

4. Gross, M. *Journal of the American Society for Mass Spectrometry* **1994**, *5*, 57.

5. Sack, T. M.; Lapp, R. L.; Gross, M. L.; Kimble, B. J. *International Journal of Mass Spectrometry and Ion processes* **1984**, *61*, 191.

6. Brenton, A. G.; Godfrey, A. R.; *J. Am. Soc. Mass Spectrom* **2010**, *21*, 1821.

7. Trimpin, S.; Inutan, E. D. *Analytical Chemistry* **2013**, *85*, 2005.

8. Trimpin, S.; Inutan, E. D. *J. Am. Soc. Mass Spectrom.* **2013**, *24*, 722.

9. http://en.wikipedia.org/wiki/Elemental_analysis

10. West, A. R. *Basic Solid State Chemistry,* 1st ed.; John Wiley & Sons, Inc, New York, 1988.

11. APEX2 V2010.11-3. Software *for the CCD Detector System*; Bruker Analytical X-ray Systems, Madison, WI (2010).

12. Sheldrick, G.M. "A short history of SHELX". *Acta Cryst*. **A64**, 2008, 112-122.

13. Dolomanov, O. V.; Bourhis, L. J.; Gildea, R. J.; Howard J. A. K.; Puschmann, H. "OLEX2: A Complete Structure Solution, Refinement and Analysis Program". *J. Appl. Cryst.* **2009**, *42*, 339.

14. Lever, A. B. P. *Journal of Chemical Education* **1974**, *51*, 612.

15. Clarck, B. J.; Forst, T.; Russell, M. A. *UV Spectroscopy: Techniques, Instrumentation, Data Handling,* 1st ed.; UV spectrometry group, Chapman and Hall, London, 1993.

16. Engelking, J.; Menzel, H. *Thin Solid Films* **1998**, *90*, 327

17. Mishra, A.; Behera, R. K.; Behera, P. K.; Mishra, B. K.; Behera, G. B. *Chem. Rev.* **2000**, *100*, 1973.

18. Menzel, H.; Weichart, B.; *Langmuir* **1994**, *10*, 1926.

19. Kissinger, P. T.; Bott, A. W. *Current Separations* **2002**, *20*, 51

20. Wang, J. *Analytical Electrochemistry*; John Wiley & Sons, Inc, New York, 2000; chapter 2.

21. Gagne, R.; Koval, C.; Licenski, G. *Inorg. Chem*. **1980**, *19*, 2854.

22. Wertz, J. E.; Bolton, J. R. *Electron Spin Resonance, Elementary Theory and Practical Applications;* New York, Chapman and Hall, 1986.

23. Gaines, G. L. *Insoluble Monolayers Liquid-Gas Interfaces; Interscience:* New York, 1966.

24. Barraud, A.; Lelou, J.; Gouzerh, A.; Palacin, S. *Thin Solid Films* **1985**, *133*, 117.

25. Hindo, S. S.; Shakya, R.; Shanmugam, R.; Heeg, M. J.; Verani, C. N. *Eur. J. Inorg. Chem*. **2009**, 4686.

26. Kundu, S.; Datta, A.; Hazra, S. *Langmuir* **2005**, *21*, 5894.

27. Kundu, S.; Datta, A.; Hazra, S. *Phys. Rev. E* **2006**, *73*, 051608.

28. Petty, M. C. *Langmuir Blodgett Films: an Introduction,* Cambridge University Press, New York, 1996.

29. Metzger, R. M. *J. Mater. Chem.* **2008**, *18*, 4364.

30. Brewster, D. "On the laws which regulate the polarisation of light by reflection from transparent bodies," *Philosophical Transactions of the Royal Society of London* **1815**, *105*, 125-159.

31. Galvan-Miyoshi, J.; Ramos, S.; Ruiz-Garcia, J.; Castillo, R. *J. Chem. Phys.* **2001**, *115*, 8178.

32. Nissink, J. W. M. *Vibrational Spectroscopy on Intermolecular Interactions in Solutions and at Interfaces*, Universiteitsbibliotheek Utrecht, 1999; chapter 2, pp 7-12.

33. Kattner, J.; Hoffmann, H. *External reflection spectroscopy of thin films on dielectric substrates, Hand book of vibrational spectroscopy;* John Wiley & Sons Ltd, Chichester, 2002; pp12-14.

34. Paul, N. D.; Rana, U.; Goswami, S.; Mondal, T. K.; Goswami, S. *J. Am. Chem. Soc.* **2012**, *134*, 6520.

35. Metzger, R. M.; Chen, B.; Höpfner, U.; Lakshmikantham, M. V.; Vuillaume, D.; Kawai, T.; Wu, X.; Tachibana, H.; Hughes, T. V.; Sakurai, H.; Baldwin, J. W.; Hosch, C.; Cava, M. P.; Brehmer, L.; Ashwell, G. J. *J. Am. Chem. Soc.* **1997**, *119*, 10455.

36. Frisch, M. J.; Trucks, G. W.; Schlegel, H. B.; Scuseria, G. E.; Robb, M. A.; Cheeseman, J. R.; Montgomery, J. A.; Vreven, T.; Kudin, K. N.; Burant, J. C.; Millam, J. M.; Iyengar, S. S.; Tomasi, J.; Barone, V.; Mennucci, B.; Cossi, M.; Scalmani, G.; Rega, N.; Petersson, G. A.; Nakatsuji, H.; Hada, M.; Ehara, M.; Toyota, K.; Fukuda, R.; Hasegawa, J.; Ishida, M.; Nakajima,T.; Honda, Y.; Kitao, O.; Nakai, H.; Klene, M.; Li, X.; Knox, J. E.; Hratchian, H. P.; Cross, J. B.; Bakken, V.; Adamo, C.; Jaramillo, J.; Gomperts, R.; Stratmann, R. E.; Yazyev, O.; Austin, A. J.; Cammi, R.; Pomelli, C.; Ochterski, J. W.; Ayala, P. Y.; Morokuma, K.; Voth, G. A.; Salvador, P.; Dannenberg, J. J.; Zakrzewski,

V. G.; Dapprich, S.; Daniels, A. D.; Strain, M. C.; Farkas, O.; Malick, D. K.; Rabuck, A. D.; Raghavachari, K.; Foresman, J. B.; Ortiz, J. V.; Cui, Q.; Baboul, A.G.; Clifford, S.; Cioslowski, J.; Stefanov, B. B.; Liu, G.; Liashenko, A.; Piskorz, P.; Komaromi, I.; Martin, R. L.; Fox, D. J.; Keith, T.; Al-Laham, M. A.; Peng, C. Y.; Nanayakkara, A.; Challacombe, M.; Gill, P. M. W.; Johnson, B.; Chen, W.; Wong, M. W.; Gonzalez, C.; Pople, J. A. GAUSSIAN 03; Gaussian, Inc.: Wallingford, CT, 2003.

37. (a) Ditchfield, R.; Hehre, W. R.; Pople, J. A. *J. Chem. Phys.* **1971**, *54*, 724; (b) Hehre, W. J.; Ditchfield, R.; Pople, J. A. *J. Chem. Phys.* **1972**, *56*, 2257; (c) Hariharan, P. C.; Pople, J. A. *Theo. Chim. Acta.* **1973**, *28*, 213; (d) Hariharan, P. C.; Pople, J. A. *Mol. Phys.* **1974**, *27*, 209; (e) Gordon, M. S. *Chem. Phys. Lett.* **1980**, *76*, 163; (f) Becke, A. D. *Phys. Rev. A* **1988**, *38*, 3098; (g) Lee, C. T.; Yang, W. T.; Parr, R. G. *Phys. Rev. B* **1988**, *37*, 785; (h) Becke, A. D. *J. Chem. Phys.* **1993**, *98*, 5648; (i) Stephens, P. J.; Devlin, F. J.; Chabalowski, C. F.; Frisch, M. J. *J. Phys. Chem.* **1994**, *98*, 11623.

38. (a) Schlegel, H. B. *J. Comput. Chem.* **1982**, *3*, 214; (b) Hratchian, H. P.; Schlegel, H. B. *In Theory and Applications of Computational Chemistry: The First 40 Years*; Dykstra, C. E.; Kim, K. S.; Frenking, G.; Scuseria, G. E.; Eds., 2005.

CHAPTER 3

INVESTIGATION OF THE ELECTRONIC, REDOX, ELECTRON DONOR/ACCEPTOR, AND FILM FORMATION PROPERTIES OF [N₂O₃]-CONTAINING GALLIUM(III) AND IRON(III) METALLOSURFACTANTS

3.1 Introduction

A theme in the microelectronic industry today is to manufacture efficient, low cost microelectronic devices with smaller feature sizes.[1,2] To achieve this goal, there is a continuing effort to manufacture devices with high aspect ratios in the nanometer scale. Furthermore, there is a continuing effort to scale down the feature sizes to the molecular level, since it is the smallest possible level known to date. These researchers suggest that the molecule-based devices would be an advanced alternative for miniaturization process of electronic components,[3,4,5] and molecules that can probe several redox states and those can form uniform thin films are the prime target in this regard. Lindsey *et al*. suggested that the molecules with at least three accessible cationic states are the most suitable candidates for the information storage.[6] Two main strategies have been adopted when designing molecules to probe these redox states. One way is to build systems with several molecules, which are redox active, and the other is to design a single molecule, which has access to several redox states.[7]

This chapter reviews the development of new redox-active transition metal complexes that are capable of acting as precursor metallosurfactants for the thin film formation toward molecular electronics. This study has considered molecules with multiple redox states and was interested of a pentadentate ligand system with phenolate/phenoxyl redox-couple seen in

nature, tyrosine hydroxylase (TyrOH),[8] which shows great redox reversibility. Nonetheless, pseudooctahedral complexes known to date do not show notable redox reversibility when compared to natural systems, such as TyrOH.[9] Therefore, a main target of this study was to form pentacoordinate complexes with improved redox properties when compared to octahedral complexes, such as reversibility and cyclability of the compound without decomposing them on the electrode surface. Also, these features are important for information storage because subsequent oxidations and reductions can be used to read and write information.[10]

Recently, the Verani group has reported that schemes of asymmetric pentadentate ligands coordinated to trivalent iron and gallium metal centers, display good redox properties.[9] To use these redox-active molecules as potential candidates in molecule-based electronics, it is necessary to deposit the molecules onto solid substrates as thin films. Herein, I present the design of a series of ligands with $[N_2O_3]$ binding moiety with modifications at the fourth and the fifth positions of the phenylenediamine ring to merge amphiphilic and redox properties together. To characterize the amphiphilic behavior of molecules, the Langmuir-Blodgett (LB) deposition method was used. The LB method is capable of forming well-organized films with controlled thickness using organic or inorganic molecules. **Scheme 3.1** shows the representative diagram of the ligands and the metal complexes of interest.

Ligands
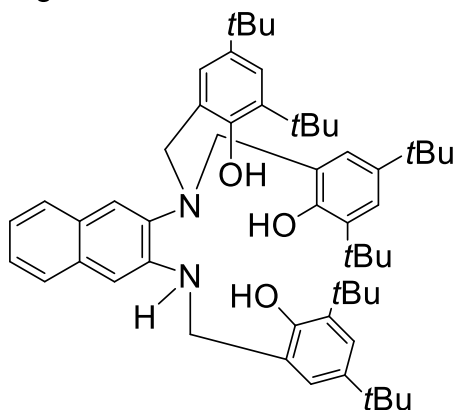
$[H_3L^1]$
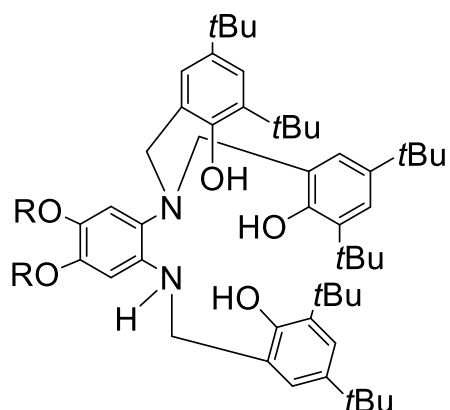
$[H_3L^2]$, R = CH_3
$[H_3L^3]$, R = $C_{18}H_{37}$
$[H_3L^4]$, R = $CH_2CH_2OCH_3$

Metal Complexes
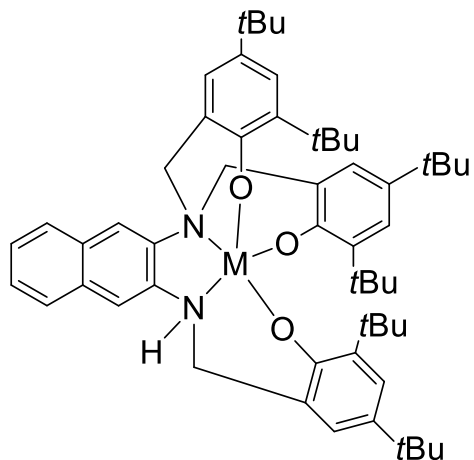
$[Ga^{III}L^1]$, M=Ga(III)   (1)
$[Fe^{III}L^1]$, M=Fe(III)   (5)
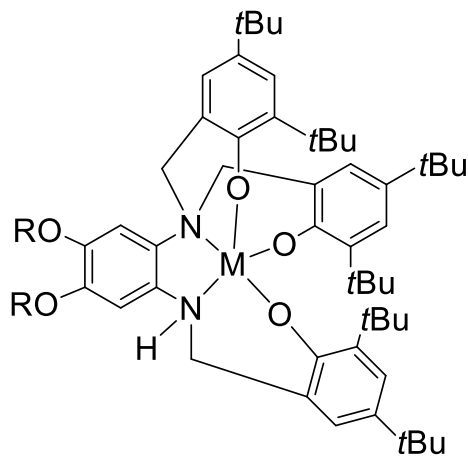
$[Ga^{III}L^2]$, R=CH_3 M=Ga(III)   (2)
$[Ga^{III}L^3]$, R=$C_{18}H_{37}$ M=Ga(III)   (3)
$[Ga^{III}L^4]$, R=$CH_2CH_2OCH_3$ M=Ga(III)   (4)
$[Fe^{III}L^2]$, R=CH_3 M=Fe(III)   (6)
$[Fe^{III}L^3]$, R=$C_{18}H_{37}$ M=Fe(III)   (7)

Scheme 3.1. Ligands and their respective iron(III) and gallium(III) metal complexes.

3.2 Experimental Section

3.2.1 X-ray Structural Determinations for complex 5'

The structure **[Fe^{III}L$^{1'}$]**, **(5')** was solved by direct methods using the SHELXS-97 program in APEX II suite and refined by least squares method on F^2, SHELXL-97. A dark red-brown crystal of **(5')** was mounted on a mitogen loop, and data were collected on a Bruker APEX-II Kappa geometry diffractometer with Mo radiation and a graphite monochromato using a Bruker CCD based diffractometer equipped with an Oxford Cryostream low-temperature apparatus at 100 K. A total of 92860 reflections were collected with 24321 unique reflections. Two independent molecules were present in the asymmetric unit cell and one disordered *tert*-butyl group was found in one of the structures. All non-hydrogen atoms are refined anisotropically. Hydrogens were calculated by geometrical methods and refined as a riding model.

3.2.2 Syntheses of Ligands

Synthesis of Organic Precursors

The ligand synthesis was a multistep process. Because the substituted 1,2-diamine precursors are air sensitive, the synthesis, isolation, and subsequent synthetic steps were carried out using standard Schlenk and glove box techniques. 1,2-Dimethoxy-4,5-dinitrobenzene,[11] 4,5-dimethoxybenzene-1,2-diamine,[11] 2,4-di-*tert*-butyl-6-(hydroxymethyl)phenol,[12] and 2,4-di-*tert*-butyl-6-(chloromethyl)phenol[9] were synthesized following reported procedures.

Synthesis of 1,2-bis(octadecyloxy)benzene (L[1a]).

To a solution of catechol (1.00 g, 9.08 mmol) and anhydrous K_2CO_3 (4.52 g, 32.7 mmol) in anhydrous *N,N*-dimethyl formamide (15 mL), a solution of 1-bromooctadecane (6.67 g, 20.00 mmol) in anhydrous *N,N*-dimethyl formamide (20 mL) was added drop wise over a period of 15 minutes under inert conditions. After refluxing for 18 h, the reaction mixture was poured into 150 mL of cold (0 °C) water and extracted with dichloromethane (100 mL). The organic layer was collected and dried over anhydrous Na_2SO_4. The solvent was removed by rotatory evaporation and the remaining yellow viscous oil was re-dissolved in a n-hexanes and ethyl acetate (19:1). The solution was filtered through silica under vacuum. The obtained pale yellow solution was concentrated to half of its original volume and was kept in the refrigerator to yield a white precipitate of 1,2-bis(octadecyloxy)benzene. Yield: 72%. APCI (m/z^+) = 637.5892 (100%) for $[C_{42}H_{78}O_2 + Na^+]$ (calculated = 637.5900) in agreement with -1.3 ppm difference. IR (KBr, cm^{-1}) 2850-2919 (ν_{C-H}), 1595 ($\nu_{C=C}$, aromatic), 1508 ($\nu_{C=C}$, aromatic), 1259 (ν_{C-O-C}). ^{1}H NMR, ppm (CDCl$_3$, 300 MHz): δ 6.866 (s, 4H^{ph}), 3.969 (t, 4H^{OCH2}), 1.790 (m, 4H^{CH2}), 1.444 (m, 4H^{CH2}), 1.239 (s, 56H^{CH2}), 0.863 (t, 6H^{CH3}).

Synthesis of 1,2-dinitro-4,5-bis(octadecyloxy)benzene (L[2a]).

1,2-Dinitro-4,5-bis(octadecyloxy)benzene was synthesized by dissolving 1,2-bis(octadecyloxy)benzene (2.05 g, 3.33 mmol) in dichloromethane (24 mL) and glacial acetic acid (24 mL). The reaction solution was cooled to 15 °C, and conc. HNO_3 acid (3.5 mL) was added to the mixture that was subsequently stirred at ambient temperature for 30 minutes. The reaction mixture was cooled back to 15 °C and fuming HNO_3 acid (8.5 mL) was added

slowly. After stirring the reaction mixture for 72 hours at ambient temperature, the solution was added to ice cold water (100 mL). The organic layer was washed sequentially with water (3 × 100 mL), saturated $NaHCO_3$ solution (100 mL), and brine solution (100 mL). After drying the organic layer over anhydrous Na_2SO_4, the solvent was removed by rotatory evaporation and recrystallized from hot acetone to yield 1,2-dinitro-4,5-bis(octadecyloxy)benzene as yellow crystals. Yield: 86%. APCI (m/z^+) = 743.5341 (100%) for $[C_{42}H_{76}N_2O_6 + K^+]$ (calculated = 743.5340) in agreement with 0.1 ppm difference. IR (KBr, cm^{-1}) 2850-2918 (ν_{C-H}), 1587 ($\nu_{C=C}$, aromatic), 1539 ($\nu_{C=C}$, aromatic), 1294 (ν_{C-O-C}), 1466 ($\nu_{N=O}$), 1335 ($\nu_{N=O}$), 873 (ν_{C-N}). ^1H NMR, ppm (CDCl$_3$, 400 MHz): δ 7.270 (s, 2H^{ph}), 4.073 (t, 4H^{OCH2}), 1.846 (m, 4H^{CH2}), 1.453 (m, 4H^{CH2}), 1.234 (s, 56H^{CH2}), 0.857 (t, 6H^{CH3}).

Synthesis of 4,5-bis(octadecyloxy)benzene-1,2-diamine (L^{3a}).

Synthesis of 4,5-bis(octadecyloxy)benzene-1,2-diamine was carried out by reacting 1,2-dinitro-4,5-bis(octadecyloxy)benzene (2.4 g, 3.4 mmol) with hydrazine monohydrate (6.3 mL) in presence of 0.1 g of 10% Pd/C in absolute ethanol (50 mL) under inert conditions. After refluxing for 18 hours, the mixture was filtered through celite under inert conditions. The solvent was reduced to dryness under vacuum to yield a white precipitate as 4,5-bis(octadecyloxy)benzene-1,2-diamine. Yield: 76%. IR (KBr, cm^{-1}) 3334 (ν_{N-H}), 2850-2917 (ν_{C-H}), 1560 ($\nu_{C=C}$, aromatic), 1532 ($\nu_{C=C}$, aromatic), 1249 (ν_{C-O-C}). ^1H NMR, ppm (CDCl$_3$, 400 MHz): δ 6.350 (s, 2H^{ph}), 3.858 (t, 4H^{OCH2}), 3.121 (s, 4H^{NH2}), 1.717 (m, 4H^{CH2}), 1.410 (m, 4H^{CH2}), 1.234 (s, 56H^{CH2}), 0.856 (t, 6H^{CH3}).

Synthesis of 1,2-bis(2-methoxyethoxy)benzene (L^{1b}).

Catechol (4.00 g, 36.3 mmol) was dissolved in a NaOH solution in ethanol (9.07 g of NaOH in 80 mL of 95% ethanol). To this was added 1-bromo-2-methoxyethane (25.7 g, 185 mmol) drop wise under inert conditions. The mixture was heated at reflux for 48 hours. The resulting dark solution was concentrated and extracted with ether and 10% NaOH solution in water. The organic layer was collected, dried over Na_2SO_4 and the resulting pale yellow viscous oil was further dried under vacuum to give 1,2-bis(2-methoxyethoxy)benzene. Yield: 80%. IR (KBr, cm^{-1}) 2820-3065 (ν_{C-H}), 1594 ($\nu_{C=C}$, aromatic), 1503 ($\nu_{C=C}$, aromatic), 1257 (ν_{C-O-C}), 1127 (ν_{C-O-C}). ^1H NMR, ppm (CDCl$_3$, 400 MHz): δ 3.427 (s, 6H^{OCH3}), 3.741 (t, 4H^{OCH2}), 4.134 (t, 4H^{OCH2}), 6.902 (m, 4H^{ph}).

Synthesis of 1,2-bis(2-methoxyethoxy)-4,5-dinitrobenzene (L^{2b}).

To a cooled (<15 °C) solution of 1,2-bis(2-methoxyethoxy)benzene (4.53 g, 20.0 mmol) in dichloromethane (140 mL) and glacial acetic acid (140 mL) was added 65% HNO$_3$ acid (20 mL) over a period of 15 minutes. The mixture was stirred at ambient temperature for 30 minutes and cooled back to 15 °C. Afterwards, fuming HNO$_3$ acid (50 mL) was added to the reaction mixture over 30 minutes and stirred for 72 hours at ambient temperature. The reaction was quenched by adding the mixture to 500 mL of ice cold water and extracted with water (3 × 500 mL), saturated NaHCO$_3$ solution (500 mL), and finally with brine solution (500 mL). The organic layer was dried over anhydrous Na_2SO_4 and the solvent was removed by rotatory evaporation. The crude product was recrystallized from methanol to give 1,2-bis(2-methoxyethoxy)-4,5-dinitrobenzene as a yellow crystalline product. Yield: 41%. IR (KBr, cm^{-1}) 2818-3129 (ν_{C-H}), 1590 ($\nu_{C=C}$, aromatic), 1522 ($\nu_{C=C}$, aromatic) 1472 ($\nu_{N=O}$),

1338 ($\nu_{N=O}$), 884 (ν_{C-N}), 1295 (ν_{C-O-C}), 1120(ν_{C-O-C}). ^{1}H NMR, ppm (CDCl$_3$, 400 MHz) : δ 3.418 (s, 6H^{OCH3}), 3.785 (t, 4H^{OCH2}), 4.259 (t, 4H^{OCH2}), 7.394 (s, 2H^{ph}).

Synthesis of 4,5-bis(2-methoxyethoxy)benzene-1,2-diamine (L^{3b}).

Hydrazine monohydrate (1.04 g, 20.7 mmol) was added slowly to a mixture of 1,2-bis(2-methoxyethoxy)-4,5-dinitrobenzene (0.601 g, 1.90 mmol) and 10% Pd/C (0.025 g) in absolute ethanol (12.5 mL). The solution was heated at reflux for 18 hours under inert conditions. The hot solution was filtered through celite under argon and reduced to dryness under vacuum to give 4,5-bis(2-methoxyethoxy)benzene-1,2-diamine as a colorless viscous oil. Yield: 97%. IR (KBr, cm^{-1}) 3343 (ν_{N-H}), 2734-2928 (ν_{C-H}), 1628 ($\nu_{C=C,}$ aromatic), 1518 ($\nu_{C=C,}$ aromatic), 1238 (ν_{C-O-C}), 1123 (ν_{C-O-C}). ^{1}H NMR, ppm (CDCl$_3$, 400 MHz): δ 3.208 (s, 4H^{NH2}), 3.374 (s, 6H^{OCH3}), 3.637 (t, 4H^{OCH2}), 4.006 (t, 4H^{OCH2}), 6.352 (s, 2H^{ph}).

Ligands

Ligand **[H$_3$L^1]** [*6,6'-(3-(3,5-di-tert-butyl-2-hydroxybenzylamino)naphthalen-2-ylazanediyl) bis(methylene)bis(2,4-di-tert-butylphenol)]*, was synthesized according to a known procedure.[13]

To a mixture of 2,4-di-*tert*-butyl-6-(chloromethyl)phenol (4.84 g, 19.0 mmol) and triethylamine (1.92 g, 19.0 mmol) in dichloromethane (125 mL), a solution of naphthalene-2,3-diamine (1.00 g, 6.32 mmol) in dichloromethane (25 mL) was added to the mixture slowly. This solution was heated at reflux for 48 hours. The resulting solution was washed sequentially with 5% Na$_2$CO$_3$ solution (3 × 150 mL) and dried over anhydrous Na$_2$SO$_4$. The solution was filtered and the solvent was removed by rotatory evaporation. The resulted

crude product was recrystallized in acetonitrile to attain a light brown micro-crystalline powder. Yield: 61.6%. Melting point = 169-171 °C. ESI (m/z^+) in CH_2Cl_2 = 813.8 for $[C_{55}H_{76}N_2O_3 + H^+]$. ^1H NMR, ppm ($CDCl_3$, 400 MHz): δ 1.220-1.447 (m, 54H^{tBu}), 3.898 (d, 2H^{CH2}), 4.339 (d, 2H^{CH2}), 4.428 (s, 2H^{CH2}), 7.017-7.633 (m, 12H^{ph}). IR (KBr, cm^{-1}) 3613 (ν_{O-H}), 3349 (ν_{N-H}), 2866-2957 (ν_{C-H}), 1630 ($\nu_{C=C}$, aromatic), 1523 ($\nu_{C=C}$, aromatic), 1236 (ν_{C-N}).

Synthesis of ligand [H₃L²], *6,6'-(2-(3,5-di-tert-butyl-2-hydroxybenzylamino)-4,5-dimethoxyphenylazanediyl)bis(methylene)bis(2,4-di-tert-butylphenol).*

To a mixture of 2,4-di-*tert*-butyl-6-(chloromethyl)phenol (6.12 g, 24.0 mmol) and triethylamine (2.43 g, 24.0 mmol) in dichloromethane (150 mL), a solution of 4,5-dimethoxybenzene-1,2-diamine (1.01 g, 6.00 mmol) in dichloromethane (25 mL) was cannulated under inert conditions. The resulting solution was heated at reflux for 72 hours. The obtained golden brown solution was extracted with brine solution (3×200 mL), dried over anhydrous Na_2SO_4, and the solvent was removed by rotatory evaporation. The resulting viscous oil was further dried under vacuum and the attained crude product was purified by column chromatography (4:1 n-hexanes/ethyl acetate) yielding a pale yellow solid product. Yield: 24%. Melting point = 102-104 °C. APCI (m/z^+) in CH_3OH = 823.6003 (100%) for $[C_{53}H_{78}N_2O_5 + H^+]$ (calculated = 823.5989) in agreement with 1.7 ppm difference. ^1H NMR, ppm ($CDCl_3$, 500 MHz): δ 1.254 (s, 18H^{tBu}), 1.320 (s, 18H^{tBu}), 1.330 (s, 9H^{tBu}), 1.433 (s, 9H^{tBu}), 3.731 (s, 3H^{OCH3}), 3.852 (s, 3H^{OCH3}), 3.933 (s, 1H^{CH2}), 3.966 (s, 1H^{CH2}), 4.126 (s, 1H^{CH2}), 4.160 (s, 1H^{CH2}), 4.237 (s, 2H^{CH2}), 6.562 (s, 1H^{ph}), 6.899 (s, 1H^{ph}), 6.956 (d, 2H^{ph}), 7.032 (d, 1H^{ph}), 7.175 (d, 2H^{ph}), 7.299 (d, 1H^{ph}). IR (KBr, cm^{-1}) 3614 (ν_{O-H}), 3328 (ν_{N-H}), 2866-2959 (ν_{C-H}), 1606 ($\nu_{C=C}$, aromatic), 1517 ($\nu_{C=C}$, aromatic), 1236 (ν_{C-O-C}).

Synthesis of ligand [H₃L³], *6,6'-(2-(3,5-di-tert-butyl-2-hydroxybenzylamino)-4,5-bis(octadecyloxy)phenylazanediyl)bis(methylene)bis(2,4-di-tert-butylphenol).*

The ligand was synthesized in a similar fashion as **[H₃L²]**. 2,4-Di-tert-butyl-6-(chloromethyl)phenol (1.02 g, 4.00 mmol), triethylamine (0.405 g, 4.00 mmol), 4,5-bis(octadecyloxy)benzene-1,2-diamine (0.645 g, 1.00 mmol). The crude product was purified by column chromatography (10:1 n-hexanes/ethyl acetate) yielding a yellow viscous oil as the product. Yield: 44%. ESI (m/z^+) = 1300.1342 (100%) for $[C_{87}H_{146}N_2O_5 + H^+]$ (calculated = 1300.1310) in agreement with 2.5 ppm difference. ^{1}H NMR, ppm (CDCl₃, 400 MHz) : δ 0.863 (t, 6H^{CH3}), 1.216 (s, 18H^{tBu}), 1.238-1.287 (m, 83H$^{tBu, CH2}$), 1.392 (s, 11H$^{tBu, CH2}$), 1.548 (m, 2H^{CH2}), 1.696 (m, 2H^{CH2}), 1.761 (m, 2H^{CH2}), 3.767 (t, 2H^{OCH2}), 3.899 (m, 4H$^{OCH2, CH2}$), 4.055 (s, 1H^{CH2}), 4.087 (s, 1H^{CH2}), 4.130 (s, 2H^{CH2}), 6.490 (s, 1H^{ph}), 6.90 (m, 3H^{ph}), 6.963 (d, 1H^{ph}), 7.140 (d, 2H^{ph}), 7.252 (d, 1H^{ph}). IR (KBr, cm^{-1}) 3614 (v_{O-H}), 3328 (v_{N-H}), 2854-2955 (v_{C-H}), 1603 ($v_{C=C}$, aromatic), 1515 ($v_{C=C}$, aromatic), 1235 (v_{C-O-C}).

Synthesis of ligand [H₃L⁴], *(6,6'-(2-(3,5-di-tert-butyl-2-hydroxybenzylamino)-4,5-bis(2-methoxyethoxy)phenylazanediyl)bis(methylene)bis(2,4-di-tert-butylphenol).*

The ligand was synthesized in a similar fashion as **[H₃L²]**. 2,4-Di-tert-butyl-6-(chloromethyl)phenol (7.54 g, 3.80 mmol), triethylamine (3.16 g, 4.00 mmol), 4,5-bis(2-methoxyethoxy)benzene-1,2-diamine (2.00 g, 7.80 mmol). The crude product was purified by column chromatography (3:1 n-hexanes/ethyl acetate) yielding a pale yellow solid as the product. Yield: 32.4%. Melting point = 71-73 °C. ESI (m/z^+) in CH₃OH = 911.6503 (100%) for $[C_{57}H_{86}N_2O_7 + H^+]$ (calculated = 911.6513) in agreement with -1.1 ppm difference. ^{1}H NMR, ppm (CDCl₃, 500 MHz): δ 1.215 (s, 18H^{tBu}), 1.283 (s, 18H^{tBu}), 1.294 (s, 9H^{tBu}) 1.392

(s, 9H^{tBu}), 3.380 (s, 3H^{OCH3}), 3.444 (s, 3H^{OCH3}), 3.648 (t, 2H^{OCH2}), 3.699 (t, 2H ^{OCH2}), 3.892 (s, 1H^{CH2}), 3.918 (s, 1H^{CH2}), 3.978 (t, 2H ^{OCH2}), 4.059 (m, 4H$^{OCH2, CH2}$), 4.124 (s, 2H^{CH2}), 6.537 (s, 1H^{ph}), 6.893 (d, 2H^{ph}), 6.969 (d, 1H^{ph}), 6.992 (s, 1H^{ph}), 7.139 (d, 2H^{ph}), 7.258 (d, 1H^{ph}). IR (KBr, cm^{-1}) 3615 (ν_{O-H}), 3329 (ν_{N-H}), 2870-2957 (ν_{C-H}), 1606 ($\nu_{C=C}$, aromatic), 1516 ($\nu_{C=C}$, aromatic), 1236 (ν_{C-O-C}), 1126 (ν_{C-O-C}).

3.2.3 Syntheses of Metal Complexes

Synthesis of complex [Ga^{III}L^1] (1).

To an anhydrous methanol (15 mL) and anhydrous dichloromethane (5 mL) solution of **[H$_3$L^1]** (0.200 g, 0.250 mmol) and anhydrous NaOCH$_3$ (0.041 g, 0.750 mmol), an anhydrous methanolic solution (5 mL) of GaCl$_3$ (0.044 g, 0.250 mmol) was slowly added under inert conditions. The solution obtained was warmed at 50 °C for 30 minutes. After reaching the reaction mixture to ambient temperature, the mixture was stirred for one and half hours under an argon blanket. Then the solvent was removed under vacuum, and the product obtained was dissolved in anhydrous dichloromethane (20 mL). The solution was filtered through celite under inert conditions, and the solvent was completely removed under reduced pressure to yield a yellow precipitate of **[Ga^{III}L^1]**. Yield: 91.7%. Melting point = 178-180 °C. ESI (*m/z*$^+$) in CH$_3$OH = 879.4958 for [C$_{55}$H$_{73}$N$_2$O$_3$Ga + H$^+$] (calculated = 879.4955) in agreement with 0.34 ppm difference. Anal. Calc. for [C$_{55}$H$_{73}$N$_2$O$_3$Ga]: C, 75.08; H, 8.36; N, 3.18%. Found: C, 74.72; H, 8.16; N, 3.29%. IR (KBr, cm^{-1}) 3251 (ν_{N-H}), 2868-2956 (ν_{C-H}), 1605 ($\nu_{C=C}$, aromatic), 1515 ($\nu_{C=C}$, aromatic).

Synthesis of complex [Ga^{III}L^2] (2).

The complex was synthesized in a similar fashion as **[Ga^{III}L^1]**. The precipitate obtained was recrystallized from methanol and dichloromethane solvent mixture (1:2) to obtain yellow crystals of **[Ga^{III}L^2]**. **[H$_3$L^2]** (0.206 g, 0.250 mmol), anhydrous NaOCH$_3$ (0.041 g, 0.75 mmol), anhydrous GaCl$_3$ (0.044 g, 0.250 mmol). Yield: 68.8%. Melting point = 287-288 °C. ESI (m/z^+) in CH$_3$OH = 889.4995 for [C$_{53}$H$_{75}$N$_2$O$_5$Ga + H$^+$] (calculated = 889.5010) in agreement with -1.69 ppm difference. Anal. Calc. for [C$_{53}$H$_{75}$N$_2$O$_5$Ga·H$_2$O]: C, 70.11; H, 8.55; N, 3.09%. Found: C, 69.81; H, 8.24; N, 3.11%. IR (KBr, cm^{-1}) 3189 (ν_{N-H}), 2866-2952 (ν_{C-H}), 1607 ($\nu_{C=C}$, aromatic), 1515 ($\nu_{C=C}$, aromatic), 1275 (ν_{C-O-C}).

Synthesis of complex [Ga^{III}L^3] (3).

The complex was synthesized in a similar fashion as **[Ga^{III}L^1]** to obtain yellow precipitate of **[Ga^{III}L^3]**. **[H$_3$L^3]** (0.546 g, 0.420 mmol), anhydrous NaOCH$_3$ (0.068 g, 1.26 mmol), anhydrous GaCl$_3$ (0.074 g, 0.420 mmol). Yield: 86.2%. Melting point = 51-52 °C. ESI (m/z^+) in CH$_2$Cl$_2$ = 1366.0287 for [C$_{87}$H$_{143}$N$_2$O$_5$Ga + H$^+$] (calculated = 1366.0331) in agreement with -3.29 ppm difference. Anal. Calc. for [C$_{87}$H$_{143}$N$_2$O$_5$Ga]: C, 76.45; H, 10.55; N, 2.05%. Found: C, 76.11; H, 10.35; N, 2.13%. IR (KBr, cm^{-1}) 3189 (ν_{N-H}), 2854-2955 (ν_{C-H}), 1607 ($\nu_{C=C}$, aromatic), 1514 ($\nu_{C=C}$, aromatic), 1267 (ν_{C-O-C}).

Synthesis of complex [Ga^{III}L^4] (4).

The complex was synthesized in a similar fashion as **[Ga^{III}L^1]**. **[H$_3$L^4]** (0.301 g, 0.330 mmol), anhydrous NaOCH$_3$ (0.054 g, 0.990 mmol), anhydrous GaCl$_3$ (0.058 g, 0.330 mmol). Yield: 71.7%. Melting point = 177-179 °C. ESI (m/z^+) in CH$_3$OH = 977.5532 for

$[C_{57}H_{83}N_2O_7Ga + H^+]$ (calculated = 977.5534) in agreement with -0.2 ppm difference. Anal. Calc. for $[C_{57}H_{83}N_2O_7Ga \cdot 2H_2O]$: C, 67.51; H, 8.65; N, 2.76%. Found: C, 67.19; H, 8.33; N, 2.84%. IR (KBr, cm^{-1}) 3189 (v_{N-H}), 2869-2954 (v_{C-H}), 1607 ($v_{C=C}$, aromatic), 1514 ($v_{C=C}$, aromatic), 1270 (v_{C-O-C}), 1131 (v_{C-O-C}).

Synthesis of complex $[Fe^{III}L^1]$ (5).

A solution of $[H_3L^1]$ (0.20 g, 0.25 mmol) and anhydrous NaOCH$_3$ (0.04 g, 0.75 mmol) in anhydrous methanol (15 mL) and anhydrous dichloromethane (5 mL) mixture was treated with an anhydrous methanolic solution (5 mL) of FeCl$_3$ (0.04 g, 0.25 mmol) under inert conditions. The resulting solution was heated at 50 °C for 30 minutes. The reaction mixture was cooled to ambient temperature and stirred for one and half hours under inert conditions. Then the solvent was removed under vacuum, and the product obtained was dissolved in anhydrous dichloromethane (20 mL). The solution was filtered through celite under inert conditions, and the solvent was completely removed under reduced pressure to yield a dark red-brown precipitate. Yield: 91.1%. Melting point = 174-177 °C. ESI (m/z^+) in CH$_3$OH = 866.5053 (100%) for $[C_{55}H_{73}N_2O_3Fe + H^+]$ (calculated = 866.5050) in agreement with 0.34 ppm difference. Anal. Calc. for $[C_{55}H_{73}N_2O_3Fe \cdot H_2O]$: C, 74.72; H, 8.55; N, 3.17%. Found: C, 74.48; H, 8.29; N, 3.17%. IR (KBr, cm^{-1}) 3203 (v_{N-H}), 2866-2956 (v_{C-H}), 1601 ($v_{C=C}$, aromatic), 1511 ($v_{C=C}$, aromatic).

Synthesis of complex $[Fe^{III}L^2]$ (6).

The complex was synthesized in a similar fashion as $[Fe^{III}L^1]$. The precipitate obtained was recrystallized from methanol and dichloromethane solvent mixture (1:2) to

obtain dark red-brown crystals of $[Fe^{III}L^2]$. $[H_3L^2]$ (0.25 g, 0.30 mmol), anhydrous $NaOCH_3$ (0.05 g, 0.90 mmol), $FeCl_3$ (0.05 g, 0.30 mmol). Yield: 72.3%. Melting point = 268-269 °C. ESI (m/z^+) in CH_3OH = 876.5089 (100%) for $[C_{53}H_{75}N_2O_5Fe + H^+]$ (calculated = 876.5105) in agreement with -1.82 ppm difference. Anal. Calc. for $[C_{53}H_{75}N_2O_5Fe \cdot 2H_2O]$: C, 69.80; H, 8.73; N, 3.07%. Found: C, 69.54; H, 8.19; N, 3.07%. IR (KBr, cm^{-1}) 3204 (ν_{N-H}), 2867-2955 (ν_{C-H}), 1606 ($\nu_{C=C}$, aromatic), 1515 ($\nu_{C=C}$, aromatic), 1272 (ν_{C-O-C}).

Synthesis of complex $[Fe^{III}L^3]$ (7).

The complex was synthesized in a similar fashion as $[Fe^{III}L^1]$ to attain deep brown precipitate of $[Fe^{III}L^3]$. $[H_3L^3]$ (0.40 g, 0.31 mmol), anhydrous $NaOCH_3$ (0.05 g, 0.93 mmol), $FeCl_3$ (0.05 g, 0.31 mmol). Yield: 87%. Melting point = 63-64 °C. ESI (m/z^+) in CH_2Cl_2 = 1353.0470 for $[C_{87}H_{143}N_2O_5Fe + H^+]$ (calculated = 1353.0428) in agreement with 3.1 ppm difference. Anal. Calc. for $[C_{87}H_{143}N_2O_5Fe]$: C, 77.24; H, 10.65; N, 2.07%. Found: C, 77.20; H, 10.49; N, 2.08%. IR (KBr, cm^{-1}) 3206 (ν_{N-H}), 2854-2954 (ν_{C-H}), 1604 ($\nu_{C=C}$, aromatic), 1509 ($\nu_{C=C}$, aromatic), 1273 (ν_{C-O-C}).

Synthesis of complex $[Fe^{III}L^{1'}]$ (5').

A solution of $[H_3L^1]$ (0.20 g, 0.25 mmol) and anhydrous $NaOCH_3$ (0.04 g, 0.75 mmol) in methanol (20 mL) and dichloromethane (5 mL) mixture was treated with an anhydrous methanolic solution (5 mL) of $FeCl_3$ (0.04 g, 0.25 mmol) under ambient conditions. The resulting solution was heated at 50 °C for 30 minutes. Then the reaction mixture was cooled to ambient temperature, stirred for one hour at ambient temperature, and bubbled with dioxygen gas for 30 minutes. The solvent was removed completely by rotatory

evaporation, and the precipitate obtained was recrystallized from methanol and dichloromethane solvent mixture (1:2) to obtain dark red-brown crystals of **[Fe^{III}L$^{1'}$]**. Yield: 86.7%. Melting point = 147-149 °C. ESI (*m/z$^+$*) in CH$_3$OH = 864.4898 for [C$_{55}$H$_{71}$N$_2$O$_3$Fe + H$^+$] (calculated = 864.4892) in agreement with 0.7 ppm difference. Anal. Calc. for [C$_{55}$H$_{71}$N$_2$O$_3$Fe·CH$_3$OH]: C, 75.06; H, 8.44; N, 3.13%. Found: C, 75.06; H, 8.44; N, 3.13%. IR (KBr, cm^{-1}) 2867-2956 (ν_{C-H}), 1611 ($\nu_{C=C}$, aromatic), 1505 ($\nu_{C=C}$, aromatic), 1579 ($\nu_{C=N}$).

Synthesis of complex [Fe^{III}L$^{2'}$] (6').

The complex was synthesized in a similar fashion as **[Fe^{III}L$^{1'}$]** using methanol as the solvent. **[H$_3$L^2]** (0.25 g, 0.30 mmol), anhydrous NaOCH$_3$ (0.05 g, 0.90 mmol), FeCl$_3$ (0.05 g, 0.30 mmol). Yield: 88.3%. Melting point = 162-165 °C. ESI (*m/z$^+$*) in CH$_3$OH = 874.4933 for [C$_{53}$H$_{73}$N$_2$O$_5$Fe + H$^+$] (calculated = 874.4949) in agreement with -1.83 ppm difference. Anal. Calc. for [C$_{53}$H$_{73}$N$_2$O$_5$Fe·0.5H$_2$O]: C, 72.09; H, 8.45; N, 3.17%. Found: C, 72.22; H, 8.09; N, 3.10%. IR (KBr, cm^{-1}) 2866-2953 (ν_{C-H}), 1610 ($\nu_{C=C}$, aromatic), 1511 ($\nu_{C=C}$, aromatic), 1582 ($\nu_{C=N}$), 1268 (ν_{C-O-C}).

3.3 Results and Discussion

3.3.1 Ligand Rationale, Synthesis, and Characterization

The incorporation of redox and film formation properties into molecules is important in addressing many issues related to molecule-based electronics. Therefore, the main goal of this project was to investigate molecules, which are highly asymmetric in nature and that can act as metallosurfactants for thin film formation. These redox-active metallosurfactants are intended to be used as potential candidates in molecular rectification. Therefore, molecules of interest should have intra electron acceptor and donor properties. To achieve these goals, novel molecules were designed and synthesized by incorporating trivalent metal ions into asymmetric phenolate-containing organic ligands. Distinct substituents have been attached to the ligand structure to modulate the film formation properties at the air/water interface. Design of these ligands are mainly focused on generating low symmetry metal complexes due to their ability to facilitate current rectification[14] as well as formation of stable redox species upon oxidation and reduction.[15] Complexes consisted of [N$_2$O$_3$]-type binding sites around metal ions to resemble the active site of the tyrosine hydroxylase enzyme and this phenolate rich environment of ligands help in stabilizing the metal complexes with trivalent iron or gallium. Previously, the Verani group has reported few complexes that resembled the head group of the designed ligands.[9,16] These studies helped in understanding the geometry of metal center, sequence of radical generation, and their stability. Furthermore, film formation properties of these systems were incorporated by mimicking the ligand design by fine tuning the phenylenediamine moiety. In this study, substituents such as naphthalene, methoxy-, and alkoxy-containing phenylenediamine moieties were investigated. These ligands are capable of forming stable radical species due to the presence of *tert*-butyl groups at *ortho* and *para*

positions of phenolate moieties. Therefore, such modifications make these molecules excellent candidates in the molecular electronic field.

Tripodal ligands were obtained by following multistep synthetic routes. To form the desired metal complexes, naphthalene or modified diamine precursors were treated with stoichiometric or excess 2,4-di-*tert*-butyl-6-(chloro-methyl)phenol in the presence of triethylamine. Recrystallization methods and column chromatography (using n-hexanes and ethyl acetate solvent mixtures) were used to purify the products. Standard Schlenk and glove box techniques were used when synthesizing air-sensitive precursors. The isolated tripodal ligands were treated with one equivalent of anhydrous salts of M(III) chlorides, where M = Ga, Fe to isolate the subsequent metal complexes. Sodium methoxide was used as the base in these reactions. The ligands and resulted complexes were characterized by ^{1}H-NMR; IR; UV-visible spectroscopic methods; high resolution ESI/APCI mass spectrometry; and CHN combustion analysis. The general synthetic pathway to obtain tripodal ligands and the respective metal complexes is shown in **Scheme 3.2**.

Another factor that needed to be addressed was the amine and imine conversions of compounds and how these conversions affect the redox, amphiphilic, and electronic properties of metal complexes. Upon running reactions under aerobic or anaerobic conditions, the amine/imine conversions of the resulting compounds were affected. The amine version of complexes can be isolated under inert conditions and the imine version can be isolated under aerobic conditions, and will result in the C=N bond formation at the C—N bond of the amine nitrogen in the coordinated ligand. This process has also been observed by Lanznaster *et. al.*[15] To carry out these studies, using **[H₃L¹]**-**[H₃L⁴]** ligands, four new gallium(III) complexes and three new iron(III) complexes, **1**-**7**, were synthesized.
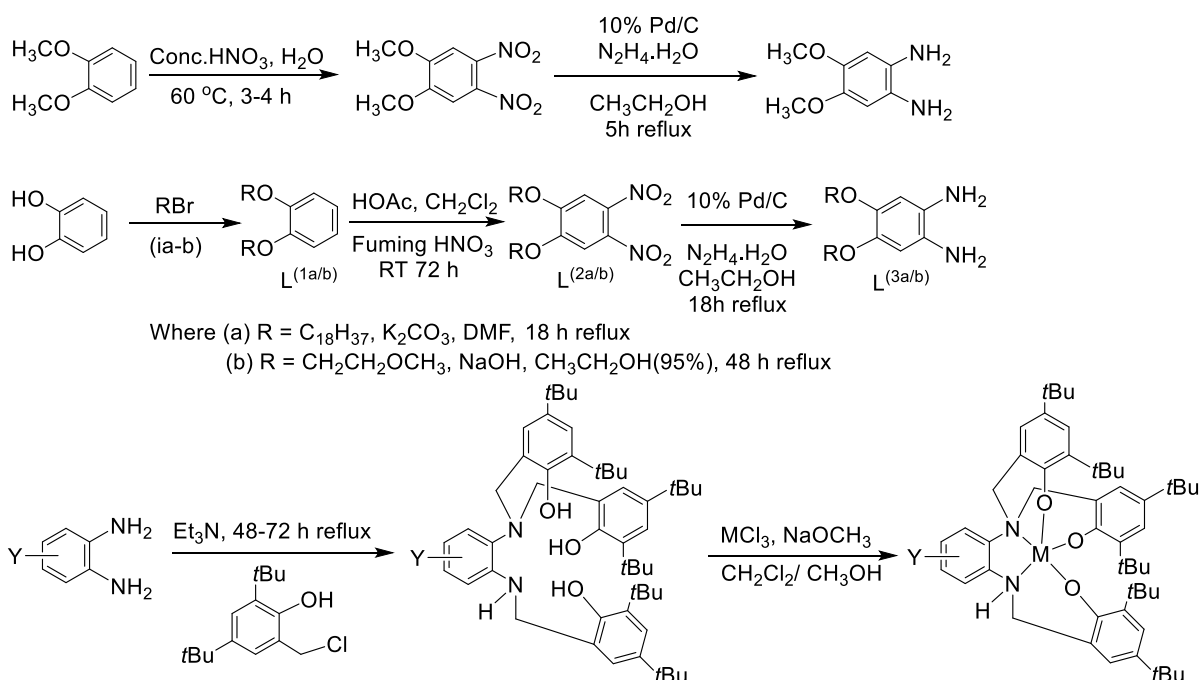
Scheme 3.2. Synthesis of ligands and trivalent metal complexes.

High resolution mass spectral data (positive ion mode) of metal complexes showed dominant peak clusters for their [M+H⁺] molecular ion peak (**Figure 3.1**). The difference between experimental and simulated data was found to be less than ±4 ppm. According to the observed data, peak positions and isotopic distribution patterns were well-approved with the simulated data (continuum) and also in good agreement with the calculated data. To gain a better understanding about the structural information such as functional groups of ligands and complexes, infrared (IR) spectroscopy was used. IR data showed prominent peaks for C—H stretching vibrations including symmetric and asymmetric modes at ~ 2800-3000 cm^{-1} for the ligands and their metal complexes. In ligands **[H₃L^1]-[H₃L^4]** the phenolic O—H stretching vibration was appeared as a sharp peak at ~ 3615 cm^{-1}. The aromatic C=C stretching bands were observed at ~ 1610 cm^{-1} and 1515 cm^{-1} for all the compounds. The N—H stretching

vibrations belonging to ligands appeared at ~ 3350 cm^{-1} and during metal complex formation it shifted to ~ 3200 cm^{-1}. Some complexes showed the C—O—C alkyl aryl stretching vibration at ~ 1275 cm^{-1}.[17,18]
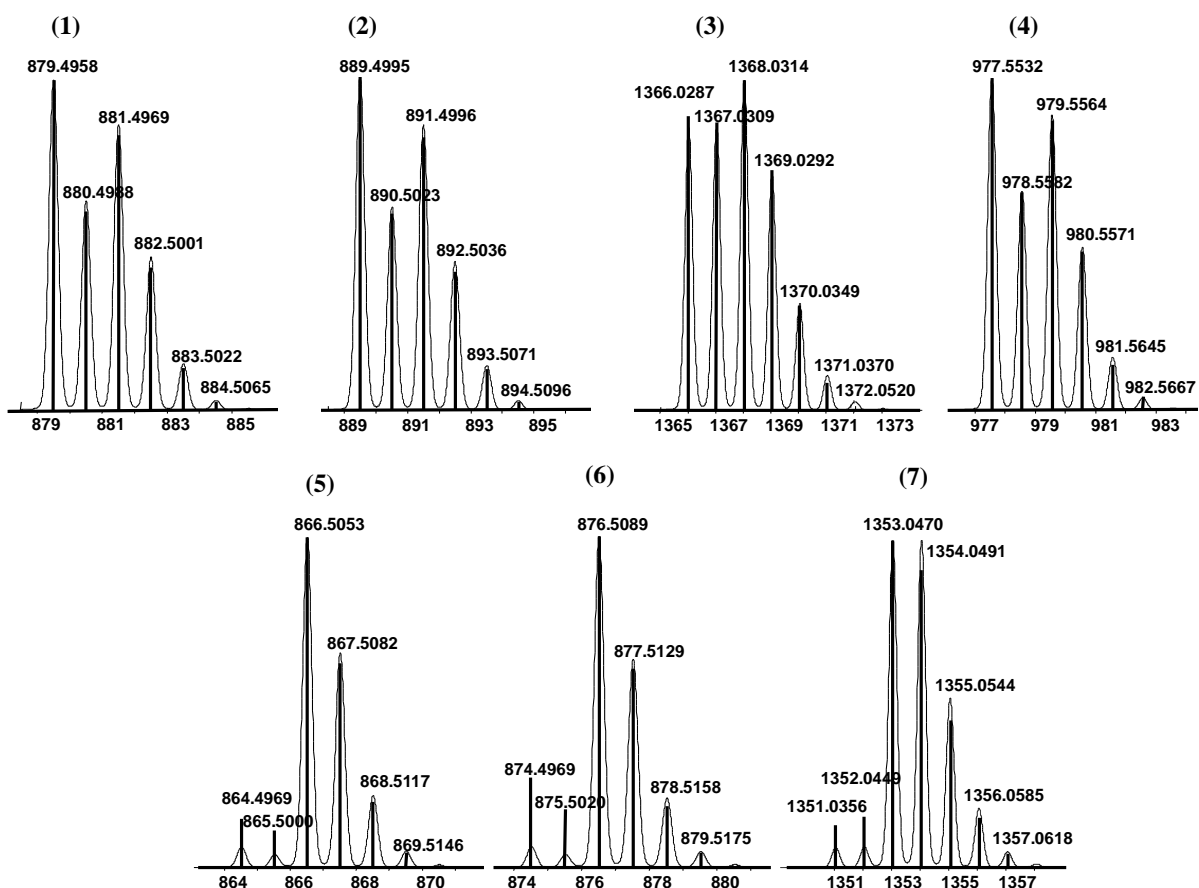
Figure 3.1. ESI (positive) peak clusters of [M+H$^+$] for metal complexes **1**-**7**. The relative abundance axis is not shown for clarity.

3.3.2 Molecular Structures

Partially solved crystal structures were attained for complexes **2** and **6** (**Figure 3.2**), and therefore bond lengths and bond angles of these structures are not discussed herein.

Nevertheless, we can depict some useful information about the coordination environment, structure, and the identity of the ligand using these structures. According to the observed data, the N1 has a single phenolate appended arm and the N2 has occupied two of these groups. Two nitrogen atoms and three phenolate moieties have been coordinated to the central metal atom in a pentacoordinated fashion as observed for other species with similar coordination environments.[9,16] Attempts to grow crystals, suitable for X-ray analysis, of other metal complexes were unsuccessful.

Ga^{III}L^2 **Fe^{III}L^2**
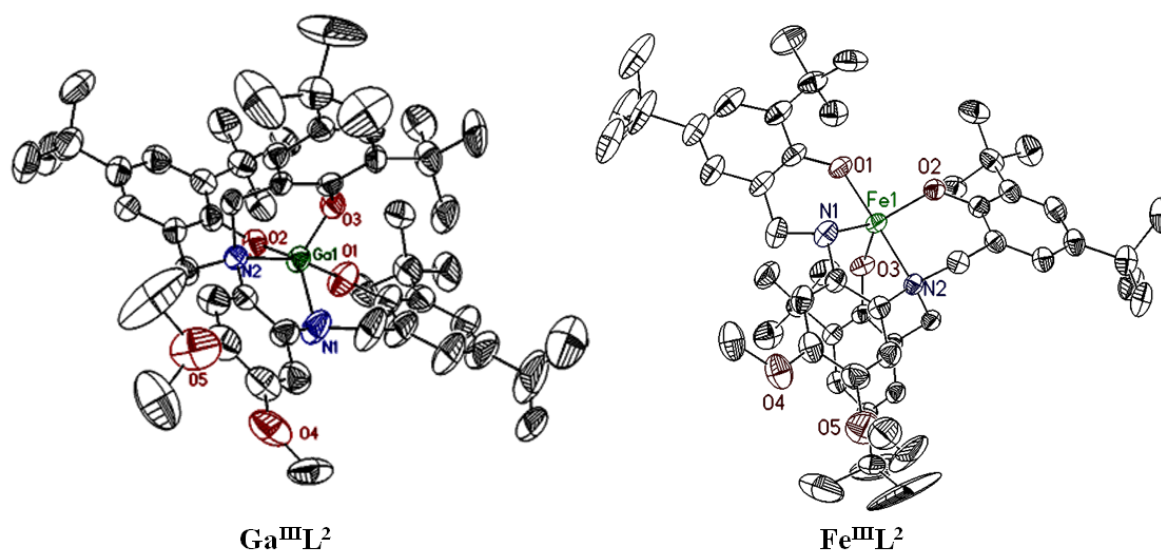
Figure 3.2. X-ray structure data for complexes **2** and **6**.

3.3.3 Electronic Spectral Properties

UV-visible spectra of ligands [**H$_3$L^1**]-[**H$_3$L^4**], were measured in dichloromethane. The uncoordinated ligands showed two absorption maxima in the UV region of the spectra. Ligand [**H$_3$L^1**] showed absorptions at 277 nm (ε, ~ 26600 L•mol^{-1}•cm^{-1}) and 341 nm (ε, ~ 6300 L•mol^{-1}•cm^{-1}), and the other three ligands showed consistent data with one another

including an intense band at ~ 285 nm and a shoulder band at ~ 300 nm, respectively (**Figure 3.3** and **Table 3.1**). These bands can be attributed to be $\pi \to \pi^*$ electronic transitions.[19]
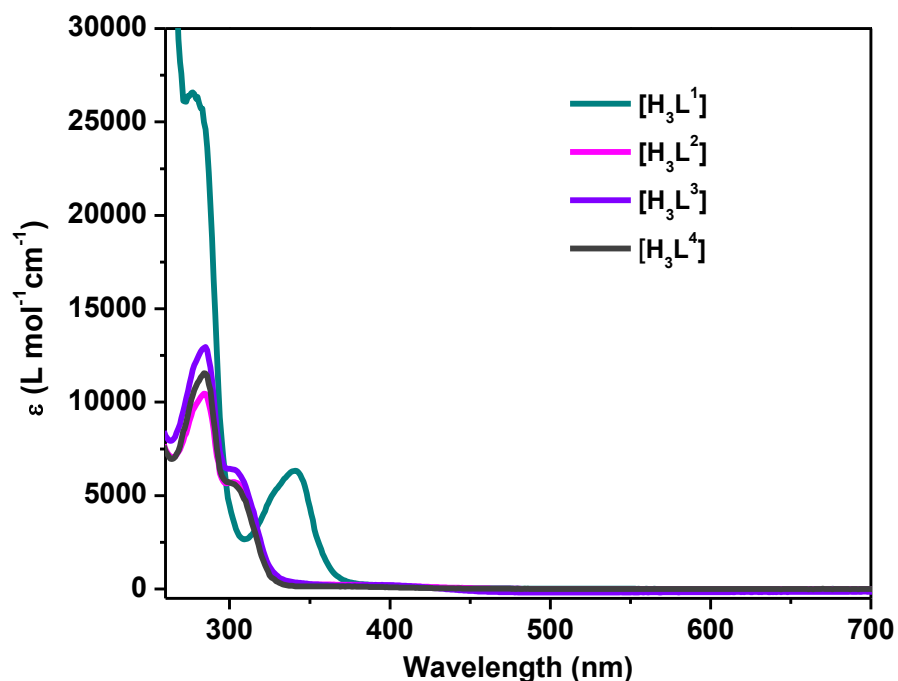
Figure 3.3. UV-visible spectra for ligands $[H_3L^1]$-$[H_3L^4]$ in 1.0×10^{-4} mol•L^{-1} dichloromethane solutions.

Compound	λ_{max}(nm), ε (L•mol^{-1}•cm^{-1}) (CH_2Cl_2)
$[H_3L^1]$	277 (26578), 341 (6330)
$[H_3L^2]$	284 (10453), 303 (5721)
$[H_3L^3]$	285 (12949), 302 (6407)
$[H_3L^4]$	284 (11553), 302 (5642)

Table 3.1. UV-visible spectroscopic data for ligands $[H_3L^1]$-$[H_3L^4]$ in 1.0×10^{-4} mol•L^{-1} dichloromethane solutions.

Gallium(III) complexes showed intense bands in the near-UV region, at ~290 nm. These spectra are presented in **Figure 3.4a** and **Table 3.2** indicating their relevant λ_{max} values. Complex **1** showed a higher molar absorptivity (ε of ~ 22250 L•mol^{-1}•cm^{-1}) when compared to that of complexes **2**-**4** (ε value of ~13350 L•mol^{-1}•cm^{-1}) due to the presence of conjugated naphthalene moiety. These transitions can be attributed to ligand-based $\pi \rightarrow \pi^*$ transitions. In gallium(III) complexes, the metal ion has filled d-orbitals. Therefore, gallium(III) complexes do not exhibit any ligand to metal charge transfer (LMCT) transitions in the UV-visible spectra.

Iron(III) complexes showed remarkable features related to the presence of iron(III) metal, when compared to respective gallium(III) complexes. Iron(III) complexes, **5-7**, showed consistent spectral features to one another. Obtained UV-visible spectra are shown in **Figure 3.4b** and the spectral data are given in **Table 3.2**. Iron(III) complexes, **5-7**, showed three well-pronounced absorption bands in the respective UV-visible spectra. These complexes showed intense broad absorption bands in the visible region, at ~ 465 nm with ε ranging from ~ 5000 to 8000 L•mol^{-1}•cm^{-1}. These bands can be assigned as phenolate to iron(III) charge transfer transition[20] originating from p_π orbital of the phenolate oxygens to $d_{\pi*}$ of the metal center. Besides these bands, there were another two absorption bands present in the near-UV region. The band at ~ 325 nm with ε values ranging from ~ 9000 to 15000 L•mol^{-1}•cm^{-1} can be designated to another LMCT transition occurring from phenolate-based p_π orbitals to $d_{\sigma*}$ of the iron(III) metal center. The band appearing at ~ 285 nm can be attributed to be ligand-based $\pi \rightarrow \pi^*$ electronic transitions. All the assignments are well-matched with the electronic spectral assignments presented in the literature for similar

compounds.[16,21,22] These assignments were further studied by spectroelectrochemical experiments and will be discussed in a later section.
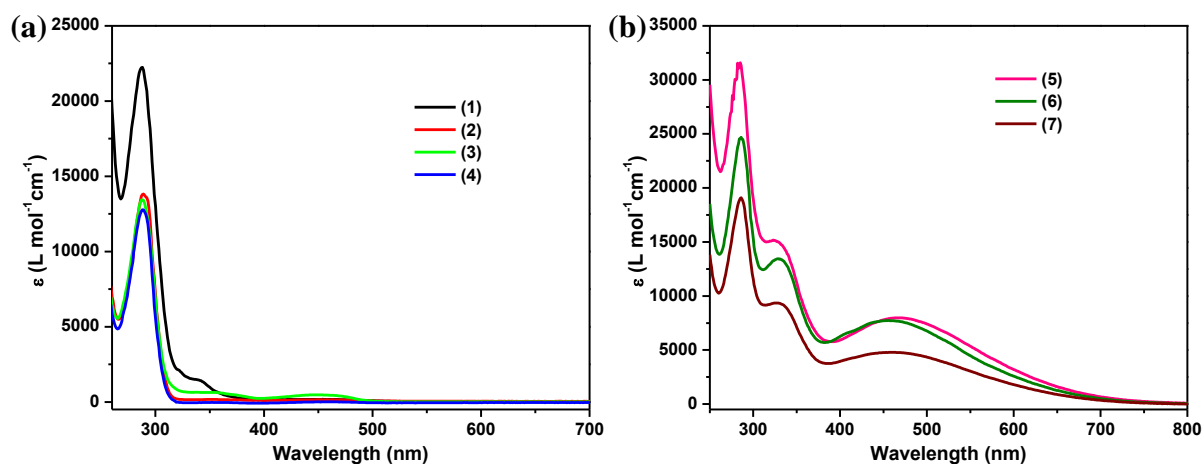
Figure 3.4. UV-visible spectra for (a) gallium(III) complexes, **1**-**4** and (b) iron(III) complexes **5-7** in 1.0×10^{-4} mol•L^{-1} dichloromethane solutions.

Compound	λ_{max} (nm), ε (L•mol^{-1}•cm^{-1})
(1)	288 (22246), 342 (1407)
(2)	289 (13824)
(3)	288 (13442)
(4)	288 (12779)
(5)	285 (31580), 323 (15178), 465 (7981)
(6)	286 (24680), 328 (13441), 461 (7711)
(7)	286 (19104), 329 (9353), 463 (4788)

Table 3.2. UV-visible spectroscopic data for complexes **1-7** in 1.0×10^{-4} mol•L^{-1} dichloromethane solutions.

3.3.4 Redox Properties

The cyclic voltammetry experiments of all the ligands and metal complexes were measured in dichloromethane using TBAPF$_6$ as the supporting electrolyte and the potential values were recorded versus the Fc$^+$/Fc couple. The ligands **[H$_3$L^1]**-**[H$_3$L^4]** showed two redox processes and one ill-defined process. Ligand **[H$_3$L^1]** showed two quasi-reversible processes at ~ 0.46 V with a peak potential separation (ΔE_p) of ~ 0.13 V and another at ~ 0.84 V with a ΔE_p of ~ 0.19 V. The other three ligands showed redox processes ~ 0.1 V and ~ 0.5 V. These two processes can be assigned as phenolate/phenoxyl redox couples and there were no cathodic processes associated with any of the ligands. The cyclic voltammograms of the ligands and their potential values (E$_{½}$ and ΔE_p) are given in **Figure 3.5** and **Table 3.3**, respectively.

	E$_{½}$, (ΔE_p) (V)	E$_{½}$, (ΔE_p) (V)
[H$_3$L^1]	0.457 (0.127)	0.843 (0.188)
[H$_3$L^2]	0.053 (0.11)	0.51 (0.247)
[H$_3$L^3]	0.069 (0.12)	0.49 (0.238)
[H$_3$L^4]	0.118 (0.112)	0.594 (0.16)

Table 3.3. Cyclic voltammetry data for ligands **[H$_3$L^1]**-**[H$_3$L^4]**.
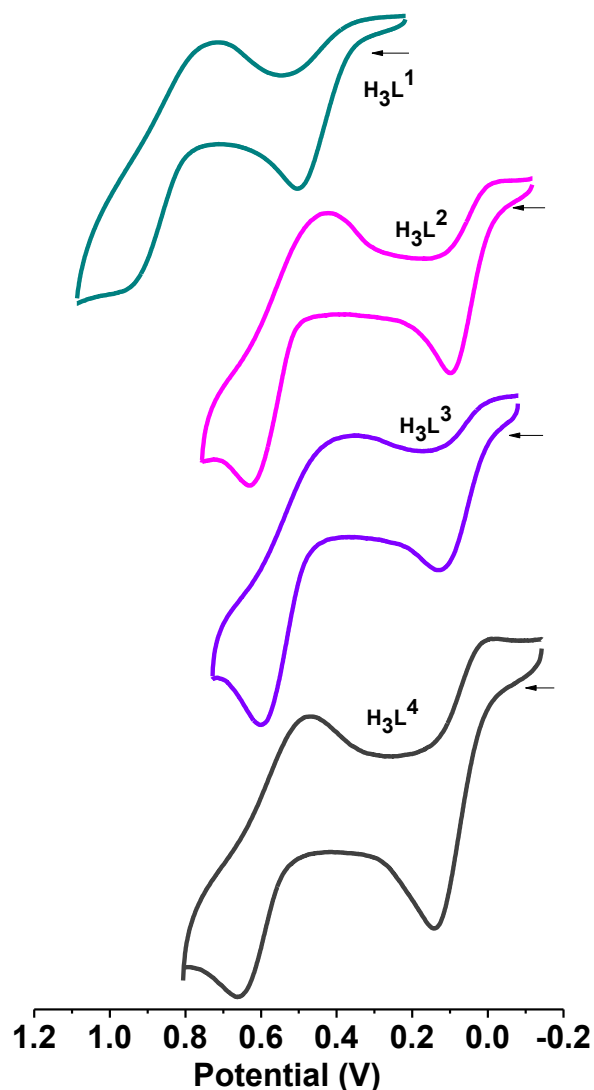
Figure 3.5. Cyclic voltammograms for ligands $[\mathbf{H_3L^1}]$-$[\mathbf{H_3L^4}]$ in 1.0×10^{-3} mol·L^{-1} dichloromethane solutions.

The cyclic voltammograms of the gallium complexes **1**-**4** also showed fairly similar characteristics to that of the respective ligands. Obtained cyclic voltammograms and their $E_{1/2}$ and ΔE_p values are shown in **Figure 3.6** and **Table 3.4**, respectively. The gallium(III) complexes showed consistent cyclic voltammograms with two anodic redox processes. There were no cathodic processes involved with the metal reduction. The reaction of gallium(III)

ions with $[N_2O_3]$-containing ligands, will result in stable neutral species with three phenolate moieties attached to the metal ion. The gallium(III) ion has filled *d*-orbitals and needs high energy (1480 kcal/mol) to break this stable configuration to form a gallium(IV) species. Therefore, gallium(III) ion behaves as an redox innocent metal. The first oxidative process for complex **1** was found to be at ~ 0.5 V (ΔE_p = ~ 0.12 V) while complexes **2**, **3**, and **4** showed the first anodic processes at ~ 0.47 (ΔE_p = ~ 0.11 V), 0.46 (ΔE_p = ~ 0.1 V), and 0.43 V (ΔE_p = ~ 0.17 V), respectively. The second anodic processes were found at ~ 0.86 V (ΔE_p = ~0.21 V) for complex **1** and at ~ 0.81 V with ΔE_p values of 0.19, 0.16, and 0.29 V for complexes **2**-**4**, respectively. According to the observed ΔE_p values, the first anodic process was quasi-reversible, and the second process was irreversible. The second anodic process found at ≥ 0.8 V can be assigned as a two electron process while the first anodic process is a one electron process. A similar behavior has been observed by other gallium(III) species under similar environments with 1:2 electron ratios.[9] According to the literature, these redox processes can be assigned as ligand-based phenolate/phenoxyl redox couples.[9,23,24]

	$E_{1/2}$, (ΔE) (V)	$E_{1/2}$, (ΔE) (V)
(1)	0.503 (0.118)	0.863 (0.210)
(2)	0.465 (0.108)	0.810 (0.186)
(3)	0.457 (0.097)	0.813 (0.158)
(4)	0.428 (0.173)	0.807 (0.291)

Table 3.4. Cyclic voltammetry data for gallium(III) complexes **1**-**4**.
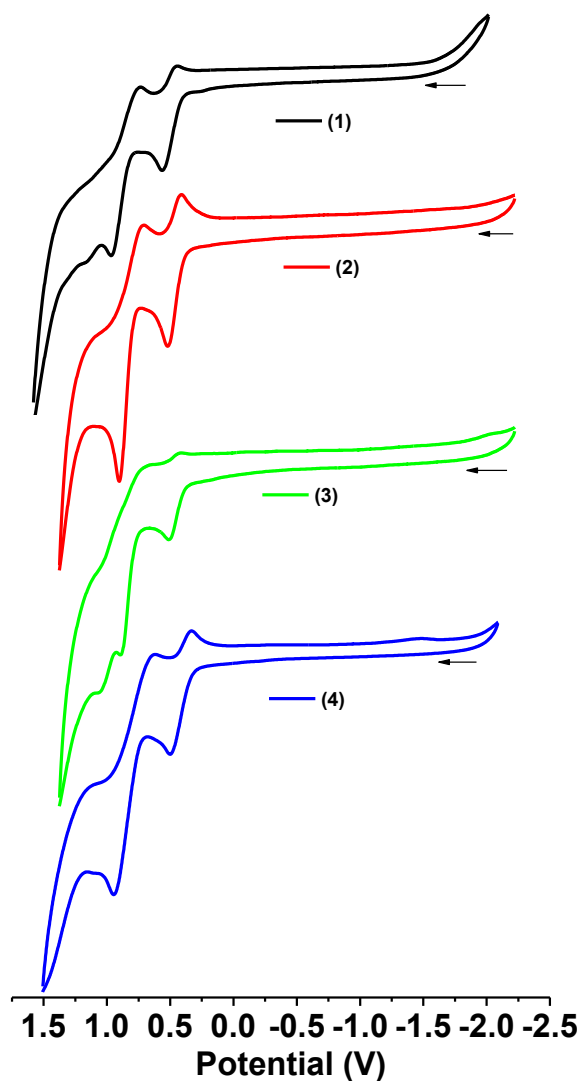
Figure 3.6. Cyclic voltammograms for gallium(III) complexes **1**-**4** in 1.0×10^{-3} mol·L^{-1} dichloromethane solutions.

Cyclic voltammetry measurements for iron(III) complexes are shown in **Figure 3.7**, and corresponding $E_{1/2}$ and ΔE_p values are tabulated in **Table 3.5**. The iron complexes showed one cathodic peak and three anodic peaks in their cyclic voltammograms. The quasi-reversible single electron cathodic processes found at ~ -1.39, -1.41, and -1.46 V with ΔE_p values of ~ 0.13, 0.15, and 0.11 V for complexes **5**, **6**, and **7** were allocated to be Fe^{III}/Fe^{II}

redox couple, respectively. The first single electron anodic processes found at ~ 0.5 V with ΔE_p values of ~ 0.1 V for complexes, **5**-**7** can attributed to be ligand assisted, phenolate/phenoxyl redox couples. The second phenolate/phenoxyl redox couples were found at ~ 0.74 V with ΔE_p of ~ 0.1 V and the third anodic processes were found at ~ 0.96 V with ΔE_p of ~ 0.2 V for all the iron(III) complexes. In complexes **5**-**7**, the first two ligand centered phenolate/ phenoxyl redox processes were found to be quasi-reversible while the third process was irreversible. When comparing the $E_{1/2}$ values of complexes **5**-**7** with literature reported iron(III) complexes with similar coordination environments it shows a good agreement between them.[9,15,16]

According to the literature, hexacoordinated iron(III) complexes with [N$_3$O$_3$]-type coordination environments exhibit the Fe^{III}/Fe^{II} reduction redox couple at ~ -1.8 V.[19,20] Nonetheless, iron(III) complexes that were discussed in this section hold a [N$_2$O$_3$]-type coordination environment around the Fe^{III} metal center and showed a potential value of ~ -1.4 V. The discrepancy between these potential values can be correlated to pentacoordinated Fe^{III} with three coordinated phenolates and hexacoordinated Fe^{III} with three coordinated phenolates. In the former case, it is easier to reduce when compared to the latter due to the lower electron density present around the metal center. This is another strong evidence to demonstrate the asymmetric pentacoordinate geometry around the metal center in complexes **5**-**7**.

An important factor that needs to be addressed in redox responsive materials is the reversibility and the cyclability of the redox processes. According to the literature, consecutive oxidations and reductions can be used to write and read information.[25,26] Iron(III) complexes that were discussed in this chapter showed redox reversible properties.

After assessing the reversibility of redox processes, experiments were carried out to assess the cyclability of the redox processes (using iron(III) and gallium(III) complexes), by cycling the cathodic and first anodic processes for thirty to fifty times. These complexes showed insignificant amounts of decomposition during the course of experiments, and suggested that iron(III) and gallium(III) complexes form stable radical species during the electrochemical experiments with minor decompositions, making them suitable candidates for redox responsive material.
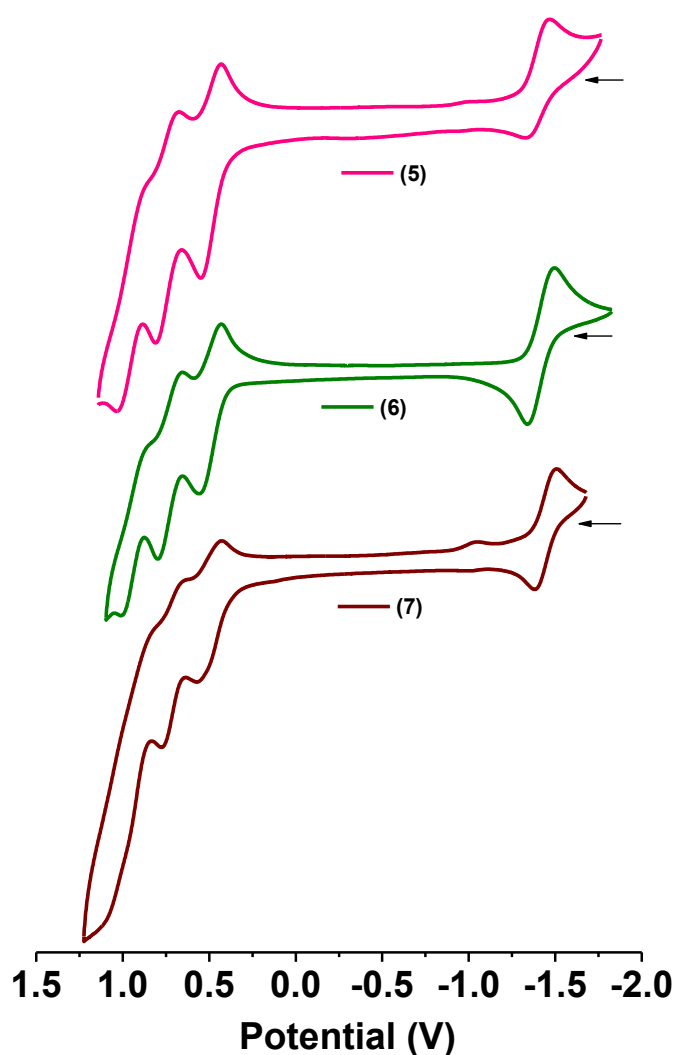
Figure 3.7. Cyclic voltammograms for iron(III) complexes **5**-**7** in 1.0×10^{-3} mol·L^{-1} dichloromethane solutions.

	$E_{1/2}$, (ΔE_p) (V) $\lvert I_{pa}/I_{pc} \rvert$	$E_{1/2}$, (ΔE_p) (V) $\lvert I_{pa}/I_{pc} \rvert$	$E_{1/2}$, (ΔE_p) (V)	$E_{1/2}$, (ΔE_p) (V)
(5)	-1.394 (0.130) $\lvert 0.48 \rvert$	0.495 (0.116) $\lvert 1.36 \rvert$	0.756 (0.114)	0.960 (0.154)
(6)	-1.409 (0.146) $\lvert 0.81 \rvert$	0.514 (0.128) $\lvert 1.83 \rvert$	0.748 (0.124)	0.959 (0.138)
(7)	-1.455 (0.108) $\lvert 0.64 \rvert$	0.512 (0.106) $\lvert 2.08 \rvert$	0.712 (0.110)	0.964 (0.223)

Table 3.5. Cyclic voltammetry data for iron(III) complexes **5**-**7**.

3.3.5 Spectroelectrochemical Properties

Spectroelectrochemical experiments were conducted to distinguish the absorption bands associated with respective electronic transitions. Herein, oxidation and reduction processes of complex **6** were studied to observe the associated spectral changes. Results obtained during spectroelectrochemical experiments for complex **6** are shown in **Figure 3.8**. Experiments were performed in dichloromethane using fixed potential method under ambient conditions and $TBAPF_6$ was used as the electrolyte.

Upon applying the respective potential value for complex **6** (0.894 V *vs*. the Fc^+/Fc), charge transfer bands appearing at ~ 460 nm due to the electronic transition from p_π (phenolate) to $d_{\pi*}$ of the metal center reduced in intensity and new bands started to appear in the region of ~ 715 nm with an isosbestic point observed at 605 nm. During the oxidation

process, Fe^{III}-phenolate will transform in to a Fe^{III}-phenoxyl radical species and, because there are three phenolate groups, each of these transformations will occur at different applied potential values. During these transformations the LMCT band occurring from p_π (phenolate) to $d_{\pi*}$ of the metal becomes weaker due to the lower charge density around the metal center. Concurrently, there could be charge transfer transition happening between the phenolate and phenoxyl moieties. In complex **6**, the increase in intensities at ~ 715 nm could be due to the appearance of this new phenolate to phenoxyl charge transfer band.[27,28,29] The reduction process of complex **6** (at -1.778 V *vs*. the Fc$^+$/Fc) showed that the lower energy band appearing at ~ 460 nm, due to the electronic transition from p_π (phenolate) to $d_{\pi*}$ of the iron(III) species, started to decrease in intensity. Also within this process, the absorption maxima showed a slight blue shift. The reason for the LMCT band to decrease in intensity is due to the reduction of Fe^{III} in to Fe^{II}, making the ligand to metal charge transfer transitions unfeasible.
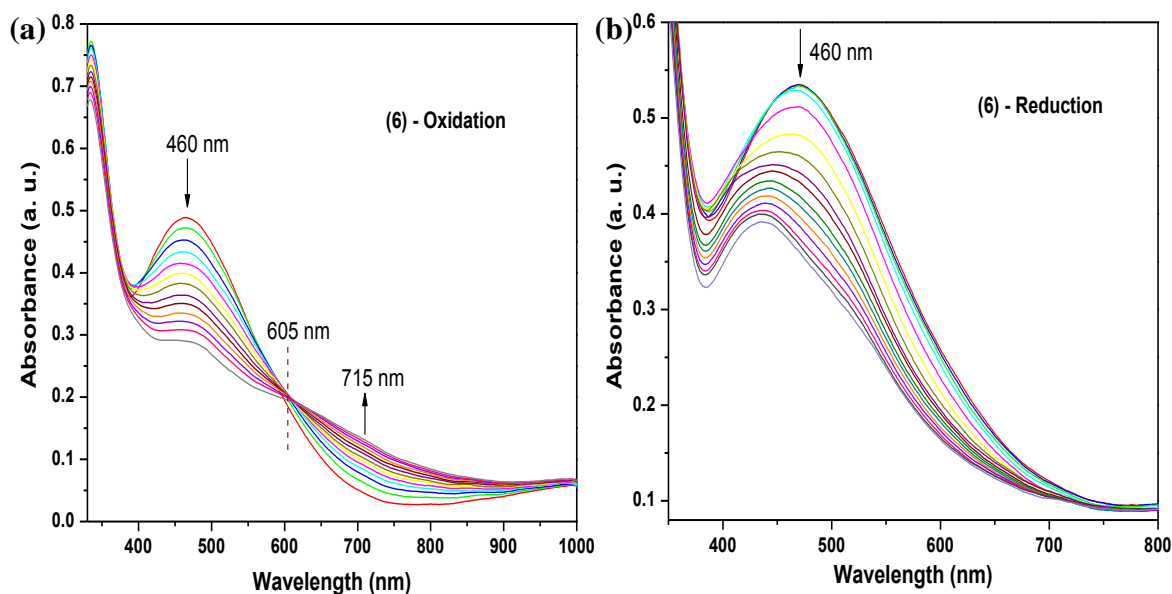
Figure 3.8. Electronic spectral changes observed (a) during oxidation and (b) during reduction for complex **6** under fixed potential conditions.

3.3.6 Electron Paramagnetic Resonance Spectroscopy Data

To acquire information regarding the oxidation state, spin state, and geometry of iron complexes, EPR measurements were carried out in dichloromethane solutions for complexes **6** and **7** at 110 K. Liquid nitrogen was used as the coolant during the cause of experiments. The parent species of complexes, **6** and **7** showed prominent signals at g = 4.23 and g = 4.28, respectively, as shown in **Figure 3.9**. These data resembled high spin iron complexes in their +3 oxidation state with D much larger than 0.3 cm^{-1} and E approximately D/3. The data also suggested that their ligand fields are highly distorted with no higher symmetry elements have been observed. This analysis further supported the presence of pentacoordinate geometry around the metal centers. Similar results were observed for literature reported pentacoordinate high spin iron(III) complexes.[9,16]
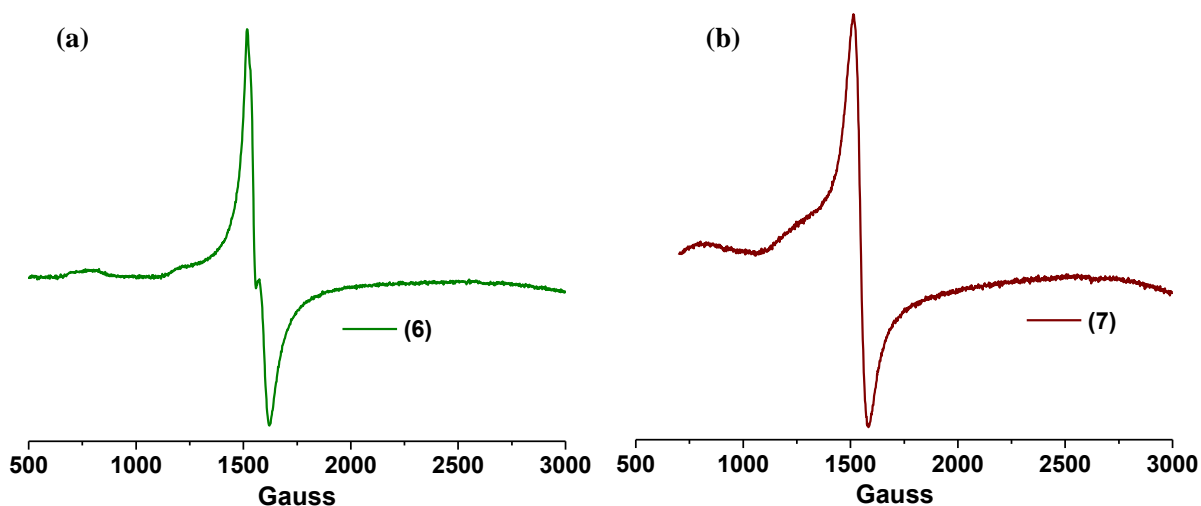
Figure 3.9. X-band EPR spectra of 1.0×10^{-3} mol•L^{-1} frozen dichloromethane solutions for (a) complex **6** and (b) complex **7** at 110 K.

3.3.7 Isothermal Compression Data

One of the main goals of this research was to design and synthesize redox active metal complexes, which can be deposited onto solid surfaces for device fabrication. Therefore, upon attaining the electrochemical properties, the film formation properties were assessed using Langmuir-Blodgett (LB) method. The LB method is used to deposit surfactant-like molecules. Therefore, hydrophilic and hydrophobic counterparts were incorporated during the design of molecules, to attain a good balance between the hydrophilic and hydrophobic characteristics to facilitate film formation properties.[30] Film formation properties of gallium(III) complexes **1**-**4** and iron(III) complexes **5**-**7** were evaluated by recording their compression isotherms and the quality of Langmuir films at the air/water interface were observed with Brewster angle microscopy. The compression isotherms and the Brewster angle micrographs obtained for gallium(III) and iron(III) complexes are presented in **Figure 3.10** and **Figure 3.11**, respectively. Important characteristics related to compression isotherms of metal complexes are given in **Table 3.6**. Ligands also presented good film formation ability at the air/water interface. However, previous studies exposed that ligands alone will not form homogeneous LB films due to disordered packing topologies.[31] Therefore, the use of coordination compounds is important to form uniform LB films. Such metal coordinated systems are known as metallosurfactants. Complexes **1**, **2**, and **4**-**6** exhibited areas of interaction ~ 180 $Å^2$ at the air/water interface while the complexes **3** and **7** showed the highest area of interaction as well as the highest critical area of < 250 $Å^2$. Complexes **3** and **7** contained alkoxy chains with eighteen carbons at the fourth and fifth positions of the phenylenediamine moiety. The free rotation of these chains around the molecule and the repulsion forces between hydrophobic carbon chains may

lead to the observed higher area of interaction before the compression and for the critical area of complexes **3** and **7**. Classical amphiphiles and surfactants contain long alkyl chains in their structure to obtain enhanced film formation properties. However, the alkoxy chain containing complexes (**3** and **7**) showed very poor performances at the air/water interface and behaved as hydrophobes. This behavior could be due to the presence of *tert*-butyl groups along with the alkoxy chains, which elevates the hydrophobic nature of the overall molecule. Complexes **1**, **2**, and **4-6** displayed critical areas of 100, 114, 96, 123, and 121 $Å^2$, respectively, and exhibited collapse pressures ~ 40-50 mN/m. In general, the metal complexes with methoxy and methoxyethoxy substituents exhibited better film formation ability at the air/water interface with higher collapse pressures when compared to other systems. This data indicate that the introduction of polar groups such as oxygen rich moieties to ligand structures help to balance the hydrophobic and hydrophilic characteristics of the overall molecule.

According to Brewster angle micrographs, complexes **1**, **2**, and **4-6** formed homogeneous, well-ordered films at the air/water interface at the steepest region of their compression isotherms. The above mentioned complexes also showed a clear collapse in the BAM images, where it started to show a decrease in the slope of the isotherms. All of the gallium(III) and iron(III) complexes showed a constant pressure collapse mechanism irrespective of the structure of the molecule. The observed data exposed comparable critical areas of ~ 100 $Å^2$ for gallium(III) complexes and ~ 120 $Å^2$ for iron(III) complexes, respectively. Because these complexes have comparable head groups with *tert*-butyl rich metal coordinated moieties, we can expect them to demonstrate similar footprints during the ordering of the monolayer. The LB film formation data of complexes **1**, **2**, and **4-6**, indicated

better film formation properties when compared to other metallosurfactants that were reported in the literature.[31]
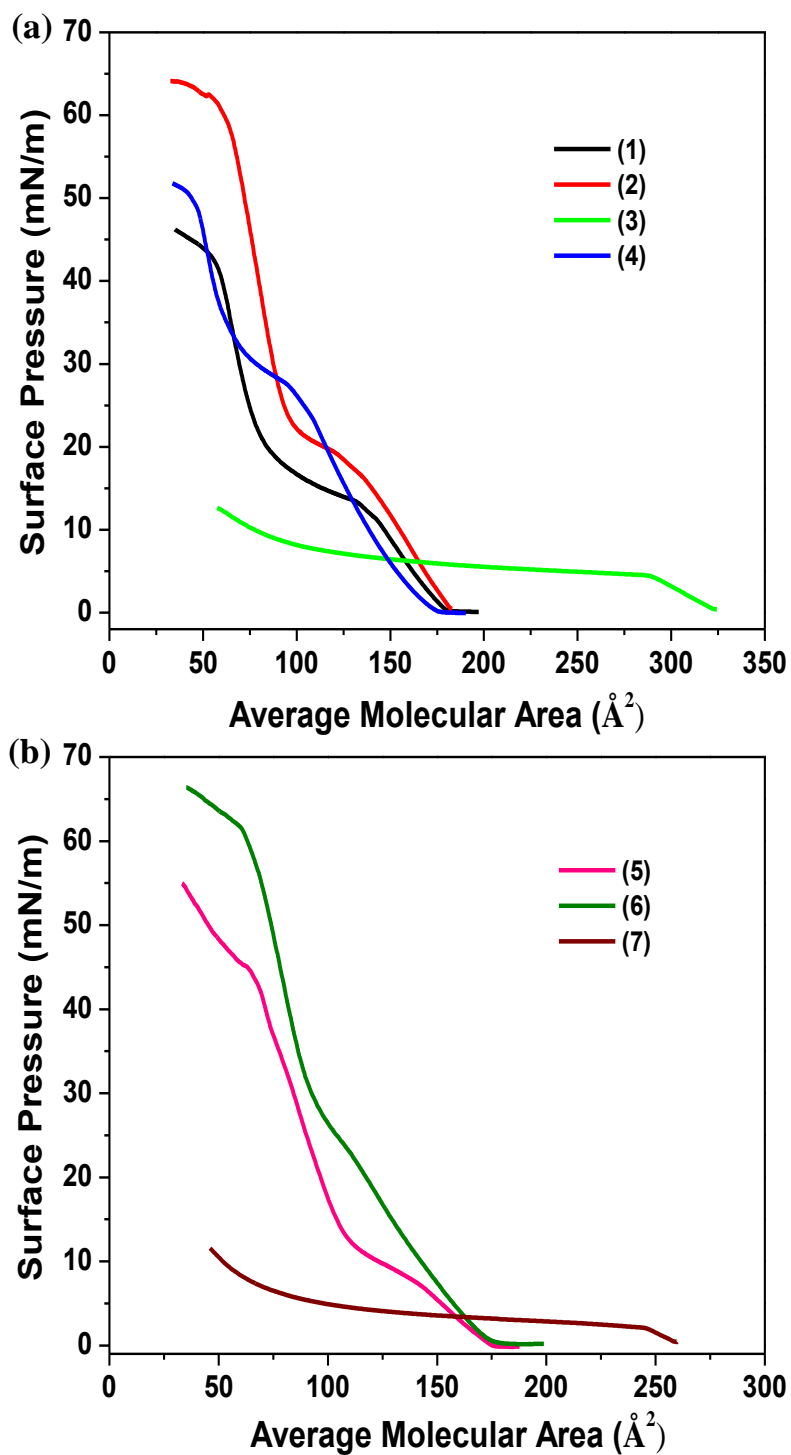
Figure 3.10. Isothermal compression data for (a) gallium(III) and (b) iron(III) complexes.
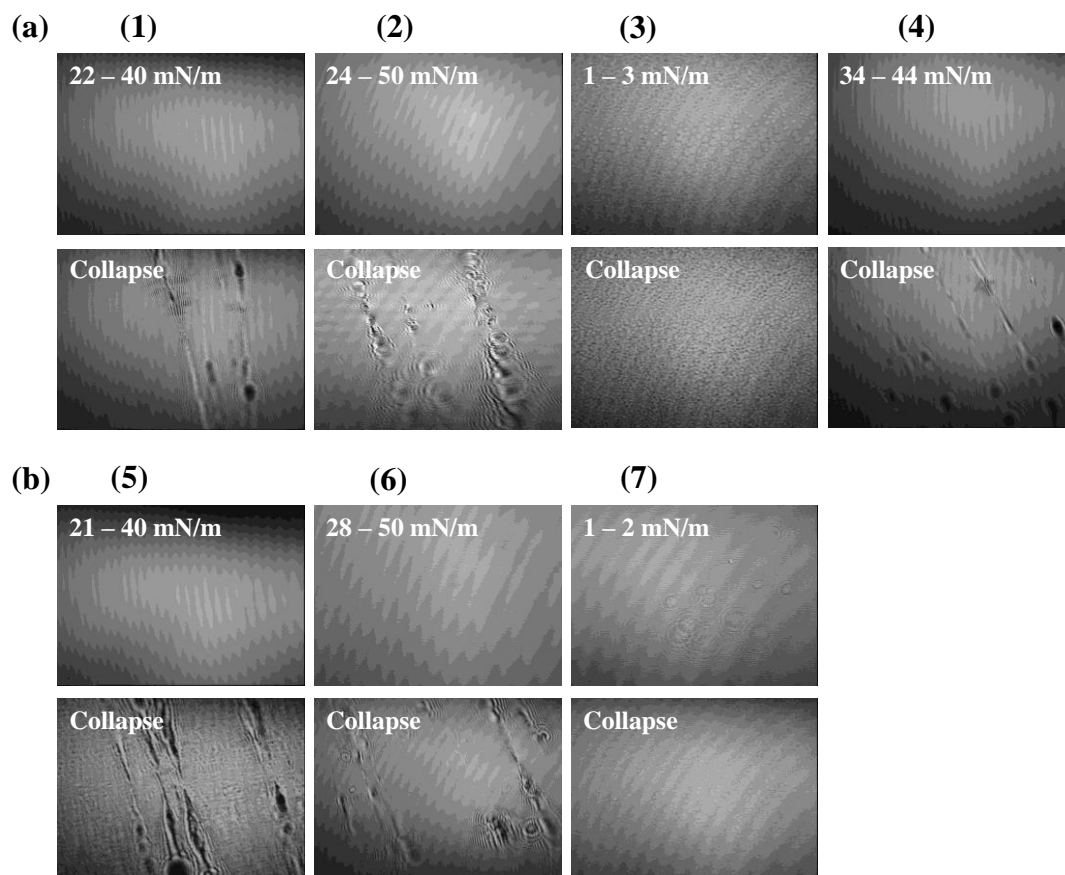
Figure 3.11. Brewster angle micrographs for (a) gallium(III) and (b) iron(III) complexes.

	(1)	**(2)**	**(3)**	**(4)**	**(5)**	**(6)**	**(7)**
Area of interaction (Å^2)	182	183	323	176	176	179	259
Phase transition pressure (mN/m)	12-20	17-23	-	26-32	7-13	22-28	-
Collapse pressure (mN/m)	42	50	4	45	42	50	2
Critical area (Å^2)	100	114	327	96	123	121	263

Table 3.6. Isothermal compression properties for complexes **1**-**7**.

3.3.8 Langmuir-Blodgett Film Characterization by UV-visible Spectroscopy

Redox-active coordination complexes, which can be organized into ordered films, are of special interest in molecular electronic field.[32] This section summarizes the UV-visible analysis of LB films of gallium(III) and iron(III) complexes.

To carry out the dipping experiment, a suitable surface pressure was identified by studying the compression isotherm and then, the LB films were deposited onto thoroughly cleaned glass substrates using y-type dipping[30] method (glass is a hydrophilic substrate). Complexes **2**, **5**, and **6** were considered for thin film characterization studies, since they showed good amphiphilic properties at the air/water interface. Fifty depositions were carried out for each of these complexes and they showed an average transfer ratio (TR) of close to unity. Complexes **2**, **5**, and **6** were deposited at surface pressures of 30, 21, and 30 mN/m, respectively. These multilayer films were held together by weak interactions such as the van der Waals forces. Complex **2** deposited on glass showed a yellow color while complexes **5** and **6** deposited on glass showed a strong red-brown color. UV-visible spectra of multilayer LB films were recorded and are shown in **Figure 3.12** in against their solution spectra. Furthermore, **Table 3.7** gives λ_{max} values, respectively. UV-visible spectroscopy of thin films gives information regarding the possible chromophore arrangements[33] that occurs during film ordering. Solid state UV-visible spectroscopy also gives information related to possible phase transitions, such as from liquid expanded state to a liquid crystalline state,[34] and molecular composition.

Observed UV-visible spectral data of complexes **2**, **5**, and **6**, LB film spectra did not exactly correlated with their solution spectra. They displayed different features > 300 nm with some similar features at lower wavelengths. According to the previous studies that were

carried out in our laboratory,[15] these changes indicated a possible imine conversion that occurs at the air/water interface for amine-based structures. Complex **2** showed the appearance of two new absorption maxima at 352 and 458 nm. Complexes **5** and **6** also showed the appearance of new bands at ~ 415 and 401 nm, respectively. These data indicate that amine complexes at the air/water interface undergo an oxidation at the amine nitogen of the tripodal ligand to form an azomethine moiety. Therefore, the bands observed in the visible region at ~ 350-600 nm correspond to a collection of charge transitions including intra-ligand charge transitions (originating from phenolate $p_\pi \rightarrow p_{\pi*}$ of the azomethine moiety) and MLCT transitions (originating from phenolate $p_\pi \rightarrow d_{\pi*}$ of the iron(III) center).

To investigate this phenomenon further, corresponding imine versions of iron(III) complexes, (**5'** and **6'**) were synthesized, isolated, and characterized (**Scheme 3.3**). Another experiment was also conducted by measuring the UV-visible spectra of complex **6** in 9:1 methanol/water solution at ambient conditions overtime. These experiments were assisted in identifying the spectral changes related to formation of imine-based complexes.
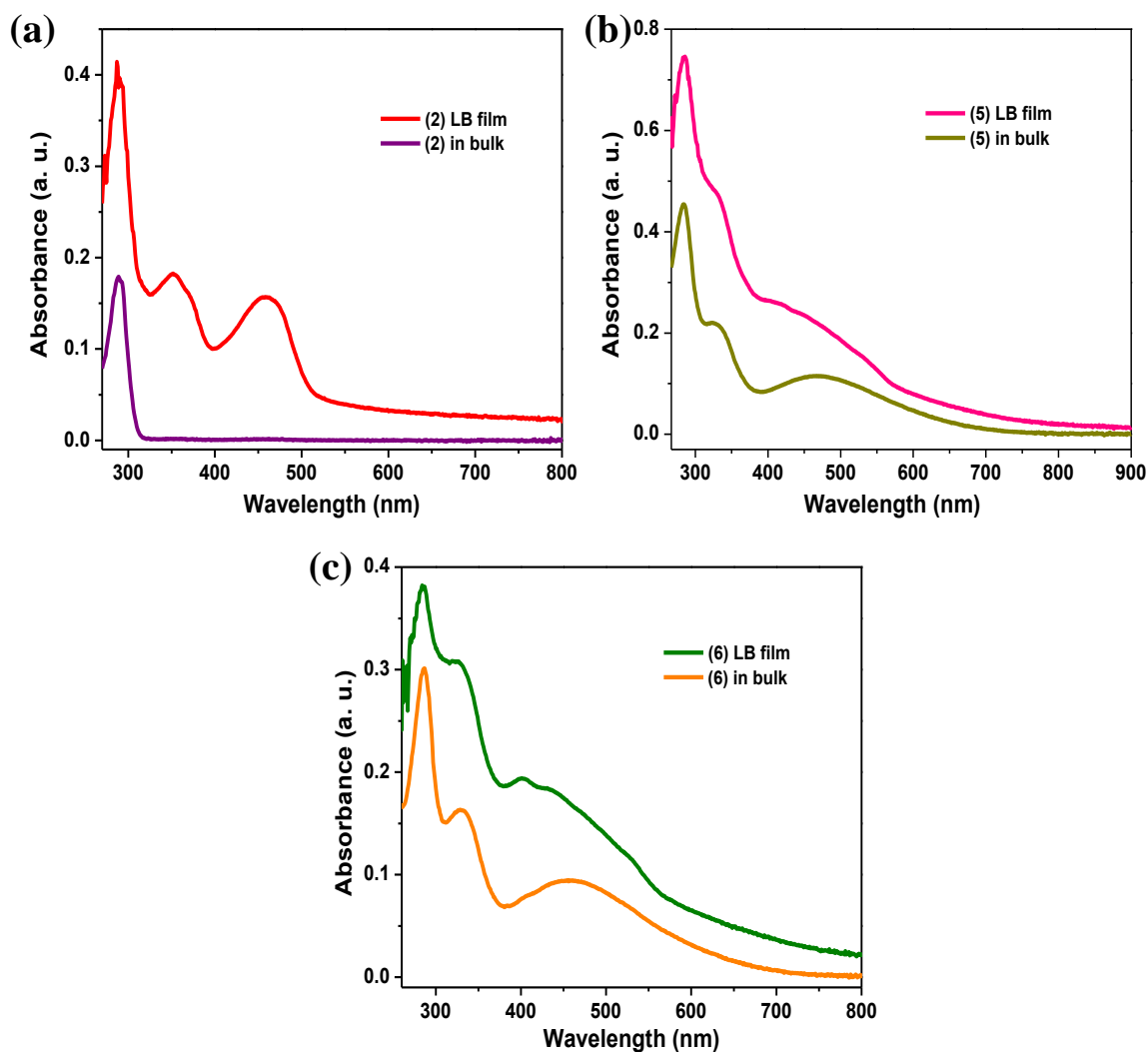
Figure 3.12. UV-visible spectra of multilayer LB films for (a) complex **2**, (b) complex **5**, and (c) complex **6** in comparison with 1.0×10^{-5} mol•L^{-1} dichloromethane solutions of respective metal complexes.

Compound	λ_{max}, nm
(2)	288, 352, 458
(5)	285, 333, ~ 415, ~ 465
(6)	284, 327, 401, ~ 440

Table 3.7. UV-visible spectroscopic data for multilayer LB films of complexes **2**, **5**, and **6**.

3.3.9 Study the Formation of Imine-based Complexes

The isolated imine form of iron(III) complexes are shown in **Scheme 3.3**. Complexes **5'** and **6'** were isolated and characterized using infrared spectroscopy, elemental analysis, and high resolution electrospray ionization mass spectrometry. In IR spectroscopy The N—H stretching vibrations of these complexes appeared around ~ 3200 cm^{-1}. These vibrations completely disappeared during the formation of imine-based complexes (**5'** and **6'**) and new bands have been appeared at ~ 1580 cm^{-1}. The appearance of this new band can be assigned to be C=N bond stretching vibration in the imine complexes.[17]
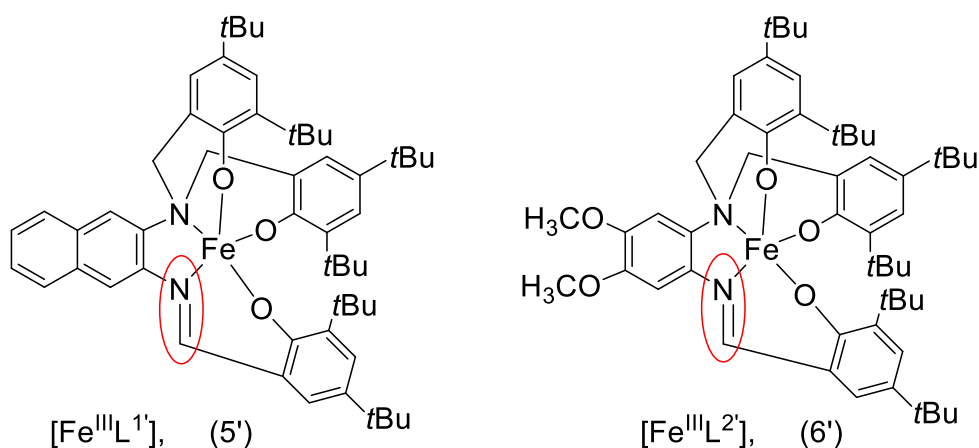
Scheme 3.3. The iron(III) imine complexes **5'** and **6'**.

Complex **5'** afforded dark brown crystals upon recrystallization in methanol and dichloromethane (1:2) solvent mixture at ambient conditions. Selected crystallographic data of complex **5'** are given in **Table 3.8**, **Table 3.9** and X-ray structural data is shown in **Figure 3.13**. In the complex **5',** three phenolate oxygen atoms, the imine N1, and the amine N2 nitrogen atoms have been coordinated to the iron(III) center in a pentacoordinate fashion, forming a neutral species. Bond lengths of complex **5'** showed N1-C7 bond distance of 1.309 Å, while the N2-C25 and N2-C18 showed 1.503 Å and 1.493 Å, respectively. These data

clearly indicated that the N1-C7 bond has a double bond character while N2-C25 and N2-C18 bonds carry a single bond character.

The calculated τ value for complex **5'** was found to be 0.686 and it depicts distorted trigonal bipyramidal geometry around the metal ion. According to the X-ray structure data of complex **5'**, the O2 and O3 phenolate oxygens were axially coordinated to the central atom while N1, N2, and O1 atoms were in the same plane as iron, and were coordinated to the central atom forming a distorted trigonal bipyramidal geometry as shown in **Figure 3.13**.

[Fe^{III}L^{1}'],   (5')
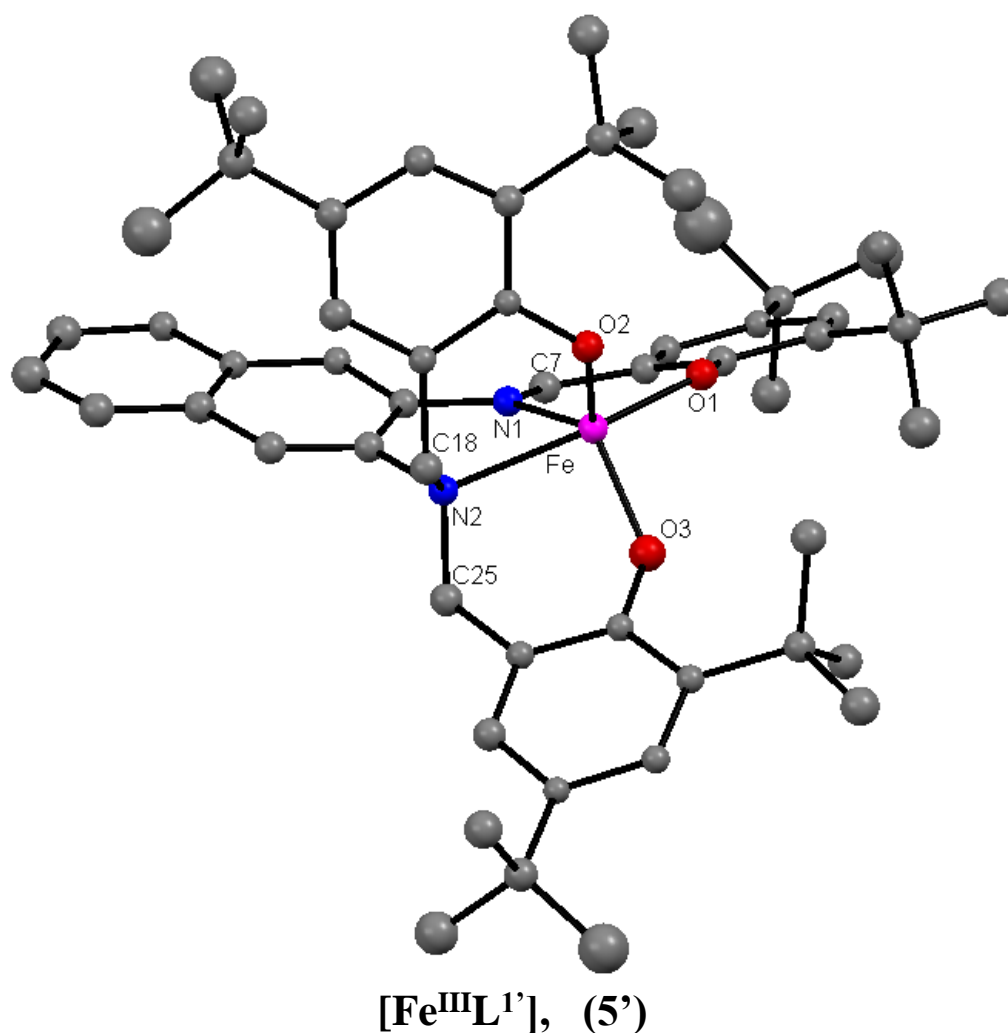
Figure 3.13. X-ray structure data for complex **5'**.

	(5')
Formula	$C_{55}H_{71}FeN_2O_3$
M	863.99
Space group	P(-1)
a / Å	15.8704(5)
b/ Å	16.2473(4)
c/ Å	21.0057(6)
α/ °	84.049(1)
β/ °	71.559(1)
γ/ °	75.613(1)
V/ Å^3	4975.2(2)
Z	4
T/ K	100(2)
λ/ Å	0.71073
D_{calc}/ g cm^{-3}	1.153
μ/ mm^{-1}	0.346
R(F) (%)	4.93
Rw(F) (%)	10.08

^{a}R(F) = $\sum \|\,|F_o| - |F_c|\,\| / \sum |F_o|$; Rw(F) = $[\sum w(F_o^2 - F_c^2)^2 / \sum w(F_o^2)^2]^{1/2}$ for I > 2σ(I)

Table 3.8. Important crystal structure parameters^a for complex **5'**.

	(5')
Fe-O1	1. 9107 (14)
Fe-O2	1. 8611 (14)
Fe-O3	1. 8664 (14)
Fe-N1	2.0746(17)
Fe-N2	2.2591(16)
N1-C7	1.309(3)
N2-C25	1.503(3)
N2-C18	1.493 (3)
O1-Fe-O2	102.56(6)
O1-Fe-O3	96.73(6)
O2-Fe-O3	115.66(6)
O1-Fe-N2	163.06(6)
O3-Fe-N2	88.77(6)
O2-Fe-N2	89.30(6)
O1-Fe-N1	86.81(6)
O3-Fe-N1	119.95(7)
O2-Fe-N1	121. 88 (7)
N2-Fe-N1	76.60(6)

Table 3.9. Selected bond lengths (Å) and angles (°) for complex **5'**.

3.3.10 Electronic, Redox, and Isothermal Compression Data of Imine-based Complexes

The UV-visible spectra of imine-based complexes **5'** and **6'** are shown in **Figure 3.14a** and corresponding data are given in **Table 3.10**. The bands appeared in the region of ~ 375 nm to ~ 650 nm were involved with a collection of intra-ligand charge transfer (ILCT) and ligand to metal charge transfer (LMCT) bands and this remains same for iron(III) imine complexes. There were two shoulder bands appearing at ~ 400 nm and ~ 450 nm. The band in the visible region at ~ 450 nm in complexes **5'** and **6'**, can be assigned as the charge transition from phenolate p_π to $d_{\pi*}$ of the iron(III) center. The band at ~ 400 nm can be assigned as ILCT associated with the phenolate p_π to $p_{\pi*}$ of the azomethine moiety. These assignments were further studied with the aid of spectroelectrochemical experiments and will be discussed in a later section. The band in the near-UV region at ~ 325 nm can be assigned as charge transfer from phenolate p_π to $d_{\sigma*}$ of the iron(III) metal. The absorption maxima found at ~ 285 nm was related to the $\pi \rightarrow \pi^*$ electronic transitions.[16,35]

The cyclic voltammograms obtained for complexes **5'** and **6'** are given in **Figure 3.14b** and the $E_{\frac{1}{2}}$, ΔE_p, and $|I_{pa}/I_{pc}|$ values are shown in **Table 3.11**. Complexes **5'** and **6'** showed a quasi-reversible single electron cathodic process at ~ -1.45 V and can be assigned as a Fe^{III}/Fe^{II} redox couple. The first and the second single electron quasi-reversible anodic processes found at ~ 0.52 V and at ~ 0.7 V with ΔE_p of ~ 0.1 V can be attributed to be ligand assisted phenolate/phenoxyl redox couples. In complexes **5'** and **6'** the third anodic processes were found to be ill-defined.
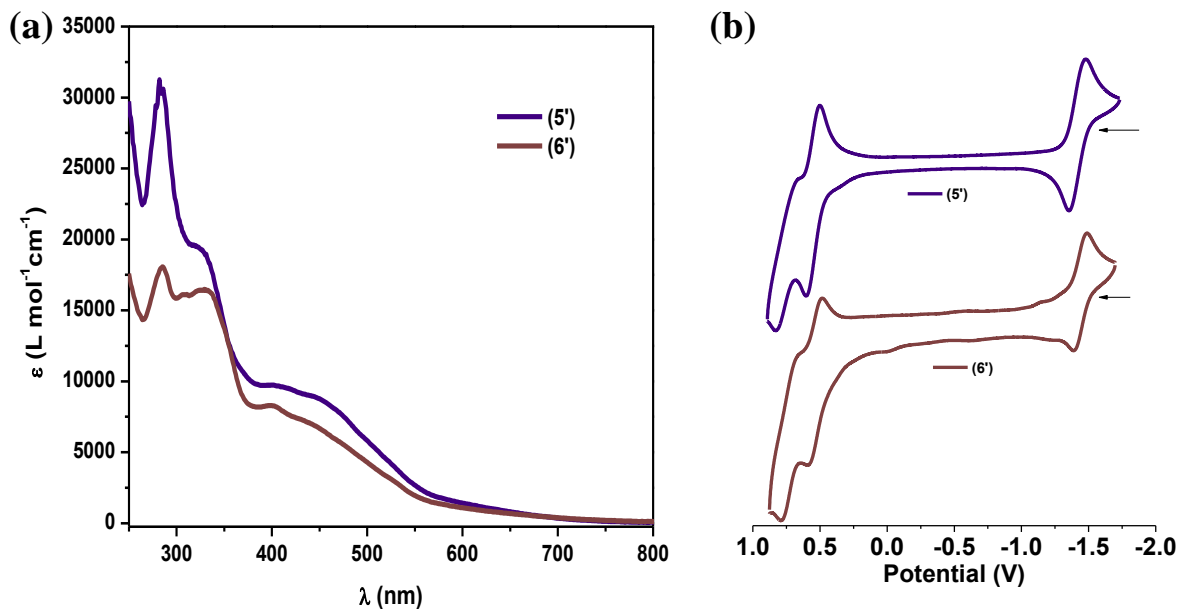
Figure 3.14. (a) UV-visible spectra of 1.0×10^{-4} mol•L^{-1} dichloromethane solutions and (b) cyclic voltammograms of 1.0×10^{-3} mol•L^{-1} solutions for complexes **5'** and **6'**.

Compound	λ_{max} (nm), ε (L•mol^{-1}•cm^{-1}) (CH$_2$Cl$_2$)
(5')	286 (30583), 321 (19479), ~ 399 (9732), ~ 448 (8811)
(6')	285 (18061), 329 (16476), ~ 398 (8294), ~ 440 (7010)

Table 3.10. UV-visible spectroscopic data for iron(III) complexes **5'** and **6'** in 1.0×10^{-4} mol•L^{-1} dichloromethane solutions.

Compound	$E_{1/2}, (\Delta E_p)$ (V) $|I_{pa}/I_{pc}|$	$E_{1/2}, (\Delta E_p)$ (V) $|I_{pa}/I_{pc}|$	$E_{1/2}, (\Delta E_p)$ (V)
(5')	-1.457 (0.110) |0.88|	0.524 (0.088) |1.47|	0.716 (0.121)
(6')	-1.443 (0.092) |0.75|	0.524 (0.110) |2.08|	0.744 (0.085)

Table 3.11. Cyclic voltammetry data for iron(III) complexes **5'** and **6'**.

Spectroelectrochemical studies of complex **5'** helped to understand the features associated with the C=N, azomethine moiety. Upon applying the respective potential of 0.898 V *vs*. Fc$^+$/Fc for complexes **5'**, the charge transfer band, which appeared in the region of ~ 400-600 nm started to decrease in intensity. Simultaneously, the region at ~ 720 nm started to increase in intensity with an isosbestic point observed at 622 nm (**Figure 3.15a**). This observation can be explained as follows. During the oxidation, the Fe^{III}-phenolate converts in to a Fe^{III}-phenoxyl species, and this radical generation happens at different applied potentials. Therefore, during the oxidation process transitions associated with phenolate to phenoxyl charge transfer transitions begin to increase in intensity around the region of ~ 650-900 nm.[27,16] During the reduction process (at -1.782 V *vs*. Fc$^+$/Fc) the bands appeared in the region of ~ 480-660 nm decreased in intensity. Also a new well-defined band

started to appear in the visible region at 436 nm (**Figure 3.15b**). During the reduction process of Fe^{III} to Fe^{II}, LMCT charge transfer transitions occurred between phenolate oxygens and Fe^{III} moiety become weak, which leads into decrease in intensity. Concurrently, the intraligand charge transitions that are allowed will start to increase in intensity. This suggests that the new band appeared at 436 nm in the spectrum is associated with charge transfer transitions taking place between p_π phenolate oxygen and $p_{\pi*}$ of C=N, azomethine moiety. Similar observations were made for complex **6'**.
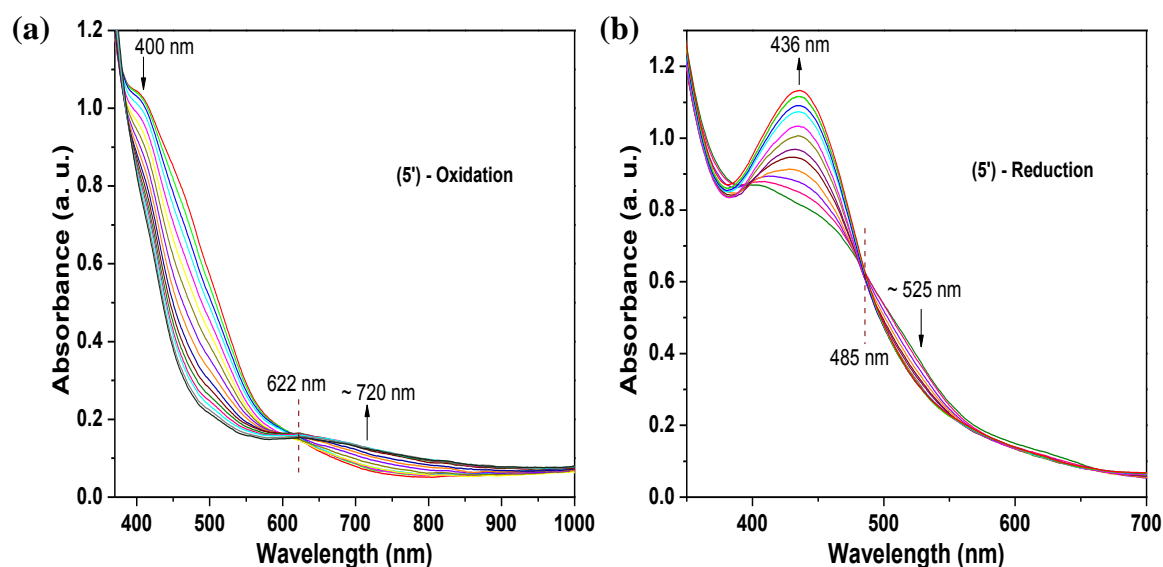
Figure 3.15. Electronic spectral changes observed for complex **5'** (a) during oxidation and (b) during reduction under fixed potential conditions.

The isolated iron(III) imine complexes **5'** and **6'** also showed film formation properties with collapse pressures ~ 40 mN/m. The area of interaction of complexes **5'** and **6'** were found to be 126 and 142 Å^2 while the critical areas were 83 and 112 Å^2. These complexes also showed a constant pressure collapse mechanism. BAM images displayed smooth film formation in regions of 16-40 and 23-38 mN/m, respectively with clear

collapses. The observed compression isotherms, BAM images, and the compression isotherm

properties of complexes **5'** and **6'** are shown in **Figure 3.16** and **Table 3.12**, respectively.
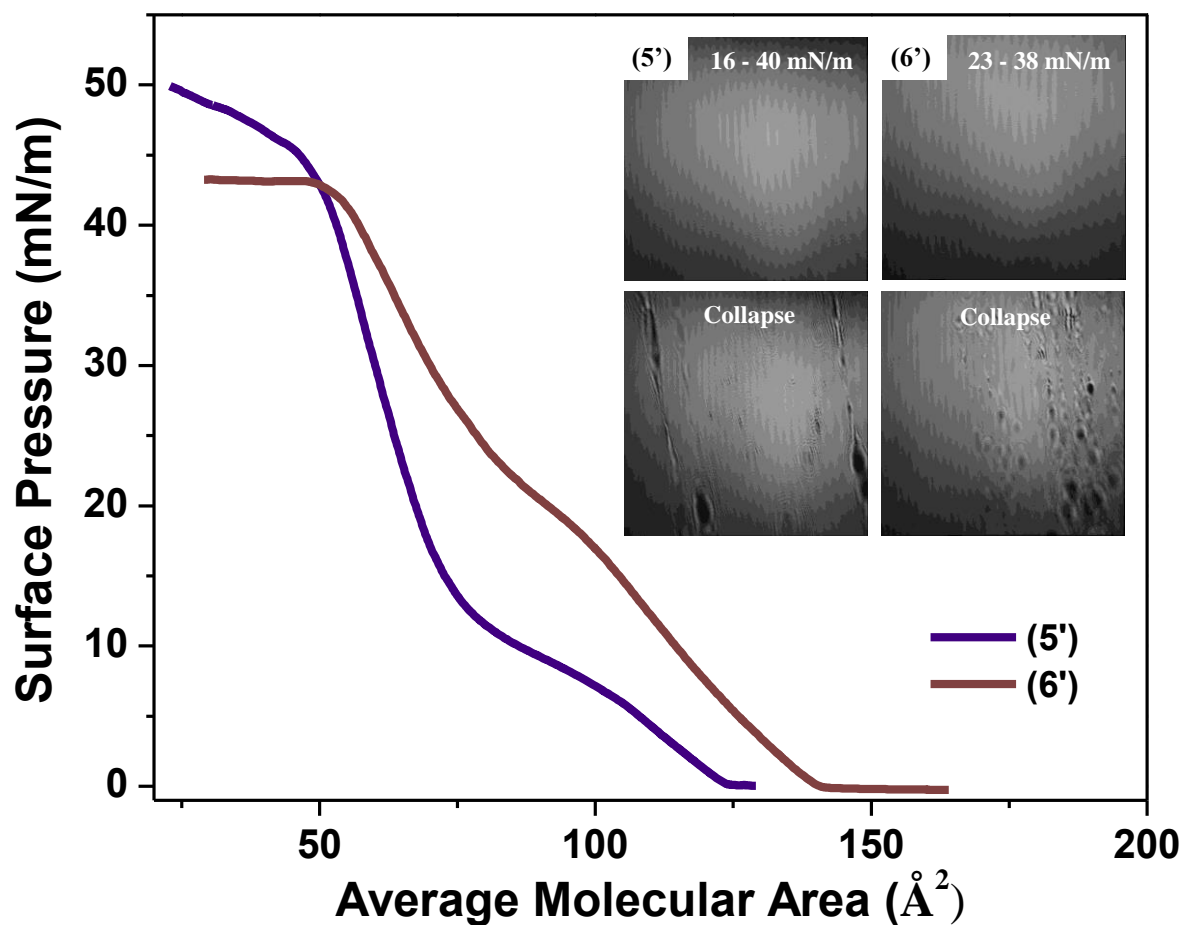
Figure 3.16. Compression isotherms and Brewster angle micrographs for iron(III) complexes

5' and **6'**.

Isothermal Properties	(5')	(6')
Area of interaction (Å^2)	126	142
Phase transition pressure (mN/m)	8-12	19-24
Collapse pressure (mN/m)	41	40
Critical area (Å^2)	83	112

Table 3.12. Compression isothermal properties for iron(III) complexes **5'** and **6'**.

3.3.11 UV-visible Spectroscopy Data of Iron(III) Imine Complexes

After the deposition of LB multilayers of complexes **5'** and **6'** on glass substrates, their UV-visible spectra were recorded. Fifty depositions were carried out for complexes **5'** and **6'** at surface pressures of 25 and 28 mN/m, respectively. UV-visible spectra of LB films of complexes **5'** and **6'** showed a good correlation with their solution spectra (**Figure 3.17a** and **Figure 3.17b**). This data strongly suggest that iron(III) imine complexes remain intact at the air/water interface. Also the UV-visible spectra obtained for LB films of complexes **5** and **6** are in good correlation with UV-visible spectra of complexes **5'** and **6'**. Therefore, these data further support that amine complexes undergo an oxidation at the amine nitrogen of the tripodal ligand to form an azomethine moiety at the air/water interface. According to the literature, shifting of absorption bands in the LB film spectra with respect to their solution spectra indicate possible chromophore aggregations.[36,37,38] A bathochromic effect or a red shift of bands indicates an antiparallel arrangement of chromophores (J-type aggregates) and a hypsochromic effect or a blue shift indicates a parallel chromophore arrangement (H-type aggregates).[34] UV-visible spectra obtained for LB films of complexes **5'** and **6'** showed a red

shift of bands, and therefore, suggested the formation of J-type aggregates or an antiparallel arrangement of chromophores within the film. An experiment carried out with methanol:water (9:1) mixture clearly demonstrated the formation of an imine complex over time by shifting the band at ~ 465 nm to lower wavelength and by the appearance of new band at ~ 400 nm (**Figure 3.17c**). This data further indicated that the imine form complexes are stable at the air/water interface.
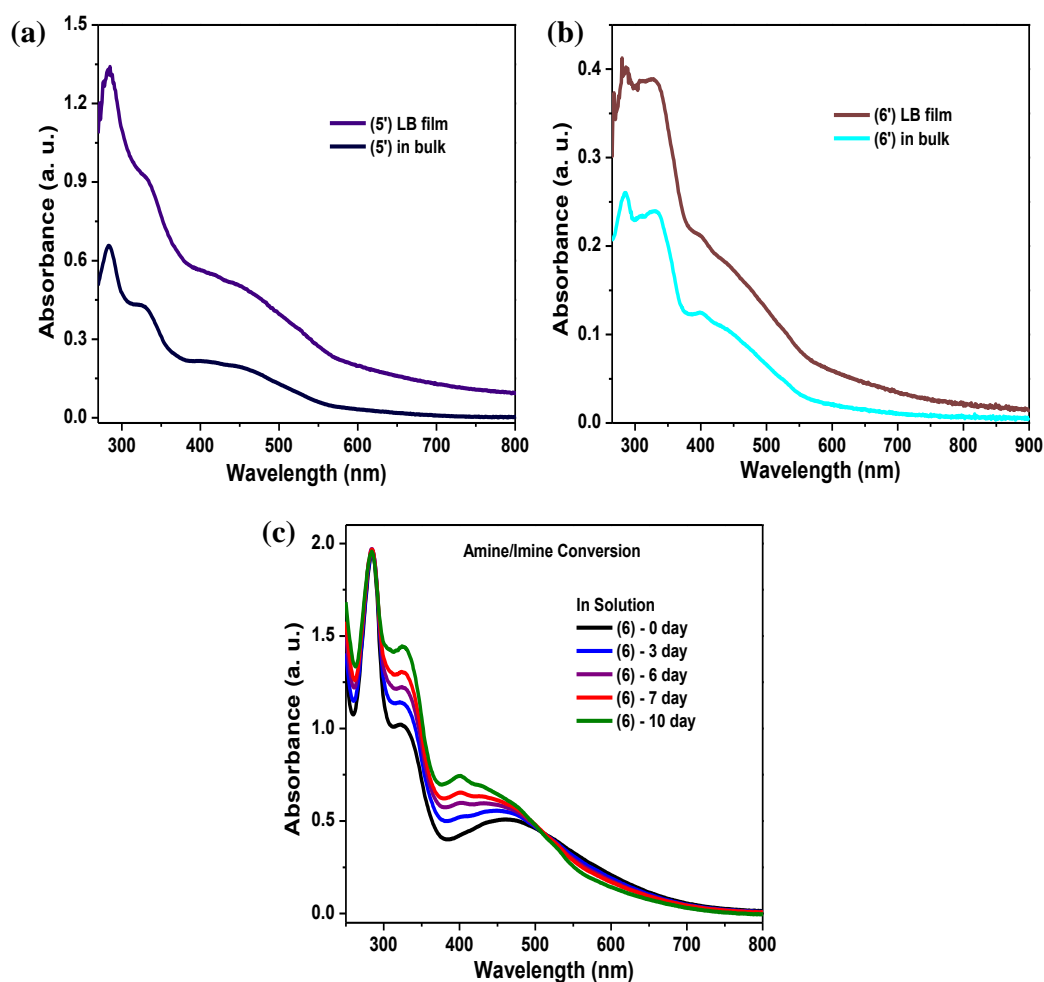
Figure 3.17. UV-visible spectra of LB films for (a) complex **5'** and (b) complex **6'** in comparison with 1.0×10^{-5} mol•L^{-1} dichloromethane solutions of the respective metal complexes. (c) The amine to imine conversion of complex **6** as detected by UV-visible spectroscopy.

3.3.12 Infrared Reflection Absorption Spectroscopy (IRRAS)

The multilayer deposited LB films were characterized using IRRA spectroscopy and this is similar to IR spectroscopy. This technique helps to infer information related to functional groups present in the compound after deposited onto solid substrates. Very importantly, IRRAS provides data associated with packing topologies and defects of organized assemblies, such as LB films.[39,40]

IRRA spectra of complexes **2**, **5**, **6**, and the isolated imine form of complexes **5'** and **6'** were recorded by varying the angle of incidence from 30 to 60° under both *s*- and *p*-polarized light. In most cases, the C-H symmetric and anti-symmetric stretching vibrations were easy to observed, whereas difficulties were encountered to observe a good finger print region due to moisture bands. IRRA spectra with most characteristics were observed at 30° (for complexes **2**, **6**, and **5'**) and at 40° (for complexes **5** and **6'**) under *p*-polarized light. IRRA spectra obtained for complexes **2**, **5**, **6**, **5'**, and **6'** are shown in **Figure 3.18**. The expanded views of the finger print region, starting from 1300 to 1800 cm^{-1} for complexes **2**, **6**, and **6'**, in comparison to their bulk infrared spectra are shown in **Figure 3.19**. The IRRA spectra of above mentioned complexes showed symmetric and asymmetric stretching vibrations in the region of ~ 2860-2965 cm^{-1}. Another important feature is that the complexes **5**, **6**, **5'**, and **6'** showed prominent peaks at ~ 1573, 1583, 1575, and 1583 cm^{-1}, respectively in the finger print region of their IRRA spectra. In complexes **5** and **6**, bands appearing at ~ 1573 and 1583 cm^{-1} can be assigned as a C=N stretching vibration, because they are in good agreement with the isolated imine complexes **5'** and **6'** (C=N stretching vibrations at 1575 and 1583 cm$^{\textbf{-1}}$). These IRRAS data further suggested the amine to imine conversions of complexes **2**, **5**, and **6** occurred at the air/water interface. Apart from C=N vibration bands,

aromatic C=C stretching and CH_n deformation bands appeared in the finger print region of their IRRA spectra. Slight shifts of symmetric and asymmetric C-H stretching vibrations with prominent asymmetric methyl stretching vibrations were observed for LB films when compared to bulk IR spectra. The IRRA spectra of complexes also showed an inversion of peaks within the same spectra. According to the literature, these features suggest the formation of anisotropic films with high molecular order.[38,39,41,42,43]

Static contact angels measured for the monolayers of complexes **5'** and **6'** on glass (at 30 mN/m for **5'** and at 28 mN/m for **6'**), showed values of 92.93° ± 1.22° and 76.82° ± 2.38°, respectively with comparison to a value of 7.45° ± 0.42° for bare glass. This data suggests that complex **5'** is more hydrophobic than **6'**. The contact angel and IRRAS data indicate that, *tert*-butyl rich metal coordinated moieties point outward in the direction of air/solid interface during the film deposition. The following assumption can be made, because glass, mica, quartz, and gold surfaces are hydrophilic in nature. During the first up stroke deposition, hydrophilic counterparts of the molecules will attach to the substrate and therefore, the hydrophobic counterparts will be at the air/solid interface making the surface more hydrophobic in nature. During the film deposition, LB layers will be held together by weak interactions, such as van der Waals forces.
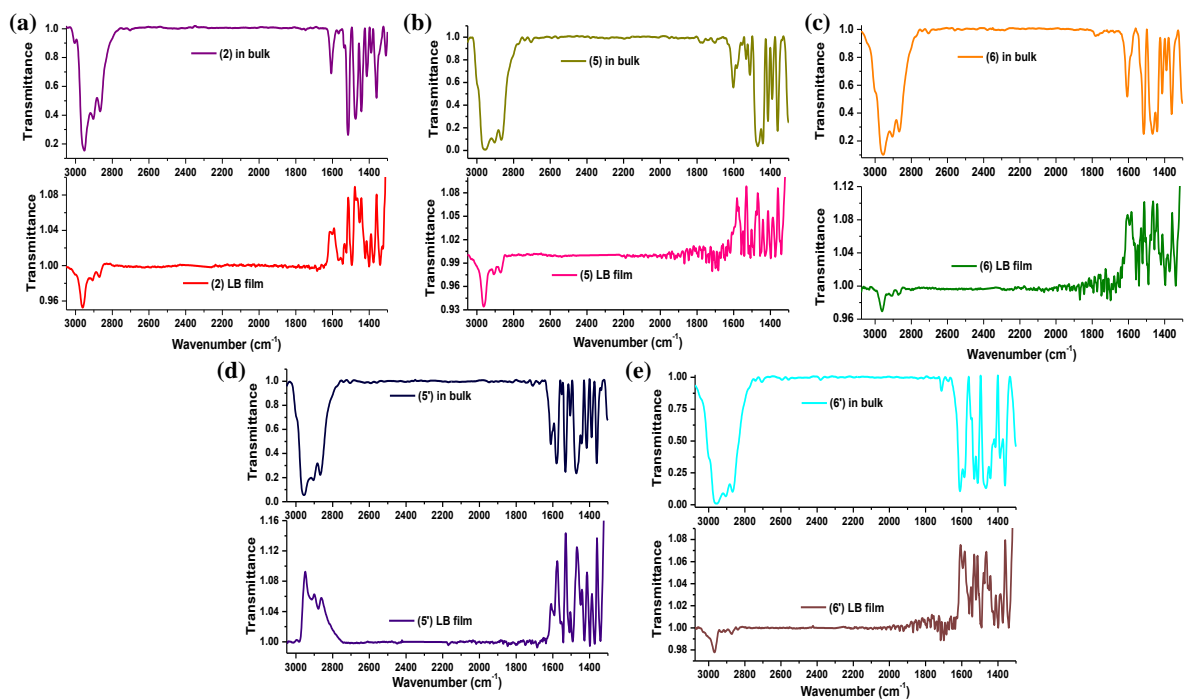
Figure 3.18. IRRA spectra for (a) complex **2**, (b) complex **5**, (c) complex **6**, (d) complex **5'**, and (e) complex **6'** in comparison with their bulk infrared spectra.
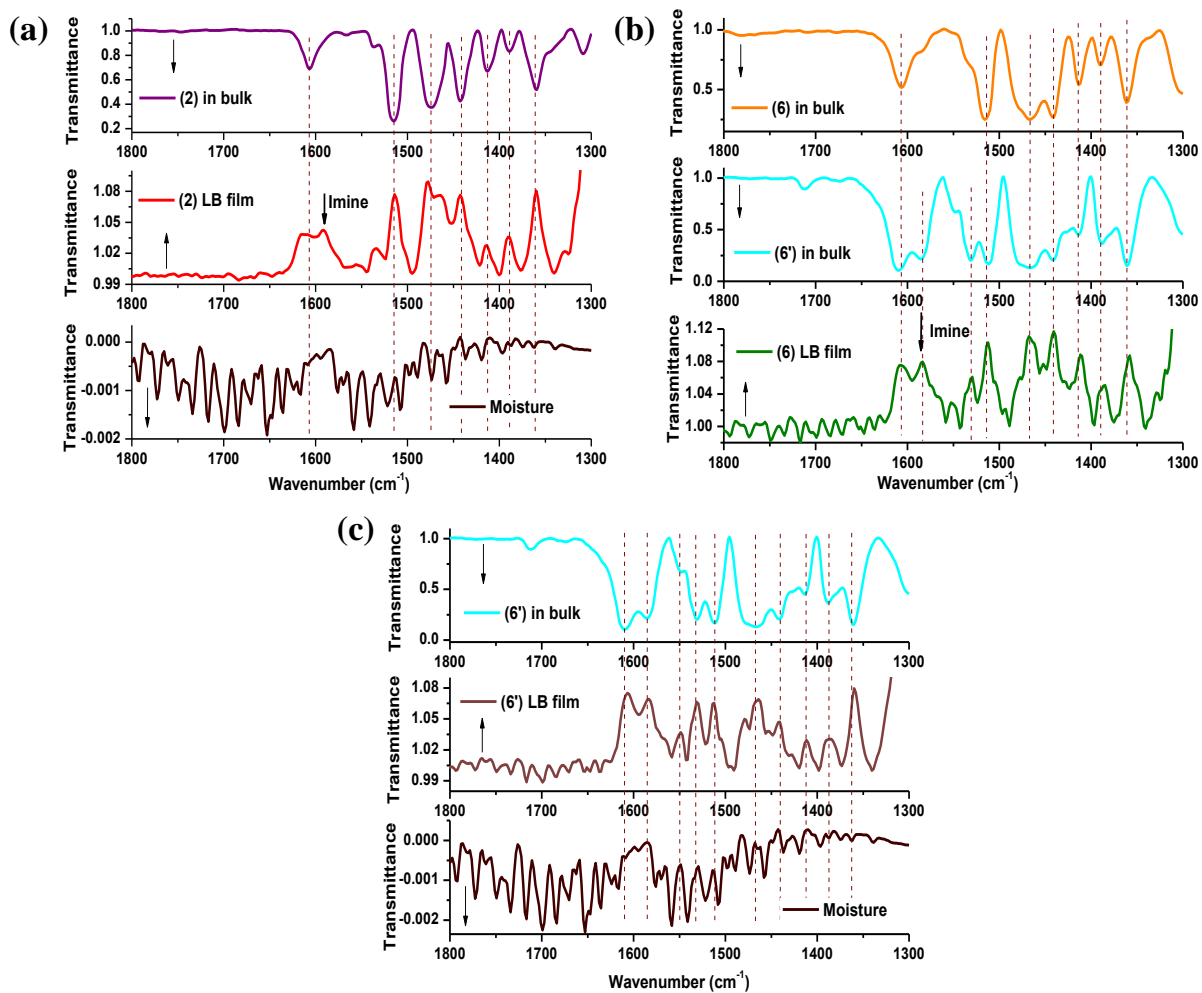
Figure 3.19. The region between 1300 and 1800 cm^{-1} for (a) complex **2**, (b) complex **6**, and (c) complex **6'** in comparison with their bulk infrared spectra.

3.3.13 Surface Characterization using AFM

Complexes **5'** and **6'** were used to carry out further surface analysis using AFM because they afforded stable thin films at the air/water interface. AFM was used to investigate the morphology of the monolayer films of complexes **5'** and **6'** on mica surfaces. AFM height images of the monolayers of complexes **5'** and **6'** at different surface pressures are shown in **Figure 3.20**. Monolayer films deposited at low surface pressures for complexes **5'** and **6'** showed defects, such as areas covered with pinholes and few aggregated particles, as shown in **Figure 3.20a**, **b**, **f**, and **g**. LB films of complexes **5'** and **6'** exhibited lesser defects at increased surface pressures of 27 and 23 mN/m, and showed a closely packed structure at 30 and 28 mN/m, respectively. In complexes **5'** and **6'**, at 36 and 37 mN/m, respectively the films became rougher, and excess material has started to deposit on the surface of the monolayer. Therefore, 28 mN/m was selected to carry out further experiments, such as roughness and thickness measurements, for complex **6'** where a uniform monolayer was observed.
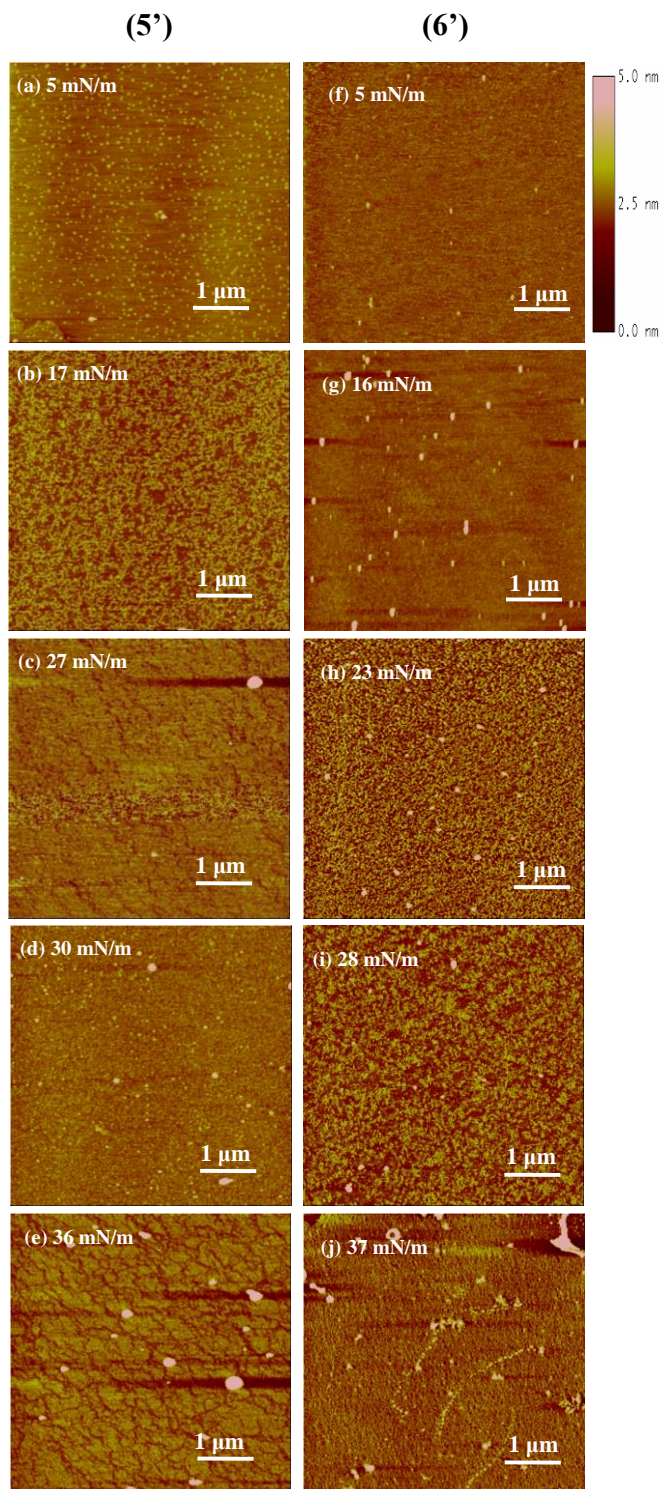
Figure 3.20. AFM height images of monolayer films deposited on mica substrates at different surface pressures for complex **5'** (a)-(e) and complex **6'** (f)-(j). The scan size was 5 μm and the Z range was 5 nm for all images.

The surface roughness measurements of mono and multilayers were estimated using AFM, where they were deposited onto mica. The height images and the corresponding 3D surface plots ranging from 1 to 15 layers are shown in **Figure 3.21** for complex **6'**. As the layer number increases, the surface roughness also started to increase exponentially and the film surface became rougher due to additional particle aggregation.
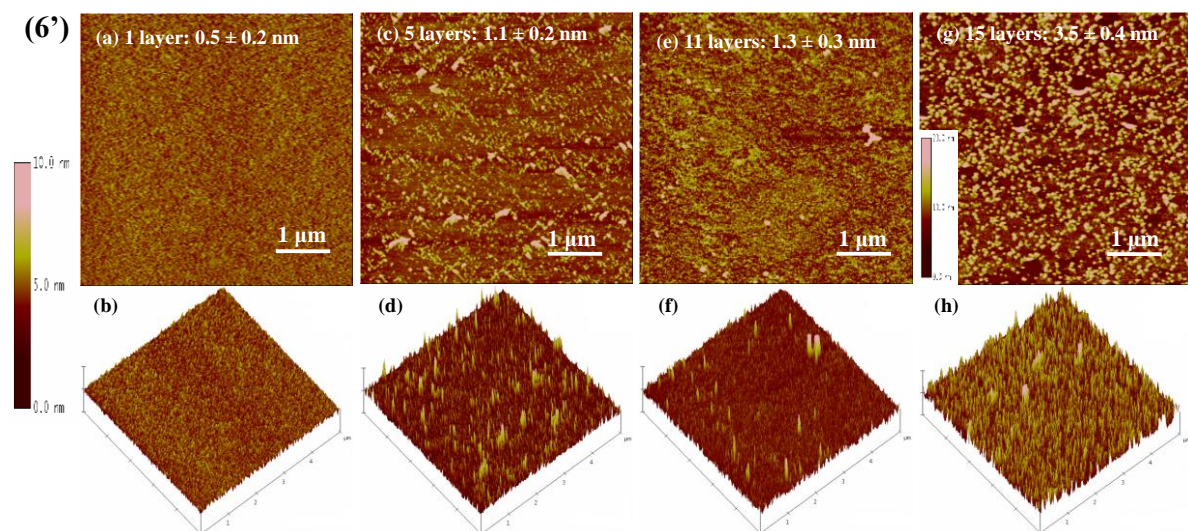
Figure 3.21. Surface roughness measurements of 1-15 LB layers for complex **6'** deposited on mica substrates. AFM height images (top) and 3D surface plots (bottom). 1 layer (a, b); 5 layers (c, d); 11 layers (e, f), the scan size is 5 μm and the Z range is 10 nm for the images; 15 layers (g, h), the scan size is 5 μm and the Z range is 20 nm for the images.

Film thicknesses of 1-15 layers deposited onto quartz substrates were examined by intentional scratching of the film with a sharp blade, followed by measuring the depth of the scratch. The AFM height image (2D), 3D surface plot, corresponding sectional analysis along the black solid line indicated in the 3D image, and the plot between number of layers and layer thickness for complexes **6'** is shown in **Figure 3.22**. Film thickness was indicated by the height differences between the red arrows as shown in **Figure 3.22c**. According to

these data, the experimental monolayer thickness of complexes **6'** was found to be 1.6 ± 0.2 nm. The plot between the number of layers *vs.* layer thickness (**Figure 3.22d**) afforded a linear relationship indicating a homogeneous film deposition. The theoretical film thickness obtained from the above plot was found to be 1.3 nm. Crystal structure data of similar compounds, showed an approximate length of 12-13 Å for a molecule.[9,16] AFM thickness measurements suggested the formation of a true monolayer at air/water and air/solid interfaces, because there was a good agreement between the experimental and theoretical data of LB film thickness. A summary of the film roughness and thickness measurements are tabulated in **Table 3.13**.

Number of Layers	Surface Roughness (nm)	Thickness of the Film (nm)
1	0.5 ± 0.2	1.6 ± 0.2
5	1.1 ± 0.2	7.9 ± 0.6
11	1.3 ± 0.3	12.6 ± 0.9
15	3.5 ± 0.4	18.0 ± 1.1

Table 3.13. Film roughness and thickness data of 1-15 LB layers for complex **6'**.
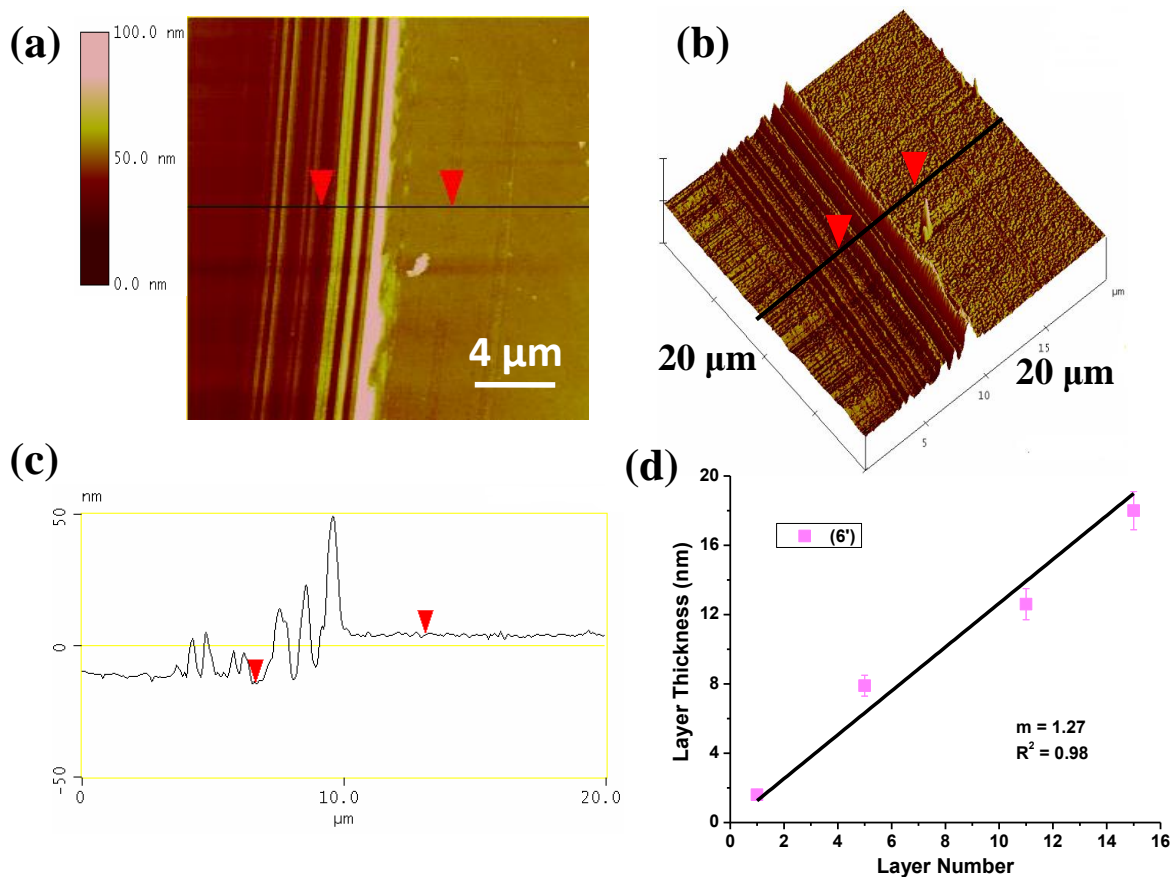
Figure 3.22. AFM height images and sectional analysis for complex **6'** (15 layers) on quartz. (a) 2D view, (b) 3D view, (c) sectional analysis along the black solid line, and (d) plot between the thicknesses (nm) *vs*. number of layers from 1 to 15 layers.

3.4 Conclusions

In conclusion, these results presented the synthesis and characterization of four new pentadentate ligands and their asymmetric gallium(III) and iron(III) complexes. Furthermore, the presence of different substituents on the phenylenediamine moiety, as well as the amine to imine conversion of gallium(III) and iron(III) complexes at the air/water interface, addressed the modulation of electronic, redox, and film formation properties. These metal complexes showed highly distorted pentacoordinate geometries around the trivalent metal

ions. The asymmetrical geometry and the presence of *tert*-butyl groups on phenylenediamine moiety facilitated the radical generation, and helped to modify the electron donor and acceptor properties of the resulting complexes. The redox properties suggested that the phenolates can act as donor moieties when coordinated to trivalent metal ions. The metal complexes presented well-behaved surfactant properties at the air/water interface and the Langmuir films were successfully transferred onto solid substrates. These LB films were characterized by UV-visible, IRRA spectroscopic methods, static contact angle measurements, and AFM analysis. Finally, the experiments that were carried out in assessing the properties of complexes **1**-**7** proposed successful results in obtaining possible electron donor and acceptor counterparts within the same molecule. The possibility of having electron donor and acceptor moieties along with the surfactant properties, make these molecules excellent candidates for device fabrication and to test them as current rectifiers.

REFERENCES

1. http://www.itrs.net/Links/2011ITRS/Home2011.htm

2. Noh, T.W., *Appl. Phys. Lett.* **2011**, *98*, 18357

3. Joachim, C.; Gimzewski, J. K.; Aviram, A. *Nature* **2000**, *408*, 541.

4. Wassel, R. A.; Gorman, C. B.; *Angew. Chem. Int. Ed.* **2004**, *43*, 5120.

5. Park, J.; Pasupathy, A. N.; Goldsmith, J. I.; Chang, C. Yaish, Y.; Petta, J. R.; Rinkoski, M.; Sethna, J. P.; Abruna, H. D.; McEuen, P. L.; Ralph, D. C. *Nature* **2002**, *417,* 722.

6. Lindsey, J. S.; Bocian, D. F.; *Accounts of Chemical Research* **2011**, *44*, 638.

7. Li, Q.; Mathur, G.; Gowda, S.; Surthi, S.; Zhao, Q.; Yu, L.; Lindsey, J. S.; Bocian, D. F.; Misra, V.; *Adv. Mater*. **2004**, *16*, 133.

8. Goodwill, K. E.; Sabatier, C.; Stevens, R. C.; *Biochemistry,* **1998**, *37,* 13437.

9. Lanznaster, M.; Hratchian, H. P.; Heeg, M. J.; Hryhorczuk, L. M.; McGarvey, B. R.; Schlegel, H. B.; Verani, C. N.; *Inorg. Chem.* **2006**, *45*, 955.

10. Hindo, S. S.; Shakya, R.; Rannulu, N. S.; Allard, M. M.; Heeg, M. J.; Rodgers, M. T.; da Rocha, R. P.; Verani, C. N.; *Inorg. Chem.* **2008**, *47*, 3119.

11. Rosa, D. T.; Reynolds, R. A.; Malinak, S. M.; Coucouvanis, D.; *Useful Reagents and Ligands. 4,5-Diaminocatechol: A Useful Building Block in Synthesis*, pp 112-115.

12. Sokolowski, A.; Müller, J.; Weyhermüller, T.; Schnepf, R.; Hildebrandt, P.; Hildenbrand, K.; Bothe, E.; Wieghardt, K.; *J. Am. Chem. Soc.* **1997**, *119*, 8889.

13. Allard, M. M.; Xavier, F. R.; Heeg, M. J.; Schlegel, H. B.; Verani, C. N. *Eur. J. Inorg. Chem.* **2012**, 4622.

14. Metzger, R. M. *Chem. Rev*. **2003**, *103*, 3803.

15. Lanznaster, M.; Heeg, M. J.; Yee, G. T.; McGarvey, B. R.; Verani, C. N.; *Inorg. Chem.* **2007**, *46*, 72.

16. Allard, M. M.; Sonk, J. A.; Heeg, M. J.; McGarvey, B. R.; Schlegel, H. B.; Verani, C. N.; *Angew. Chem. Int. Ed.* **2012**, *51*, 3178.

17. Nakamoto, K. *Infrared and Raman Spectra of Inorganic and Coordination Compounds, Part B: Applications in Coordination, Organometallic and Bioinorganic Chemistry,* 6th ed.; John Wiley & Sons, Inc, 2008; chapter 1, pp 1-275.

18. Silverstein, R. M.; Bassler, G. C.; Morrill, T. C. *Spectrometric Identification of Organic Compounds,* 5th ed.; John Wiley & Sons, Inc, 1991; chapter 3, pp 91-163, pp 289.

19. Auerbach, U.; Eckert, U.; Wieghardt, K.; Nuber, B.; Weiss, J.; *Inorg. Chem.* **1990,** *29,* 938.

20. Adam, B.; Bill, E.; Bothe, E.; Goerdt, B.; Haselhorst, G.; Hildenbrand, K.; Sokolowski, A.; Steenken, S.; Weyhermüller, T.; Wieghardt, K.; *Chem.-Eur. J.* **1997**, *3*, 308.

21. Shongwe, M. S.; Kaschula, C. H.; Adsetts, M. S.; Ainscough, E. W.; A. M.Brodie,; Morris, M.J.; *Inorg. Chem.* **2005**, *44*, 3070.

22. Gaber, B. P.; Miskowski, V.; Spiro, T. G.; *J. Am. Chem. Soc.* **1974**, *96*, 6868.

23. Maki, T.; Araki, Y.; Ishida, Y.; Onomura, O.; Matsumura, Y.; *J. Am. Chem. Soc.* **2001**, *123*, 3371.

24. Benisvy, L.; Blake, A. J.; Collison, D.; Davies, E. S.; Garner, C. D.; McInnes, E. J. L.; McMaster, J.; Whittaker, G.; Wilson, C.; *Dalton Trans.* **2003**, 1975.

25. Padmaja, K; Youngblood, W. J.; Wei, L.; Bocian, D. F.; Lindsey,J. S.; *Inorg. Chem.* **2006**, *45*, 5479.

26. Roth, K. M.; Dontha, N.; Dabke, R. B.; Gryko, D. T.; Clausen, C.; Lindsey, J. S.; Bocian, D. F.; Kuhr, W. G.; *J. Vac. Sci. Technol.* **2000**, *18B*, 2359.

27. Anjos, A.; Bortoluzzi, A. J.; Caro, M. S. B.; Peralta, R. A.; Friedermann, G. R.; Mangrich, A. S.; Neves, A.; *J. Braz. Chem. Soc.* **2006**, *17*, 1540.

28. Kurahashi, T.; Kikuchi, A.; Tosha, T.; Shiro, Y.; Kitagawa, T.; Fujii, H.; *Inorg. Chem.* **2008**, *47*, 1674.

29. Itoh, S.; Kumei, H.; Nagatomo, S.; Kitagawa, T.; Fukuzumi, S.; *J. Am. Chem. Soc.* **2001**, *123*, 2165.

30. Petty, M. C. *Langmuir Blodgett Films: an Introduction,* Cambridge University Press, New York, 1996.

31. Jayathilake, H. D.; Driscoll, J. A.; Bordenyuk, A. N.; Wu, L.; da Rocha, S. R. P.; Verani, C. N.; Benderskii, A. V.; *Langmuir* **2009**, *25*, 6880.

32. Shakya, R.; Imbert, C.; Hratchian, H. P.; Lanznaster, M.; Heeg, M. J.; McGarvey, B. R.; Allard, M.; Schlegel, H. B.; Verani, C. N.; *Dalton Trans.* **2006**, 2517.

33. Engelking, J.; Menzel, H.; *Thin Solid Films* **1998**, *90*, 327.

34. Menzel, H.; McBride, J. S.; Weichart, B.; Ruther, M.; *Thin Solid Films* **1996**, *284-285*, 640.

35. Pyrz, J. W.; Roe, A. L.; Stern, L. J.; Que, Jr. L.; *J. Am. Chem. Soc.* **1985**, *107* , 614.

36. Menzel, H.; Weichart, B.; *Langmuir* **1994**, *10*, 1926.

37. Pal, P.; Dutta, A. K.; Pal, A. J.; Misra, T. N.; *Langmuir* **1994**, *10*, 2339.

38. Joy, S.; Pal, P.; Mondal,T. K.; Talapatra, G. B.; Goswami, S.; *Chem. Eur. J.* **2012**, *18*, 1761.

39. Brezesinski, G.; Dobner, B.; Stefaniu, C.; Vollhardt, D.; *J. Phys. Chem. C*. **2011**, *115*, 8206.

40. Wang, L.; Cruz, A.; Flach, C. R.; Pérez-Gil, J.; Mendelsohn, R.; *Langmuir* **2007,** *23,* 4950.

41. Brezesinski, G.; Dobner, B.; Stefaniu, C.; Vollhardt, D.; *Langmuir* **2011**, 27, 5386.

42. Kattner, J.; Hoffmann, H. *External reflection spectroscopy of thin films on dielectric substrates: Hand book of vibrational spectroscopy;* John Wiley & Sons Ltd., Chichester, 2002; pp 12-14.

43. Hasegawa, T.; Umemura, J.; Takenaka, T.; *J. Phys. Chem.* **1993**, *97*, 9009.

CHAPTER 4

ASSESSMENT OF THE PROPERTIES OF NITRO-SUBSTITUTED IRON(III) COMPLEXES WITH [N_2O_3] AND [N_2O_2] ENVIRONMENTS

4.1 Introduction

There is a growing interest of using coordination metal complexes in the modern molecular-based electronic field. Recent examples include the use of cobalt(II)-terpyridine and divanadium complexes as potential single molecule transistors,[1,2] ruthenium(II) coordinated to a conjugated bipyridine system to demonstrate current rectifying properties,[3] metal containing porphyrin systems as single molecule diodes,[4] azo-containing rhodium(III) complexes for random-access memory (RAM) and read-only memory (ROM) applications in potential memory devices,[5] and metal complexes with photoelectrochemical photocurrent switching properties (eg. iron(II)-cyano and ruthenium-containing polypyridine complexes on titanium dioxide) as optoelectronic logic devices.[6,7] Our laboratory has recently demonstrated the feasibility of using redox active iron(III) complexes with [N_2O_3] binding moieties for current rectification.[8] The rectification behavior can be identified by an asymmetric, unidirectional flow of electric current, and rectification can involve three different mechanisms, namely Schottky, unimolecular, and asymmetric mechanisms.[9] The Schottky mechanism usually involves electrodes with different work functions, and unimolecular and asymmetric mechanisms involve the frontier molecular orbitals of the involved system with accessible Fermi energy levels of the electrodes.

Although it is not obvious at this point, what mechanism drives rectification in [Fe(III)-N_2O_3] complex,[8] some variables seem necessary to attain molecular rectification.

The most important characteristics are as follows: (i) the species of interest should be electrochemically active with distinguished donor-acceptor [D-A] moieties,[10] (ii) the energetic synchronicity between donor/acceptor and electrodes with proper HOMO-LUMO energy gap, and (iii) the ability to deposit onto solid surfaces to establish contact with metal electrodes.[11] The introduction of the electrochemical properties can be done by introducing redox non-innocent ligands and metal ions. One of the most stable redox active species with organic-inorganic combination is the phenolate systems when coordinated to iron(III) metal ions. In these systems, the iron(III) center shows distorted hexa or pentacoordinate geometries. This duet is commonly found in nature[12] as well as synthetically, and shows exceptional electron transfer properties.[13] Also, the electrochemical properties of metal complexes can be altered by the introduction of different substituents to the backbone of the ligand structure. A hypothesis made during the investigation of properties of nitro-substituted iron(III) complexes was the nature of substituents on phenylenediamine moiety would allow for modulation of energies of HOMO and LUMO. Strongly electron-withdrawing nitro substituents ($—NO_2$) are electro-active by themselves, and the introduction of such moieties can enhance the electrochemical properties of the overall system. Also, to introduce pure unimolecular rectifiers, precursors of interest should show low HOMO-LUMO energy gaps with accessible energies when compared to metal Fermi levels.

The mode of attachment of molecules onto metal electrodes is also important in having a good electrical conductivity between the molecule and the electrode. The deposition of molecules onto metal electrode surfaces can be achieved via chemisorption or physisorption. A common chemisorption method is the self-assembly of molecules onto substrate surfaces.[14] In self-assembled monolayers (SAM) covalent bonds are formed

between molecules and the electrode.[15] In self-assembly, a monolayer is easy to deposit with maximum surface coverage, but the main limitation is that during multilayer formation, SAMs tend to show low surface coverage with defects.[16] The self-assembly method is known to form dissimilar contacts with the two metal|molecule junctions. In one end, the molecule is chemically bound to the metal surface, and on the other end, the molecule is bound via physisorption. Therefore, the formation of different interfacial dipole moments (Schottky barriers)[17] at the two metal|molecule junctions is inevitable. Physisorption methods, such as the Langmuir-Blodgett (LB) method,[18] which can form highly oriented films, are advantageous in overcoming Schottky barriers. Devices which are fabricated using LB films, show weak van der Waal's interactions on both ends of metal|molecule junctions. In the LB method, molecules of interest should behave as surfactants to form uniform films at the air/water interface. In this chapter, two new nitro substituted iron(III) complexes with $[N_2O_3]$, (**1**) and $[N_2O_2]$, (**2**) environments were studied, interrogating their electronic, redox, and surface properties by means of a concerted experimental and theoretical approach. A representative view of the metal complexes is shown in **Scheme 4.1**. In these systems, the coordination environment and substituent effect can also influence redox and surface properties, which are important for device fabrication.

Ligands

[H₃L^trisPhO-NO2]

[H₂L^bisPhO-NO2]

Metal Complexes

[Fe^III L^trisPhO-NO2l], (1)

[Fe^III L^bisPhO-NO2], (2)
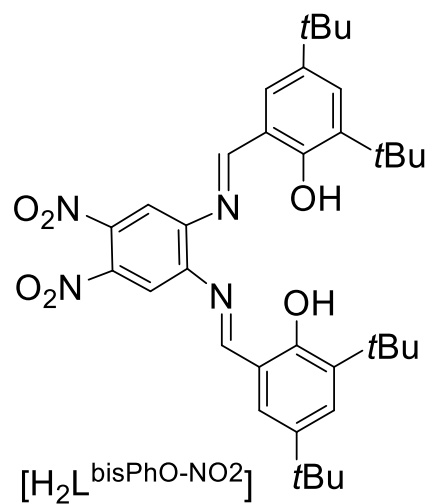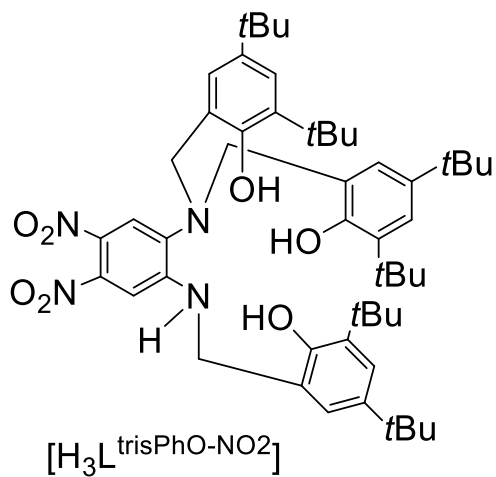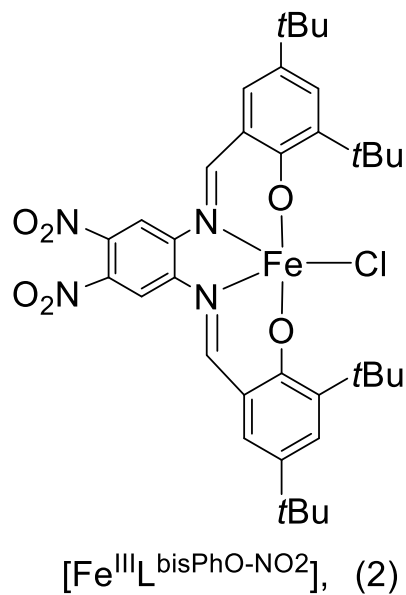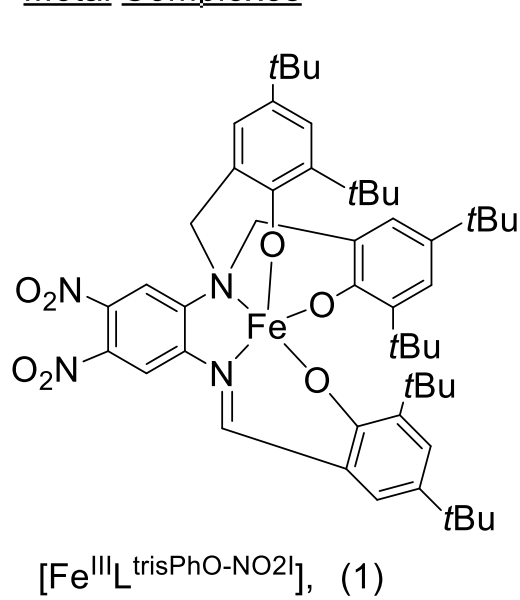
Scheme 4.1. Ligands and their respective iron(III) complexes.

4.2 Experimental Section

4.2.1 X-ray Structural Determinations for complexes 1 and 2

Structures were solved by direct methods using the SHELXS-97 program in APEX II suite and refined by least squares method on F^2, SHELXL-97. A red hexagonal crystal of **[Fe^{III}L$^{trisPhO-NO2I}$], (1)** with dimensions $0.37 \times 0.25 \times 0.23$ mm was mounted on a nylon loop, and data were collected using a Bruker CCD (charge coupled device) based diffractometer equipped with an Oxford Cryostream low-temperature apparatus operating at 173 K. Data were measured using omega and phi scans of $0.5°$ per frame for 30 s. A total of 149130 reflections were collected with 18732 unique reflections. Two independent molecules along with one methanol and one water molecule were present in the unit cell. A dark brown-green crystals of **[Fe^{III}L$^{bisPhO-NO2}$], (2)** with dimensions of $0.908 \times 0.691 \times 0.422$ mm was mounted on a mitogen loop using paratone oil. Data were collected on a Bruker APEX-II Kappa geometry diffractometer with Mo radiation and a graphite monochromato using a Bruker CCD based diffractometer equipped with an Oxford Cryostream low-temperature apparatus at 100 K. A total of 167698 reflections were collected with 56127 unique reflections. Four independent molecules were present in the asymmetric unit cell. All non-hydrogen atoms are refined anisotropically. Hydrogens were calculated by geometrical methods and refined as a riding model.

4.2.2 Syntheses of Ligands

2,4-di-*tert*-butyl-6-(hydroxymethyl)phenol,[19]   2,4-di-*tert*-butyl-6-(chloromethyl) phenol,[20] and 4,5-dinitrobenzene-1,2-diamine[21] were synthesized according to known procedures.

Synthesis of ligand [H₃L$^{trisPhO-NO2}$], *6,6'-(2-(3,5-di-tert-butyl-2-hydroxybenzylamino)-4,5-dinitrophenylazanediyl)bis (methylene)bis(2,4-di-tert-butylphenol).*

A mixture of 2,4-di-*tert*-butyl-6-(chloromethyl)phenol (6.12 g, 24.0 mmol) and triethylamine (2.43 g, 24.0 mmol) in dichloromethane (150 mL), was treated with a solution of 4,5-dinitrobenzene-1,2-diamine (1.19 g, 6.00 mmol). The resulting solution was heated at reflux for 72 hours. Then the mixture was extracted with brine solution (3×200 mL) and dried over anhydrous Na_2SO_4. The solvent was removed by rotatory evaporation, and the resulting crude product was purified by column chromatography (6:1 n-hexanes/ethyl acetate), yielding a yellow solid product. Yield: 22.7%. ESI (m/z^+) in CH_3OH = 859.55 for $[C_{51}H_{72}N_4O_7 + Li^+]$ (calculated = 859.56). ^{1}H NMR, ppm ($CDCl_3$, 400 MHz): δ 1.228-1.417 (m, 54H^{tBu}), 3.838-4.355 (m, 6H^{CH2}), 6.928-7.919 (m, 8H^{ph}). IR (KBr, cm^{-1}) 3607 (ν_{O-H}), 3326 (ν_{N-H}), 2869-2960 (ν_{C-H}), 1597 ($\nu_{C=C}$, aromatic), 1546 ($\nu_{C=C}$, aromatic), 1481 ($\nu_{N=O}$), 1364 ($\nu_{N=O}$).

Synthesis of ligand [H₂L$^{bisPhO-NO2}$], *6,6'-(1E,1'E)-(4,5-dinitro-1,2-phenylene)bis(azan-1-yl-1-ylidene)bis(methan-1-yl-1-ylidene)bis(2,4-di-tert-butylphenol).*

To a stirred solution of 3,5-di-*tert*-butyl-2-hydroxybenzaldehyde (1.183 g, 5.047 mmol) in methanol (40 mL) was added a solution of 4,5-dinitrobenzene-1,2-diamine (0.5001 g, 2.524 mmol) in methanol (30 mL). The mixture was heated at reflux for 28 hours to obtain a brown solution. The solvent was removed to half of its original volume by rotatory evaporation and the crude product was stored at 4 °C for recrystallization. The obtained precipitate was filtered and dried under vacuum to attain an orange powder. Yield: 67.9%. ESI (m/z^+) in CH_3OH = 631.1046 for $[C_{36}H_{46}N_4O_6 + H^+]$ (calculated = 631.3496). ^{1}H NMR,

ppm (CD$_3$OD, 400 MHz): δ 1.330-1.461 (m, 36H$^{t\text{Bu}}$), 7.059 (s, 2H$^{\text{ph}}$), 7.475 (d, 2H$^{\text{ph}}$), 7.537 (d, 2H$^{\text{ph}}$), 7.894 (s, 2H$^{\text{CH}}$). IR (KBr, cm^{-1}) 3502 ($\nu_{\text{O-H}}$), 2843-2959 ($\nu_{\text{C-H}}$), 1650, 1619, and 1517 ($\nu_{\text{C=C}}$, aromatic and $\nu_{\text{C=N}}$), ($\nu_{\text{C=C}}$, aromatic), 1466 ($\nu_{\text{N=O}}$), 1361 ($\nu_{\text{N=O}}$).

4.2.3 Syntheses of Iron(III) Complexes

Synthesis of complex [Fe$^{\text{III}}$L$^{\text{trisPhO-NO2I}}$] (1).

A solution of [H$_3$L$^{\text{trisPhO-NO2}}$] (0.21 g, 0.25 mmol) and anhydrous NaOCH$_3$ (0.04 g, 0.75 mmol) in methanol (15 mL) was treated with a methanolic solution (5 mL) of Fe(ClO$_4$)$_3$·xH$_2$O (0.12 g, 0.25 mmol), under ambient conditions. The resulting solution was heated at 50 °C for 2 hours. Then the reaction mixture was cooled to ambient temperature, stirred for one hour at ambient temperature, and bubbled with dioxygen gas for 30 minutes. The reaction mixture was recrystallized at ambient temperature to obtain dark red-brown crystals of [Fe$^{\text{III}}$L$^{\text{trisPhO-NO2I}}$]. Yield: 59.3%. Melting point = 184-186 °C. ESI (m/z^+) in CH$_3$OH = 904.4453 for [C$_{51}$H$_{67}$N$_4$O$_7$Fe + H$^+$] (calculated = 904.4437) in agreement with 1.8 ppm difference. Anal. Calc. for [C$_{51}$H$_{67}$N$_4$O$_7$Fe·H$_2$O]: C, 66.44; H, 7.54; N, 6.08 %. Found: C, 65.84; H, 7.42; N, 5.99 %. IR (KBr, cm^{-1}) 2868-2957 ($\nu_{\text{C-H}}$), 1615 ($\nu_{\text{C=C}}$, aromatic), 1530 ($\nu_{\text{C=C}}$, aromatic), 1574 ($\nu_{\text{C=N}}$), 1471 ($\nu_{\text{N=O}}$), 1360 ($\nu_{\text{N=O}}$).

Synthesis of complex [Fe$^{\text{III}}$L$^{\text{bisPhO-NO2}}$] (2).

A solution of [H$_2$L$^{\text{bisPhO-NO2}}$] (0.250 g, 0.396 mmol) and anhydrous NaOCH$_3$ (0.043 g, 0.793 mmol) in methanol (20 mL) was treated with a methanolic solution (5 mL) of FeCl$_3$·6H$_2$O (0.107 g, 0.396 mmol). The resulting solution was heated at 50 °C for 4 hours. The reaction mixture was cooled to ambient temperature. Then the solution was filtered and

recrystallized at ambient conditions to yield dark brown-green crystals of **[Fe^{III}L$^{bisPhO-NO2}$]**. Yield: 48.1%. ESI (m/z^+) in CH$_3$OH = 684.2610 for [C$_{36}$H$_{44}$FeN$_4$O$_6^+$] (calculated = 684.2611). Anal. Calc. for [C$_{36}$H$_{44}$ClFeN$_4$O$_6$]: C, 60.05; H, 6.16; N, 7.78 %. Found: C, 59.97; H, 6.24; N, 7.82 %. IR (KBr, cm^{-1}) 2869-2958 (ν_{C-H}), 1611 ($\nu_{C=C}$, aromatic), 1526 ($\nu_{C=C}$, aromatic) 1573 ($\nu_{C=N}$), 1462 ($\nu_{N=O}$), 1360 ($\nu_{N=O}$).

4.3 Results and Discussion

4.3.1 Synthesis and Characterization of Compounds

The ligand **[H$_3$L$^{trisPhO-NO2}$]** was synthesized by treating one equivalent of 4,5-dinitrobenzene-1,2-diamine with four equivalents of 2,4-di-*tert*-butyl-6-(chloromethyl) phenol. The reaction was carried out in dichloromethane for 72 hours under reflux conditions, and triethylamine was used as the base. The purified ligand was obtained by column chromatography. The synthesis of the ligand **[H$_2$L$^{bisPhO-NO2}$]** was carried out by the treatment of two equivalents of 3,5-di-*tert*-butyl-2-hydroxybenzaldehyde with one equivalent of 4,5-dinitrobenzene-1,2-diamine in methanol media. The resulting mixture was refluxed for 28 hours and the pure ligand was obtained by recrystallization from methanol. The synthesis route followed to obtain ligands and metal complexes are shown in **Scheme 4.2**. After isolating the purified ligands, one equivalent of the corresponding ligand was treated with one equivalent of iron(III) metal salt in the presence of anhydrous NaOCH$_3$.
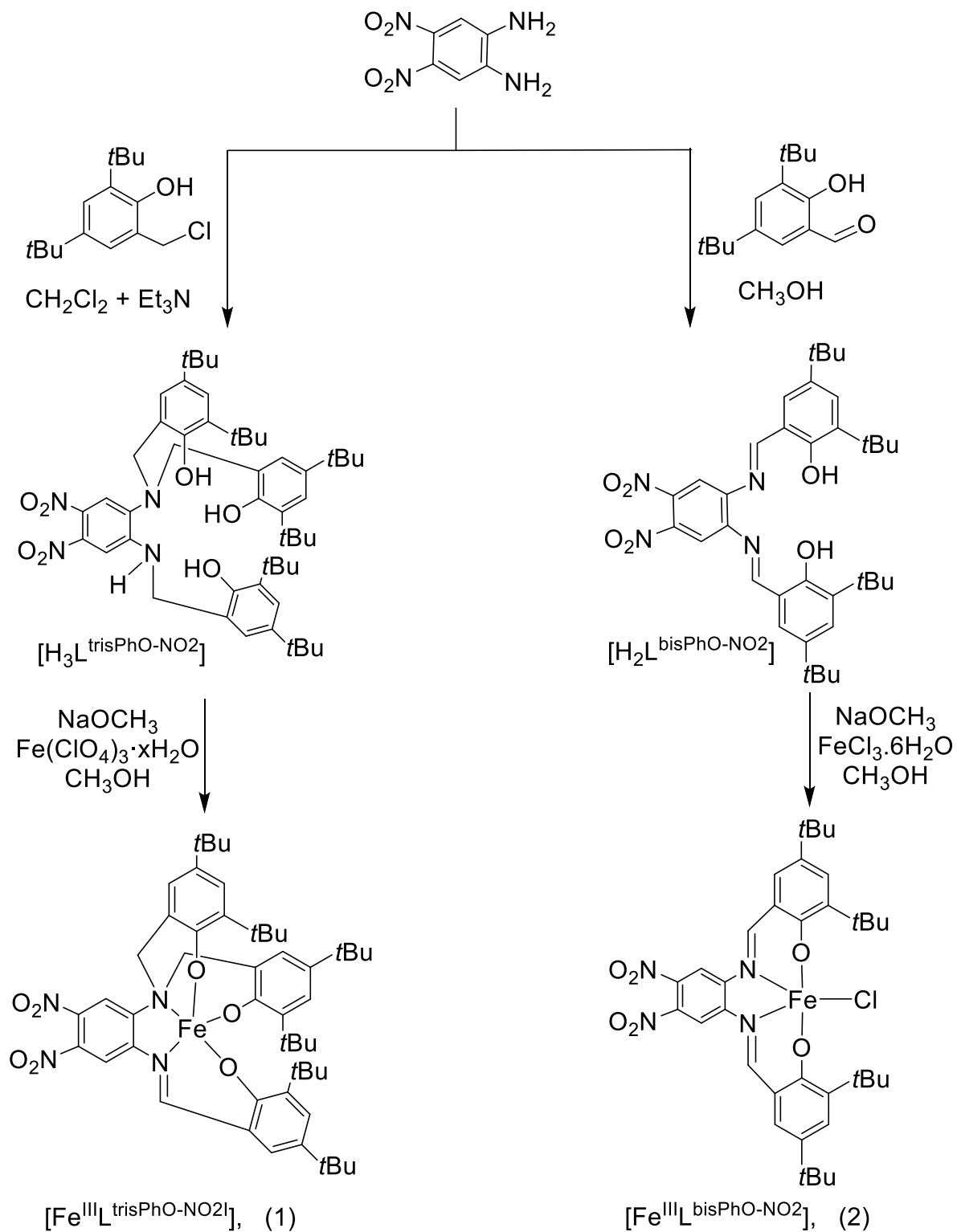
Scheme 4.2. Synthetic routes followed to obtain ligands and iron(III) complexes.

All the ligands and iron(III) complexes were characterized using multiple techniques, namely, infrared and NMR spectroscopic methods, ESI-mass spectrometry, and CHN elemental analysis. The mass spectrometry data were measured in the positive ion mode. The peak positions and the isotopic distribution patterns of the molecular ion peaks matched with simulated data. In IR spectra, the O—H stretching vibrations of the ligands appeared at 3607 and 3502 cm^{-1} for [$H_3L^{trisPhO-NO2}$] and [$H_2L^{bisPhO-NO2}$]. In complexes **1** and **2** the O—H stretching vibrations were not observed. During the formation of complex **1**, the N—H stretching vibration (at 3326 cm^{-1}), which was present in [$H_3L^{trisPhO-NO2}$] disappeared. In complex **1**, a new band appeared at 1574 cm^{-1} belonging to a C=N stretching vibration. This suggests a possible imine conversion of the ligand structure, during the complex synthesis. In complex **2**, the C=N stretching vibration appeared at 1573 cm^{-1}. Additionally, the ligands and the complexes showed bands ~ 1470 and 1360 cm^{-1}, belonging to N=O stretching vibrations. The IR spectra also displayed prominent bands belonging to asymmetric and symmetric C—H, C=C aromatic stretching vibrations, and CH_n deformations.[22]

4.3.2 Molecular Structure Data

X-ray quality crystals were obtained for complexes **1** (dark red-brown) and **2** (dark brown-green), upon recrystallization in methanol at ambient conditions. Selected crystallographic data of complexes **1** and **2** are given in **Table 4.1** and the ORTEP view is shown in **Figure 4.1**. The selected bond lengths and angles of complexes **1** and **2** are tabulated in **Table 4.2**. In complex **1**, there are two types of nitrogens present namely, the N1, a mono-substituted imine with one 2,4-di-*tert*-butyl substituted phenolate arm, and N2, di-substituted tertiary amine with two of the same phenolate arms. The three phenolate

oxygen atoms and the imine, and amine nitrogen atoms were coordinated to the iron(III) center in a pentacoordinated fashion forming a neutral species. When considering bond lengths, complex **1** showed a N1-C7 bond distance of 1.307 Å, while N2-C37 and N2-C22 were found to be 1.506 Å and 1.513 Å, respectively. This data suggested that N1-C7 is a double bond, while N2-C25 and N2-C18 are single bonds. The core of complex **1** showed bond distances of Fe-O1, 1.911 Å; Fe-O2 and Fe-O3, ~ 1.86 Å; and Fe-N1 and Fe-N2 distance of ~ 2.1 Å and ~ 2.2 Å, respectively. These data are well-suited with other pentacoordinate iron(III) complexes that have been reported in the literature.[23,24] The X-ray structural data of complex **1** consisted of two molecules in the crystal lattice with minor differences. The calculated τ values for these two molecules were found to be 0.599 and 0.317. Therefore, the structure of the complex **1** could occupy a distorted trigonal bipyramidal or distorted square pyramidal geometry.

On the contrary, complex **2** consisted with a single type of two imine nitrogen atoms, N25 and N26, which were coordinated to 2,4-di-*tert*-butyl substituted phenolate entities. In complex **2**, the iron(III) center was surrounded by two nitrogen atoms (N25 and N26), two phenolate oxygen atoms (O14 and O22), and one chloro ligand, in a pentacoordinate fashion. The calculated τ value was found to be 0.148. Therefore, complex **2** showed a distorted square pyramidal geometry around the metal atom. In the X-ray structure, the two nitrogen atoms and the two phenolate oxygen atoms occupied the four corners of the square pyramid whereas the chloro ligand was found to be axially coordinated to the metal atom. The oxygen and nitrogen atoms were found to be *trans* to each other. Complex **2** showed a Fe-N bond distance of ~ 2.09 Å and a Fe-O bond distance of ~ 1.88 Å. The Fe-Cl bond distance was found to be 2.21 Å. The N25-C66 and N26-C39 bonds showed a double bond character with

a distance of ~ 1.3 Å. These bond distances and angles are well-matched with the literature reported saloph-type iron(III) complexes.[25,26] Complexes **1** and **2** showed the presence of nitro substituents at the phenylenediamine moiety and showed a typical N=O bond distance of ~ 1.2 Å.
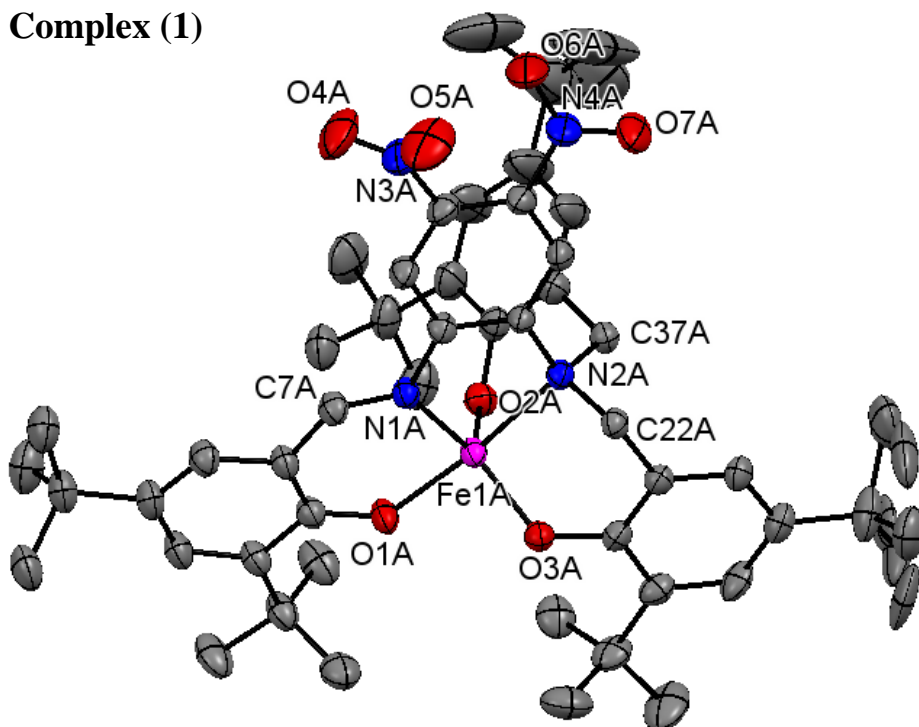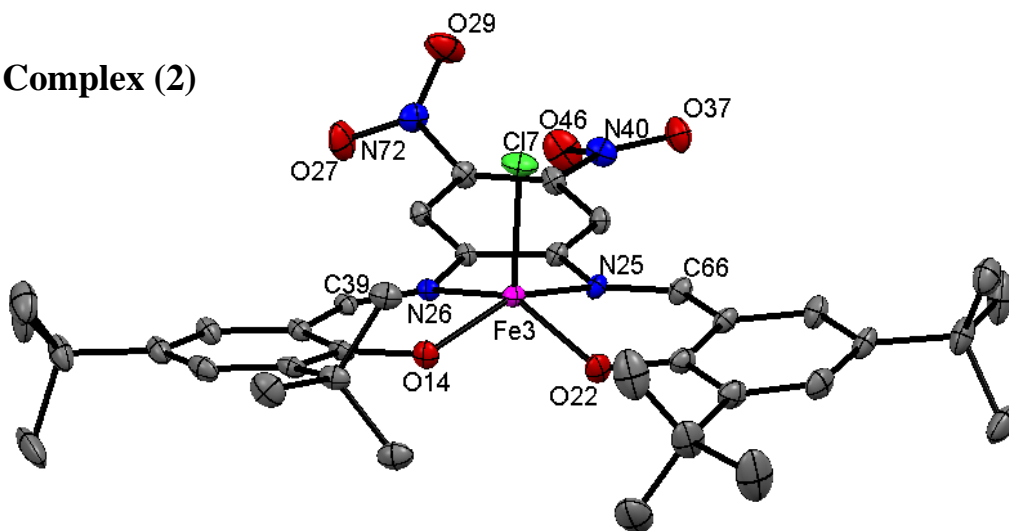
Figure 4.1. ORTEP diagrams for complexes **1** and **2**.

	(1)	(2)
Formula	$C_{51.5}H_{69.5}FeN_4O_8$	$C_{144}H_{176}Cl_4Fe_4N_{16}O_{24}$
M	928.46	2880.21
Space group	$P2_1/n$	P1
a / Å	21.5860(17) Å	18.5576 (10) Å
b/ Å	19.7699(16) Å	20.0263 (11) Å
c/ Å	25.059(2) Å	21.5406 (10) Å
α/ °	90°	74.430 (2)°
β/ °	106.9200(10)°	75.669 (2)°
γ/ °	90°	72.390 (2)°
V/ Å^3	10231.2(14)	7228.6 (6)
Z	8	2
T/ K	173(2)	100
λ/ Å	0.71073	0.71073
D_{calc}/ g cm^{-3}	1.206	1.323
μ/ mm^{-1}	0.349	0.54
R(F) (%)	5.69	5.6
Rw(F) (%)	15.41	15.7

$^aR(F) = \sum \|F_o| - |F_c\| / \sum |F_o|$; $Rw(F) = [\sum w(F_o^2 - F_c^2)^2 / \sum w(F_o^2)^2]^{1/2}$ for $I > 2\sigma(I)$

Table 4.1. Crystal data^a for complexes **1** and **2**.

(1)		(2)	
Fe(1A)-O(1A)	1.911(2)	Fe3-Cl7	2.2110 (5)
Fe(1A)-O(2A)	1.856(2)	Fe3-O14	1.8786 (12)
Fe(1A)-O(3A)	1.862(2)	Fe3-O22	1.8817 (13)
Fe(1A)-N(1A)	2.100(3)	Fe3-N25	2.0932 (15)
Fe(1A)-N(2A)	2.213(2)	Fe3-N26	2.0870 (14)
N(1A)-C(7A)	1.307(4)	N26-C39	1.305 (2)
N(2A)-C(37A)	1.506(4)	N25-C66	1.310 (2)
N(2A)-C(22A)	1.513(4)	O27-N72	1.211 (2)
O(4A)-N(3A)	1.190(4)	O29-N72	1.220 (2)
O(5A)-N(3A)	1.216(4)	N40-O46	1.231 (2)
O(6A)-N(4A)	1.204(4)	O37-N40	1.230 (2)
O(7A)-N(4A)	1.217(4)	O14-Fe3-Cl7	107.61 (4)
O(2A)-Fe(1A)-O(3A)	119.16(10)	O14-Fe3-O22	91.23 (6)
O(2A)-Fe(1A)-O(1A)	101.97(10)	O14-Fe3-N25	149.69 (6)
O(3A)-Fe(1A)-O(1A)	93.74(9)	O14-Fe3-N26	86.63 (5)
O(2A)-Fe(1A)-N(1A)	112.36(10)	O22-Fe3-Cl7	112.36 (5)
O(3A)-Fe(1A)-N(1A)	127.09(10)	O22-Fe3-N25	85.60 (6)
O(1A)-Fe(1A)-N(1A)	86.65(9)	O22-Fe3-N26	140.83 (6)
O(2A)-Fe(1A)-N(2A)	90.89(9)	N25-Fe3-Cl7	101.42 (4)
O(3A)-Fe(1A)-N(2A)	89.50(9)	N26-Fe3-Cl7	105.50 (4)
O(1A)-Fe(1A)-N(2A)	163.04(10)	N26-Fe3-N25	77.28 (5)
N(1A)-Fe(1A)-N(2A)	78.17(9)		

Table 4.2. Selected bond lengths (Å) and angles (°) for complexes **1** and **2**.

4.3.3 Electronic Spectral Properties

The UV-visible spectra of complexes **1** and **2** were recorded in dichloromethane. The observed electronic spectra for complexes **1** and **2** are shown in **Figure 4.2**, and their spectral positions are given in **Table 4.3**. The UV-visible spectrum of complex **1** showed an intense absorption maxima at 283 nm (ε = 23336 L•mol^{-1}•cm^{-1}) belonging to $\pi \rightarrow \pi^*$ electronic transitions.[24,27] In complex **1**, the broad band appearing in the region of ~ 400-600 nm is typical for imine type of pentacoordinate iron(III) complexes. This band consists of two shoulder peaks. The second shoulder, which was observed at ~ 550 nm (ε = 6115 L•mol^{-1}•cm^{-1}), can be attributed to the charge transfer transitions from phenolate p_π to $d_{\pi*}$ of the iron(III) center. The first shoulder, which was observed at ~ 455 nm (ε = 9794 L•mol^{-1}•cm^{-1}), can be assigned as the intra-ligand charge transfer transitions (ILCT) associated with the phenolate p_π to $p_{\pi*}$ of the azomethine moiety.[8] The spectroelectrochemical studies also supported these assignments, and the results will be discussed in a later section. The band in the near-UV region (at 325 nm with ε of 21882 L•mol^{-1}•cm^{-1}) can be assigned to the charge transfer transitions from phenolate p_π to $d_{\sigma*}$ of the iron(III) metal. These attributions are well-correlated with the literature.[28,29,30] Complex **1** also showed a band at 370 nm (ε = 18657 L•mol^{-1}•cm^{-1}) associated to $\pi \rightarrow \pi^*$ electronic transitions, due to the presence of nitro groups. Complex **2** showed similar charge transfer transitions to that of complex **1**. Complex **2** showed the intraligand $\pi \rightarrow \pi^*$ electronic transitions at ~ 240 nm (ε = 35783 L•mol^{-1}•cm^{-1}). In this spectrum, the region between ~ 400-700 nm showed bands associated woth ILCT (at 450 nm) and LMCT (phenolate p_π to $d_{\pi*}$ of the iron(III) center) transitions.[31] Apart from these absorption bands the phenolate p_π to $d_{\sigma*}$ and the nitro related intraligand $\pi \rightarrow \pi^*$ electronic transitions appeared in the region of 300-400 nm.
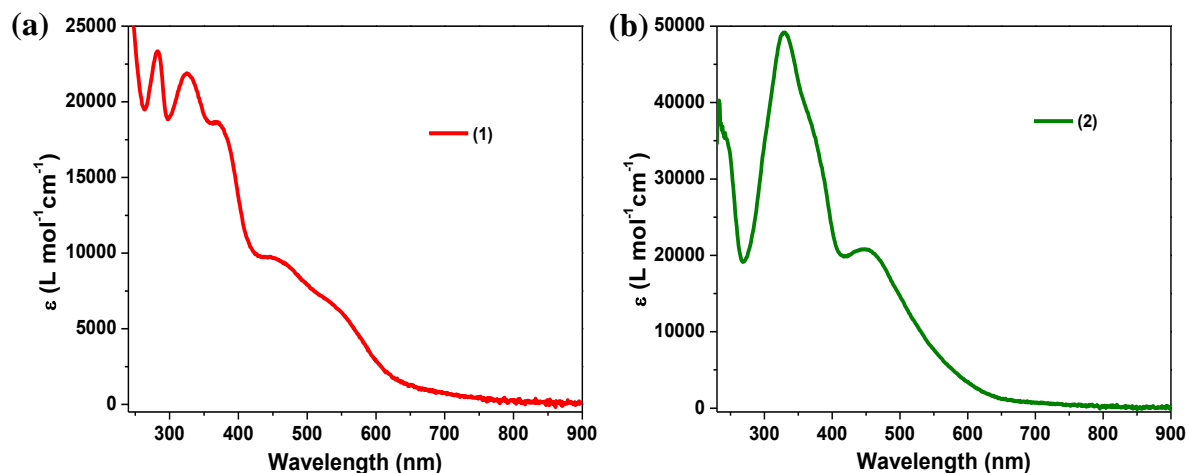
Figure 4.2. UV-visible spectra of 1.0×10^{-5} mol•L^{-1} dichloromethane solutions for (a) complex **1** and (b) complex **2**.

Compound	λ_{max}, nm (ε, L· mol^{-1} · cm^{-1})
(1)	283 (23336), 325 (21882), 370 (18657), ~ 455 (9794), ~ 552 (6115)
(2)	~ 240 (35783), 330 (49175), ~ 372 (36332), 450 (20798)

Table 4.3. UV-visible spectral data of 1.0×10^{-5} mol•L^{-1} dichloromethane solutions for complexes **1** and **2**.

4.3.4 Electrochemical Properties

The redox properties of the metal complexes **1** and **2** were measured in 1.0×10^{-3} mol•L^{-1} dichloromethane solutions using TBAPF$_6$ as the electrolyte. All the potential values were recorded versus Fc^{+}/Fc couple. The cyclic voltammograms of complexes **1** and **2** are shown in **Figure 4.3**. In **Table 4.4** the potential values and $\left| I_{pa}/I_{pc} \right|$ ratios have been

tabulated. Both complexes showed complicated cyclic voltammograms with a combination of ligand- and metal-assisted redox processes. One of the main reasons to use nitro substituents on the phenylenediamine moiety is to introduce more redox accessible states into iron(III) complexes. Complex **1** showed three cathodic and three anodic processes in the cyclic voltammogram. The reversible one electron reduction process found at -1.06 V *vs.* Fc^+/Fc (ΔE_p = 0.07 V, $|I_{pa}/I_{pc}|$ = 1.09) can be allocated to the Fe^{III}/Fe^{II} redox couple. The other two reversible single electron reduction processes at -1.36 V *vs.* Fc^+/Fc (ΔE_p = 0.08 V, $|I_{pa}/I_{pc}|$ = 1.07) and at -1.61 V *vs.* Fc^+/Fc (ΔE_p = 0.06 V, $|I_{pa}/I_{pc}|$ = 1.01) can be attributed to ligand-based nitro reduction processes. The density functional theory (DFT) calculations were performed to analyze these three cathodic processes in detail, especially regarding the sequence of the redox processes. DFT calculations reinforced the above mentioned assignments, and will be discussed in a separate section. Complex **1** also showed two quasi-reversible single electron anodic processes at 0.54 V *vs.* Fc^+/Fc (ΔE_p = 0.18 V, $|I_{pa}/I_{pc}|$ = 1.03) and at 0.8 V *vs.* Fc^+/Fc (ΔE_p = 0.09 V) belonging to ligand-centered phenolate/phenoxyl redox couple. The third phenolate/phenoxyl redox couple (at ~ 1.1 V) was ill-defined. These redox potential values are in good agreement with the literature.[20,23,24] When considering the redox properties of iron(III) complexes with electron-donating substituents (which were discussed in chapter 3), complex **1** showed well-behaved redox properties with lower reduction potential for Fe(III)/Fe(II) redox couple. Complex **2** showed the Fe^{III}/Fe^{II} redox couple at -0.77 V *vs.* Fc^+/Fc (ΔE_p = 0.1 V, $|I_{pa}/I_{pc}|$ = 0.72). The quasi-reversible ligand-centered oxidation processes appeared at 0.99 V *vs.* Fc^+/Fc (ΔE_p = 0.11 V, $|I_{pa}/I_{pc}|$ = 1.37) and at 1.2 V *vs.* Fc^+/Fc (ΔE_p = 0.14 V). According to DFT calculations performed for a similar salophen-type iron(III) complex (Chapter 6) suggested that the first oxidation is a ligand-

based event giving rise to a radical delocalized over the phenylenediamine moiety, while the second oxidation is a phenolate/phenoxyl redox couple. There are a number of ligand-based reduction moieties present in complex **2**, such as nitro and azomethine moieties. Therefore, they appeared as disordered irreversible redox processes in the region from -1 to -2.5 V (**Figure 4.3a**).

	$E_{1/2}$, (ΔE_p) (V) | I_{pa}/I_{pc} |	$E_{1/2}$, (ΔE_p) (V) | I_{pa}/I_{pc} |	$E_{1/2}$, (ΔE_p) (V) | I_{pa}/I_{pc} |	$E_{1/2}$, (ΔE_p) (V) | I_{pa}/I_{pc} |	$E_{1/2}$, (ΔE_p) (V)
(1)	-1.056 (0.072) | 1.088 |	-1.364 (0.076) | 1.075 |	-1.611 (0.062) | 1.006 |	0.541 (0.178) | 1.031 |	0.803 (0.086)
(2)	-0.774 (0.104) | 0.72 |	0.987 (0.106) | 1.37 |	1.2 (0.14)		

Table 4.4. Cyclic voltammetry data for complexes **1** and **2**.
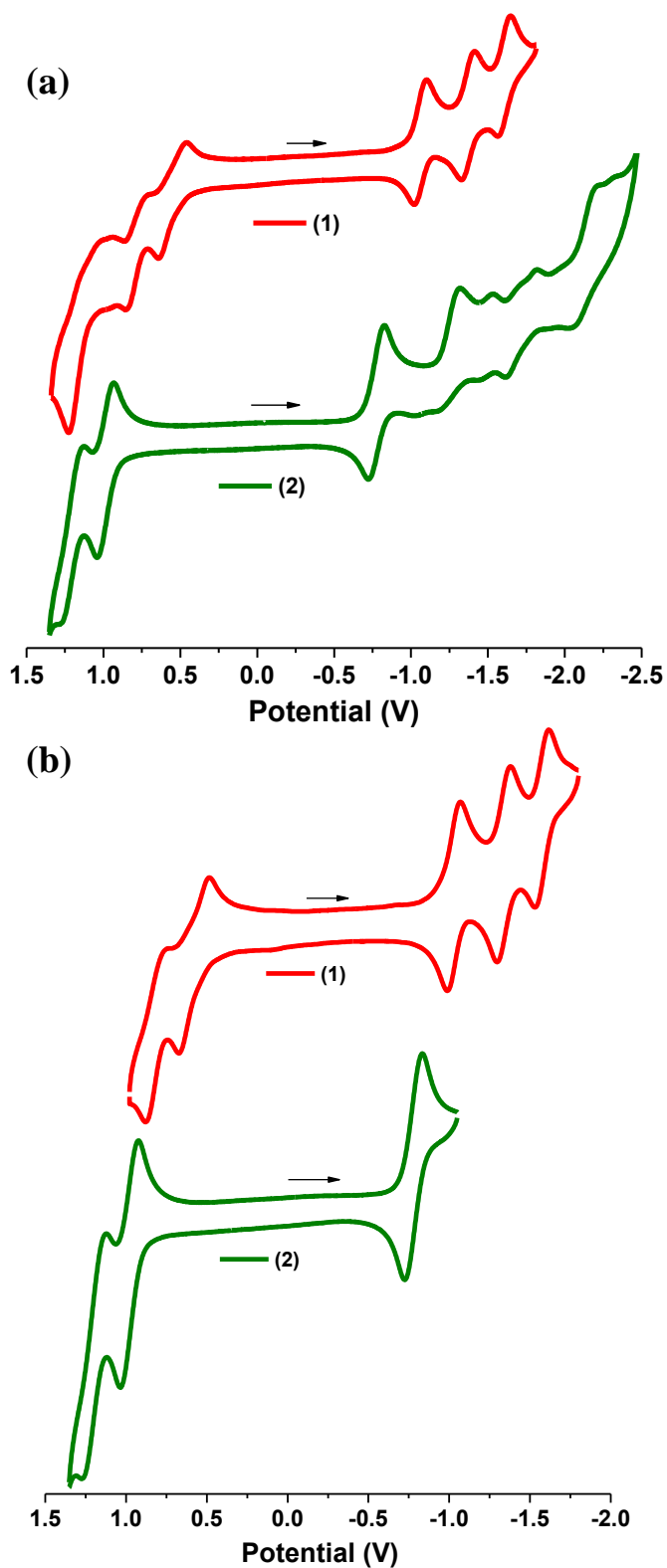
Figure 4.3. Cyclic voltammograms of 1.0×10^{-3} mol•L^{-1} solutions for iron(III) complexes **1** and **2**. (a) Full scale and (b) isolated region with most reversible redox processes.

4.3.5 Spectroelectrochemical Properties

Spectroelectrochemical experiments were carried out to clarify the spectral assignments of complex **1** and to identify the absorption bands associated with the C=N, azomethine moiety. The experiments were performed using fixed potential method in dichloromethane solutions of complex **1** with TBAPF$_6$ as the electrolyte. The results obtained for complex **1** during the spectroelectrochemical experiments are shown in **Figure 4.4**.

The oxidation process of complex **1** was studied by applying a fixed potential at 0.982 V *vs*. Fc$^+$/Fc. During this process, charge transfer bands appeared in the region of ~ 400-600 nm started to decrease in intensity. At the same time, the region between ~ 650 and 900 nm started to increase in intensity, with an isosbestic point observed at 630 nm (**Figure 4.4a**). The reason for this observation can be explained as follows. During the oxidation Fe^{III}-phenolate moieties will convert in to Fe^{III}-phenoxyl species. Therefore, LMCT transitions start to decrease in intensity. At the same time, because there can be charge transfer transitions between phenolate to phenoxyl moieties, a new band (at ~750 nm) starts to increase in intensity.[24]

During the reduction process of complex **1** (-1.092 V *vs*. the Fc$^+$/Fc), bands appeared in the region of ~ 550-800 nm decreased in intensity. Also, a new well-defined band started to increase at 460 nm with an isosbestic point observed at 402 nm (**Figure 4.4b**). This observation can be explained as follows. During the reduction of Fe(III) to Fe(II), LMCT charge transfers initiating from phenolate oxygens to Fe(III) becomes unfavorable. Therefore, those bands start to decrease in intensity. Concurrently, the more favorable ILCT transitions will start to increase in intensity. With these observations, the new absorption

band appeared at 460 nm can be assigned as charge transfers taking place from p_π phenolate oxygen to $p_{\pi*}$ of the azomethine moiety.
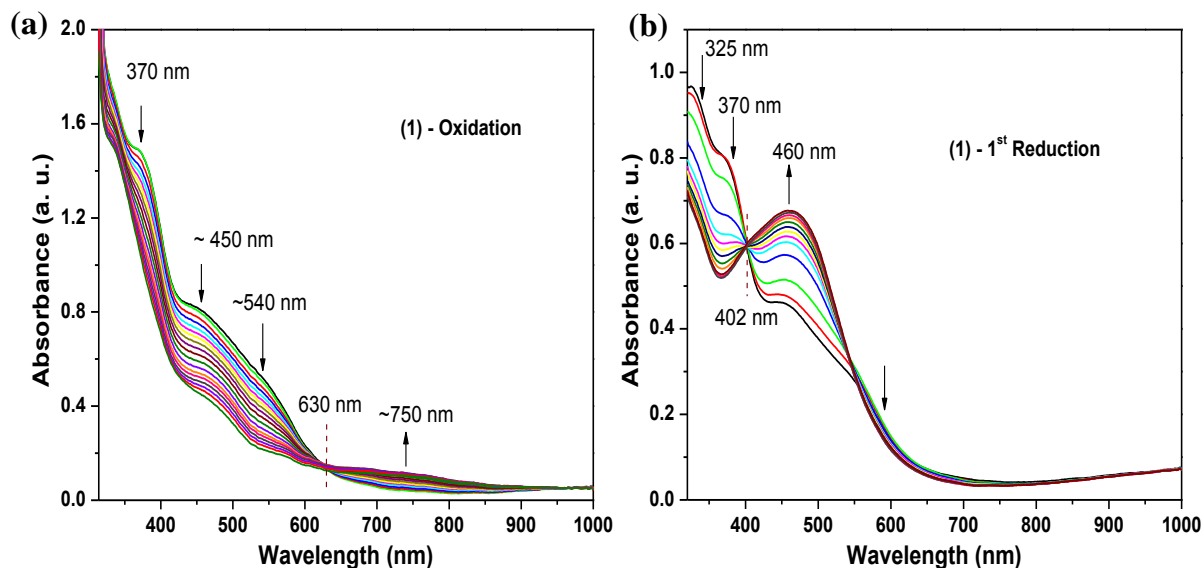
Figure 4.4. Electronic spectral changes observed during (a) oxidation and (b) first reduction for complex **1** under fixed potential conditions.

4.3.6 DFT Calculations

DFT[32] calculations, using a developed version of Gaussian,[33] were carried out for complexes **1** and **2**, to establish the redox sequence of the cathodic processes appeared in their cyclic voltammograms (**Figure 4.5a**). B3LYP functional[34] with SDD basis set[35] on iron and 6-31G(d,p) basis on the other atoms were used. Geometry optimizations were performed in the gas phase without any symmetry constraints. Solvation effects were included using SMD solvation model[36] on the gas-phase optimized geometry. The solvent used was dichloromethane. The optimized geometry of complex **1** is shown in **Figure 4.5b**, the C-N(nitro) bond distance was calculated to be 1.469Å for the *p*-nitro moiety while it was 1.476Å for the *m*-nitro functionality (*para-* and *meta*-nitro moieties were labeled with respect

to the C=N, azomethine moiety). The nitro group *para* to the azomethine moiety was found to be about 9° more coplanar with the phenyl ring when compared to the nitro group *meta* to the azomethine moiety. Therefore, the two nitro functionalities were expected to be electronically different.
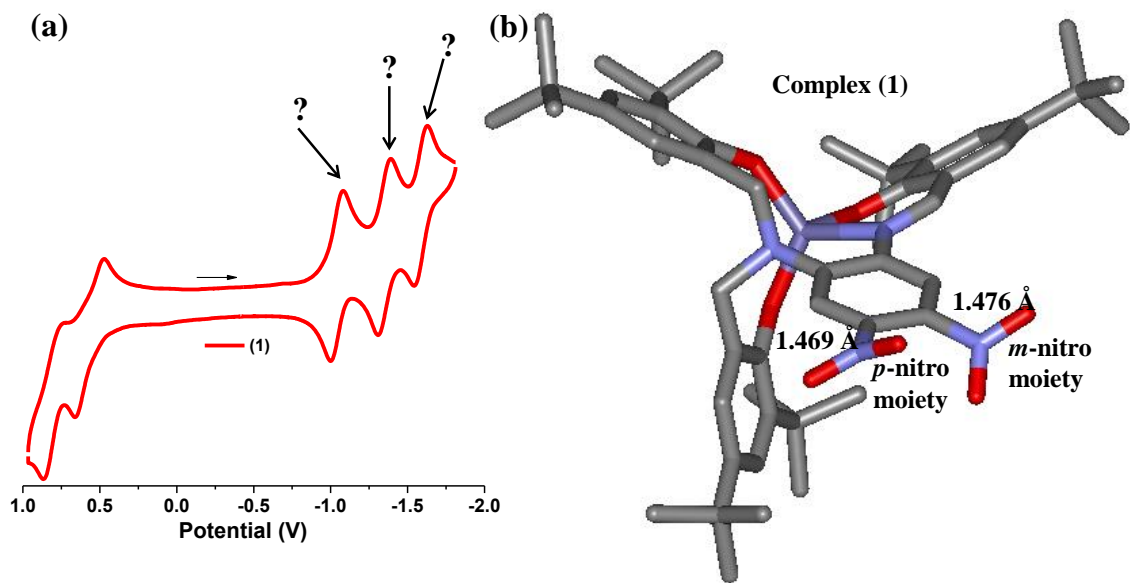
Figure 4.5. (a) Cyclic voltammogram and (b) DFT-optimized structure of complex **1**. Hydrogen atoms are omitted for clarity.

According to DFT calculations, the high spin (S = 5/2) iron(III) configuration is energetically more favorable than the low spin (S = 3/2) state by about 17 kcal/mol. Hence, complex **1** should have sextet spin state configuration as the ground state. After the first reduction of complex **1**, the calculated Mulliken spin density was found to be 3.75 on the iron center and suggested the formation of a high spin iron(II) center with a quintet (S = 4/2) spin state (**Figure 4.6**). During the reduction process of Fe(III) to Fe(II), the metal-ligand bond distances were elongated by 0.03 to 0.13 Å. The second reduction process gives rise to two possible spin states: S = 5/2 and S = 3/2. DFT calculations showed that these two configurations are isoenergetic, i.e. with 1 kcal/mol. The spin density plot of S = 5/2

configuration showed a Mulliken spin density of 0.348 on the *p*-nitro moiety and 0.278 on the *m*-nitro group as shown in **Figure 4.6**. The iron center retains the high spin configuration with a Mulliken spin density of about 4. These results indicate that unlike the first reduction, the second electron transfer happens on the nitro functionality and initially, the *p*-nitro moiety gets reduced. Because the two adjacent nitro groups are coplanar and electronically connected, the spin becomes delocalized over both the nitro functionalities after the initial reduction of the *p*-nitro moiety. The spin density plot obtained after the third electron reduction showed considerable amount of spin density around the azomethine moiety and the phenolate ring (**Figure 4.6**). Inspection of the two nitro groups revealed that the spin density on the *p*-nitro moiety being 0.338 is essentially same to what was found (0.348) in the doubly reduced species while the spin density on the *m*-nitro group is significantly increased from 0.278 in the doubly reduced species to 0.508. Therefore, we can predict that the third electron transfer happens to the *m*-nitro functionality and the spin density gets delocalized over the phenolate ring via the azomethine moiety. This delocalization is facile because the *m*-nitro group is coplanar to the azomethine functionality and the phenolate ring, and hence, they are electronically connected in the π-space. The third reduction process was found to be on the *m*-nitro functionality. This event was strongly assisted by the presence of the imine, because the azomethine moiety can help delocalization of the spin. Therefore, the resulting reduced species is stable. In order to support this phenomenon, two model systems **I** and **II** were designed (**Figure 4.7**), which can be considered as the essential simplified versions of complex **1**, where the redox active part of the ligand framework was retained. Model **I** has two nitro moieties, the azomethine unit, and the phenolate ring conjugated to each other, while in model **II**, two nitro groups were disconnected in the π-space from the azomethine

unit and the phenolate fragments. The first reduction process was found to be on one of the nitro functionalities for both the models. Model **I** has the second reduction event happening on the second nitro group, but this event was strongly assisted by the imine and the phenolate ring (as found for complex **1**), because of delocalization of the spin from nitro to imine and phenolate fragments. This kind of delocalization was not possible in the case of Model **II** and hence, the second reduction event happens on the imine and phenolate fragments, and not on the nitro moiety. As a result, unlike model **I**, the reduced species cannot gain the required stability. This phenomenon was reflected on the computed second reduction potentials for the two model systems (**Figure 4.7**). The potential for model system **II** was calculated to be more negative than that for model system **I**. Finally, we conclude that the first reduction event observed in the cyclic voltammogram of complex **1** (**Figure 4.5a**) was iron-based reduction, Fe(III)/Fe(II), while the other two reductions were based on the nitro functionalities, and not on the imine moiety. However, the imine moiety plays an important role providing significant stability to the resulting species formed after the third reduction, and as a result, the observed third reduction potential being -1.69V (*vs.* Fc$^+$/Fc couple) was not too negative. The observed imine reduction potential for complex **1** has been found at very high negative potential, about -2.5 V *vs*. Fc$^+$/Fc couple in the presence of acetonitrile solvent and TBAPF$_6$ electrolyte.
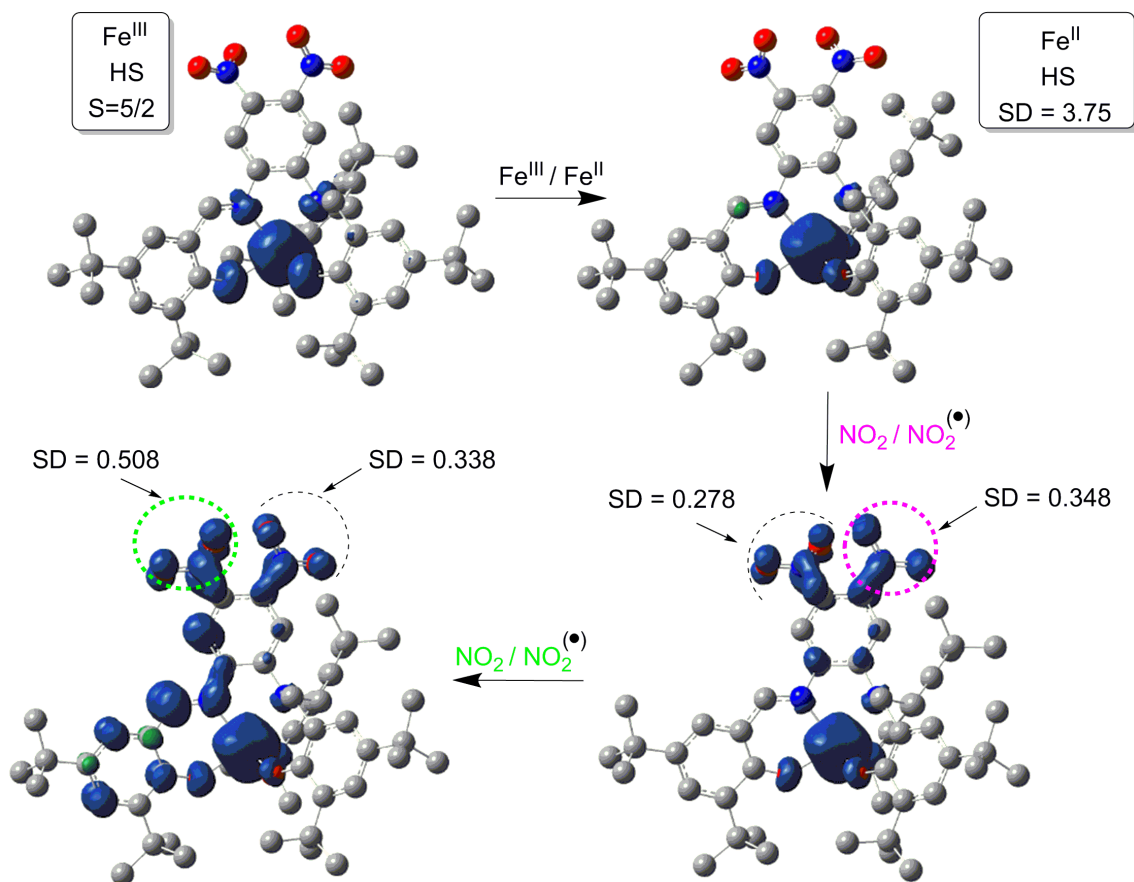
Figure 4.6. Spin Density (SD) plots of the redox active species involved in the electrochemical pathway of complex **1**. An isodensity value of 0.004 a.u. was used for plotting the spin density. Hydrogen atoms are omitted for clarity.

	Model system I	Model system II
Computed redox potential (V) second reduction	1.92	1.36

Figure 4.7. Computed potentials of the second reduction event for the simplified model systems of complex **1**.

As expected, experimental results and theoretical calculations showed that complex **1** with electron-withdrawing nitro substituents present at fourth and fifth positions of the phenylenediamine moiety can attain the Fe(III)/(II) reduction at a lower negative redox potential when compared to iron(III) complexes with electron-donating methoxy groups. This is illustrated in **Figure 4.8**. All the potentials are reported with respect to Fc$^+$/Fc couple. The calculated potential, E, has been obtained from the standard thermodynamic equation: $\Delta G_{(Solution)} = -nFE$, while $\Delta G_{(Solution)}$ has been calculated as: $G_{(reduced)} - G_{(oxidized)}$. The potential for the Fc$^+$/Fc couple was calculated at the same level of theory mentioned above. Experimentally, the difference between the first oxidation and the first reduction potentials for the nitro-substituted complex was found to be smaller than that for the methoxy substituted complex. The difference between potentials is a measure of the HOMO-LUMO energy gap of the complex. Therefore, a lower HOMO-LUMO energy gap can be expected for the nitro substituted species than that for the methoxy substituted species. This was also

supported by the DFT calculations, when we compared the calculated energy gap (of those two complexes) between the orbitals that are active for the first oxidation and the first reduction events.

Comparison of the first reduction [Fe(III)/Fe(II)] potentials
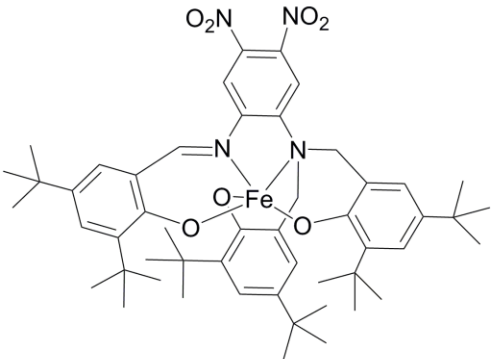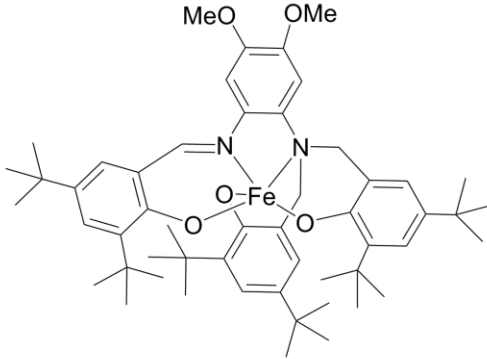
Experimental	-1.06 V	-1.45 V
Calculated	-0.63 V	-0.85 V

Figure 4.8. Change of the first reduction potential as a result of substituting the nitro functionalities with the methoxy groups on the phenylenediamine moiety of complex **1**.

The calculated electrochemical pathway of complex **2** is shown in **Figure 4.9**. Similar to what were found for complex **1**, the first reduction process was based on the reduction of Fe(III) → Fe(II), and the second and third reductions were found to be nitro-based events.
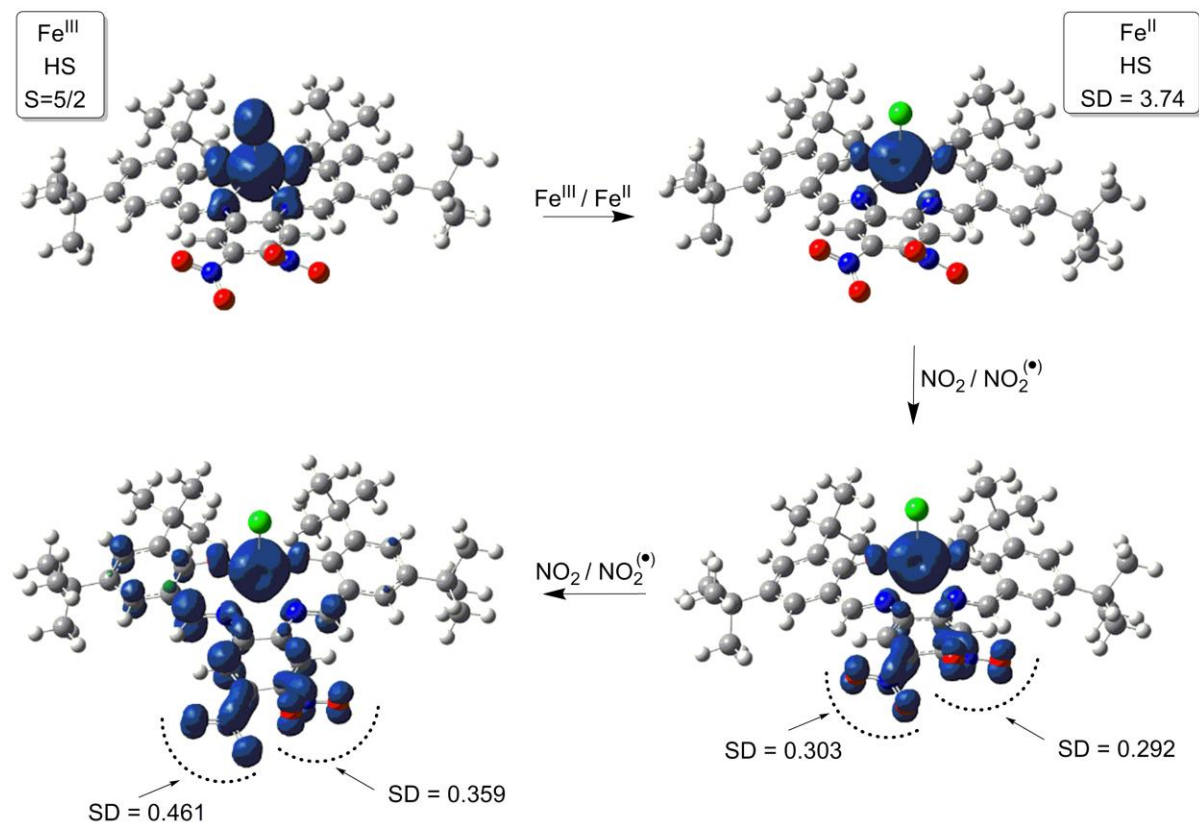
Figure 4.9. Spin Density (SD) plots of the redox active species involved in the electrochemical pathway of complex **2**. An isodensity value of 0.004 a.u. was used for plotting the spin density.

The experimental data and theoretical calculations of complexes **1** and **2** suggested that the Fe(III)/Fe(II) reduction can be obtained at a lower negative potential when there are electron-withdrawing nitro substituents present at the fourth and fifth positions of the phenylenediamine moiety. The potential gap between the first reduction and first oxidation half waves also provided an insight about the HOMO-LUMO energy gap. Therefore, we observed a lower HOMO-LUMO energy gap for nitro substituted iron(III) complexes. Low HOMO-LUMO energy gaps with accessible energies are useful when designing molecules as

unimolecular current rectifiers. Furthermore, these studies indicated that electronic and redox properties can be modulated by changing the substituents on the phenylenediamine moiety.

4.3.7 Isothermal Compression Data

The film formation ability at the air/water interface of complexes **1** and **2** were assessed using Langmuir-Blodgett (LB) and Brewster angle microscopy (BAM) methods. The obtained isothermal compression data and BAM micrographs are shown in **Figure 4.10**. To incorporate hydrophilic and hydrophobic characteristics to the molecule, polar nitro and non-polar *tert*-butyl groups were introduced. According to compression isotherms of complexes **1** and **2**, molecules started to interact with each other around *ca*. 140 and 70 $Å^2$. Complex **1** showed a phase transition in the region between 9 and 14 mN/m, but complex **2** did not show such a phase rearrangement. The phase rearrangement of complex **1** was visible in the BAM micrographs because Newton rings started to appear in that surface pressure region. The BAM micrographs observed between 20 and 35 mN/m for complex **1** did not show any additional features or defects, hence, showed a homogeneous film formation at the air/water interface. Complex **2** did not show many features in the BAM micrographs and showed a homogeneous film formation between ~ 5 and 25 mN/m.
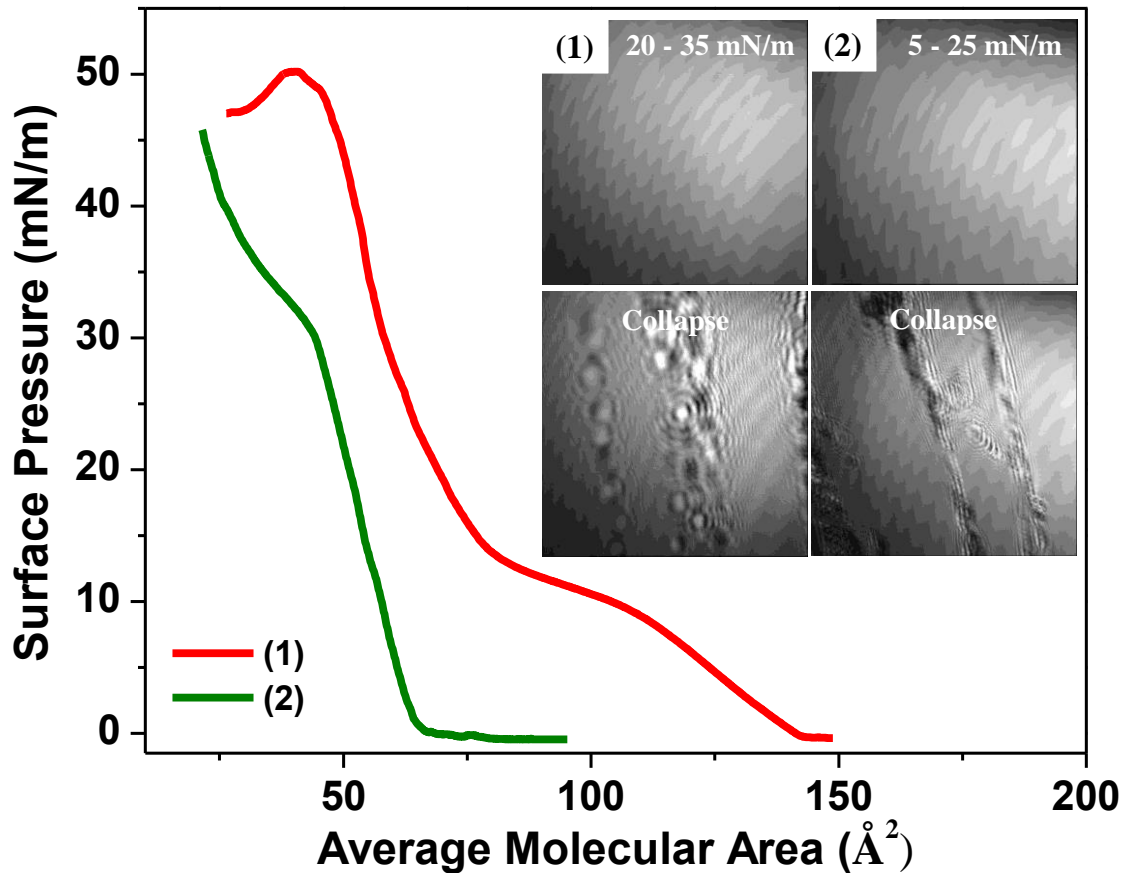
Figure 4.10. Isothermal compression and Brewster angle micrographs for complexes **1** and **2**.

The minimum average area (critical area) occupied by a molecule, after the formation of a compact well-ordered film, was calculated by extrapolating the steepest portion of the isotherm. The critical areas observed for complexes **1** and **2** were *ca*. 90 and 65 Å^2, respectively. The films started to collapse by following the classic Ries mechanism,[37,38] and this was evident in the BAM micrographs by the formation of arrays of Newton rings. Complexes **1** and **2** started to collapse at *ca*. 40 and 30 mN/m, respectively, by following a constant pressure collapse mechanism.

4.3.8 Langmuir-Blodgett Film Characterization using UV-visible Spectroscopy, Infrared Reflection Absorption Spectroscopy, and Mass Spectrometry Methods

The spectroscopic characterizations of thin films are important in gaining information regarding the structure composition and packing topology.[39] Multilayers of complexes **1** and **2** were deposited onto glass substrates, and then, they were characterized using UV-visible and infrared reflection absorption spectroscopic methods. For each of these experiments, fifty depositions were carried out using y-type dipping method at 22 mN/m. Complex **1** showed a transfer ratio close to unity, and complex **2** showed a transfer ratio ≤ 0.5, due to poor adhesion. The UV-visible spectra obtained for LB films when compared to their solution spectra are shown in **Figure 4.11**. LB film spectra of complexes **1** and **2** showed similar spectral features to their solution spectra, but with slight peak shifts. The intraligand $\pi \rightarrow \pi^*$ and LMCT transitions, which appeared in solution spectra were retained in LB film spectra. Therefore, this supports that the molecular structure of complexes **1** and **2** were remained intact. The UV-visible spectra of LB films for **1** and **2** showed a bathochromic shift of absorption bands when compared to their solution spectra. This feature suggests the formation of J-type aggregates during the LB film deposition.[40,41]
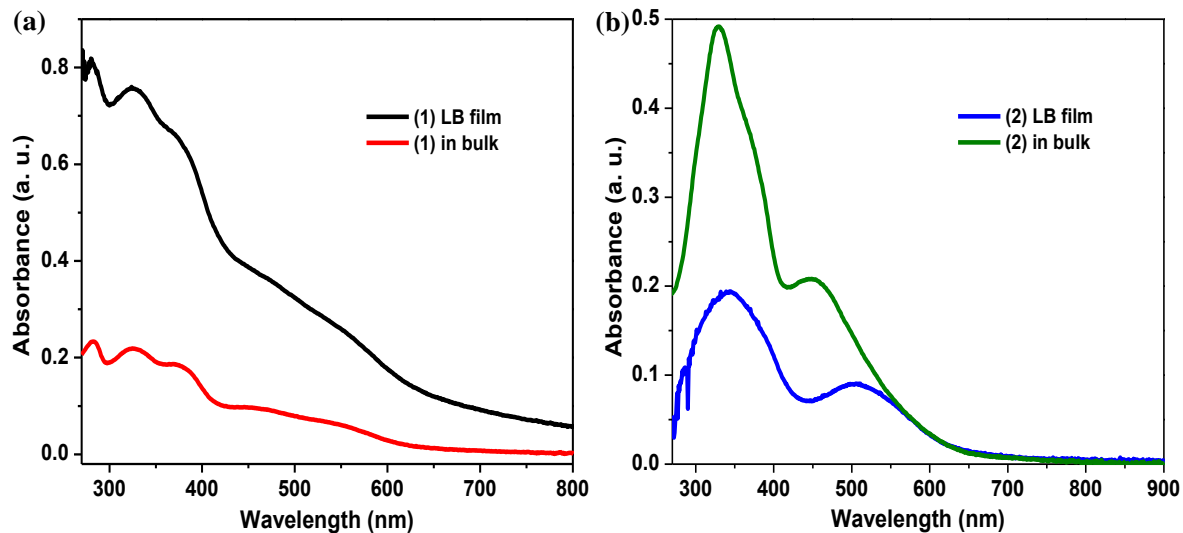
Figure 4.11. UV-visible spectra of LB films in comparison with 1.0×10^{-5} mol•L^{-1} dichloromethane solutions for (a) complex **1** and (b) complex **2**.

The IRRA spectroscopy was also used to characterize the LB films of complexes **1** and **2**. IRRA spectra of complexes **1** and **2** (50 layers) in comparison with KBr infrared spectra are shown in **Figure 4.12**. IRRA spectra of complexes **1** and **2** were measured at 30° and 40° under *p*-polarized light, respectively. The spectral features of IRRA and IR spectra of complexes **1** and **2** were comparable with each other, suggesting that the molecular structure remains intact during the film deposition. In complexes **1** and **2**, aromatic C=C stretching vibrations and CH$_n$ deformation bands appeared in the region of 1650-1300 cm^{-1}. In addition to these bands, C=N stretching vibrations appeared at 1574 and 1572 cm^{-1} for complexes **1** and **2**, respectively. The bands associated with the N=O stretching vibrations appeared at ~ 1470 and 1360 cm^{-1}.
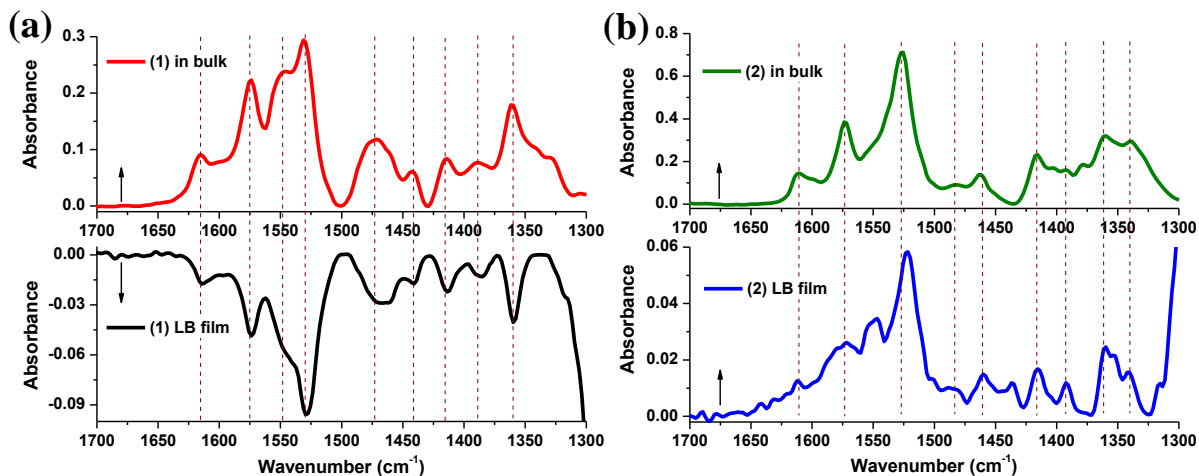
Figure 4.12. IRRA spectra of LB films (50 layers) for (a) complex **1** and (b) complex **2** in comparison with KBr infrared spectra.

In IRRA spectra, asymmetric and symmetric C-H stretching vibrations appeared in the region of 2870-2970 cm^{-1}, with a slight shift of bands when compared to their IR spectra (**Figure 4.13**). In complex **1**, IR bands were observed at 2957, 2905, and 2868 cm^{-1}, but in the film these bands have been shifted to 2966, 2916, and 2874 cm^{-1}, respectively. Likewise, in complex **2** the IR bands were observed at 2960, 2907, and 2869 cm^{-1}, and have been shifted to 2960, 2922, and 2872 cm^{-1} in the film. In addition, the films of complexes **1** and **2** showed prominent asymmetric methyl stretching vibrations as well as positive and negative bands within the same spectrum. These characteristics resembled anisotropic films with well packed topologies for complexes **1** and **2**,[42,43] where the nitro groups are attached to the glass substrate and the *tert*-butyl rich metal coordinated moiety pointing in air/solid interface. The suggested arrangement of molecules was further approved by the contact angle measurements. A monolayer of complex **1** showed a static contact angle of 89.14° ± 1.35° compared to 7.46° ± 0.42° obtained for a clean glass surface. This demonstrates the intense hydrophobic nature of complex **1**.
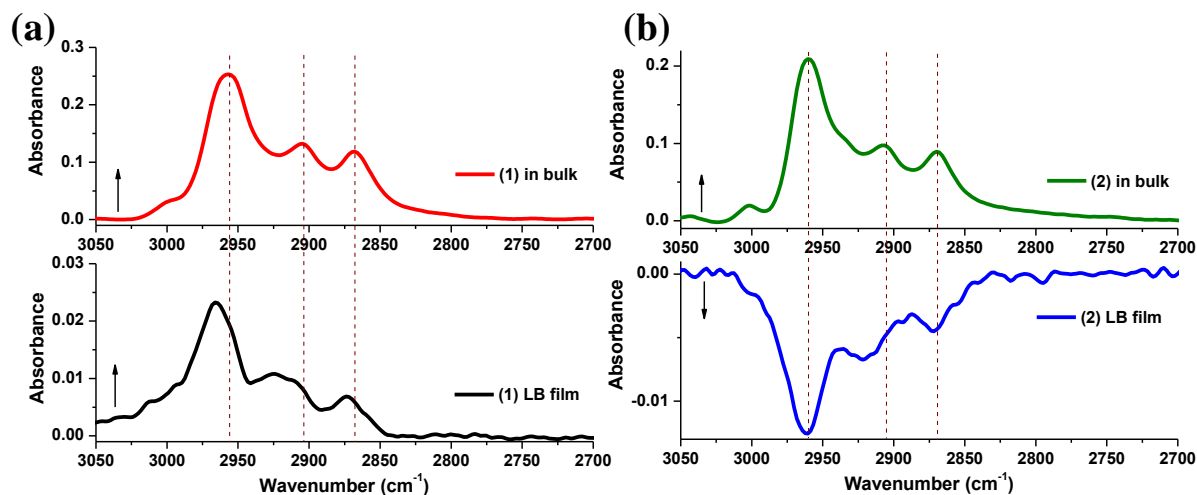
Figure 4.13. C-H stretching region of IRRA spectra for (a) complex **1** and (b) complex **2** in comparison to their bulk IR spectra.

To further analyze the structure composition of LB films, matrix assisted ionization vacuum (MAIV) mass spectrometry[44,45] was used. For this experiment, a LB monolayer of complex **1** was deposited onto a glass substrate at 22 mN/m and then the mass spectrum was recorded. The obtained mass spectrum for the LB monolayer when compared to bulk sample is shown in **Figure 4.14**. According to the observed data, the LB monolayer as well as the bulk sample of complex **1** showed molecular ion peaks at (m/z) 904.6 belonging to $[C_{51}H_{67}N_4O_7Fe + H^+]$. Therefore, this mass spectrometry data further indicated the intact molecular structure of complex **1** in the LB film.
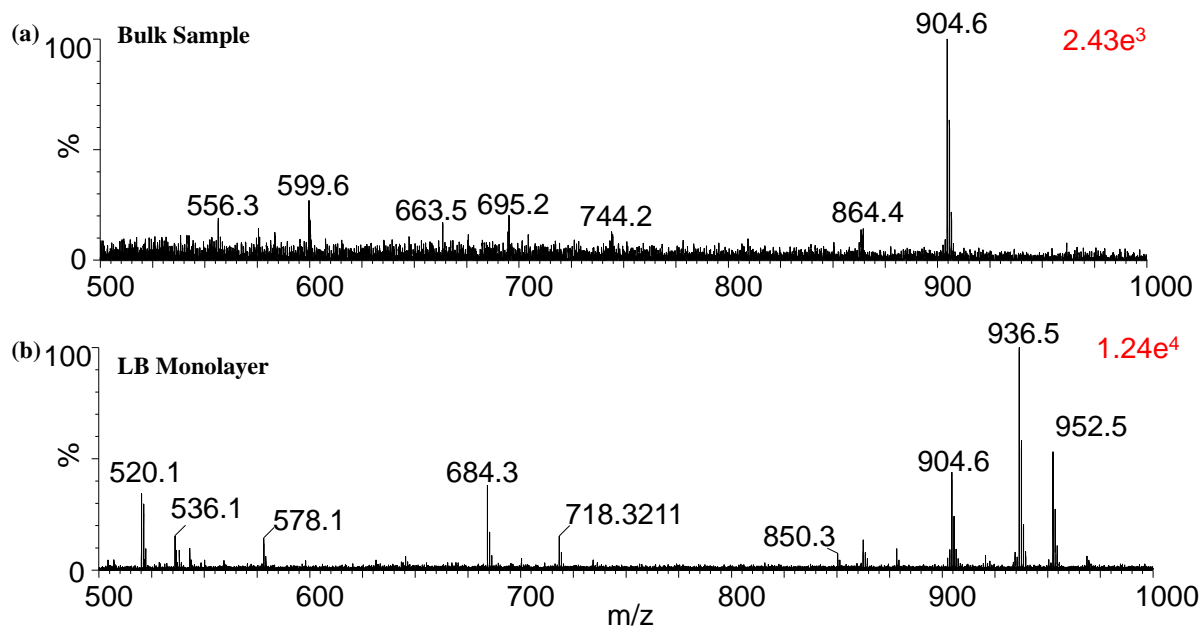
Figure 4.14. MAIV mass analysis for complex **1** (a) bulk sample and (b) LB monolayer.

4.3.9 Surface Characterization of LB films using Atomic Force Microscopy (AFM)

The surface analysis of mono and multilayer LB films were carried out using AFM method. The surface topology of LB films of complex **1** was investigated by depositing monolayer films onto mica substrates at surface pressures of 12, 20, 22, 30, 35 mN/m, and at monolayer collapse. AFM height images of monolayers at different surface pressures are shown in **Figure 4.15**. The monolayer deposited at a lower surface pressure, 12 mN/m, showed an irregular film deposition with surface defects. At 20 mN/m, the LB monolayer showed fewer defects, due to the transformation of the Langmuir film from a gaseous 2D phase to a condensed 2D phase at the air/water interface. The monolayer showed a smooth film formation at 22 mN/m. At higher surface pressures, the film became rougher due to

excess material deposition on the surface of the monolayer. Therefore, to measure the surface roughness and thickness, LB mono and multilayers were deposited at 22 mN/m.
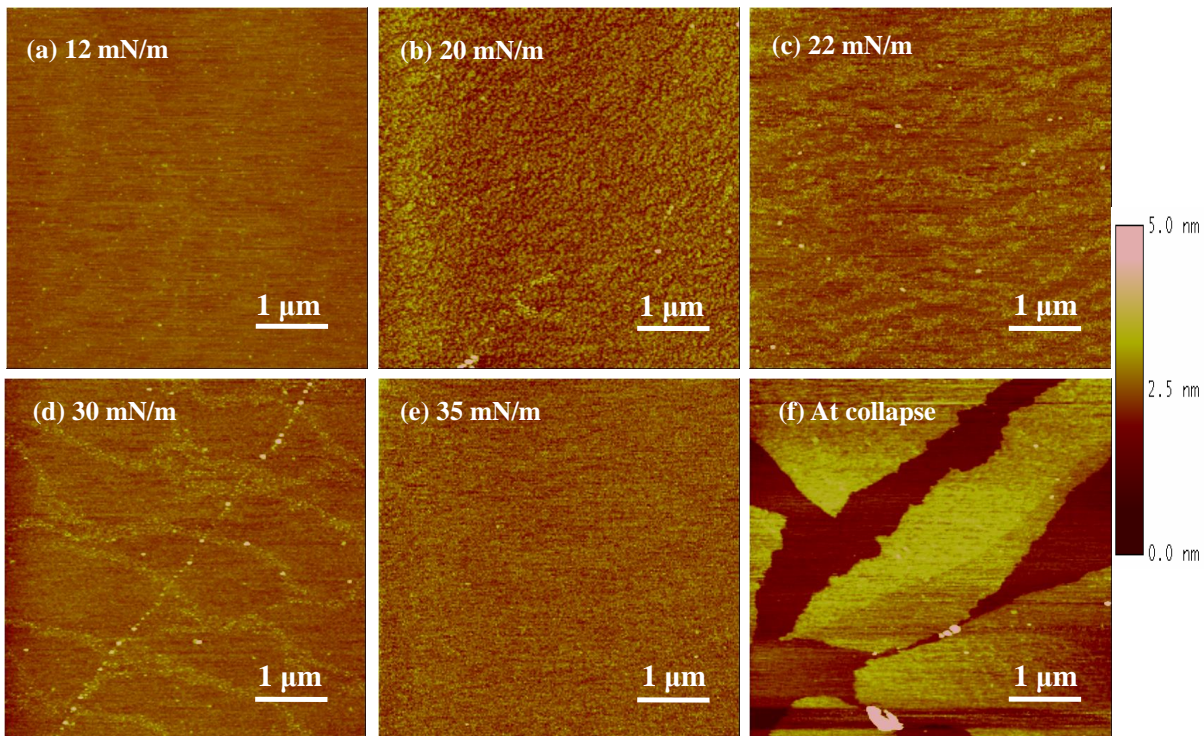
Figure 4.15. AFM height images of monolayer films for complex **1** deposited on mica substrate at (a) 12 mN/m, (b) 20 mN/m, (c) 22 mN/m, (d) 30 mN/m, (e) 35 mN/m, and (f) at collapse; the scan size is 5 μm and the Z range is 5 nm for all images.

The surface roughness of mono and multilayer LB films were measured using AFM. Mica substrates were used to deposit the LB films. Height images and the corresponding 3D surface images of complex **1** ranging from 1 to 15 layers are shown in **Figure 4.16**. As the number of the layers increased, the film surface became rougher due to particle aggregation on the surface of the film.
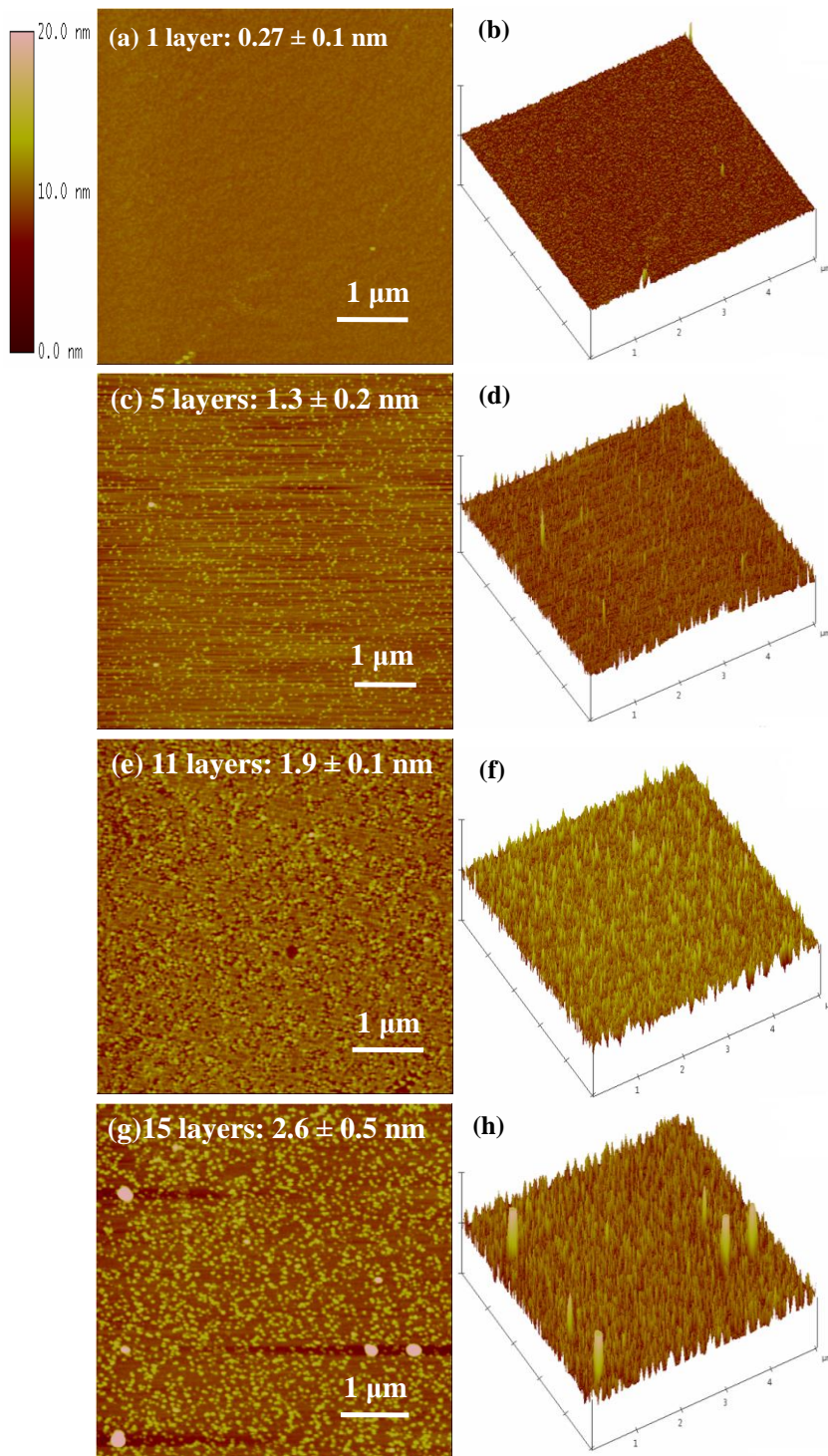
Figure 4.16. Surface roughness measurements of 1-15 LB layers for complex **1** deposited on mica substrates. AFM height images (left) and 3D surface plots (right). (a, b) 1; (c, d) 5; (e, f) 11; (g, h) 15 layers, the scan size is 5 μm and the Z range is 20 nm for the images.

The thickness of the films ranging from 1 to 15 layers deposited onto quartz substrates were examined by intentional scratching of the film with a sharp blade, and by measuring the depth of the scratch. **Figure 4.17** shows the AFM height image (2D), the 3D surface image, the corresponding sectional analysis along the black solid line indicated in the 3D image for an 11 layer LB film, and the plot between number of layers and the layer thickness for complex **1**. Height differences between the red arrows indicated the film thickness. According to this data, the experimental monolayer thickness for complex **1** was found to be 1.3 ± 0.3 nm. The plot obtained between the number of layers *vs.* the layer thickness (**Figure 4.17d**) showed a linear relationship indicating a homogeneous film deposition. According to the crystal structure data of complex **1**, the approximate length of the molecule is 12-13 Å. Therefore, this result is in excellent agreement with the monolayer thickness obtained from the AFM analysis. A summary of the film roughness and thickness measurements are tabulated in **Table 4.5**.

Number of Layers	Surface Roughness (nm)	Thickness of the Film (nm)
1	0.27 ± 0.1	1.3 ± 0.3
5	1.3 ± 0.2	4.7 ± 0.5
11	1.9 ± 0.1	9.1 ± 0.4
15	2.6 ± 0.5	14.0 ± 1.7

Table 4.5. Surface roughness and thickness data of 1-15 layers for complex **1**.
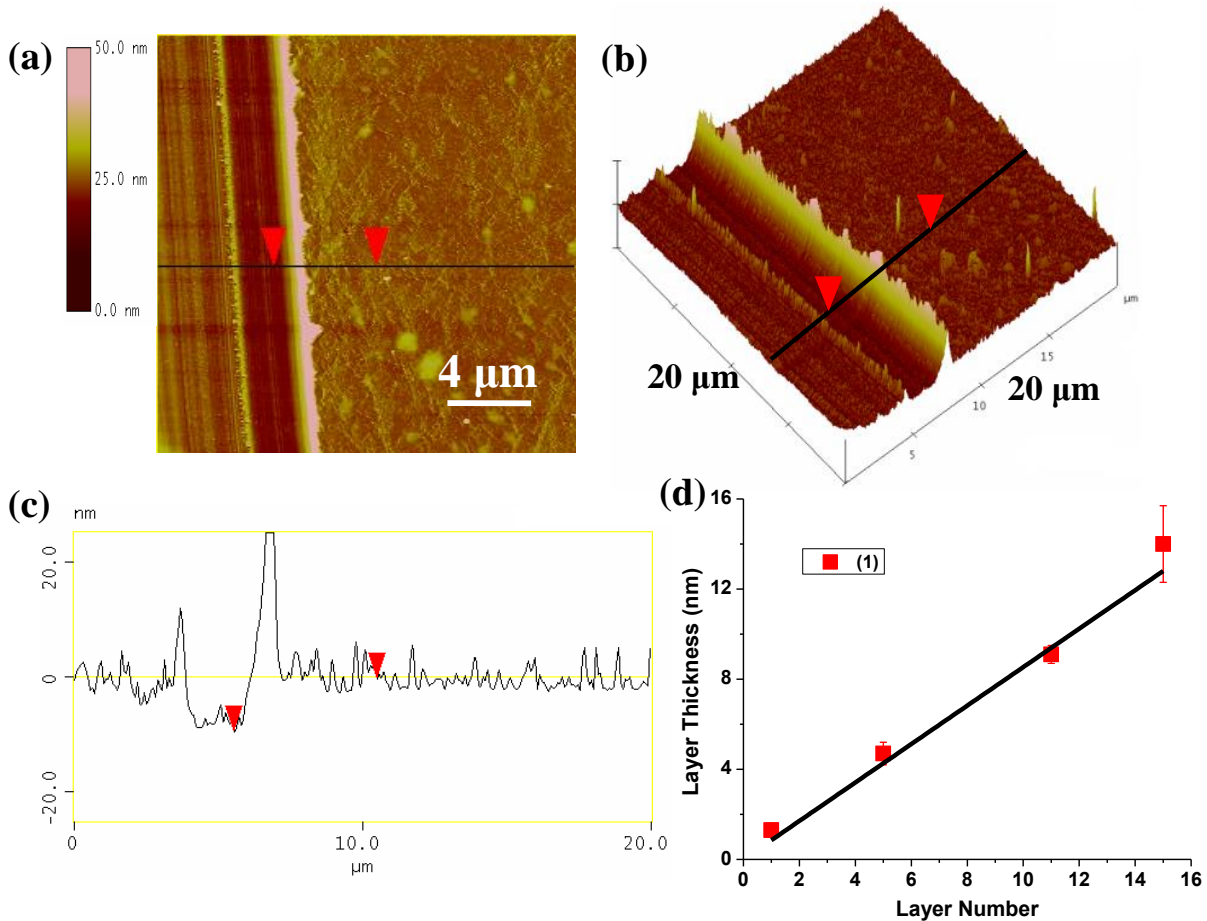
Figure 4.17. AFM height images and sectional analysis of complex **1** (11 layers) on quartz. (a) 2D view, (b) 3D view, (c) sectional analysis along the black solid line, and (d) plot between the thickness (nm) *vs*. number of layers from 1 to 15 layers.

4.4 Conclusions

Two new nitro substituted asymmetric iron(III) complexes with pentacoordinate geometry were successfully synthesized and characterized. Due to the introduction of nitro substituents, complex **1** exhibited well-behaved redox properties. Complex **1** showed metal- and ligand-centered reduction processes and showed that the Fe(III)/Fe(II) reduction can be obtained at much lower potentials compared to iron(III) complexes with

electron-donating substituents. Electrochemical and DFT data revealed a decrease in HOMO-LUMO energy gap when compared to other iron(III) complexes with electron-donating substituents, due to the lowering of the LUMO energy level. Both of these complexes showed a homogeneous film formation at the air/water interface. The LB films of complexes **1** and **2** were able to deposit onto solid substrates, but complex **2** showed poor adhesive properties. The LB films were thoroughly characterized using different spectroscopic, spectrometric, and microscopic methods. According to these data, the molecular structure remained intact in both complexes. Well-ordered LB films of complexes **1** and **2** were observed, with possible J-type aggregates. Experiments that were carried out to understand the properties of complexes **1** and **2**, proposed successful results in obtaining better redox and electronic properties with possible donor and acceptor moieties. Electrochemical data and DFT calculations suggested that the introduction of nitro substituents were important for modulation of HOMO and LUMO energies of the iron(III) complexes, which is an important factor when designing molecule-based current rectifiers.

REFERENCES

1. Park, J.; Pasupathy, A. N.; Goldsmith, J. I.; Chang, C.; Yaish, Y.; Petta, J. R.; Rinkoski, M.; Sethna, J. P.; Abruña, H. D.; McEuen, P. L.; Ralph, D. C. *Nature* **2002**, *417*, 722.

2. Liang, W.; Shores, M. P.; Bockrath, M.; Long, J. R.; Park, H. *Nature* **2002**, *417*, 725.

3. Lee, Y.; Yuan, S.; Sanchez, A.; Yu, L. *Chem. Commun*. **2008**, 247.

4. Handayani, M.; Gohda, S.; Tanaka, D.; Ogawa, T. *Chem. Eur. J.* **2014**, DOI: 10.1002/chem.201402052

5. Paul, N. D.; Rana, U.; Goswami, S.; Mondal, T. K.; Goswami, S. *J. Am. Chem. Soc.* **2012**, *134*, 6520.

6. Szaciłowski, K.; Macyk, W.; Stochel, G. *J. Am. Chem. Soc*. **2006**, *128*, 4550.

7. Oszajca, M. F.; McCall, K. L.; Robertson, N.; Szacizowski, K. *J. Phys. Chem. C* **2011**, *115*, 12187.

8. Wickramasinghe, L. D.; Perera, M. M.; Li, L.; Mao, G.; Zhou, Z.; Verani, C. N. *Angew. Chem. Int. Ed*. **2013**, *52*, 13346.

9. Metzger, R. M. *Chem. Rev.* **2003,** *103,* 3803.

10. Aviram, A.; Ratner, M. *Chem. Phys. Lett.* **1974**, *29*, 277.

11. Metzger, R. M. *J. Mater. Chem.* **2008**, *18*, 4364.

12. Ramsey, A. J.; Hillas, P. J.; Fitzpatrick, P. F. *J. Biol. Chem.* **1996**, *271*, 24395.

13. (a) Pratt, R. C.; Mirica, L. M.; Stack, T. D. P. *Inorg. Chem.* **2004**, *43*, 8030. (b) Chaudhuri, P.; Wieghardt, K. *Prog. Inorg. Chem.* **2001**, *50*, 151. (c) Jadzewski, B. A.; Tolman, W. B *Coord. Chem. ReV.* **2000**, *200-202*, 633.

14. Bigelow, W. C.; Pickett D. L.; Zisman, W. A. *J. Colloid Sci.* **1946**, *1*, 513.

15. Sagiv, J. *J. Am. Chem. Soc.* **1980**, *102*, 92.

16. Bain, C. D.; Troughton, E. B.; Tao, Y. T.; Evail, J.; Whitesides G. M.; Nuzzo, R. G. *J. Am. Chem. Soc.* **1989**, *111*, 321.

17. Schottky, W. *Z. Phys.* **1942**, *118*, 539.

18. (a) Blodgett, K. B. *J. Am. Chem. Soc.* **1935**, *57*, 1007. (b) Blodgett K. B.; Langmuir, I. *Phys. Rev.* **1937**, *51*, 964.

19. Sokolowski, A.; Müller, J.; Weyhermüller, T.; Schnepf, R.; Hildebrandt, P.; Hildenbrand, K.; Bothe, E.; Wieghardt, K. *J. Am. Chem. Soc.* **1997**, *119*, 8889.

20. Lanznaster, M.; Hratchian, H. P.; Heeg, M. J.; Hryhorczuk, L. M.; McGarvey, B. R.; Schlegel, H. B.; Verani, C. N. *Inorg. Chem.* **2006**, *45*, 955.

21. (a) Shang, X. F.; Lin, H.; Lin, H. K. *Journal of Fluorine Chemistry* **2007**, *128*, 530. (b) Cheeseman, G. W. H. *J. Chem. Soc.* **1962**, 1170.

22. Nakamoto, K. *Infrared and Raman Spectra of Inorganic and Coordination Compounds, Part B: Applications in Coordination, Organometallic and Bioinorganic Chemistry,* 6th ed.; John Wiley & Sons, Inc., Hoboken, New Jersey, 2008; chapter 1, pp 1-222.

23. Lanznaster, M.; Heeg, M. J.; Yee, G. T.; McGarvey, B. R.; Verani, C. N.; *Inorg. Chem.* **2007**, *46*, 72.

24. Allard, M. M.; Sonk, J. A.; Heeg, M. J.; McGarvey, B. R.; Schlegel, H. B.; Verani, C. N.; *Angew. Chem. Int. Ed*. **2012**, *51*, 3178.

25. Mayilmurugan, R; Stoeckli-Evans, H.; Suresh, E.; Palaniandavar, M. *Dalton Trans.* **2009**, 5101.

26. Mayilmurugan, R.; Suresh E.; Palaniandavar, M. *Inorg. Chem.* **2007**, *46*, 6038.

27. Pyrz, J. W.; Roe, A. L.; Stern, L. J.; Que, Jr. L.; *J. Am. Chem. Soc.* 1985, 107 , 614.

28. Auerbach, U.; Eckert, U.; Wieghardt, K.; Nuber, B.; Weiss, J.; *Inorg. Chem.* **1990,** *29,* 938.

29. Shongwe, M. S.; Kaschula, C. H.; Adsetts, M. S.; Ainscough, E. W.; A. M.Brodie,; Morris, M.J.; *Inorg. Chem.* **2005**, *44*, 3070.

30. Gaber, B. P.; Miskowski, V.; Spiro, T. G.; *J. Am. Chem. Soc.* **1974**, *96*, 6868.

31. Bania, K. K.; Bharali, D.; Viswanathan, B.; Deka, R. C. *Inorg. Chem.* **2012**, *51*, 1657.

32. Parr, R. G.; Yang, W. *Density-functional theory of atoms and molecules*; Oxford University Press: New York, 1989.

33. Frisch, M. J.; Trucks, G. W.; Schlegel, H. B.; Scuseria, G. E.; Robb, M. A.; Cheeseman, J. R.; Scalmani, G.; Barone, V.; Mennucci, B.; Petersson, G. A.; Nakatsuji, H.; Caricato, M.; Li, X.; Hratchian, H. P.; Izmaylov, A. F.; Bloino, J.; Zheng, G.; Sonnenberg, J. L.; Hada, M.; Ehara, M.; Toyota, K.; Fukuda, R.; Hasegawa, J.; Ishida, M.; Nakajima, T.; Honda, Y.; Kitao, O.; Nakai, H.; Vreven, T.; Montgomery, J., J. A.; Peralta, J. E.; Ogliaro, F.; Bearpark, M.; Heyd, J. J.; Brothers, E.; Kudin, K. N.; Staroverov, V. N.; Kobayashi, R.; Normand, J.; Raghavachari, K.; Rendell, A.; Burant, J. C.; Iyengar, S. S.; Tomasi, J.; Cossi, M.; Rega, N.; Millam, J. M.; Klene, M.; Knox, J. E.; Cross, J. B.; Bakken, V.; Adamo, C.; Jaramillo, J.; Gomperts, R.; Stratmann, R. E.; Yazyev, O.; Austin, A. J.; Cammi, R.; Pomelli, C.; Ochterski, J. W.; Salvador, P.; Dannenberg, J. J.; Dapprich, S.; Parandekar, P. V.; Mayhall, N. J.; Daniels, A. D.; Farkas, O.; Foresman, J. B.; Ortiz, J. V.; Cioslowski, J.; Fox, D. J. Gaussian Development Version; Revision H.31 ed.; Gaussian, Inc.: Wallingford, CT, 2010.

34. (a) Vosko, S. H.; Wilk, L.; Nusair, M. *Can. J. Phys.* **1980**, *58*, 1200. (b) Lee, C. T.; Yang, W. T.; Parr, R. G. *Phys. Rev. B* **1988**, *37*, 785.

35. (a) Dunning, T. H. Jr.; Hay, P. J. *In Modern Theoretical Chemistry*; Schaefer, H. F., III, Ed.; Plenum: New York, **1976**, *3*, 1. (b) Andrae, D.; Haussermann, U.; Dolg, M.; Stoll, H.; Preuss, H. *Theor.Chim.Acta* **1990**, *77*, 123.

36. (a) Marenich, A. V.; Cramer, C. J.; Truhlar, D. G. *J. Phys. Chem. B* **2009**, *113*, 6378. (b) Miertus, S.; Scrocco, E.; Tomasi, *J. Chem. Phys.* **1981**, *55*, 117. (c) Scalmani, G.; Frisch, M. J. *J. Chem. Phys.* **2010**, *132*, 114110. (d) Scalmani, G.; Frisch, M. J.; Mennucci, B.; Tomasi, J.; Cammi, R.; Barone, V. *J. Chem. Phys.* **2006**, *124*, 9410. (e) Tomasi, J.; Mennucci, B.; Cammi, R. *Chem. Rev*. **2005**, *105*, 2999.

37. Ries Jr., H. E. *Nature* **1979**, *281*, 287.

38. Ries, H. E.; Swift, H. *Langmuir* **1987**, *3*, 853.

39. Menzel, H.; McBride, J. S.; Weichart, B.; Ruther, M. *Thin Solid Films* **1996**, *284-285*, 640.

40. Menzel, H.; Weichart, B. *Langmuir* **1994**, *10*, 1926.

41. Joy, S.; Pal, P.; Mondal,T. K.; Talapatra, G. B.; Goswami, S. *Chem. Eur. J.* **2012**, *18*, 1761.

42. Brezesinski, G.; Stefaniu, C.; Nandy, D.; Dutta Banik, S.; Nandi, N.; Vollhardt, D. *J. Phys. Chem. C*. **2010**, *114*, 15695.

43. Wang, L.; Cruz, A.; Flach, C. R.; Pérez-Gil, J.; Mendelsohn, R.; *Langmuir* **2007,** *23,* 4950.

44. Trimpin, S.; Inutan, E. D. *Analytical Chemistry* **2013**, *85*, 2005.

45. Trimpin, S.; Inutan, E. D. *J. Am. Soc. Mass Spectrom.* **2013**, *24*, 722.

CHAPTER 5

STUDY OF THE RECTIFICATION BEHAVIOR IN NANOSCALE DEVICES BASED OF AN ASYMMETRIC FIVE-COORDINATE IRON(III)/PHENOLATE COMPLEX

The data described in this chapter has been published by Lanka D. Wickramasinghe, Meeghage Madusanka Perera, Li Li, Guangzhao Mao, Zhixian Zhou, and Cláudio N. Verani* in *Angew. Chem. Int. Ed.* **2013**, *52*, 13346-13350. Copyright 2013 WILEY-VCH Verlag GmbH & Co. KGaA, Weinheim.

5.1 Introduction

Rectification is characterized by an asymmetric flow of electric current. In macroscopic electrical circuitry, rectifiers such as vacuum tubes or solid state diodes control the mobility of current enabling it to flow in one direction and preventing reversibility. This directionality is fundamental to the conversion of alternating into direct current. Molecular rectification, proposed in the celebrated Aviram-Ratner ansatz,[1] anticipates the feasibility of the same directional current flow taking place in an electrode|molecule|electrode junction. Central to this paradigm is the existence of asymmetric molecules that incorporate electron-donor and electron-acceptor moieties, [DA], with an excited state [D$^+$A$^-$] of higher but accessible energy.[2] Usually, donor and acceptor are separated by a σ- or π-bridge to decrease electronic coupling[3] and, if the requirements are fulfilled, rectification occurs with contributions from Schottky, asymmetric, and/or unimolecular mechanisms. Schottky rectification is based on interfacial dipoles from electrode contact or on covalent bonding between the molecule and the electrode.[4] Asymmetric and unimolecular mechanisms rely on

the use of frontier molecular orbitals of the molecule; while the former relies on asymmetric placement of the HOMO or the LUMO in the electrode|molecule|electrode assembly, the latter is based on small HOMO-LUMO gaps that allow for through-molecule current flow.[4a,5] While experimental distinction between asymmetric and unimolecular contributions can be ambiguous, there is consensus that electroactive molecules with local low-symmetry[6] constitute good candidates for the enterprise, and well-documented cases of molecular rectification rely heavily on the formation of high-quality Langmuir-Blodgett films.[7]

Although it has been shown that self-assembled monoayers of polypyridine-cobalt(II) complexes in octahedral environments[8] can act as single-electron transistors and induce increased resistance (Coulomb blockade) at cryogenic temperatures, the incorporation of transition metal complexes into electrode|molecule junctions has favored symmetric molecules and has been rather slow in development. Examples involve assemblies based on metallo-porphyrins,[9] terpyridine-ruthenium(II),[10] as well as trivalent cobalt[11] and rhodium[12] azo-containing species in octahedral environments and capable of symmetrical conductance relevant for memory switching devices. An example of rectification based on an octahedral bipyridine/acac-ruthenium(II) system has been reported,[13] but the effect of lowering global symmetries around the metal center is yet to be tested.

The Verani group is engaged in an effort to integrate bioinspired asymmetry principles into new molecular materials, aiming to develop redox-responsive metallosurfactants with topologies that display unique structural, spectroscopic, and surface patterning behavior. The Verani group recently reported the redox and electronic behavior of five-coordinate complexes where the iron(III) ion is bound to low-symmetry, phenolate-rich, $[N_2O_3]$ environments and have shown that geometric and electronic constraints determine the

sequence by which the metal and each of the phenolates is oxidized.[14] In this account, a new iron(III) species **[Fe^{III}L^4] (1)** (**Scheme 5.1**) is reported. This species shows marked local asymmetries and is based on a newly synthesized amphiphilic and redox-active [N$_2$O$_3$] ligand. The complex takes advantage of the presence of phenylenediamino-metal and phenyl/phenolate moieties that can act respectively as electron-acceptors and donors. The viability of **1** as precursor for Langmuir-Blodgett (LB) films, as well as its use in the fabrication of nanoscale rectifying devices was probed.
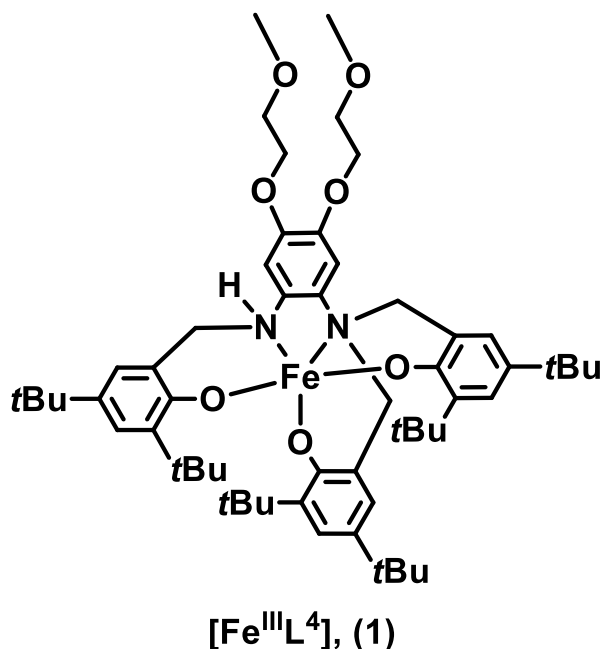
[Fe^{III}L^4], (1)

Scheme 5.1. The five-coordinate iron(III)/N$_2$O$_3$ complex **[Fe^{III}L^4]**.

5.2 Experimental Section

5.2.1 Synthesis of the Ligand and Iron(III) Complex (1)

The synthesis of the ligand **[H$_3$L^4]**, *(6,6'-(2-(3,5-di-tert-butyl-2-hydroxybenzylamino)-4,5-bis(2-methoxyethoxy)phenylazanediyl)bis(methylene)bis(2,4-di-tert-butylphenol),* was described in chapter 3.

Synthesis of complex [Fe^{III}L^4] (1).

Complex **[Fe^{III}L^4]** (**1**) was synthesized as follows: A solution containing 1 equivalent of **[H$_3$L^4]** (0.300 g, 0.330 mmol) in methanol (25 mL) was treated with 3 equivalents of anhydrous NaOCH$_3$ (0.054 g, 0.990 mmol) and followed by addition of 1 equivalent of methanolic FeCl$_3$ (0.054 g, 0.330 mmol) under an inert atmosphere. The resulting solution was heated at 50 °C for 30 minutes. The reaction mixture was cooled to ambient temperature and stirred for 1.5 h. The solvent was removed under vacuum, and the crude product was dissolved in anhydrous dichloromethane and filtered through celite. Solvent evaporation yielded a reddish-brown precipitate of **[Fe^{III}L^4]**. Yield: 77.6%. Melting point = 140-143 °C. ESI (m/z^+) in CH$_3$OH = 964.5606 for [C$_{57}$H$_{83}$N$_2$O$_7$Fe + H$^+$] (calculated = 964.5629) in agreement with -2.38 ppm difference. Anal. Calc. for [C$_{57}$H$_{83}$N$_2$O$_7$Fe]: C, 71.01; H, 8.68; N, 2.91%. Found: C, 71.38; H, 8.57; N, 2.97%. IR (KBr, cm^{-1}) 3205 (ν_{N-H}), 2868-2954 (ν_{C-H}), 1604 ($\nu_{C=C}$, aromatic), 1512 ($\nu_{C=C}$, aromatic), 1273 (ν_{C-O-C}), 1129 (ν_{C-O-C}).

5.3 Results and Discussion

5.3.1 Synthesis and Characterization of Ligand and Iron(III) Complex

The ligand **[H$_3$L^4]** was obtained via treatment of an alkoxylated phenylenediamine obtained by multistep protocols[15] with 2,4-di-*tert*-butyl-6-(chloromethyl)phenol in presence of triethylamine (**Scheme 5.2**). The ligand **[H$_3$L^4]** was treated with anhydrous FeCl$_3$ in methanol in presence of sodium methoxide under inert conditions.
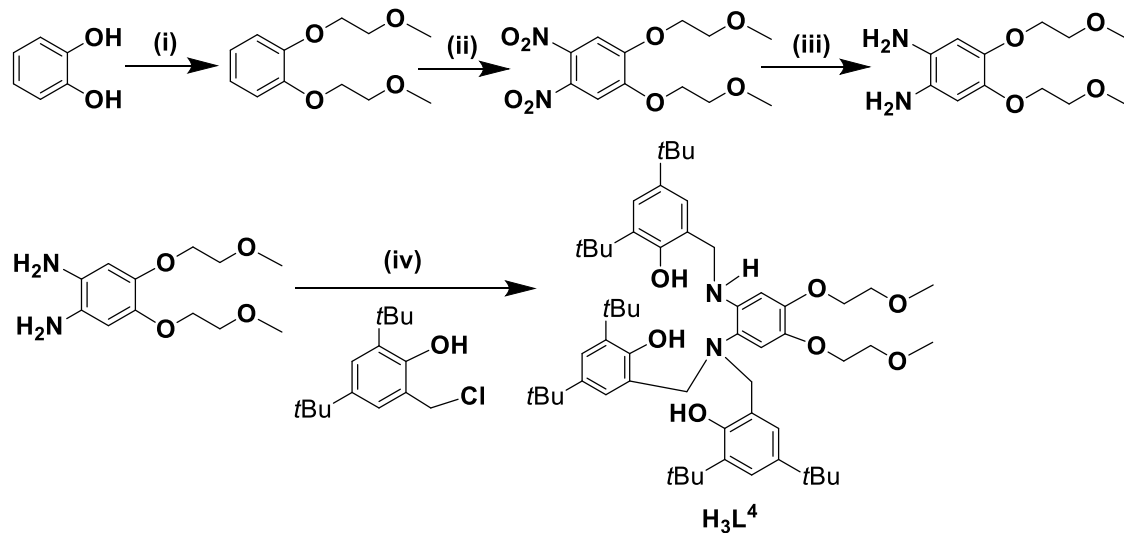
Scheme 5.2. Multistep synthesis of **[H₃L⁴]**; (i) CH₃OCH₂CH₂Br, NaOH, ethanol, 48 h reflux; (ii) HOAc, HNO₃, CH₂Cl₂, RT, 72 h; (iii) Pd/C, hydrazine, ethanol, 18 h reflux; (iv) Et₃N, CH₂Cl₂, 72 h reflux.

Species **[Fe^{III}L⁴]** (**1**) was characterized by exact mass spectrometry (**Figure 5.1**) IR and UV-visible spectroscopic methods and was in excellent agreement with combustion analysis results.
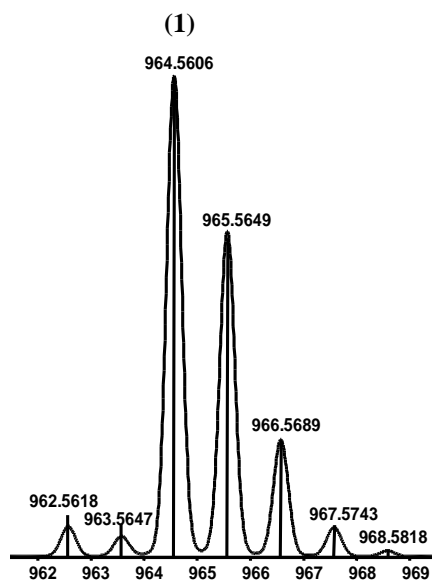
Figure 5.1. ESI (positive) peak cluster for [M+H⁺] of metal complex **1**.

5.3.2 X-ray Structural Data

Limited X-ray structural information obtained for the methoxy-substituted analogue (**Figure 5.2**), supported that **1** contains an iron(III) metal ion surrounded by three phenolate oxygen atoms and two amine nitrogen atoms of the respective ligand in a distorted trigonal bipyramidal geometry. This description was in excellent agreement with experimental and calculated species described previously by the Verani laboratory,[16] where average Fe-N and Fe-O bond distances reach 2.20 and 1.87 Å, respectively.[17] UV-visible and IR evidence suggested that **1** retains its amine character, rather than being converted by ligand oxidation into the equivalent imine species **1ⁱ**, as usually observed.[16a] This amine/imine conversion will be only observed at the air/water interface and in LB films.
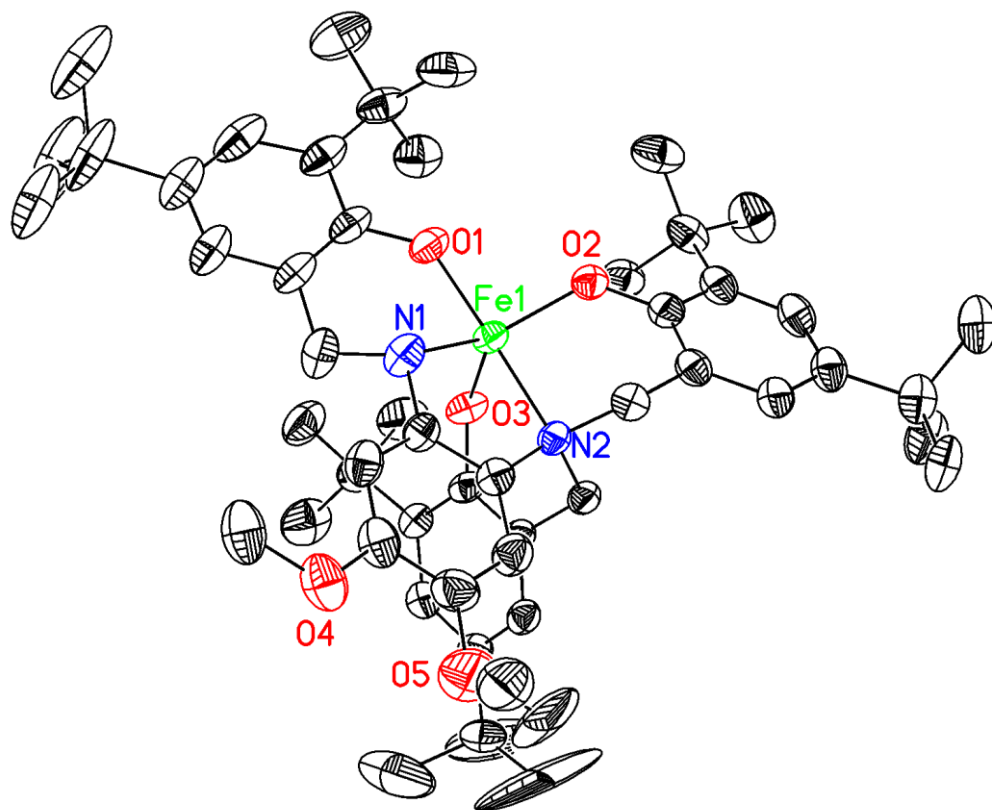
Figure 5.2. Snapshot of the methoxy substituted iron(III) complex [**FeIIILOCH3**].

5.3.3 Electronic Spectral Properties

The UV-visible spectrum of complex **1** was measured in dichloromethane. **Table 5.1** and **Figure 5.3** show the spectrum and the spectral positions obtained for metal complex **1**. Metal complex **1** showed an intense band in the near-UV region at 286 nm with ε value of ~ 23,400 L•mol^{-1}•cm^{-1} due to ligand based $\pi \rightarrow \pi^*$ electronic transitions. Also, it showed a band in the visible region, at 466 nm with ε value of ~ 6,100 L•mol^{-1}•cm^{-1}. This band can be assigned as phenolate to Fe^{III} charge transfer transition originating from p_π orbital of the phenolate oxygens to d_{π^*} of the metal center. Besides the above mentioned bands, there was another absorption band present in the near-UV region at 329 nm with ε value of ~ 10,300 L•mol^{-1}•cm^{-1} due to another ligand to metal charge transfer (LMCT) transition originating from phenolate p_π orbitals to d_{σ^*} of the metal center. The spectroelectrochemical experiments were carried out using fixed potentials for complex **1**, and the results obtained from the experiments were also approved the electronic spectral assignments (results will follow). In addition, the spectral assignments are well suited with literature reported iron(III) complexes under similar coordination environments.[18]

Compound	λ_{max}, nm (ε, L•mol^{-1}•cm^{-1})
(1)	286 (23423), 329 (10319), 466 (6094)

Table 5.1. UV-visible data of 1.0×10^{-4} mol•L^{-1} dichloromethane solution for complex **1**.
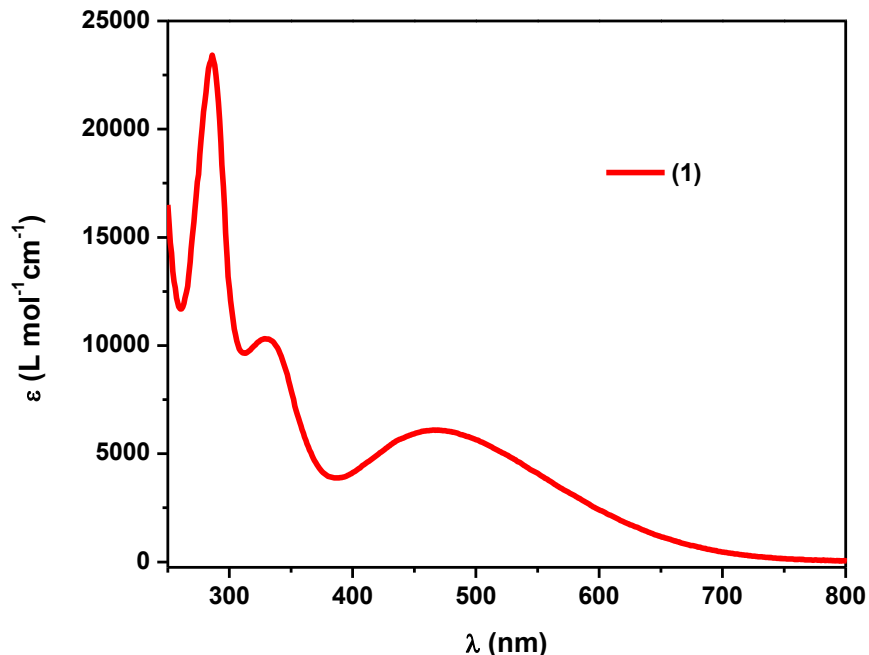
Figure 5.3. UV-visible spectrum of 1.0×10^{-4} mol•L^{-1} dichloromethane solution of **1**.

5.3.4 Electrochemical Properties

Complex **1** showed well-defined metal- and ligand-centered redox processes in dichloromethane with TBAPF$_6$ as the supporting electrolyte. The obtained cyclic voltammogram and the redox potentials are shown in **Figure 5.4** and **Table 5.2**. A cathodic process that appeared at ~ -1.49 V *vs.* Fc$^+$/Fc (ΔE_p = 0.18 V, $|\mathrm{I_{pa}/I_{pc}}|$ = 0.81) was assigned to the Fe^{III}/Fe^{II} redox couple; whereas, three consecutive phenolate/ phenoxyl processes were observed at 0.43 V (ΔE_p = 0.09 V), 0.69 V (ΔE_p = 0.12 V) and 0.9 V *vs.* Fc$^+$/Fc. The first two processes were quasi-reversible, and the third was ill-defined. The electronic origin of these attributions has been investigated in detail along with the consequences of the lack of orbital degeneracy to redox-cycling brought by the low symmetry of this five-coordinate species.[14]
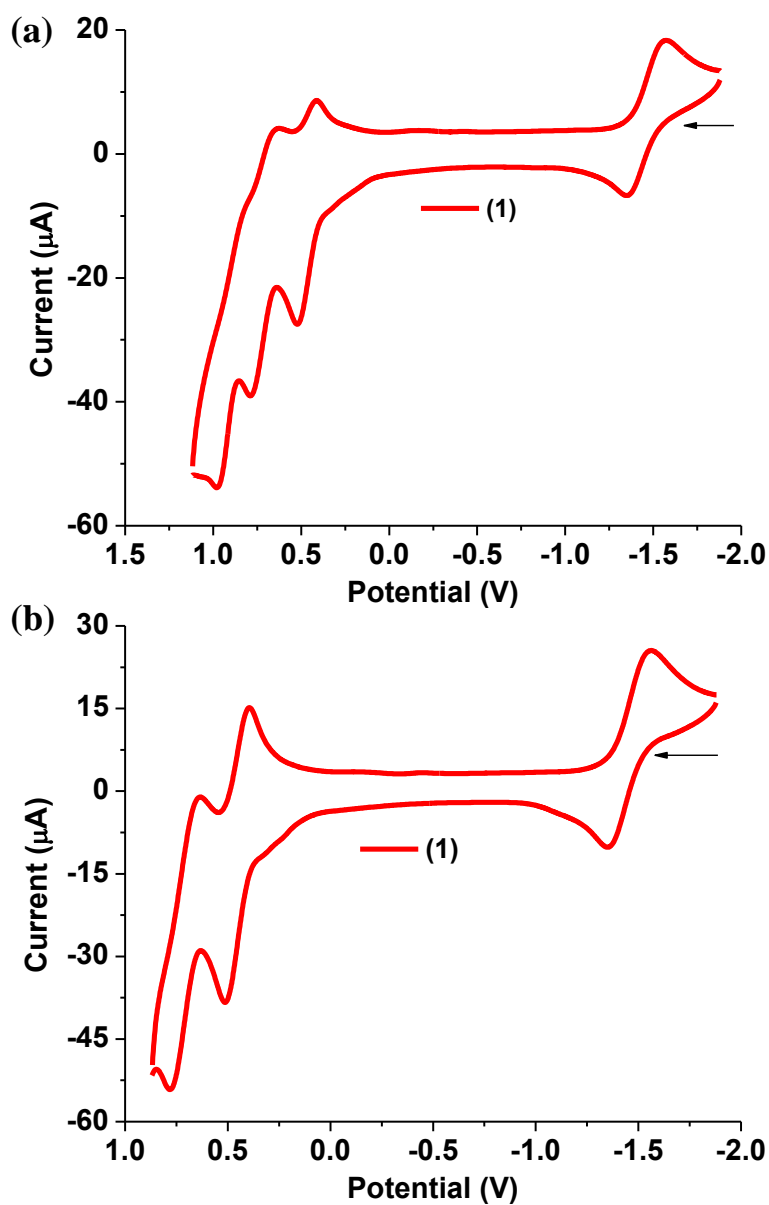
Figure 5.4. Cyclic voltammogram of complex **1** (a) from 1.5 to -2 V and (b) isolated redox

processes from 1 to -2 V in dichloromethane.

Process (*vs.* Fc$^+$/Fc) Compound	E$_{\frac{1}{2}}$, (ΔE$_p$) (V) | I$_{pa}$/I$_{pc}$ |	E$_{\frac{1}{2}}$, (ΔE$_p$) (V) | I$_{pa}$/I$_{pc}$ |	E$_{\frac{1}{2}}$, (ΔE$_p$) (V)	E$_{\frac{1}{2}}$, (ΔE$_p$) (V)
(1)	-1.494 (0.177) | 0.81 |	0.434 (0.093) | 1.09 |	0.690 (0.122) -	0.86 (0.14) -

Table 5.2. Redox processes (E$_{\frac{1}{2}}$ and ΔE$_p$ values) *vs.* Fc$^+$/Fc for complex **1**.

5.3.5 Spectroelectrochemical Properties

In complex **1**, when the reduction process occurred, the lower energy LMCT band at ~ 465 nm started to decrease in intensity. The reason for this observation is that during the reduction, the Fe^{III} reduces to Fe^{II} and this transformation results in a weakening of the ligand- to -metal charge transfer transition. During the oxidation process of complex **1**, the band at ~ 465 nm decreased in intensity, and the region ~ 700 nm increased in intensity. When the Fe^{III}-phenolate transforms into Fe^{III}-phenoxyl radical species, the LMCT band occurring from p_π (phenolate) to $d_{\pi*}$ of the metal becomes weaker due to the lower charge density around the metal center and, therefore, decreases in intensity. Nevertheless, there could be charge transfer transitions between the phenolate and phenoxyl moieties, the band at ~ 700 nm can be assigned as a phenolate to phenoxyl charge transfer. **Figure 5.5** shows the observed spectral changes for complex **1** during reduction and oxidation processes. The experiments for complex **1** were conducted using fixed potential method. To study the oxidation and reduction processes, potentials of 0.869 V and -1.881 V *vs.* the Fc$^+$/Fc were applied, respectively.
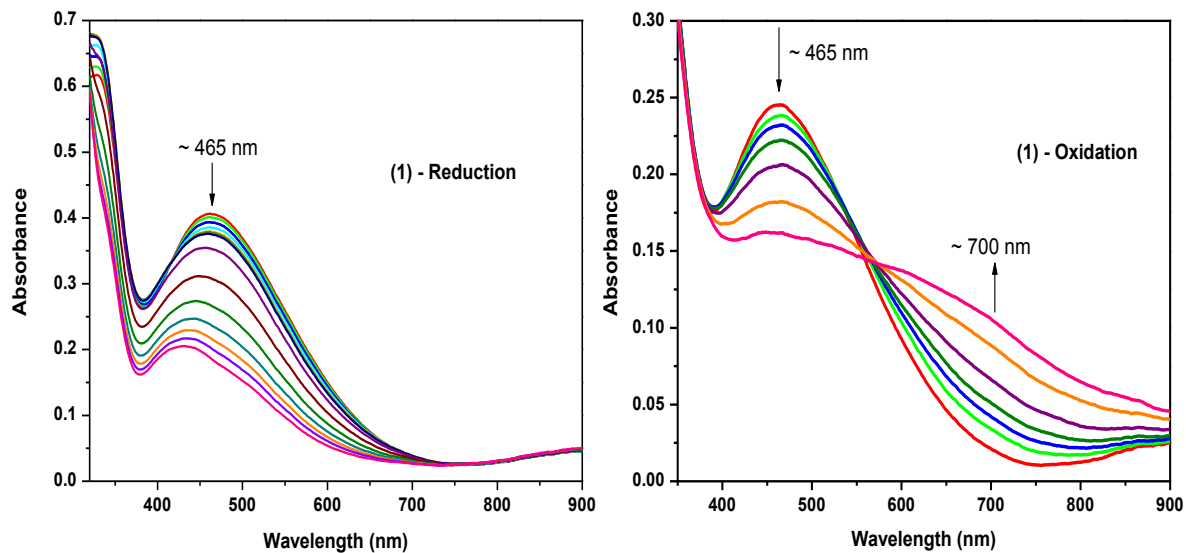
Figure 5.5. Electronic spectral changes observed for **1** during spectroelctrochemical experiments.

5.3.6 Isothermal Compression Data

To build nanoscale devices based on LB films of **1**, the first step was the evaluation of interfacial properties at the air/water interface. Therefore, isothermal compression associated with Brewster angle microscopy (BAM)[19] was used at 23 ± 0.5 °C to assess average area per molecule, collapse pressure of the monolayers, and film topology and homogeneity. The data obtained are shown in **Figure 5.6**. Species **1** presented a good amphiphilic distribution between the hydrophobic *tert*-butyl groups attached to the phenolate moieties and the hydrophilic methoxyethane chains. As a consequence, complex **1** started to show intermolecular interactions at the air/water interface around 260 Å^2/molecule. Further compression led to the formation of a homogeneous film at surface pressures of around 10-20 mN/m, as observed by BAM images. Formation of Newton rings associated with film instability was eventually observed. An apparent phase rearrangement was observed between

25 and 35 mN/m was indicated by a change in the slope of the isotherm, as well as by the absence of Newton rings. The microscopic homogeneity of the film tracked by BAM seemed to remain unaltered until ridge formation indicative of collapse which appeared at 63 mN/m.
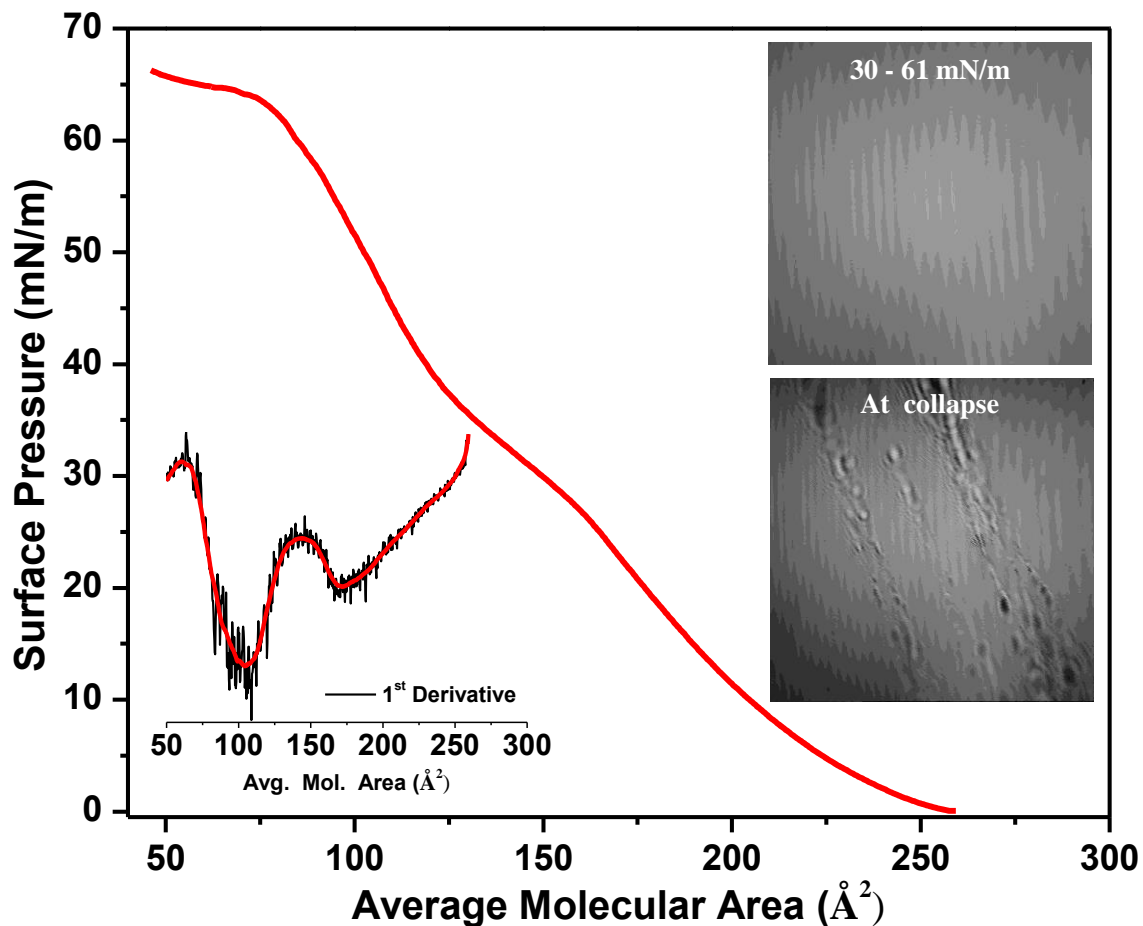
Figure 5.6. Compression isotherm for complex **1** with its first derivative and selected BAM micrographs (Insets).

In the classic Ries mechanism,[20] collapse involves folding, bending, and breaking of the monolayer. The simplest model for molecular arrangement at the air/water interface suggested the methoxyethane moiety submerged in water, whereas the hydrophobic iron/phenolate core remains at the air subphase. Thus, the approximate area occupied by this

core is equivalent to a circle with radius corresponding to the distance between the outermost *tert*-butyl group in the ligand and the metal ion. This distance is *ca.* 7.9 Å in known structures,[14,16b] resulting in an area of about 200 Å^2 for optimal packing. Hence, the critical areas towards the end of the phase transition at 35 mN/m should yield a tightly packed film with optimized topology.

5.3.7 Langmuir-Blodgett Film Characterization using UV-visible and IRRAS Spectroscopy Methods

LB films were deposited either as monolayers or multilayers onto glass substrates at 33 mN/m and studied by UV-visible, IR reflection/absorption spectroscopy (IRRAS),[21] and contact angle measurements. This characterization yielded pivotal understanding of the chemical composition and orientation of the resulting films. The UV-visible and IRRAS response of a single monolayer cannot be detected accurately and best results were obtained for films with 25-50 layers on glass. The general $\pi \rightarrow \pi^*$ and LMCT features present in the solution spectrum of **1** were clearly maintained,[14,16a] but evident changes were observed: the intensification of the N-Fe(III) LMCT band at 330 nm, the hypsochromic shift of the in- and out-of-the-plane PhO$^-$-Fe(III) band at 470 nm, and a new component at *ca.* 400 nm. The UV-visible spectrum obtained for LB film in comparison to its solution spectrum is shown in **Figure 5.7**.
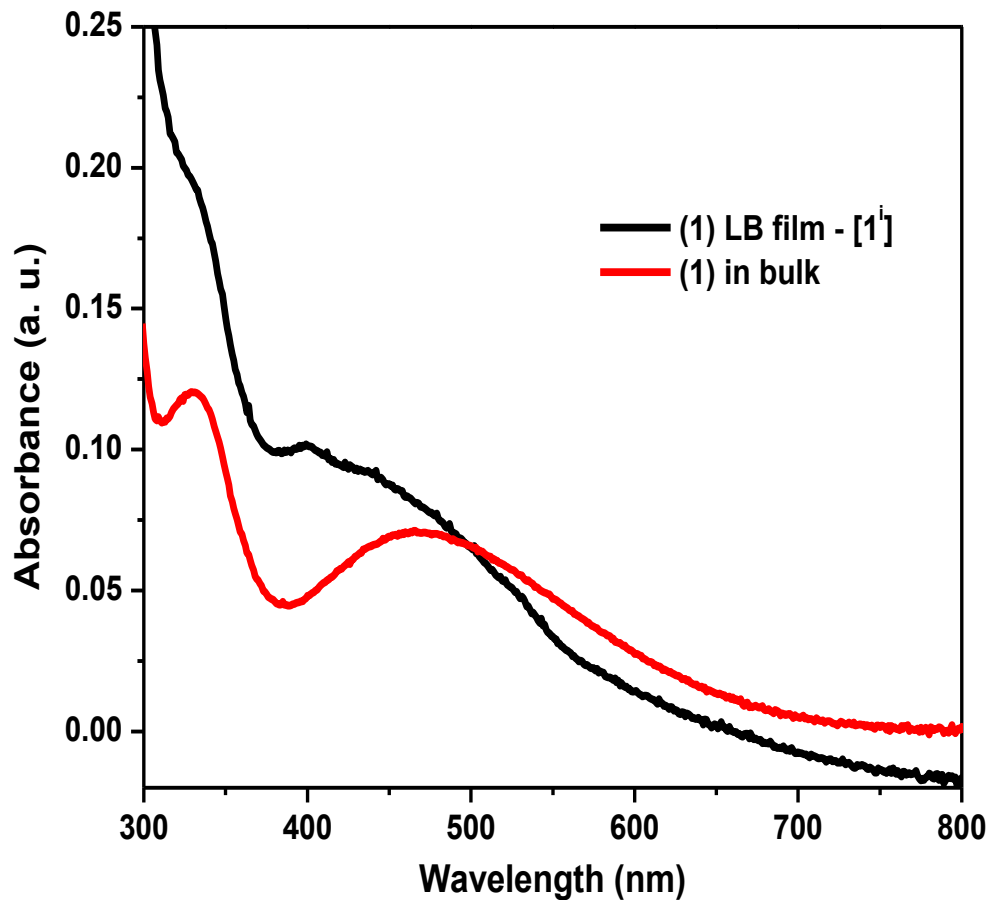
Figure 5.7. Comparison between UV-visible spectra of complex **1** and its LB film (50 layers) on glass.

This new band is a phenolate-to-azomethine CT associated to amine/imine conversion of the ligand that takes place at the air/water interface. The conversion of **1** to **1^i** (**Scheme 5.3**) was followed by UV-visible and ESI mass spectrometry methods.
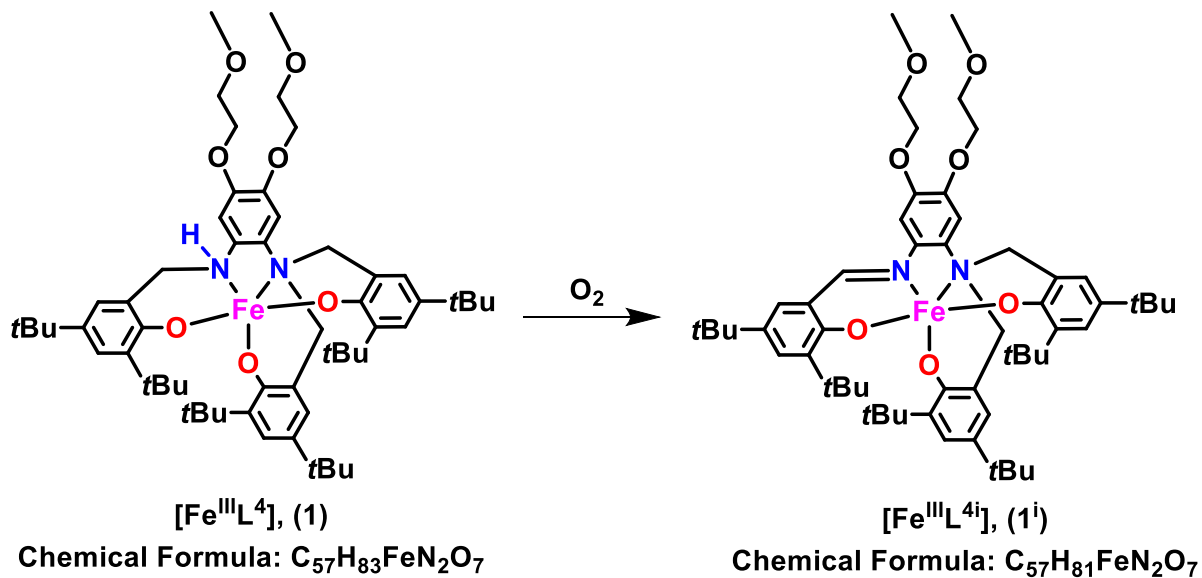
Scheme 5.3. Amine/imine conversion.

The amine/imine conversion was monitored by UV-visible spectroscopy and mass spectrometry using two methods. During the first method, the measurement was carried out using a freshly prepared solution of complex **1** in 9:1 methanol/water under constant concentration of dioxygen gas contained in the cuvette. The observed spectral changes are shown in **Figure 5.8** and the mass spectrometry data obtained for the product recovered from **1** in 9:1 methanol/water is shown in **Figure 5.9**.
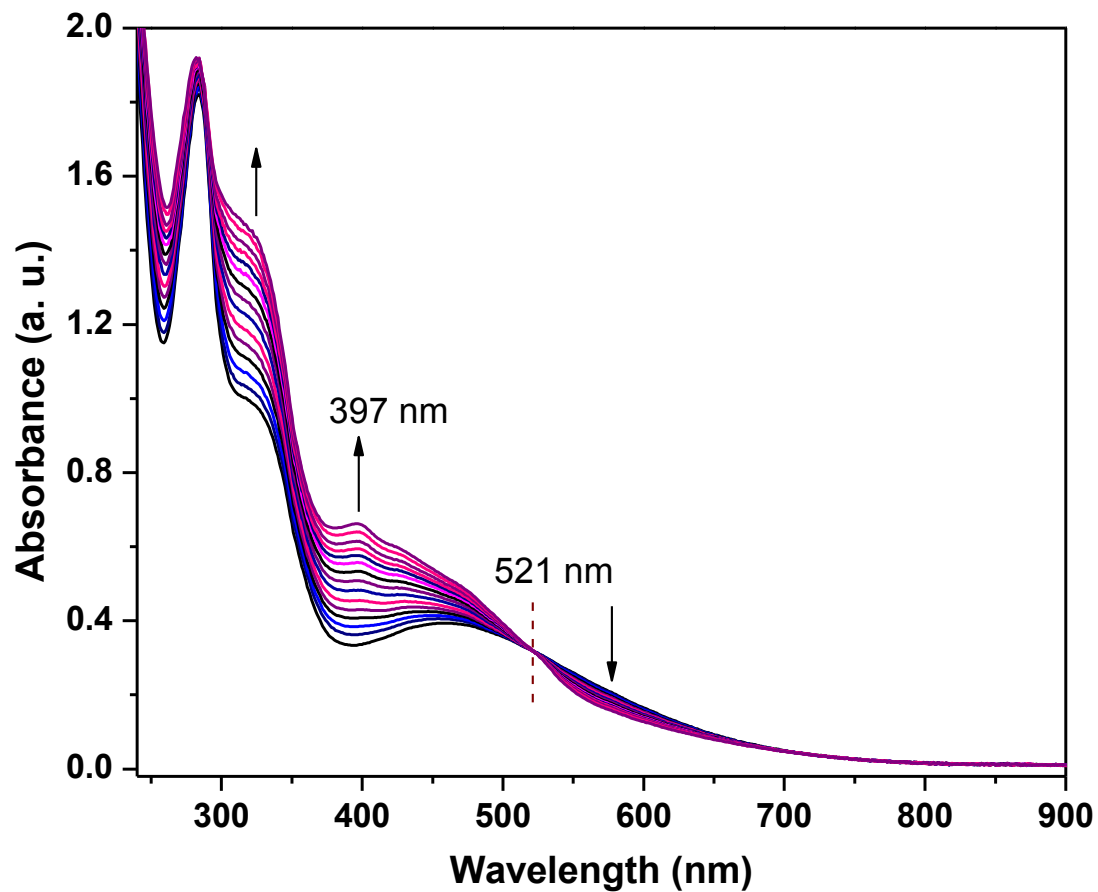
Figure 5.8. UV-visible monitoring of amine/imine conversion in 9:1 methanol/water mixture.
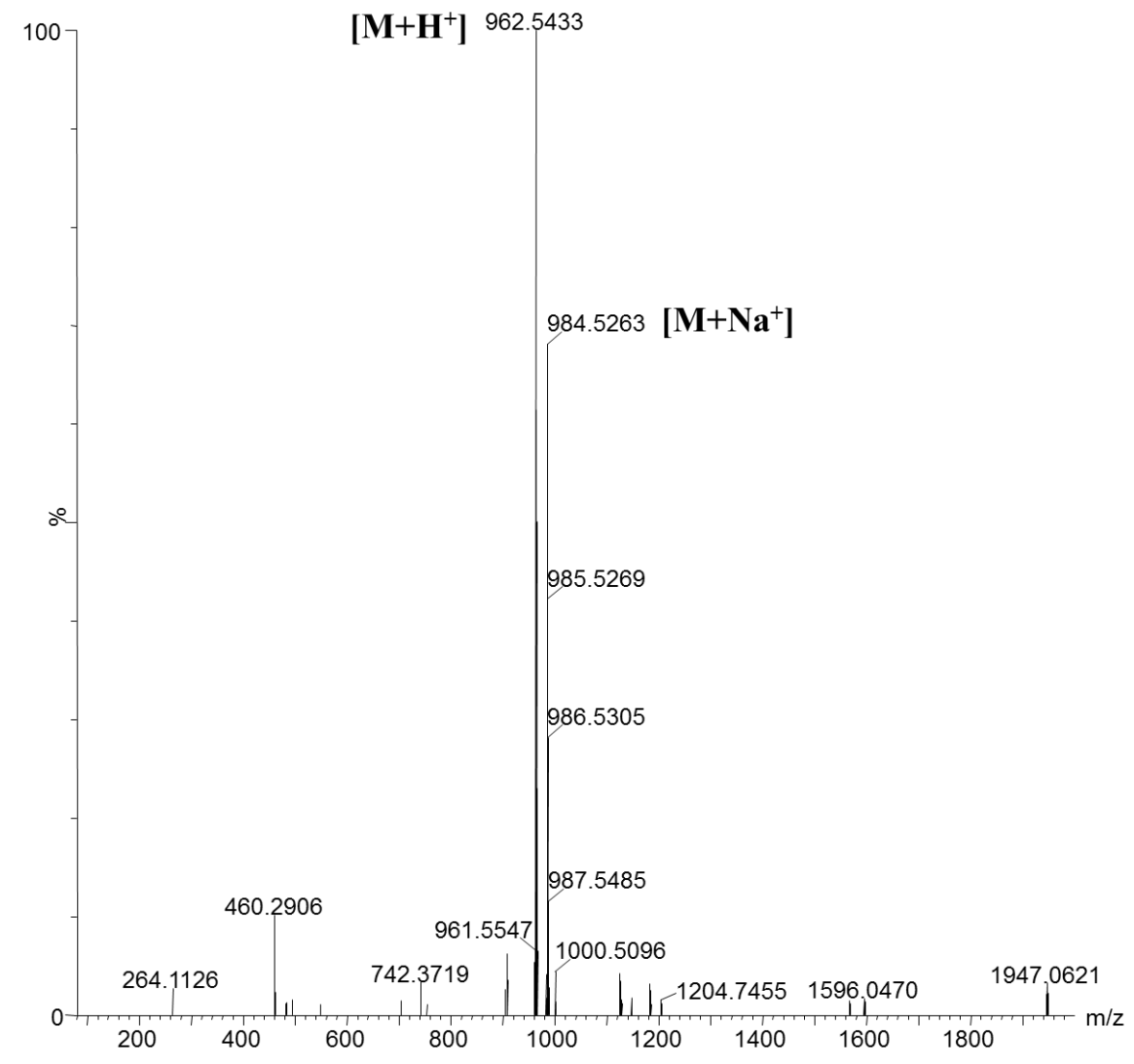
Figure 5.9. Mass spectrum of product recovered from 9:1 methanol/water. ESI (m/z^+) in CH$_3$OH = 962.5433 for [C$_{57}$H$_{81}$N$_2$O$_7$Fe + H$^+$].

During the second method, the LB film that was deposited onto a glass substrate was dissolved in dichloromethane and then UV-visible and mass spectrometry data were measured. The observed UV-visible spectrum for the dissolved LB film in comparison to complex **1** (in solution) and LB film (solid) are shown in **Figure 5.10**. The mass spectrometry data obtained for the dissolved LB film is shown in **Figure 5.11**.
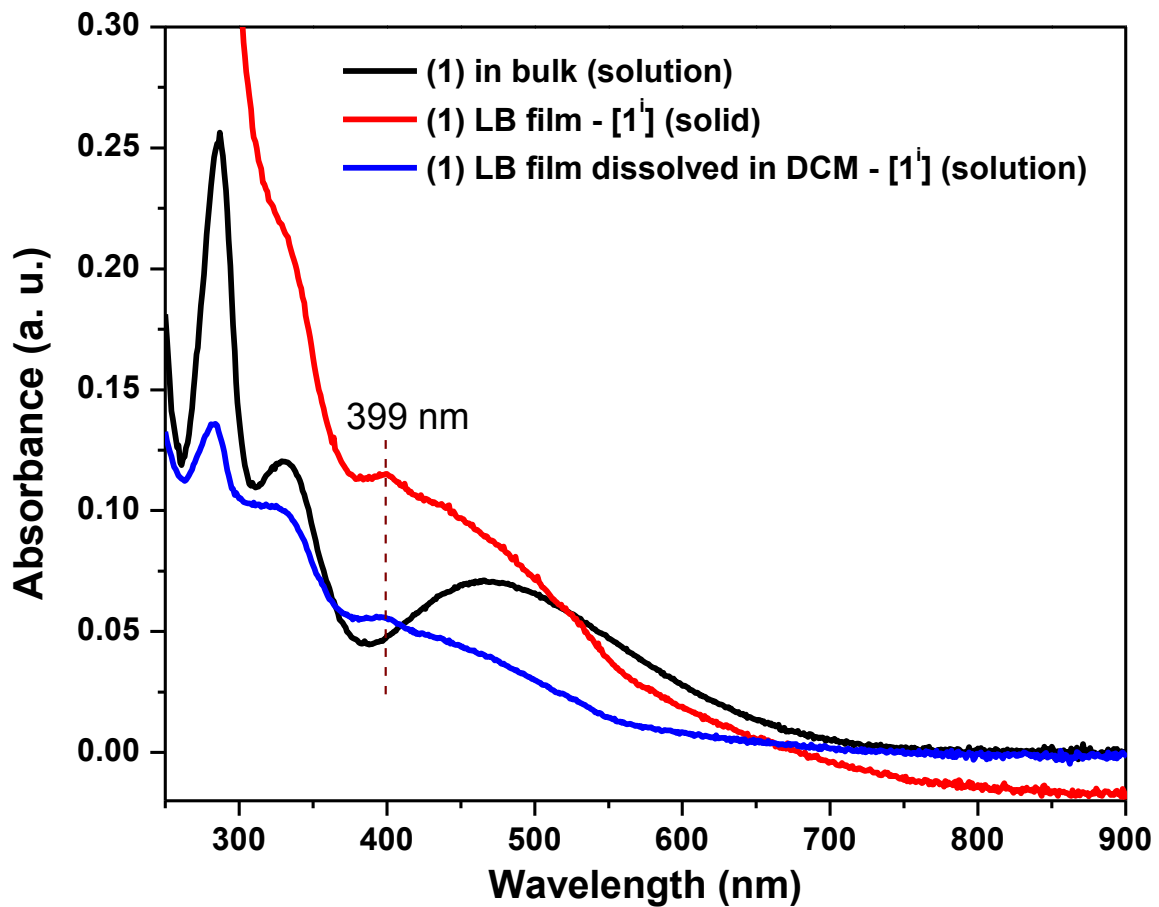
Figure 5.10. UV-visible spectral data for LB film dissolved in dichloromethane.
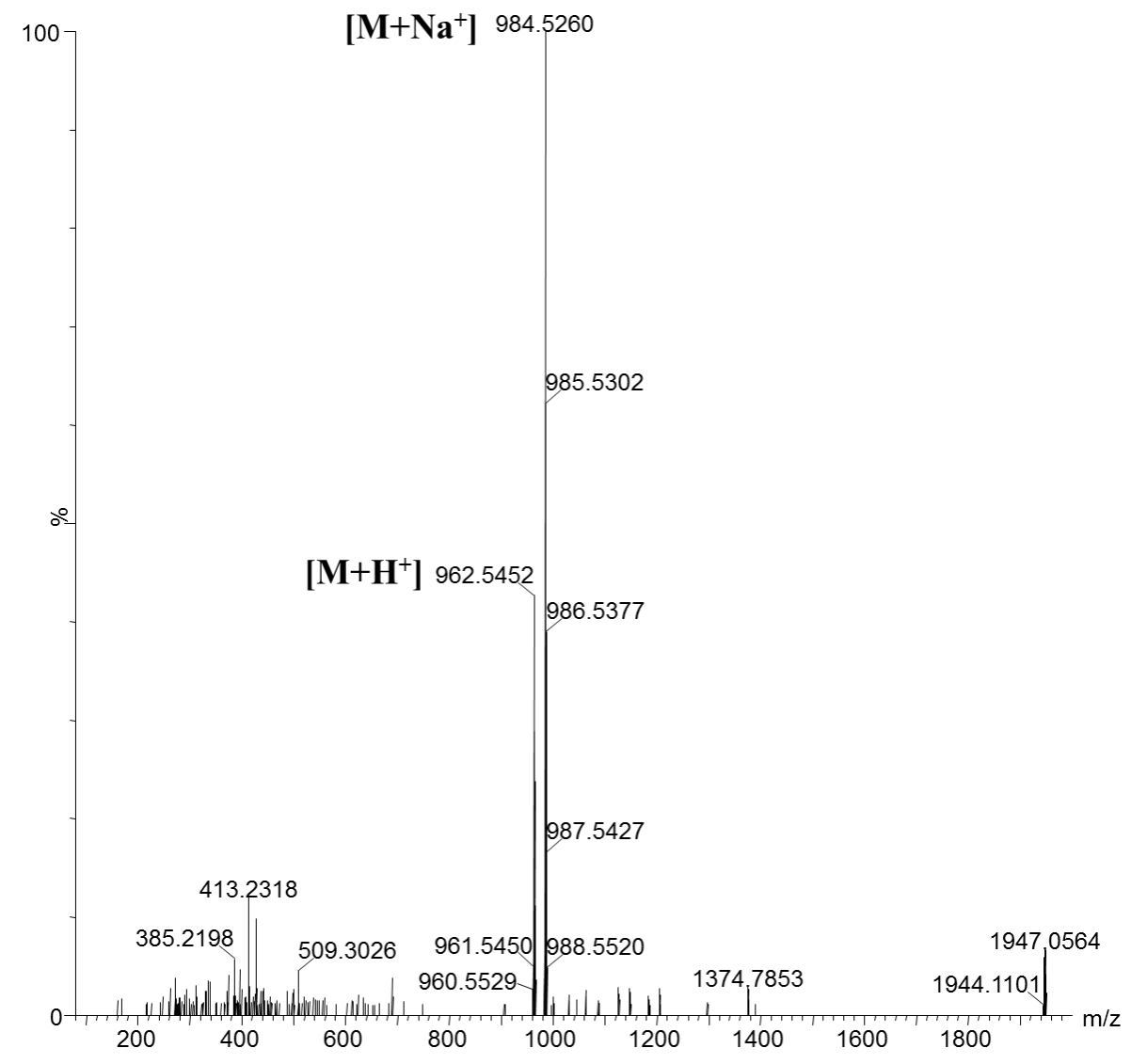
Figure 5.11. Mass spectrum of recovered LB film. ESI (m/z^+) in CH_2Cl_2 = 962.5452 for $[C_{57}H_{81}N_2O_7Fe + H^+]$.

Except for these two methods, the amine/imine conversion of complex **1** was directly monitored by matrix assisted ionization vacuum (MAIV) mass spectrometry.[22,23] In this method, the LB monolayer of complex **1** that was deposited onto a glass substrate was directly analyzed. The LB monolayer of **1** was introduced to the mass spectrometer using

3-nitrobenzonitrole (3-NBN) as a matrix in acetonitrile/water. Then, the results were compared with the bulk sample that was measured under similar conditions. The results obtained for the LB monolayer and bulk sample are shown in **Figure 5.12**. According to the observed data, the bulk sample of complex **1** showed a molecular ion peak at (m/z) 964.8 which belongs to $[C_{57}H_{83}N_2O_7Fe + H^+]$, and the LB monolayer showed the molecular ion peak at (m/z) 962.7 which belongs to $[C_{57}H_{81}N_2O_7Fe + H^+]$. A shift of 2 Da was observed for the mass spectrum of LB film when compared to the bulk material. Therefore, MAIV mass spectrometry data further suggested that an amine/imine conversion of **1** to **1**[i] was taking place at the air/water interface.
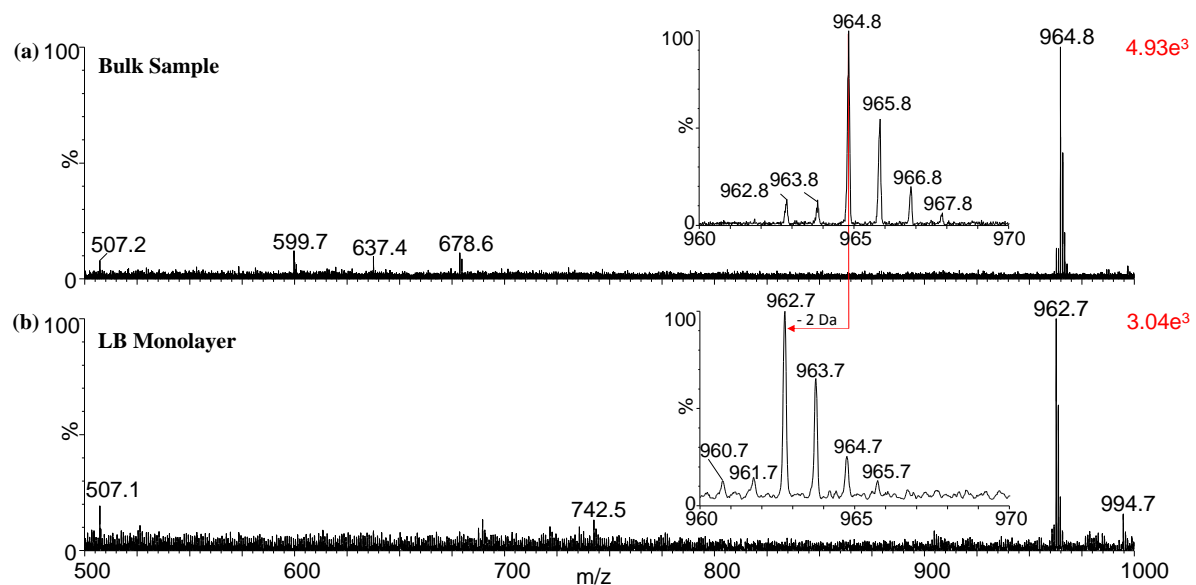
Figure 5.12. MAIV mass analysis for complex **1** (a) bulk sample and (b) LB monolayer (Isotopic distributions are shown in the insets).

The conversion of **1** to **1**[i] was also observed by IRRAS on glass at 30° under *s*-polarized light. **Figure 5.13** shows a new peak at 1583 cm^{-1} associated with the C=N group.

As this peak is absent in the bulk IR of **1** and not associated with adventitious moisture, it further validates the intraligand conversion.
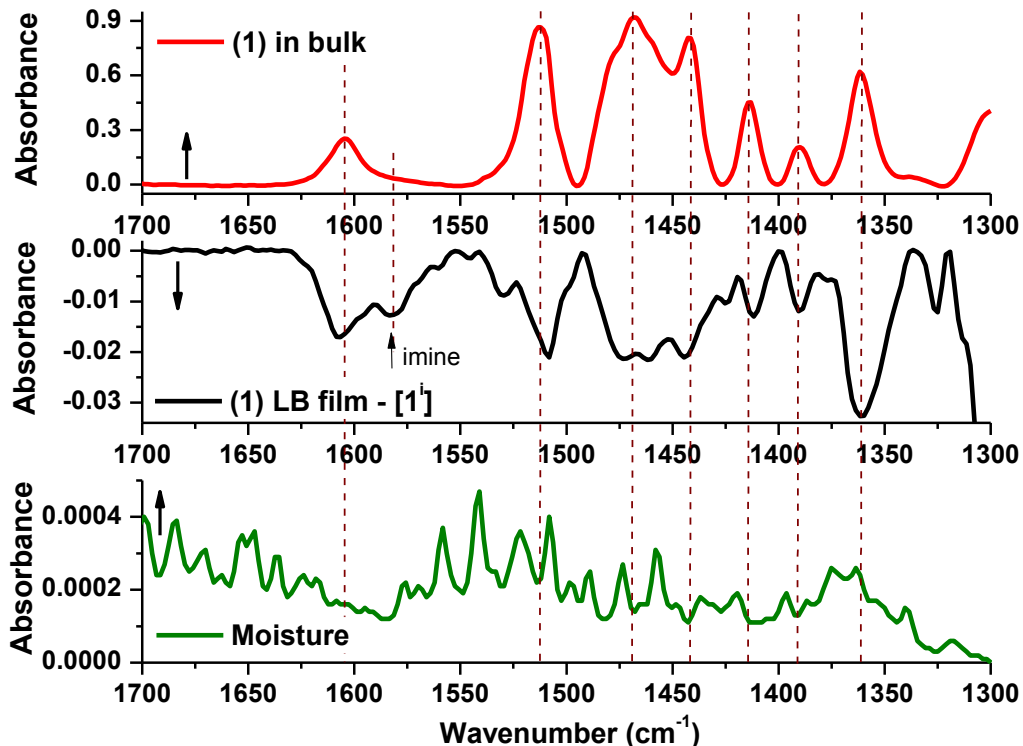
Figure 5.13. Comparison between IR of **1** in KBr, the IRRAS of **1**[i] LB film (50 layers), and moisture at 30°, *s*-polarized light.

Other features include the fingerprint region, where aromatic C=C stretchings (1610 to 1510 cm^{-1}) and angular -CH$_2$- and -CH$_3$ deformations (1360 to 1470 cm^{-1}) appear[24] (**Figure 5.14**). Relevant CH$_2$ symmetric and antisymmetric stretching vibrations were observed between 2850 to 2920 cm^{-1} and a prominent asymmetric CH$_3$ feature appears at 2962 cm^{-1}. In previous studies,[21,25] a correlation was drawn between the high intensity of the CH$_2$ vibrations of alkyl chains along with its shifting to lower wavenumbers, as associated

with a highly ordered and well packed film. This relationship requires caution because the CH$_2$ contribution is smaller than that observed for the CH$_3$ groups.

Full-length spectra

Fingerprint region
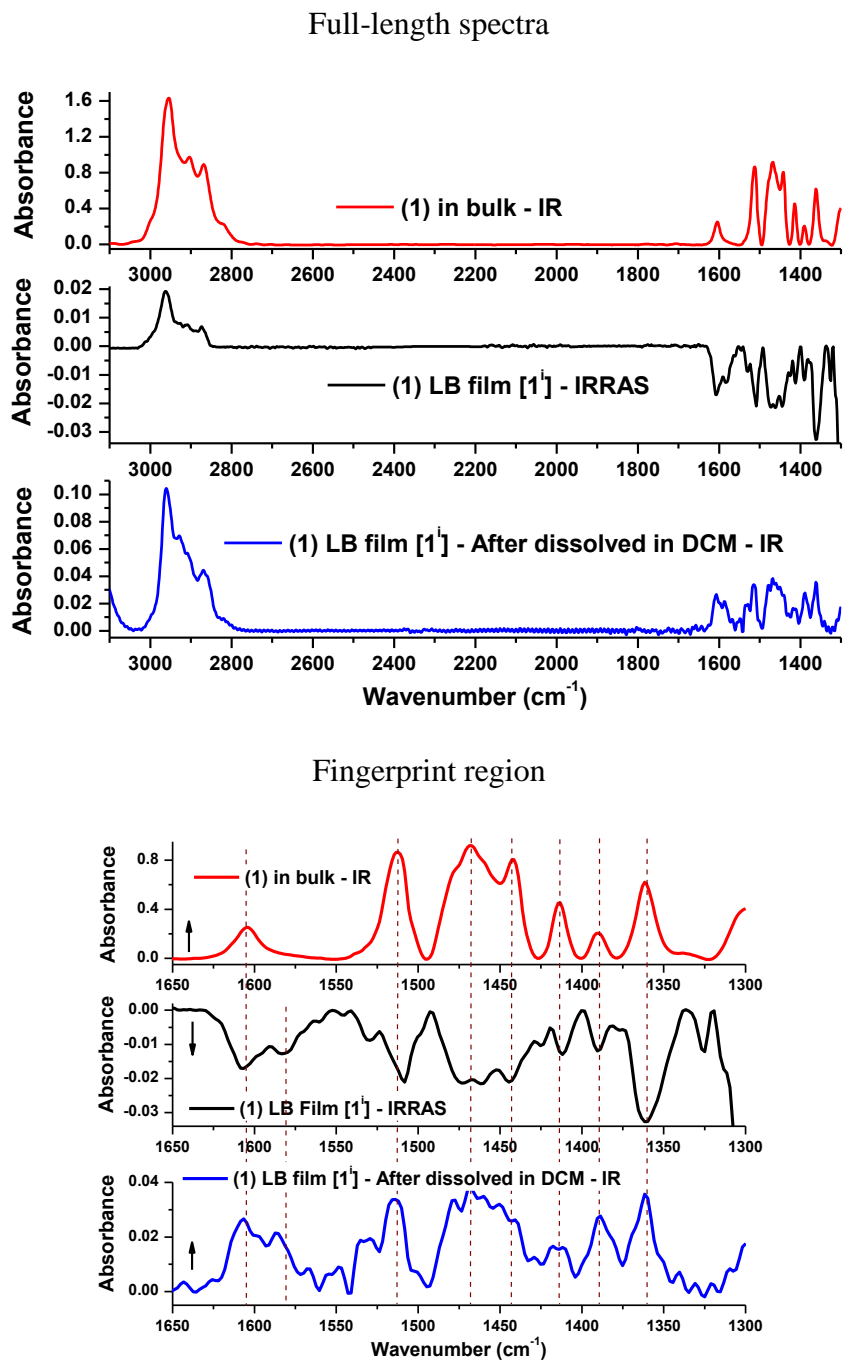
Figure 5.14. Comparative IR and IRRA spectra for **1, 1^i**, and LB film.

Each molecule of 1^i contains twenty methyl groups (eighteen attached to the phenolates and two to the alkoxy chain) and only six CH_2 groups (four in the alkoxy chains and two in the methylaminophenolate moiety). Therefore, analysis of the film cannot be based on the intensity of the signals but rather on the peak position. Indeed the CH_3 peaks shift from 2954 cm^{-1} in the bulk sample to 2962 cm^{-1} in the film (**Figure 5.15**).
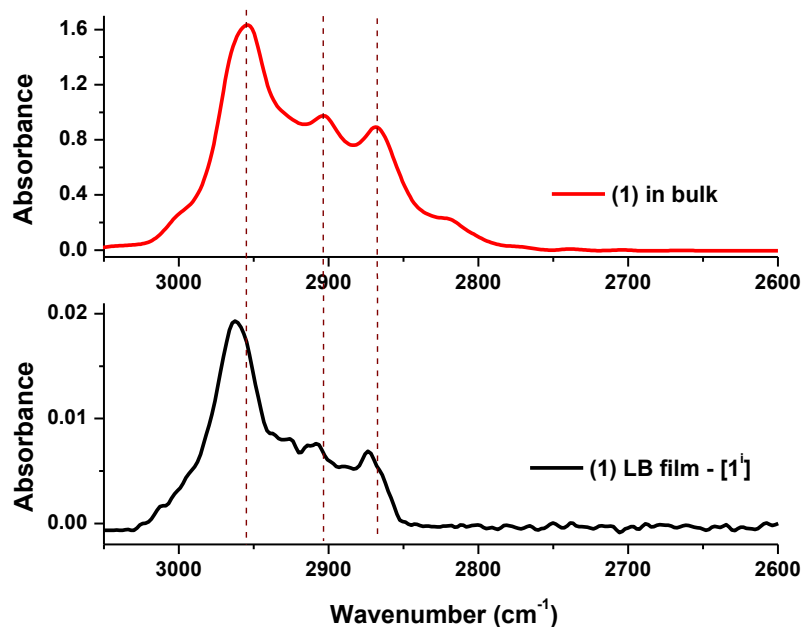
Figure 5.15. IRRA spectrum (50 layers deposited onto glass substrates, s-polarization and incidence angle of 30°) of CH_n stretching region for 1^i compared to its bulk infrared spectrum.

Another significant feature observed in IRRAS is that bands in the C—H stretching region are pointing upward while bands in the finger print region are pointing downward. In IRRAS this inversion is related to the detection of two forms of bands namely positive (upward) and negative bands (downward). This phenomenon can be generally explained using the surface selection rules which states that when the films are deposited on metal

substrates, the vibrations with perpendicular transition dipole moments show positive absorption bands while the vibrations with parallel transition dipole moments are undetectable. On the other hand, if the films are deposited on to dielectric substrates, then the positive bands are shown for vibrations with perpendicular transition dipole moments, and negative bands for vibrations with parallel transition dipole moments can be detected where $\theta < \theta_B$. This type of inversion of absorption bands can be observed for anisotropic films with high molecular order within the film.[26]

Considering the average area at collapse reported above, this data corroborates the notion of a well packed film where the iron/phenolate moiety points outwards. Although the intrinsically complex molecular structure of $\mathbf{1^i}$ prevents proposing a tilt angle of alignment, further information about the orientation of the molecules can be gathered by the static contact angle of the compound on glass as measured by a KSV CAM 200 goniometer at room temperature. The film yields a value of $85.30° \pm 0.65°$, compared to $7.45° \pm 0.42°$ for the glass substrate alone, thus confirming its hydrophobic nature.

5.3.8 Langmuir-Blodgett Film Characterization using Atomic Force Microscopy (AFM)

LB films were deposited either as monolayers or multilayers onto quartz and mica substrates to investigate by AFM. This characterization was helpful in understanding the morphology, surface roughness, and thickness of the resulted films. The morphology of the LB-monolayer of $\mathbf{1^i}$ deposited on mica at surface pressures of 10, 25, 30, 33, and 40 mN/m was measured by AFM. At low surface pressures the monolayer showed large pinhole defects that become smaller and less frequent as the surface pressure increases as shown in

Figure 5.16. At 33 mN/m the monolayer becomes smooth, being optimal for nanofabrication.
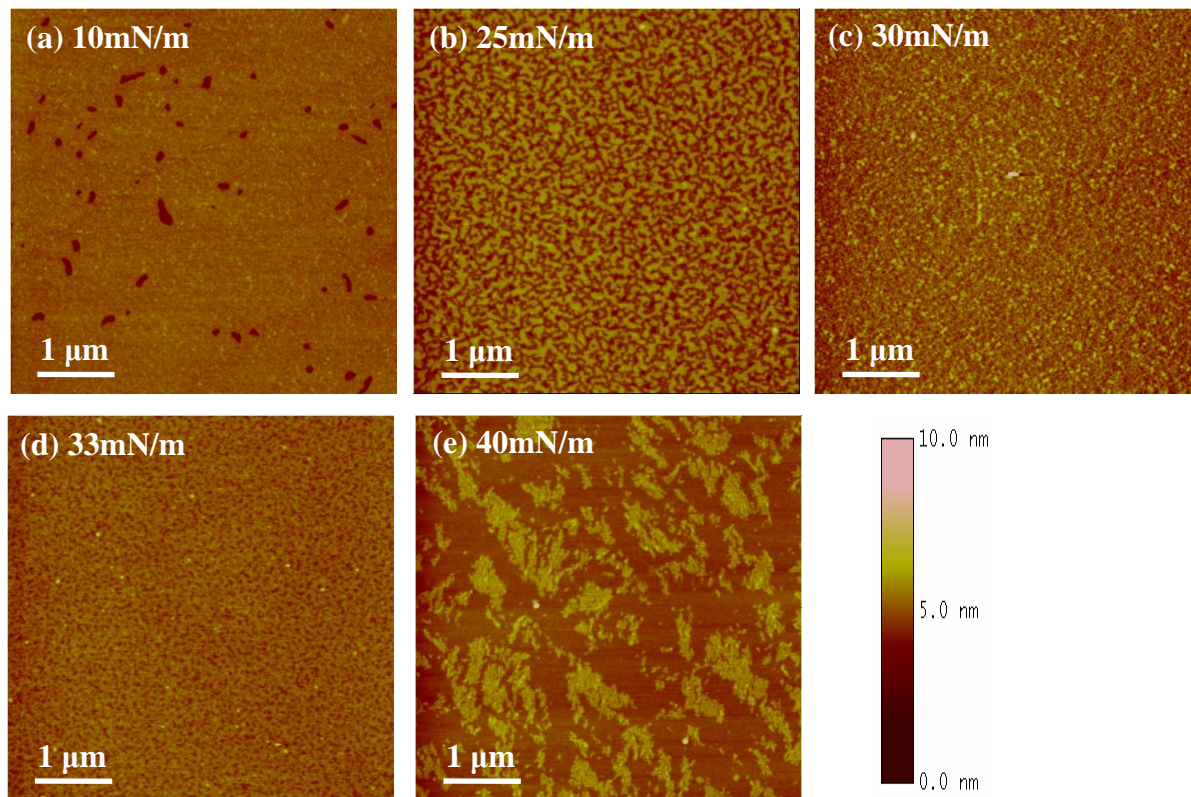
Figure 5.16. Surface morphology of monolayers of **1^i** at different surface pressures. LB monolayer deposited on mica substrates (a) at 10 mN/m, (b) at 25 mN/m, (c) at 30 mN/m, (d) at 33 mN/m, and (e) at 40 mN/m for complex **1^i**. The scan size is 5 μm and the Z range is 10 nm for all images.

At higher surface pressures the film becomes rougher due to material aggregation. In multilayer films, the surface roughness increases with an increasing number of layers (**Figure 5.17 and Table 5.3**) and more particles tend to aggregate to the surface of the film.
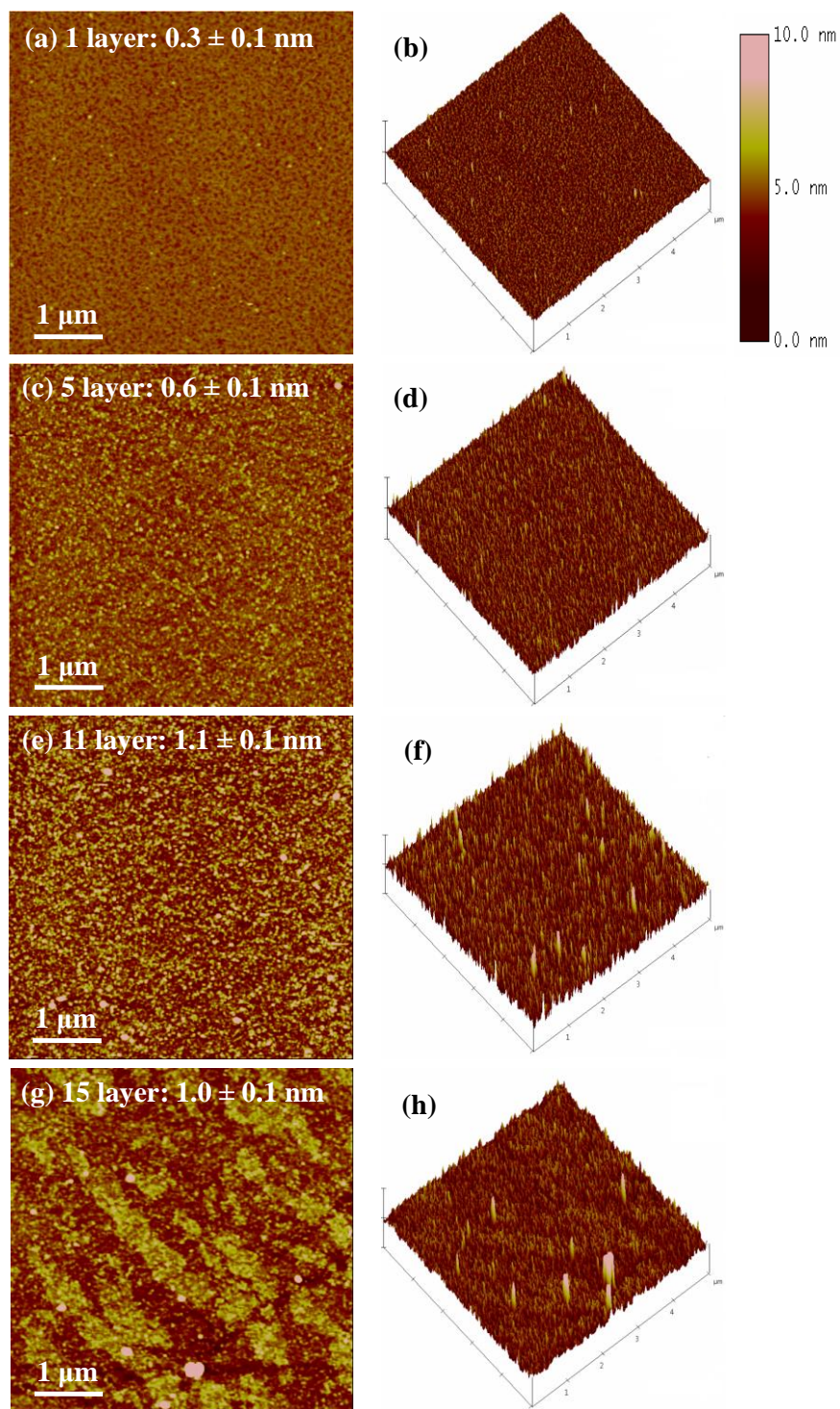
Figure 5.17. Surface roughness measurements of 1-15 LB layers of **1**[i]. AFM height images (left) and 3D surface plots (right) of complex **1** deposited on mica substrate with (a, b) 1; (c, d) 5; (e, f) 11; (g, h) 15 layers. The scan size is 5 μm and the Z range is 10 nm for all images.

The thickness of a single monolayer was determined on quartz substrates containing 1 to 15 layers by blade-scratching the film and measuring the scratch depth in the tapping mode (**Figure 5.18** and **Table 5.3**). The resulting values yielded a linear relationship between thickness and number of layers indicating homogeneous film deposition (**Figure 5.18d**).
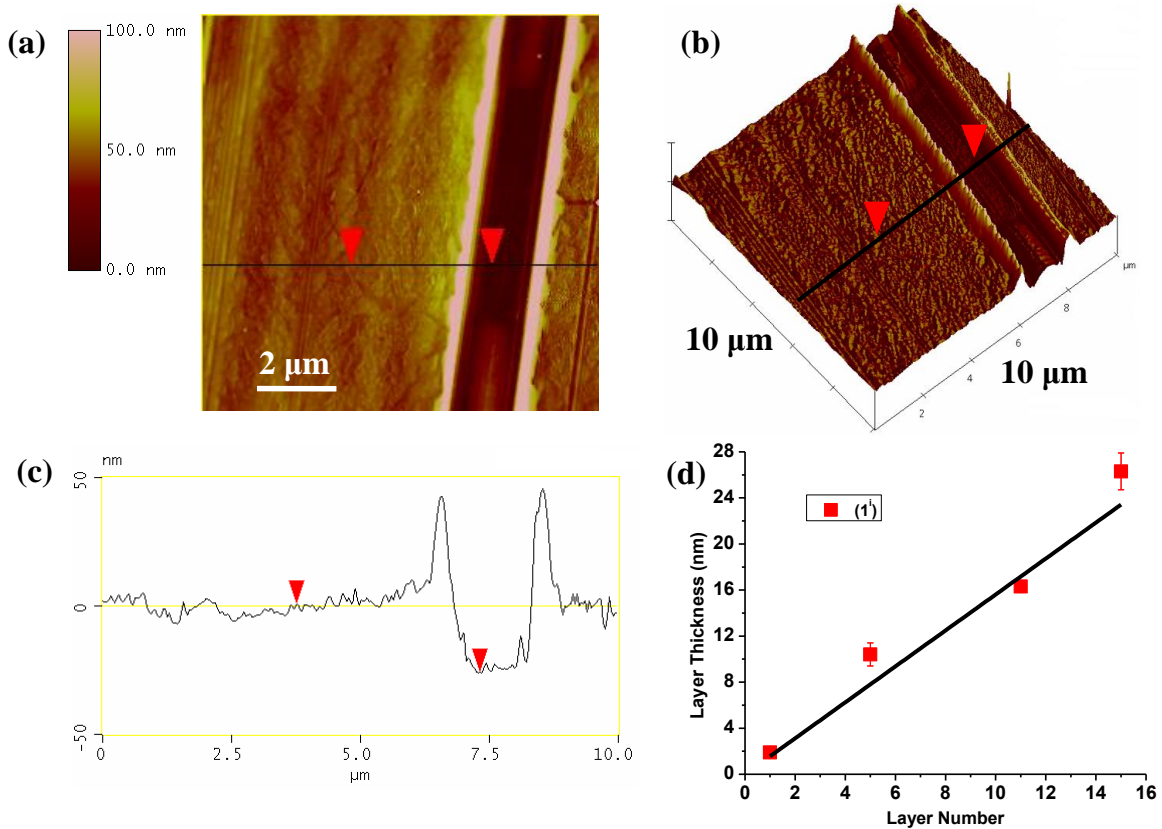
Figure 5.18. AFM height images and sectional analysis of **1**[i] (15 layers) on quartz. (a) 2D view, (b) 3D view, (c) sectional analysis along the black solid line, and (d) plot between the thickness (nm) *vs*. number of layers from 1 to 15 layers.

Number of Layers	Surface Roughness (nm)	Thickness of the Film (nm)
1	0.3 ± 0.1	1.9 ± 0.2
5	0.6 ± 0.1	10.4 ± 1.0
11	1.1 ± 0.1	16.3 ± 0.5
15	1.0 ± 0.1	26.3 ± 1.6

Table 5.3. Summary of AFM data for mono- and multilayers of **1^{i}**.

Each layer was approximately 19 ± 2 Å thick, and based on available crystallographic data for related complexes, the approximate length of **1^{i}** reaches 15-17 Å. With an estimated 12 Å between the catechol-like oxygen atoms and the bulky terminal *tert*-butyl groups,[14,16] these results are in excellent agreement with the notion of a true monolayer. Thus, taking into account the shift in the pronounced CH_3 peak from IRRAS, the thickness of the monolayer gathered by AFM, and the hydrophobic nature of the film, it is possible to conclude that the LB film of **1^{i}** is composed of well-packed molecules where the alkoxy chains are in contact with the solid substrate and the *tert*-butyl rich iron/phenolate moiety points outwards at the air/solid interface.

5.3.9 Device Fabrication and Current-Voltage Measurements

After gaining knowledge about the monolayers at air/water and air/solid interfaces, the device fabrication was carried out for complex **1**. The Langmuir monolayer of **1^{i}** was transferred at 33 mN/m onto a precleaned gold-coated mica substrate to yield a defect-free film. After drying the monolayer for 5 days under reduced pressure, an Au|**1^{i}**LB|Au device

was built. The top gold electrode was deposited with an EffaCoater gold sputter via the shadow masking method using argon as the carrier. Three assemblies with an average of 16 devices each were fabricated and the current–voltage (I-V) characteristics were reproducibly measured in four to five devices per assembly using a Keithley 4200 semiconductor parameter analyzer and a Signatone S-1160 Probe Station at ambient conditions. A few devices were short-circuited, likely because of monolayer defects.[6d] An optical micrograph of the fabricated devices and the schematic view of the device layout are shown in **Figures 5.19**.
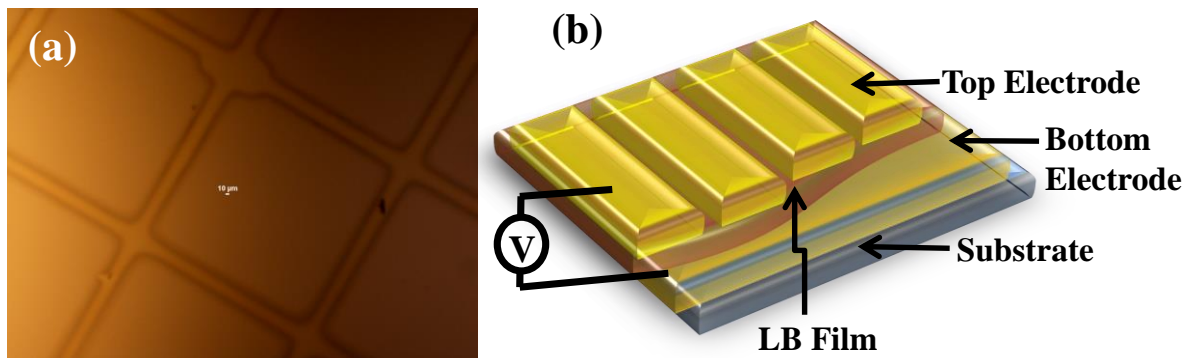
Figure 5.19. (a) An optical micrograph of the device and (b) schematic view of device layout.

In each of these I-V measurements, a higher current was observed in the third quadrant than in the first quadrant. This asymmetric I-V characteristic of a sharp negative response and a negligible positive response was indicative of rectification behavior, as shown in **Figure 5.20**.
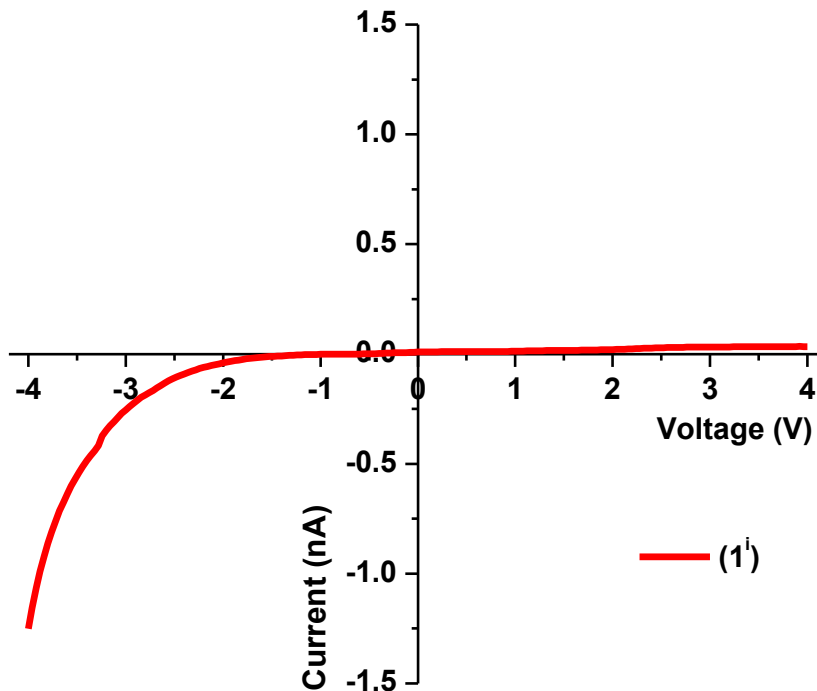
Figure 5.20. I-V characteristic of complex **1^i** from 4 to -4 V.

The rectification ratio (RR = [I at -V$_o$/I at +V$_o$])[6d] for the monolayer of **1^i** varied from 4.52 to 12 between -2 to +2 V and from 2.95 to 36.7 between -4 to +4 V, respectively. Reversing the drain and the source contacts led to a reversed current response, thus demonstrating the retention of the rectification behavior (**Figure 5.21c**). Upon repeating scans, the current responce droped and the I-V behavior displayed increased symmetry (**Figure 5.21e, f**). This phenomenon has been observed for organic materials and is tentatively explained by the reorganization of dipole moments in presence of high electric fields in order to attain a stable monolayer by decreasing their energy.[6d] These results further indicate that the rectifying behavior of the current response is directly associated with the presence of the LB film of **1^i**.
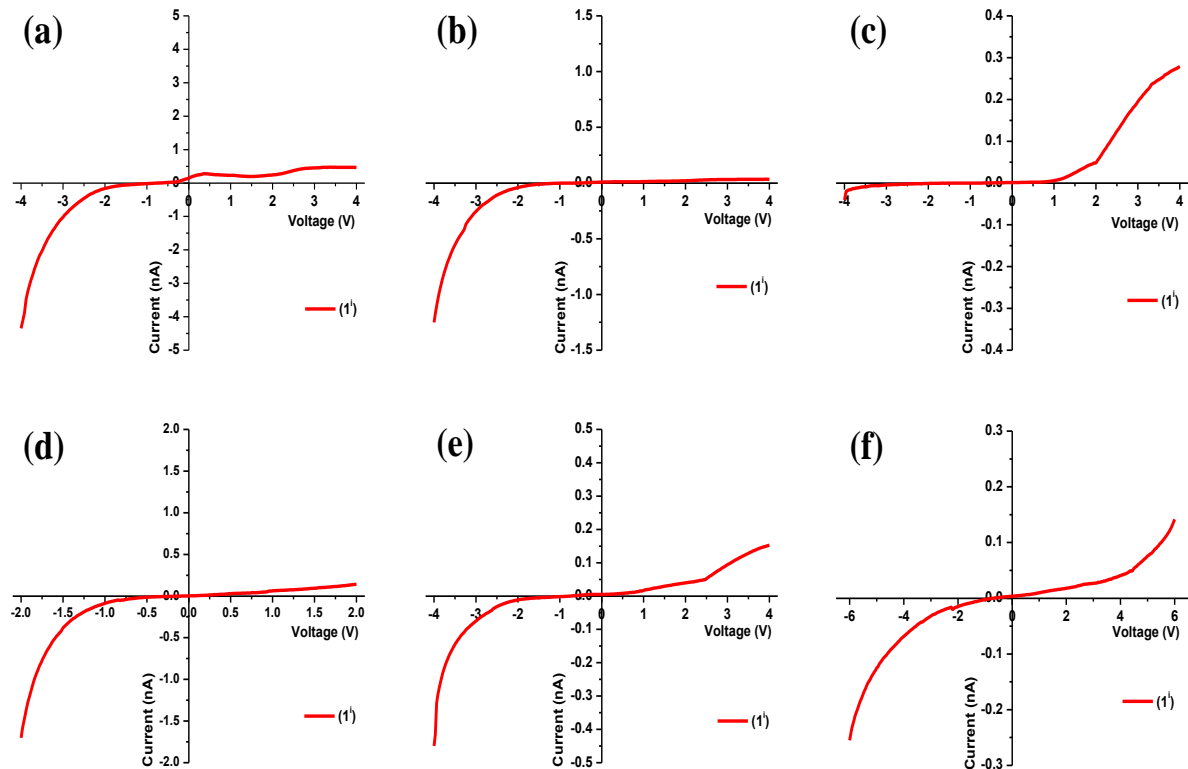
Figure 5.21. I-V characteristic of complex **1^i**. (a) from 4 to -4 V, (b) response observed after multiple scans between 4 to -4 V, (c) response observed for reversed applied potentials, (d) response observed from 2 to -2 V, and (e), (f) the symmetrical response observed after multiple scans.

Although the exact origin of the rectifying behavior is not certain, unimolecular contribution can be assumed as viable, and a description of the possible [DA] and [D$^+$A$^-$] states becomes relevant.[4b,c,5b,6d,27] The redox behavior of **1** in dichloromethane gives clues of allowed oxidation states, as the reduction Fe(III) → Fe(II) has been observed, but not the oxidation Fe(III) → Fe(IV). Conversely, the PhO$^-$ → PhO$^•$ oxidation from phenolate to phenoxyl has been observed while the formation of any reduced anionic radical remains unseen for these ligand systems. Thus, it is viable to propose the involvement of

Au|PhO$^-$—Fe^{III}|Au and Au|PhO$^{\bullet}$—Fe^{II}|Au states, where the LUMO of the ansatz is metal-based and the HOMO is ligand-centered. Although further consideration will be necessary, DFT calculations for similar systems[14] suggest that partially occupied metal-based SOMOs might be energetically accessible.

5.4 Conclusions

This chapter presented the synthesis and thorough characterization of a new [N$_2$O$_3$] ligand and its pentacoordinate iron(III) complex. The balanced amphiphilic nature of **1**, along with imine conversion into **1^i** at the air/water interface, was pivotal in optimizing the properties of defect-free LB monolayers, as confirmed by spectroscopic and microscopic methods. Furthermore, the asymmetric nature of the complex seemed useful in designing suitable precursors with current rectifying properties, as indicated by the I-V characteristics of fabricated devices. Asymmetrical responses indicative of rectifying behavior were observed for well-ordered LB monolayers of **1^i** sandwiched between two gold electrodes. Considering the molecular structure of **1^i** along with the associated I-V characteristics, suggested that the phenolate moiety and the metal center play a role as electron-donors and electron-acceptors in the generation of a directional flow of current. This example of rectification based on an asymmetric coordination complex paves the road towards the investigation of enhanced nanoscale rectifying devices in greater detail. Also, this study indicated that the optimization of molecular structures containing new iron(III) complexes with different donating and withdrawing substituents is able to modulate the Fe(III) to Fe(II) and the PhO$^-$ to PhO$^{\bullet}$ redox couples and amphiphilic or hydrophobic characters to yield defect-free LB films. The determination of the extent by which redox potentials enhance

rectification will allow to consider the magnitude of asymmetric versus unimolecular contributions.

REFERENCES

1. Aviram, A.; Ratner, M. *Chem. Phys. Lett.* **1974**, *29*, 277.

2. (a) Franco, I.; Solomon, G. C.; Schatz, G. C.; Ratner, M. A. *J. Am. Chem. Soc.* **2011**, *133*, 15714. (b) Ashwell, G. J.; Urasinska-Wojcik, B.; Phillips, L. J. *Angew. Chem. Int. Ed.* **2010**, *49*, 3508. (c) Shumate, W. J.; Mattern, D. L.; Jaiswal, A.; Dixon, D. A.; White, T. R.; Burgess, J.; Honciuc, A.; Metzger, R. M. *J. Phys. Chem. B* **2006**, *110,* 11146. (d) Troisi, A.; Ratner, M. A. *Nano Lett.* **2004**, *4*, 591. (e) Troisi, A.; Ratner, M. A. *J. Am. Chem. Soc.* **2002**, *124*, 14528. (f) Joachim, C.; Gimzewski, J. K.; Aviram, A. *Nature* **2000**, *408*, 541. (g) Metzger, R. M. *Acc. Chem. Res.* **1999**, *32*, 950.

3. Metzger, R. M. *Chem. Rev.* **2003**, *103,* 3803.

4. (a) Metzger, R. M. *J. Mater. Chem.* **2008**, *18*, 4364. (b) Ashwell, G. J.; Urasinska, B.; Tyrrell, W. D. *Phys. Chem. Chem. Phys.* **2006**, *8*, 3314. (c) Ashwell, G. J.; Mohib, A. *J. Am. Chem. Soc.* **2005**, *127*, 16238. (d) Liu, Y.; Xu, Y.; Zhu, D. *Synth. Met.* **1997**, *90*, 143. (e) Liu, Y.; Xu, Y.; Wu, J.; Zhu, D. *Solid State Commun.* **1995**, *95*, 695.

5. (a) Mujica, V.; Ratner, M. A.; Nitzan, A. *Chem. Phys.* **2002**, *281*,147. (b) Chabinyc, M. L.; Chen, X.; Holmlin, R. E.; Jacobs, H.; Skulason, H.; Frisbie, C. D.; Mujica, V.; Ratner, M. A.; Rampi, M. A.; Whitesides, G. M. *J. Am. Chem. Soc.* **2002**, *124*, 11730. (c) Krzeminski, C.; Delerue, C.; Allan, G.; Vuillaume, D.; Metzger, R. M. *Phys. Rev. B* **2001**, *64*, 085405-1.

6. (a) Nerngchamnong, N.; Yuan, L.; Qi, D.-C.; Li, J.; Thompson, D.; Nijhuis, C. A. *Nature Nanotechnology* **2013**, *8*, 113. (b) Azzaroni, O.; Alvarez, M.; Abou-Kandil, A. I.; Yameen, B.; Knoll, W. *Adv. Funct. Mater.* **2008**, *18*, 3487. (c) Oh, S.-K.; Baker, L. A.;

Crooks, R. M. *Langmuir* **2002**, *18,* 6981. (d) Metzger, R. M.; Chen, B.; Hopfner, U.; Lakshmikantham, M. V.; Vuillaume, D.; Kawai, T.; Wu, X.; Tachibana, H.; Hughes, T. V.; Sakurai, H.; Baldwin, J. W.; Hosch, C.; Cava, M. P.; Brehmer, L.; Ashwell, G. J. *J. Am. Chem. Soc.* **1997**, *119*, 10455.

7. (a) Jaiswal, A.; Rajagopal, D.; Lakshmikantham, M. V.; Cava, M. P.; Metzger, R. M. *Phys. Chem. Chem. Phys.* **2007**, *9*, 4007. (b) Ashwell, G. J.; Robinson, B. J.; Amiri, M. A.; Locatelli, D.; Quici, S.; Roberto, D. *J. Mater. Chem.* **2005**, *15*, 4203. (c) Ng, M.-K.; Yu, L. *Angew. Chem., Int. Ed.* **2002**, *41*, 3598. (d) Xu, T.; Peterson, I. R.; Lakshmikantham, M. V.; Metzger, R. M. *Angew. Chem. Int. Ed.* **2001**, *40*, 1749. (e) Collier, C. P.; Mattersteig, G.; Wong, E. W.; Beverly, K.; Sampaio, J.; Raymo, F. M.; Stoddart, J. F.; Heath, J. R. *Science* **2000**, *289*, 1172.

8. Liang, W.; Shores, M. P.; Bockrath, M.; Long, J. R.; Park, H. *Nature* **2002**, *417*, 725.

9. Lindsey, J. S.; Bocian D. F. *Acc. Chem. Res.* **2011**, *44*, 638.

10. (a) Lee, J.; Chang, H.; Kim, S.; Bang, G. S.; Lee, H. *Angew. Chem. Int. Ed.* **2009**, *48*, 8501. (b) Seo, K.; Konchenko, A. V.; Lee, J.; Bang, G. S.; Lee, H. *J. Am. Chem. Soc.* **2008**, *130*, 2553.

11. Bandyopadhyay, A.; Sahu, S.; Higuchi, M. *J. Am. Chem. Soc.* **2011**, *133*, 1168.

12. Paul, N. D.; Rana, U.; Goswami, S.; Mondal, T. K.; Goswami, S. *J. Am. Chem. Soc.* **2012**, *134*, 6520.

13. Lee, Y.; Yuan, S.; Sanchez, A.; Yu L. *Chem. Commun.* **2008**, 247.

14. Allard, M. M.; Sonk, J. A.; Heeg, M. J.; McGarvey, B. R.; Schlegel, H. B.; Verani, C. N. *Angew. Chem. Int. Ed*. **2012**, *51*, 3178.

15. (a) Hu, J.; Zhang, D.; Jin, S.; Cheng, S. Z. D.; Harris, F. W. *Chem. Mater.* **2004**, *16*, 4912. (b) Rosa, D. T.; Reynolds III, R. A.; Malinak, S. M.; Coucouvanis, D.; Ali, M.; MacDonnell, F. M. *Inorganic Syntheses* **2002**, *33*, 112. (c) Antonisse, M. M. G.; Snellink-Ruel, B. H. M.; Yigit, I.; Engbersen, J. F. J.; Reinhoudt, D. N. *J. Org. Chem.* **1997**, *62*, 9034. (d) Kyba, E. P.; Raymond, E. D.; Hudson, C. W.; John, A. M.; Brown, S. B.; McPhaul, M. J.; Liu, L.; Glover, A. C. *J. Am. Chem. Soc.***1981**, *103*, 3868.

16. (a) Lanznaster, M.; Heeg, M. J.; Yee, G. T.; McGarvey, B. R.; Verani, C. N. *Inorg. Chem.* **2007**, *46*, 72. (b) Lanznaster, M.; Hratchian, H. P.; Heeg, M. J.; Hryhorczuk, L. M.; McGarvey, B. R.; Schlegel, H. B.; Verani, C. N. *Inorg. Chem.* **2006**, *45*, 955.

17. (a) Tong, L. H.; Wong, Y.-L.; Pascu, S. I.; Dilworth, J. R. *Dalton Trans*. **2008**, 4784. (b) Nairn, A. K.; Bhalla, R.; Foxon, S. P.; Liu, X.; Yellowlees, L. J.; Gilbert, B. C.; Walton, P. H. *Dalton Trans.* **2002**, 1253. (c) Snodin, M. D.; Ould-Moussa, L.; Wallmann, U.; Lecomte, S.; Bachler, V.; Bill, E.; Hummel, H.; Weyhermüller, T.; Hildebrandt, P.; Wieghardt, K. *Chem. Eur. J.* **1999**, 5, 2554.

18. (a) Auerbach, U.; Eckert, U.; Wieghardt, K.; Nuber, B.; Weiss, J. *Inorg. Chem.* **1990**, *29,* 938. (b) Adam, B.; Bill, E.; Bothe, E.; Goerdt, B.; Haselhorst, G.; Hildenbrand, K.; Sokolowski, A.; Steenken, S.; Weyhermüller, T.; Wieghardt, K. *Chem.-Eur. J.* **1997**, *3*, 308. (c) Shongwe, M. S.; Kaschula, C. H.; Adsetts, M. S.; Ainscough, E. W.; Brodie, A. M.; Morris, M. J. *Inorg. Chem.* **2005**, *44*, 3070. (d) Gaber, B. P.; Miskowski, V.; Spiro, T. G. *J. Am. Chem. Soc.* **1974**, *96*, 6868. (e) Pyrz, J. W.; Roe, A. L.; Stern, L. J.; Que, Jr. L. *J. Am. Chem. Soc.* **1985**, *107* , 614. (f) Karsten, P.; Neves, A.; Bortoluzzi, A. J.;

Strahel, J.; -Mossmer, C. M. *Inorganic Chemistry communications* **2002**, *5*, 434. (g) Anjos, A.; Bortoluzzi, A. J.; Caro, M. S. B.; Peralta, R. A.; Friedermann, G. R.; Mangrich, A. S.; Neves, A. *J. Braz. Chem. Soc.* **2006**, *17*, 1540.

19. (a) Kundu, S.; Datta, A.; Hazra, S. *Phys. Rev. E* **2006**, *73*, 051608-1. (b) Kundu, S.; Datta, A.; Hazra, S. *Langmuir* **2005**, *21*, 5894. (c) Galvan-Miyoshi, J.; Ramos, S.; Ruiz-Garcia, J.; Castillo, R. *J. Chem. Phys.* **2001**, *115*, 8178.

20. Ries Jr., H. E. *Nature* **1979**, *281*, 287.

21. (a) Brezesinski, G.; Dobner, B.; Stefaniu, C.; Vollhardt, D. *Langmuir* **2011**, 27, 5386. (b) Hamoudi, H.; Chesneau, F.; Patze, C.; Zharnikov, M. *J. Phys. Chem. C.* **2011**, *115,* 534. (c) Brezesinski, G.; Dobner, B.; Stefaniu, C.; Vollhardt, D. *J. Phys. Chem. C*. **2011**, *115*, 8206. (d) Wang, L.; Cruz, A.; Flach, C. R.; Pérez-Gil, J.; Mendelsohn, R. *Langmuir* **2007**, *23,* 4950. (e) Wang, Y.; Du, X.; Guo, L.; Liu, H. *J. Chem. Phys.* **2006**, *124*, 134706-1.

22. Trimpin, S.; Inutan, E. D. *Analytical Chemistry* **2013**, *85*, 2005.

23. Trimpin, S.; Inutan, E. D. *J. Am. Soc. Mass Spectrom.* **2013**, *24*, 722.

24. Nakamoto, K. *Infrared and Raman Spectra of Inorganic and Coordination Compounds, Part B: Applications in Coordination, Organometallic and Bioinorganic Chemistry,* 6th ed.; John Wiley & Sons, Inc., Hoboken, New Jersey, 2008; chapter 1, pp 1-222.

25. Lipert, R. J.; Lamp, B. D.; Porter M. D. *Modern Techniques in Applied Molecular Spectroscopy* (Ed.: F. M. Mirabella), Wiley, New York, 1998; pp 83-126.

26. Kattner, J.; Hoffmann, H. *External reflection spectroscopy of thin films on dielectric substrates: Hand book of vibrational spectroscopy;* John Wiley & Sons Ltd., Chichester, 2002; pp 12-14.

27. (a) Ashwell, G. J.; Mohib, A.; Miller, J. R. *J. Mater. Chem.* **2005**, *15*, 1160. (b) Ashwell, G. J.; Chwialkowska, A.; High, L. R. H. *J. Mater. Chem.* **2004**, *14*, 2848.

CHAPTER 6

EVALUATION OF THE BEHAVIOR OF SALOPH-TYPE IRON(III) COMPLEXES WITH [N_2O_2] DONOR SETS IN RECTIFYING DEVICES

6.1 Introduction

As stated by Moore's law,[1] due to the miniaturization process of electronic components,[2,3,4] the use of inorganic semiconductor materials will face challenges in the near future. Inevitable problems associated with reducing the size of semiconductor chips are the leakage of current due to heat dissipation and the cost associated with necessary technology to reduce the chip size.[5] As an innovative concept to overcome these problems, the molecular electronics field emerged. As a first attempt to address the use of small molecules in electronics field, Aviram and Ratner[6] proposed a theoretical model of a single molecule that could act as a molecular rectifier. Molecular rectifiers can be defined as molecules with unidirectional flow of electrical current or which, can direct electrical current to flow only in one direction (asymmetric flow of current). With the concept of using molecules in electronics field, new organic and inorganic materials with different geometric, electronic, and magnetic properties were developed as potential candidates to be used as molecular switches,[7] molecular wires,[8] transistors,[9] capacitors,[10] and molecular diodes.[10] The most important characteristic that should be fulfilled by these molecules is to have an efficient electron transfer process. Therefore, redox-active molecules play an important role when designing precursors for molecule-based electronics. Redox behavior can be introduced by incorporating redox-active ligands or redox-active metals into a system. However, if one can incorporate redox-active ligands with redox-active metals, then the overall redox

properties of a particular system can be improved making them effective candidates for molecule-based electronics, because metal ions can be behaved as carriers for radial-containing ligand systems.

In previous chapters, I reported a large number of new asymmetric molecules with well-behaved redox properties. In these systems, phenolate moieties played a huge role in achieving the redox properties.[11,12,13,14,15] Recently, I presented a new redox active iron(III) metallosurfactant that demonstrated current rectification behavior when sandwiched between two gold electrodes.[16] This iron(III) complex exhibited a phenolate-based, electron-donor (D) and an iron(III)-based, electron-acceptor (A). However, the current rectifying mechanism for this system was not well-understood. Current rectification can occur via different mechanisms, namely Schottky, asymmetric, and unimolecular.[17] Because the Schottky mechanism relies on electrodes with different work functions, this is not be viable for the above mentioned iron(III) system. In search of new systems for current rectification and to propose a plausible current rectifying mechanism for iron(III) complexes, a new class of saloph-type iron(III) complexes were designed.

This chapter will present the development of new saloph-type iron(III) complexes as well as their electronic, redox, and current rectifying behavior. With the aid of electrochemical and density functional theory (DFT) calculations, a plausible electron transfer pathway during current rectification will also be discussed in this chapter. These new iron(III) complexes showed a $[N_2O_2]$-type binding cavity. However, the pentacoordinate geometry was maintained to create an asymmetric nature around the metal atom. By varying the substituents on the phenolate moiety, the electronic, redox, and amphiphilic properties of

the resulting complexes were modulated. The desired ligands and iron(III) complexes are shown in **Scheme 6.1**.

Ligands
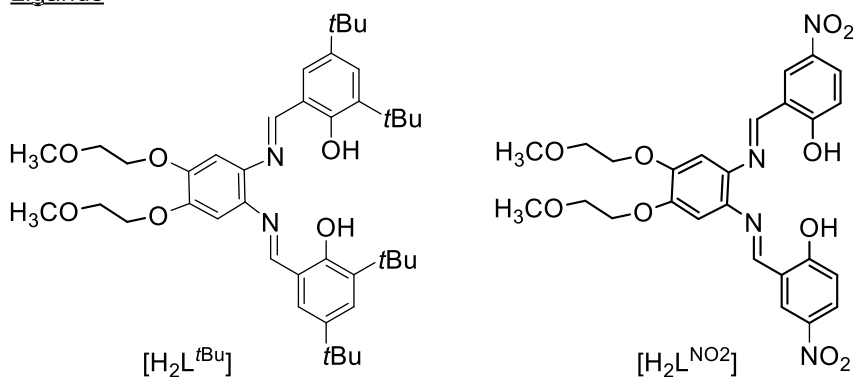
Metal Complexes
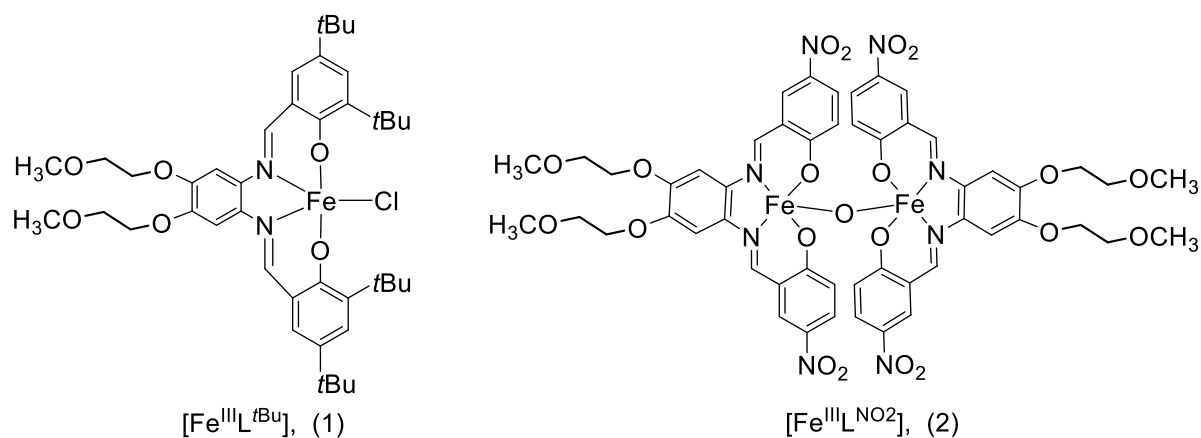
Scheme 6.1. Ligands described in chapter **6** and their respective iron(III) complexes.

6.2 Experimental Section

6.2.1 X-ray Structural Determinations for complex 2

A dark green crystal of **[Fe^{III}L^{NO2}], (2)** with dimensions $0.36 \times 1.09 \times 0.25$ mm was mounted on a mitogen loop using paratone oil. Data were collected on a Bruker APEX-II Kappa geometry diffractometer with Mo radiation and a graphite monochromato using a

Bruker CCD (charge coupled device) based diffractometer equipped with an Oxford Cryostream low-temperature and was measured at a temperature of 100 K with omega and phi scans of 0.5° per frame for 20 s. The crystal was solved to a resolution of 0.74 Å with a completeness of 100%. The structures were solved by direct methods using the SHELXS-97 program in APEX II suite and refined by least squares method on F^2, SHELXL-97 and OLEX2. A total of 200653 reflections were collected with 17566 unique reflections. An independent molecule along with four dimethyl sulfoxide molecules was present in the asymmetric unit cell. Hydrogen atoms were placed in calculated positions.

6.2.2 Computational methods used for complex 1

All the calculations were performed using DFT[18] with a development version of Gaussian,[19] using B3LYP[20,21] functional with SDD basis set and pseudopotentials[22,23,24] on the metal centers, iron and copper, and 6-31G(d,p) basis[25,26] on the other atoms. To reduce the computational cost, a slightly modified model was used where the methoxyethoxy substituents of the phenylenediamine moiety were replaced by methoxy groups. All optimized structures were confirmed as minima by analyzing the harmonic vibrational frequencies. Solvation effects (in dichloromethane) were accounted for using the implicit SMD[27] continuum solvation model and were included during structure optimization. Isodensity plots of orbitals were visualized using Gauss View.[28] Vertical electronic excitation energies and intensities were evaluated using time-dependent DFT (TD-DFT),[29,30,31] and the orbital transitions of each excited state were characterized using the natural transition orbital (NTO) method.[32] The calculations of the oxidation and reduction potentials of the complexes included zero-point energy and thermal corrections and standard thermodynamic equation

$\Delta G = -nFE$ was used. The calculated potentials were referenced to a calculated value of $E_{1/2} =$ 4.35 V for the ferrocene/ferrocenium couple under the level of theory used.

6.2.3 Syntheses of Ligands

Synthesis of 4,5-bis(2-methoxyethoxy)benzene-1,2-diamine was carried out as previously described.[16] 3,5-Di-*tert*-butyl-2-hydroxybenzaldehyde and 2-hydroxy-5-nitrobenzaldehyde were used as received from Sigma Aldrich.

Synthesis of ligand [H$_2$L^{tBu}], *6,6'-(1E,1'E)-(4,5-bis(2-methoxyethoxy)-1,2-phenylene)bis(azan-1-yl-1-ylidene)bis(methan-1-yl-1-ylidene)bis(2,4-di-tert-butylphenol).*

To a stirred solution of 3,5-di-*tert*-butyl-2-hydroxybenzaldehyde (1.99 g, 8.51 mmol) in dry methanol (30 mL) was added a solution of 4,5-bis(2-methoxyethoxy)benzene-1,2-diamine (1.09 g, 4.25 mmol) in anhydrous methanol (20 mL). The mixture was heated at reflux for 18 hours under inert conditions. The resulting dark orange turbid solution was stored at 4 C° for 18 hours. The obtained precipitate was filtered, washed with cold methanol, and dried under vacuum to attain a dark orange microcrystalline powder. Yield: 78.3%. ESI (m/z^+) in CH$_2$Cl$_2$ = 689.4525 for [C$_{42}$H$_{60}$N$_2$O$_6$ + H$^+$] (calculated = 689.4530) in agreement with -0.7 ppm difference. ^{1}H NMR, ppm (CDCl$_3$, 400 MHz): δ 1.305-1.453 (m, 36H^{tBu}), 3.459 (s, 6H^{OCH3}), 3.794 (t, 4H^{OCH2}), 4.236 (t, 4H^{OCH2}), 6.884 (s, 2H^{ph}), 7.196 (d, 2H^{ph}), 7.411 (d, 2H^{ph}), 8.635 (s, 2H^{CH}). IR (KBr, cm^{-1}) 3245 (ν_{O-H}), 2811-2957 (ν_{C-H}), 1616 ($\nu_{C=C}$, aromatic), 1511 ($\nu_{C=C}$, aromatic), 1578 ($\nu_{C=N}$), 1266 (ν_{C-O-C}), 1129 (ν_{C-O-C}).

Synthesis of ligand [H$_2$L^{NO2}], *2,2'-(1E,1'E)-(4,5-bis(2-methoxyethoxy)-1,2-phenylene)bis(azan-1-yl-1-ylidene)bis(methan-1-yl-1-ylidene)bis(4-nitrophenol).*

To a stirred mixture of 2-hydroxy-5-nitrobenzaldehyde (1.29 g, 7.714 mmol) in anhydrous methanol (10 mL) and dichloromethane (40 mL) was added a solution of 4,5-bis(2-methoxyethoxy)benzene-1,2-diamine (0.66 g, 2.575 mmol) in anhydrous methanol (30 mL). The mixture was heated at reflux for 18 hours under dark and inert conditions. The reaction mixture was cooled to ambient temperature and the solvent was removed to half of its original volume under reduced pressure. The dark orange precipitate obtained was filtered and washed with methanol. Then the precipitate was recrystallized from hot dimethyl sulfoxide. The obtained dark orange crystalline product was filtered, washed with methanol, and dried under vacuum. Yield: 46.8%. ESI (m/z^+) = 555.1736 for [C$_{26}$H$_{26}$N$_4$O$_{10}$ + H$^+$] (calculated = 555.1727) in agreement with 0.9 ppm difference. ^{1}H NMR, ppm (DMSO-d$_6$, 400 MHz): δ 3.347 (s, 6H^{OCH3}), 3.721 (t, 4H^{OCH2}), 4.237 (t, 4H ^{OCH2}), 7.046 (d, 2H^{ph}), 7.303 (s, 2H^{ph}), 8.2 (dd, 2H^{ph}), 8.697 (d, 2H^{ph}), 9.182 (s, 2H^{CH}). IR (KBr, cm^{-1}) 2827-3077 (ν_{C-H}), 1612 ($\nu_{C=C}$, aromatic), 1528 ($\nu_{C=C}$, aromatic), 1568 ($\nu_{C=N}$), 1479 ($\nu_{N=O}$), 1336 ($\nu_{N=O}$), 1264 (ν_{C-O-C}), 1130 (ν_{C-O-C}).

6.2.4 Syntheses of Metal Complexes

Synthesis of complex [Fe^{III}L^{tBu}] (1).

A mixture of **[H$_2$L^{tBu}]** (0.250 g, 0.363 mmol) and anhydrous NaOCH$_3$ (0.040 g, 0.730 mmol) in methanol (15 mL) and dichloromethane (5 mL) was treated with a methanolic solution (5 mL) of FeCl$_3$.6H$_2$O (0.098 g, 0.363 mmol). The resulting solution was heated at 50 °C for 4-5 hours. The reaction mixture was cooled to ambient temperature and stirred for

1 hour. Then, the solution was filtered and the solvent was removed to half of its original volume under reduced pressure. The solution was recrystallized at ambient conditions to yield dark brown crystals. Yield: 87.2%. ESI (m/z^+) in CH_3OH = 742.3641 (100%) for $[C_{42}H_{58}N_2O_6Fe^+]$ (calculated = 742.3644) in agreement with -0.4 ppm difference. Anal. Calc. for $[C_{42}H_{58}ClFeN_2O_6]$: C, 64.82; H, 7.51; N, 3.60%. Found: C, 65.19; H, 7.48; N, 3.69%. IR (KBr, cm^{-1}) 2819-2956(ν_{C-H}), 1606($\nu_{C=C}$, aromatic), 1507($\nu_{C=C}$, aromatic) 1585 ($\nu_{C=N}$), 1273 (ν_{C-O-C}), 1131 (ν_{C-O-C}).

Synthesis of complex [Fe^{III}L^{NO2}] (2).

A mixture of **[H$_2$L^{NO2}]** (0.200 g, 0.361 mmol) and anhydrous $NaOCH_3$ (0.039 g, 0.720 mmol) in dichloromethane (30 mL) and dimethyl sulfoxide (5 mL) was treated with a methanolic solution (10 mL) of $FeCl_3.6H_2O$ (0.098 g, 0.361 mmol). The resulting solution was heated at reflux for 20 hours. The reaction mixture was cooled to ambient temperature. The solvent was concentrated to half of its original volume, and diethyl ether (50 mL) was added to the solution to give a dark green microcrystalline product. The microcrystalline product was recrystallized from dichloromethane and dimethyl sulfoxide mixture (6:1, 21 mL) to obtain X-ray quality single crystals. Yield: 33.1%. ESI (m/z^+) = 1233.1945 for $[C_{52}H_{48}Fe_2N_8O_{21} + H^+]$. Anal. Calc. for $[C_{52}H_{48}Fe_2N_8O_{21}.4(CH_3)_2SO]$: C, 46.64; H, 4.70; N, 7.25%. Found: C, 46.69; H, 4.13; N, 7.84%. IR (KBr, cm^{-1}) 2828-2932(ν_{C-H}), 1608($\nu_{C=C}$, aromatic), 1517($\nu_{C=C}$, aromatic) 1585 ($\nu_{C=N}$), 1271 (ν_{C-O-C}), 1133 (ν_{C-O-C}), 1461 ($\nu_{N=O}$), 1334 ($\nu_{N=O}$).

6.3 Results and Discussion

6.3.1 Ligand Rationale, Synthesis, and Characterization

This chapter will address the development of new precursors which can behave as current rectifiers and propose a plausible current rectifying mechanism for phenolate coordinate iron(III) complexes. Therefore, new saloph-type ligands with $[N_2O_2]$ donor sets and their iron(III) complexes were designed and synthesized. In these metal complexes, electron-donating *tert*-butyl groups and electron-withdrawing nitro groups were occupied on the phenolate moieties to modulate the redox and electronic properties. Methoxyethoxy groups were substituted on the fourth and fifth positions of the phenylenediamine moiety to introduce amphiphilic character into these systems. Ligands **[H₂L^{*tBu*}]** and **[H₂L^{NO2}]** were synthesized by reacting one equivalent of 4,5-bis(2-methoxyethoxy)benzene-1,2-diamine with two equivalents of 3,5-di-*tert*-butyl-2-hydroxybenzaldehyde and 2-hydroxy-5-nitrobenzaldehyde, respectively under inert atmospheric conditions. The reaction mixtures were heated at reflux for 18 h and for the synthesis of **[H₂L^{NO2}]**, dark condition were used (2-hydroxy-5-nitrobenzaldehyde is light sensitive). After following recrystallization methods, **[H₂L^{*tBu*}]** from methanol and **[H₂L^{NO2}]** from hot dimthyl sulfoxide, purified ligands were isolated. Then ligands were reacted with one equivalent of $FeCl_3.6H_2O$ and two equivalents of $NaOCH_3$ to result in the metal complexes **[Fe^{III}L^{*tBu*}]** (**1**) and **[Fe^{III}L^{NO2}]** (**2**). The synthetic pathway to obtain ligands and metal complexes are shown in **Scheme 6.2**. These ligands and metal complexes were structurally characterized using multiple techniques such as infrared, NMR, ESI-mass spectrometry, and CHN elemental analysis. IR spectroscopic data showed symmetric and asymmetric C–H stretching vibrations in the regions of ~ 2820-2960 cm⁻¹. The C=N stretching vibrations appeared at 1585 cm⁻¹. High resolution ESI-mass

spectrometry data showed peak clusters of [M$^+$] for complex **1** and [M+H$^+$] for ligands as well as for complex **2**. Peak positions and isotopic distribution patterns matched between experimental and simulated data.
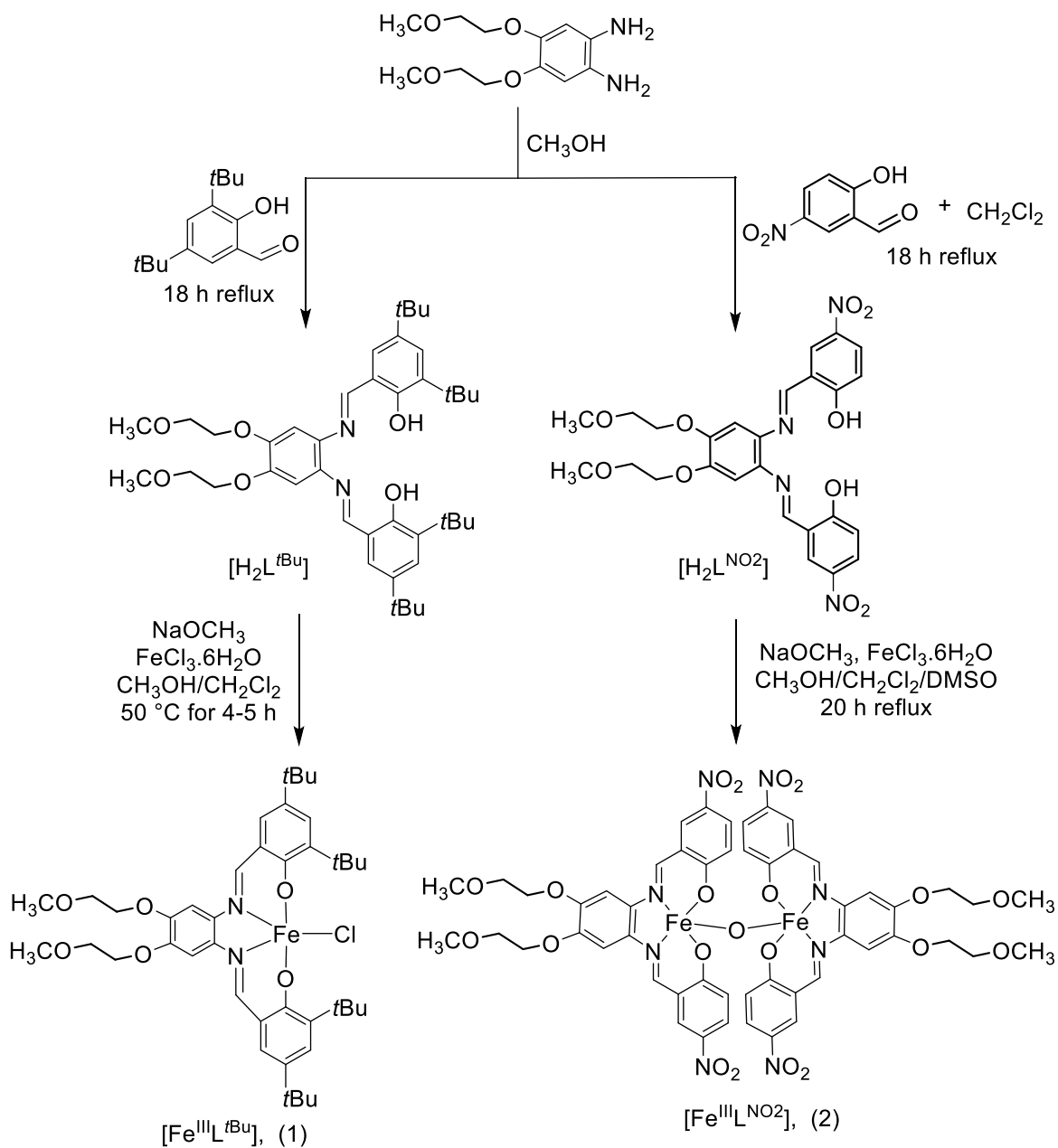
Scheme 6.2. Synthesis of ligands and iron(III) complexes.

6.3.2 Molecular Structure Data

X-ray quality dark green single crystals were obtained for complex **2** from dichloromethane and dimethyl sulfoxide solvent mixture (6:1). Attempts to grow X-ray quality single crystals for complex **1** were unsuccessful. Complex **1** was isolated as fibrous bundles of dark brown crystals from methanol dichloromethane solvent mixture (2:1). In these cases, slow evaporation method was used for the recrystallization of metal complexes. The X-ray crystallographic structure of complex **2** is shown in **Figure 6.1**. Important structure parameters, and selected bond distances and angles are given in **Table 6.1** and **6.2**, respectively. The crystal structure data of complex **2** showed the formation of a μ-oxo-bridged di-iron species with a Fe1–O3–Fe2 core. The two imine nitrogens and the two phenolate oxygens of the ligand occupied the same plane, and the bridging oxygen atom, O3 occupied the axial position. The two iron(III) centers (Fe1 and Fe2) showed τ value of 0.119 and 0.097, hence showed a distorted square pyramidal geometry around both the iron(III) centers. The μ-oxo bridge showed bond distances of, 1.782 Å for Fe1-O3 and 1.779 Å for Fe2-O3 bonds, respectively. Complex **2** also showed a Fe1—Fe2 distance of 3.561 Å. These bond distances are in the same range as other reported μ-oxo-bridged di-iron species, where Fe—O bond is between 1.75 and 1.80 Å and Fe—Fe distance is ~3.35-3.55 Å.[33,34,35,36,37] The cavity of the crystal structure showed Fe—O$_{phenolate}$ bond distances of Fe1—O2, 1.932; Fe1—O1, 1.913; Fe2—O4, 1.924; Fe2—O5, 1.921 Å and Fe—N$_{imine}$ bond distances of Fe1—N3, 2.103; Fe1—N4, 2.110; Fe2—N1, 2.102; Fe2—N2, 2.111 Å. Therefore, the Fe—O$_{phenolate}$ bond distances were found to be longer than the other observed saloph-type iron(III) monomeric species, but with usual Fe—N$_{imine}$ bond distances of other reported μ-oxo bridged diiron complexes.[38] Fe1–O3–Fe2 angle was found to be 150.69°. This data further indicated

that the Fe1 and Fe2 centers were distorted in geometry and were asymmetrically bonded to the ligand. The C-N imine bonds (N1—C7, 1.285; N2—C13, 1.288; N3—C39, 1.301; N4—C26, 1.293 Å) showed an average bond distance of 1.29 Å, which is typical for C=N bond found in the literature.[39]
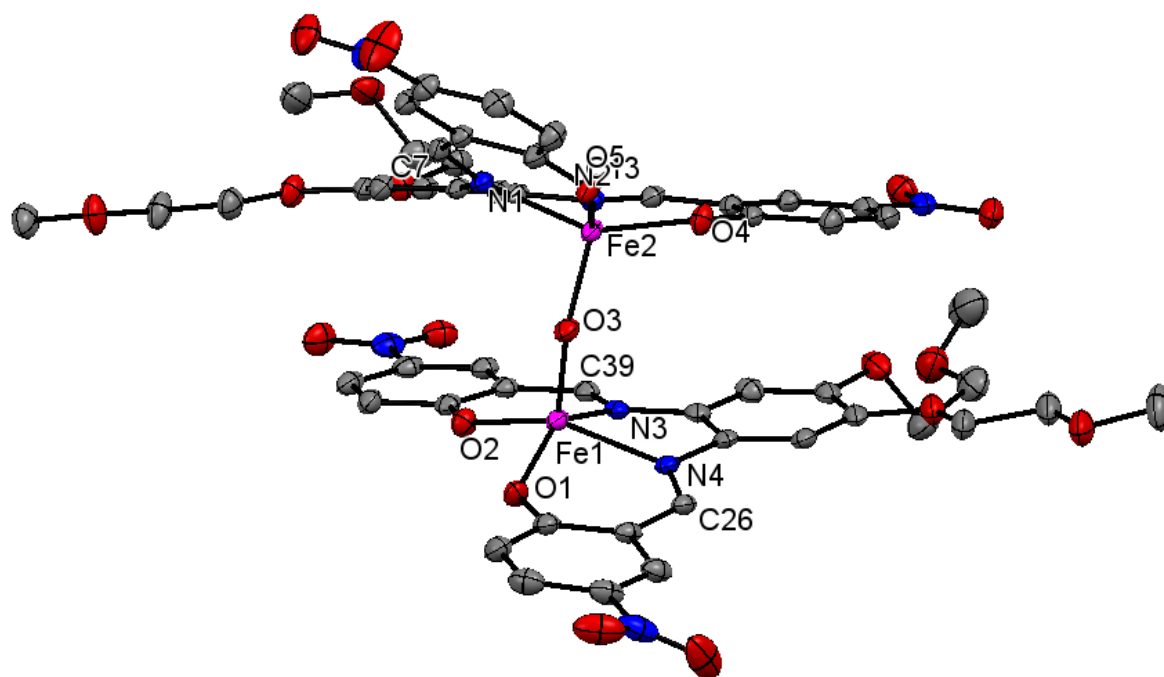
Figure 6.1. X-ray crystal structure data of complex **2**.

	Complex (2)
Formula	$C_{60}H_{72}N_8O_{25}S_4Fe_2$
M	1545.20
T/K	100.1
Space group	P(-1)
a/Å	14.2608(9)
b/Å	14.9219(9)
c/Å	18.1654(11)
α/°	76.882(4)
β/°	69.115(4)
γ/°	72.261(4)
V/Å^3	3409.3(4)
Z	2
D_{calc}/ g cm^{-3}	1.505
μ/ mm^{-1}	0.634
λ/ Å	0.71073
R(F) (%)	6.69
Rw(F) (%)	16.26

^{a}R(F) = $\sum \left\| F_o \right| - \left| F_c \right\| / \sum \left| F_o \right|$; Rw(F) = $[\sum w(F_o^2 - F_c^2)^2 / \sum w(F_o^2)^2]^{1/2}$ for I > 2σ(I)

Table 6.1. Important crystal structure parameters^a for complex 2.

Complex (2)			
Fe1-O3	1.782(2)	O4-Fe2-N1	149.00(11)
Fe1-N3	2.103(3)	N1-Fe2-N2	76.85(11)
Fe1-O2	1.932(2)	O5-Fe2-O4	90.42(11)
Fe1-N4	2.110(3)	O5-Fe2-N2	143.16(11)
Fe1-O1	1.913(3)	O5-Fe2-N1	87.15(11)
Fe2-O3	1.779(2)	O3-Fe1-N3	106.60(11)
Fe2-O4	1.924(2)	O3-Fe1-O2	110.48(11)
Fe2-N2	2.111(3)	O3-Fe1-N4	97.88(11)
Fe2-N1	2.102(3)	O3-Fe1-O1	108.33(12)
Fe2-O5	1.921(3)	N3-Fe1-N4	77.05(11)
N1-C7	1.285(4)	O2-Fe1-N3	86.95(11)
N2-C13	1.288(5)	O2-Fe1-N4	150.50(11)
N3-C39	1.301(5)	O1-Fe1-N3	143.36(11)
N4-C26	1.293(5)	O1-Fe1-O2	90.99(11)
O3-Fe2-O4	110.13(11)	O1-Fe1-N4	87.54(11)
O3-Fe2-N2	104.02(11)	Fe2-O3-Fe1	150.69(17)
O3-Fe2-N1	99.48(11)		
O3-Fe2-O5	111.30(12)		
O4-Fe2-N2	87.02(11)		

Table 6.2. Selected bond lengths (Å) and angles (°) for complex **2**.

6.3.3 Electronic Spectral Properties

UV-visible spectra of [H$_2$L^{tBu}] and complex **1** were measured in 1.0×10^{-5} mol•L^{-1} dichloromethane solutions. The ligand [H$_2$L^{NO2}] and complex **2** were dissolved in dichloromethane and dimethyl sulfoxide solvent mixture (19:1) to prepare a 1.0×10^{-3} mol•L^{-1} solution, and then the dilution was carried out using dichloromethane to make 1.0×10^{-5} mol•L^{-1} solutions. The observed UV-visible spectra for ligands and metal complexes are shown in **Figure 6.2**, and the λ_{max} values are given in **Table 6.3**. Uncoordinated ligands, [H$_2$L^{tBu}] and [H$_2$L^{NO2}] showed intense absorption bands in the range of 275-370 nm. These bands can be attributed to intraligand $\pi \rightarrow \pi^*$ charge transitions. Time-dependent DFT (TD-DFT)[29,40,41] calculations along with the natural transition orbital (NTO) method[42] were used to characterize these bands using ligand [H$_2$L^{tBu}]. All these absorptions were assigned as intraligand $\pi \rightarrow \pi^*$ charge transitions (**Figure 6.3**). Two types of excitations were observed: (i) from the donor orbitals having predominant phenylenediamine character to the acceptor orbitals which are mainly π^* on imine and (ii) from the phenoxyl-based donor orbitals to the imine-based π^* acceptor orbitals.

Iron(III) complexes showed intense absorption bands in the region of 300-600 nm. Complex **1** showed bands at 310, ~ 351, ~ 395, and ~ 447 nm with ε ranging from 19210 to 49920 L•mol^{-1}•cm^{-1}. Complex **2** showed absorption bands at 280, 312, 341, 373, and ~ 440 nm with ε ranging from 23620 to 53075 L•mol^{-1}•cm^{-1}. Bands at ~ 310-400 nm can be assigned as ligand to metal charge transfer transitions (LMCT), originating from phenolate p_π orbitals to $d_{\sigma*}$ and $d_{\pi*}$ of the iron(III) metal center.[43,44,45] The other bands belong to intraligand $\pi \rightarrow \pi^*$ charge transfer transitions (ILCT) as observed for similar species.[46] TD-DFT calculations on complex **1** showed that there are three intense absorption bands in

the region of 367-383 nm. All of them can be characterized as LMCT transitions. The donor orbitals are (i) the π orbital delocalized on the phenylenediamine moiety, (ii) the *p*-orbital of phenolate oxygens, and (iii) the p_π orbital on the chloride ligand. The acceptor orbitals are $d_{\pi*}$ and $d_{\sigma*}$ orbitals of the metal center. A new absorption was found at 459 nm, which is characterized to be a $\pi \rightarrow \pi*$ intraligand charge transfer transition (**Figure 6.4**).
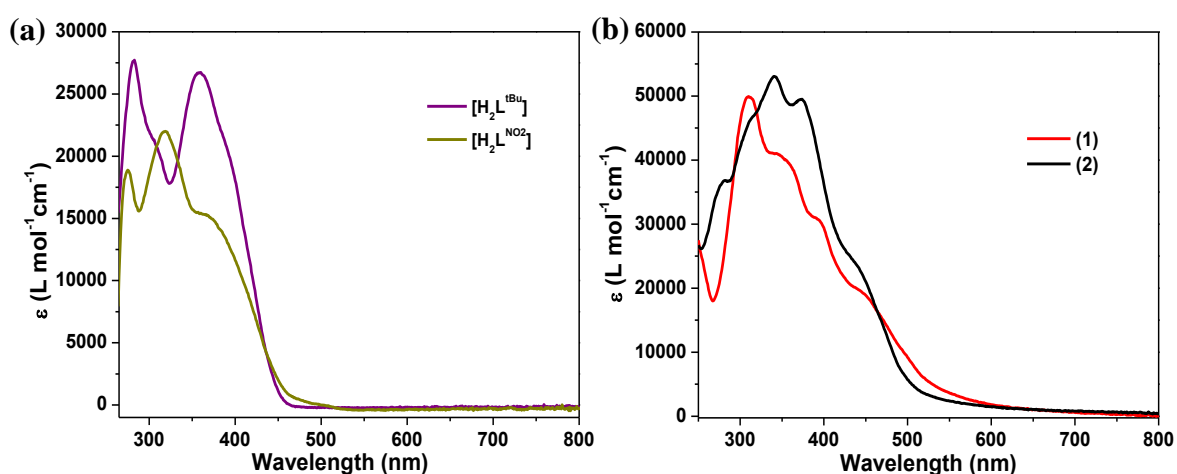
Figure 6.2. UV-visible spectra of (a) ligands (**H₂L***$^{t\mathbf{Bu}}$* and **H₂L**$^{\mathbf{NO2}}$) and (b) iron(III) complexes (**1** and **2**) in 1.0×10^{-5} mol•L^{-1} solutions.

Compound	λ_{max} (nm), ε (L•mol^{-1}•cm^{-1})
[H$_2$L^{tBu}]	283 (27720), 358 (26719)
[H$_2$L^{NO2}]	276 (18836), 319 (22005), 370 (15097)
(1)	310 (49917), ~351 (40362), ~395 (30516), ~447 (19210)
(2)	280 (36984), 312 (46688), 341 (53075), 373 (49493), ~440 (23620)

Table 6.3. UV-visible spectroscopic data for ligands (**H$_2$L^{tBu}** and **H$_2$L^{NO2}**) and their iron(III) complexes (**1** and **2**) in 1.0×10^{-5} mol•L^{-1} solutions.

UV-VIS Spectrum

λ = 424.66 nm

f (Oscillator strength) = 0.496

Transition 1

MO 163 (occupied) → MO 164 (unoccupied)

λ = 381.20 nm

f (Oscillator strength) = 0.280

Transition 2

MO 163 (occupied) → MO 164 (unoccupied)

λ = 355.24 nm

f (Oscillator strength) = 0.345

Transition 3

MO 163 (occupied) → MO 164 (unoccupied)
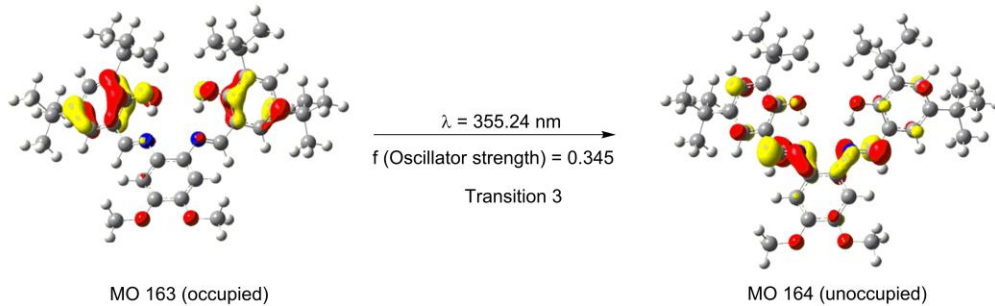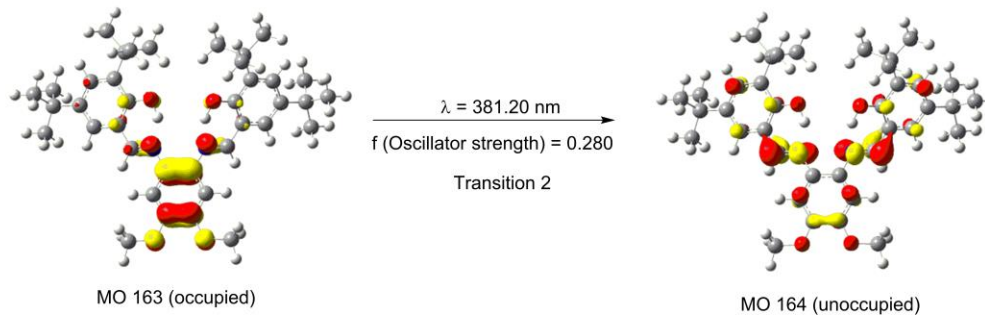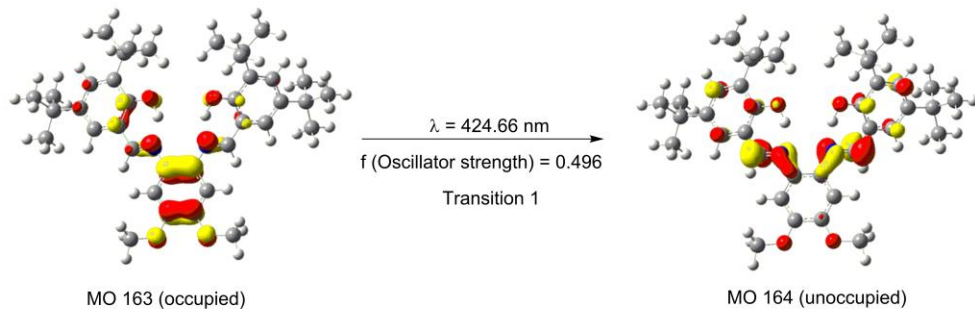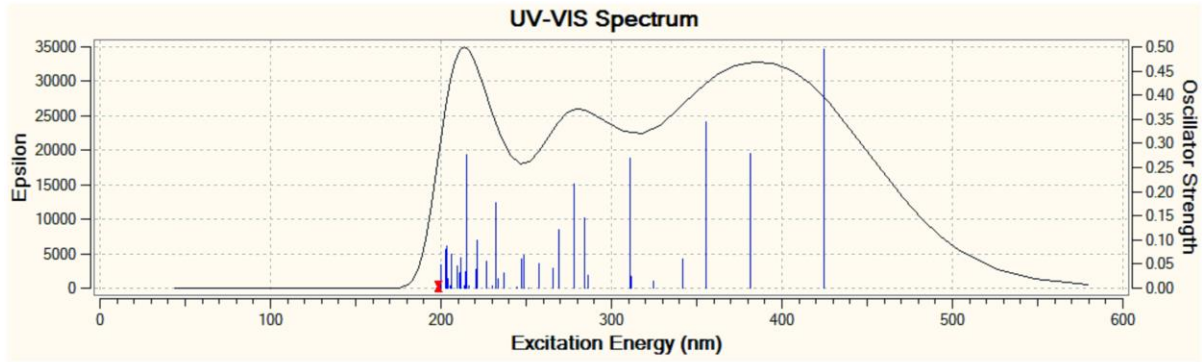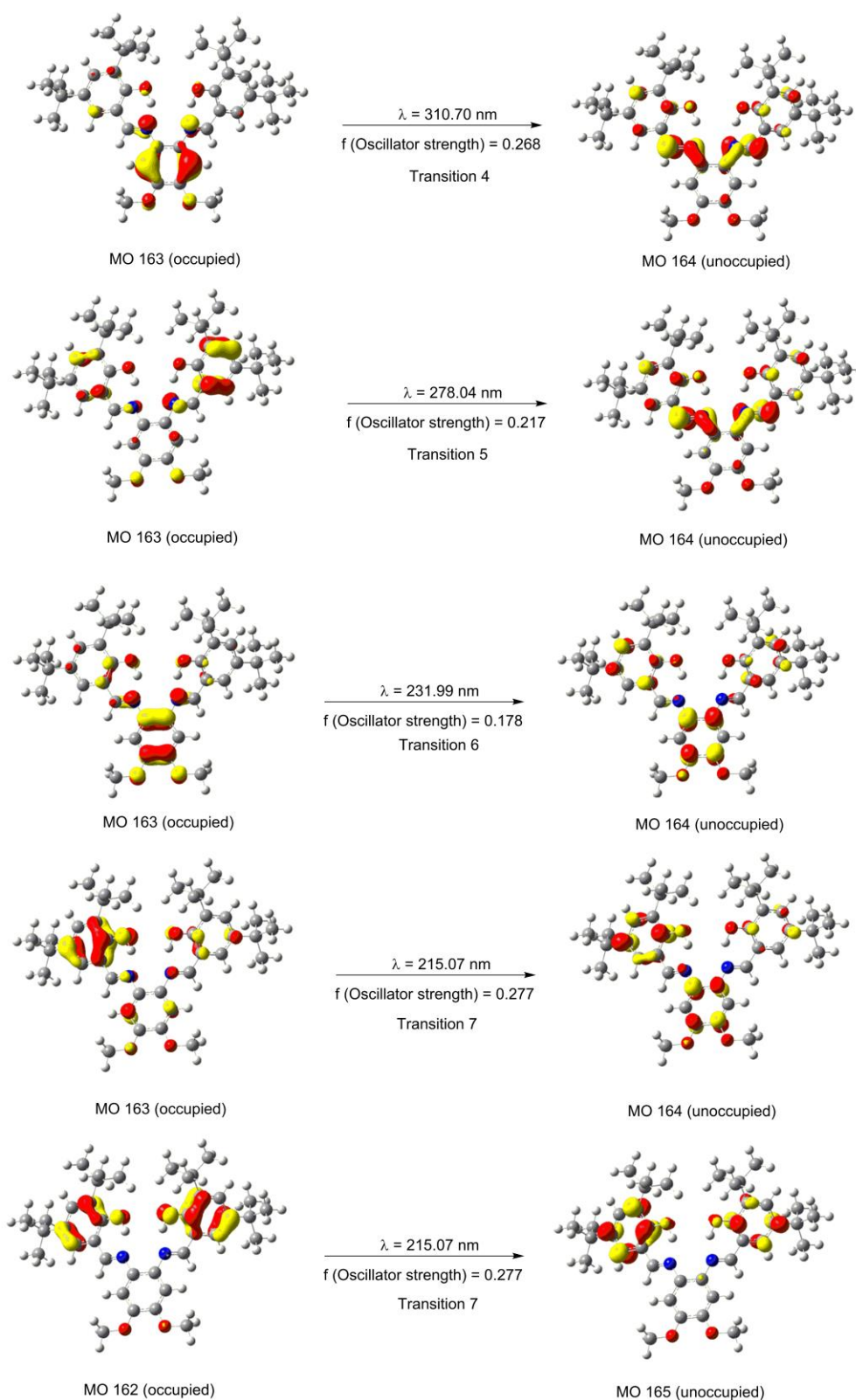
Figure 6.3. TD-DFT spectrum and NTOs (isodensity value of 0.05 a.u.) of the excitations of reasonable intensity for the uncoordinated ligand [$\mathbf{H_2L^{tBu}}$].

UV-VIS Spectrum

λ = 459.32 nm
f (Oscillator strength) = 0.184

MO 181a (occupied) → MO 182a (unoccupied)

λ = 459.32 nm
f (Oscillator strength) = 0.184

MO 176b (occupied) → MO 177b (unoccupied)

λ = 383.27 nm
f (Oscillator strength) = 0.155

MO 176b (occupied) → MO 177b (unoccupied)

MO 176b (occupied) $\lambda = 372.50$ nm   MO 177b (unoccupied)

f (Oscillator strength) = 0.145

MO 176b (occupied) $\lambda = 367.20$ nm   MO 177b (unoccupied)

f (Oscillator strength) = 0.175

MO 175b (occupied) $\lambda = 367.20$ nm   MO 178b (unoccupied)

f (Oscillator strength) = 0.175

Figure 6.4. TD-DFT spectrum and NTOs (isodensity value of 0.05 a.u.) of the excitations of reasonable intensity for the complex **1**.

6.3.4 Electrochemical Data of Iron(III) Complexes

The cyclic voltammograms of iron(III) complexes **1** and **2** were recorded in 1.0×10^{-3} mol•L^{-1} dichloromethane and 19:1 dichloromethane/dimethyl sulfoxide solutions, respectively, using TBAPF$_6$ as the supporting electrolyte. All the potential values were recorded versus the Fc$^+$/Fc couple. The cyclic voltammograms and their redox potential values are shown in **Figure 6.5** and **Table 6.4**, respectively. Complexes **1** and **2** showed

metal- and ligand-centered redox processes in their cyclic voltammograms. Complex **1** showed a single electron reversible redox process at -1.02 V with ΔE_p of 0.12 V, and complex **2** showed reversible process at -0.57 V with ΔE_p of 0.12 V. According to DFT calculations, these two cathodic processes can be assigned as Fe^{III}/Fe^{II} redox couple. The lower redox potential observed for complex **2**, when compared to complex **1** can be related to the electron-withdrawing nitro and electron-donating *tert*-butyl substituents present on the phenolate moieties. In complex **2**, the nitro groups present on the phenolate moiety creates a lower electron density around the metal center when compared to complex **1**. Therefore, in complex **2**, the Fe^{III}/Fe^{II} reduction can happen at a lower potential when compared to complex **1**. Apart from the metal-centered process, complex **1** showed one reversible process at 0.64 V (ΔE_p, 0.12 V) and one quasi-reversible single electron anodic process at 1.05 V (ΔE_p, 0.11 V). These two processes can be attributed to ligand-centered oxidations. According to DFT calculations, the first reversible oxidation process can be assigned as the oxidation of the phenylenediamine moiety. Thomas *et al*. also observed a similar oxidation process for copper(II) salophen systems.[39] The second oxidation process can be assigned as phenolate/phenoxyl redox process.[11,14,47] Complex **2** showed an irreversible ligand-based oxidation process at ~ 1 V. This data further indicated that the phenoxyl radical can be stabilized better when there are sterically bulky electron-donating *tert*-butyl substituents when compared to electron-withdrawing nitro groups.[48] Complex **2** showed another quasi-reversible reduction process at ~ -1.9 V with ΔE_p of 0.14 V belonging to nitro reduction.
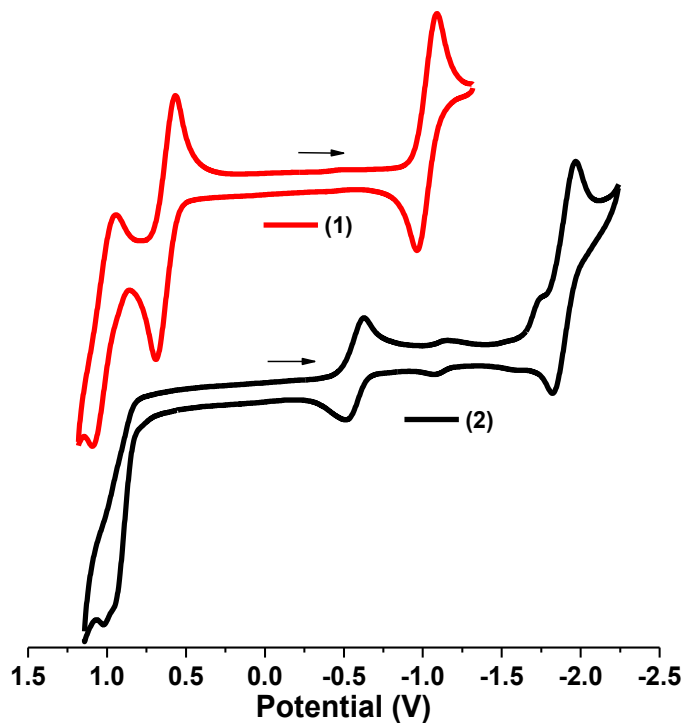
Figure 6.5. Cyclic voltammograms of 1.0×10^{-3} mol•L^{-1} solutions of iron(III) complexes **1** and **2**.

Complex	$E_{1/2}$, (ΔE_p) (V) $\lvert I_{pa}/I_{pc} \rvert$	$E_{1/2}$, (ΔE_p) (V) $\lvert I_{pa}/I_{pc} \rvert$	$E_{1/2}$, (ΔE_p) (V)
(1)	-1.018 (0.122) $\lvert 0.932 \rvert$	0.643 (0.124) $\lvert 1.078 \rvert$	1.050 (0.110)
(2)	-1.897 (0.136) $\lvert 0.638 \rvert$	-0.567 (0.116) $\lvert 0.872 \rvert$	1.013 (E_{pa})

Table 6.4. Cyclic voltammetry data for iron(III) complexes **1** and **2**.

To understand the electrochemical events of complex **1**, a number of electronic structures were investigated using DFT.[18] Complex **1** is found to be a sextet (S = 5/2) with high spin $3d^5$ iron(III). As shown in **Figure 6.6**, spin densities were computed for all the relevant structures to understand the electron transfer phenomena in first oxidation and first reduction processes.[49]
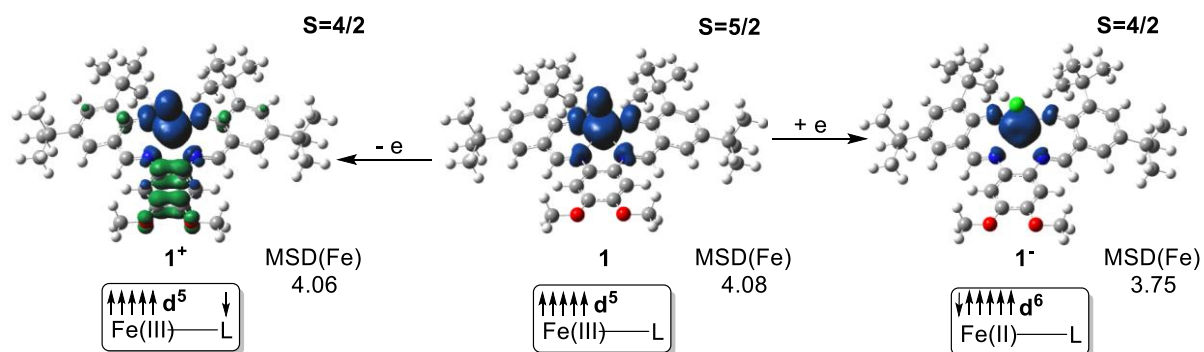
Figure 6.6. DFT-calculated spin density plots (isodensity value of 0.004 a.u.) with Mulliken spin density values (MSD) showing the oxidation and reduction processes of complex **1**.

The first reduction for complex **1** was found to be Fe(III)/Fe(II) reduction leading to high spin (S = 4/2) **1⁻** with $3d^6$ Fe(II) center. On the other hand, the first oxidation is a ligand-based event giving rise to a radical delocalized over the di(methoxy)phenylenediamine moiety. This radical, being π in nature, can be coupled with a singly occupied d_π orbital of iron and DFT calculations show that the antiferromagnetically (AF) coupled **1⁺** with S = 4/2 is lower in energy than the high spin state (S = 6/2) by 3.66 kcal/mol. The second oxidation process of complex **1** is a ligand-based phenolate/phenoxyl redox process as shown in **Figure 6.7**.

239
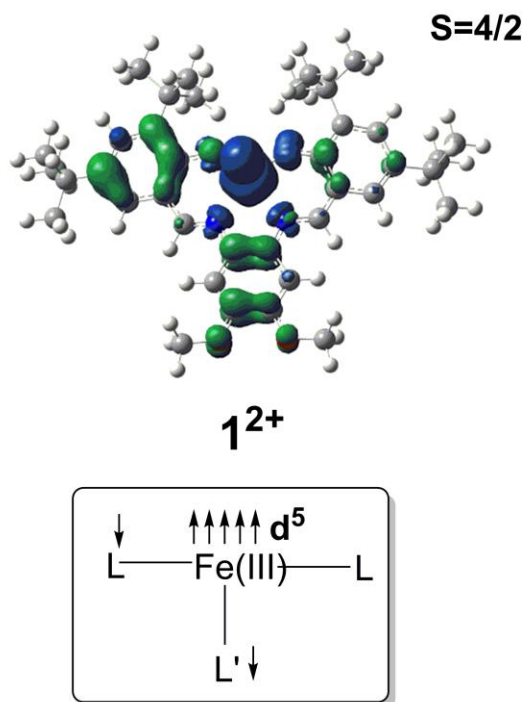
Figure 6.7. DFT-calculated spin density plot (isodensity value of 0.004 a.u.) of **1²⁺**, the doubly-oxidized species of complex **1**. As illustrated in the diagram, the second oxidation is a ligand-based (phenolate/phenoxyl) for complex **1**.

	Spin state	G (a.u.)	ΔG (kcal/mol)
1	Quartet	-2472.184881	10.06
	Sextet	-2472.200917	0.00
1$^+$	Triplet	-2472.000552	10.61
	Quintet	-2472.017458	0.00
	Septet	-2472.011630	3.66
1^{2+}	Doublet	-2471.785440	9.08
	Quartet	-2471.799911	0.00
	Sextet	-2471.799556	0.22
1$^-$	Singlet	-2472.294994	25.40
	Triplet	-2472.311667	14.93
	Quintet	-2472.335465	0.00
	Septet	-2472.286940	30.45

Table 6.5. DFT-calculated energetics of the possible spin states for each of the complexes generated electrochemically from **1**.

6.3.5 Spectroelectrochemical Data

The spectroelectrochemical experiments were carried out using a dichloromethane solution of complex **1** to distinguish the bands associated with the electronic transitions under fixed potential conditions. The spectral changes observed during reduction and oxidation for complex **1** are shown in **Figure 6.8**. The measurements were recorded at ambient conditions using TBAPF$_6$ as the electrolyte. The reduction experiment was carried out at -1.38 V *vs.*

Fc$^+$/Fc. During the reduction, the bands in the region between 300-400 nm and 550-750 nm started to decrease in intensity, with a new band appearing at 451 nm. In the course of this conversion two isosbestic points appeared at 438 and 531 nm. During the reduction, because iron(III) transforms into iron(II), the LMCT transitions become unfavorable and start to decrease in intensity.[50] Simultaneously, intraligand charge transfer transition start to increase in intensity. TD-DFT calculations carried out on the reduced species found new bands at 394, 448, and 460 nm. These can be characterized as ILCT $\pi \to \pi^*$ transitions. The donor orbitals are (i) π orbitals delocalized on the phenolate rings with significant contributions from the p_π orbitals of oxygens and (ii) π orbitals delocalized on the phenylenediamine moiety, while the acceptor orbitals are mainly imine-based π^* orbitals (**Figure 6.9**). During the reduction process, the metal center becomes reduced which in turn makes the nearby phenolate oxygen atoms electron rich and the intensity of the ILCT transitions increase in that region (400-450 nm). Spectroelectrochemical experiments carried out for the first oxidation process at 0.88 V *vs.* Fc$^+$/Fc showed increase in intensity of all the bands, and these can be attributed to ILCT $\pi \to \pi^*$ transitions.[39] The appearance of new absorption bands in the near infrared region has been found in the spectrum. This included a prominent band at 1370 nm and a shoulder at ~ 1160 nm, which were absent in the parent species. According to the literature, these bands can be attributed to intraligand charge transfer transitions originating from delocalized π system.[39] TD-DFT calculations demonstrate a new band at 1274 nm in the oxidized species, which is absent in the neutral complex. Calculations showed that this new band is a result of ILCT $\pi \to \pi^*$ transition, where the acceptor orbital is mainly phenylenediamine-based (**Figure 6.10**). As illustrated in **Figure 6.6**, the oxidation of complex **1** results in a cationic radical on

the phenylenediamine moiety and hence, the intensity of charge transfer transitions on this moiety increases significantly leading to the appearance of a new band.
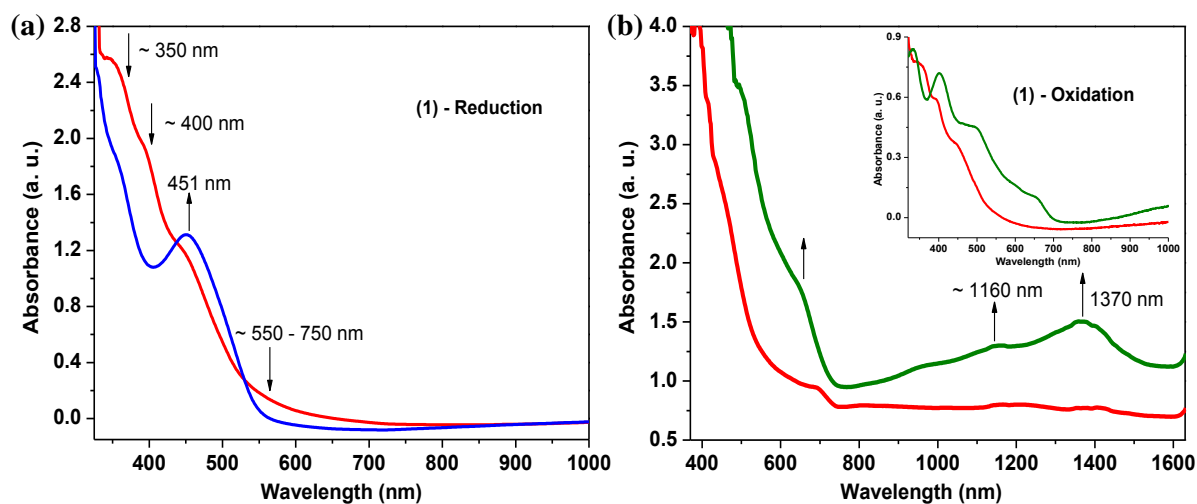
Figure 6.8. Electronic spectral changes observed for (a) reduction and (b) oxidation for complex **1** under fixed potential conditions, inset: UV-visible region of one electron oxidized species. Red line; parent complex, blue line; one electron reduced species, green line; one electron oxidized species.
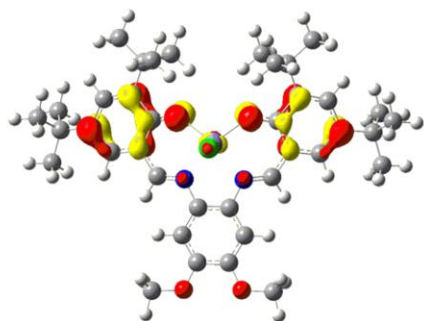
MO 181a (occupied)

λ = 460.52 nm
f (Oscillator strength) = 0.1886
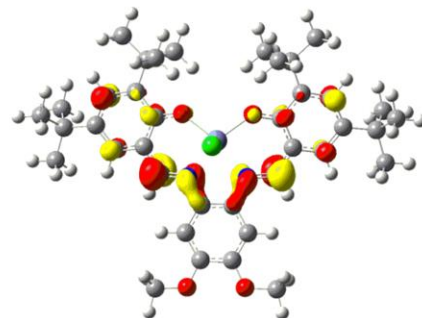
MO 182a (unoccupied)
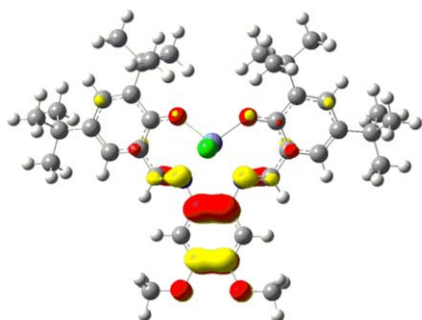
MO 177b (occupied)

λ = 460.52 nm
f (Oscillator strength) = 0.1886
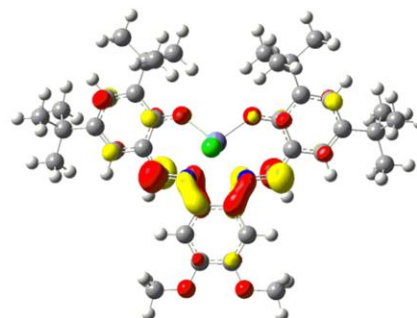
MO 178b (unoccupied)
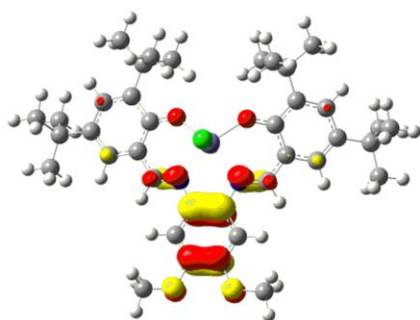
MO 181a (occupied)

λ = 448.91nm
f (Oscillator strength) = 0.1501

MO 182a (unoccupied)

λ = 448.91nm
f (Oscillator strength) = 0.1501

MO 177b (occupied)

MO 178b (unoccupied)

λ = 394.10nm
f (Oscillator strength) = 0.5056

MO 181a (occupied)

MO 182a (unoccupied)

λ = 394.10nm
f (Oscillator strength) = 0.5056

MO 177b (occupied)
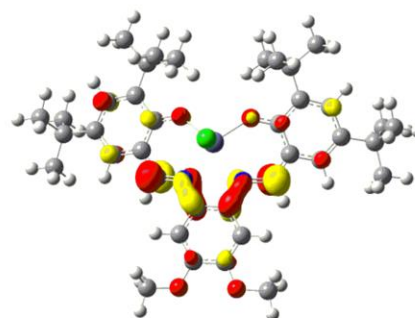
MO 178b (unoccupied)
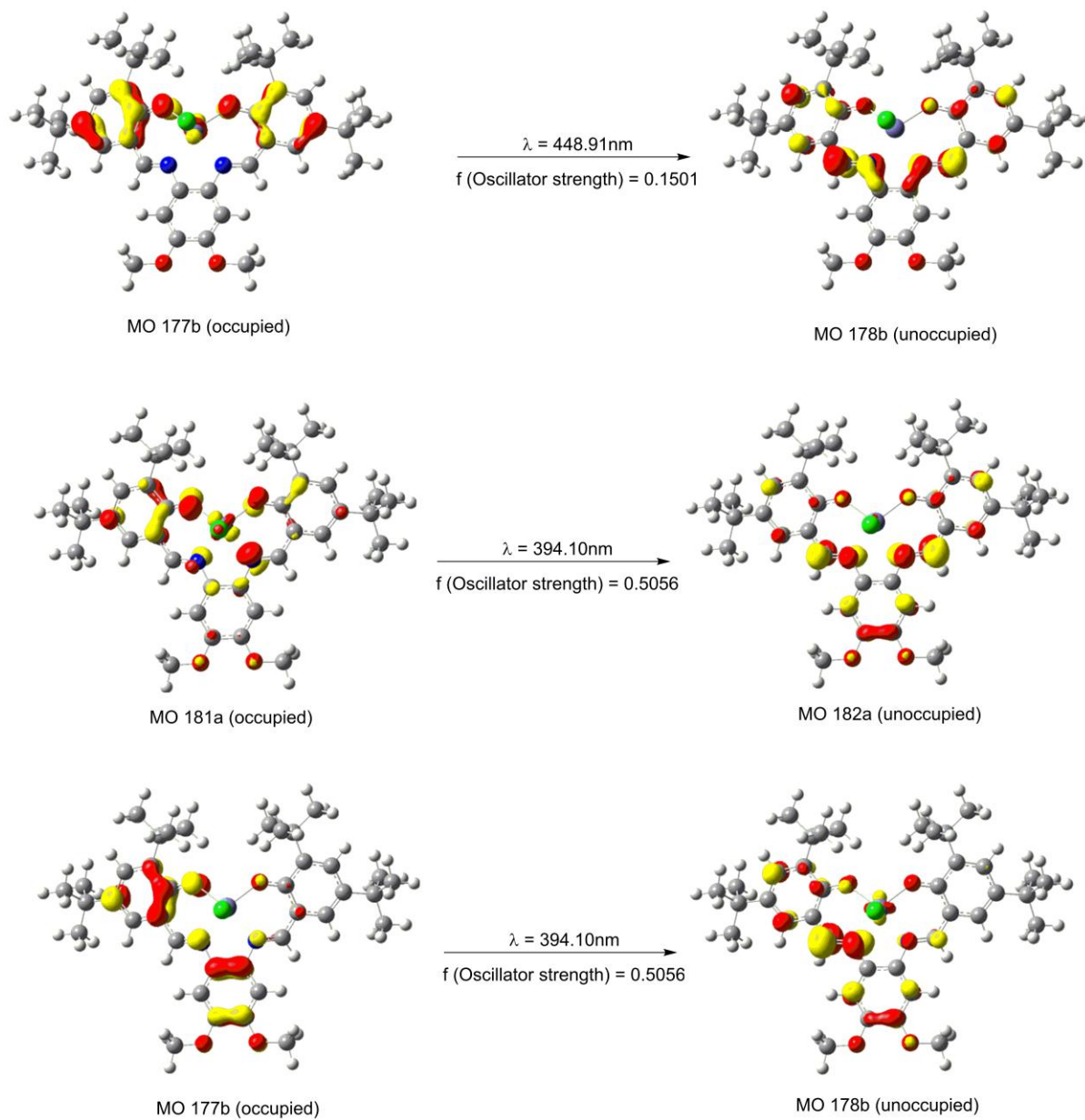
Figure 6.9. NTOs (isodensity value of 0.05 a.u.) of the excitations of reasonable intensity for the complex **1**⁻.

λ = 1274.72 nm
f (Oscillator strength) = 0.0766

MO 180a (occupied)

MO 181a (unoccupied)
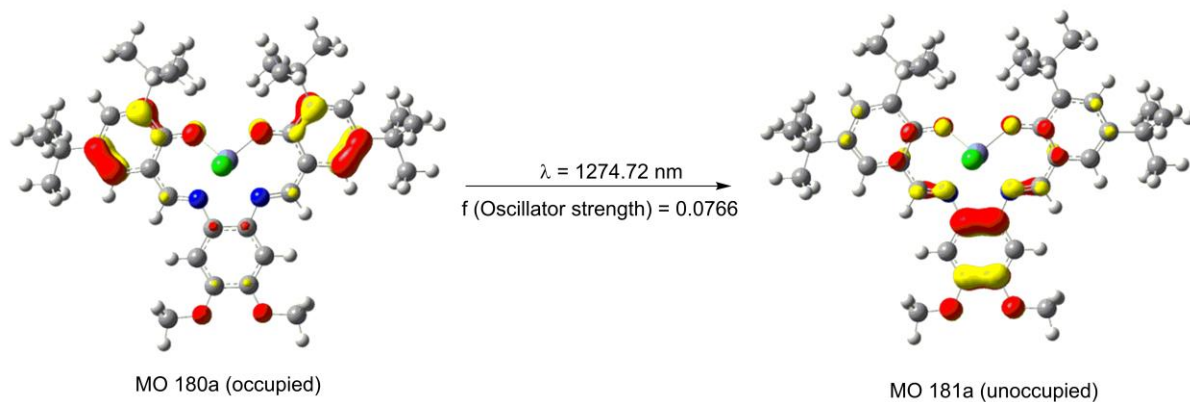
Figure 6.10. NTOs (isodensity value of 0.05 a.u.) of the excitation above 1200 nm region with reasonable intensity for the complex $\mathbf{1}^{+}$.

6.3.6 Isothermal Compression Data

The LB film formation ability of iron(III) complexes was measured using isothermal compression data and Brewster angle microscopy. Solubility tests showed that complex **2** dissolved in solvent mixtures (e.g. dichloromethane and dimethyl sulfoxide) and showed poor solubility in highly volatile solvents (e.g. dichloromethane, chloroform, and hexane). Therefore, complex **1** was further investigated for film formation and fabrication studies. Isothermal compression data and BAM images obtained for metal complex **1** are shown in **Figure 6.11**. When designing metal complex **1**, methoxyethoxy and *tert*-butyl substituents were introduced onto phenylenediamine and phenolate moieties, respectively. This allows achieving a good balance between hydrophilic and hydrophobic characteristics, and facilitates the formation of a stable Langmuir film at the air/water interface. In complex **1**, the molecules started to interact with each other at ~ 74 $Å^2$ molecule$^{-1.}$ The critical area of the compacted film was found to be ~ 71 $Å^2$ molecule^{-1}. The isotherm obtained for complex **1** did not show any phase transitions and showed a collapse pressure of *ca*. 40 mN/m. Complex **1**

showed a constant pressure collapse[51] by following the Ries mechanism[52] as observed for many other metallosurfactants.[53] Brewster angle micrographs obtained during the LB experiment showed a homogeneous film formation from *ca.* 9 to 38 mN/m without any defects, such as domain or Newton ring formation. Arrays of Newton rings were started to form at *ca.* 40 mN/m, to denote the collapse of the Langmuir film.[54]
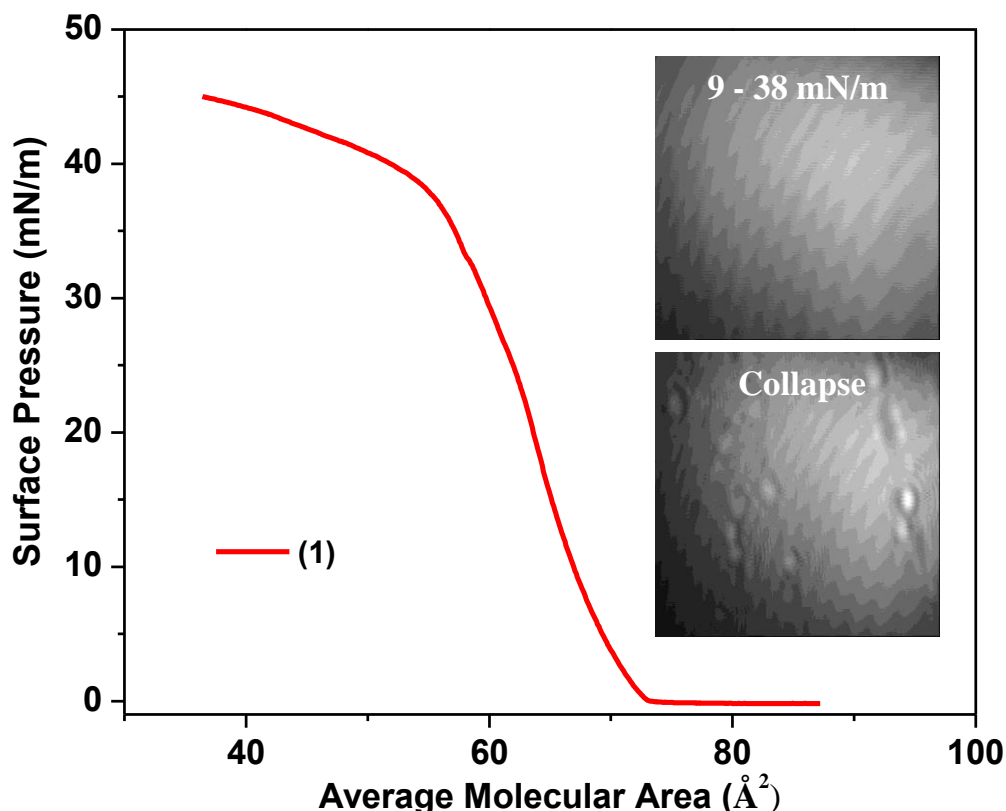
Figure 6.11. Compression isotherm data of complex **1** and selected BAM micrographs.

6.3.7 Langmuir-Blodgett Film Characterization using UV-visible and Infrared Reflection Absorption Spectroscopy

The UV-visible spectrum of LB film was recorded to evaluate the molecular composition of complex **1** after being deposited onto solid substrate. UV-visible spectrum of the films also provides additional information, such as packing topologies. Menzel *et. al*

explained that the type of peak shift provides information about the chromophore aggregation. A hypsochromic shift of bands demonstrates a H-type chromophore aggregation where as a bathochromic shift of bands denotes a J-type chromophore aggregation.[55,56] During the experiment, fifty depositions at 25 mN/m on glass were carried out using y-type dipping method. Depositions showed a transfer ratio close to unity. The film and solution spectra are shown in **Figure 6.12**. The UV-visible spectrum of the LB film of complex **1** showed intense absorption maxima at 312 nm and 452 nm. When compared to the solution spectrum, absorptions at ~ 350 nm and 395 nm have been weakened in the LB film spectrum. Such behavior has been observed due to possible rearrangements and conformational changes that take place during the deposition mechanism of the molecules.[57] The LB film spectrum showed a slight red shift of peaks when compared to the solution spectrum due to J-type chromophore aggregation.
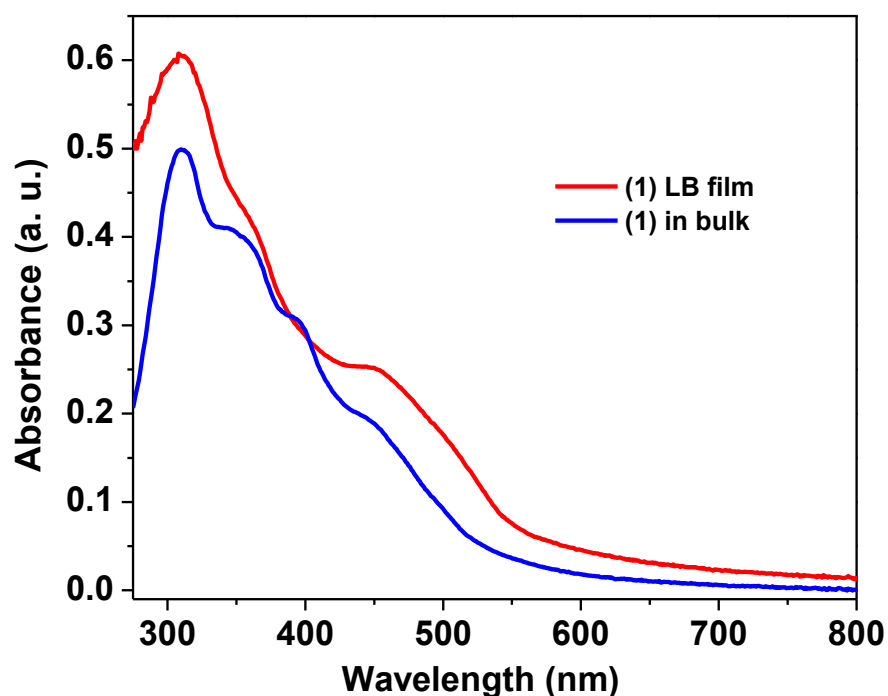
Figure 6.12. UV-visible spectra of solution and multilayer LB film of complex **1**.

The infrared reflection absorption spectrum of complex **1** was measured after depositing fifty layers onto a well cleaned glass substrate using *p*-polarized light at an angle of incidence of 30°. IRRAS data provide information related to composition and ordering of the molecules in the LB film.[58,59] The IRRA spectrum of complex **1** in comparison to KBr IR spectrum is shown in **Figure 6.13**. The IRRA spectrum of complex **1** showed bands at 2964, 2906, and 2874 cm^{-1}, belonging to asymmetric and symmetric C—H stretching vibrations. $C=C_{(aromatic)}$ stretching vibration and CH_n deformation bands were observed in the region of ~ 1610-1350 cm^{-1}. A well-pronounced band at 1581 cm^{-1} was observed due to C=N stretching vibrations. The LB film spectrum of complex **1** showed very similar peak patterning to its bulk IR spectrum, but showed slight shift in band positioning. Positive and negative bands along with well-pronounced asymmetric C—H stretching vibrations were observed to denote the anisotropic behavior of the LB film.[58,60,61,62,63] The spectroscopic data of LB film of complex **1** suggest that the molecular structure of complex **1** remains intact.
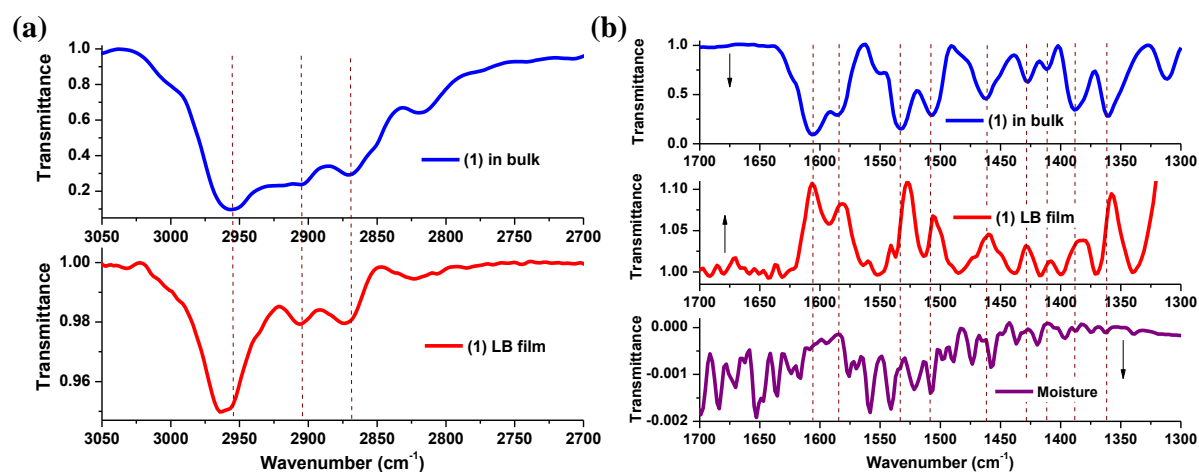
Figure 6.13. IRRAS spectrum of complex **1** (a) region between 3050 and 2700 cm^{-1} and (b) expanded region between 1700 and 1300 cm^{-1}, in comparison with KBr bulk infrared spectrum.

6.3.8 Surface Characterization using AFM

The surface topologies of LB films of complex **1** were analyzed using AFM. Measurements were carried out by depositing LB monolayers onto mica substrates using y-type dipping method with a transfer ratio close to unity. The monolayers were deposited at 15, 25, 30, 35, 37, and 40 mN/m. The obtained AFM height images are shown in **Figure 6.14**. According to the observed AFM data, the monolayers deposited at lower surface pressures, at 15 and 25 mN/m, showed a random film deposition with defects, such as pinholes. The monolayer film deposited at 30 mN/m showed the formation of an ordered film with fewer defects when compared to **Figure 6.14a** and **6.14b**. At surface pressures of 35 and 37 mN/m, completely homogeneous films have formed. However, the LB film transferred at 40 mN/m, where the LB film is closer to collapse, showed a rougher film due to aggregate formation. A rougher surface can be observed due to multilayer formation that takes place near film collapse owing to molecular tumbling and film folding.[52]
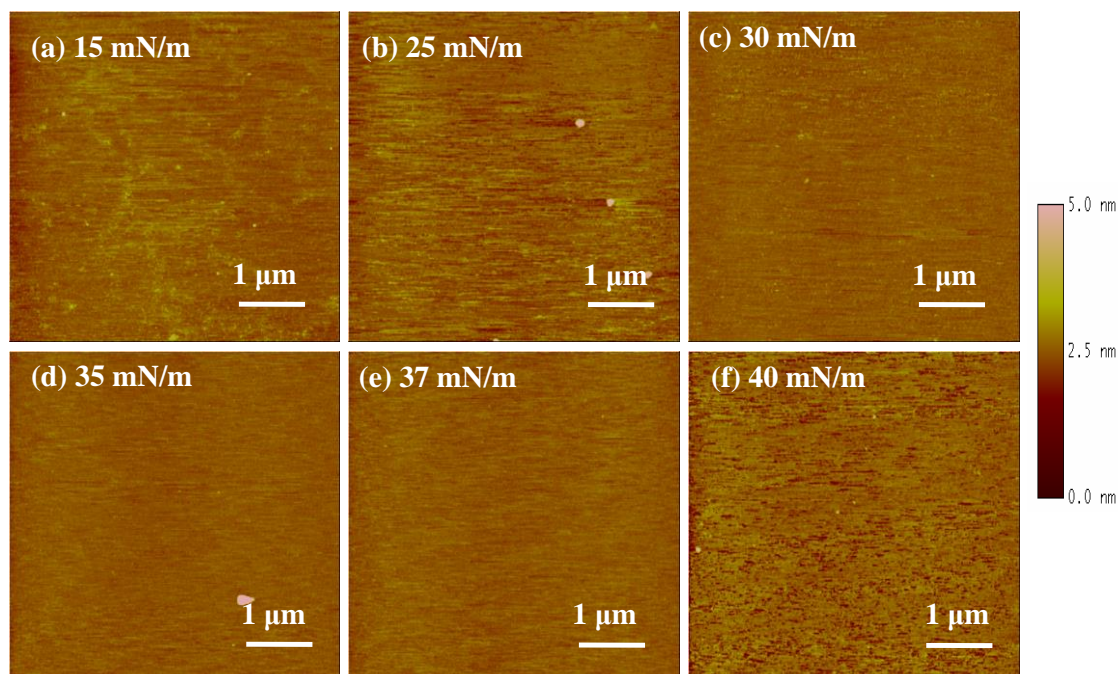
Figure 6.14. AFM height images of monolayer films deposited on mica substrates at different surface pressures for complex **1**. The Z range was 5 nm and the scan size was 5 μm for all the images.

6.3.9 Device Fabrication and Current-Voltage Characterization

According to the observed AFM data, 35 mN/m was chosen to carry out the device fabrication studies. At 35 mN/m, a smooth homogeneous monolayer formed at the air/water interface. During the device fabrication, a LB monolayer of complex **1** was deposited onto a gold coated mica substrate and dried in a desiccator for five days. The AFM images of a LB monolayer deposited gold substrate in comparison to a bare gold electrode are shown in **Figure 6.15a** and **6.15b**. Then the top gold layer was deposited using the shadow masking method to create a metal|LB-monolayer|metal junction by sandwiching the LB monolayer in between two non-oxidizable gold electrodes. An optical micrograph of the assembly and a schematic representation of the assembly layout are shown in **Figure 6.15c** and **6.15d**.
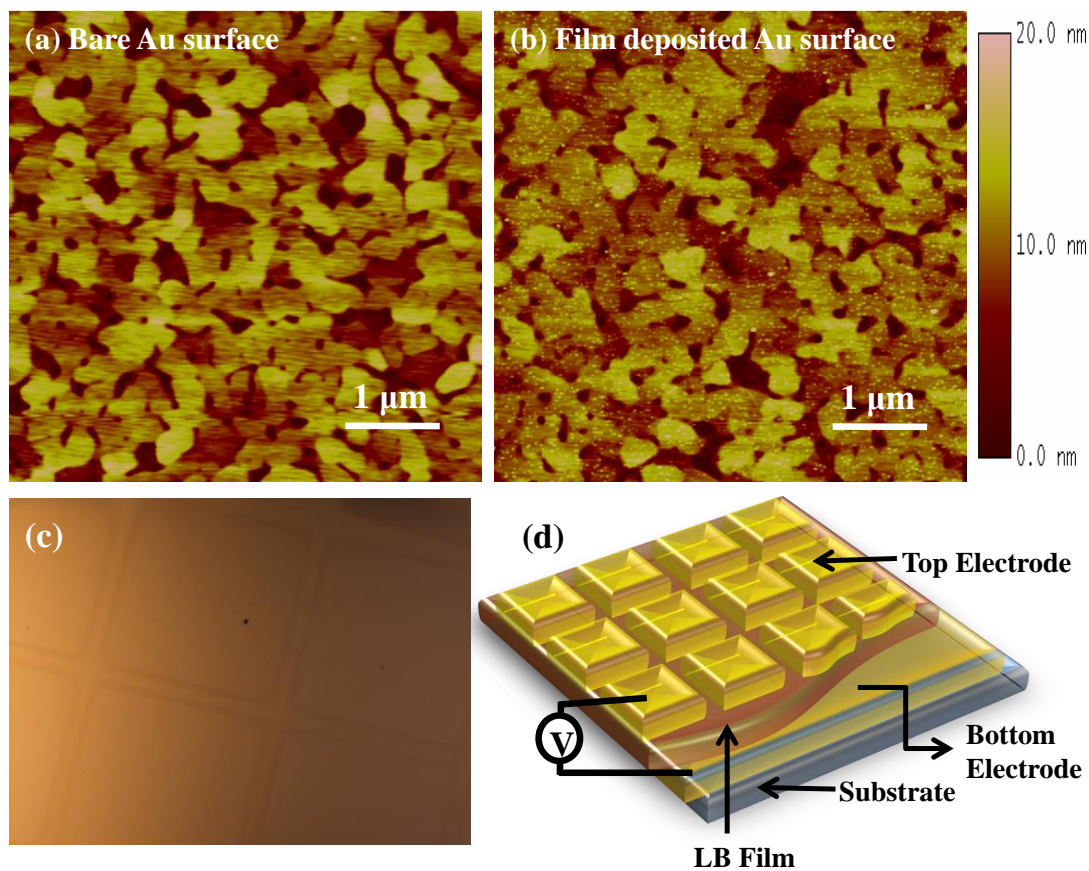
Figure 6.15. AFM height images of (a) bare gold substrate, (b) monolayer film deposited on gold substrate, (c) optical micrograph of the assembly, and (d) schematic representation of the assembly. The Z range was 20 nm and the scan size was 5 μm for the AFM images.

The current-voltage (I-V) characteristics of complex **1** were measured using the Au|LB-monolayer|Au device at ambient conditions (**Figure 6.16**). The reproducibility of the I-V characteristics were probed by measuring few devices in the same sample as well as by measuring few samples that were fabricated using the same procedure. Complex **1** showed an asymmetric current response with high electrical current in the negative quadrant and a negligible current in the positive quadrant, which is indicative of the current rectifying behavior (**Figure 6.16**, **6.17a**, and **6.17c**). According to the observed data, complex **1** showed

a rectification ratio (RR = [I at -V$_o$/I at +V$_o$])[64] ranging from 3.99 to 28.6 between -2 and +2 V and from 2.04 to 31 between -4 and +4 V, respectively. The experiment performed by reversing the source and the drain contacts, reversed the I-V response indicating the true rectification behavior of complex **1** as shown in **Figure 6.17e-f**. After several repeats of the I-V measurements, the magnitude of the current response as well the rectification ratio started to decrease (**Figure 6.17b** and **6.17d**). Then a more symmetric current response was appeared (**Figure 6.17g**). This behavior has been observed in other organic systems, which showed current rectification. The main reason for the observed symmetric current response is that in the presence of an electric field the molecules in the LB film start to reorient to minimize the dipole moment to create a more stable monolayer.[10,17]
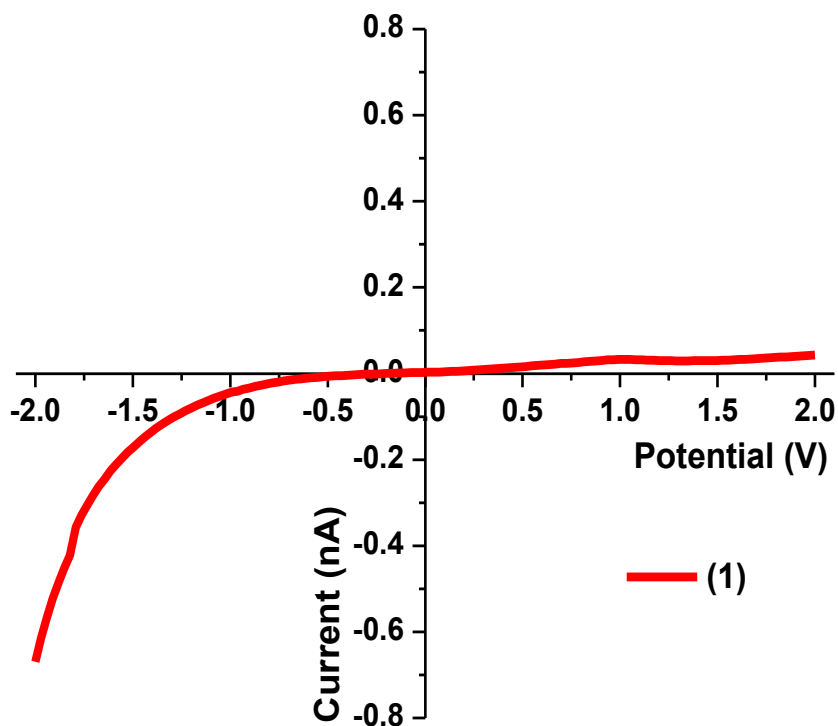
Figure 6.16. I-V characteristics observed for complexes **1**.
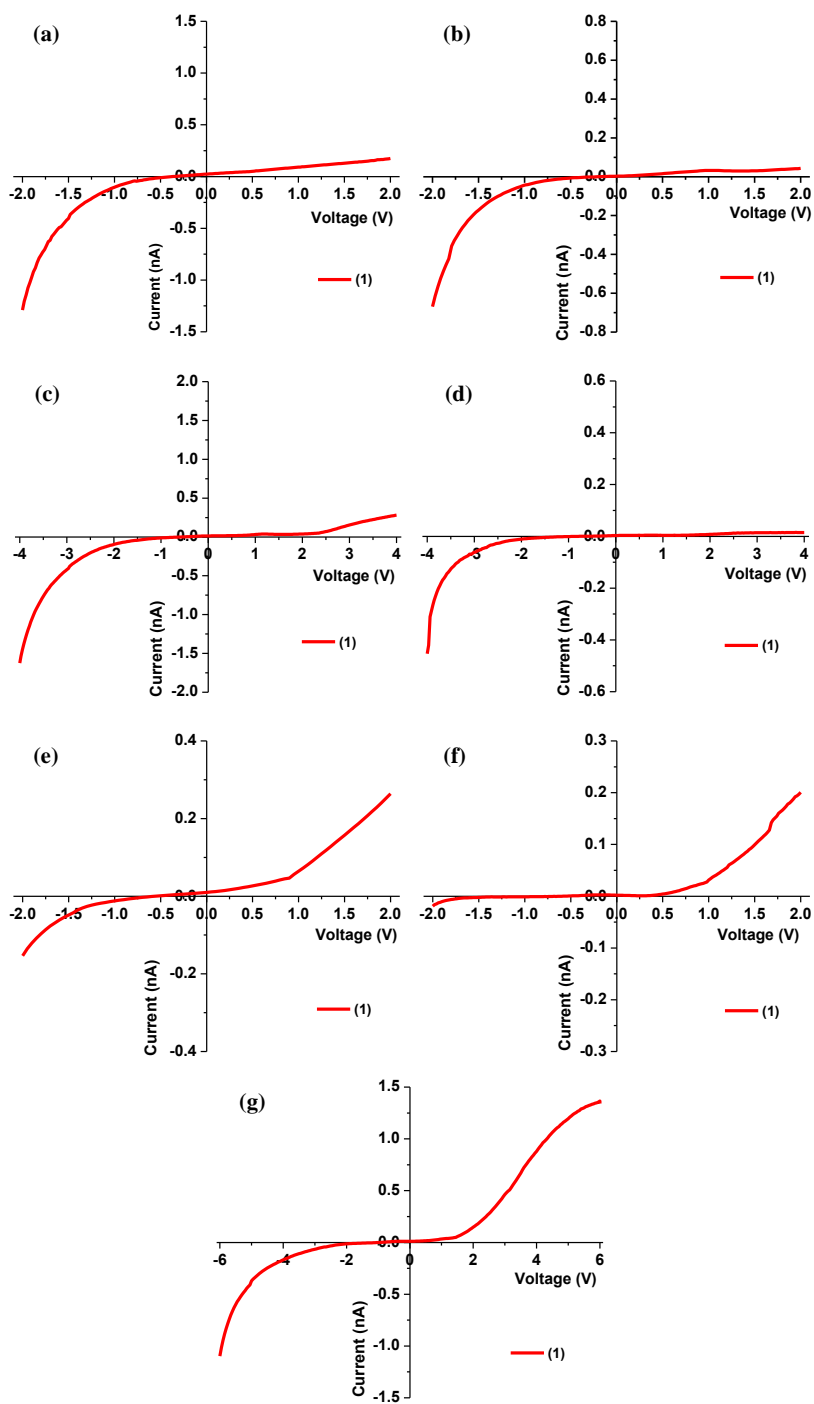
Figure 6.17. I-V characteristic of complex **1** (a) from 2 to -2 V, (b) lower current observed after multiple scans between 2 and -2 V, (c) from 4 to -4 V, (d) lower current observed after multiple scans between 4 and -4 V, (e, f) I-V response observed for reversed applied potentials, (g) symmetric response observed after multiple scans.

Because the LB monolayer of complex **1** is sandwiched between two symmetric electrodes, the involvement of a Schottky mechanism[10] is unfavorable. In this metal|molecule|metal junction the LB monolayer is physisorbed onto both gold electrodes via weak van der Waals forces. Therefore, the formation of a Schottky barrier[65] is unfavorable, due to the presence of similar interfacial electrical dipole moments. According to the observed cyclic votammetry data of complex **1**, the phenylenediamine and the phenolate moieties were behaving as electron donor moieties (D) whereas the iron(III) center was behaving as an electron acceptor moiety (A). Therefore, the molecule is consisting of a [D-A] type structure. The Verani laboratory studied a square planar copper(II) analogue under similar conditions and this complex did not show any current rectification behavior. Nevertheless, showed poor current responces which were similar to leakage current. Major differences that were observed between the copper(II) and iron(III) complexes were the oxidation state of the metal ion [Cu(II) *vs.* Fe(III)], geometry of the complex [square planner *vs.* square pyramidal], coordination mode around the metal atom [four-coordinate *vs.* five-coordinate], and electronic configuration [d^9 *vs.* d^5]. Also, the iron(III) complex adupted a distorted geometry, when compared to copper(II) complex. According to the cyclic voltammetry data and DFT calculations of copper(II) system, the copper(II) center acted as an electron acceptor where as the the phenylenediamine and the phenolate moieties acted as electron donors. Therefore, the copper(II) complex also had a [D-A] type structure which was similar to the iron(III) complex. A true [D-A] system with a unimolecular rectification mechanism,[66] should show asymmetric current responces despite of the molecular symmetry. However, the observed I-V characterictics suggested that the copper(II) complex behaved as an insulator where as the iron(III) complex behaved as a plausible current rectifier. Another

possible reason that could account for the observed I-V behavior in copper(II) complex is the unfitting of HOMO and LUMO energies with Fermi levels of the metal electrode. As a first step to distinguish the current rectification mechamism between asymmetric and unimolecular, the understanding of the possible electron transfer pathway is important. Therefore, complex **1** was further investigated using electrochemical and DFT calculations.

The cyclic voltammogram of a particular system provides an insight regarding the HOMO-LUMO energy gap. The difference between the half wave potential of the first oxidation process (E^{ox}) and the half wave potential of the first reduction process (E^{red}) are accountable for the HOMO-LUMO energy gap. The cyclic voltammetry data of iron(III) complex exhibited a smaller ΔE between (E^{ox}) and (E^{red}) when compared to copper(II) complex. Therefore, a smaller HOMO-LUMO gap can be observed for complex **1** compared to copper(II) system.

To show current rectification using a [D-A] type structure, the donor moiety should show a small ionization potential (I_D) and the acceptor moiety should show a large electron affinity (A_A).[66] The ionization potential and the electron affinity associated with the donor and the acceptor can be calculated using half wave potentials of first oxidation (E^{ox}) and reduction (E^{red}) processes, respectively.[67,68] To calculate the electron affinity associated with the reduction process, equation (1) can be used.[67,68,69,70]

$$V_a = 4.7 \text{ eV} + E^{red}(SCE)_{½} \text{ ………(1)}$$

To calculate the ionization energy associated with the oxidation process equation (2) can be used.[70,71]

$$V_i = 4.7 \text{ eV} + (1.7) E^{ox}(SCE)_{½} \text{ ………(2)}$$

When applying equations (1) and (2), the half wave potentials should be reported versus the standard calomel electrode (SCE). The half wave potential of first reduction and oxidation processes of complex **1** were found to be -0.61 and 1.051 V *vs*. SCE, respectively. DFT calculations of complex **1**, suggested that the LUMOs are metal-centered and the HOMO are ligand-centered. Therefore, after applying equations (1) and (2) to complex **1**, the energies associated with LUMO [4.7 eV + (-0.61)] and HOMO [4.7 eV + 1.7 (1.051)] were found to be -4.09 and -6.49 eV, respectively. After understanding these calculations, a model system was built to compare these energies with the Fermi levels of the metal electrode (**Figure 6.18**). The Fermi level of gold electrode was calculated to be -5.1 eV.[68] After applying a bias voltage to one of the elctrodes, the Fermi energy of that electrode get adjusted to be situated between the HOMO and LUMO energy levels.[72,73] The electrochemical calculations showed that there is a energy difference of 1.01 eV between Fermi level and LUMO energy level, and a difference of 1.39 eV between Fermi level and HOMO energy level for complex **1**. Therefore, the electron transfer can happen efficiently via the LUMO energy level because in complex **1** the LUMO is closer to the Fermi level compared to the HOMO. The copper(II) complex showed -3.24 and -6.05 eV associated with the LUMO and HOMO, respectively. Because the LUMO of copper(II) complex is far away from the metal Fermi level, the electron transfer will be difficult in copper(II) complex when compared to complex **1**. This could be the potential reason, for copper(II) complex to behave as an insulator. However, according to DFT calculations singly occupied molecular orbitals (SOMOs) can act as LUMOs in these iron(III) and copper(II) complexes, due to the presence of partially filled *d*-orbitals. Also, as demonstrated in the **Figure 6.19b**, the relative increase of the energy of the orbitals by 1.0 eV from iron(III) complex to copper(II) complex supports

the model described in **Figure 6.19a**. Therefore, the proposed model can qualitatively explain that the electron transfer via SOMO is favorable in the iron(III) complex. This explains the different I-V characteristics observed for iron(III) and copper(II) complexes. Electrochemical and DFT calculations of complex **1** indicated that the electron transfer occur via singly occupied molecular orbitals (as LUMO) and HOMOs are not involved in the electron transfer pathway. Therefore, the asymmetric I-V behavior observed for complex **1** suggests an asymmetric current rectification mechanism.
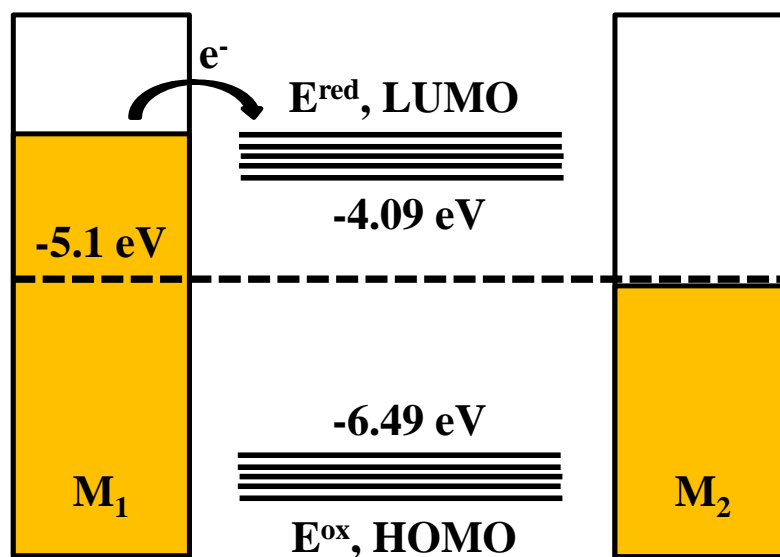
Figure 6.18. Proposed model for complex **1** to compare the HOMO and LUMO energies with Fermi energy of gold electrodes.
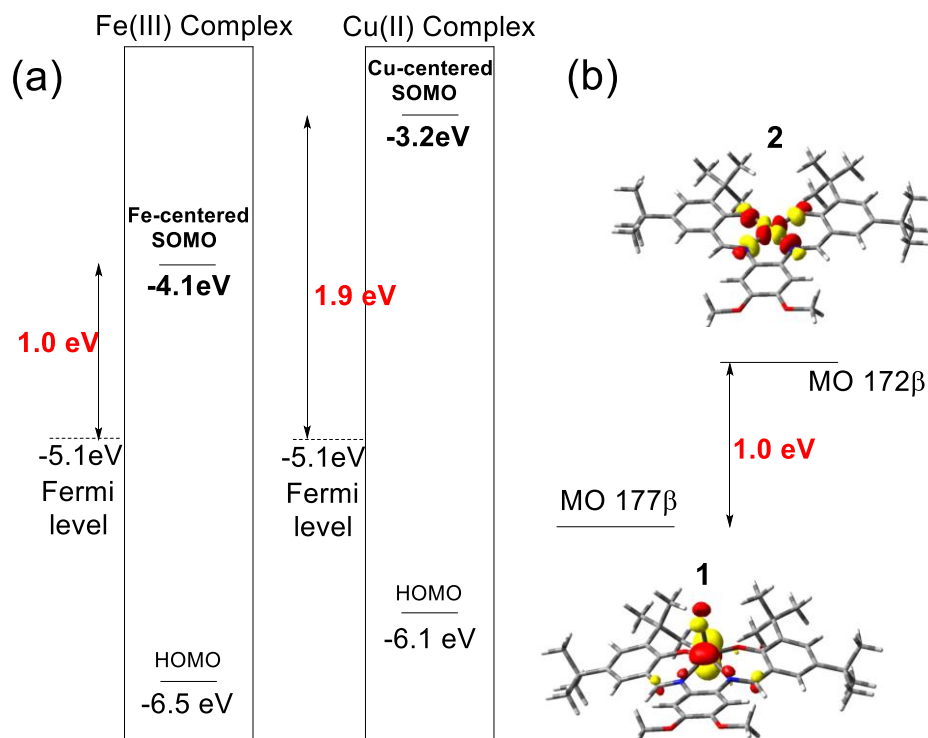
Figure 6.19. (a) Electron transfer model involving the charge transfer from the Fermi levels of the electrode into the metal-based SOMO. (b) Increase of the DFT-calculated energy of the metal-centered acceptor orbital from iron(III) complex to copper(II) complex.

6.4 Conclusions

In conclusion, two salophen-type iron(III) complexes with $[N_2O_2]$ coordination environments were successfully synthesized and structurally characterized using multiple techniques. X-ray crystal structure data revealed the formation of a µ-oxo bridged species for complex **2**. Nevertheless, both complexes showed asymmetric pentacoordinate species with distorted square pyramidal geometry. Complex **1** showed well-behaved redox and amphiphilic properties. The UV-visible and IRRAS data revealed that the molecular structure of complex **1** remains intact at the air/water interface. AFM data of complex **1** indicated the formation of a homogeneous film at 35 mN/m. After device fabrication, complex **1** showed

current rectification and was further investigated to understand the mechanism involved in current rectification. Cyclic voltammetry data revealed that the iron(III) center acts as an electron acceptor moiety while the phenylenediamine and phenolate moieties act as electron donor moieties. Redox properties along with the DFT calculations suggested that LUMOs are metal-centered and HOMOs are ligand-centered. Furthermore, the calculations carried out using redox potentials showed that the electron transfer is easy to occur via the LUMO energy level in this [D-A] type iron(III) system. DFT calculations revealed that singly occupied molecular orbitals act as LUMOs because there are five partially filled *d*-orbitals present in the iron(III) complex. These data suggested that Fermi levels are further away from the HOMO compared to SOMO in complex **1**, and the electron transfer occurs via the SOMO. Due to the distorted geometry of complex **1** and because SOMOs (as LUMOs) are involved in the electron transfer pathway, an asymmetric current rectification mechanism is proposed for complex **1**.

REFERENCES

1. Moore, G. E. *Electronics* 19 April **1965**, *38*, 114.

2. Strukov, D. B.; Snider, G. S.; Stewart, D. R.; Williams, R. S. *Nature* **2008**, *453*, 80.

3. Staikov, G.; Szot, K. *Adv. Mater*. **2009**, *21*, 2632.

4. Bandyopadhyay, A.; Sahu, S.; Higuchi, M. *J. Am. Chem. Soc*. **2011**, *133*, 1168.

5. Wassel, R. A.; Gorman, C. B. *Angew. Chem. Int. Ed.* **2004**, *43*, 5120.

6. Aviram, A.; Ratner, M. A. *Chem. Phys. Lett.* **1974**, *29*, 277.

7. Lindsey, J. S.; Bocian, D. F. *Accounts of Chemical Research* **2011**, *44*, 638.

8. Low, P. J. *Dalton Trans*. **2005**, 2821.

9. Park, J.; Pasupathy, A. N.; Goldsmith, J. I.; Chang, C.; Yaish, Y.; Petta, J. R.; Rinkoski, M.; Sethna, J. P.; Abruña, H. D.; McEuen, P. L.; Ralph, D. C *Nature* **2002**, *417*, 722-725.

10. Metzger, R. M. *J. Mater. Chem.* **2008**, *18*, 4364.

11. Lanznaster, M.; Hratchian, H. P.; Heeg, M. J.; Hryhorczuk, L. M.; McGarvey, B. R.; Schlegel, H. B.; Verani, C. N.; *Inorg. Chem.* **2006**, *45*, 955.

12. Lanznaster, M.; Heeg, M. J.; Yee, G. T.; McGarvey, B. R.; Verani, C. N.; *Inorg. Chem.* **2007**, *46*, 72.

13. Allard, M. M.; Xavier, F. R.; Heeg, M. J.; Schlegel, H. B.; Verani, C. N. *Eur. J. Inorg. Chem.* **2012**, 4622.

14. Allard, M. M.; Sonk, J. A.; Heeg, M. J.; McGarvey, B. R.; Schlegel, H. B.; Verani, C. N.; *Angew. Chem. Int. Ed*. **2012**, *51*, 3178.

15. Lesh, F. D.; Shanmugam, R.; Allard, M. M.; Lanznaster, M.; Heeg, M. J.; Rodgers, M. T.; Shearer, J. M.; Verani, C. N. *Inorg. Chem.* **2010**, *49*, 7226.

16. Wickramasinghe, L. D.; Perera, M. M.; Li, L.; Mao, G.; Zhou, Z.; Verani, C. N. *Angew. Chem. Int. Ed.* **2013**, *52*, 13346.

17. Metzger, R. M. *Chem. Rev.* **2003**, *103,* 3803.

18. Parr, R. G.; Yang, W. *Density-functional theory of atoms and molecules; Oxford University Press: New York*, 1989.

19. Frisch, M. J.; Trucks, G. W.; Schlegel, H. B.; Scuseria, G. E.; Robb, M. A.; Cheeseman, J. R.; Scalmani, G.; Barone, V.; Mennucci, B.; Petersson, G. A.; Nakatsuji, H.; Caricato, M.; Li, X.; Hratchian, H. P.; Izmaylov, A. F.; Bloino, J.; Zheng, G.; Sonnenberg, J. L.; Hada, M.; Ehara, M.; Toyota, K.; Fukuda, R.; Hasegawa, J.; Ishida, M.; Nakajima, T.; Honda, Y.; Kitao, O.; Nakai, H.; Vreven, T.; Montgomery, J., J. A.; Peralta, J. E.; Ogliaro, F.; Bearpark, M.; Heyd, J. J.; Brothers, E.; Kudin, K. N.; Staroverov, V. N.; Kobayashi, R.; Normand, J.; Raghavachari, K.; Rendell, A.; Burant, J. C.; Iyengar, S. S.; Tomasi, J.; Cossi, M.; Rega, N.; Millam, J. M.; Klene, M.; Knox, J. E.; Cross, J. B.; Bakken, V.; Adamo, C.; Jaramillo, J.; Gomperts, R.; Stratmann, R. E.; Yazyev, O.; Austin, A. J.; Cammi, R.; Pomelli, C.; Ochterski, J. W.; Salvador, P.; Dannenberg, J. J.; Dapprich, S.; Parandekar, P. V.; Mayhall, N. J.; Daniels, A. D.; Farkas, O.; Foresman, J. B.; Ortiz, J. V.; Cioslowski, J.; Fox, D. J. Gaussian Development Version; Revision H.31 ed.; Gaussian, Inc.: Wallingford, CT, 2010.

20. Vosko, S. H.; Wilk, L.; Nusair, M. *Can. J. Phys.* **1980**, *58*, 1200.

21. Lee, C. T.; Yang, W. T.; Parr, R. G. *Phys. Rev. B* **1988**, *37*, 785

22. Andrae, D.; Haussermann, U.; Dolg, M.; Stoll, H.; Preuss, H., *Theor. Chim. Acta* **1990**, *77*, 123.

23. Igelmann, G.; Stoll, H.; Preuss, H., *Molecular Physics* **1988**, *65*, 1321.

24. Dunning, T. H., Jr.; Hay, P. J. In *Modern Theoretical Chemistry*, Vol. **3**; Schaefer, H. F., III, Ed. Plenum New York, 1976; p 1.

25. Francl, M. M.; Petro, W. J.; Hehre, W. J.; Binkley, J. S.; Gordon, M. S.; DeFrees, D. J.; Pople, J. A., *J. Chem. Phys.* **1982**, *77*, 3654.

26. Hariharan, P. C.; Pople, J. A., *Theor. Chim. Acta* **1973**, *28*, 213.

27. Marenich, A. V.; Cramer, C. J.; Truhlar, D. G., *J. Phys. Chem. B* **2009**, *113*, 6378.

28. Dennington, R.; Keith, T.; Millam, J. M. *GaussView, Version 5*, Semichem, Inc.: Shawnee Mission, KS, 2009.

29. Petit, L.; Maldivi, P.; Adamo, C. *J. Chem. Theory Comput.* **2005**, *1*, 953.

30. Runge, E.; Gross, E. K. U. *Phys. Rev. Lett.* **1984**, 52.

31. Stratmann, R. E.; Scuseria, G. E.; Frisch, M. J. *J. Chem. Phys.* **1998**, *109*, 8218.

32. Martin, R. L. *J. Chem. Phys.* **2003**, *118*, 4775.

33. Dong, Y.; Fujii, H.; Hendrich, M. P.; Leising, R. A.; Pan, G.; Randall, C. R.; Wilkinson, E. C.; Zang, Y.; Que Jr., L. *J. Am. Chem. Soc.* **1995**, *117*, 2778.

34. Kojima, T.; Leising, R. A.; Yan S.; Que, Jr., L. *J. Am. Chem. Soc.* **1993**, *115*, 11328.

35. Fish, R. H.; Konnings, M. S.; Oberhausen, K. J.; Fong, R. H.; Yu, W. M.; Christou, G.; Vincent, J. B.; Coggin, D. K.; Buchanan, R. M. *Inorg. Chem.* **1991**, *30*, 3002.

36. Buchanan, R. M.; Chen, S.; Richardson, J. F.; Bressan, M.; Forti, L.; Morvillo, A.; Fish, R. H. *Inorg. Chem.* **1994**, *33*, 3208.

37. Wang, X.; Wang, S.; Li, L.; Sundberg, E. B.; Gacho, G. P. *Inorg. Chem.* **2003**, *42*, 7799.

38. Mayilmurugan, R; Stoeckli-Evans, H.; Suresh, E.; Palaniandavar, M. *Dalton Trans.* **2009**, 5101.

39. Kochem, A.; Jarjayes, O.; Baptiste, B.; Philouze, C.; Vezin, H.; Tsukidate, K.; Tani, F.; Orio, M.; Shimazaki, Y.; Thomas, F. *Chem. Eur. J.* **2012**, *18*, 1068.

40. Petit, L.; Maldivi, P.; Adamo, C. *J. Chem. Theory Comput.* **2005**, *1*, 953.

41. Stratmann, R. E.; Scuseria, G. E.; Frisch, M. J. *J. Chem. Phys.* **1998**, *109*, 8218.

42. Martin, R. L. *J. Chem. Phys.* **2003**, *118*, 4775.

43. Gaber, B. P.; Miskowski V.; Spiro, T. G. *J. Am. Chem. Soc.* **1974**, *96*, 6868.

44. Mayilmurugan, R.; Suresh E.; Palaniandavar, M. *Inorg. Chem.* **2007**, *46*, 6038.

45. Velusamy, M.; Palaniandavar, M.; Srinivasa, R.; Gopalan; Kulkarni, G. U. *Inorg. Chem.* **2003**, *42*, 8283.

46. Rotthaus, O.; Jarjayes, O.; Philouze, C.; Valle, C. P. D.; Thomas, F. *Dalton Trans.* **2009**, 1792.

47. Pratt, R. C.; Mirica, L. M.; Stack, T. D. P. *Inorg. Chem.* **2004**, *43*, 8030.

48. Chaudhuri, P.; Wieghardt, K. *Prog. Inorg. Chem.* **2001**, *50*, 151.

49. Mulliken, R. S. *J. Chem. Phys.***1955**, *23*, 1833-1840.

50. Anjos, A.; Bortoluzzi, A. J.; Caro, M. S. B.; Peralta, R. A.; Friedermann, G. R.; Mangrich, A. S.; Neves, A.; *J. Braz. Chem. Soc.* **2006**, *17*, 1540.

51. Kundu, S.; Datta, A.; Hazra, S. *Langmuir* **2005**, *21*, 5894.

52. Ries, H. E., Jr. *Nature* **1979**, *281*, 287.

53. Shakya, R.; Hindo, S. S.; Wu, L.; Allard, M. M.; Heeg, M. J.; Hratchian, H. P.; McGarvey, B. R.; da Rocha, S. R. P.; Verani, C. N. *Inorg. Chem*. **2007**, *46*, 9808.

54. Galvan-Miyoshi, J.; Ramos, S.; Ruiz-Garcia, J.; Castillo, R. *J. Chem. Phys.* **2001**, *115*, 8178.

55. Menzel, H.; McBride, J. S.; Weichart, B.; Ruther, M.; *Thin Solid Films* **1996**, *284-285*, 640.

56. Menzel, H.; Weichart, B.; *Langmuir* **1994**, *10*, 1926.

57. Dhanabalan, A.; Mello, S. V.; Oliveira Jr, O. N.; *Macromolecules* **1998**, *31,* 1827.

58. Brezesinski, G.; Dobner, B.; Stefaniu, C.; Vollhardt, D.; *J. Phys. Chem. C*. **2011**, *115*, 8206.

59. Wang, L.; Cruz, A.; Flach, C. R.; Pérez-Gil, J.; Mendelsohn, R.; *Langmuir* **2007,** *23,* 4950.

60. Joy, S.; Pal, P.; Mondal,T. K.; Talapatra, G. B.; Goswami, S.; *Chem. Eur. J.* **2012**, *18*, 1761.

61. Brezesinski, G.; Dobner, B.; Stefaniu, C.; Vollhardt, D.; *Langmuir* **2011**, 27, 5386.

62. Kattner, J.; Hoffmann, H.; External reflection spectroscopy of thin films on dielectric substrates, *Hand book of vibrational spectroscopy*; John Wiley and Sons Ltd, Chichester, 2002; pp 12-14.

63. Hasegawa, T.; Umemura, J.; Takenaka, T.; *J. Phys. Chem.* **1993**, *97*, 9009.

64. Metzger, R. M.; Chen, B.; Ho1pfner, U.; Lakshmikantham, M. V.; Vuillaume, D.; Kawai, T.; Wu, X.; Tachibana, H.; Hughes, T. V.; Sakurai, H.; Baldwin, J. W.; Hosch, C.; Cava, M. P.; Brehmer, L.; Ashwell, G. J. *J. Am. Chem. Soc.* **1997**, *119*, 10455.

65. Schottky, W. *Naturwissenschaften* **1938**, *26*, 843.

66. Metzger, R. M. *Acc. Chem. Res.* **1999**, *32*, 950.

67. Hipps, K. W. *Scanning Tunneling Spectroscopy. In Handbook of Applied Solid State Spectroscopy*; Vij, D. R., Ed.; Springer-Verlag: Berlin, 2006; chapter 7.

68. Seo, K.; Konchenko, A. V.; Lee, J.; Bang, G. S.; Lee, H. *J. Am. Chem. Soc.* **2008**, *130*, 2553.

69. He, J.; Fu, Q.; Lindsay, S.; Ciszek, J. W.; Tour, J. M. *J. Am. Chem. Soc.* **2006**, *127*, 11932.

70. Scudiero, L.; Barlow, D. E.; Hipps, K. W. *J. Phys. Chem. B* **2002**, *106*, 996.

71. Schmidt, A.; Armstrong, N. R.; Goeltner, C.; Muellen, K. *J. Phys. Chem.* **1994**, *98*, 11780.

72. Zhang, L.; Bain, J. A.; Zhu, J. G.; Abelmann, L.; Onoue, T. *IEEE Trans. Magn.* **2004**, *40*, 2549.

73. Kitagawa, K.; Morita, T.; Kimura, S. *Langmuir* **2005**, *21*, 10624.

CHAPTER 7

INVESTIGATION OF THE BEHAVIOR OF REDOX-ACTIVE MANGANESE COMPLEXES WITH [N₂O₃] AND [N₂O₂] COORDINATION ENVIRONMENTS FOR THIN FILM FORMATION AND CURRENT RECTIFICATION

7.1 Introduction

The advancement of future microelectronic devices is heavily based on the development of new nanoscale organic and inorganic molecular materials. These molecular materials should demonstrate efficient electron transfer mechanisms to be used in microelectronic devices. With the development of scanning tunneling microscopy (STM), novel approaches were developed to measure the conductivity of nanoscale molecular materials.[1] Along with the experimental achievements, theoretical methods were also developed in recent years to understand the conductivity properties of these molecular materials.[1,2] These molecular materials with electron conduction properties are expected to be used in the molecular electronics field.[3,4,5] In addition, a new approach has been developed in the recent years to immobilize these transition metal complexes onto semiconductor materials to be used as solar energy conversion catalysts.[6] Nature conducts solar energy conversion via photosynthesis in photosystem II by following efficient proton-coupled electron transfer processes.[7] In PS II, chemical reactions happen in a well-distinguished and well-separated manner to avoid charge recombination. Therefore, when designing synthetic catalysts to carry out water oxidation, systems should demonstrate good charge separation with slow recombination rates in forward and backward electron transfer processes. In other words, the immobilized molecules should show a rectification behavior during electron transfer processes to exhibit maximum catalytic activity.[8,9]

Manganese can be found in the oxygen evolving complex of the photosystem II[10,11] and in the active site of various enzyme categories namely, catalases and superoxide dismutase.[12,13] Therefore, the development of novel manganese-containing molecular systems and the investigation of their properties become relevant to study asymmetric intramolecular electron transfer processes. Considerable effort has been undertaken in past years to develop molecular catalysts that use multiple oxidation states of manganese ion.[14] To date, several water oxidation catalysts, particularly ruthenium containing systems, have demonstrated improved activity when anchored onto surfaces.[15,16,17,18,19] However, manganese-containing redox-active metallosurfactants immobilized onto solid surfaces are poorly understood.

The Verani group is engaged in the development of new amphiphilic[20,21,22,23,24] and hydrophobic[25] metal containing systems, along with the scrupulous study of their electronic and redox properties.[26,27,28] Recently, Lesh *et al.* have used a modular synthetic approach to integrate ruthenium antennae complexes with surfactant ligands[29] and have studied their behavior at the air/water interface. Similar approaches can be successful in the incorporation of amphiphilic properties to manganese-containing organic systems.

This chapter summarizes the development of a series of manganese-containing surfactants, which merge amphiphilic and redox properties, as a primary step toward device fabrication and current-voltage measurements. Interested ligands were synthesized by multistep synthetic protocols with $[N_2O_3]$ and $[N_2O_2]$ donor sets related to Jacobsen's catalyst[30,31] and other potential catalysts described by Akermark,[32] Pecoraro,[33] and Fujii.[34] The chelating portion of these ligands is suitable for stabilizing a trivalent manganese ion, in an asymmetric nature. These ligands and the manganese complexes are shown in **Scheme 7.1**. All of these complexes were isolated, and their redox and electronic properties were

characterized. The film formation behavior of these compounds at the air/water interface was examined by isothermal compression and Brewster angle microscopy, whereas the structure and surface properties of resulting Langmuir-Blodgett (LB) films were interrogated by spectroscopic, spectrometric, and nanoscopic methods. Then, current-voltage characteristics were measured to investigate current rectification behavior.

Ligands

[H₃L²],   R = CH₃
[H₃L³],   R = C₁₈H₃₇
[H₃L⁴],   R = CH₂CH₂OCH₃

[H₂L^{t}Bu],   R₁ = OCH₂CH₂OCH₃, X = Y = tBu
[H₂L$^{bisPhO-NO2}$], R₁ = NO₂, X = Y = tBu
[H₂L^{NO2}],   R₁= OCH₂CH₂OCH₃, X = NO₂, Y = H

Metal Complexes

[Mn^{III}L^{2l}], R = CH₃   (1)
[Mn^{III}L^{3l}], R = C₁₈H₃₇   (2)
[Mn^{III}L^{4l}], R = CH₂CH₂OCH₃   (3)

[Mn^{III}L^{t}Bu],   R₁ = OCH₂CH₂OCH₃ (4)
[Mn^{III}L$^{bisPhO-NO2}$], R₁ = NO₂   (5)

[Mn^{II}L^{NO2}],   (6)
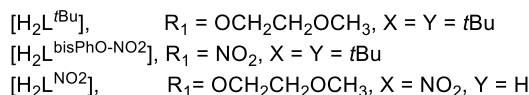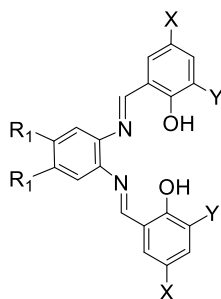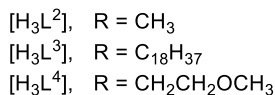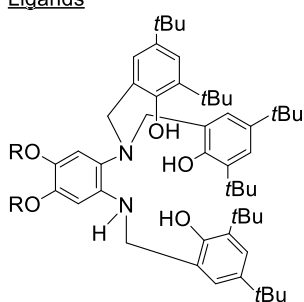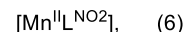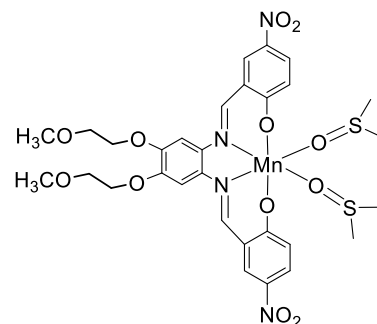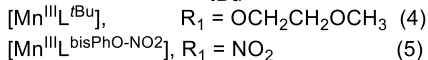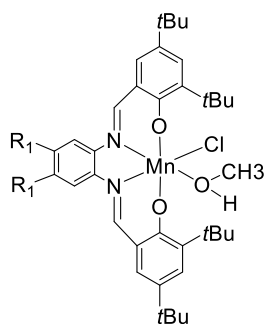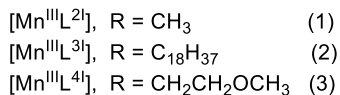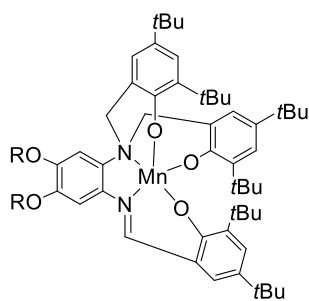
Scheme 7.1. Ligands and their respective manganese complexes.

7.2 Experimental Section

7.2.1 X-ray Structural Determinations for complexes 4, 5, and 6

Structures were solved by direct methods using the SHELXS-97 program in APEX II suite and refined by least squares method on F^2, SHELXL-97 and OLEX2. The crystals were mounted on a mitogen loop using paratone oil. Data were collected on a Bruker APEX-II Kappa geometry diffractometer with Mo radiation and a graphite monochromato using a Bruker CCD (charge coupled device) based diffractometer equipped with an Oxford Cryostream low-temperature. Complex **[Mn^{III}L^{tBu}] (4)** crystallized as dark green rhombic crystals and was measured at a temperature of 293 K. Unique reflections of 8910 were collected to solve the structure of complex **4**. An independent molecule along with one methanol molecule and a chloride anion was present in the asymmetric unit cell. A dark brown crystal with dimensions $0.902 \times 0.891 \times 0.81$ mm of **[Mn^{III}L$^{bisPho-NO2}$] (5)** was mounted and data were collected at 100 K. A total of 88443 reflections were collected with 10706 unique reflections. An independent molecule of complex **5** and one methanol molecule were present in the asymmetric unit cell. A molecule of 4,5-dinitrobenzene-1,2-diamine was also co-crystallized along with complex **5**. A dark greenish brown crystal with dimensions $0.315 \times 0.207 \times 0.099$ mm of **[Mn^{II}L^{NO2}] (6)** was mounted and data were collected at 100 K. A total of 79410 reflections were collected with 6154 unique reflections. Hydrogen atoms were placed in calculated positions. An independent molecule along with one dimethyl sulfoxide molecule was present in the asymmetric unit cell.

7.2.2 Syntheses of Ligand and Metal complexes

The synthesis of ligands **[H₃L²]**-**[H₃L⁴]**, **[H₂L^{tBu}]**, **[H₂L^{bisPho-NO2}]**, and **[H₂L^{NO2}]** were carried out as previously discussed in chapters 3, 4, and 6.

Synthesis of Metal Complexes

Synthesis of complex [Mn^{III}L^{2I}] (1).

A mixture of **[H₃L²]** (0.823 g, 1.00 mmol) and anhydrous $NaOCH_3$ (0.162 g, 3.00 mmol) in anhydrous methanol (80 mL) was treated with an anhydrous methanolic solution (10 mL) of $MnCl_2 \cdot 4H_2O$ (0.198 g, 1.00 mmol) under inert conditions. The resulting mixture was heated at 50 °C for one hour. The reaction mixture was cooled to ambient temperature, stirred at ambient conditions for one hour, then bubbled O_2 gas for 30 minutes. The solvent was completely removed by rotatory evaporation. The product was dissolved in dichloromethane (50 mL) and filtered through celite. The solution was reduced to dryness by rotatory evaporation to yield a dark brown precipitate. Yield: 74.4%. Melting point = 162-164 °C. ESI (m/z^+) in CH_3OH = 873.4962 (100%) for $[C_{53}H_{73}N_2O_5Mn + H^+]$ (calculated = 873.4978) in agreement with -1.8 ppm difference. Anal. Calc. for $[C_{53}H_{73}N_2O_5Mn \cdot CH_3OH]$: C, 71.66; H, 8.57; N, 3.09%. Found: C, 71.33; H, 8.23; N, 3.29%. IR (KBr, cm^{-1}) 2868-2956 (v_{C-H}), 1608 ($v_{C=C}$, aromatic), 1512 ($v_{C=C}$, aromatic), 1587 ($v_{C=N}$), 1275 (v_{C-O-C}).

Synthesis of complex [Mn^{III}L^{3I}] (2).

Complex **2** was synthesized in a similar fashion as **[Mn^{III}L^{2I}]**. **[H₃L³]** (1.30 g, 1.00 mmol), anhydrous $NaOCH_3$ (0.162 g, 3.00 mmol), $MnCl_2 \cdot 4H_2O$ (0.198 g, 1.00 mmol). The product was obtained as brown viscous oil. Yield: 71.8%. ESI (m/z^+) = 1350.0317 (100%)

for $[C_{87}H_{141}N_2O_5Mn + H^+]$ (calculated = 1350.0299) in agreement with 1.3 ppm difference. Anal. Calc. for $[C_{87}H_{141}N_2O_5Mn \cdot 2H_2O]$: C, 75.39; H, 10.54; N, 2.02%. Found: C, 74.93; H, 10.38; N, 2.43%. IR (KBr, cm^{-1}) 2854-2957 (v_{C-H}), 1605 ($v_{C=C}$, aromatic), 1509 ($v_{C=C}$, aromatic), 1587 ($v_{C=N}$), 1263 (v_{C-O-C}).

Synthesis of complex $[Mn^{III}L^{4I}]$ (3).

Complex **3** was synthesized in a similar fashion as $[Mn^{III}L^{2I}]$. $[H_3L^4]$ (0.911 g, 1.00 mmol), anhydrous NaOCH$_3$ (0.162 g, 3.00 mmol), MnCl$_2\cdot$4H$_2$O (0.198 g, 1.00 mmol). Yield: 62%. Melting point = 116-118 °C. ESI (m/z^+) in CH$_3$OH = 961.5481 (100%) for $[C_{57}H_{81}N_2O_7Mn + H^+]$ (calculated = 961.5503) in agreement with -2.3 ppm difference. Anal. Calc. for $[C_{57}H_{81}N_2O_7Mn]$: C, 71.22; H, 8.49; N, 2.91%. Found: C, 71.67; H, 8.40; N, 2.94%. IR (KBr, cm^{-1}) 2869-2955 (v_{C-H}), 1611 ($v_{C=C}$, aromatic), 1512 ($v_{C=C}$, aromatic), 1591 ($v_{C=N}$), 1273 (v_{C-O-C}), 1129 (v_{C-O-C}).

Synthesis of complex $[Mn^{III}L^{tBu}]$ (4).

A methanol and dichloromethane solution (10:1) of $[H_2L^{tBu}]$ (0.250 g, 0.363 mmol) and anhydrous NaOCH$_3$ (0.040 g, 0.730 mmol) was treated with a methanolic solution (5 mL) of MnCl$_2$.4H$_2$O (0.072 g, 0.360 mmol). The resulting mixture was heated at 50 °C for 4-5 hours. The reaction mixture was cooled to ambient temperature and stirred for 1 hour. Then, the solution was filtered and set for recrystallization at ambient conditions to yield dark green crystals. The crystals were filtered and washed with water. Yield: 85.7%. ESI (m/z^+) in CH$_3$OH = 741.3658 (100%) for $[C_{42}H_{58}N_2O_6Mn^+]$ (calculated = 741.3675) in agreement with -2.3 ppm difference. Anal. Calc. for $[C_{43}H_{62}ClMnN_2O_7.CH_3OH]$: C, 62.81;

H, 7.91; N, 3.33%. Found: C, 62.12; H, 7.13; N, 3.46%. IR (KBr, cm^{-1}) 2869-3093 (v_{C-H}), 1605 ($v_{C=C}$, aromatic), 1517 ($v_{C=C}$, aromatic) 1586 ($v_{C=N}$), 1271 (v_{C-O-C}), 1132 (v_{C-O-C}).

Synthesis of complex [Mn^{III}L$^{bisPho-NO2}$] (5).

A mixture of [H$_2$L$^{bisPho-NO2}$] (0.250 g, 0.396 mmol) and anhydrous NaOCH$_3$ (0.043 g, 0.793 mmol) in methanol (20 mL) was treated with a methanolic solution (5 mL) of MnCl$_2$.4H$_2$O (0.078 g, 0.396 mmol). The resulting mixture was heated at 50 °C for 4 hours. The reaction mixture was cooled to ambient temperature, and the solution was filtered and set for recrystallization at ambient conditions to yield dark brown crystals. The crystals were washed with water and dried under vacuum. Yield: 92.6%. ESI (m/z^+) in CH$_3$OH = 683.2641 (100%) for [C$_{36}$H$_{44}$MnN$_4$O$_6^+$] (calculated = 683.2642). Anal. Calc. for [C$_{36}$H$_{44}$ClMnN$_4$O$_6$]: C, 60.13; H, 6.17; N, 7.79%. Found: C, 59.74; H, 6.52; N, 8.26%. IR (KBr, cm^{-1}) 2869-2958 (v_{C-H}), 1613 ($v_{C=C}$, aromatic), 1524 ($v_{C=C}$, aromatic) 1573 ($v_{C=N}$), 1462 ($v_{N=O}$), 1361 ($v_{N=O}$).

Synthesis of complex [Mn^{II}L^{NO2}] (6).

A mixture of [H$_2$L^{NO2}] (0.200 g, 0.361 mmol) and anhydrous NaOCH$_3$ (0.039 g, 0.720 mmol) in dichloromethane (20 mL) and dimethyl sulfoxide (6 mL) was treated with a methanolic solution (4 mL) of MnCl$_2$.4H$_2$O (0.072 g, 0.361 mmol). The resulting mixture was heated at reflux for 18-20 hours. The reaction mixture was cooled to ambient temperature. The solvent was concentrated to half of its original volume, and diethyl ether (30 mL) was added to the solution to give a dark greenish brown microcrystalline product. The microcrystalline product was crystallized in dichloromethane and dimethyl sulfoxide mixture (3:1, 16 mL) to obtain x-ray quality single crystals. Yield: 44.6%. ESI (m/z^+) =

685.0994 for $[C_{28}H_{30}MnN_4O_{11}S^+]$ (calculated = 685.1012) in agreement with -2.6 ppm difference. Anal. Calc. for $[C_{30}H_{36}MnN_4O_{12}S_2 \cdot (CH_3)_2SO]$: C, 45.66; H, 5.03; N, 6.66%. Found: C, 46.00; H, 4.89; N, 6.79%. IR (KBr, cm^{-1}) 2818-3008 (ν_{C-H}), 1613 ($\nu_{C=C}$, aromatic), 1514 ($\nu_{C=C}$, aromatic) 1592 ($\nu_{C=N}$), 1261 (ν_{C-O-C}), 1130 (ν_{C-O-C}), 1462 ($\nu_{N=O}$), 1333 ($\nu_{N=O}$).

7.3 Results and Discussion

7.3.1 Synthesis and Characterization of Manganese Complexes

Six new manganese(III) complexes were designed to investigate the spectroscopic, redox, amphiphilic, and current-voltage properties. This study included the synthesis of redox-active manganese(III) complexes with $[N_2O_3]$ and $[N_2O_2]$ environments to accommodate trivalent manganese ions in a pentacoordinate or hexacoordinate geometries. All the ligand structures were designed in a way to facilitate film formation at the air/water and air/solid interfaces. Electron donating and electron withdrawing substituents were introduced to the backbone of the ligand to modulate electronic and redox properties. All of the ligands were synthesized using multistep synthetic processes and were characterized by spectroscopic methods (IR and ^{1}H-NMR spectroscopy) and ESI/APCI mass spectrometry as discussed in earlier chapters. Treatment of ligands (**[H$_3$L^2]**-**[H$_3$L^4]**, **[H$_2$L^{tBu}]**, **[H$_2$L$^{bisPho-NO2}$]**, and **[H$_2$L^{NO2}]**) with manganese(II) chloride tetrahydrate (MnCl$_2 \cdot$4H$_2$O) and sodium methoxide under reflux conditions yielded a series of stable neutral monometallic manganese complexes (**Scheme 7.2**). Except for complex **2**, all the other manganese complexes were isolated in the solid form. Multiple analysis techniques were used to characterize the products including, IR spectroscopy, high-resolution mass spectrometry, and combustion analysis. Complexes **1**-**3** showed the formation of C=N, azomethine moiety upon metal coordination at

the C—N amine nitrogen bond of the ligand structure.[35] Attempts to grow X-ray quality crystals of complexes **1**-**3** were unsuccessful. Complexes **4**-**6** did not show any change in the ligand structure. According to the observed data complexes **1**-**5** indicated the formation of manganese(III) complexes whereas the complexes **6** suggested the formation of a manganese(II) species.

[Mn^{III}L^{2l}], R = CH$_3$ (1)
[Mn^{III}L^{3l}], R = C$_{18}$H$_{37}$ (2)
[Mn^{III}L^{4l}], R = CH$_2$CH$_2$OCH$_3$ (3)

[Mn^{III}L^{tBu}], R$_1$ = OCH$_2$CH$_2$OCH$_3$ (4)
[Mn^{III}L$^{bisPhO-NO2}$], R$_1$ = NO$_2$ (5)

[Mn^{II}L^{NO2}], (6)
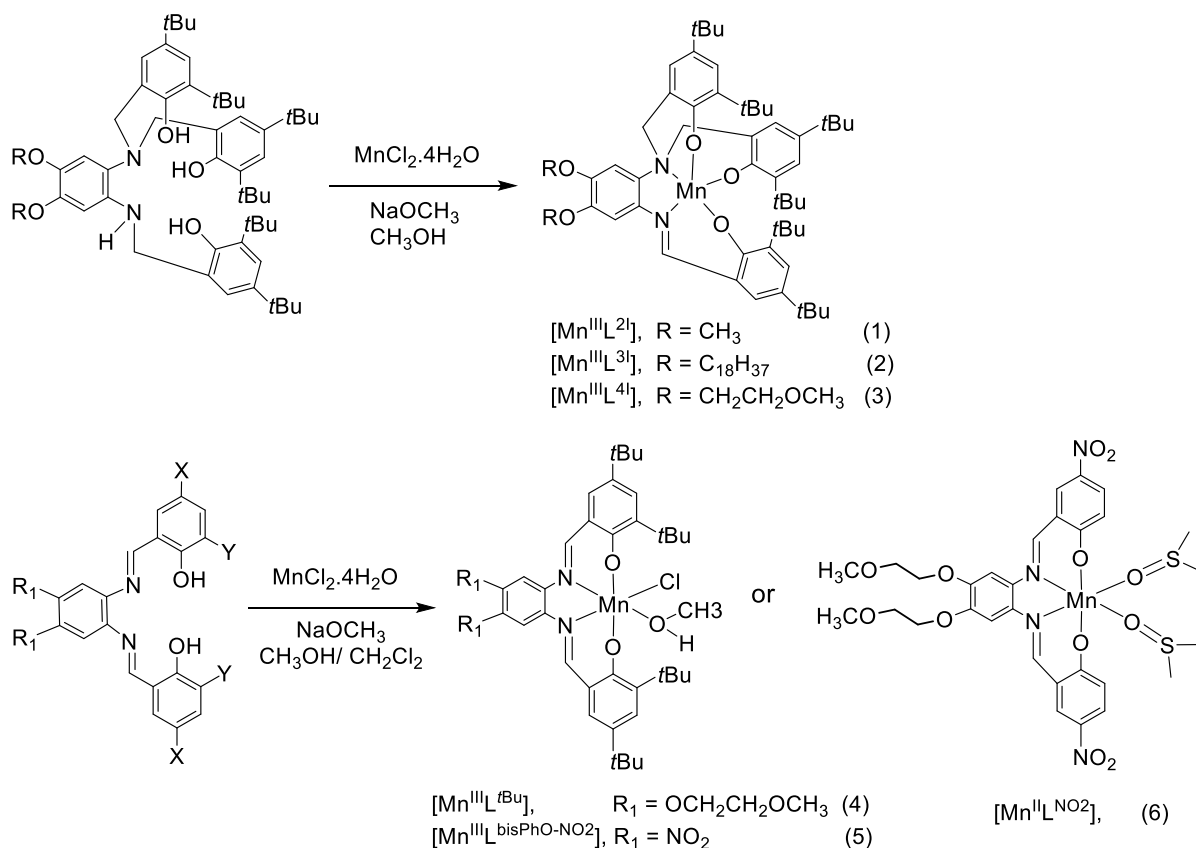
Scheme 7.2. Synthesis of manganese complexes

Furthermore, another manganese complex **[Mn^{III}L•CH$_3$OH]**, was synthesized without modification on phenelynediamine moiety to explore the electrochemistry and spectroscopic properties of manganese(III) ion when coordinated to [N$_2$O$_3$] pocket of the ligand. The hexacoordinate geometry of complex **[Mn^{III}L•CH$_3$OH]** was established by

crystal structure information (crystal structure is known with one methanol molecule coordinated to the sixth coordination position). Thermogravimetric analyses (TGA) were performed and compared with hexacoordinate manganese(III) complex **[Mn^{III}L•CH$_3$OH]**, to establish the pentacoordinate geometry of complexes **1**-**3**. A Perkin-Elmer Pyris 1 thermogravimetric analyzer was used to study the decomposition temperatures and relative weight losses of complex **1**, **3**, and **[Mn^{III}L•CH$_3$OH]**. These compounds were heated from 25 to 250 °C with a temperature ramp rate of 2 °C min^{-1} and 250 to 500 °C with a temperature ramp rate of 5 °C min^{-1} in a flow of air. Complexes **1** and **3** showed similar behavior and showed no weight loss below 200 °C; whereas, complex **[Mn^{III}L•CH$_3$OH]** showed a weight loss of 3.732% at ∼ 135 °C which corresponds to loss of one molecule of methanol. The pentacoordinate geometry of complexes **1** and **3** can be confirmed, because these complexes did not show weight loss in the above temperature region (**Figure 7.1**). These three complexes started to show the decomposition of organic material > 200 °C.
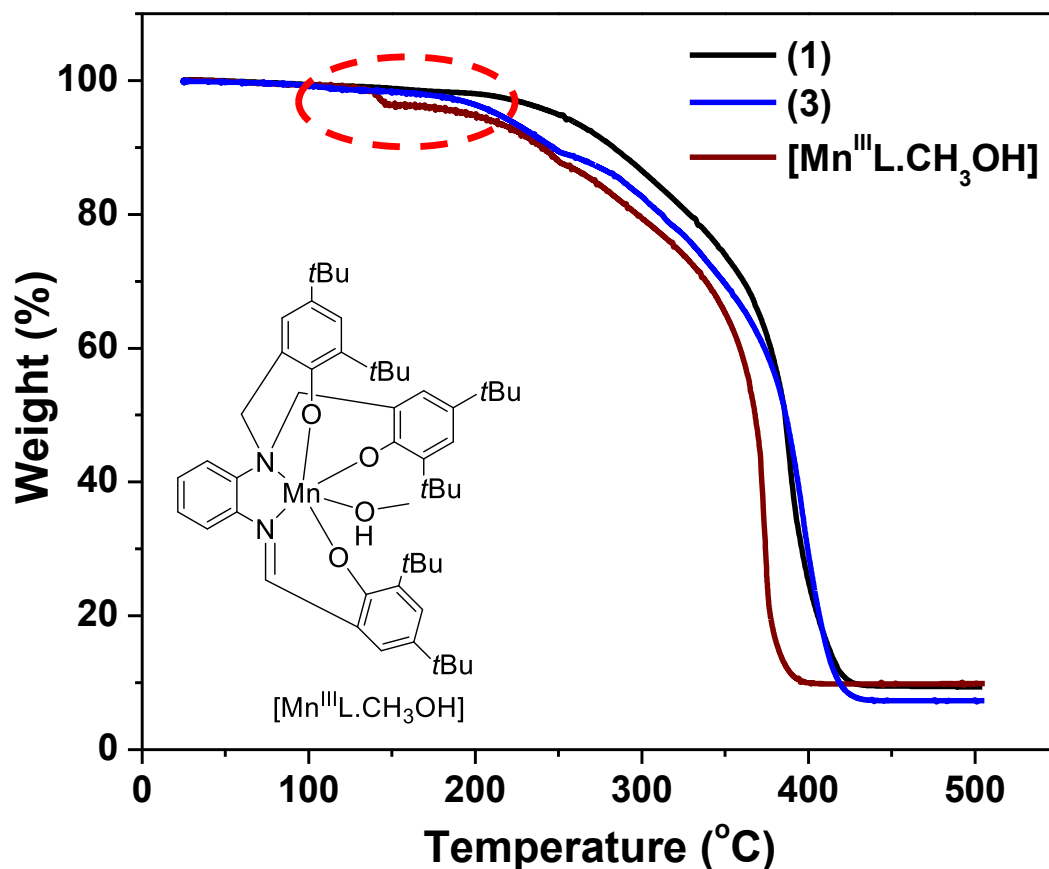
Figure 7.1. TGA data of complexes **1** and **3** in comparison with **[M^{III}L•CH$_3$OH]**.

High resolution ESI mass spectra (positive ion mode) of the isolated products of complexes **1-6** showed dominant peaks for their molecular ion peaks (M+H$^+$) with a difference between the calculated and experimental data to be less than ±3 ppm. The peak positions and isotopic distribution patterns were in agreement with the expected data. These data suggest that the elemental compositions of the isolated products match well with the desired compounds. IR spectroscopy was also used to characterize the isolated compounds. The asymmetric and symmetric C—H stretches appeared ~ 3000-2800 cm^{-1}. Complexes **1-6** showed peaks around ~ 1585 cm^{-1} referenced to the C=N stretching vibration. This information suggests a possible amine to imine conversion that takes place during the metal

complexation of complexes **1**-**3**. In addition, IR spectra showed C=C aromatic stretching and CH$_n$ deformation bands in the finger print region. These data were in good agreement with the literature.[36]

7.3.2 Molecular Structure Data

Attempts to grow X-ray quality crystals of complexes **1**-**3** were unsuccessful. Single crystals were isolated for complexes **4** (from methanol/dichloromethane; dark green), **5** (from methanol; dark brown), and **6** (from dichloromethane/dimethyl sulfoxide; dark greenish brown) using slow evaporation method. Selected crystallographic data of complexes **4**-**6** are given in **Table 7.1**-**Table 7.4** and the ORTEP views are shown in **Figure 7.2**. Crystal structure data of complexes **4**-**6** confirmed the presence of monomeric manganese species and the ligand identity. According to the crystallographic data, complexes **4**-**6** showed that the two imine nitrogen atoms and the two phenolate oxygen atoms have been coordinated to the manganese ion on the same plane. Saloph-type manganese complexes showed a distorted octahedral geometry around the metal ion. In complexes **4** and **5**, a choloro ligand and a methanol molecule; and in complex **6**, two dimethyl sulfoxide molecules were axially coordinated to form hexacoordinate species. Mn-N bond distances of complexes **4** and **5** ranged between 1.98 and 1.99 Å and a Mn-O bond distance of ~ 1.87 Å was found in each complex. Also, complexes **4** and **5** showed bond distances of 2.3 and 2.6 Å, respectively for the Mn-Cl bond. Complex **6** showed Mn-N bond distance of ~ 2.2 Å and Mn-O bond distance of ~ 2.08 Å. These bond distances and angles are comparable to other saloph-type manganese(III) complexes.[37,38,39]
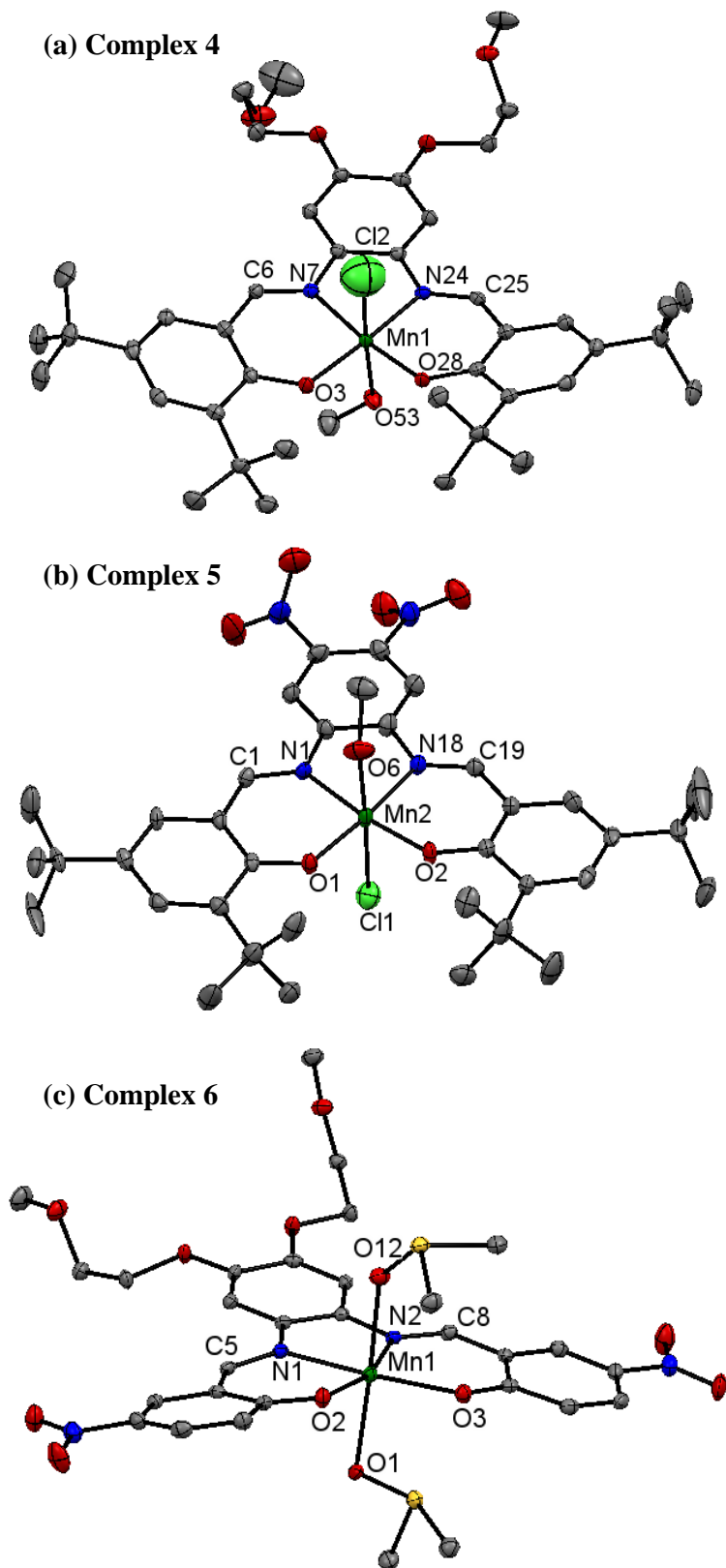
Figure 7.2. X-ray crystal structure data of complexes (a) **4**, (b) **5**, and (c) **6**.

	(4)	**(5)**	**(6)**
Formula	$C_{44}H_{66}Cl_2MnN_2O_8$	$C_{44}H_{58}ClMnN_8O_{12}$	$C_{32}H_{42}MnN_4O_{13}S_3$
M	876.82	981.38	841.85
Space group	P-1	Cc	P-1
a / Å	10.7364(5)	12.3951(9)	11.5544(7)
b/ Å	14.1651(6)	43.834(3)	13.0314(8)
c/ Å	16.3530(7)	9.5402(6)	13.7212(8)
α/ °	71.703(2)	90.00	104.484(3)
β/ °	77.979(3)	113.281(3)	104.060(4)
γ/ °	80.303(3)	90.00	104.707(3)
V/ Å³	2295.22(18)	4761.4(5)	1828.3(2)
Z	2	4	2
T/ K	293(2)	100.1	100.1
λ/ Å	0.71073	0.71073	0.71073
D_{calc}/ g cm^{-3}	1.269	1.241	1.5291
μ/ mm^{-1}	0.455	0.391	0.603
R(F) (%)	6.34	6.59	3.03
wR (F) (%)	18.03	16.85	10.47

[a]$R(F) = \sum \left\| F_o \right| - \left| F_c \right\| / \sum \left| F_o \right|$; $Rw(F) = [\sum w(F_o{}^2 - F_c{}^2)^2 / \sum w(F_o{}^2)^2]^{1/2}$ for $I > 2\sigma(I)$

Table 7.1. Crystal structure data[a] for complexes **4-6**.

Complex 4			
Mn1	Cl2	2.277(3)	
Mn1	O3	1.865(2)	
Mn1	N7	1.993(3)	
Mn1	N24	1.975(3)	
Mn1	O28	1.866(2)	
Mn1	O53	2.236(3)	
C6	N7	1.296(4)	
N24	C25	1.292(4)	
O3	Mn1	Cl2	94.38(10)
O3	Mn1	N7	91.66(11)
O3	Mn1	N24	172.68(10)
O3	Mn1	O28	93.89(10)
O3	Mn1	O53	90.09(10)
N7	Mn1	Cl2	87.69(10)
N7	Mn1	O53	91.38(11)
N24	Mn1	Cl2	89.66(10)

N24	Mn1	N7	82.39(11)
N24	Mn1	O53	85.81(10)
O28	Mn1	Cl2	87.85(10)
O28	Mn1	N7	173.13(10)
O28	Mn1	N24	92.36(10)
O28	Mn1	O53	92.65(10)
O53	Mn1	Cl2	175.46(9)

Table 7.2. Selected bond lengths (Å) and angles (°) for complex **4**.

Complex 5			
Cl1	Mn2	2.6172(16)	
Mn2	O1	1.870(3)	
Mn2	N1	1.979(3)	
Mn2	O2	1.871(3)	
Mn2	O6	2.268(4)	
Mn2	N18	1.980(4)	
N1	C1	1.312(6)	
N18	C19	1.298(6)	
O1	Mn2	Cl1	89.66(11)
O1	Mn2	N1	92.33(14)

O1	Mn2	O2	93.76(10)
O1	Mn2	O6	88.39(14)
O1	Mn2	N18	174.48(15)
N1	Mn2	Cl1	91.73(12)
N1	Mn2	O6	87.26(15)
N1	Mn2	N18	82.18(11)
O2	Mn2	Cl1	91.43(11)
O2	Mn2	N1	173.16(15)
O2	Mn2	O6	89.78(15)
O2	Mn2	N18	91.76(15)
O6	Mn2	Cl1	177.76(13)
N18	Mn2	Cl1	89.92(13)
N18	Mn2	O6	91.91(16)

Table 7.3. Selected bond lengths (Å) and angles (°) for complex **5**.

Complex 6			
N1	Mn1	2.1847(17)	
N2	Mn1	2.2299(16)	
O1	Mn1	2.3123(15)	
O2	Mn1	2.0781(14)	
O3	Mn1	2.0691(15)	
O12	Mn1	2.2394(15)	

C5	N1	1.295(2)	
C8	N2	1.295(3)	
N2	Mn1	N1	75.84(6)
O1	Mn1	N1	86.13(6)
O1	Mn1	N2	89.64(6)
O2	Mn1	N1	87.41(6)
O2	Mn1	N2	162.87(6)
O2	Mn1	O1	92.85(5)
O3	Mn1	N1	161.73(6)
O3	Mn1	N2	86.49(6)
O3	Mn1	O1	89.22(5)
O3	Mn1	O2	110.48(5)
O12	Mn1	N1	89.56(6)
O12	Mn1	N2	85.86(6)
O12	Mn1	O1	174.41(5)
O12	Mn1	O2	90.51(6)
N2	Mn1	N1	75.84(6)
O1	Mn1	N1	86.13(6)
O12	Mn1	O3	93.79(6)

Table 7.4. Selected bond lengths (Å) and angles (°) for complex **6**.

7.3.3 Electronic Spectral Properties

UV-visible spectra of complexes **1**-**5** were recorded in dicholoromethane and complex **6** was measured in a 19:1 dichloromethane/dimethyl sulfoxide mixture. UV-visible spectra obtained for the metal complexes are shown in **Figure 7.3** and **Table 7.5** presents spectral data obtained for 1.0×10^{-5} mol•L^{-1} solutions of metal complexes. UV-visible spectra of complexes **1**-**6** showed ligand-based $\pi \rightarrow \pi*$ electronic transitions[40] below 300 nm. Complexes **1**-**5** showed intense absorption maxima in the near-UV region ~ 350 nm. According to Karsten *et al.* this band can be designated as ligand to metal charge transfer (LMCT) originating from the phenolate oxygen (p_π orbital) to $d_{\sigma*}$ of the metal center.[41] The other absorption maxima in the visible region at ~ 465 nm for complexes **1**-**3**, at 494 nm for complex **4**, and at 523 nm for complex **5**, can also be assigned as a LMCT transition originating from p_π orbital of the phenolate oxygen to $d_{\pi*}$ of the manganese(III) center.[41,42,43] In complex **6**, intraligand $\pi \rightarrow \pi*$ and other charge transfer transitions appear at ~ 384 nm as an intense broad band. In addition to these LMCT transitions, complexes **4** and **5** showed intraligand $\pi \rightarrow \pi*$ electronic transitions in the region of ~ 300-450 nm associated with phenyl, azomethine, and nitro moieties.[44]
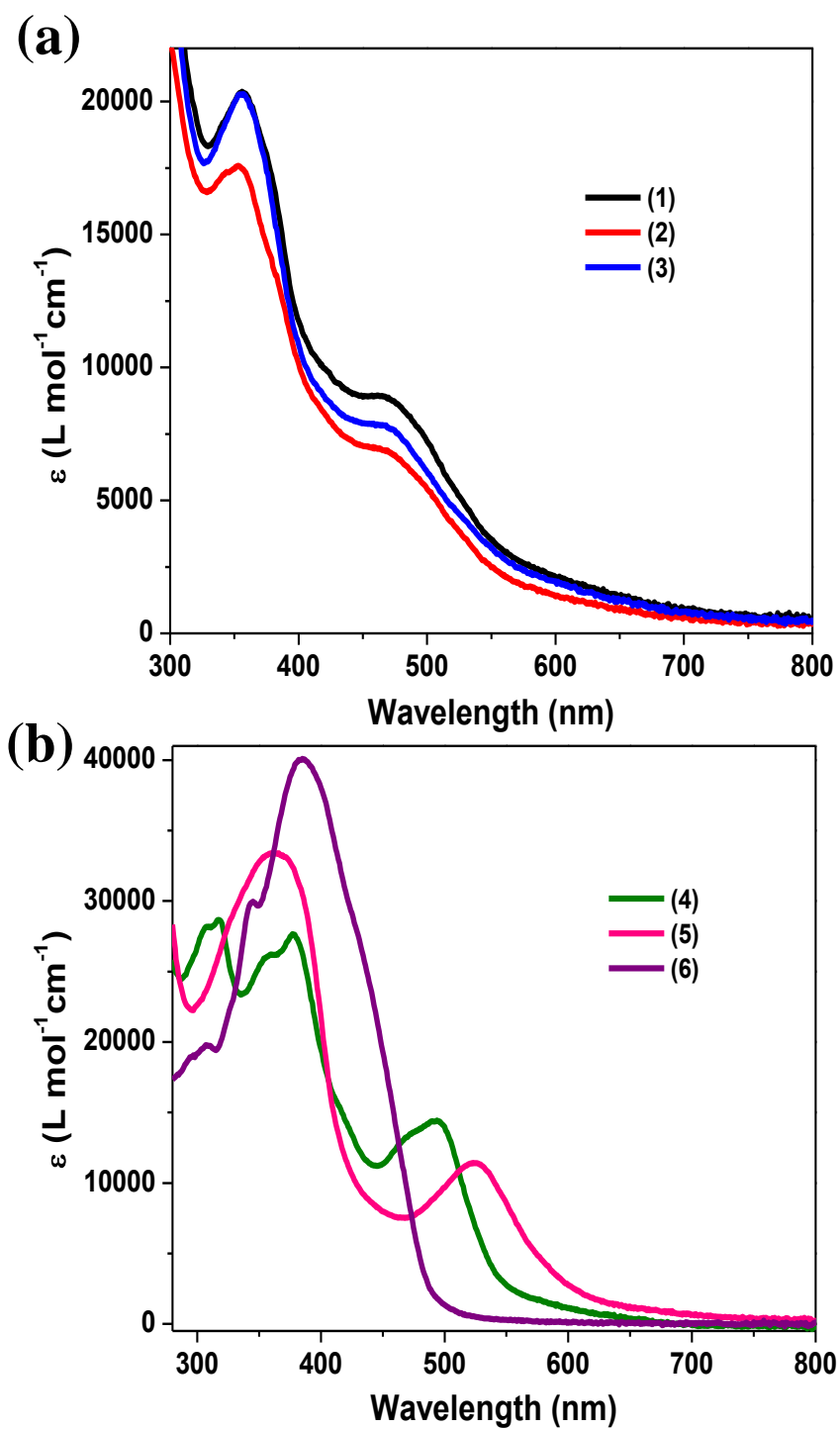
Figure 7.3. UV-visible spectra of complexes (a) **1**-**3** and (b) **4**-**6** in 1.0×10^{-5} mol•L^{-1} solutions.

Compound	λ_{max}, nm (ε, L•mol^{-1}•cm^{-1})
(1)	356 (20366), 465 (8934)
(2)	353 (17586), 468 (6850)
(3)	357 (20281), 465 (7834)
(4)	308 (28180), 317 (28655), 360 (26218), 377 (27657), 494 (14432)
(5)	366 (33387), 523 (11433)
(6)	345 (29959), 384 (40020)

Table 7.5. UV-visible spectroscopic data for complexes **1**-**6** in 1.0×10^{-5} mol•L^{-1} solutions.

7.3.4 Redox Properties

Cyclic voltammetry experiments for complexes **1-5** and **6** were carried out in dichloromethane and 19:1 dichloromethane/dimethyl sulfoxide solutions to examine the redox properties. TBAPF$_6$ was used as the supporting electrolyte, and all potential values were recorded against the Fc$^+$/Fc couple. Cyclic voltammograms obtained for complexes **1-6** are shown in **Figure 7.4**, and their potentials are tabulated in **Table 7.6**. Complexes **1-6** showed defined metal- and ligand-based redox processes in their cyclic voltammograms. In complexes **1**-**3**, a single electron cathodic processes found at ~ -0.92, -0.97, and -0.94 V, with ΔE_p of ~ 0.17, 0.2, and 0.21 V, which can be assigned as Mn(III)/Mn(II) redox couple. Neves and co-workers and Wieghardt and co-workers reported similar electrochemical behavior for Mn(III)/Mn(II) redox couple.[37,45,46,47] Furthermore, in complexes **4-6** a single electron cathodic process found at ~ -0.77, -0.45, and -0.27 V, with ΔE_p of ~ 0.12, 0.2, and 0.24 V, respectively, which can be assigned as Mn(III)/Mn(II) redox couples.[48,49,50] The Mn(III)/Mn(II) redox couple was found to be quasi-reversible in nature. In complexes **1**-**3**,

single electron quasi-reversible processes found at more positive potentials (at ~ 0.14, 0.15, and 0.13 V with ΔE_p of ~ 0.09, 0.08, and 0.1 V, respectively) can be ascribed to be ligand-centered, phenolate/phenoxyl redox couple.[43,45] Single electron quasi-reversible processes at ~ 0.69, 0.71, 0.68, 0.53, and 0.9 V for complexes **1**-**5** can also be attributed to ligand-centered redox processes.[26,27] In complexes **1**-**6**, other phenolate/phenoxyl redox couples appeared as ill-defined processes in their cyclic voltammograms. In complexes **5** and **6**, cathodic processes appearing at ~ -1.5 and -1.9 V, respectively, can be attributed to be nitro reductions.
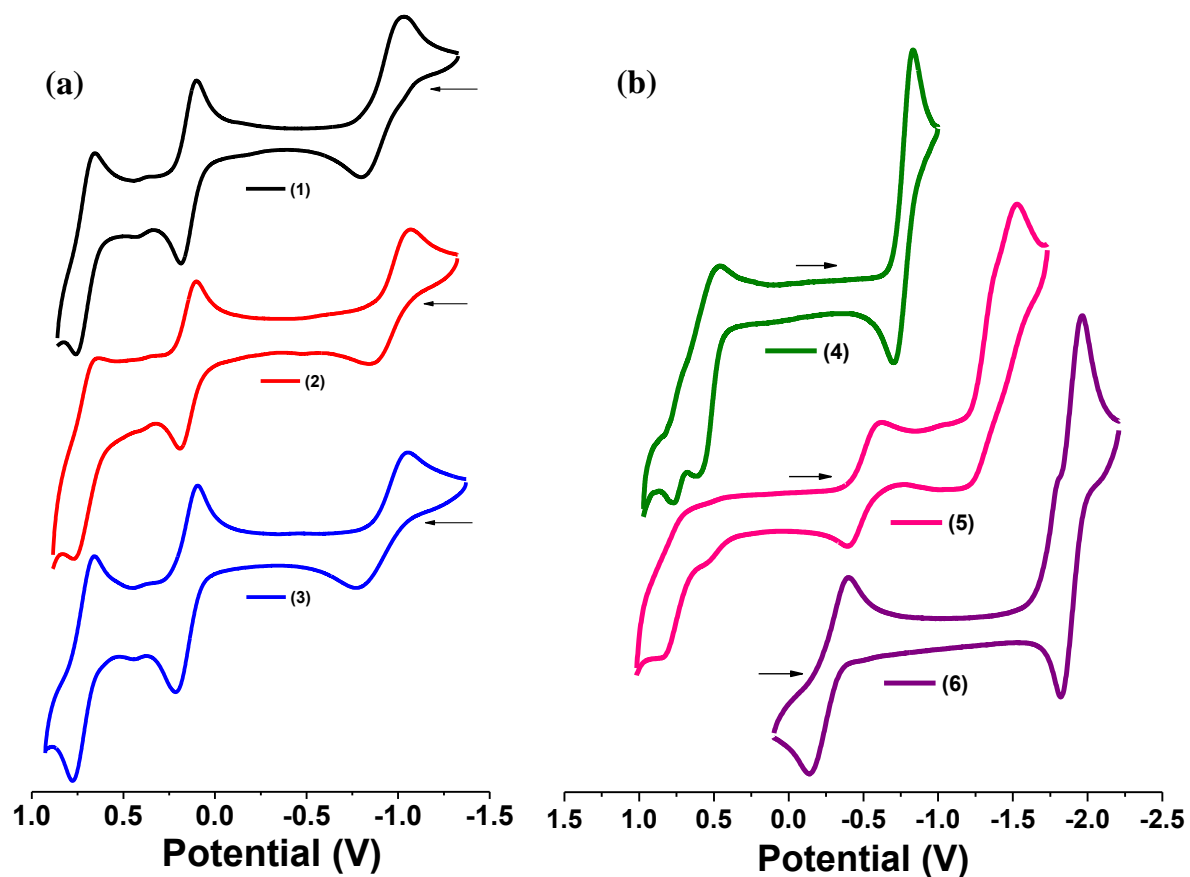
Figure 7.4. Cyclic voltammograms of 1.0×10^{-3} mol•L^{-1} solutions of complexes (a) **1**-**3** and (b) **4**-**6**.

Compound	$E_{1/2}$, (ΔE_p) (V) $\lvert I_{pa}/I_{pc} \rvert$	$E_{1/2}$, (ΔE_p) (V) $\lvert I_{pa}/I_{pc} \rvert$	$E_{1/2}$, (ΔE_p) (V)
(1)	-0.924 (0.172) $\lvert 1.114 \rvert$	0.135 (0.090) $\lvert 1.045 \rvert$	0.694 (0.112)
(2)	-0.966 (0.195) $\lvert 0.655 \rvert$	0.148 (0.083) $\lvert 1.107 \rvert$	0.708 (0.123)
(3)	-0.935 (0.212) $\lvert 0.656 \rvert$	0.133 (0.112) $\lvert 1.219 \rvert$	0.676 (0.146)
(4)	-0.765 (0.122) $\lvert 0.88 \rvert$	0.529 (0.162) $\lvert 2.43 \rvert$	-
(5)	~ -1.5	-0.450 (0.202) $\lvert 0.961 \rvert$	~ 0.9
(6)	-1.892 (0.132) $\lvert 1.13 \rvert$	-0.268 (0.240) $\lvert 1.492 \rvert$	-

Table 7.6. Electrochemical data (*vs.* Fc$^+$/Fc) for complexes **1**-**6**.

7.3.5 Spectroelectrochemical Properties

Spectroelectrochemical experiments were carried out for complexes **1**, **3**, and **4** to validate the above mentioned spectral assignments. In this regard, the reduction process associated with the $Mn^{III/II}$ redox couple was probed. Experiments were performed in dichloromethane at ambient conditions by applying fixed potentials at -1.38 V *vs.* Fc^+/Fc for complexes **1** and **3** and at -1.22 V *vs.* Fc^+/Fc for complex **4**. $TBAPF_6$ was used as the supporting elctrolyte during the experiments. Spectroelectrochemical experiments carried out for complexes **1**, **3**, and **4** showed that ligand to metal charge transfer transitions associated with phenolate to manganese metal center (regions between ~ 350 and 400 nm and ~ 485 and 800 nm) appeared to decrease in intensity. Also, new charge transfer bands appeared at 432, 441, and 428 nm for complexes **1**, **3**, and **4**, respectively. Besides the above features, complexes showed two isosbestic points for each reduction process (at 406 and 486 nm for complex **1**, at 404 and 496 nm for complex **3**, and at 400 and 475 nm for complex **4**). The spectral changes observed for complexes **1**, **3**, and **4** upon reduction are shown in **Figure 7.5**. The LMCT transitions become unfavorable[43] during the reduction of the metal ion from Mn(III) to Mn(II). Therefore, the LMCT related bands appeared to decrease in intensity. The appearance of new bands at 432, 441, and 428 nm can be assigned as intraligand charge transfer transitions originating from p_π of phenolate oxygen to $p_{\pi*}$ of azomethine moiety.
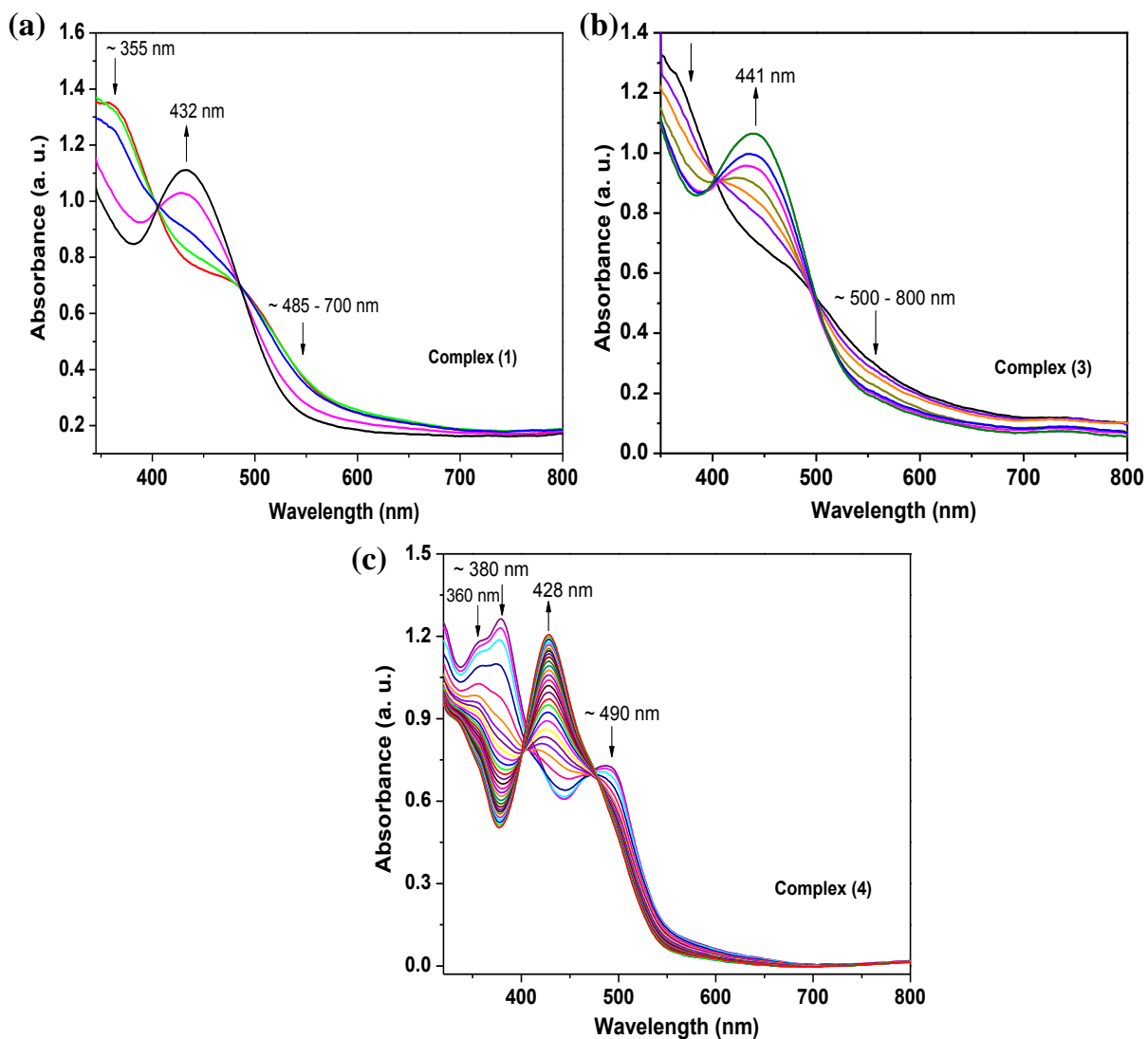
Figure 7.5. Electronic spectral changes observed for complexes (a) **1**, (b) **3**, and (c) **4** during spectroelectrochemistry experiments

7.3.6 Isothermal Compression Data

Ligand structures consisted of hydrophobic and hydrophilic moieties to obtain well-behaved film formation at the air/water interface.[51] The film formation ability of complexes **1**-**5** was assessed by studying their compression isotherms and Brewster angle micrographs. Complex **6** was not used for this study due to insolubility. Complex **2** showed

weak properties with low collapse pressure at the air/water interface and displayed a very large area of interaction of *ca.* 257 $Å^2$. In complex **2**, the presence of two alkoxy chains on the phenylenediamine moiety gives rise to free rotation[52] of carbon chains about the C—C backbone. Therefore, alkoxy chains will repel each other, when they are at close proximity, leads to the observed higher critical area of *ca.* 240 $Å^2$. Brewster angle micrographs showed homogeneous Langmuir film formation between 9 and 45 mN/m for complex **1**, 8 and 40 mN/m for complex **3**, 20 and 45 mN/m for complex **4**, and 15 and 33 mN/m for complex **5**. Complexes **1**-**5** showed critical areas of *ca.* 112, 240, 151, 78, and 63 $Å^2$, respectively, in their isotherms. These Langmuir films did not exhibit defects until they reached the respective collapse pressures. Complexes **1**-**5** showed collapse pressures at *ca.* 50, 8, 42, 50, and 35 mN/m, respectively, which were denoted with the linearly oriented Newton rings[53] in their Brewster angle micrographs. These data suggested constant pressure collapse mechanisms[54] for all the manganese(III) complexes reported herein. Compression isotherms and Brewster angle micrographs obtained for complexes **1**-**5** are shown in **Figure 7.6** and **Figure 7.7**. Results obtained from these experiments showed that the introduction of oxygen rich moieties help to form homogeneous films at the air/water interface, because they help to balance the hydrophilicity and hydrophobicity of the designed molecules.
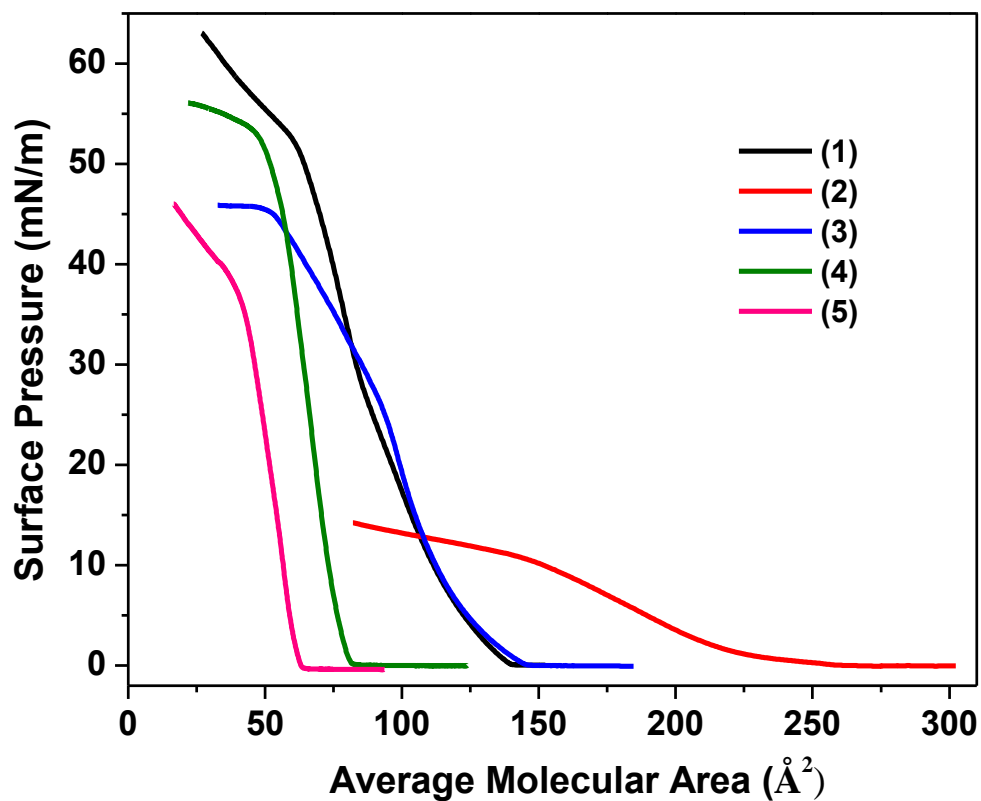
Figure 7.6. Isothermal compression data of complexes **1**-**5**.
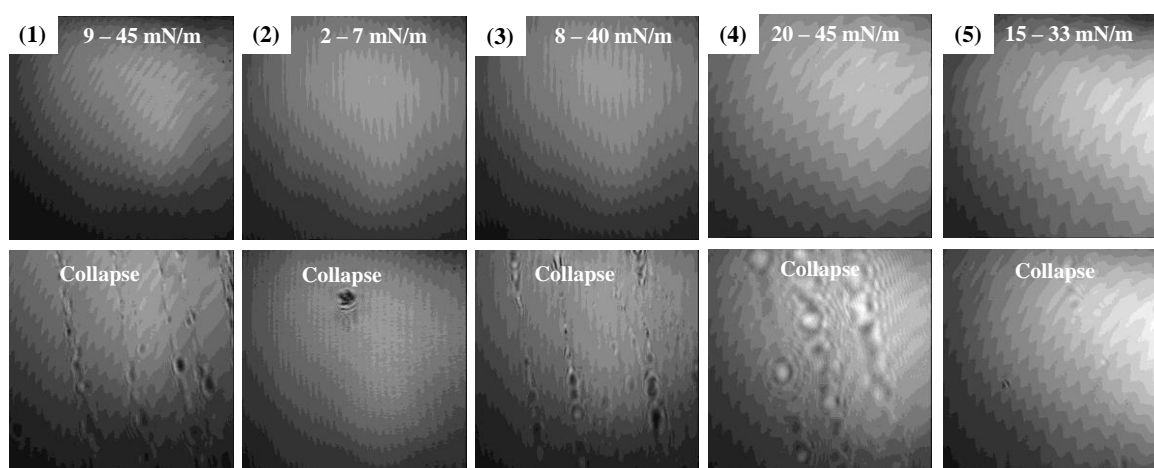
Figure 7.7. Brewster angle micrographs obtained for complexes **1**-**5**.

7.3.7 Langmuir-Blodgett Film Characterization using Spectroscopic and Spectrometric Methods

The LB films of complexes **1**, **3**, **4**, and **5** were further investigated using spectroscopic and spectrometric methods to understand the molecular composition and integrity of films.[55] Homogeneous Langmuir films (complexes **1** and **3** at 30 mN/m, complex **4** at 32 mN/m, and complex **5** at 25 mN/m) were transferred onto well-cleaned glass substrates using the y-type dipping method.[51] Fifty depositions were carried out for each of the forementioned complexes. Complexes **1**, **3**, and **4** showed transfer ratios close to unity for both up- and down-stroke dipping methods, and complex **5** showed a transfer ratio of ≤ 0.5. Thin film-deposited glass substrates showed an intense brown to dark green color. UV-visible studies conducted on complex **2** showed weak absorptions in the spectrum due to low adhesive properties of complex **2**. Therefore, further studies were not carried out with complex **2**. LB film spectra of complexes **1**, **3**, **4**, and **5** showed intense absorption maxima at ~ 345, 342, 373, and 359 nm, respectively. Relative to their solution spectra, the blue-shifting of bands and the diminished absorptions in the lower energy region (between ~ 450 and 600 nm) can be attributed to possible rearrangements and conformational changes of molecules.[56] These hypsochromic shifts of bands demonstrate H-type chromophore aggregation present in LB films.[57,58,59] The UV-visible spectra of LB films and solution spectra are shown in **Figure 7.8**. The stability of complexes **1** and **3** were investigated by aging their chloroform solutions at 4 °C. UV-visible spectra recorded for these aged solutions did not show any noticeable changes to denote the stable structure of these complexes (**Figure 7.8d**).
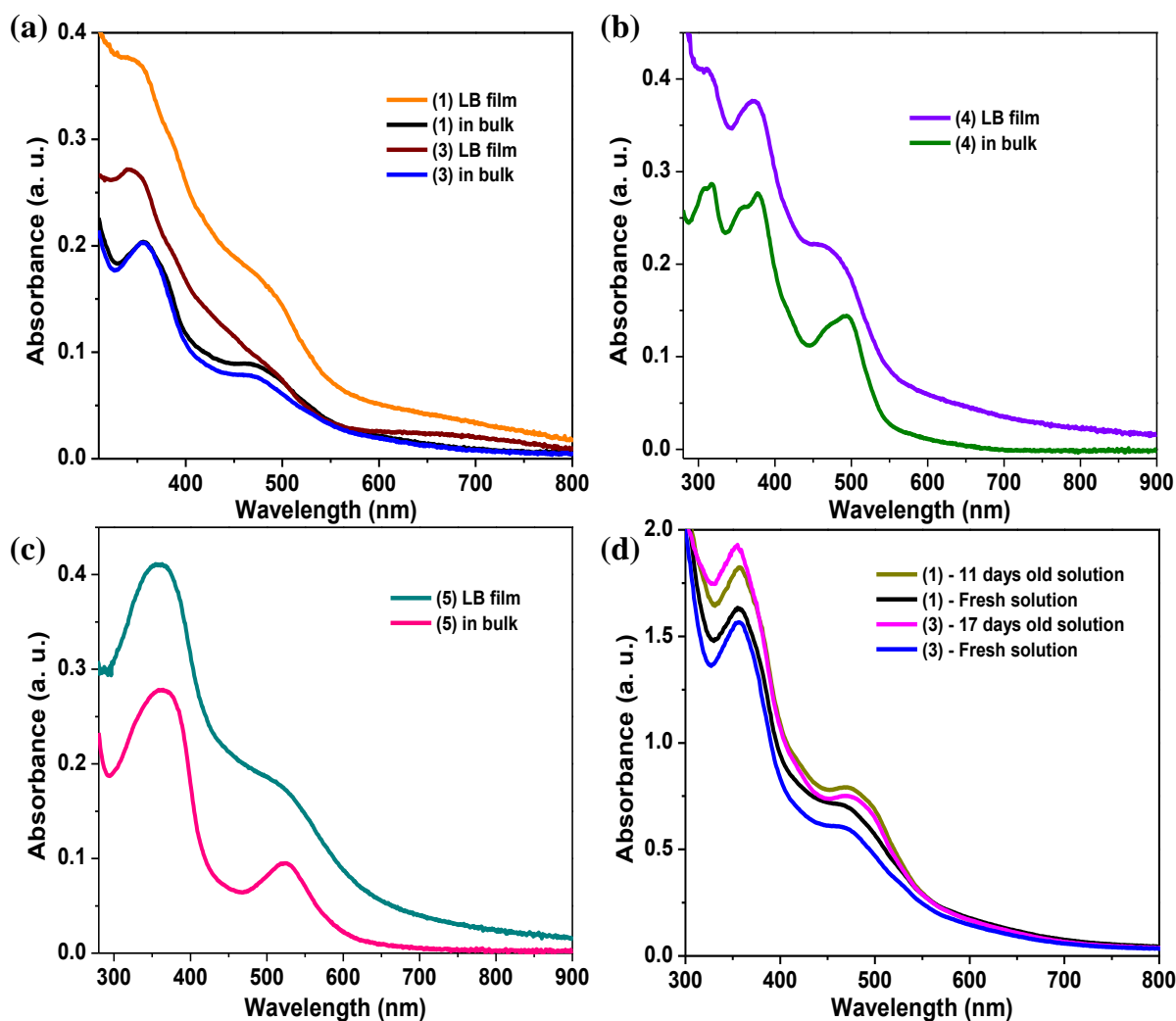
Figure 7.8. UV-visible spectra of LB films (50 depositions) of complexes (a) **1** and **3**, (b) **4**, and (c) **5** in comparison with solution spectra (1.0×10^{-5} mol•L^{-1}, dichloromethane); (d) the comparison of UV-visible spectra of fresh and aged solutions of complexes **1** and **3**.

Infrared reflection absorption spectroscopy (IRRAS) was also used to analyze the composition of LB films (fifty layers on glass). IRRA spectra of complexes **1** and **4** were measured at 30° and complexes **3** and **5** were measured at 40° using *p*-polarized light. A comparison of IRRS spectra of complexes **1**, **3**, **4**, and **5** with their bulk IR spectra are shown in **Figure 7.9** and **Figure 7.10**. IRRA spectra of these manganese(III) complexes showed

prominent asymmetric and symmetric C—H stretching vibrations with a slight shift of bands. Also, in the IRRA spectra, enhanced asymmetric C—H stretching vibrations were observed relative to their bulk IR spectra. These features indicate well-ordered film deposition for manganese(III) complexes with *tert*-butyl rich metal-containing moieties pointing outward.[60,61,62,63] These complexes showed C=N stretching vibrations at ~ 1585 cm^{-1}.

Static contact angles were measured for complexes **1** and **3** to evaluate their surface wetting ability. Monolayers of complexes **1** and **3**, deposited onto glass substrates, showed contact angles of 81.75° ± 4.28° and 68.88° ± 2.49°, respectively, compared to 7.46° ± 0.42° for bare glass. These measurements indicated the hydrophobic nature of monolayer deposited glass surfaces. The data also suggested that complex **1** has a more hydrophobic character compared to complex **3**.
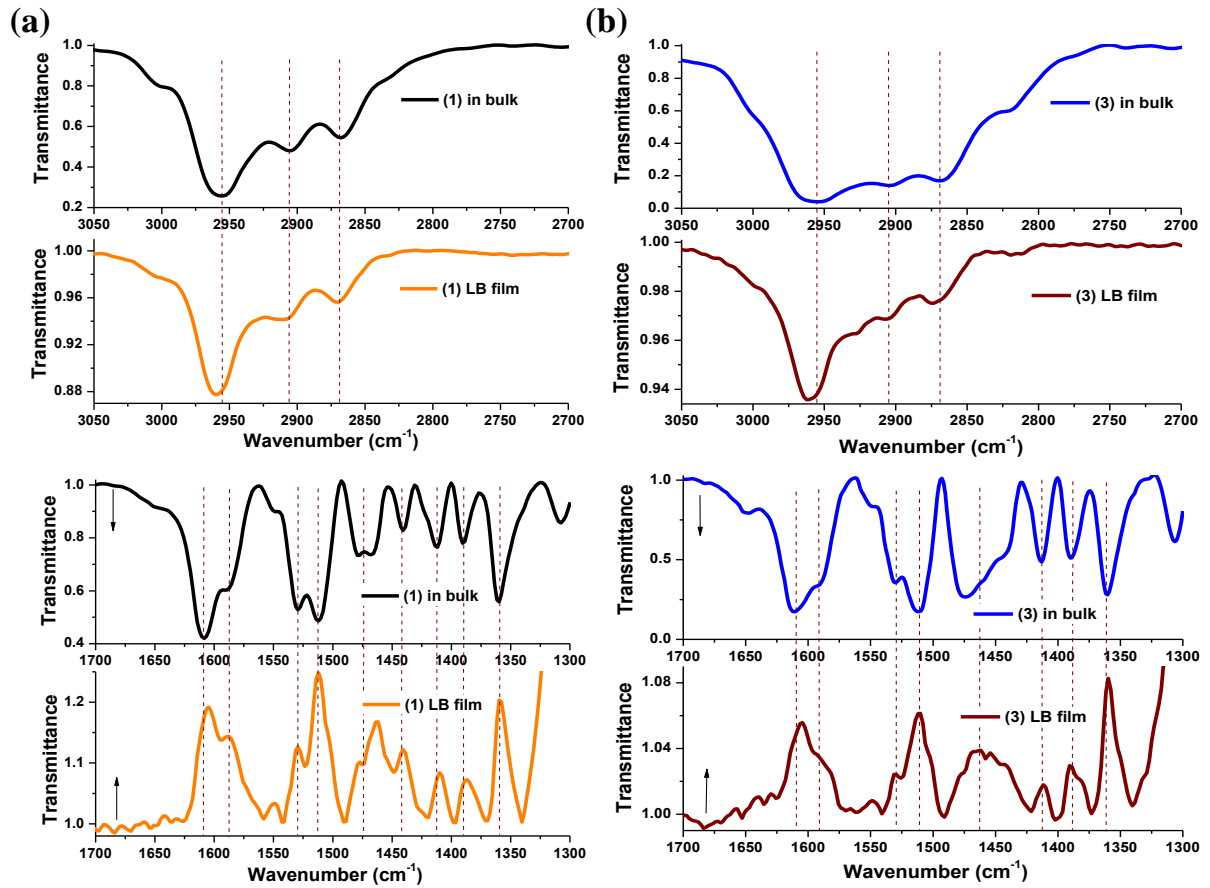
Figure 7.9. IRRAS spectra of LB films (50 depositions) of (a) complex **1** and (b) complex **3** and the bulk IR spectra of these complexes.
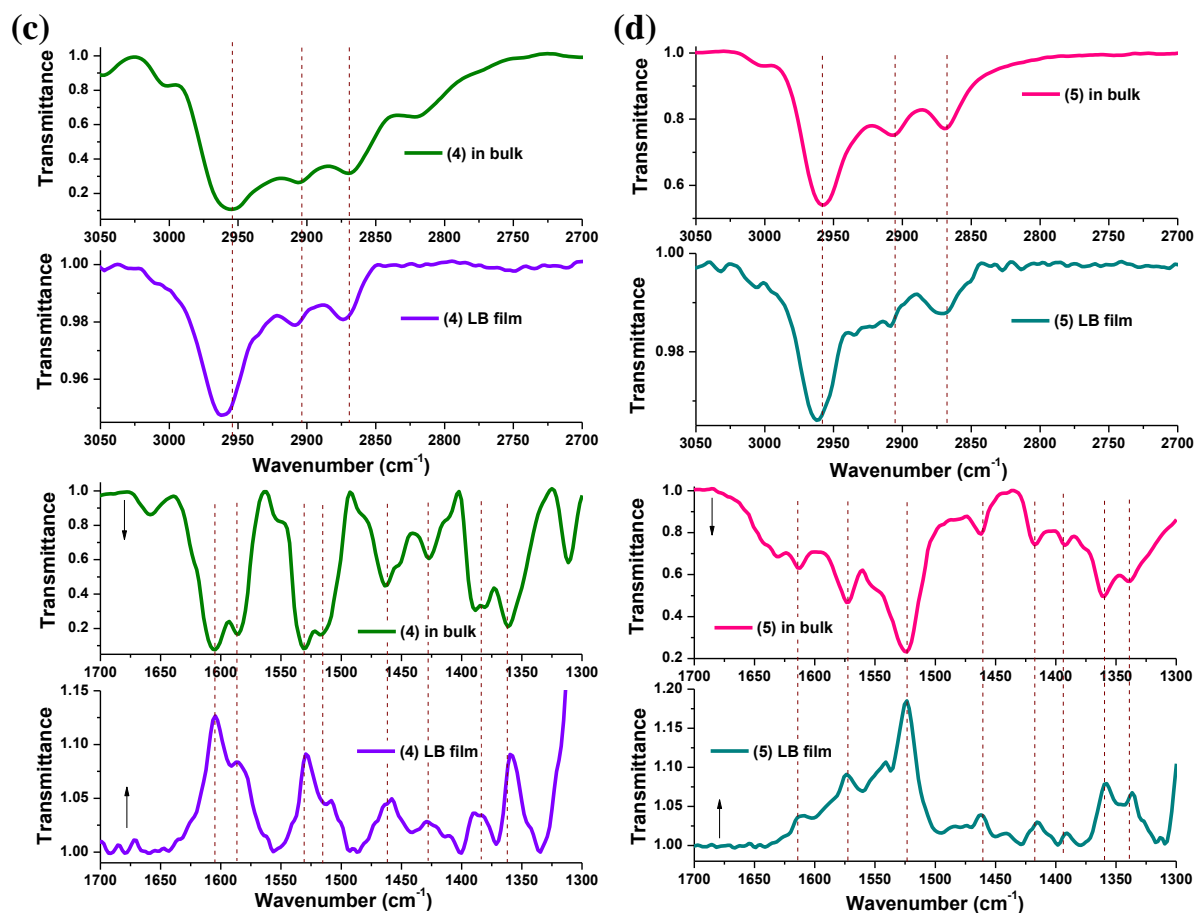
Figure 7.10. IRRAS spectra of LB films (50 depositions) of (c) complex **4** and (d) complex **5** and the bulk IR spectra of these complexes.

A monolayer film of complex **3** was further analyzed by matrix assisted ionization vacuum (MAIV) mass spectrometry[64] to understand the composition of deposited LB films. Mass spectra of the bulk sample and the LB monolayer showed a peak at m/z 961.7 belonging to $[C_{57}H_{81}MnN_2O_7 + H^+]$, corresponding to the molecular ion peak (**Figure 7.11**). Overall, the UV-visible, IRRAS, contact angle measurements, and mass spectrometry data indicated the anisotropic behavior of LB films with high molecular order[65] and the intact nature of manganese-containing molecular structures.
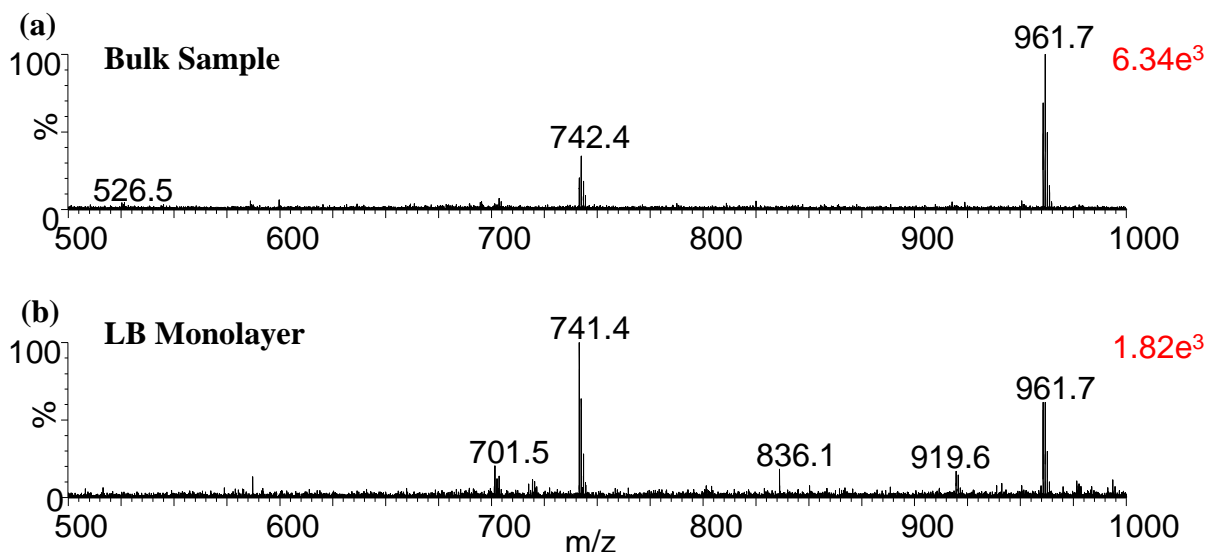
Figure 7.11. MAIV mass analysis for complex **3**, (a) bulk sample and (b) LB monolayer.

7.3.8 Surface Characterization using Atomic Force Microscopy (AFM)

The morphology of monolayer films of complexes **1-3** deposited on mica at various surface pressures were measured by AFM. AFM height images and their corresponding 3D surface plots of the monolayer films that were deposited onto mica at different surface pressures are shown in **Figures 7.12**-**7.14**. For complexes **1** and **3**, monolayers deposited at low surface pressures showed significant surface defects, such as areas covered with pinholes. Defected areas became smaller and fewer as the surface pressure increased to 20 mN/m and 15 mN/m for complexes **1** and **3**, respectively. When surface pressures increased to 25 mN/m and 30 mN/m for **1** and **3**, respectively, monolayer films became smooth with few or no defects. Therefore, films at 25 mN/m and 30 mN/m were suitable for film fabrication. Monolayer films of complexes **1** and **3**, at much higher surface pressures ≥ 30 and ~ 39 mN/m, respectively, became rougher due to excess material aggregation. On the contrary, monolayer films of complex **2** behaved different than complexes **1** and **3**. At 5

mN/m the film showed formation of small domains with sparse particles and when the surface pressure increased to 10 mN/m the domains became larger and connected. Therefore, these films showed a random, discontinued film deposition with defects on the monolayers such as large cracks and pinholes (**Figure 7.13**).
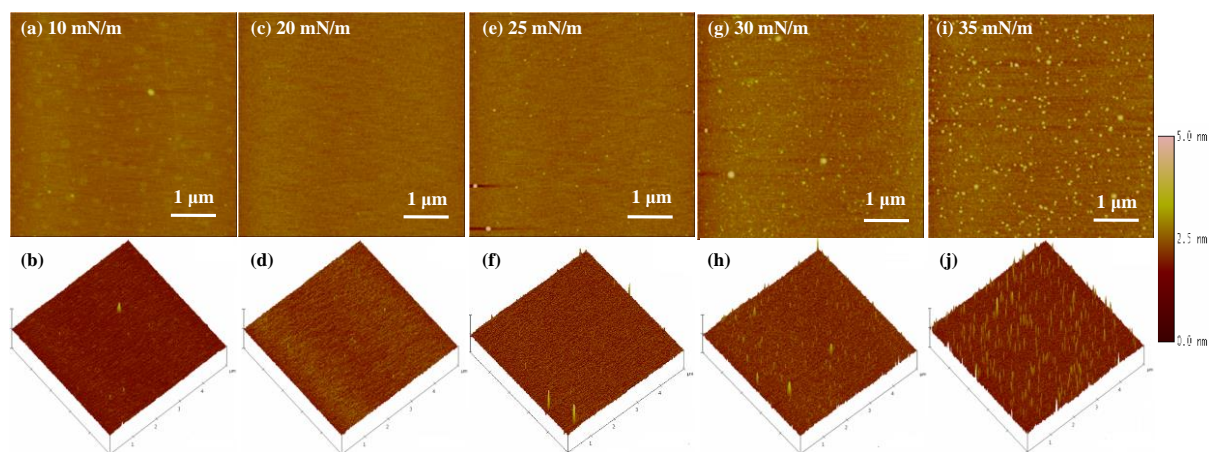
Figure 7.12. AFM height images (top) and 3D views (bottom) of monolayer films deposited on mica substrates for complex **1**: (a, b) at 10 mN/m, (c, d) at 20 mN/m, (e, f) at 25 mN/m, (g, h) at 30 mN/m, and (i, j) at 35 mN/m; the scan size is 5 μm and Z range is 5 nm for all images.
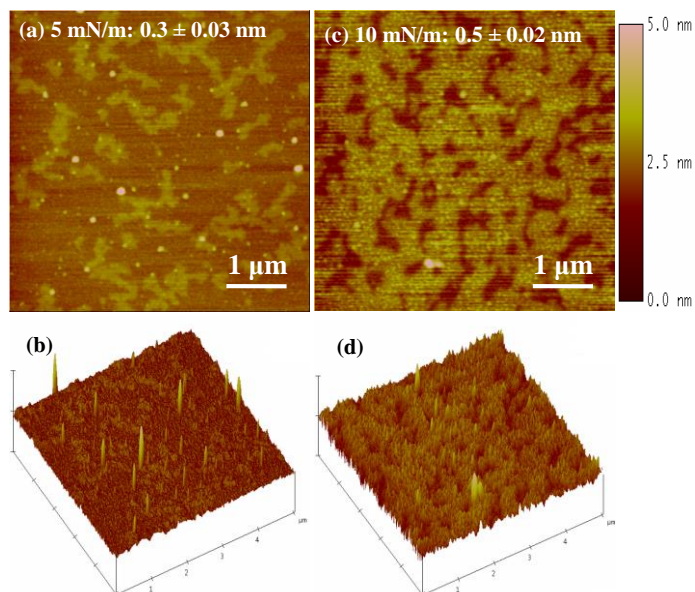
Figure 7.13. AFM height images (top) and 3D views (bottom) of monolayer films deposited on mica substrates for complex **2**: (a, b) at 5 mN/m and (c, d) at 10 mN/m; the scan size is 5 μm and the Z range is 5 nm for all images.
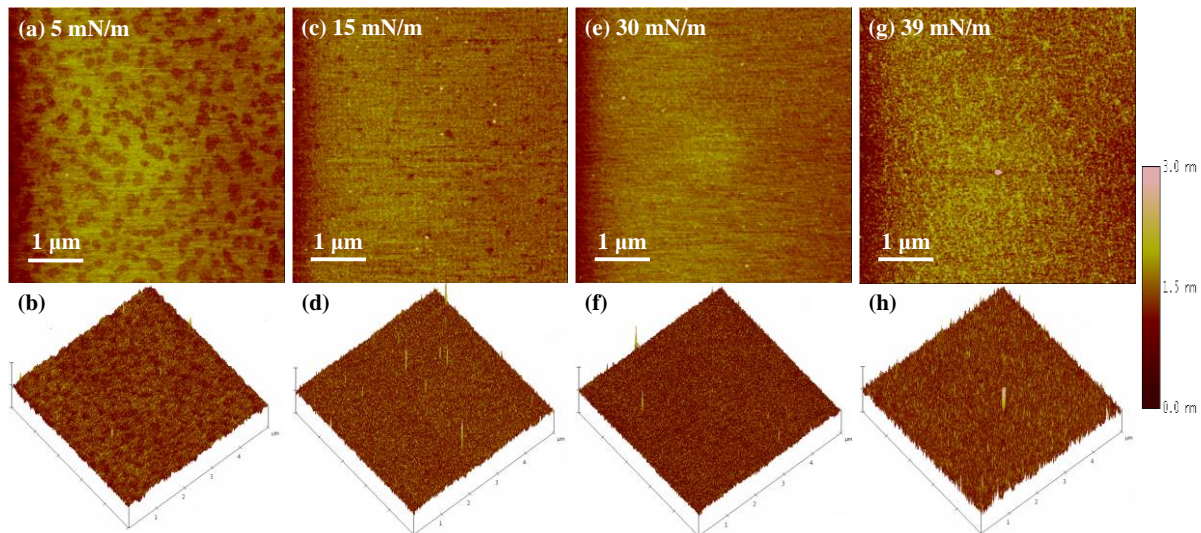
Figure 7.14. AFM height images (top) and 3D views (bottom) of monolayer films deposited on mica substrates at different surface pressures for complex **3**: (a, b) at 5 mN/m, (c, d) at 15 mN/m, (e, f) at 30 mN/m, and (g, h) at 39 mN/m; the scan size is 5 μm and the Z range is 3 nm for all images.

Surface roughness of the multilayer films was analyzed using AFM by depositing 1 to 15 layers onto mica substrates. AFM height images and the 3D plots obtained for complexes **1** and **3** are shown in **Figure 7.15** and **Figure 7.16**, respectively. Upon increasing the number of layers, surface roughness increased. Also the film became rougher with more particles aggregated on the surface of the film.
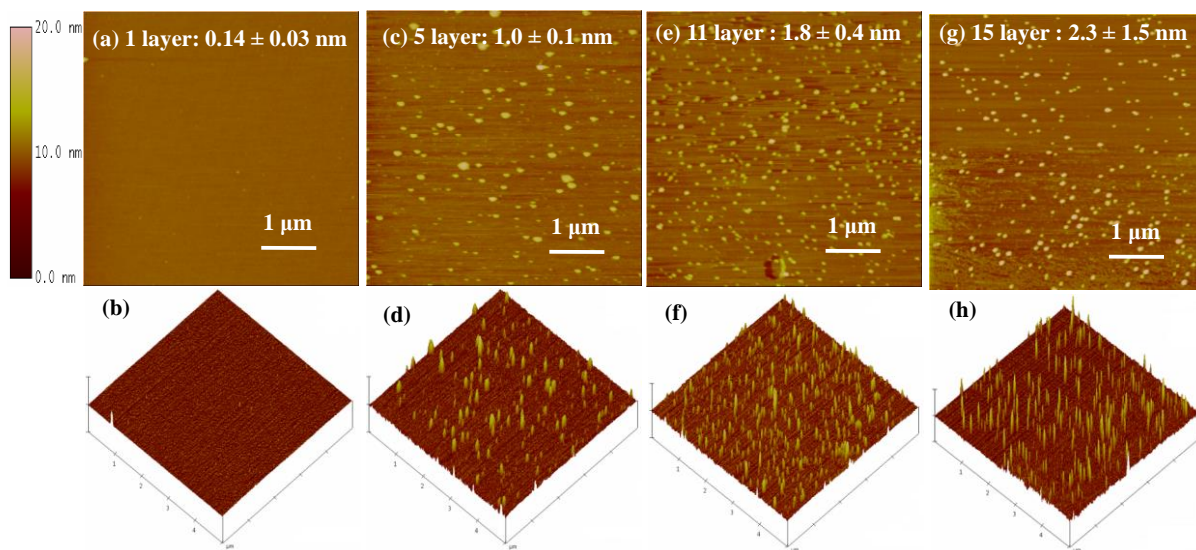
Figure 7.15. Surface roughness measurements of 1-15 LB layers deposited on mica substrates at 25 mN/m. AFM height images (top) and 3D surface plots (bottom) for complex **1**: (a, b) 1, (c, d) 5, (e, f) 11, and (g, h) 15 layers; the scan size is 5 μm and the Z range is 20 nm for all images.
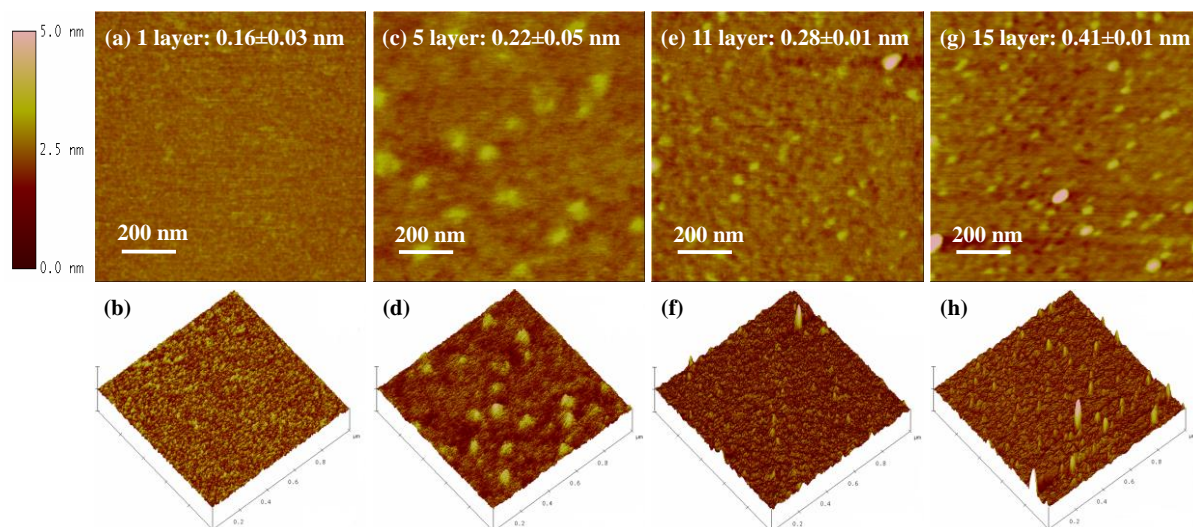
Figure 7.16. Surface roughness measurements of 1-15 LB layers deposited on mica substrates at 30 mN/m. AFM height images (top) and 3D surface plots (bottom) for complex **3**: (a, b) 1, (c, d) 5, (e, f) 11, and (g, h) 15 layers; the scan size is 1 μm and the Z range is 5 nm for the images.

Thickness measurements of mono and multilayer films up to 15 layers deposited onto quartz substrates were determined by carefully blade-scratching the films and measuring the depth of the scratch. AFM height images as well as their sectional analysis along the scratches for 15 layer films of complexes **1** and **3** are shown in **Figure 7.17** and **Figure 7.18**, respectively. Graphs obtained upon plotting layer number *vs.* layer thickness for complexes **1** and **3** showed a linear relationship indicating a homogeneous film deposition. The slopes of these plots indicate the monolayer thickness for complexes **1** and **3** were found to be 0.9 nm and 1.2 nm, respectively. According to the measured depth of the monolayer scratch, the thicknesses of the monolayer films were found to be approximately 1.2 nm. The surface roughness and thickness measurements are tabulated in **Table 7.7**. AFM results of complexes

1 and **3**, suggested the formation of smooth mono and multilayer films with low surface roughness to indicate homogeneous film deposition.
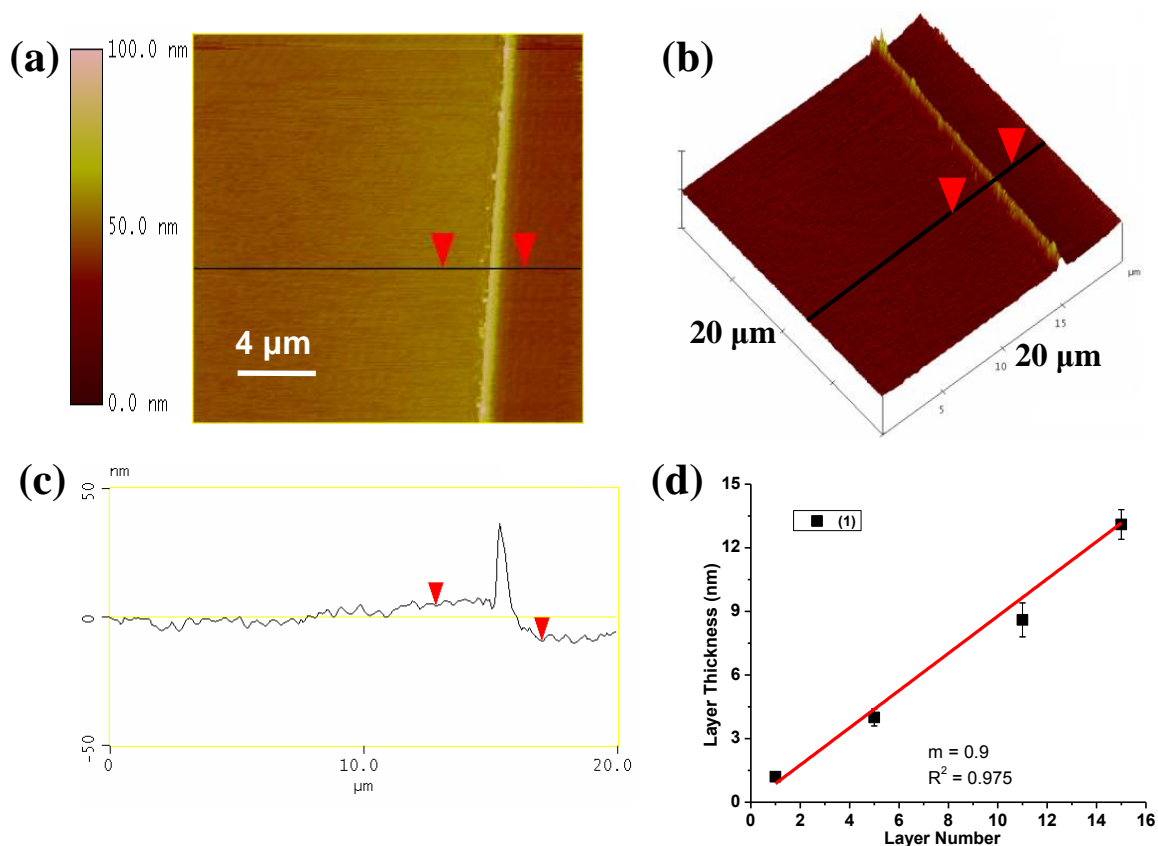
Figure 7.17. AFM height images and sectional analysis of complex **1** (15 layers) on quartz at 25 mN/m: (a) 2D view, (b) 3D view, (c) sectional analysis along the black solid line, and (d) plot between the thickness (nm) *vs*. number of layers from 1 to 15 layers.
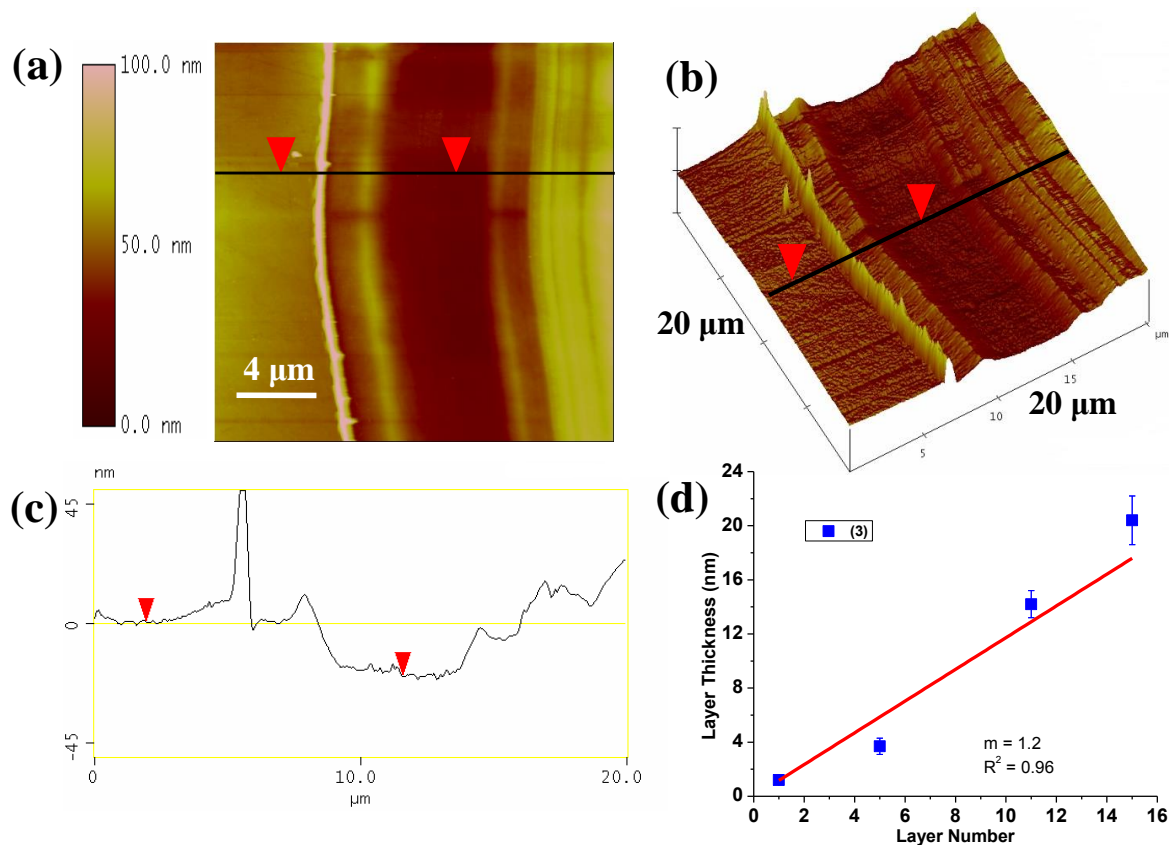
Figure 7.18. AFM height images and sectional analysis of complex **3** (15 layers) on quartz at 30 mN/m: (a) 2D view, (b) 3D view, (c) sectional analysis along the black solid line, and (d) plot between the thickness (nm) *vs.* number of layers from 1 to 15 layers.

Compound	Number of Layers	Surface Roughness (nm)	Thickness of the Film (nm)
(1)	1	0.14 ± 0.03	1.2 ± 0.1
	5	1.0 ± 0.1	4.0 ± 0.4
	11	1.8 ± 0.4	8.6 ± 0.8
	15	2.3 ± 1.5	13.1 ± 0.7
(3)	1	0.16 ± 0.03	1.2 ± 0.1
	5	0.22 ± 0.05	3.7 ± 0.6
	11	0.28 ± 0.01	14.2 ± 1.0
	15	0.41 ± 0.01	20.4 ± 1.8

Table 7.7. Summary of surface roughness and thickness data of 1-15 LB layers for complexes **1** and **3**

7.3.9 Device Fabrication and Current-Voltage Characterization

Complex **3** was used for device fabrication and I-V characterization, because it was the most promising candidate among the other manganese(III) complexes. Also the iron(III) complex which was synthesized using the ligand, **[H₃L⁴]** showed current rectification behavior. Complex **3** was also comprised of a [donor-acceptor][66] type structure similar to the iron(III) complex.[35] After the formation of a homogeneous film at the air/water interface, a monolayer of complex **3** was deposited onto pre-cleaned gold coated mica substrate at 30 mN/m. After drying the monolayer film inside a desiccator for 5 days, the top gold electrode

was deposited using shadow masking method. Using this method, a monolayer was sandwiched between two non-oxidizable gold electrodes to afford Au|LB-monolayer|Au device. Then, current-voltage (I-V) characteristics of the devices were measured at ambient conditions. Complex **3** showed an asymmetric I-V characteristic indicative of rectification behavior, nevertheless with a small magnitude of current (**Figure 7.19**). Rectification ratio (RR)[67] for complex **3** varied from 1.41 to 4.45 between -2 and +2 V and from 1.76 to 10.7 between -4 and +4 V. I-V characteristic data of complex **3** suggested the formation of an insulating layer, because complex **3** displayed very low current responses with negligible leakage currents even at high voltages. Therefore, complex **3** has the potential to be used as a dielectric layer in electronic components such as transistors.
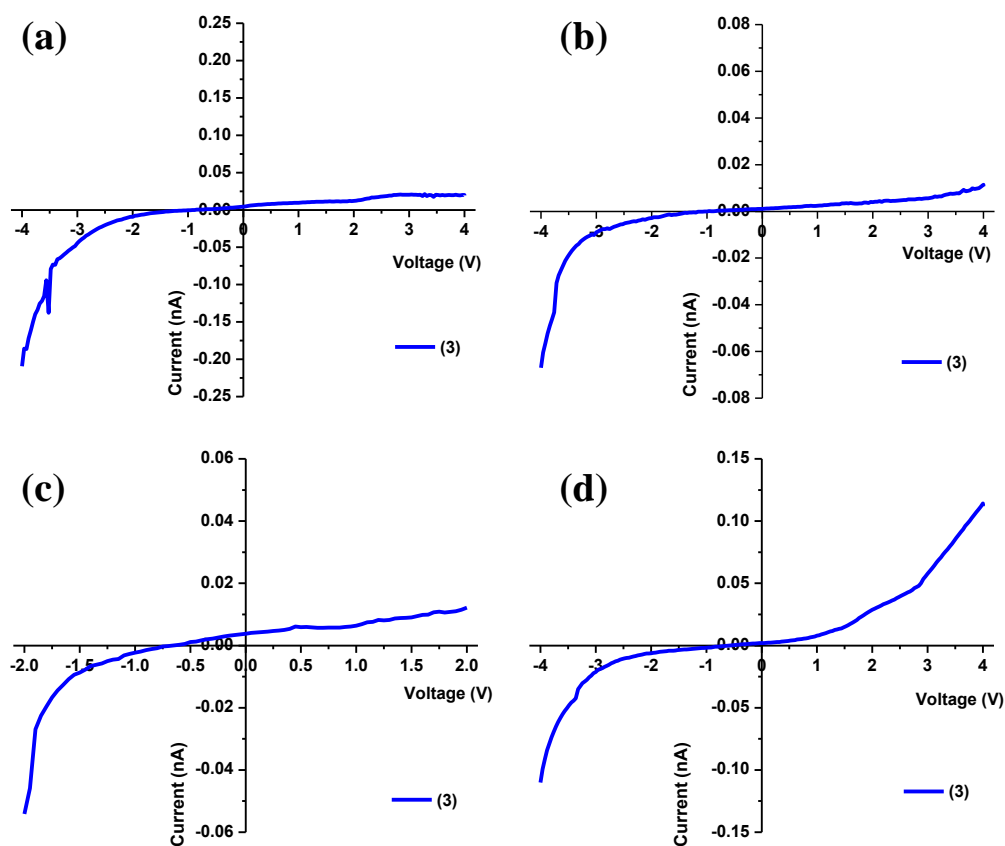
Figure 7.19. I-V characteristics of complex **3** (a) from 4 to -4 V, (b) lower current observed after multiple scans between 4 and -4 V (c) from 2 to -2 V, and (d) symmetrical response observed after multiple scans.

The observed small magnitude of current response could be related either to molecular, electronic, or film formation properties of complex **3**. According to the AFM studies, complex **3** showed highly homogeneous film formation properties and the surface passivation experiments showed at least five monolayers are necessary to observe complete surface passivation. The surface passivation experiment was carried out by immersing a gold working electrode with an area of 2 cm^2 in an aqueous solution of 1×10^{-3} $mol \cdot L^{-1}$

K$_3$[Fe(CN)$_6$] and 0.1 mol•L^{-1} in KCl. Then the redox response obtained for the Fe(II)/Fe(III) couple was recorded. During the experiment a Ag/AgCl Reference electrode and a Pt Auxiliary electrode were used and scans were recorded at a rate of 50 mV/s. Initially, the redox response was recorded using a bare gold electrode. Then redox responses were recoded with electrodes which were modified by depositing LB monolayers of complex **3** (at different surface pressures) and 5 layers at 30 mN/m (**Figure 7.20**). According to these results, the insulating behavior of complex **3** could arise due to electronic, structure, or unfitting HOMO-LUMO energy gaps with Fermi levels of metal electrodes.
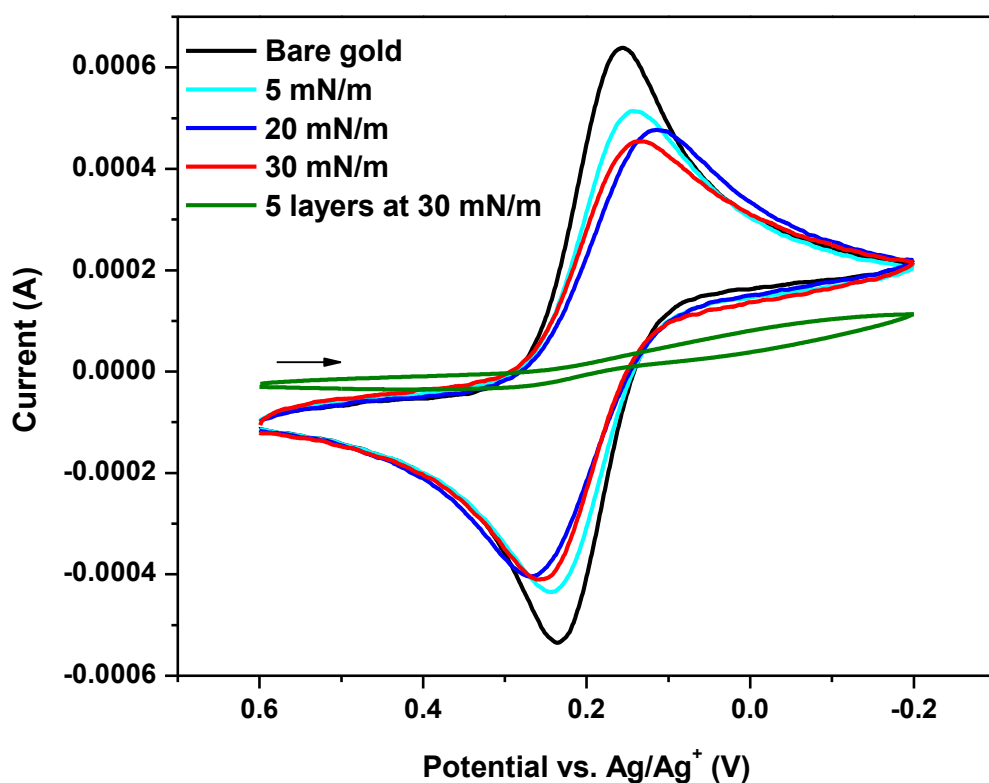
Figure 7.20. Cyclic voltammograms obtained for complex **3** during the surface passivation experiment.

7.4 Conclusions

This chapter described the characterization of new series of $[N_2O_3]$- and $[N_2O_2]$-containing manganese complexes that were synthesized in an attempt to merge amphiphilic and redox properties. The ligand systems in this chapter were able to stabilize manganese(III) ions in pentacoordinate or hexacoordinate geometries. Mononuclear metal complexes showed ligand- and metal-centered redox properties. Complexes **1**-**5** showed diverse amphiphilic properties at the air/water interface. Complexes **1**, **3**, **4**, and **5** showed homogeneous film formation properties. According to mass spectrometry, UV-visible and IRRAS spectroscopic studies, LB films exhibited crystalline-like well-packed topologies on solid substrates without structure decomposition. The film formation ability of complex **2** at the air/water interface was found to be weak due to the elevated hydrophobic nature of the compound. Studies that were performed in assessing the properties of complexes **1**-**6**, suggested that both amphiphilic and redox properties can be merged into a single molecule. Current-voltage measurements carried out for Au|LB-monolayer|Au devices of complex **3** displayed poor current responses and suggested an insulator-like behavior.

REFERENCES

1. Rocha, A. R.; García-Suárez, V. M.; Bailey, S.; Lambert, C.; Ferrer, J.; Sanvito, S. *Physical Review B* **2006**, *73*, 085414.

2. Ding, W.; Negre, C. F. A.; Vogt, L.; Batista, V. S. *J. Phys. Chem. C* **2014**, *118*, 8316.

3. Feng, M.; Guo, X.; Lin, X.; He, X.; Ji, W.; Du, S.; Zhang, D.; Zhu, D.; Gao, H. *J. Am. Chem. Soc.* **2005**, *127*, 15338.

4. Collier, C. P.; Wong, E. W.; Belohradsky, M.; Raymo, F. M.; Stoddart, J. F.; Kuekes, P. J.; Williams, R. S.; Heath, J. R. *Science* **1999**, *285*, 391.

5. Huang, Y.; Duan, X.; Cui, Y.; Lauhon, L. J.; Kim, K.-H.; Lieber, C. M. *Science* **2001**, *294*, 1313.

6. McNamara, W. R.; Snoeberger III, R. C.; Li, G.; Schleicher, J. M.; Cady, C. W.; Poyatos, M.; Schmuttenmaer, C. A.; Crabtree, R. H.; Brudvig, G. W.; Batista, V. S. *J. Am. Chem. Soc*. **2008**, *130*, 14329.

7. Ding, W.; Negre, C. F. A.; Palma, J. L.; Durrell, A. C.; Allen, L. J.; Young, K. J.; Milot, R. L.; Schmuttenmaer, C. A.; Brudvig, G. W.; Crabtree, R. H.; Batista, V. S. *ChemPhysChem* **2014**, *15*, 1138.

8. Palma, J. L.; Cao, C.; Zhang, X.-G.; Krstic, P. S.; Krause J. L.; Cheng, H.-P. *J. Phys. Chem. C* **2010**, *114*, 1655.

9. Palma, J. L.; Allen, L. J.; Young, K. J.; Milot, R. L.; Schmuttenmaer, C. A.; Brudvig, G. W.; Crabtree, R. H.; Batista, V. S. *Preprints of Symposia - American Chemical Society, Division of Fuel Chemistry* **2012**, *57*, 32.

10. Meyer, T. J.; Huynh, M. H. V.; Thorp, H. H.; *Angew. Chem. Int. Ed.* **2007**, *46*, 5284.

11. Sunatsuki, Y.; Kishima, Y.; Kobayashi, T.; Yamaguchi, T.; Suzuki, T.; Kojima, M.; Krzystek, J.; Sundberg, M. R.; *Chem. Commun.* **2011**, *47*, 9149.

12. Law, N. A.; Claudle, M. T.; Pecoraro, V. L. *Adv. Inorg. Chem.* **1998**, *46*, 305.

13. Dempsey, J. L.; Esswein, A. J.; Manke, D. R.; Rosenthal, J.; Soper, J. D.; Nocera, D. G. *Inorg. Chem.* **2005**, *44*, 6879.

14. Cady, C. W.; Crabtree, R. H.; Brudvig, G. W. *Coord. Chem. Rev.* **2008**, *252*, 444.

15. Jurss, J. W.; Concepcion, J. C.; Norris, M. R.; Templeton, J. L.; Meyer, T.J. *Inorg. Chem.* **2010**, *49*, 3980.

16. Chen, Z.; Concepcion, J. J.; Hull, J. F.; Hoertz, P.G.; Meyer, T. J. *Dalton Trans.* **2010**, *39*, 6950.

17. Concepcion, J. J.; Jurss, J. W.; Hoertz, P. G.; Meyer, T. J. *Angew. Chem. Int. Ed.* **2009**, *48*, 9473.

18. Brennaman, M. K.; Patrocinio, A. O. T.; Song, W.; Jurss, J. W.; Concepcion, J. J.; Hoertz, P. G.; Traub, M. C.; Murakami Iha, N. Y.; Meyer, T. J. *ChemSusChem* **2011**, *4*, 216.

19. McNamara, W. R.; Milot, R. L.; Song, H.; Snoeberger III, R. C.; Batista, V. S.; Schmuttenmaer, C. A.; Brudvig, G. W.; Crabtree, R. H. *Energy Environ. Sci.* **2010**, *3*, 917.

20. Shakya, R.; Hindo, S. S.; Wu, L.; Ni, S.; Allard, M.; Heeg, M. J.; da Rocha, S. R. P.; Yee, G. T.; Hratchian, H. P.; Verani, C. N. *Chem. Eur. J.* **2007**, *13*, 9948.

21. Shakya, R.; Hindo, S. S.; Wu, L.; Allard, M. M.; Heeg, M. J.; Hratchian, H. P.; McGarvey, B. R.; da Rocha, S. R. P.; Verani, C. N. *Inorg. Chem.* **2007**, *46*, 9808.

22. Driscoll, J. A.; Allard, M. M.; Wu, L.; Heeg, M. J.; da Rocha, S. R. P.; Verani, C. N. *Chem. Eur. J.* **2008**, *14*, 9665.

23. Hindo, S. S.; Shakya, R.; Rannulu, N. S.; Allard, M. M.; Heeg, M. J.; Rodgers, M. T.; da Rocha, S. R. P.; Verani, C. N. *Inorg. Chem.* **2008**, *47*, 3119.

24. Lesh, F. D.; Hindo, S. S.; Heeg, M. J.; Allard, M. M.; Jain, P.; Peng, B.; Hryhorczuk, L.; Verani, C. N. *Eur. J. Inorg. Chem.* **2009**, 345.

25. Lesh, F. D.; Shanmugam, R.; Allard, M. M.; Lanznaster, M.; Heeg, M. J.; Rodgers, M. T.; Shearer, J. M.; Verani, C. N. *Inorg. Chem.* **2010**, *49*, 7226.

26. Lanznaster, M.; Hratchian, H. P.; Heeg, M. J.; Hryhorczuk, L. M.; McGarvey, B. R.; Schlegel, H. B.; Verani, C. N. *Inorg. Chem.* **2006**, *45*, 955.

27. Lanznaster, M.; Heeg, M. J.; Yee, G. T.; McGarvey, B. R.; Verani, C. N. *Inorg. Chem.* **2007**, *46*, 72.

28. Shakya, R.; Allard, M. M.; Johann, M.; Heeg, M. J.; Rentschler, E.; Shearer, J. M.; McGarvey, B.; Verani, C. N. *Inorg. Chem.* **2011**, *50*, 8356.

29. Lesh, F. D.; Allard, M. M.; Shanmugam, R.; Hryhorczuk, L. M.; Endicott, J. F.; Schlegel, H. B.; Verani, C. N. *Inorg. Chem.* **2011**, *50*, 969.

30. Zhang, W.; Loebach, J. L.; Wilson, S. R.; Jacobsen, E. N. *J. Am. Chem. Soc.* **1990**, *112,* 2801.

31. Yoon, T. P.; Jacobsen, E. N. *Science* **2003**, *299*, 1691.

32. Schmitt, H.; Lomoth, R.; Magnuson, A.; Park, J.; Fryxelius, J.; Kritikos, M.; Martensson, J.; Hammarstrom, L.; Sun, L.; Akermark, B. *Chem. Eur. J.* **2002**, *8*, 3757.

33. Bonadies, J. A.; Kirk, M. L.; Lah, M. S.; Kessissoglou, D. P.; Hatfield, W. E.; Pecoraro, V. L. *Inorg. Chem.* **1989**, *28*, 2037.

34. Kurahashi, T.; Fujii, H. *J. Am. Chem. Soc.* **2011**, *133*, 8307.

35. Wickramasinghe, L. D.; Perera, M. M.; Li, L.; Mao, G.; Zhou, Z.; Verani, C. N. *Angew. Chem. Int. Ed*. **2013**, *52*, 13346.

36. Nakamoto, K. *Infrared and Raman Spectra of Inorganic and Coordination Compounds, Part B: Applications in Coordination, Organometallic and Bioinorganic Chemistry,* 6th ed.; John Wiley & Sons, Inc, Hoboken, New Jersey, 2008; chapter 1, pp 1-275.

37. Miyasaka, H.; Clerac, R.; Ishii, T.; Chang, H-C.; Kitagawa, S.; Yamashita, M. *J. Chem. Soc., Dalton Trans.* **2002**, 1528.

38. Chandra, S. K.; Chakraborty, P.; Chakravorty, A. *J. Chem. Soc., Dalton Trans.* **1993**, 863.

39. Kochem, A.; Jarjayes, O.; Baptiste, B.; Philouze, C.; Vezin, H.; Tsukidate, K.; Tani, F.; Orio, M.; Shimazaki, Y.; Thomas, F. *Chem. Eur. J*. **2012**, *18*, 1068.

40. Auerbach, U.; Eckert, U.; Wieghardt, K.; Nuber, B.; Weiss, J. *Inorg. Chem.* **1990,** *29,* 938.

41. Karsten, P.; Neves, A.; Bortoluzzi, A. J.; Strahel, J.; Maichle-Mossmer, C. *Inorganic Chemistry communications* **2002**, *5*, 434.

42. Shongwe, M. S.; Mikuriya, M.; Nukada, R.; Ainscough, E. W.; Brodie, A. M.; Waters, J. M. *Inorganica Chimica Acta* **1999**, *290*, 228.

43 Anjos, A.; Bortoluzzi, A. J.; Caro, M. S. B.; Peralta, R. A.; Friedermann, G. R.; Mangrich, A. S.; Neves, A. *J. Braz. Chem. Soc.* **2006**, *17*, 1540.

44. Rotthaus, O.; Jarjayes, O.; Philouze, C.; Valle, C. P. D.; Thomas, F. *Dalton Trans.* **2009**, 1792.

45. Neves, A.; Erthal, S. M. D.; Vencato, I.; Ceccato, A. S. *Inorg. Chem.* **1992,** *31,* 4749.

46. Belal, A. A.; Chaudhuri, P.; Fallis, I.; Farrugia, L. J.; Hartung, R.; Macdonald, N. M.; Nuber, B.; Peacock, R. D.; Weiss, J.; Wieghardt, K. *Inorg. Chem*. **1991,** *30***,** 4397.

47. Bonadies, J. A.; Maroney, M. J.; Pecoraro, V. L. *Inorg. Chem.* **1989,** *28*, 2044.

48. Panja, A.; Shaikh, N.; Gupta, S.; Butcher R. J.; Banerjee, P. *Eur. J. Inorg. Chem.* **2003**, 1540.

49. Hoogenraad, M.; Ramkisoensing, K.; Gorter, S.; Driessen, W. L.; Bouwman, E.; Haasnoot, J. P.; Reedijk, J.; Mahabiersing T.; Hartl, F. *Eur. J. Inorg. Chem.* **2002**, 377.

50. Gandolfi, C.; Cotting, T.; Martinho, P. N.; Sereda, O.; Neels, A.; Morgan, G. G.; Albrecht, M. *Dalton Trans*. **2011**, *40*, 1855.

51. Petty, M. C. *Langmuir Blodgett Films: an Introduction,* Cambridge University Press, New York, 1996.

52. Nagel, J.; Oertel, U.; Friedel, P.; Komber, H.; Möbius, D. *Langmuir* **1997**, *13*, 4693.

53. Galvan-Miyoshi, J.; Ramos, S.; Ruiz-Garcia, J.; Castillo, R. *J. Chem. Phys.* **2001**, *115*, 8178.

54. (a) Kundu, S.; Datta, A.; Hazra, S. *Langmuir* **2005**, *21*, 5894. (b) Kundu, S.; Datta, A.; Hazra, S. *Phys. Rev. E* **2006**, *73*, 051608.

55. Flach, C. R.; Xu, Z.; Bi, X.; Brauner, J. W.; Mendelsohn, R. *Applied Spectroscopy* **2001**, *55*, 1060.

56. Dhanabalan, A.; Mello, S. V.; Oliveira Jr, O. N. *Macromolecules* **1998**, *31,* 1827.

57. Menzel, H.; McBride, J. S.; Weichart, B.; Ruther, M. *Thin Solid Films* **1996**, *284-285*, 640.

58. Menzel, H.; Weichart, B. *Langmuir* **1994**, *10*, 1926.

59. Engelking, J.; Menzel, H. *Thin Solid Films* **1998**, *90*, 327.

60. Wang, L.; Cruz, A.; Flach, C. R.; Pérez-Gil, J.; Mendelsohn, R. *Langmuir* **2007,** *23,* 4950.

61. Brezesinski, G.; Dobner, B.; Stefaniu, C.; Vollhardt, D. *Langmuir* **2011**, 27, 5386.

62. Hamoudi, H.; Chesneau, F.; Patze, C.; Zharnikov, M. *J. Phys. Chem. C.* **2011,** *115,* 534.

63. Brezesinski, G.; Dobner, B.; Stefaniu, C.; Vollhardt, D. *J. Phys. Chem. C*. **2011**, *115*, 8206.

64. Trimpin, S.; Inutan, E. D. *Analytical Chemistry* **2013**, *85*, 2005.

65. Kattner, J.; Hoffmann, H. *External reflection spectroscopy of thin films on dielectric substrates: Hand book of vibrational spectroscopy;* John Wiley & Sons Ltd., Chichester, 2002; pp 12-14.

66. (a) Ashwell, G. J.; Urasinska, B.; Tyrrell, W. D. *Phys. Chem. Chem. Phys.* **2006**, *8*, 3314. (b) Ashwell, G. J.; Mohib A.; Miller, J. R. *J. Mater. Chem.* **2005**, *15*, 1160. (c) Ashwell, G. J.; Chwialkowska, A.; High, L. R. H. *J. Mater. Chem.* **2004**, *14*, 2848.

67. Metzger, R. M.; Chen, B.; Ho1pfner, U.; Lakshmikantham, M. V.; Vuillaume, D.; Kawai, T.; Wu, X.; Tachibana, H.; Hughes, T. V.; Sakurai, H.; Baldwin, J. W.; Hosch, C.; Cava, M. P.; Brehmer, L.; Ashwell, G. J. *J. Am. Chem. Soc.* **1997**, *119*, 10455.

CHAPTER 8

CONCLUSIONS AND PERSPECTIVES

In recent years, with the development of organic field effect transistors (FET)[1] and organic light emitting diodes,[2] organic soft materials have gained vast interest in the electronics field. Also, after introducing metal ions into these organic ligands, their electronic, redox, photochemical, and magnetic properties can be controlled.[3] Therefore, organic and inorganic systems that exhibit efficient electron transfers and that organize onto highly ordered assemblies are promising candidates in the molecule-based electronics field. Because the number of electrical components present on a chip doubles in every two years according to Moore's Law,[4] a huge barrier has formed in the development of high-tech electronic devices. Hence, molecule-based electronics have the potential to overcome the miniaturization of electrical components by eliminating the difficulties associated with semiconductor-based electronics, such as the leakage of current.[5]

For the first time in the field of molecular electronics, a current rectifier was theoretically analyzed by Aviram and Ratner.[6] Afterwards, many other groups provided experimental details regarding the use of organic materials as current rectifiers.[7] In search of new materials that can be used for current rectification and to improve the knowledge of inorganic metal complexes as current rectifiers, this dissertation research are involved in the development of [Donor-Acceptor] type redox non-innocent metal complexes for current rectification. These complexes have asymmetric molecular structures, and many of them have hydrophilic and hydrophobic moieties attached to the main ligand structure. Therefore, they display surfactant properties, and hence, they behave as metallosurfactants.

Film-formation studies have been carried out using the Langmuir-Blodgett (LB) method,[8,9] which is a method to develop ordered thin films with controlled thickness.

To serve this purpose, phenolate-containing ligand systems with $[N_2O_3]$ and $[N_2O_2]$ donor sets and their gallium(III), iron(III), and manganese(III) complexes have been designed and synthesized. These ligand systems were able to stabilize the low global symmetries which are necessary for molecular rectification. Mostly pentacoordinate geometries were observed around the trivalent metal ions. The ligand structures were also functionalized with various electron-donating and -withdrawing substituents to modulate the electronic, redox, and film formation properties of the systems. The primary goals of my dissertation research was focused on the investigation of structure, electronic, redox, and film formation properties of $[N_2O_3]$- and $[N_2O_2]$-containing gallium(III), iron(III), and manganese(III) complexes and the study of the rectification behavior of these complexes in nanoscale devices. Infrared, NMR, UV-visible, and electron paramagnetic resonance spectroscopic methods; mass spectrometry; elemental analysis; and X-ray diffraction were carried out to characterize the compounds. Redox properties of the compounds were assessed by cyclic voltammetry. Film formation properties and thin film characterization were investigated by Langmuir-Blodgett (LB) isothermal compression, Brewster angle microscopy, atomic force microscopy, contact angle measurements, and IR reflection/absorption spectroscopy. Finally, device fabrication was carried out to measure the current-voltage characteristics of the metallosurfactants that I synthesized.

Chapter 3 discussed the synthesis and characterization of asymmetric gallium(III) and iron(III) complexes coordinated to two nitrogen and three phenolate moieties. EPR studies showed that the iron(III) complexes are in their high spin state. These complexes

showed well-behaved redox properties with three ligand centered phenolate/phenoxyl redox couples. Iron(III) complexes showed one metal-centered cathodic redox process, and the gallium(III) complexes did not exhibit any metal mediated redox processes, due to its [Ar] $3d^{10}$ $4s^1$ state, which needs 1480 kcal/mol to form the gallium(IV) species. Therefore, the study of gallium(III) complexes was helpful in identifying the ligand mediated redox properties and to distinguish the redox processes belonging to the iron(III) center. Additionally, the gallium(III) ion has a radius of 7.6 Å, which is comparable to the high spin iron(III) (radius = 7.8 Å), and therefore, gallium(III) complexes are good comparisons for iron(III) complexes. The iron(III) and gallium(III) complexes showed good film formation properties at the air/water and air/slid interfaces, and suggested a possible amine/imine conversion at the air/water interface. However, when the alkoxy substituents are present on the phenylenediamine moiety, the complexes showed poor film formation properties and behaved as hydrophobes. The results obtained from this project suggested that film-formation and redox properties can be merged into a single molecule. Furthermore, the observed redox properties suggested that phenolate moieties can act as donors when coordinated trivalent metal ions and the iron(III) center can act as an electron acceptor. Finally, the data of this project proposed that, the properties of iron(III) complexes are suitable to carry out device fabrication to measure the current-voltage characteristics.

Chapter 4 presented the structure, electronic, redox, and film formation properties of two iron(III) complexes with different coordination environments. The ligands contained electron-withdrawing nitro substituents on the phenylenediamine moiety, and the introduction of redox-active nitro substituents were important in achieving more redox accessible states. Well-behaved redox properties were observed when iron(III) was

coordinated to the $[N_2O_3]$-containing ligand rather than to the $[N_2O_2]$ system. Thin film characterization data showed tightly packed, well-ordered anisotropic film deposition at the air/solid interface, and further evidence suggested that the molecular structure remained intact. Density functional theory (DFT) calculations were carried out to assign the redox sequence of the cathodic redox processes, and showed that the first reduction belonged to the Fe(III)/Fe(II) redox couple. Also, the introduction of nitro groups helped to lower the energy gap between highest occupied and lowest unoccupied molecular orbitals (HOMO-LUMO) and suggested that it is possible to access the Fe(III)/Fe(II) redox processes, when compared to complexes with electron-donating substituents on the phenylenediamine moiety. The data of this research project proposed that, different substituents on the phenylenediamine moiety help to fine-tune the electronic and redox properties.

Chapter 5 focused on the analysis of an iron(III)/phenolate system, which is suitable for device fabrication. This pentacoordinate iron(III) complex also showed an amine/imine conversion at the air/water interface and showed well-distinguished redox properties. The device fabrication was carried out by sandwiching a well-ordered LB monolayer between two gold electrodes. The current-voltage characteristics were measured across the LB monolayer. The Au|LB-monlayer|Au devices showed asymmetrical current responses, which were indicative of current rectifying behavior. This study showed that triphenolate-coordinated iron(III) systems are suitable for current rectification and suggested that the phenolate moieties and the metal center act as electron-donor (D) and electron-acceptor (A).

Chapter 6 investigated the possibility of using iron(III) complexes with $[N_2O_2]$ coordination environments for device fabrication and current rectification. To address these matters, two iron(III) complexes were synthesized using $[N_2O_2]$-containing salophen-type

ligands. Phenolate moieties were substituted with *tert*-butyl and nitro groups to modulate the redox and surfactant properties. The nitro substituted iron(III) complex formed a μ-oxo bridged species and showed poor solubility, and was not a suitable candidate for device fabrication studies. The *tert*-butyl substituted iron(III) complex showed well-behaved redox processes. Also, the spectroscopic analyses performed on LB films showed closely packed, well-ordered, anisotropic thin films with intact molecular structures. Then, Au|LB-monlayer|Au nanoscale devices were fabricated and current-voltage characteristics were measured. The electrical data of *tert*-butyl substituted iron(III) complex demonstrated asymmetrical current responses, indicative of current rectification. The DFT calculations and comparison studies carried out with a copper(II) analogue suggested, that the pentacoordinate geometry, which gives rise to the asymmetric nature of the metal complex, is crucial for current rectification. The data also suggested that the LUMO energy levels are metal-centered and the HOMO energy levels are ligand-centered. The DFT data showed that the singly occupied molecular orbitals (SOMO) can act as LUMOs due to the presence of five partially filled *d*-orbitals in the high spin iron(III) complex. Furthermore, calculations carried out using DFT and redox potentials for this [D-A] type iron(III) complex suggested that the SOMO energy level is accessible during the electron transfer process and HOMO is not involved in the electron transfer pathway. Therefore, the asymmetric current rectification mechanism is potentially applicable in this iron(III) complex.

In **Chapter 7**, a series of manganese(III) complexes were investigated to study the film formation and current rectification behavior. These manganese(III) complexes were synthesized with penta and hexacoordinate geometries. Manganese(III) complexes showed well-behaved redox properties with metal-centered manganese(III)/(II) redox processes.

Most of the complexes exhibited homogeneous film formation properties. The films were characterized with UV-visible and infrared reflection absorption spectroscopic methods to suggest that the molecular composition remained unchanged during the film formation and deposition processes. The complexes also displayed the formation of well-ordered films. The device fabrication was carried out for the most promising candidate, **[Mn^{III}L^{4I}]**, and showed asymmetric current responses with poor current amplitudes. The observed discrepancy of current responses between the iron(III) and manganese(III) complexes could be due to structure, electronic properties, to unfitting energies in the HOMO-LUMO energy gaps with Fermi levels of the metal electrode, or to both reasons. Thus, further investigations are necessary to unveil the cause to the observed discrepancy.

In summary, successful results were obtained in the synthesis and characterization of new [N$_2$O$_3$] and [N$_2$O$_2$] ligands, and their gallium(III), iron(III), and manganese(III) complexes. The investigations carried out on different phenolate based gallium(III), iron(III), and manganese(III) complexes showed successful results in merging redox and film formation properties into single molecular systems, where the different substituents on the phenylenediamine and phenolate moieties assisted the fine-tuning of redox and amphiphilic properties. The iron(III) complexes with both [N$_2$O$_3$] and [N$_2$O$_2$] environments showed asymmetrical current responses for Au|LB-monolayer|Au devices, indicative of current rectifying behavior. In iron(III)/phenolate systems, the asymmetrical nature of the complex helps in current rectification. The DFT and electrochemical calculations carried out for an iron(III) complex, suggested a possible asymmetric current rectification mechanism.

To improve the understanding of current rectification behavior in metallosurfactants, and to develop this research project further, a few studies can be suggested: one key

requirement for molecular rectification is the distinguished [D-A] type molecular structure. Typically, these two entities are separated via σ- or π-type bridge. Therefore, new molecular designs can be introduced to identify the role of the donors and acceptors. By introducing pyridine-containing groups (**Figure 8.1**), can hypothesize that the current rectification behavior to diminish, because the pyridine unit acts as an acceptor. Therefore, the typical [D-A] structure will become imbalanced.
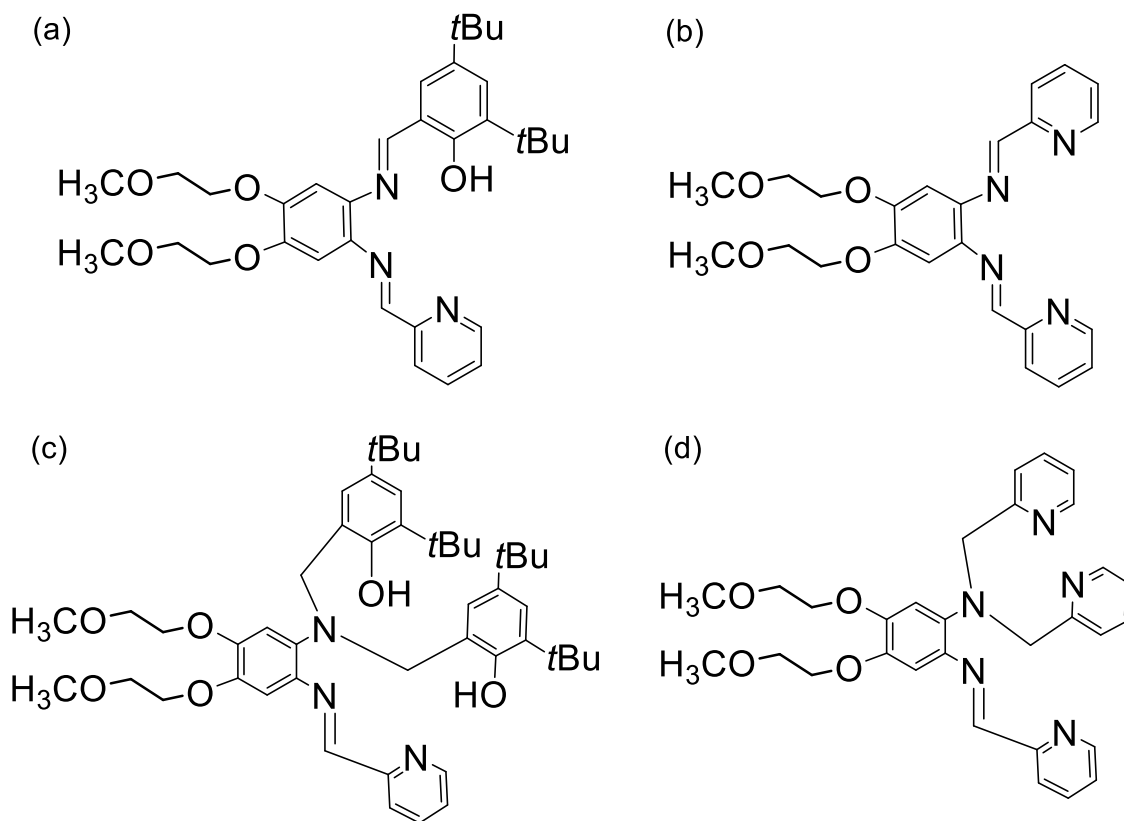
Figure 8.1. Proposed pyridine-containing ligands.

To have efficient electron transfer at the metal|molecule junction, the energy of the frontier molecular orbitals should be comparable to the metal Fermi level. Therefore, modulating the HOMO and LUMO energies with different substituents is expected to provide a better understanding about this phenomenon. The dissertation research (chapter 4

and 6) discussed some of the possibilities that can affect the energies of the frontier molecular orbitals. To analyze this concept further, a few possible ligand designs are shown in **Figure 8.2**.
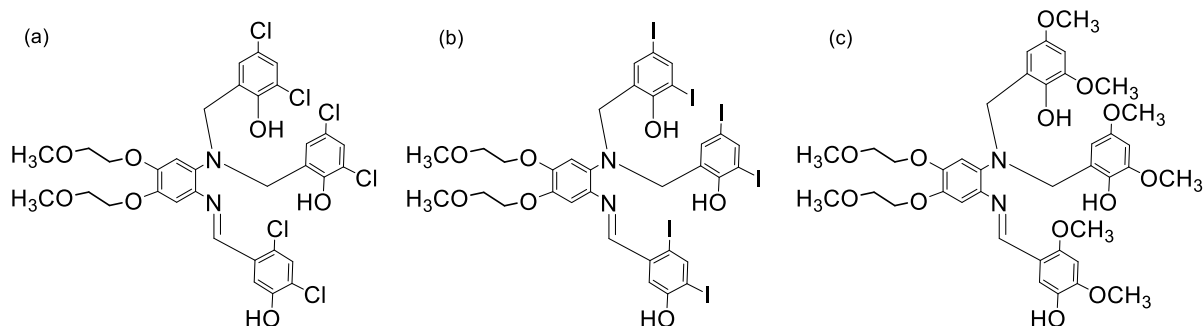
Figure 8.2. Proposed ligands to modulate the orbital energies.

The data discussed in this thesis, provide evidence to support, that iron(III) metal centers act as electron acceptors (A) and phenolate moieties act as electron donors (D). However, there was no clear evidence of a bridge between the two entities. Structures with distinguished donor and acceptor moieties that are separated via σ- or π-bridges are well-known.[7,10] In [D-σ-A] and [D-π-A] structures, the bridge helps avoid charge recombination. Therefore, to understand electrical communication between donor and acceptor moieties of iron(III)-containing metallosurfactants, iron(III) centers could be replaced by redox inactive metals, and a well-separated electron acceptor moiety could be introduced as shown in **Figure 8.3**.
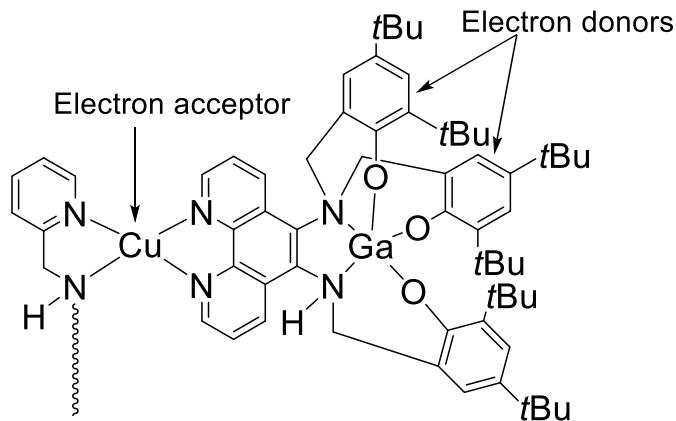
Figure 8.3. Proposed structure with distinguished donor and acceptor moieties.

This dissertation research discussed molecular systems with metal-based acceptors and ligand-based donors for current rectification. Therefore, the investigation of new molecular designs, which are based on ligand-mediated acceptors and donors (catechol-containing ligands), and metal-mediated donors, such as iron(II), cobalt(II), and ruthenium(II) ions, and ligand-mediated acceptors, such as terpyridine entities, are important for the development of molecular rectifiers. Proposed molecular designs are shown in **Figure 8.4**.
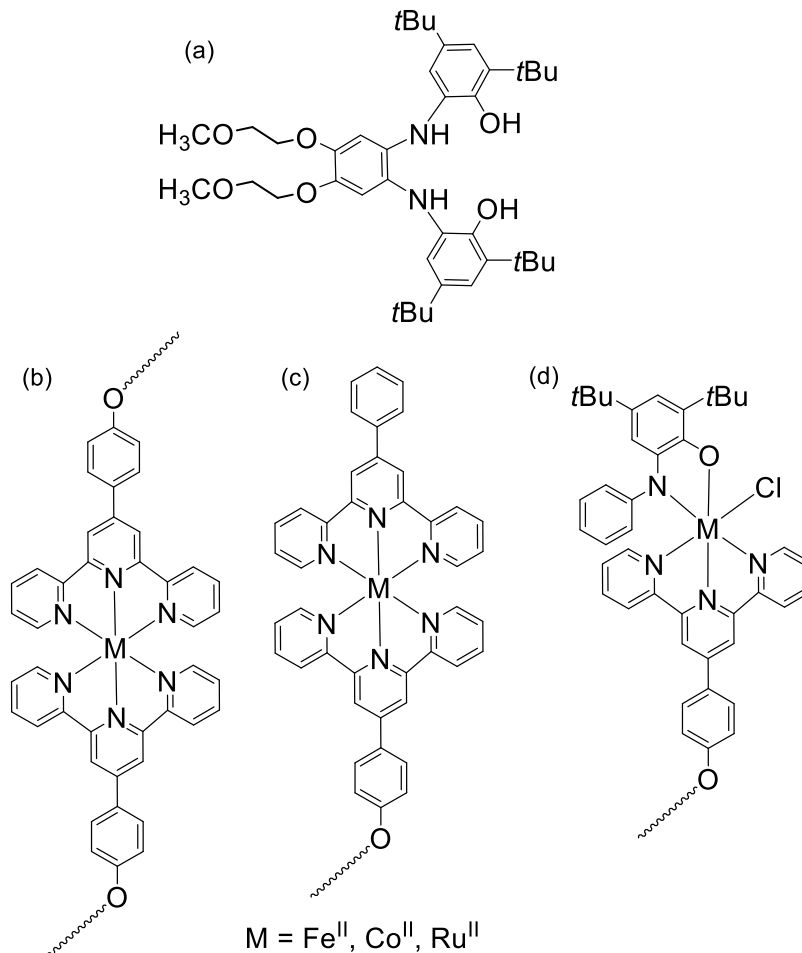
Figure 8.4. Proposed (a) ligand-based, and (b, c, d) metal- and ligand-based molecular structures.

Molecular rectification can occur via different mechanisms, such as Schottky, asymmetric, and unimolecular.[10] The Schottky rectification occurs when two different electrodes are used to fabricate the metal|molecule|metal devices. The other possibility is to form devices with different dipole moments at the two electrodes. Different dipole moments originate, when the monolayer attaches to one electrode via physisorption and to the other via chemisorption interactions. If devices are fabricated using the LB method, monolayers will attach to both electrodes via physisorption interactions. Self-assembly is also widely used for

device fabrication. During this method, self-assembled monolayers (SAM) will attach to the electrodes via physisorption and chemisorption interactions. Therefore, two similar metal-containing molecular structures can be used to study this concept. The proposed molecules for the formation of chemisorbed and physisorbed monolayers are shown in **Figure 8.5**. During this dissertation research, only the physisorption method was followed to obtain the nanoscale devices.
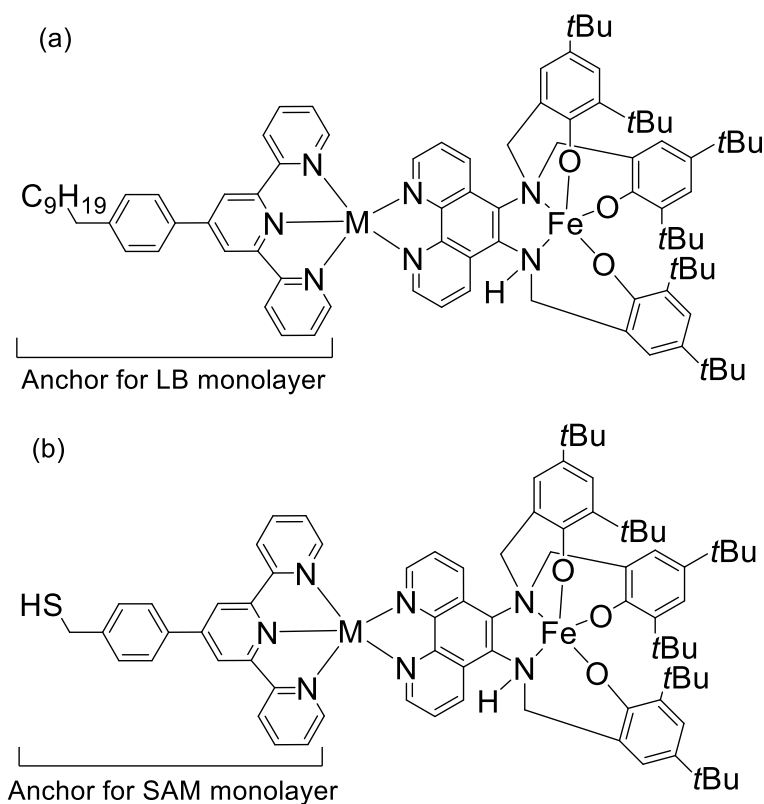
Figure 8.5. Proposed molecules for LB and SAM monolayers.

REFERENCE

1. Tans, S. J.; Devoret, M. H.; Dai, H.; Thess, A.; Smalley, R. E.; Geerligs L. J.; Dekker, C. *Nature* **1997**, *386*, 474.

2. Sun, Y.; Giebink, N. C.; Kanno, H.; Ma, B.; Thompson, M. E.; Forrest, S. R. *Letters to Nature* **2006**, *440*, 908.

3. Low, P. J. *Dalton Trans.* **2005**, 2821.

4. Lundstrom, M. *Science* **2003**, *299*, 210.

5. Roth, K. M.; Yasseri, A. A.; Liu, Z.; Dabke, R. B.; Malinovskii, V.; Schweikart, K.-H.; Yu, L.; Tiznado, H.; Zaera, F.; Lindsey, J. S.;Kuhr, W. G.; Bocian,D. F. *J. Am. Chem. Soc.* **2003**, *125*, 505.

6. Aviram, A.; Ratner, M. A. *Chem. Phys. Lett.* **1974**, *29*, 277.

7. Metzger, R. M. *J. Mater. Chem.* **2008**, *18*, 4364.

8. Blodgett, K. B. *J. Am. Chem. Soc.* **1935**, *57*, 1007.

9. Blodgett, K. B.; Langmuir, I. *Phys. Rev*. **1937**, *51*, 964.

10. Metzger, R. M. *Chem. Rev*. **2003**, *103*, 3803.

APPENDIX A

Characterization of Compounds Not Included in Chapters

N,N'-(4,5-Bis(octadecyloxy)-1,2-phenylene)dipicolinamide and its gallium(III) complex were synthesized and structurally characterized using multiple methods.
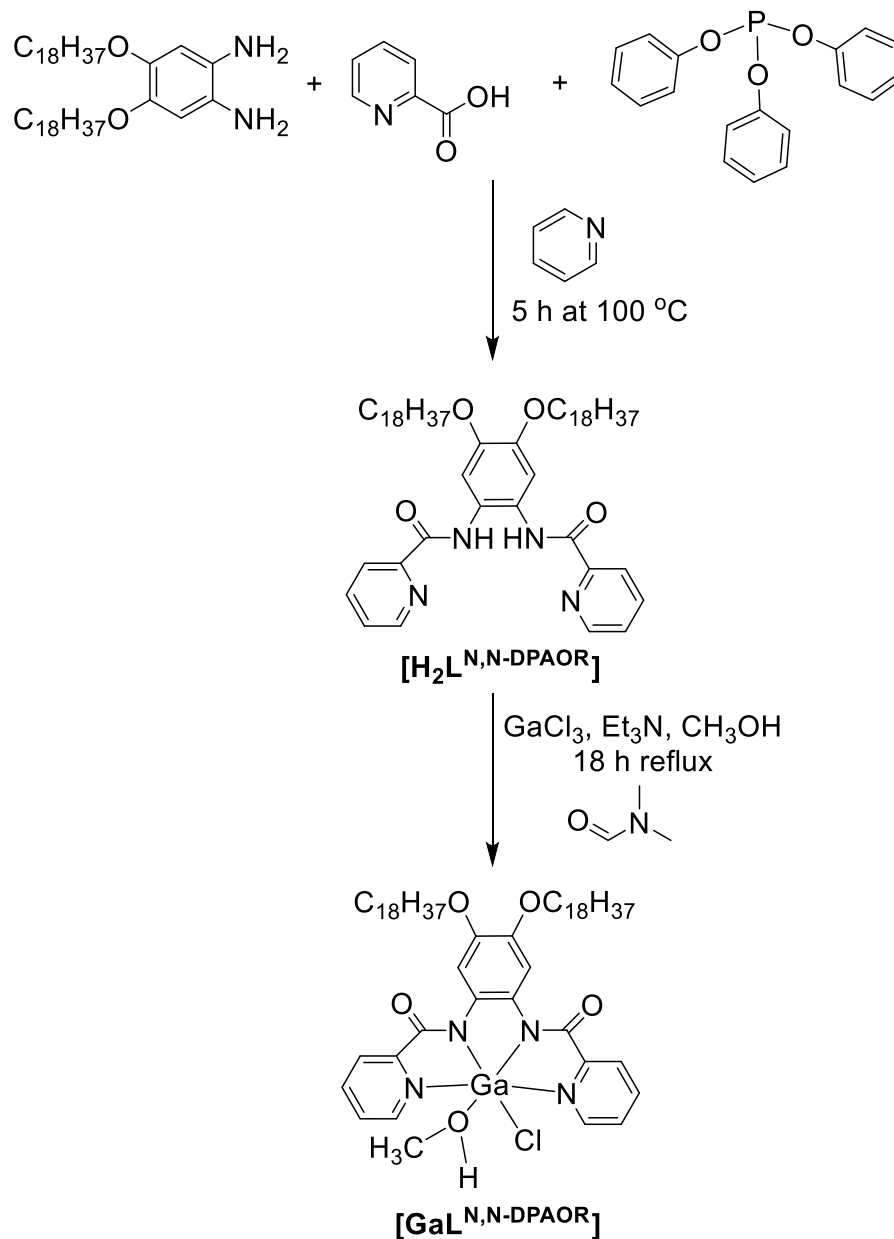
Scheme A.1. Synthesis of ligand **[H₂L$^{N,N-DPAOR}$]** and its gallium(III) complex **[GaL$^{N,N-DPAOR}$]**.

Synthesis of [H₂L^{N,N-DPAOR}], *N,N'-(4,5-bis(octadecyloxy)-1,2-phenylene)dipicolinamide.*

To a mixture of picolinic acid (0.401 g, 3.26 mmol) and triphenyl phosphite (1.01 g, 0.860 ml, 3.26 mmol) in anhydrous pyridine (10 mL), a solution of 4,5-bis(octadecyloxy)benzene-1,2-diamine (1.05 g, 1.63 mmol) in anhydrous pyridine (20 mL) was cannulated under inert conditions. This solution was heated in a water bath for 5 hours. Then the solution was stored at ambient conditions for 18 hours and ~ 5 mL of methanol was added to the obtained golden brown solution. The pale brown precipitate obtained after standing at room temperature for 18 hours was filtered and washed with methanol to obtain a pale yellow precipitate of **[H₂L^{N,N-DPAOR}]**. Yield: 55.9%. ESI (m/z^+) = 855.6721 (100%) for [$C_{54}H_{86}N_4O_4 + H^+$] (calculated = 855.6727) in agreement with -0.7 ppm difference. ^{1}H NMR, ppm (CDCl₃, 400 MHz): δ 0.855 (t, 6H^{CH3}), 1.233 (s, 56H^{CH2}), 1.448 (quin, 4H^{CH2}), 1.812 (quin, 4H^{CH2}), 4.021 (t, 4H^{OCH2}), 7.407 (s, 2H^{ph}), 7.433 (td, 2H^{py}), 7.875 (td, 2H^{py}), 8.283 (dd, 2H^{py}), 8.533 (dd, 2H^{py}), 10.096 (s, 2H^{NH}). IR (KBr, cm⁻¹) 3301 (ν_{N-H}), 2850-2920 (ν_{C-H}), 1660-1680 ($\nu_{C=O}$), 1609, 1591, 1570, and 1529 ($\nu_{C=C}$, aromatic and $\nu_{C=N}$, pyridine), 1236 (ν_{C-O-C}).

Synthesis of complex [GaL^{N,N-DPAOR}].

To a anhydrous N,N-dimethylformamide solution (15 mL) of **[H₂L^{N,N-DPAOR}]** (0.150 g, 0.175 mmol) and triethylamine (0.110 ml, 0.750 mmol) was slowly added a methanolic solution (5 mL) of GaCl₃ (0.031 g, 0.175 mmol) under inert conditions. The obtained solution was heated at reflux for 18 hours. After allowing the reaction mixture to reach ambient temperature, 10 mL of methanol was added, and the resulting mixture was stored at 4 °C for 18 h. The precipitate was filtered, washed with methanol, and dried to yield an

orange solid of **[GaL$^{N,N-DPAOR}$]**. Yield: 91.4%. ESI (m/z^+) = 953.6012 for [C$_{55}$H$_{88}$N$_4$O$_5$Ga$^+$] (calculated = 953.6011) in agreement with 0.1 ppm difference. Anal. Calc. for [C$_{55}$H$_{88}$N$_4$O$_5$ClGa]: C, 66.69; H, 8.96; N, 5.66%. Found: C, 67.04; H, 9.20; N, 5.29%. IR (KBr, cm^{-1}) 2850-3070 (v_{C-H}), 1626-1680 ($v_{C=O}$), 1596, 1566, and 1529 ($v_{C=C}$, aromatic and $v_{C=N}$, pyridine), 1232 (v_{C-O-C}).

Electronic and Redox Properties of [H$_2$L$^{N,N-DPAOR}$] and [GaL$^{N,N-DPAOR}$]

The UV-visible spectra of ligand, **[H$_2$L$^{N,N-DPAOR}$]** and gallium(III) complex were measured using 1×10^{-4} mol•L^{-1} dichloromethane solution. The uncoordinated ligand, **[H$_2$L$^{N,N-DPAOR}$]** showed two bands at 253 nm (ε, ~ 16100 L•mol^{-1}•cm^{-1}) and 312 nm (ε, ~ 9900 L•mol^{-1}•cm^{-1}). Complex **[GaL$^{N,N-DPAOR}$]** showed absorption bands at 252 nm (ε, ~ 17000 L•mol^{-1}•cm^{-1}), 321 nm (ε, ~ 7970 L•mol^{-1}•cm^{-1}), and ~ 425 nm (ε, ~ 3880 L•mol^{-1}•cm^{-1}). These bands can be assigned to be intra-ligand $\pi \rightarrow \pi^*$ charge transitions.[1,2] The obtained UV-visible spectra are shown in the **Figure A.1** and the data are tabulated in **Table A.1**.

Compound	λ_{max}(nm), ε (L•mol^{-1}•cm^{-1}) (CH$_2$Cl$_2$)
[H$_2$L$^{N,N-DPAOR}$]	253 (16112), 312 (9895)
[GaL$^{N,N-DPAOR}$]	252 (17006), 321 (7966), ~ 425 (3882)

Table A.1. The UV-visible spectroscopic data of ligand, **[H$_2$L$^{N,N-DPAOR}$]** and **[GaL$^{N,N-DPAOR}$]** in 1.0×10^{-4} mol•L^{-1} dichloromethane solutions.
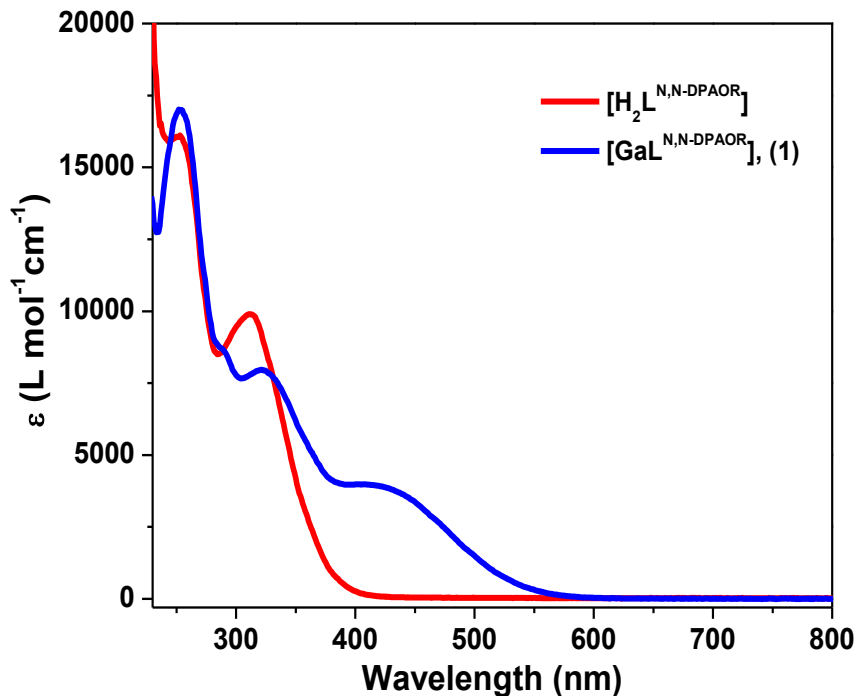
Figure A.1. The UV-visible spectra of **[H₂L^{N,N-DPAOR}]** and **[GaL^{N,N-DPAOR}]** in 1.0×10^{-4} mol•L^{-1} dichloromethane solutions.

The cyclic voltammetry data of **[GaL^{N,N-DPAOR}]** was recorded in dichloromethane using TBAPF₆ as the supporting electrolyte. All potential values were recorded versus the Fc$^+$/Fc couple. The cyclic voltammogram of **[GaL^{N,N-DPAOR}]** is given in **Figure A.2** and its potential values are given in **Table A.2**. **[GaL^{N,N-DPAOR}]** showed a ligand-centered oxidation and reduction processes in its cyclic voltammogram. The cathodic process appeared at ~ -2 V can be attributed to the pyridine reduction. **[GaL^{N,N-DPAOR}]** showed three well-defined quasi-reversible oxidation processes in its cyclic voltammogram. The oxidation process at ~ 0.22 V *vs.* Fc$^+$/Fc (ΔE_p = 0.09 V, $|I_{pa}/I_{pc}|$ = 1.27) can be assigned to the phenylenediamine bridge oxidation to form a delocalized π-radical species as seen in the literature.[2] The other two oxidation processes at ~ 0.53 V (ΔE_p = 0.12 V) and ~ 0.72 V (ΔE_p = 0.15 V, $|I_{pa}/I_{pc}|$ = 0.92)

vs. Fc⁺/Fc can be assigned to be ligand-based amide oxidations. Further experiments are necessary to distinguish each of these oxidation processes.
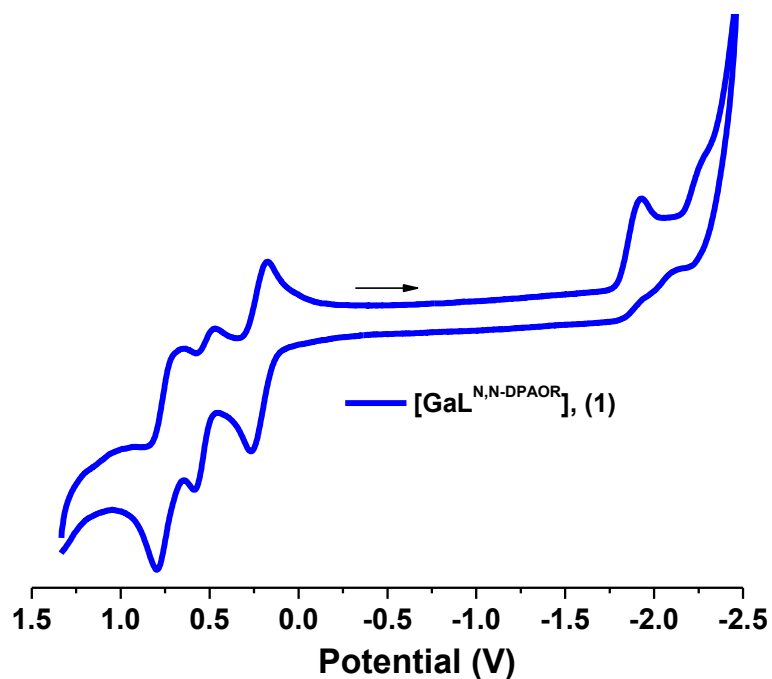
Figure A.2. Cyclic voltammogram of **[GaL$^{N,N\text{-}DPAOR}$]** in 1.0×10^{-3} mol•L^{-1} dichloromethane solutions.

E_{pc} (V)	$E_{1/2}$, (ΔE_p) (V) $\mid I_{pa}/I_{pc} \mid$	$E_{1/2}$, (ΔE_p) (V)	$E_{1/2}$, (ΔE_p) (V) $\mid I_{pa}/I_{pc} \mid$
-1.930	0.217 (0.094) $\mid 1.27 \mid$	0.527 (0.121)	0.722 (0.151) $\mid 0.92 \mid$

Table A.2. $E_{1/2}$ and ΔE_p values *vs.* Fc⁺/Fc for each of the redox processes shown by **[GaL$^{N,N\text{-}DPAOR}$]**.

2-Hydroxy-5-methylisophthalaldehyde and its copper(II) dimer-complex were synthesized and structurally characterized using multiple methods.
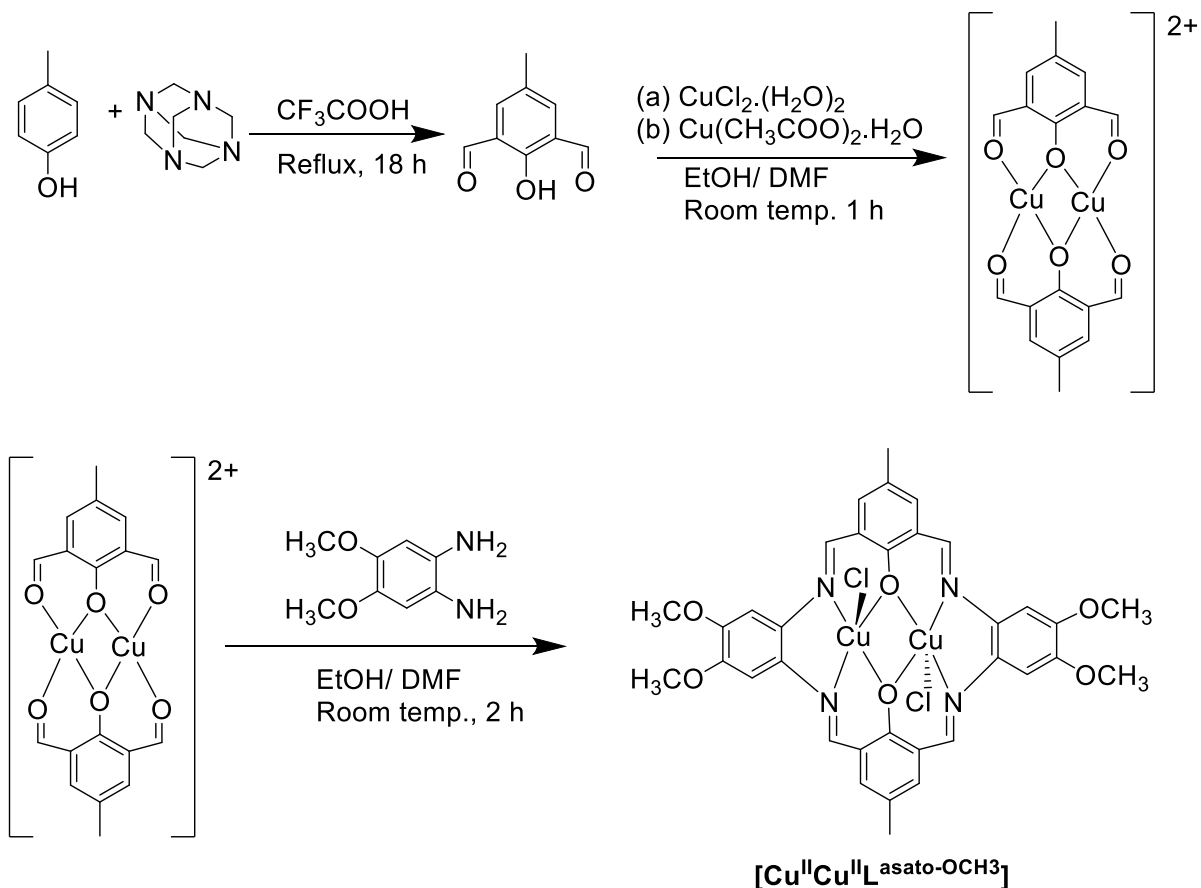
Scheme A.2. Synthesis of copper(II) complex **[Cu^II Cu^II L^asato-OCH3]**.

Templating reactions were followed to synthesize symmetrical bicompartmental copper(II) complex. 4,5-dimethoxybenzene-1,2-diamine[3] and 2-hydroxy-5-methylisophthalaldehyde[4] were used as precursor ligands (**Scheme A.2**).

Synthesis of metal complex [Cu^{II}Cu^{II}L$^{asato-OCH3}$]

After isolating 2-hydroxy-5-methylisophthalaldehyde, the compound was treated with metal salts [Cu(CH$_3$COO)$_2$·(H$_2$O) and CuCl$_2$·(H$_2$O)$_2$, (1:1)] for one hour at ambient temperature in anhydrous 10:1 ethanol/N,N-dimethylformamide solvent mixture (11 mL) to obtain the bi-metalated species. The mixture was further treated with 4,5-dimethoxybenzene-1,2-diamine in anhydrous ethanol for two hours under reflux conditions to obtain the Robson-type symmetric bimetallic macrocycle **[Cu^{II}Cu^{II}L$^{asato-OCH3}$]**. The metal complex **[Cu^{II}Cu^{II}L$^{asato-OCH3}$]** was insoluble in most organic solvents except for N,N-dimethylformamide and dimethyl sulfoxide. Yield: 25.2%. ESI (m/z^+) = 751.0438 for [C$_{34}$H$_{30}$N$_4$O$_6$ClCu$_2^+$]. Anal. Calc. for [C$_{34}$H$_{30}$N$_4$O$_6$Cl$_2$Cu$_2$·2H$_2$O]: C, 49.52; H, 4.16; N, 6.79%. Found: C, 49.37; H, 4.61; N, 7.53%. IR (KBr, cm^{-1}) 3005, 2942, 2837, 1609, 1571, 1509, 1465, 1439, 1410, 1377, 1352, 1331, 1303, 1277, 1223, 1182, 1113, 1063, 1031, 1002, 763.

REFERENCES

1. Fry, N. L.; Heliman, B. J.; Mascharank, P. K. *Inorg. Chem.* **2011**, *50*, 317.

2. Kochem, A.; Jarjayes, O.; Baptiste, B.; Philouze, C.; Vezin, H.; Tsukidate, K.; Tani, F.; Orio, M.; Shimazaki, Y.; Thomas, F. *Chem. Eur. J.* **2012**, *18*, 1068.

3. Rosa, D. T.; Reynolds, R. A.; Malinak, S. M.; Coucouvanis, D.; *Useful Reagents and Ligands. 4,5-Diaminocatechol: A Useful Building Block in Synthesis*, pp 112-115.

4. Knight, P. D.; White, A. J. P.; Williams, C. K. *Inorg. Chem.* **2008**, *47*, 11711.

APPENDIX B

Crystal structure data of complex **[Fe^{III}L$^{1'}$], (5'**) in **Chapter 3**
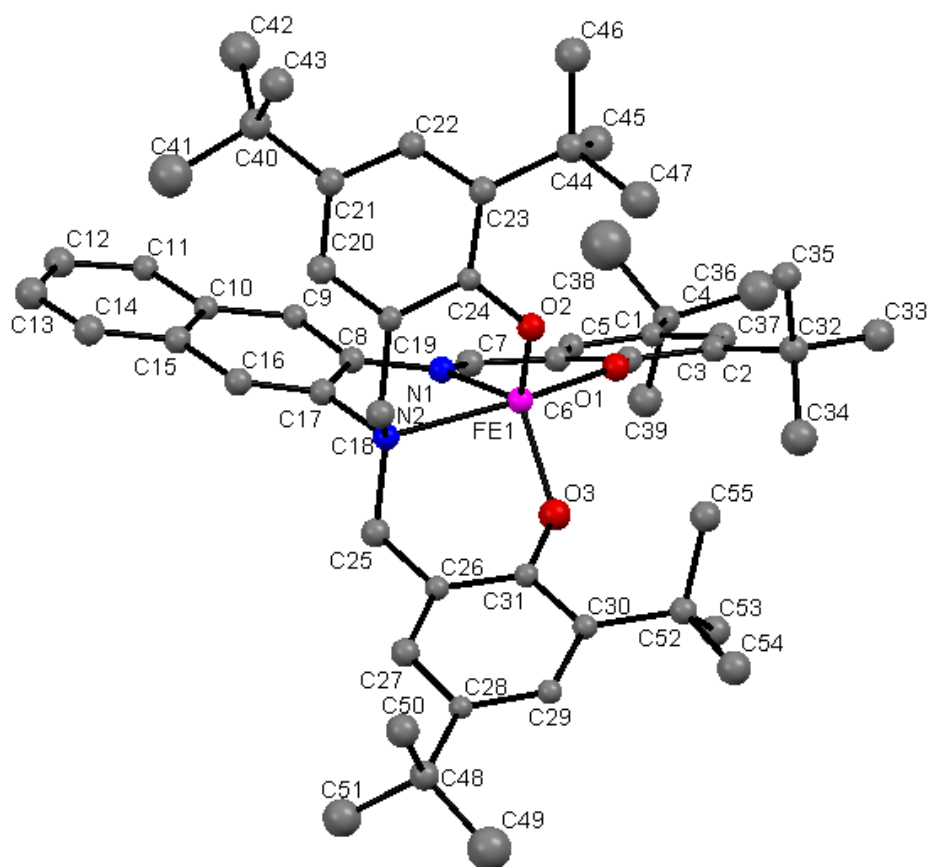
Figure B.1. X-ray crystal structure data of complex **[Fe^{III}L$^{1'}$], (5')**.

Formula	$C_{55}H_{71}FeN_2O_3$
M	863.99
Space group	P(-1)
a / Å	15.8704(5)
b/ Å	16.2473(4)
c/ Å	21.0057(6)
α/ °	84.049(1)
β/ °	71.559(1)
γ/ °	75.613(1)
V/ Å^3	4975.2(2)
Z	4
T/ K	100(2)
λ/ Å	0.71073
D_{calc}/ g cm^{-3}	1.153
μ/ mm^{-1}	0.346
R(F) (%)	4.93
Rw(F) (%)	10.08

$^a R(F) = \sum \| F_o | - | F_c \| / \sum | F_o | $; $Rw(F) = [\sum w(F_o^2 - F_c^2)^2 / \sum w(F_o^2)^2]^{1/2}$ for $I > 2\sigma(I)$

Table B.1. Important crystal structure parameters^a of complex **[Fe^{III}L$^{1'}$], (5')**.

Atom1	Atom2	Length	Atom1	Atom2	Length
FE1	O1	1.9107	C20	H20	1.0267
FE1	N1	2.0746	C21	C22	1.4020
FE1	N2	2.2591	C21	C40	1.5340
FE1	O2	1.8611(1)	C22	C23	1.3902
FE1	O3	1.8664	C22	H22	0.9912
O1	C1	1.3150	C23	C24	1.4178
C1	C2	1.4278	C23	C44	1.5343
C1	C6	1.4271	C24	O2	1.3554
C2	C3	1.3850	C25	C26	1.5006
C2	C32	1.5411	C25	H25A	0.9361
C3	C4	1.4128	C25	H25B	0.9726
C3	H3	0.9381	C26	C27	1.3940
C4	C5	1.3704	C26	C31	1.4031
C4	C36	1.5393	C27	C28	1.3939
C5	C6	1.4151	C27	H27	0.9497
C5	H5	0.9492	C28	C29	1.4054
C7	N1	1.3086	C28	C48	1.5357
C7	H7	0.9525	C29	C30	1.3931
N1	C8	1.4189	C29	H29	0.9427
C8	C9	1.3843	C30	C31	1.4179
C8	C17	1.4201	C30	C52	1.5413
C9	C10	1.4217	C31	O3	1.3454
C9	H9	0.9831	C32	C33	1.5333
C10	C11	1.4200	C32	C34	1.5405
C10	C15	1.4216	C32	C35	1.5419
C11	C12	1.3739	C33	H33A	0.9800
C11	H11	0.9240	C33	H33B	0.9800
C12	C13	1.4083	C33	H33C	0.9800
C12	H12	0.9844	C34	H34A	0.9800
C13	C14	1.3678	C34	H34B	0.9800
C13	H13	0.9516	C34	H34C	0.9800
C14	C15	1.4184	C35	H35A	0.9800
C14	H14	0.9185	C35	H35B	0.9800
C15	C16	1.4180	C35	H35C	0.9800
C16	C17	1.3641	C36	C37	1.5167
C16	H16	0.9141	C36	C38	1.5468
C17	N2	1.4543	C36	C39	1.5177
N2	C18	1.4934	C37	H37A	0.9800
N2	C25	1.5026	C37	H37B	0.9800
C18	C19	1.4993	C37	H37C	0.9800
C18	H18A	1.0082	C38	H38A	0.9800
C18	H18B	0.9835	C38	H38B	0.9800
C19	C20	1.4004	C38	H38C	0.9800
C19	C24	1.4047	C39	H39A	0.9800

C20	C21	1.3838	C52	C53	1.5360
C39	H39C	0.9800	C52	C54	1.5291
C40	C41	1.5339	C52	C55	1.5406
C40	C42	1.5425	C53	H53A	0.9800
C40	C43	1.5305	C53	H53B	0.9800
C41	H41A	0.9800	C53	H53C	0.9800
C41	H41B	0.9800	C54	H54A	0.9800
C41	H41C	0.9800	C54	H54B	0.9800
C42	H42A	0.9800	C39	H39B	0.9800
C42	H42B	0.9800	C54	H54C	0.9800
C42	H42C	0.9800	C55	H55A	0.9800
C43	H43A	0.9800	C55	H55B	0.9800
C43	H43B	0.9800	C55	H55C	0.9800
C43	H43C	0.9800	C48	C50	1.5331
C44	C45	1.5361	C48	C51	1.5337
C44	C46	1.5301	C49	H49A	0.9800
C44	C47	1.5376	C49	H49B	0.9800
C45	H45A	0.9800	C49	H49C	0.9800
C45	H45B	0.9800	C50	H50A	0.9800
C45	H45C	0.9800	C50	H50B	0.9800
C46	H46A	0.9800	C50	H50C	0.9800
C46	H46B	0.9800	C51	H51A	0.9800
C46	H46C	0.9800	C51	H51B	0.9800
C47	H47A	0.9800	C51	H51C	0.9800
C47	H47B	0.9800			
C47	H47C	0.9800			
C48	C49	1.5338			

Table B.2. Bond lengths (Å) for complex **[Fe^{III}L$^{1'}$], (5')**.

Crystal structure data of complex [Fe^{III}L$^{trisPhO-NO2I}$] (1) in **Chapter 4**
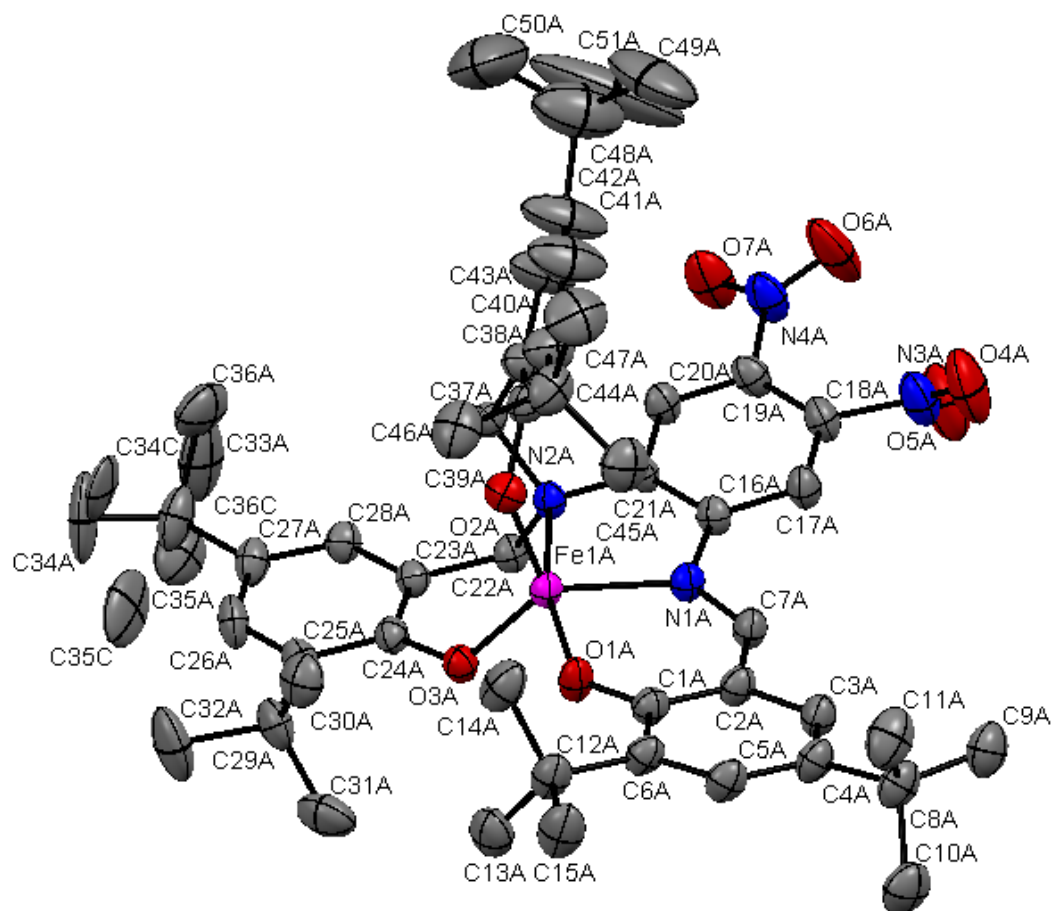
Figure B.2. ORTEP diagram of complex [Fe^{III}L$^{trisPhO-NO2I}$] (1).

Identification code	CNV312_0m
Empirical formula	$C_{51.5}H_{69.5}FeN_4O_8$
Formula weight	928.46
Temperature/K	173(2)
Crystal system	monoclinic
Space group	$P2_1/n$
a/Å	21.5860(17)
b/Å	19.7699(16)
c/Å	25.059(2)
α/°	90.00
β/°	106.9200(10)
γ/°	90.00
Volume/Å^3	10231.2(14)
Z	8
ρ_{calc}mg/mm^3	1.206
m/mm^{-1}	0.349
F(000)	3972.0
Crystal size/mm^3	$0.37 \times 0.25 \times 0.23$
Radiation	MoKα ($\lambda = 0.71073$)
2Θ range for data collection	3.4 to 50.72°
Index ranges	$-25 \leq h \leq 25, -23 \leq k \leq 23, -30 \leq l \leq 30$
Reflections collected	149130
Independent reflections	18732 [$R_{int} = 0.0745$, $R_{sigma} = 0.0453$]
Data/restraints/parameters	18732/0/1229
Goodness-of-fit on F^2	0.992
Final R indexes [I>=2σ (I)]	$R_1 = 0.0569$, $wR_2 = 0.1541$
Final R indexes [all data]	$R_1 = 0.0863$, $wR_2 = 0.1765$
Largest diff. peak/hole / e Å^{-3}	1.20/-0.61

Table B.3. Crystal data and structure refinement for **[Fe^{III}L$^{trisPhO-NO2I}$] (1)**.

Atom	Atom	Length/Å		Atom	Atom	Length/Å
Fe1A	O1A	1.911(2)		C48A	C51A	1.576(11)
Fe1A	O2A	1.856(2)		Fe1B	O1B	1.911(2)
Fe1A	O3A	1.862(2)		Fe1B	O2B	1.865(2)
Fe1A	N1A	2.100(3)		Fe1B	O3B	1.864(2)
Fe1A	N2A	2.213(2)		Fe1B	N1B	2.096(3)
O1A	C1A	1.306(4)		Fe1B	N2B	2.233(3)
O2A	C39A	1.341(4)		O1B	C1B	1.311(4)
O3A	C24A	1.346(4)		O2B	C39B	1.357(4)
O4A	N3A	1.190(4)		O3B	C24B	1.349(4)
O5A	N3A	1.216(4)		O4B	N3B	1.199(4)
O6A	N4A	1.204(4)		O5B	N3B	1.224(4)
O7A	N4A	1.217(4)		O6B	N4B	1.207(4)
N1A	C7A	1.307(4)		O7B	N4B	1.194(5)
N1A	C16A	1.415(4)		N1B	C7B	1.319(4)
N2A	C21A	1.442(4)		N1B	C16B	1.398(4)
N2A	C22A	1.513(4)		N2B	C21B	1.448(4)
N2A	C37A	1.506(4)		N2B	C22B	1.508(4)
N3A	C18A	1.472(4)		N2B	C37B	1.502(4)
N4A	C19A	1.457(4)		N3B	C18B	1.472(4)
C1A	C2A	1.417(4)		N4B	C19B	1.465(4)
C1A	C6A	1.431(4)		C1B	C2B	1.418(4)
C2A	C3A	1.423(4)		C1B	C6B	1.427(4)
C2A	C7A	1.415(4)		C2B	C3B	1.427(4)
C3A	C4A	1.367(5)		C2B	C7B	1.407(4)
C4A	C5A	1.417(5)		C3B	C4B	1.366(5)
C4A	C8A	1.529(4)		C4B	C5B	1.415(5)
C5A	C6A	1.383(5)		C4B	C8B	1.540(5)
C6A	C12A	1.538(5)		C5B	C6B	1.377(5)
C8A	C9A	1.531(5)		C6B	C12B	1.538(5)
C8A	C10A	1.533(5)		C8B	C9B	1.522(6)
C8A	C11A	1.535(5)		C8B	C10B	1.524(5)
C12A	C13A	1.526(5)		C8B	C11B	1.529(6)
C12A	C14A	1.528(5)		C12B	C13B	1.540(5)
C12A	C15A	1.530(5)		C12B	C14B	1.532(5)
C16A	C17A	1.399(4)		C12B	C15B	1.544(5)
C16A	C21A	1.402(4)		C16B	C17B	1.406(4)
C17A	C18A	1.369(4)		C16B	C21B	1.399(4)
C18A	C19A	1.390(5)		C17B	C18B	1.362(5)
C19A	C20A	1.372(4)		C18B	C19B	1.385(5)
C20A	C21A	1.384(4)		C19B	C20B	1.376(5)
C22A	C23A	1.497(4)		C20B	C21B	1.378(4)
C23A	C24A	1.403(4)		C22B	C23B	1.502(4)
C23A	C28A	1.386(4)		C23B	C24B	1.400(4)
C24A	C25A	1.406(4)		C23B	C28B	1.390(4)

C25A	C26A	1.394(5)		C24B	C25B	1.420(4)
C25A	C29A	1.543(5)		C25B	C26B	1.393(4)
C26A	C27A	1.393(5)		C25B	C29B	1.540(4)
C27A	C28A	1.385(4)		C26B	C27B	1.395(4)
C27A	C33A	1.532(5)		C27B	C28B	1.382(4)
C29A	C30A	1.533(5)		C27B	C33B	1.537(4)
C29A	C31A	1.530(6)		C29B	C30B	1.529(5)
C29A	C32A	1.534(5)		C29B	C31B	1.522(5)
C33A	C34A	1.50(2)		C29B	C32B	1.531(5)
C33A	C35A	1.497(9)		C33B	C34B	1.537(5)
C33A	C36A	1.638(10)		C33B	C35B	1.537(5)
C33A	C34C	1.49(3)		C33B	C36B	1.534(5)
C33A	C35C	1.682(15)		C37B	C38B	1.494(5)
C33A	C36C	1.375(13)		C38B	C39B	1.399(5)
C37A	C38A	1.496(4)		C38B	C43B	1.390(5)
C38A	C39A	1.406(5)		C39B	C40B	1.407(5)
C38A	C43A	1.369(5)		C40B	C41B	1.409(5)
C39A	C40A	1.412(5)		C40B	C44B	1.535(6)
C40A	C41A	1.376(6)		C41B	C42B	1.405(6)
C40A	C44A	1.532(5)		C42B	C43B	1.375(5)
C41A	C42A	1.390(6)		C42B	C48B	1.534(5)
C42A	C43A	1.388(6)		C44B	C45B	1.532(6)
C42A	C48A	1.576(7)		C44B	C46B	1.525(6)
C44A	C45A	1.541(5)		C44B	C47B	1.536(5)
C44A	C46A	1.528(6)		C48B	C49B	1.528(6)
C44A	C47A	1.543(5)		C48B	C50B	1.523(7)
C48A	C49A	1.418(9)		C48B	C51B	1.524(7)
C48A	C50A	1.595(11)		O1S	C1S	1.481(10)

Table B.4. Bond lengths (Å) of [$Fe^{III}L^{trisPhO-NO2I}$] (**1**).

Atom	Atom	Atom	Angle/°		Atom	Atom	Atom	Angle/°
O1A	Fe1A	N1A	86.65(9)		C46A	C44A	C47A	108.3(3)
O1A	Fe1A	N2A	163.04(10)		C42A	C48A	C50A	108.2(6)
O2A	Fe1A	O1A	101.97(10)		C42A	C48A	C51A	106.9(6)
O2A	Fe1A	O3A	119.16(10)		C49A	C48A	C42A	112.1(6)
O2A	Fe1A	N1A	112.36(10)		C49A	C48A	C50A	107.1(6)
O2A	Fe1A	N2A	90.89(9)		C49A	C48A	C51A	103.9(7)
O3A	Fe1A	O1A	93.74(9)		C51A	C48A	C50A	118.7(8)
O3A	Fe1A	N1A	127.09(10)		O1B	Fe1B	N1B	85.36(9)
O3A	Fe1A	N2A	89.50(9)		O1B	Fe1B	N2B	156.94(10)
N1A	Fe1A	N2A	78.17(9)		O2B	Fe1B	O1B	106.59(10)
C1A	O1A	Fe1A	135.8(2)		O2B	Fe1B	N1B	106.34(10)
C39A	O2A	Fe1A	128.2(2)		O2B	Fe1B	N2B	92.81(10)
C24A	O3A	Fe1A	126.04(19)		O3B	Fe1B	O1B	94.75(9)
C7A	N1A	Fe1A	124.5(2)		O3B	Fe1B	O2B	113.78(10)
C7A	N1A	C16A	119.8(3)		O3B	Fe1B	N1B	137.91(10)
C16A	N1A	Fe1A	115.43(19)		O3B	Fe1B	N2B	88.49(9)
C21A	N2A	Fe1A	109.81(17)		N1B	Fe1B	N2B	77.12(9)
C21A	N2A	C22A	110.3(2)		C1B	O1B	Fe1B	133.4(2)
C21A	N2A	C37A	112.1(2)		C39B	O2B	Fe1B	120.1(2)
C22A	N2A	Fe1A	108.16(17)		C24B	O3B	Fe1B	125.92(18)
C37A	N2A	Fe1A	106.95(17)		C7B	N1B	Fe1B	121.5(2)
C37A	N2A	C22A	109.4(2)		C7B	N1B	C16B	119.1(3)
O4A	N3A	O5A	124.5(4)		C16B	N1B	Fe1B	117.44(19)
O4A	N3A	C18A	117.8(3)		C21B	N2B	Fe1B	110.99(18)
O5A	N3A	C18A	117.5(3)		C21B	N2B	C22B	110.3(2)
O6A	N4A	O7A	123.1(3)		C21B	N2B	C37B	109.7(2)
O6A	N4A	C19A	118.5(3)		C22B	N2B	Fe1B	109.18(18)
O7A	N4A	C19A	118.3(3)		C37B	N2B	Fe1B	104.88(18)
O1A	C1A	C2A	120.1(3)		C37B	N2B	C22B	111.7(2)
O1A	C1A	C6A	120.3(3)		O4B	N3B	O5B	125.7(3)
C2A	C1A	C6A	119.6(3)		O4B	N3B	C18B	118.5(3)
C1A	C2A	C3A	119.9(3)		O5B	N3B	C18B	115.5(3)
C7A	C2A	C1A	123.2(3)		O6B	N4B	C19B	118.1(3)
C7A	C2A	C3A	116.5(3)		O7B	N4B	O6B	124.0(4)
C4A	C3A	C2A	121.5(3)		O7B	N4B	C19B	117.9(3)
C3A	C4A	C5A	117.0(3)		O1B	C1B	C2B	120.5(3)
C3A	C4A	C8A	123.8(3)		O1B	C1B	C6B	120.6(3)
C5A	C4A	C8A	119.0(3)		C2B	C1B	C6B	118.9(3)
C6A	C5A	C4A	125.0(3)		C1B	C2B	C3B	120.5(3)
C1A	C6A	C12A	120.7(3)		C7B	C2B	C1B	122.8(3)
C5A	C6A	C1A	116.9(3)		C7B	C2B	C3B	116.7(3)
C5A	C6A	C12A	122.3(3)		C4B	C3B	C2B	121.2(3)
N1A	C7A	C2A	127.7(3)		C3B	C4B	C5B	116.7(3)
C4A	C8A	C9A	111.5(3)		C3B	C4B	C8B	123.5(3)

C4A	C8A	C10A	110.5(3)	C5B	C4B	C8B	119.8(3)
C4A	C8A	C11A	108.7(3)	C6B	C5B	C4B	125.6(3)
C9A	C8A	C10A	108.8(3)	C1B	C6B	C12B	120.1(3)
C9A	C8A	C11A	108.2(3)	C5B	C6B	C1B	117.2(3)
C10A	C8A	C11A	109.0(3)	C5B	C6B	C12B	122.7(3)
C13A	C12A	C6A	110.5(3)	N1B	C7B	C2B	127.0(3)
C13A	C12A	C14A	110.0(3)	C9B	C8B	C4B	111.4(3)
C13A	C12A	C15A	107.5(3)	C9B	C8B	C10B	108.9(4)
C14A	C12A	C6A	109.4(3)	C9B	C8B	C11B	109.2(4)
C14A	C12A	C15A	107.8(3)	C10B	C8B	C4B	109.3(3)
C15A	C12A	C6A	111.7(3)	C10B	C8B	C11B	108.5(3)
C17A	C16A	N1A	124.8(3)	C11B	C8B	C4B	109.5(3)
C17A	C16A	C21A	118.6(3)	C6B	C12B	C13B	111.2(3)
C21A	C16A	N1A	116.5(3)	C6B	C12B	C15B	108.7(3)
C18A	C17A	C16A	120.4(3)	C13B	C12B	C15B	109.4(3)
C17A	C18A	N3A	117.0(3)	C14B	C12B	C6B	111.0(3)
C17A	C18A	C19A	120.7(3)	C14B	C12B	C13B	109.1(3)
C19A	C18A	N3A	122.2(3)	C14B	C12B	C15B	107.3(3)
C18A	C19A	N4A	122.2(3)	N1B	C16B	C17B	124.7(3)
C20A	C19A	N4A	118.0(3)	N1B	C16B	C21B	117.2(3)
C20A	C19A	C18A	119.6(3)	C21B	C16B	C17B	118.1(3)
C19A	C20A	C21A	120.6(3)	C18B	C17B	C16B	120.1(3)
C16A	C21A	N2A	118.4(3)	C17B	C18B	N3B	116.1(3)
C20A	C21A	N2A	121.5(3)	C17B	C18B	C19B	121.4(3)
C20A	C21A	C16A	120.1(3)	C19B	C18B	N3B	122.2(3)
C23A	C22A	N2A	111.5(2)	C18B	C19B	N4B	121.7(3)
C24A	C23A	C22A	118.2(3)	C20B	C19B	N4B	118.9(3)
C28A	C23A	C22A	121.4(3)	C20B	C19B	C18B	119.2(3)
C28A	C23A	C24A	120.3(3)	C19B	C20B	C21B	120.4(3)
O3A	C24A	C23A	118.4(3)	C16B	C21B	N2B	117.2(3)
O3A	C24A	C25A	122.0(3)	C20B	C21B	N2B	122.0(3)
C23A	C24A	C25A	119.6(3)	C20B	C21B	C16B	120.7(3)
C24A	C25A	C29A	120.4(3)	C23B	C22B	N2B	110.7(3)
C26A	C25A	C24A	117.4(3)	C24B	C23B	C22B	118.5(3)
C26A	C25A	C29A	122.2(3)	C28B	C23B	C22B	120.2(3)
C27A	C26A	C25A	124.2(3)	C28B	C23B	C24B	121.2(3)
C26A	C27A	C33A	122.1(3)	O3B	C24B	C23B	118.7(3)
C28A	C27A	C26A	116.6(3)	O3B	C24B	C25B	122.0(3)
C28A	C27A	C33A	121.3(3)	C23B	C24B	C25B	119.3(3)
C27A	C28A	C23A	121.8(3)	C24B	C25B	C29B	121.3(3)
C30A	C29A	C25A	109.9(3)	C26B	C25B	C24B	116.8(3)
C30A	C29A	C32A	107.2(3)	C26B	C25B	C29B	121.9(3)
C31A	C29A	C25A	109.7(3)	C25B	C26B	C27B	124.7(3)
C31A	C29A	C30A	109.9(3)	C26B	C27B	C33B	119.6(3)
C31A	C29A	C32A	108.6(4)	C28B	C27B	C26B	116.9(3)

C32A	C29A	C25A	111.5(3)	C28B	C27B	C33B	123.5(3)
C27A	C33A	C36A	107.8(4)	C27B	C28B	C23B	121.1(3)
C27A	C33A	C35C	103.9(5)	C30B	C29B	C25B	110.0(3)
C34A	C33A	C27A	115.2(9)	C30B	C29B	C32B	108.1(3)
C34A	C33A	C35A	115.6(8)	C31B	C29B	C25B	109.6(3)
C34A	C33A	C36A	104.1(10)	C31B	C29B	C30B	110.1(3)
C34A	C33A	C35C	78.8(9)	C31B	C29B	C32B	107.2(3)
C35A	C33A	C27A	110.1(4)	C32B	C29B	C25B	111.7(3)
C35A	C33A	C36A	102.8(6)	C34B	C33B	C27B	109.5(3)
C35A	C33A	C35C	47.1(6)	C34B	C33B	C35B	108.5(3)
C36A	C33A	C35C	142.9(7)	C35B	C33B	C27B	108.8(3)
C34C	C33A	C27A	108.4(9)	C36B	C33B	C27B	111.8(3)
C34C	C33A	C34A	22.5(13)	C36B	C33B	C34B	108.1(3)
C34C	C33A	C35A	134.8(9)	C36B	C33B	C35B	109.9(3)
C34C	C33A	C36A	86.7(11)	C38B	C37B	N2B	110.4(3)
C34C	C33A	C35C	101.2(10)	C39B	C38B	C37B	118.7(3)
C36C	C33A	C27A	118.1(6)	C43B	C38B	C37B	119.8(3)
C36C	C33A	C34A	123.0(11)	C43B	C38B	C39B	121.4(3)
C36C	C33A	C35A	62.1(10)	O2B	C39B	C38B	118.4(3)
C36C	C33A	C36A	40.8(9)	O2B	C39B	C40B	122.1(3)
C36C	C33A	C34C	116.7(14)	C38B	C39B	C40B	119.5(3)
C36C	C33A	C35C	106.2(10)	C39B	C40B	C41B	116.0(4)
C38A	C37A	N2A	112.9(3)	C39B	C40B	C44B	121.6(3)
C39A	C38A	C37A	118.4(3)	C41B	C40B	C44B	122.4(3)
C43A	C38A	C37A	120.9(3)	C42B	C41B	C40B	124.7(4)
C43A	C38A	C39A	120.5(3)	C41B	C42B	C48B	121.1(4)
O2A	C39A	C38A	118.9(3)	C43B	C42B	C41B	116.4(4)
O2A	C39A	C40A	121.3(3)	C43B	C42B	C48B	122.4(4)
C38A	C39A	C40A	119.8(3)	C42B	C43B	C38B	121.1(4)
C39A	C40A	C44A	122.0(3)	C40B	C44B	C47B	111.8(4)
C41A	C40A	C39A	116.9(4)	C45B	C44B	C40B	110.8(3)
C41A	C40A	C44A	121.0(3)	C45B	C44B	C47B	107.9(3)
C40A	C41A	C42A	124.3(4)	C46B	C44B	C40B	109.5(3)
C41A	C42A	C48A	119.9(4)	C46B	C44B	C45B	109.0(4)
C43A	C42A	C41A	117.3(4)	C46B	C44B	C47B	107.8(4)
C43A	C42A	C48A	122.6(4)	C49B	C48B	C42B	108.0(4)
C38A	C43A	C42A	121.1(4)	C50B	C48B	C42B	111.7(4)
C40A	C44A	C45A	108.9(3)	C50B	C48B	C49B	107.2(5)
C40A	C44A	C47A	112.1(3)	C50B	C48B	C51B	107.9(5)
C45A	C44A	C47A	107.4(3)	C51B	C48B	C42B	110.3(4)
C46A	C44A	C40A	110.2(3)	C51B	C48B	C49B	111.7(4)
C46A	C44A	C45A	110.0(3)				

Table B.5. Bond angles (°) for [**Fe^{III}L^{trisPhO-NO2I}**] (**1**).

Crystal structure data of complex [Fe^{III}L$^{bisPhO-NO2}$] (2) in **Chapter 4**
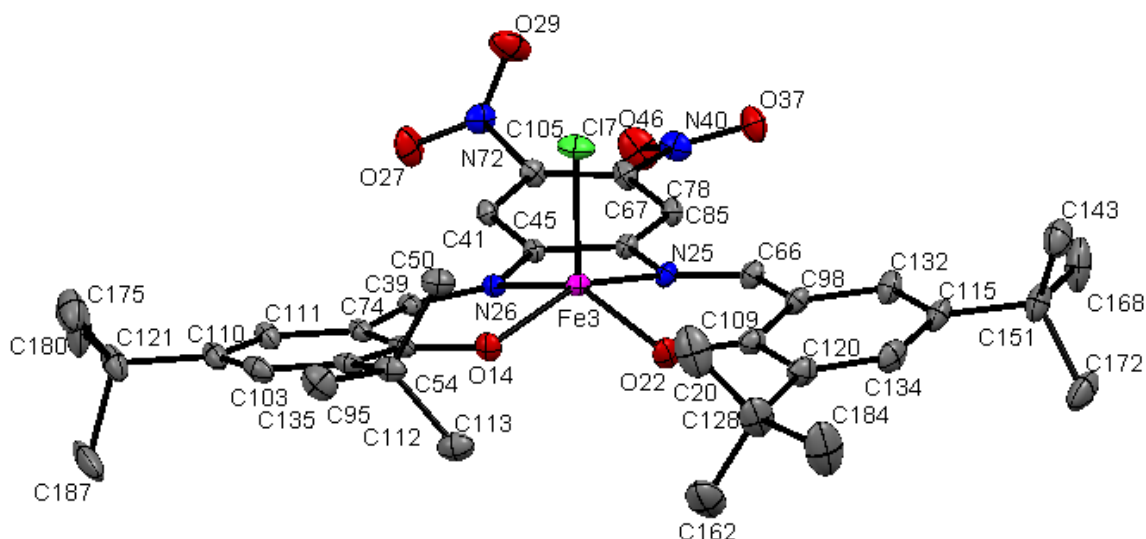
Figure B.3. ORTEP diagram of complex [Fe^{III}L$^{bisPhO-NO2}$] (2).

Identification code	la103run2_0m
Empirical formula	C$_{144}$H$_{176}$Cl$_4$Fe$_4$N$_{16}$O$_{24}$
Formula weight	2880.21
Temperature/K	100.1
Crystal system	triclinic
Space group	P-1
a/Å	18.5576(10)
b/Å	20.0263(11)
c/Å	21.5406(10)
α/°	74.430(2)
β/°	75.669(2)
γ/°	72.390(2)
Volume/Å^3	7228.6(6)
Z	2
ρ$_{calc}$mg/mm^3	1.323
m/mm^{-1}	0.540
F(000)	3032.0
Crystal size/mm^3	0.908 × 0.691 × 0.422

Radiation	MoKα (λ = 0.71073)	
2Θ range for data collection	2.64 to 67.72°	
Index ranges	-28 ≤ h ≤ 29, -31 ≤ k ≤ 30, -33 ≤ l ≤ 33	
Reflections collected	167698	
Independent reflections	56127 [R_{int} = 0.0392, R_{sigma} = 0.0602]	
Data/restraints/parameters	56127/0/1777	
Goodness-of-fit on F^2	1.091	
Final R indexes [I>=2σ (I)]	R_1 = 0.0563, wR_2 = 0.1430	
Final R indexes [all data]	R_1 = 0.0954, wR_2 = 0.1568	
Largest diff. peak/hole / e Å^{-3}	1.93/-1.38	

Table B.6. Crystal data and structure refinement for **[Fe^{III}L$^{bisPhO-NO2}$] (2)**.

Atom	Atom	Length/Å		Atom	Atom	Length/Å
Fe1	O9	1.8866(11)		C81	C90	1.423(2)
Fe1	O10	1.8846(12)		C86	C90	1.414(2)
Fe1	N16	2.1062(13)		C87	C91	1.430(2)
Fe1	N21	2.0926(14)		C88	C136	1.539(2)
Fe1	Cl1	2.2310(5)		C88	C138	1.535(3)
Fe3	Cl7	2.2110(5)		C88	C142	1.530(3)
Fe3	O14	1.8786(12)		C89	C96	1.400(2)
Fe3	O22	1.8817(13)		C89	C13	1.536(2)
Fe3	N25	2.0932(15)		C90	C101	1.414(2)
Fe3	N26	2.0870(14)		C91	C107	1.534(2)
Fe4	Cl8	2.2118(5)		C92	C119	1.393(3)
Fe4	O3	1.8776(13)		C92	C140	1.380(3)
Fe4	N1	2.0903(15)		N93	O102	1.216(3)
Fe4	O1	1.8819(14)		N93	O137	1.229(2)
Fe4	N4	2.0769(16)		N93	C140	1.466(3)
Cl6	Fe2	2.2294(5)		C95	C103	1.379(3)
O9	C87	1.3126(19)		C95	C112	1.530(2)
O10	C75	1.3144(19)		C98	C109	1.424(2)
O11	C100	1.3070(19)		C98	C132	1.414(3)
O11	Fe2	1.8845(11)		C99	C130	1.421(2)
O12	C81	1.3154(19)		C103	C110	1.419(3)
O12	Fe2	1.8872(12)		C106	C107	1.541(3)
O13	N28	1.2227(19)		C107	C131	1.542(3)
O14	C54	1.310(2)		C107	C146	1.529(3)
N16	C47	1.408(2)		C109	C120	1.421(2)

N16	C48	1.3131(19)		C110	C111	1.371(2)
N17	C34	1.407(2)		C110	C121	1.531(3)
N17	C101	1.315(2)		C112	C113	1.541(3)
N17	Fe2	2.0916(13)		C112	C135	1.534(3)
O19	N30	1.2236(19)		C114	C118	1.528(3)
O20	N35	1.2200(19)		C114	C127	1.537(2)
N21	C43	1.408(2)		C114	C133	1.532(2)
N21	C61	1.313(2)		C115	C132	1.375(2)
O22	C109	1.314(2)		C115	C134	1.410(3)
O23	N35	1.2273(19)		C115	C151	1.526(3)
O24	N28	1.2216(19)		C119	C148	1.412(3)
N25	C66	1.310(2)		C119	N1	1.407(2)
N25	C78	1.401(2)		C120	C128	1.526(3)
N26	C39	1.305(2)		C120	C134	1.375(3)
N26	C45	1.411(2)		C121	C175	1.520(3)
O27	N72	1.211(2)		C121	C180	1.534(3)
N28	C58	1.461(2)		C121	C187	1.540(3)
O29	N72	1.220(2)		C124	C139	1.537(3)
N30	C32	1.464(2)		C124	C145	1.534(3)
N30	O49	1.2233(19)		C124	C157	1.532(3)
C32	C33	1.374(2)		O125	N150	1.208(2)
C32	C51	1.396(2)		C128	C162	1.534(3)
C33	C43	1.399(2)		C128	C184	1.540(3)
C34	C56	1.400(2)		C128	C20	1.532(4)
C34	C71	1.412(2)		C129	C141	1.414(3)
N35	C51	1.464(2)		C130	C141	1.367(3)
O36	N44	1.225(2)		C140	C149	1.392(3)
O37	N40	1.230(2)		C141	C171	1.527(3)
C39	C74	1.426(2)		C143	C151	1.523(3)
N40	O46	1.231(2)		C144	C148	1.394(3)
N40	C67	1.467(2)		C144	C149	1.360(3)
C41	C45	1.399(2)		C148	N4	1.406(3)
C41	C105	1.376(2)		C149	N150	1.474(3)
C42	C62	1.368(2)		N150	O167	1.213(2)
C42	C69	1.417(2)		C151	C168	1.534(3)
C43	C47	1.407(2)		C151	C172	1.530(3)
N44	O63	1.213(2)		C154	C163	1.409(3)
N44	C82	1.463(2)		C154	C169	1.439(3)
C45	C78	1.408(2)		C154	O1	1.304(2)
C47	C64	1.402(2)		C159	C188	1.528(3)
C48	C69	1.420(2)		C163	C164	1.424(3)
C50	C112	1.537(2)		C163	C11	1.414(3)
C51	C64	1.374(2)		C164	C179	1.369(3)
C52	C86	1.372(2)		C169	C185	1.374(3)
C52	C96	1.401(3)		C169	C25	1.515(4)

C52	C12	1.537(2)		C171	C174	1.510(3)
C53	C60	1.369(2)		C171	C191	1.480(4)
C53	C65	1.420(2)		C171	C196	1.554(5)
C54	C74	1.428(2)		C179	C185	1.402(4)
C54	C95	1.427(2)		C179	C188	1.540(3)
C55	C62	1.418(2)		C186	C25	1.528(4)
C55	C91	1.378(2)		C188	C189	1.521(4)
C56	C58	1.374(2)		C188	C190	1.547(4)
C58	C82	1.394(2)		N2	C4	1.3127(19)
C59	C71	1.398(2)		N2	Fe2	2.1155(14)
C59	C82	1.375(2)		O3	C2	1.308(2)
C60	C94	1.414(2)		N1	C1	1.307(2)
C60	C114	1.532(2)		N4	C11	1.315(3)
C61	C99	1.408(2)		C1	C3	1.431(2)
C62	C80	1.535(2)		C3	C2	1.420(2)
C65	C100	1.424(2)		C3	C6	1.423(2)
C65	C4	1.419(2)		C2	C8	1.429(2)
C66	C98	1.421(2)		C6	C7	1.375(3)
C67	C85	1.380(2)		C7	C5	1.532(3)
C67	C105	1.392(2)		C7	C14	1.413(3)
C68	C94	1.378(2)		C8	C9	1.529(3)
C68	C100	1.422(2)		C8	C14	1.375(3)
C68	C124	1.535(2)		C9	C10	1.541(3)
C69	C87	1.420(2)		C9	C19	1.525(3)
C71	N2	1.406(2)		C9	C23	1.532(3)
N72	C105	1.474(2)		C5	C21	1.539(3)
C74	C111	1.415(2)		C5	C26	1.523(3)
C75	C79	1.429(2)		C5	C1D	1.541(3)
C75	C99	1.421(2)		C25	C27	1.544(3)
C78	C85	1.396(2)		C25	C15	1.534(3)
C79	C88	1.535(3)		C12	C1A	1.520(3)
C79	C129	1.383(2)		C12	C1B	1.527(3)
C80	C83	1.528(2)		C12	C1C	1.524(3)
C80	C104	1.538(2)		C13	C16	1.539(3)
C80	C117	1.532(2)		C13	C17	1.532(3)
C81	C89	1.422(2)		C13	C18	1.534(3)

Table B.7. Bond lengths (Å) for $[Fe^{III}L^{bisPhO\text{-}NO2}]$ **(2)**.

Atom	Atom	Atom	Angle/°		Atom	Atom	Atom	Angle/°
O9	Fe1	N16	85.67(5)		C132	C98	C109	120.01(15)
O9	Fe1	N21	140.64(5)		C61	C99	C75	123.48(15)
O9	Fe1	Cl1	107.48(4)		C61	C99	C130	115.83(16)
O10	Fe1	O9	93.47(5)		C130	C99	C75	120.53(15)
O10	Fe1	N16	151.75(5)		O11	C100	C65	121.31(14)
O10	Fe1	N21	86.99(5)		O11	C100	C68	120.15(15)
O10	Fe1	Cl1	107.46(4)		C68	C100	C65	118.49(14)
N16	Fe1	Cl1	99.66(4)		N17	C101	C90	126.73(15)
N21	Fe1	N16	76.33(5)		C95	C103	C110	125.17(16)
N21	Fe1	Cl1	109.86(4)		C41	C105	C67	120.47(15)
O14	Fe3	Cl7	107.61(4)		C41	C105	N72	116.26(16)
O14	Fe3	O22	91.23(6)		C67	C105	N72	122.67(15)
O14	Fe3	N25	149.69(6)		C91	C107	C106	111.17(14)
O14	Fe3	N26	86.63(5)		C91	C107	C131	109.10(15)
O22	Fe3	Cl7	112.36(5)		C106	C107	C131	110.02(15)
O22	Fe3	N25	85.60(6)		C146	C107	C91	111.83(15)
O22	Fe3	N26	140.83(6)		C146	C107	C106	107.30(16)
N25	Fe3	Cl7	101.42(4)		C146	C107	C131	107.34(16)
N26	Fe3	Cl7	105.50(4)		O22	C109	C98	120.83(15)
N26	Fe3	N25	77.28(5)		O22	C109	C120	119.88(16)
O3	Fe4	Cl8	110.71(4)		C120	C109	C98	119.27(17)
O3	Fe4	N1	86.06(6)		C103	C110	C121	119.27(16)
O3	Fe4	O1	90.75(6)		C111	C110	C103	117.14(17)
O3	Fe4	N4	142.49(6)		C111	C110	C121	123.59(17)
N1	Fe4	Cl8	101.16(4)		C110	C111	C74	121.33(17)
O1	Fe4	Cl8	109.46(5)		C50	C112	C113	109.55(16)
O1	Fe4	N1	148.26(6)		C95	C112	C50	109.84(14)
O1	Fe4	N4	86.10(7)		C95	C112	C113	111.65(15)
N4	Fe4	Cl8	105.53(5)		C95	C112	C135	111.40(16)
N4	Fe4	N1	77.67(6)		C135	C112	C50	106.85(15)
C87	O9	Fe1	133.25(11)		C135	C112	C113	107.41(15)
C75	O10	Fe1	136.62(11)		C60	C114	C127	108.60(14)
C100	O11	Fe2	135.85(11)		C118	C114	C60	111.75(14)
C81	O12	Fe2	136.10(11)		C118	C114	C127	108.64(15)
C54	O14	Fe3	132.55(10)		C118	C114	C133	108.46(15)
C47	N16	Fe1	115.26(10)		C133	C114	C60	110.30(14)
C48	N16	Fe1	123.99(11)		C133	C114	C127	109.03(14)
C48	N16	C47	120.70(14)		C132	C115	C134	117.05(17)
C34	N17	Fe2	115.90(10)		C132	C115	C151	124.05(17)
C101	N17	C34	119.37(14)		C134	C115	C151	118.90(16)
C101	N17	Fe2	124.73(11)		C92	C119	C148	120.11(16)
C43	N21	Fe1	115.77(10)		C92	C119	N1	124.98(17)
C61	N21	Fe1	124.37(11)		N1	C119	C148	114.64(16)
C61	N21	C43	119.86(14)		C109	C120	C128	120.52(18)

C109	O22	Fe3	129.60(11)	C134	C120	C109	117.37(17)
C66	N25	Fe3	122.04(11)	C134	C120	C128	122.09(17)
C66	N25	C78	122.44(15)	C110	C121	C180	110.87(17)
C78	N25	Fe3	113.63(11)	C110	C121	C187	108.53(18)
C39	N26	Fe3	124.85(11)	C175	C121	C110	111.96(17)
C39	N26	C45	121.42(14)	C175	C121	C180	107.5(2)
C45	N26	Fe3	113.04(10)	C175	C121	C187	109.5(2)
O13	N28	C58	117.68(14)	C180	C121	C187	108.40(18)
O24	N28	O13	124.81(15)	C68	C124	C139	110.61(15)
O24	N28	C58	117.42(14)	C145	C124	C68	109.43(15)
O19	N30	C32	117.84(14)	C145	C124	C139	110.00(15)
O49	N30	O19	124.59(15)	C157	C124	C68	111.14(14)
O49	N30	C32	117.48(14)	C157	C124	C139	109.00(16)
C33	C32	N30	117.47(14)	C157	C124	C145	106.57(16)
C33	C32	C51	120.55(15)	C120	C128	C162	110.32(19)
C51	C32	N30	121.74(15)	C120	C128	C184	111.44(18)
C32	C33	C43	119.66(15)	C120	C128	C20	109.47(17)
N17	C34	C71	115.32(13)	C162	C128	C184	107.07(19)
C56	C34	N17	124.82(14)	C20	C128	C162	110.6(2)
C56	C34	C71	119.81(14)	C20	C128	C184	107.9(2)
O20	N35	O23	125.18(16)	C79	C129	C141	125.51(17)
O20	N35	C51	117.51(14)	C141	C130	C99	121.19(17)
O23	N35	C51	117.29(14)	C115	C132	C98	121.23(17)
N26	C39	C74	126.05(15)	C120	C134	C115	125.03(17)
O37	N40	O46	124.93(16)	C92	C140	N93	117.51(19)
O37	N40	C67	117.49(15)	C92	C140	C149	120.66(19)
O46	N40	C67	117.52(16)	C149	C140	N93	121.40(17)
C105	C41	C45	119.74(16)	C129	C141	C171	120.59(17)
C62	C42	C69	121.04(15)	C130	C141	C129	116.89(16)
C33	C43	N21	125.14(14)	C130	C141	C171	122.51(18)
C33	C43	C47	119.62(14)	C149	C144	C148	119.32(19)
C47	C43	N21	115.21(14)	C144	C148	C119	119.71(18)
O36	N44	C82	116.99(15)	C144	C148	N4	124.35(18)
O63	N44	O36	125.27(16)	N4	C148	C119	115.89(16)
O63	N44	C82	117.70(15)	C140	C149	N150	122.6(2)
C41	C45	N26	124.53(15)	C144	C149	C140	121.31(18)
C41	C45	C78	119.65(14)	C144	C149	N150	116.0(2)
C78	C45	N26	115.46(14)	O125	N150	C149	118.43(18)
C43	C47	N16	114.65(14)	O125	N150	O167	124.11(19)
C64	C47	N16	125.50(14)	O167	N150	C149	117.36(18)
C64	C47	C43	119.84(14)	C115	C151	C168	111.26(16)
N16	C48	C69	125.72(15)	C115	C151	C172	110.05(18)
C32	C51	N35	121.28(14)	C143	C151	C115	109.77(16)
C64	C51	C32	120.69(15)	C143	C151	C168	108.27(19)
C64	C51	N35	117.89(14)	C143	C151	C172	108.75(17)

C86	C52	C96	116.90(15)	C172	C151	C168	108.67(19)
C86	C52	C12	119.81(16)	C163	C154	C169	120.0(2)
C96	C52	C12	123.29(15)	O1	C154	C163	120.54(19)
C60	C53	C65	121.14(16)	O1	C154	C169	119.5(2)
O14	C54	C74	120.57(15)	C154	C163	C164	119.6(2)
O14	C54	C95	119.73(15)	C154	C163	C11	122.57(19)
C95	C54	C74	119.70(16)	C11	C163	C164	117.9(2)
C91	C55	C62	124.97(15)	C179	C164	C163	121.3(2)
C58	C56	C34	118.79(14)	C154	C169	C25	121.0(2)
C56	C58	N28	117.26(14)	C185	C169	C154	116.2(2)
C56	C58	C82	121.36(15)	C185	C169	C25	122.7(2)
C82	C58	N28	121.24(15)	C141	C171	C196	107.4(2)
C82	C59	C71	119.06(15)	C174	C171	C141	112.83(17)
C53	C60	C94	116.85(15)	C174	C171	C196	105.8(2)
C53	C60	C114	123.59(15)	C191	C171	C141	109.5(2)
C94	C60	C114	119.41(14)	C191	C171	C174	110.5(3)
N21	C61	C99	127.11(16)	C191	C171	C196	110.6(3)
C42	C62	C55	117.20(15)	C164	C179	C185	117.2(2)
C42	C62	C80	123.00(15)	C164	C179	C188	122.4(2)
C55	C62	C80	119.57(14)	C185	C179	C188	120.2(2)
C51	C64	C47	119.37(15)	C169	C185	C179	125.7(2)
C53	C65	C100	120.58(14)	C159	C188	C179	107.34(19)
C4	C65	C53	117.05(15)	C159	C188	C190	107.6(2)
C4	C65	C100	121.97(14)	C179	C188	C190	111.7(2)
N25	C66	C98	125.64(16)	C189	C188	C159	109.3(2)
C85	C67	N40	117.33(16)	C189	C188	C179	111.3(2)
C85	C67	C105	120.45(15)	C189	C188	C190	109.4(2)
C105	C67	N40	122.02(15)	C71	N2	Fe2	115.20(10)
C94	C68	C100	117.62(15)	C4	N2	C71	119.71(14)
C94	C68	C124	122.31(15)	C4	N2	Fe2	125.06(11)
C100	C68	C124	119.98(14)	C2	O3	Fe4	129.43(11)
C42	C69	C48	116.38(14)	C119	N1	Fe4	112.44(11)
C42	C69	C87	120.63(14)	C1	N1	Fe4	124.87(12)
C87	C69	C48	122.67(14)	C1	N1	C119	122.17(15)
C59	C71	C34	120.10(14)	C154	O1	Fe4	135.90(15)
C59	C71	N2	125.30(14)	N2	C4	C65	125.95(15)
N2	C71	C34	114.59(14)	C148	N4	Fe4	112.33(12)
O27	N72	O29	124.69(16)	C11	N4	Fe4	124.63(14)
O27	N72	C105	117.95(15)	C11	N4	C148	122.37(17)
O29	N72	C105	117.21(16)	N1	C1	C3	124.86(16)
C39	C74	C54	122.45(16)	C2	C3	C1	122.29(16)
C111	C74	C39	117.61(15)	C2	C3	C6	119.88(16)
C111	C74	C54	119.87(15)	C6	C3	C1	117.80(16)
O10	C75	C79	120.66(15)	O3	C2	C3	120.97(16)
O10	C75	C99	120.25(14)	O3	C2	C8	119.74(16)

C99	C75	C79	119.08(15)	C3	C2	C8	119.28(17)
N25	C78	C45	115.15(14)	C7	C6	C3	121.30(17)
C85	C78	N25	125.30(15)	C6	C7	C5	124.48(18)
C85	C78	C45	119.51(15)	C6	C7	C14	116.78(18)
C75	C79	C88	121.26(15)	C14	C7	C5	118.73(17)
C129	C79	C75	116.79(16)	C2	C8	C9	120.58(17)
C129	C79	C88	121.93(16)	C14	C8	C2	117.06(17)
C62	C80	C104	107.98(13)	C14	C8	C9	122.35(17)
C83	C80	C62	111.54(13)	C8	C9	C10	111.74(15)
C83	C80	C104	109.06(14)	C8	C9	C23	108.96(16)
C83	C80	C117	108.57(15)	C19	C9	C8	111.54(18)
C117	C80	C62	110.87(14)	C19	C9	C10	106.79(16)
C117	C80	C104	108.78(14)	C19	C9	C23	106.55(16)
O12	C81	C89	121.03(15)	C23	C9	C10	111.15(18)
O12	C81	C90	120.25(15)	N4	C11	C163	126.9(2)
C89	C81	C90	118.70(15)	C7	C5	C21	109.97(17)
C58	C82	N44	120.83(15)	C7	C5	C1D	108.71(17)
C59	C82	N44	118.38(15)	C21	C5	C1D	108.62(18)
C59	C82	C58	120.61(15)	C26	C5	C7	111.99(17)
C67	C85	C78	119.74(16)	C26	C5	C21	108.10(19)
C52	C86	C90	121.47(16)	C26	C5	C1D	109.39(18)
O9	C87	C69	121.22(14)	C8	C14	C7	125.42(17)
O9	C87	C91	119.82(15)	C169	C25	C186	111.4(2)
C69	C87	C91	118.92(14)	C169	C25	C27	108.3(2)
C79	C88	C136	109.21(15)	C169	C25	C15	112.1(2)
C79	C88	C138	110.51(15)	C186	C25	C27	110.6(2)
C138	C88	C136	110.03(16)	C186	C25	C15	106.6(2)
C142	C88	C79	111.72(16)	C15	C25	C27	107.7(2)
C142	C88	C136	107.78(16)	C1A	C12	C52	108.61(15)
C142	C88	C138	107.53(16)	C1A	C12	C1B	109.12(17)
C81	C89	C13	121.66(15)	C1A	C12	C1C	110.06(19)
C96	C89	C81	117.16(15)	C1B	C12	C52	111.67(16)
C96	C89	C13	121.18(15)	C1C	C12	C52	109.12(15)
C86	C90	C81	120.66(15)	C1C	C12	C1B	108.26(18)
C101	C90	C81	123.44(15)	C89	C13	C16	108.59(15)
C101	C90	C86	115.80(15)	C17	C13	C89	110.91(14)
C55	C91	C87	117.19(15)	C17	C13	C16	109.99(16)
C55	C91	C107	122.16(15)	C17	C13	C18	106.93(16)
C87	C91	C107	120.56(14)	C18	C13	C89	111.86(15)
C140	C92	C119	118.77(19)	C18	C13	C16	108.53(16)
O102	N93	O137	124.6(2)	O11	Fe2	Cl6	107.55(4)
O102	N93	C140	118.32(17)	O11	Fe2	O12	93.60(5)
O137	N93	C140	117.1(2)	O11	Fe2	N17	140.56(5)
C68	C94	C60	125.10(15)	O11	Fe2	N2	85.05(5)
C54	C95	C112	120.75(16)	O12	Fe2	Cl6	107.70(4)

C103	C95	C54	116.63(16)		O12	Fe2	N17	86.81(5)
C103	C95	C112	122.53(15)		O12	Fe2	N2	150.85(5)
C89	C96	C52	125.09(16)		N17	Fe2	Cl6	109.82(4)
C66	C98	C109	122.40(16)		N17	Fe2	N2	76.36(5)
C132	C98	C66	117.55(16)		N2	Fe2	Cl6	100.40(4)

Table B.8. Bond angles (°) for **[Fe^{III}L$^{bisPhO-NO2}$]** **(2)**.

Crystal structure data of complex **[Fe^{III}L^{NO2}] (2)** in **Chapter 6**
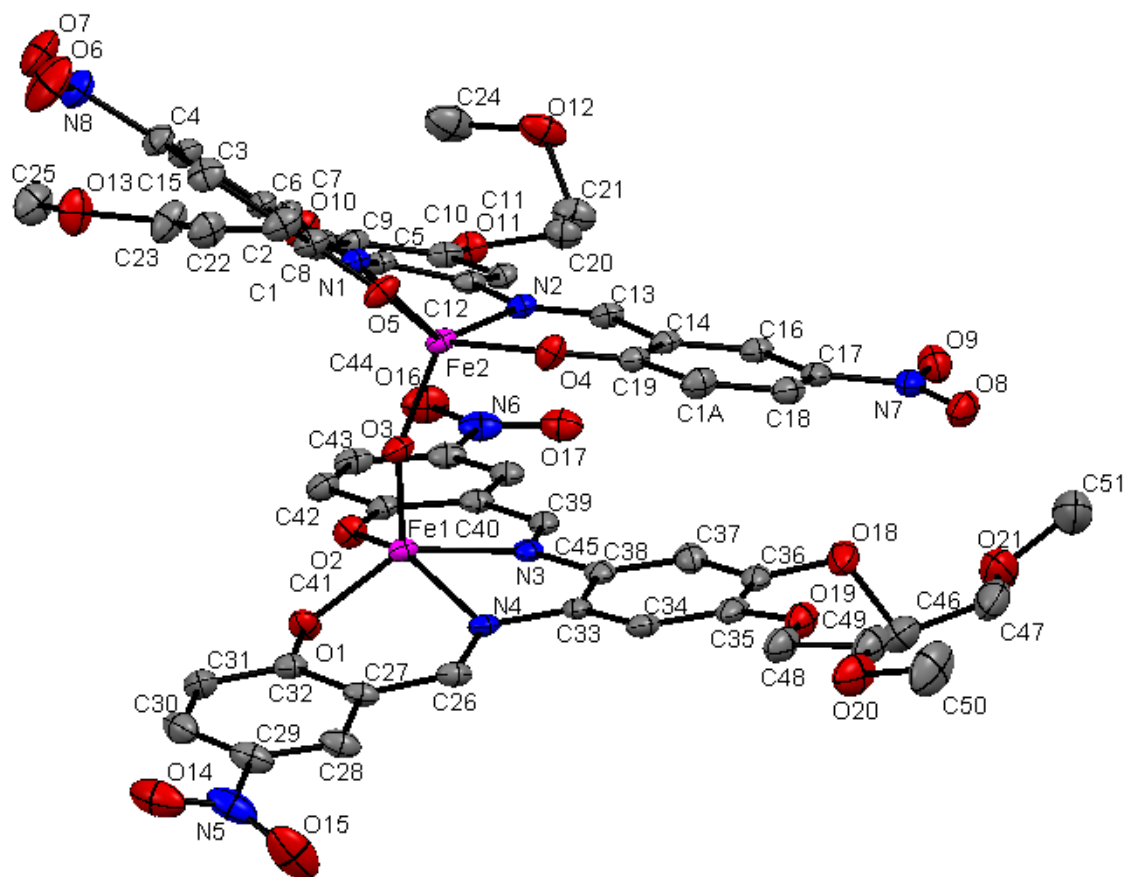
Figure B.4. ORTEP diagram of complex **[Fe^{III}L^{NO2}] (2)**.

Identification code	la099(1)
Empirical formula	$C_{60}H_{72}N_8O_{25}S_4Fe_2$
Formula weight	1545.20
Temperature/K	100.1
Crystal system	triclinic
Space group	P-1
a/Å	14.2608(9)
b/Å	14.9219(9)
c/Å	18.1654(11)
α/°	76.882(4)
β/°	69.115(4)
γ/°	72.261(4)

Volume/Å^3	3409.3(4)
Z	2
ρ_{calc}mg/mm^3	1.505
m/mm^{-1}	0.634
F(000)	1608.0
Crystal size/mm^3	1.09 × 0.36 × 0.25
Radiation	MoKα (λ = 0.71073)
2Θ range for data collection	2.42 to 57.4°
Index ranges	-19 ≤ h ≤ 19, -20 ≤ k ≤ 20, -24 ≤ l ≤ 24
Reflections collected	200653
Independent reflections	17566 [R$_{int}$ = 0.0798, R$_{sigma}$ = 0.0467]
Data/restraints/parameters	17566/0/1125
Goodness-of-fit on F^2	1.099
Final R indexes [I>=2σ (I)]	R$_1$ = 0.0669, wR$_2$ = 0.1626
Final R indexes [all data]	R$_1$ = 0.1019, wR$_2$ = 0.1927
Largest diff. peak/hole / e Å^{-3}	2.04/-1.67

Table B.9. Crystal data and structure refinement for **[Fe^{III}L^{NO2}] (2)**.

Atom	Atom	Length/Å		Atom	Atom	Length/Å
Fe2	O3	1.779(2)		C12	C11	1.400(5)
Fe2	O4	1.924(2)		O11	C10	1.355(4)
Fe2	N2	2.111(3)		O11	C20	1.434(5)
Fe2	N1	2.102(3)		C5	C8	1.400(5)
Fe2	O5	1.921(3)		C6	C7	1.442(5)
Fe1	O3	1.782(2)		C6	C1	1.439(5)
Fe1	N3	2.103(3)		C6	C15	1.393(5)
Fe1	O2	1.932(2)		N8	C4	1.454(5)
Fe1	N4	2.110(3)		N7	C17	1.444(5)
Fe1	O1	1.913(3)		N6	C44	1.459(5)
S2	O24	1.499(3)		C33	C38	1.394(5)
S2	C52	1.782(4)		C33	C34	1.398(5)
S2	C53	1.773(5)		O20	C50	1.405(5)
S3	O25	1.497(3)		O20	C49	1.411(6)
S3	C55	1.778(5)		O21	C47	1.414(6)
S3	C54	1.795(4)		O21	C51	1.404(6)
S4	O22	1.503(3)		C19	C1A	1.419(5)
S4	C57	1.779(5)		C11	C10	1.377(5)
S4	C56	1.779(5)		C10	C9	1.413(5)
O4	C19	1.291(4)		C20	C21	1.505(5)

N2	C13	1.288(5)		C9	C8	1.376(5)
N2	C12	1.422(4)		C22	C23	1.508(5)
O12	C21	1.412(5)		C1	C2	1.405(5)
O12	C24	1.407(6)		C2	C3	1.375(5)
O10	C9	1.361(4)		C3	C4	1.397(5)
O10	C22	1.416(5)		C4	C15	1.370(5)
O13	C23	1.409(5)		C16	C17	1.379(5)
O13	C25	1.416(5)		C17	C18	1.393(6)
N1	C5	1.414(4)		C18	C1A	1.365(5)
N1	C7	1.285(4)		C39	C40	1.436(5)
O5	C1	1.292(4)		C40	C41	1.419(5)
O6	N8	1.225(5)		C40	C45	1.398(5)
O7	N8	1.223(5)		C41	C42	1.419(5)
O9	N7	1.236(4)		C42	C43	1.366(5)
O8	N7	1.235(4)		C43	C44	1.403(6)
N3	C39	1.301(5)		C44	C45	1.375(5)
N3	C38	1.413(4)		C38	C37	1.400(5)
O2	C41	1.303(4)		C26	C27	1.434(5)
O17	N6	1.221(4)		C27	C28	1.408(5)
O16	N6	1.226(4)		C27	C32	1.430(5)
N4	C33	1.426(4)		C28	C29	1.378(6)
N4	C26	1.293(5)		C29	C30	1.398(6)
O1	C32	1.306(4)		C29	N5	1.454(5)
O15	N5	1.242(5)		C30	C31	1.369(6)
O14	N5	1.220(5)		C31	C32	1.415(5)
O19	C35	1.356(4)		C34	C35	1.386(5)
O19	C48	1.427(5)		C35	C36	1.422(6)
O18	C36	1.371(5)		C48	C49	1.512(5)
O18	C46	1.430(5)		C36	C37	1.371(5)
C14	C13	1.441(5)		C46	C47	1.495(7)
C14	C19	1.430(5)		S1	O23	1.454(4)
C14	C16	1.397(5)		S1	C58	1.782(7)
C12	C5	1.390(5)		S1	C59	1.841(8)

Table B.10. Bond lengths (Å) for [Fe^{III}L^{NO2}] (2).

Atom	Atom	Atom	Angle/°		Atom	Atom	Atom	Angle/°
O3	Fe2	O4	110.13(11)		O4	C19	C14	122.7(3)
O3	Fe2	N2	104.02(11)		O4	C19	C1A	119.9(3)
O3	Fe2	N1	99.48(11)		C1A	C19	C14	117.3(3)
O3	Fe2	O5	111.30(12)		C10	C11	C12	119.8(3)
O4	Fe2	N2	87.02(11)		O11	C10	C11	124.5(3)
O4	Fe2	N1	149.00(11)		O11	C10	C9	115.7(3)
N1	Fe2	N2	76.85(11)		C11	C10	C9	119.7(3)
O5	Fe2	O4	90.42(11)		O11	C20	C21	108.3(3)
O5	Fe2	N2	143.16(11)		O12	C21	C20	115.6(3)
O5	Fe2	N1	87.15(11)		O10	C9	C10	114.5(3)
O3	Fe1	N3	106.60(11)		O10	C9	C8	124.8(3)
O3	Fe1	O2	110.48(11)		C8	C9	C10	120.7(3)
O3	Fe1	N4	97.88(11)		O10	C22	C23	106.0(3)
O3	Fe1	O1	108.33(12)		O13	C23	C22	107.9(3)
N3	Fe1	N4	77.05(11)		C9	C8	C5	119.1(3)
O2	Fe1	N3	86.95(11)		N1	C7	C6	124.7(3)
O2	Fe1	N4	150.50(11)		O5	C1	C6	122.6(3)
O1	Fe1	N3	143.36(11)		O5	C1	C2	119.3(3)
O1	Fe1	O2	90.99(11)		C2	C1	C6	118.1(3)
O1	Fe1	N4	87.54(11)		C3	C2	C1	122.1(4)
Fe2	O3	Fe1	150.69(17)		C2	C3	C4	118.3(4)
O24	S2	C52	106.9(2)		C3	C4	N8	118.9(3)
O24	S2	C53	106.7(2)		C15	C4	N8	119.0(3)
C53	S2	C52	97.8(2)		C15	C4	C3	122.1(3)
O25	S3	C55	107.3(2)		C4	C15	C6	120.2(3)
O25	S3	C54	107.3(2)		C17	C16	C14	120.5(4)
C55	S3	C54	97.3(3)		C16	C17	N7	118.9(4)
O22	S4	C57	105.3(2)		C16	C17	C18	121.4(3)
O22	S4	C56	105.7(2)		C18	C17	N7	119.6(3)
C57	S4	C56	98.4(3)		C1A	C18	C17	118.7(3)
C19	O4	Fe2	133.6(2)		C18	C1A	C19	122.6(4)
C13	N2	Fe2	126.2(2)		N3	C39	C40	125.2(3)
C13	N2	C12	121.3(3)		C41	C40	C39	123.6(3)
C12	N2	Fe2	112.1(2)		C45	C40	C39	116.4(3)
C24	O12	C21	114.7(3)		C45	C40	C41	120.0(3)
C9	O10	C22	117.7(3)		O2	C41	C40	122.8(3)
C23	O13	C25	111.6(3)		O2	C41	C42	119.0(3)
C5	N1	Fe2	111.7(2)		C42	C41	C40	118.1(3)
C7	N1	Fe2	127.2(2)		C43	C42	C41	121.4(4)
C7	N1	C5	121.1(3)		C42	C43	C44	119.3(3)
C1	O5	Fe2	134.2(2)		C43	C44	N6	119.9(3)
C39	N3	Fe1	125.9(2)		C45	C44	N6	118.6(3)
C39	N3	C38	120.4(3)		C45	C44	C43	121.4(4)
C38	N3	Fe1	113.2(2)		C44	C45	C40	119.8(4)

C41	O2	Fe1	133.3(2)		C33	C38	N3	116.5(3)
C33	N4	Fe1	112.7(2)		C33	C38	C37	119.7(3)
C26	N4	Fe1	125.0(2)		C37	C38	N3	123.8(3)
C26	N4	C33	121.9(3)		N4	C26	C27	124.5(3)
C32	O1	Fe1	129.7(2)		C28	C27	C26	117.0(3)
C35	O19	C48	117.9(3)		C28	C27	C32	118.9(3)
C36	O18	C46	115.3(3)		C32	C27	C26	124.1(3)
C19	C14	C13	123.4(3)		C29	C28	C27	119.8(4)
C16	C14	C13	117.2(3)		C28	C29	C30	122.0(4)
C16	C14	C19	119.4(3)		C28	C29	N5	118.4(4)
N2	C13	C14	125.1(3)		C30	C29	N5	119.6(4)
C5	C12	N2	115.7(3)		C31	C30	C29	118.9(4)
C5	C12	C11	119.9(3)		C30	C31	C32	121.6(4)
C11	C12	N2	124.4(3)		O1	C32	C27	122.5(3)
C10	O11	C20	117.2(3)		O1	C32	C31	118.9(3)
C12	C5	N1	115.4(3)		C31	C32	C27	118.6(3)
C12	C5	C8	120.4(3)		O15	N5	C29	117.6(4)
C8	C5	N1	124.1(3)		O14	N5	O15	123.7(4)
C1	C6	C7	123.3(3)		O14	N5	C29	118.7(4)
C15	C6	C7	117.5(3)		C35	C34	C33	119.2(4)
C15	C6	C1	119.1(3)		O19	C35	C34	124.7(4)
O6	N8	O7	123.2(3)		O19	C35	C36	115.2(3)
O6	N8	C4	118.8(3)		C34	C35	C36	120.1(3)
O7	N8	C4	118.1(3)		O19	C48	C49	105.3(4)
O9	N7	C17	118.6(3)		O18	C36	C35	121.5(3)
O8	N7	O9	122.7(3)		O18	C36	C37	118.3(4)
O8	N7	C17	118.7(3)		C37	C36	C35	120.0(3)
O17	N6	O16	123.8(4)		O18	C46	C47	107.7(4)
O17	N6	C44	118.4(3)		O21	C47	C46	112.6(4)
O16	N6	C44	117.8(3)		C36	C37	C38	120.2(4)
C38	C33	N4	114.7(3)		O20	C49	C48	106.8(4)
C38	C33	C34	120.7(3)		O23	S1	C58	108.7(3)
C34	C33	N4	124.6(3)		O23	S1	C59	104.3(3)
C50	O20	C49	111.2(4)		C58	S1	C59	96.8(4)
C51	O21	C47	113.8(4)					

Table B.11. Bond angles (°) for [**Fe^{III}L^{NO2}**] (**2**).

Crystal structure data of complex **[Mn^{III}L^{*t*Bu}] (4)** in **Chapter 7**
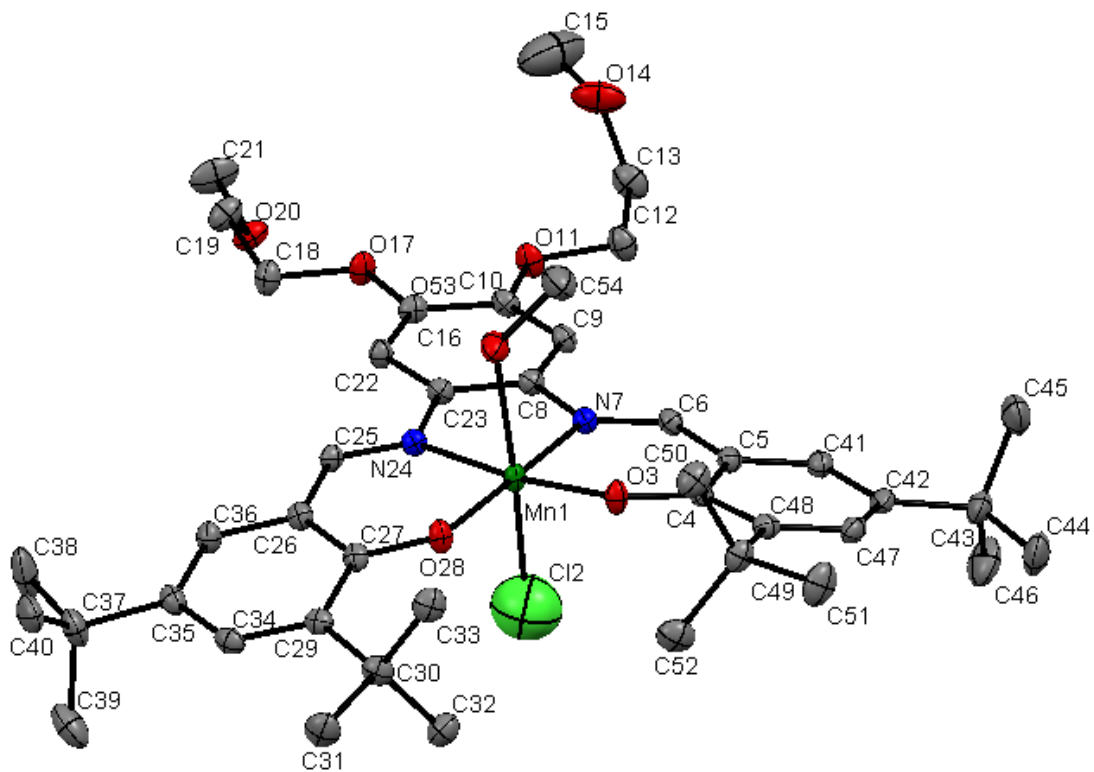
Figure B.5. ORTEP diagram of complex **[Mn^{III}L^{*t*Bu}] (4)**.

Identification code	FileName()
Empirical formula	$C_{44}H_{66}Cl_2MnN_2O_8$
Formula weight	876.82
Temperature/K	293(2)
Crystal system	triclinic
Space group	P-1
a/Å	10.7364(5)
b/Å	14.1651(6)
c/Å	16.3530(7)
α/°	71.703(2)
β/°	77.979(3)
γ/°	80.303(3)
Volume/Å^3	2295.22(18)
Z	2
ρ_{calc}mg/mm^3	1.269
m/mm^{-1}	0.455
F(000)	934.0
Crystal size/mm^3	$? \times ? \times ?$
2Θ range for data collection	3.416 to 52.132°
Index ranges	$? \leq h \leq ?, ? \leq k \leq ?, ? \leq l \leq ?$
Reflections collected	?
Independent reflections	8910[R(int) = ?]
Data/restraints/parameters	8910/3/534
Goodness-of-fit on F^2	1.019
Final R indexes [I>=2σ (I)]	$R_1 = 0.0634$, $wR_2 = 0.1803$
Final R indexes [all data]	$R_1 = 0.0822$, $wR_2 = 0.1959$
Largest diff. peak/hole / e Å^{-3}	0.60/-2.01

Table B.12. Crystal data and structure refinement for **[Mn^{III}L^{tBu}] (4)**.

Atom	Atom	Length/Å		Atom	Atom	Length/Å
Mn1	Cl2	2.277(3)		N24	C25	1.292(4)
Mn1	O3	1.865(2)		C25	C26	1.430(4)
Mn1	N7	1.993(3)		C26	C27	1.418(4)
Mn1	N24	1.975(3)		C26	C36	1.409(5)
Mn1	O28	1.866(2)		C27	O28	1.316(4)
Mn1	O53	2.236(3)		C27	C29	1.427(4)
O3	C4	1.323(4)		C29	C30	1.530(5)
C4	C5	1.415(5)		C29	C34	1.384(5)
C4	C48	1.414(4)		C30	C31	1.537(5)
C5	C6	1.431(4)		C30	C32	1.536(5)
C5	C41	1.410(5)		C30	C33	1.545(5)
C6	N7	1.296(4)		C34	C35	1.403(5)
N7	C8	1.416(4)		C35	C36	1.370(5)
C8	C9	1.394(4)		C35	C37	1.534(5)
C8	C23	1.392(5)		C37	C38	1.532(6)
C9	C10	1.372(5)		C37	C39	1.532(6)
C10	O11	1.363(4)		C37	C40	1.527(6)
C10	C16	1.416(5)		C41	C42	1.371(5)
O11	C12	1.436(4)		C42	C43	1.531(5)
C12	C13	1.506(5)		C42	C47	1.402(5)
C13	O14	1.403(5)		C43	C44	1.534(5)
O14	C15	1.394(7)		C43	C45	1.525(5)
C16	O17	1.357(4)		C43	C46	1.515(6)
C16	C22	1.375(5)		C47	C48	1.384(5)
O17	C18	1.437(4)		C48	C49	1.536(5)
C18	C19	1.491(5)		C49	C50	1.524(5)
C19	O20	1.421(4)		C49	C51	1.531(5)
O20	C21	1.413(4)		C49	C52	1.533(5)
C22	C23	1.398(4)		O53	C54	1.399(5)
C23	N24	1.419(4)		O56	C57	1.394(5)

Table B.13. Bond lengths (Å) for **[Mn^{III}L^{tBu}] (4)**.

Atom	Atom	Atom	Angle/°		Atom	Atom	Atom	Angle/°
O3	Mn1	Cl2	94.38(10)		C25	N24	C23	122.0(3)
O3	Mn1	N7	91.66(11)		N24	C25	C26	125.5(3)
O3	Mn1	N24	172.68(10)		C27	C26	C25	123.5(3)
O3	Mn1	O28	93.89(10)		C36	C26	C25	115.8(3)
O3	Mn1	O53	90.09(10)		C36	C26	C27	120.5(3)
N7	Mn1	Cl2	87.69(10)		C26	C27	C29	118.7(3)
N7	Mn1	O53	91.38(11)		O28	C27	C26	121.7(3)
N24	Mn1	Cl2	89.66(10)		O28	C27	C29	119.6(3)
N24	Mn1	N7	82.39(11)		C27	O28	Mn1	130.1(2)
N24	Mn1	O53	85.81(10)		C27	C29	C30	120.3(3)
O28	Mn1	Cl2	87.85(10)		C34	C29	C27	117.3(3)
O28	Mn1	N7	173.13(10)		C34	C29	C30	122.2(3)
O28	Mn1	N24	92.36(10)		C29	C30	C31	111.3(3)
O28	Mn1	O53	92.65(10)		C29	C30	C32	109.0(3)
O53	Mn1	Cl2	175.46(9)		C29	C30	C33	111.5(3)
C4	O3	Mn1	130.9(2)		C31	C30	C33	106.8(3)
O3	C4	C5	121.4(3)		C32	C30	C31	108.3(3)
O3	C4	C48	119.5(3)		C32	C30	C33	109.9(3)
C48	C4	C5	119.1(3)		C29	C34	C35	124.8(3)
C4	C5	C6	123.8(3)		C34	C35	C37	120.1(3)
C41	C5	C4	120.1(3)		C36	C35	C34	117.1(3)
C41	C5	C6	116.0(3)		C36	C35	C37	122.8(3)
N7	C6	C5	125.9(3)		C35	C36	C26	121.4(3)
C6	N7	Mn1	124.4(2)		C38	C37	C35	110.9(3)
C6	N7	C8	122.4(3)		C39	C37	C35	108.5(3)
C8	N7	Mn1	113.1(2)		C39	C37	C38	109.0(4)
C9	C8	N7	124.6(3)		C40	C37	C35	110.2(3)
C23	C8	N7	115.2(3)		C40	C37	C38	108.9(4)
C23	C8	C9	120.3(3)		C40	C37	C39	109.3(3)
C10	C9	C8	119.6(3)		C42	C41	C5	121.3(3)
C9	C10	C16	120.2(3)		C41	C42	C43	120.2(3)
O11	C10	C9	124.9(3)		C41	C42	C47	117.2(3)
O11	C10	C16	114.9(3)		C47	C42	C43	122.6(3)
C10	O11	C12	117.6(3)		C42	C43	C44	111.4(3)
O11	C12	C13	107.1(3)		C45	C43	C42	109.0(3)
O14	C13	C12	109.4(3)		C45	C43	C44	108.2(3)
C15	O14	C13	114.1(4)		C46	C43	C42	109.4(3)
O17	C16	C10	115.1(3)		C46	C43	C44	108.0(3)
O17	C16	C22	124.8(3)		C46	C43	C45	110.8(4)
C22	C16	C10	120.1(3)		C48	C47	C42	124.3(3)
C16	O17	C18	117.1(3)		C4	C48	C49	120.6(3)
O17	C18	C19	107.7(3)		C47	C48	C4	117.6(3)
O20	C19	C18	109.6(3)		C47	C48	C49	121.8(3)
C21	O20	C19	112.2(3)		C50	C49	C48	109.7(3)

C16	C22	C23	119.5(3)		C50	C49	C51	107.6(3)
C8	C23	C22	120.2(3)		C50	C49	C52	109.6(3)
C8	C23	N24	115.8(3)		C51	C49	C48	111.9(3)
C22	C23	N24	124.0(3)		C51	C49	C52	107.8(3)
C23	N24	Mn1	113.1(2)		C52	C49	C48	110.2(3)
C25	N24	Mn1	124.7(2)		C54	O53	Mn1	127.8(2)

Table B.14. Bond angles (°) for **[Mn^{III}L^{tBu}] (4)**.

Crystal structure data of complex [**Mn^{III}L^{bisPho-NO2}**] (**5**) in **Chapter 7**
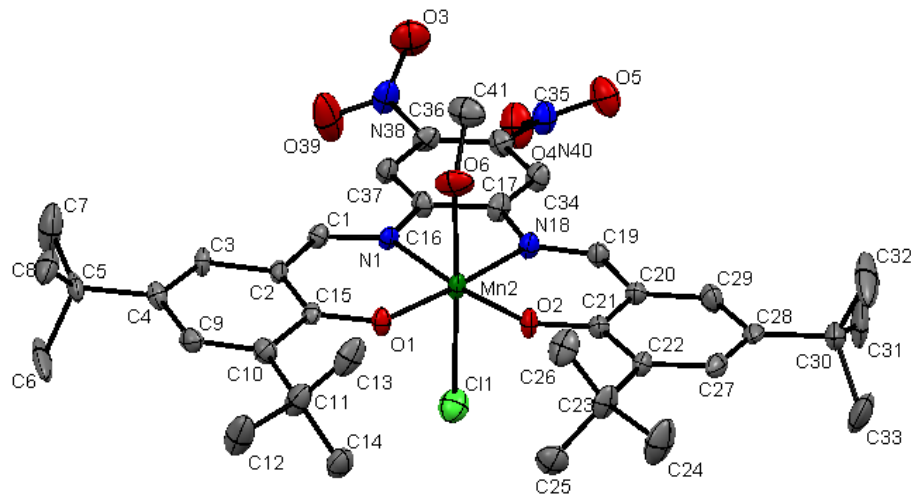
Figure B.6. ORTEP diagram of complex [**Mn^{III}L^{bisPho-NO2}**] (**5**).

Identification code	LA102(3)
Empirical formula	$C_{44}H_{58}O_{12}ClMnN_8$
Formula weight	889.27
Temperature/K	100.1
Crystal system	monoclinic
Space group	Cc
a/Å	12.3951(9)
b/Å	43.834(3)
c/Å	9.5402(6)
α/°	90.00
β/°	113.281(3)
γ/°	90.00
Volume/Å^3	4761.4(5)
Z	4
ρ_{calc}mg/mm^3	1.241
m/mm^{-1}	0.391
F(000)	1864.0
Crystal size/mm^3	$0.902 \times 0.891 \times 0.81$
Radiation	MoKα (λ = 0.71073)
2Θ range for data collection	3.7 to 55.76°
Index ranges	-16 ≤ h ≤ 16, -57 ≤ k ≤ 57, -12 ≤ l ≤ 12
Reflections collected	88443

Independent reflections   10706 [R_{int} = 0.0632, R_{sigma} = 0.0495]
Data/restraints/parameters 10706/5/613
Goodness-of-fit on F^2 1.084
Final R indexes [I>=2σ (I)] R_1 = 0.0659, wR_2 = 0.1685
Final R indexes [all data] R_1 = 0.0868, wR_2 = 0.1848
Largest diff. peak/hole / e $Å^{-3}$ 1.23/-0.47
Flack parameter   0.10(2)

Table B.15. Crystal data and structure refinement for **[Mn^{III}L^{bisPho-NO2}]** (**5**).

Atom	Atom	Length/Å		Atom	Atom	Length/Å
Cl1	Mn2	2.6172(16)		C17	N18	1.413(6)
Mn2	O1	1.870(3)		C17	C34	1.397(6)
Mn2	N1	1.979(3)		N18	C19	1.298(6)
Mn2	O2	1.871(3)		C19	C20	1.412(6)
Mn2	O6	2.268(4)		C20	C21	1.433(6)
Mn2	N18	1.980(4)		C20	C29	1.407(7)
O1	C15	1.307(5)		C21	C22	1.427(6)
N1	C1	1.312(6)		C22	C23	1.543(6)
N1	C16	1.403(5)		C22	C27	1.392(6)
O2	C21	1.304(5)		C23	C24	1.528(7)
O3	N38	1.225(6)		C23	C25	1.552(8)
O4	N40	1.229(6)		C23	C26	1.529(8)
O5	N40	1.207(5)		C27	C28	1.423(7)
O6	C41	1.424(6)		C28	C29	1.359(7)
O7	N47	1.240(6)		C28	C30	1.520(6)
O8	N49	1.233(6)		C30	C31	1.578(10)
O9	N49	1.212(7)		C30	C32	1.470(9)
O10	C53	1.424(6)		C30	C33	1.524(8)
C1	C2	1.417(6)		C34	C35	1.366(6)
C2	C3	1.426(6)		C35	C36	1.388(6)
C2	C15	1.413(6)		C35	N40	1.469(5)
C3	C4	1.375(6)		C36	C37	1.378(6)
C4	C5	1.530(6)		C36	N38	1.468(5)
C4	C9	1.413(6)		N38	O39	1.178(6)
C5	C6	1.541(8)		N42	C43	1.364(7)
C5	C7	1.530(8)		C43	C44	1.393(7)
C5	C8	1.525(7)		C43	C50	1.437(7)
C9	C10	1.380(7)		C44	C45	1.370(8)
C10	C11	1.533(7)		C45	C46	1.387(7)
C10	C15	1.436(6)		C45	N49	1.446(7)
C11	C12	1.538(7)		C46	N47	1.451(7)

C11	C13	1.553(9)	C46	C52	1.382(7)
C11	C14	1.550(8)	N47	O48	1.216(7)
C16	C17	1.413(5)	C50	N51	1.351(6)
C16	C37	1.398(6)	C50	C52	1.390(7)

Table B.16. Bond lengths (Å) for [Mn^{III}L$^{bisPho-NO2}$] (**5**).

Atom	Atom	Atom	Angle/°	Atom	Atom	Atom	Angle/°
O1	Mn2	Cl1	89.66(11)	C29	C20	C19	117.0(4)
O1	Mn2	N1	92.33(14)	C29	C20	C21	121.4(4)
O1	Mn2	O2	93.76(10)	O2	C21	C20	123.2(4)
O1	Mn2	O6	88.39(14)	O2	C21	C22	119.7(4)
O1	Mn2	N18	174.48(15)	C22	C21	C20	117.1(4)
N1	Mn2	Cl1	91.73(12)	C21	C22	C23	119.7(4)
N1	Mn2	O6	87.26(15)	C27	C22	C21	118.3(4)
N1	Mn2	N18	82.18(11)	C27	C22	C23	122.0(4)
O2	Mn2	Cl1	91.43(11)	C22	C23	C25	108.7(4)
O2	Mn2	N1	173.16(15)	C24	C23	C22	112.3(4)
O2	Mn2	O6	89.78(15)	C24	C23	C25	106.7(5)
O2	Mn2	N18	91.76(15)	C24	C23	C26	108.6(4)
O6	Mn2	Cl1	177.76(13)	C26	C23	C22	110.8(4)
N18	Mn2	Cl1	89.92(13)	C26	C23	C25	109.6(5)
N18	Mn2	O6	91.91(16)	C22	C27	C28	124.8(4)
C15	O1	Mn2	130.7(3)	C27	C28	C30	121.1(4)
C1	N1	Mn2	124.5(3)	C29	C28	C27	116.1(4)
C1	N1	C16	121.7(4)	C29	C28	C30	122.8(5)
C16	N1	Mn2	113.8(3)	C28	C29	C20	122.4(4)
C21	O2	Mn2	130.7(3)	C28	C30	C31	110.2(4)
C41	O6	Mn2	126.5(3)	C28	C30	C33	109.2(5)
N1	C1	C2	125.9(4)	C32	C30	C28	109.3(5)
C1	C2	C3	115.6(4)	C32	C30	C31	109.0(6)
C15	C2	C1	123.6(4)	C32	C30	C33	115.8(6)
C15	C2	C3	120.8(4)	C33	C30	C31	103.1(6)
C4	C3	C2	121.5(4)	C35	C34	C17	119.1(4)
C3	C4	C5	123.0(4)	C34	C35	C36	121.6(4)
C3	C4	C9	116.3(4)	C34	C35	N40	116.7(4)
C9	C4	C5	120.7(4)	C36	C35	N40	121.3(4)
C4	C5	C6	107.9(4)	C35	C36	N38	122.7(4)
C7	C5	C4	112.5(4)	C37	C36	C35	120.2(4)
C7	C5	C6	109.0(6)	C37	C36	N38	116.9(4)
C8	C5	C4	110.8(4)	C36	C37	C16	119.7(4)

C8	C5	C6	109.5(5)		O3	N38	C36	116.9(4)
C8	C5	C7	107.1(5)		O39	N38	O3	123.2(4)
C10	C9	C4	125.3(4)		O39	N38	C36	119.1(4)
C9	C10	C11	122.4(4)		O4	N40	C35	116.7(4)
C9	C10	C15	117.9(4)		O5	N40	O4	124.2(4)
C15	C10	C11	119.7(4)		O5	N40	C35	118.8(4)
C10	C11	C12	111.9(4)		N42	C43	C44	121.4(5)
C10	C11	C13	111.1(4)		N42	C43	C50	120.7(4)
C10	C11	C14	110.1(4)		C44	C43	C50	117.8(5)
C12	C11	C13	108.0(5)		C45	C44	C43	122.9(5)
C12	C11	C14	106.1(5)		C44	C45	C46	119.7(5)
C14	C11	C13	109.5(4)		C44	C45	N49	118.7(5)
O1	C15	C2	122.8(4)		C46	C45	N49	121.4(5)
O1	C15	C10	119.2(4)		C45	C46	N47	124.3(5)
C2	C15	C10	118.0(4)		C52	C46	C45	118.9(5)
N1	C16	C17	115.5(4)		C52	C46	N47	116.3(5)
C37	C16	N1	125.2(4)		O7	N47	C46	118.5(5)
C37	C16	C17	119.2(4)		O48	N47	O7	123.9(5)
C16	C17	N18	114.5(4)		O48	N47	C46	117.2(5)
C34	C17	C16	120.1(4)		O8	N49	C45	117.6(5)
C34	C17	N18	125.3(4)		O9	N49	O8	123.4(5)
C17	N18	Mn2	114.0(3)		O9	N49	C45	119.0(5)
C19	N18	Mn2	124.6(3)		N51	C50	C43	120.6(4)
C19	N18	C17	121.4(4)		N51	C50	C52	121.7(4)
N18	C19	C20	127.6(4)		C52	C50	C43	117.7(4)
C19	C20	C21	121.6(4)		C46	C52	C50	123.0(5)

Table B.17. Bond angles (°) for **[Mn^{III}L$^{bisPho-NO2}$] (5)**.

Crystal structure data of complex **[Mn^{II}L^{NO2}] (6)** in chapter 7
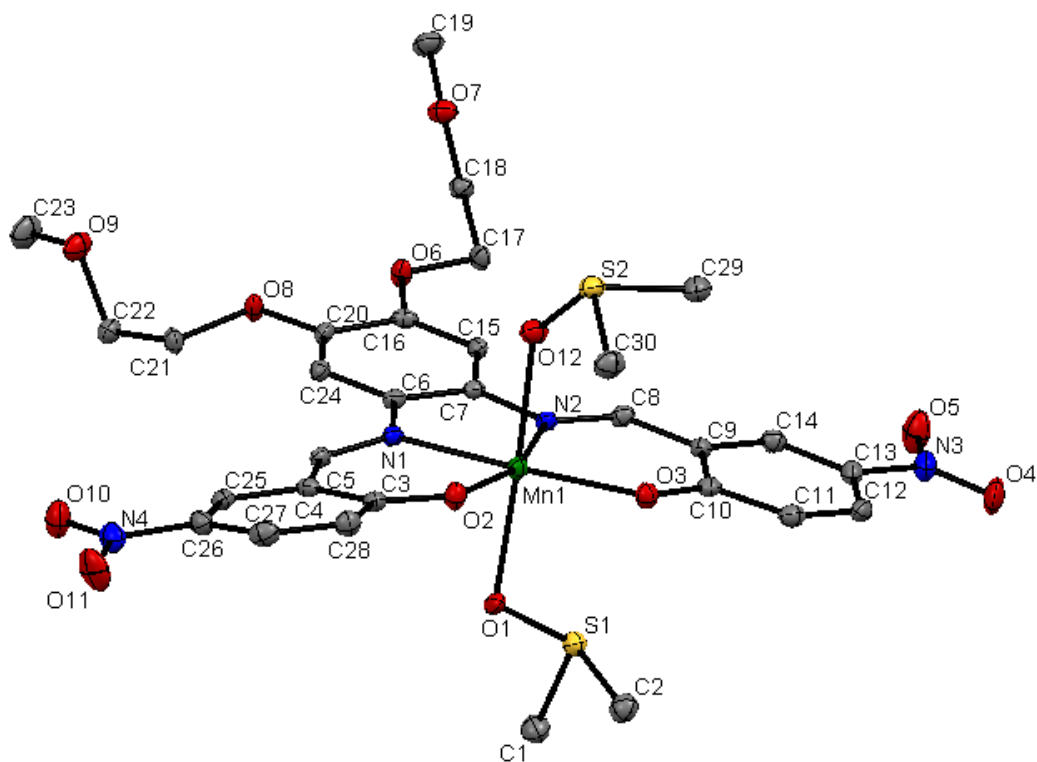
Figure B.7. ORTEP diagram of complex **[Mn^{II}L^{NO2}] (6)**.

Identification code	LA100_COPY
Empirical formula	$C_{32}H_{42}MnN_4O_{13}S_3$
Formula weight	841.85
Temperature/K	100.1
Crystal system	triclinic
Space group	P-1
a/Å	11.5544(7)
b/Å	13.0314(8)
c/Å	13.7212(8)
α/°	104.484(3)
β/°	104.060(4)
γ/°	104.707(3)
Volume/Å^3	1828.3(2)
Z	2
ρ_{calc}mg/mm^3	1.5291

m/mm^{-1}	0.603	
F(000)	879.9	
Crystal size/mm^3	$0.315 \times 0.207 \times 0.099$	
2Θ range for data collection	3.24 to 50°	
Index ranges	$-13 \le h \le 13$, $-15 \le k \le 15$, $-16 \le l \le 16$	
Reflections collected	79410	
Independent reflections	6154[R(int) = 0.0555]	
Data/restraints/parameters	6154/0/485	
Goodness-of-fit on F^2	0.808	
Final R indexes [I>=2σ (I)]	R_1 = 0.0303, wR_2 = N/A	
Final R indexes [all data]	R_1 = 0.0397, wR_2 = 0.1047	
Largest diff. peak/hole / e Å^{-3}	0.40/-0.53	

Table B.18. Crystal data and structure refinement for **[Mn^{II}L^{NO2}] (6)**.

Atom	Atom	Length/Å	Atom	Atom	Length/Å
C1	S1	1.785(2)	C19	O7	1.424(3)
C2	S1	1.789(2)	C20	C24	1.371(3)
C3	C4	1.440(3)	C20	O8	1.370(2)
C3	C28	1.432(3)	C21	C22	1.489(3)
C3	O2	1.288(2)	C21	O8	1.443(2)
C4	C5	1.441(3)	C22	O9	1.413(3)
C4	C25	1.396(3)	C23	O9	1.419(3)
C5	N1	1.295(2)	C25	C26	1.378(3)
C6	C7	1.403(3)	C26	C27	1.403(3)
C6	C24	1.399(3)	C26	N4	1.440(3)
C6	N1	1.418(3)	C27	C28	1.362(3)
C7	C15	1.406(3)	C29	S2	1.790(2)
C7	N2	1.421(3)	C30	S2	1.792(2)
C8	C9	1.451(3)	N1	Mn1	2.1847(17)
C8	N2	1.295(3)	N2	Mn1	2.2299(16)
C9	C10	1.444(3)	N3	O4	1.238(2)
C9	C14	1.394(3)	N3	O5	1.226(2)
C10	C11	1.425(3)	N4	O10	1.229(2)
C10	O3	1.292(2)	N4	O11	1.236(2)
C11	C12	1.365(3)	O1	S1	1.5281(15)
C12	C13	1.396(3)	O1	Mn1	2.3123(15)
C13	C14	1.386(3)	O2	Mn1	2.0781(14)
C13	N3	1.451(3)	O3	Mn1	2.0691(15)
C15	C16	1.381(3)	O12	S2	1.5162(14)

C16	C20	1.410(3)		O12	Mn1	2.2394(15)
C16	O6	1.361(2)		C31	S3	1.784(2)
C17	C18	1.510(3)		C32	S3	1.796(3)
C17	O6	1.438(2)		O13	S3	1.4976(16)
C18	O7	1.415(3)				

Table B.19. Bond lengths (Å) for **[Mn^{II}L^{NO2}]** (**6**).

Atom	Atom	Atom	Angle/°	Atom	Atom	Atom	Angle/°
C28	C3	C4	116.86(18)	C6	N1	C5	120.75(17)
O2	C3	C4	123.93(18)	Mn1	N1	C5	123.72(13)
O2	C3	C28	119.20(18)	Mn1	N1	C6	115.04(12)
C5	C4	C3	125.90(18)	C8	N2	C7	120.97(16)
C25	C4	C3	119.31(17)	Mn1	N2	C7	113.85(12)
C25	C4	C5	114.74(18)	Mn1	N2	C8	124.97(14)
N1	C5	C4	126.75(18)	O4	N3	C13	118.05(18)
C24	C6	C7	119.43(18)	O5	N3	C13	119.36(18)
N1	C6	C7	117.97(18)	O5	N3	O4	122.59(18)
N1	C6	C24	122.57(17)	O10	N4	C26	118.92(17)
C15	C7	C6	118.81(19)	O11	N4	C26	118.33(18)
N2	C7	C6	116.95(17)	O11	N4	O10	122.73(18)
N2	C7	C15	124.24(17)	Mn1	O1	S1	113.75(7)
N2	C8	C9	126.35(18)	Mn1	O2	C3	130.17(13)
C10	C9	C8	125.88(18)	Mn1	O3	C10	131.93(13)
C14	C9	C8	115.33(18)	C17	O6	C16	118.29(15)
C14	C9	C10	118.76(19)	C19	O7	C18	109.94(16)
C11	C10	C9	117.22(18)	C21	O8	C20	115.24(15)
O3	C10	C9	124.03(19)	C23	O9	C22	110.97(17)
O3	C10	C11	118.74(18)	Mn1	O12	S2	133.87(9)
C12	C11	C10	122.83(19)	C2	S1	C1	97.70(11)
C13	C12	C11	118.9(2)	O1	S1	C1	105.27(10)
C14	C13	C12	120.90(19)	O1	S1	C2	107.16(9)
N3	C13	C12	119.76(19)	C30	S2	C29	98.12(11)
N3	C13	C14	119.34(19)	O12	S2	C29	106.27(9)
C13	C14	C9	121.40(19)	O12	S2	C30	104.64(10)
C16	C15	C7	121.17(18)	N2	Mn1	N1	75.84(6)
C20	C16	C15	119.41(17)	O1	Mn1	N1	86.13(6)
O6	C16	C15	125.88(17)	O1	Mn1	N2	89.64(6)
O6	C16	C20	114.69(18)	O2	Mn1	N1	87.41(6)
O6	C17	C18	106.56(16)	O2	Mn1	N2	162.87(6)
O7	C18	C17	108.73(16)	O2	Mn1	O1	92.85(5)

C24	C20	C16	119.70(19)		O3	Mn1	N1	161.73(6)
O8	C20	C16	116.18(17)		O3	Mn1	N2	86.49(6)
O8	C20	C24	124.12(18)		O3	Mn1	O1	89.22(5)
O8	C21	C22	108.40(16)		O3	Mn1	O2	110.48(5)
O9	C22	C21	110.11(17)		O12	Mn1	N1	89.56(6)
C20	C24	C6	121.32(18)		O12	Mn1	N2	85.86(6)
C26	C25	C4	121.25(19)		O12	Mn1	O1	174.41(5)
C27	C26	C25	120.71(19)		O12	Mn1	O2	90.51(6)
N4	C26	C25	118.91(19)		O12	Mn1	O3	93.79(6)
N4	C26	C27	120.37(18)		C32	S3	C31	96.37(12)
C28	C27	C26	119.25(19)		O13	S3	C31	105.59(11)
C27	C28	C3	122.54(19)		O13	S3	C32	107.32(10)

Table B.20. Bond angles (°) for [Mn^{II}L^{NO2}] (6).

APPENDIX C

Permission/License Agreements for Copyrighted Material

JOHN WILEY AND SONS LICENSE
TERMS AND CONDITIONS

Mar 14, 2014

This is a License Agreement between Lanka Wickramasinghe ("You") and John Wiley and Sons ("John Wiley and Sons") provided by Copyright Clearance Center ("CCC"). The license consists of your order details, the terms and conditions provided by John Wiley and Sons, and the payment terms and conditions.

All payments must be made in full to CCC. For payment instructions, please see information listed at the bottom of this form.

License Number	3347730516651
License date	Mar 14, 2014
Licensed content publisher	John Wiley and Sons
Licensed content publication	Angewandte Chemie
Licensed content title	Rectification in Nanoscale Devices Based on an Asymmetric Five-Coordinate Iron(III) Phenolate Complex
Licensed copyright line	Copyright © 2013 WILEY-VCH Verlag GmbH & Co. KGaA, Weinheim
Licensed content author	Lanka D. Wickramasinghe,Meeghage Madusanka Perera,Li Li,Guangzhao Mao,Zhixian Zhou,Cláudio N. Verani
Licensed content date	Oct 14, 2013
Start page	13588
End page	13592
Type of use	Dissertation/Thesis
Requestor type	Author of this Wiley article
Format	Print and electronic
Portion	Full article
Will you be translating?	No
Title of your thesis / dissertation	REDOX-ACTIVE TRIVALENT METALLOSURFACTANTS WITH LOW GLOBAL SYMMETRY FOR MOLECULE-BASED

ELECTRONICS: SPECTROSCOPIC, ELECTROCHEMICAL, AND AMPHIPHILIC PROPERTIES OF NEW MOLECULAR MATERIALS FOR CURRENT-VOLTAGE MEASUREMENTS IN M|LB-MONOLAYER|M DEVICES

Expected completion date	Apr 2014
Expected size (number of pages)	300
Total	0.00 USD

Terms and Conditions

TERMS AND CONDITIONS

the Materials without the prior permission of the respective copyright owner. You may not alter, remove or suppress in any manner any copyright, trademark or other notices displayed by the Materials. You may not license, rent, sell, loan, lease, pledge, offer as security, transfer or assign the Materials, or any of the rights granted to you hereunder to any other person.

4. The Materials and all of the intellectual property rights therein shall at all times remain the exclusive property of John Wiley & Sons Inc or one of its related companies (WILEY) or their respective licensors, and your interest therein is only that of having possession of and the right to reproduce the Materials pursuant to Section 2 herein during the continuance of this Agreement. You agree that you own no right, title or interest in or to the Materials or any of the intellectual property rights therein. You shall have no rights hereunder other than the license as provided for above in Section 2. No right, license or interest to any trademark, trade name, service mark or other branding ("Marks") of WILEY or its licensors is granted hereunder, and you agree that you shall not assert any such right, license or interest with respect thereto.

5. NEITHER WILEY NOR ITS LICENSORS MAKES ANY WARRANTY OR REPRESENTATION OF ANY KIND TO YOU OR ANY THIRD PARTY, EXPRESS, IMPLIED OR STATUTORY, WITH RESPECT TO THE MATERIALS OR THE ACCURACY OF ANY INFORMATION CONTAINED IN THE MATERIALS, INCLUDING, WITHOUT LIMITATION, ANY IMPLIED WARRANTY OF MERCHANTABILITY, ACCURACY, SATISFACTORY QUALITY, FITNESS FOR A PARTICULAR PURPOSE, USABILITY, INTEGRATION OR NON-INFRINGEMENT AND ALL SUCH WARRANTIES ARE HEREBY EXCLUDED BY WILEY AND ITS LICENSORS AND WAIVED BY YOU.

6. WILEY shall have the right to terminate this Agreement immediately upon breach of this Agreement by you.

7. You shall indemnify, defend and hold harmless WILEY, its Licensors and their respective directors, officers, agents and employees, from and against any actual or threatened claims, demands, causes of action or proceedings arising from any breach of this Agreement by you.

8. IN NO EVENT SHALL WILEY OR ITS LICENSORS BE LIABLE TO YOU OR ANY OTHER PARTY OR ANY OTHER PERSON OR ENTITY FOR ANY SPECIAL, CONSEQUENTIAL, INCIDENTAL, INDIRECT, EXEMPLARY OR PUNITIVE DAMAGES, HOWEVER CAUSED, ARISING OUT OF OR IN CONNECTION WITH THE DOWNLOADING, PROVISIONING, VIEWING OR USE OF THE MATERIALS REGARDLESS OF THE FORM OF ACTION, WHETHER FOR BREACH OF CONTRACT, BREACH OF WARRANTY, TORT, NEGLIGENCE, INFRINGEMENT OR OTHERWISE (INCLUDING, WITHOUT LIMITATION, DAMAGES BASED ON LOSS OF PROFITS, DATA, FILES, USE, BUSINESS OPPORTUNITY OR CLAIMS OF THIRD PARTIES), AND WHETHER OR NOT THE PARTY HAS BEEN ADVISED OF THE POSSIBILITY OF SUCH DAMAGES. THIS LIMITATION SHALL APPLY

NOTWITHSTANDING ANY FAILURE OF ESSENTIAL PURPOSE OF ANY LIMITED REMEDY PROVIDED HEREIN.

9. Should any provision of this Agreement be held by a court of competent jurisdiction to be illegal, invalid, or unenforceable, that provision shall be deemed amended to achieve as nearly as possible the same economic effect as the original provision, and the legality, validity and enforceability of the remaining provisions of this Agreement shall not be affected or impaired thereby.

10. The failure of either party to enforce any term or condition of this Agreement shall not constitute a waiver of either party's right to enforce each and every term and condition of this Agreement. No breach under this agreement shall be deemed waived or excused by either party unless such waiver or consent is in writing signed by the party granting such waiver or consent. The waiver by or consent of a party to a breach of any provision of this Agreement shall not operate or be construed as a waiver of or consent to any other or subsequent breach by such other party.

11. This Agreement may not be assigned (including by operation of law or otherwise) by you without WILEY's prior written consent.

12. Any fee required for this permission shall be non-refundable after thirty (30) days from receipt

13. These terms and conditions together with CCC's Billing and Payment terms and conditions (which are incorporated herein) form the entire agreement between you and WILEY concerning this licensing transaction and (in the absence of fraud) supersedes all prior agreements and representations of the parties, oral or written. This Agreement may not be amended except in writing signed by both parties. This Agreement shall be binding upon and inure to the benefit of the parties' successors, legal representatives, and authorized assigns.

14. In the event of any conflict between your obligations established by these terms and conditions and those established by CCC's Billing and Payment terms and conditions, these terms and conditions shall prevail.

15. WILEY expressly reserves all rights not specifically granted in the combination of (i) the license details provided by you and accepted in the course of this licensing transaction, (ii) these terms and conditions and (iii) CCC's Billing and Payment terms and conditions.

16. This Agreement will be void if the Type of Use, Format, Circulation, or Requestor Type was misrepresented during the licensing process.

17. This Agreement shall be governed by and construed in accordance with the laws of the State of New York, USA, without regards to such state's conflict of law rules. Any legal action, suit or proceeding arising out of or relating to these Terms and Conditions or the breach thereof shall be instituted in a court of competent jurisdiction in New York County

in the State of New York in the United States of America and each party hereby consents and submits to the personal jurisdiction of such court, waives any objection to venue in such court and consents to service of process by registered or certified mail, return receipt requested, at the last known address of such party.

Wiley Open Access Terms and Conditions

Wiley publishes Open Access articles in both its Wiley Open Access Journals program [http://www.wileyopenaccess.com/view/index.html] and as Online Open articles in its subscription journals. The majority of Wiley Open Access Journals have adopted the Creative Commons Attribution License (CC BY) which permits the unrestricted use, distribution, reproduction, adaptation and commercial exploitation of the article in any medium. No permission is required to use the article in this way provided that the article is properly cited and other license terms are observed. A small number of Wiley Open Access journals have retained the Creative Commons Attribution Non Commercial License (CC BY-NC), which permits use, distribution and reproduction in any medium, provided the original work is properly cited and is not used for commercial purposes.

Online Open articles - Authors selecting Online Open are, unless particular exceptions apply, offered a choice of Creative Commons licenses. They may therefore select from the CC BY, the CC BY-NC and the Attribution-NoDerivatives (CC BY-NC-ND). The CC BY-NC-ND is more restrictive than the CC BY-NC as it does not permit adaptations or modifications without rights holder consent.

Wiley Open Access articles are protected by copyright and are posted to repositories and websites in accordance with the terms of the applicable Creative Commons license referenced on the article. At the time of deposit, Wiley Open Access articles include all changes made during peer review, copyediting, and publishing. Repositories and websites that host the article are responsible for incorporating any publisher-supplied amendments or retractions issued subsequently. Wiley Open Access articles are also available without charge on Wiley's publishing platform, **Wiley Online Library** or any successor sites.

Conditions applicable to all Wiley Open Access articles:

- The authors' moral rights must not be compromised. These rights include the right of "paternity" (also known as "attribution" - the right for the author to be identified as such) and "integrity" (the right for the author not to have the work altered in such a way that the author's reputation or integrity may be damaged).

- Where content in the article is identified as belonging to a third party, it is the obligation of the user to ensure that any reuse complies with the copyright policies of the owner of that content.

- If article content is copied, downloaded or otherwise reused for research and other purposes as permitted, a link to the appropriate bibliographic citation (authors, journal, article title, volume, issue, page numbers, DOI and the link to the definitive

published version on Wiley Online Library) should be maintained. Copyright notices and disclaimers must not be deleted.

- o Creative Commons licenses are copyright licenses and do not confer any other rights, including but not limited to trademark or patent rights.

- Any translations, for which a prior translation agreement with Wiley has not been agreed, must prominently display the statement: "This is an unofficial translation of an article that appeared in a Wiley publication. The publisher has not endorsed this translation."

Conditions applicable to non-commercial licenses (CC BY-NC and CC BY-NC-ND)

For non-commercial and non-promotional purposes individual non-commercial users may access, download, copy, display and redistribute to colleagues Wiley Open Access articles. In addition, articles adopting the CC BY-NC may be adapted, translated, and text- and data-mined subject to the conditions above.

Use by commercial "for-profit" organizations

Use of non-commercial Wiley Open Access articles for commercial, promotional, or marketing purposes requires further explicit permission from Wiley and will be subject to a fee. Commercial purposes include:

- o Copying or downloading of articles, or linking to such articles for further redistribution, sale or licensing;

- o Copying, downloading or posting by a site or service that incorporates advertising with such content;

- o The inclusion or incorporation of article content in other works or services (other than normal quotations with an appropriate citation) that is then available for sale or licensing, for a fee (for example, a compilation produced for marketing purposes, inclusion in a sales pack)

- o Use of article content (other than normal quotations with appropriate citation) by for-profit organizations for promotional purposes

- o Linking to article content in e-mails redistributed for promotional, marketing or educational purposes;

- o Use for the purposes of monetary reward by means of sale, resale, license, loan, transfer or other form of commercial exploitation such as marketing products

o Print reprints of Wiley Open Access articles can be purchased from: corporatesales@wiley.com

The modification or adaptation for any purpose of an article referencing the CC BY-NC-ND License requires consent which can be requested from RightsLink@wiley.com .

Other Terms and Conditions:

BY CLICKING ON THE "I AGREE..." BOX, YOU ACKNOWLEDGE THAT YOU HAVE READ AND FULLY UNDERSTAND EACH OF THE SECTIONS OF AND PROVISIONS SET FORTH IN THIS AGREEMENT AND THAT YOU ARE IN AGREEMENT WITH AND ARE WILLING TO ACCEPT ALL OF YOUR OBLIGATIONS AS SET FORTH IN THIS AGREEMENT.

v1.8

If you would like to pay for this license now, please remit this license along with your payment made payable to "COPYRIGHT CLEARANCE CENTER" otherwise you will be invoiced within 48 hours of the license date. Payment should be in the form of a check or money order referencing your account number and this invoice number RLNK501251400.
Once you receive your invoice for this order, you may pay your invoice by credit card. Please follow instructions provided at that time.

Make Payment To:
Copyright Clearance Center
Dept 001
P.O. Box 843006
Boston, MA 02284-3006

For suggestions or comments regarding this order, contact RightsLink Customer Support: customercare@copyright.com or +1-877-622-5543 (toll free in the US) or +1-978-646-2777.

Gratis licenses (referencing $0 in the Total field) are free. Please retain this printable license for your reference. No payment is required.

ABSTRACT

REDOX-ACTIVE TRIVALENT METALLOSURFACTANTS WITH LOW GLOBAL SYMMETRY FOR MOLECULE-BASED ELECTRONICS: SPECTROSCOPIC, ELECTROCHEMICAL, AND AMPHIPHILIC PROPERTIES OF NEW MOLECULAR MATERIALS FOR CURRENT-VOLTAGE MEASUREMENTS IN M|LB-MONOLAYER|M DEVICES

by

LANKA D. W. WICKRAMASINGHE ARACHCHILAGE

August 2014

Advisor: Professor Cláudio N. Verani

Major: Chemistry (Inorganic)

Degree: Doctor of Philosophy

The silicon-based microelectronic industry has made remarkable technological advancements. Among these, new generation consumer electronics, telecommunication devices, and high performance data processing smart devices are of special interest. At present, electronic components existing on a single silicon chip grow rapidly, and soon the miniaturization process of electrical components will face limitations due to heat dissipation. Therefore, as an advanced alternative for silicon-based electronic components, the investigation of nanoscale molecular electronic devices is of great importance. This dissertation research is focused on the development of redox-active asymmetric metallosurfactants as potential candidates for molecule-based electronics. Asymmetric donor-acceptor type [D-A] molecules are promising candidates to study the current rectification behavior. In order to address this phenomenon, a series of ligands with phenolate moieties and, their gallium(III), iron(III), and manganese(III) complexes with $[N_2O_3]$ and $[N_2O_2]$ coordination environments were synthesized and structurally

characterized using multiple methods. Ligands were designed with different electron-donating and electron-withdrawing substituents, to modulate structural, chemical, and physical properties, such as geometry, spectroscopic, redox, film formation, and electrical properties.

As an initial attempt, low symmetry gallium(III) and iron(III) complexes with [N_2O_3] binding moieties were developed. Different alkyl substituents are introduced to the phenylenediamine moiety of the main ligand structure to allow for film formation of the metal complexes. The electrochemical properties of gallium(III) complexes show ligand-based redox processes, while the iron(III) complexes show metal- and ligand-centered redox processes. The EPR data of iron(III) complexes indicate the formation of high spin species under [N_2O_3] coordination environment. Metal complexes with methoxy and methoxyethoxy substituents on the phenylenediamine moiety, show formation of homogeneous conformal thin films at the air/water and air/solid interfaces. However, a possible amine/imine conversion is observed for gallium(III) and iron(III) complexes at the air/water interface. This interconversion is evident in the spectroscopic data of gallium(III) and iron(III) thin films. This study exhibits promising results in merging surfactant and redox properties into a single molecule. The iron(III) complexes indicate, that phenolate moieties act as donors when coordinated trivalent metal ions and the iron(III) center acts as an electron-acceptor moiety. These data suggest further investigations for iron(III) complexes to study their electrical properties followed by device fabrication.

When designing a current rectifier, energy of frontier molecular orbitals should be comparable to energy of the metal Fermi levels. Then, the potential candidate can show an efficient electron transfer between the molecule and metal electrodes. In addition, if the

molecule shows lower HOMO-LUMO energy gap, a unimolecular current rectification mechanism is applicable. Such situations facilitate efficient internal electron transfer pathways. The best possible way to modulate the HOMO-LUMO energy difference is the introduction of electron-withdrawing substituents into the molecular design. If these substituents are redox-active, then the overall redox properties of the molecule can be enhanced. In order to achieve this goal, two nitro substituted iron(III) complexes with $[N_2O_3]$ and $[N_2O_2]$ coordination environments were investigated. Both complexes showed pentacoordinate geometry around the metal ion. These two iron(III) complexes showed excellent redox properties with lower potential differences between the first oxidation and reduction peaks, when compared to alkyl substituted iron(III) complexes. However, the iron(III) complex with $[N_2O_3]$ donor set was found to be a better redox candidate when compared to the other. The density functional theory (DFT) calculations suggest, that the first cathodic process to be iron(III)/(II) redox couple, and the other cathodic and anodic redox processes to be nitro reductions and phenolate oxidations, respectively. Both complexes form mono and multilayers at the air/solid interface. Spectroscopic and surface analyses of these two complexes show formation of well-ordered conformal LB films with intact molecular structures. Therefore, this investigation suggests that nitro substituted iron(III) complexes are successful in obtaining more redox accessible states with low HOMO-LUMO energies when compared to iron(III) complexes with electron-donating substituents. The modulation of HOMO and LUMO energies is important when designing molecular rectifiers.

Device fabrication studies were performed to investigate the feasibility of applying iron(III) complexes with $[N_2O_3]$ environments in molecule-based electronics. An iron(III) complex **[Fe^{III}L^4]** with methoxyethoxy substituents was investigated, and this complex

showed the iron(III)/(II) reduction process at -1.49 V *vs.* Fc^+/Fc. The iron(III) complex formed well-organized uniform thin films at air/water and air/solid interfaces with a collapse pressure of ~ 60 mN/m. The device with gold|LB-monolayer|gold configuration shows asymmetrical current responses with rectification ratios varying from 4.52 to 12 between -2 and +2 V and from 2.95 to 36.7 between -4 and +4 V, respectively. Therefore, this study showed that triphenolate coordinated iron(III) complexes are able to act as potential current rectifiers.

Further studies are performed to identify the possibility of using iron(III) complexes with $[N_2O_2]$ donor sets for current rectification. This study also examined a probable current rectifying mechanism for iron(III) systems. In order to address this, two iron(III) complexes with salophen-type ligands were synthesized and structurally characterized. These iron(III) complexes have substituted phenolate moieties (*tert*-butyl and nitro) to facilitate different physical and chemical properties. The nitro substituted iron(III) complex forms a μ-oxo bridged species due to electronic and steric effects. The *tert*-butyl substituted iron(III) complex showed current rectifying properties with rectification ratios ranging from 3.99 to 28.6 between -2 and +2 V and from 2.04 to 31 between -4 and +4 V, respectively. This study also showed, that the asymmetrical nature of the iron(III) complex is fundamental for the observed current rectification. The *tert*-butyl substituted iron(III) complex displays metal-centered, singly occupied molecular orbitals (SOMO), and ligand-centered, highest occupied molecular orbitals (HOMO). Additionally, the electrochemical and DFT calculations of this system suggest, that the SOMO energy level is closer to the metal Fermi level when compared to the HOMO energy level. Therefore, electron transfer through SOMO energy level is energetically more favorable than electron transfer through the HOMO energy level.

According to this data, an asymmetric current rectification mechanism is plausible for this [D-A] type iron(III) complex.

Manganese(III) complexes that are immobilized onto solid surfaces are another important class of compounds that can be used in electronic applications. Therefore, a series of manganese complexes with $[N_2O_3]$ and $[N_2O_2]$ donor sets were investigated. These complexes show metal-based manganese(III)/(II) and ligand-based oxidation redox processes in their cyclic voltammograms. The majority of manganese(III) complexes form well-ordered uniform LB films. The LB film analyses, also suggest that the molecular structure remains intact during the film formation processes. These manganese(III) complexes display possible [D-A] structures, nevertheless gold|LB-monolayer|gold devices of the most promising candidate show asymmetric current responses with poor current amplitudes, thus behaved as an insulator. The observed current insulating behavior could be due to structural and/or electronic parameters of manganese(III) complex and further investigations are necessary to identify the foundation.

This dissertation research presented new classes of saloph-type and triphenolate ligand systems and their gallium(III), iron(III), and manganese(III) complexes, which can merge redox and amphiphilic properties together. More importantly, this project facilitated the understanding of geometric, electronic, redox, and amphiphilic properties of different classes of metal complexes. Finally, this project allowed the study electrical properties of iron(III) complexes with $[N_2O_3]$ and $[N_2O_2]$ donor sets and reveled directional flow of electrical current to denote the rectifying behavior.

AUTOBIOGRAPHICAL STATEMENT

Lanka D. W. Wickramasinghe Arachchilage

Professional Preparation: Education
Wayne State University (MI, USA), Inorganic Chemistry, Ph.D., **2014**
Institute of Chemistry Ceylon (Sri Lanka), Chemistry, B.S.(Honors), **2006**

Appointments
2009-2014: Graduate Research Assistant, Department of Chemistry, Wayne State University (MI, USA)
2008-2009: Graduate Teaching Assistant, Department of Chemistry, Wayne State University (MI, USA)

Publications
1. Wickramasinghe, L. D.; Perera, M. M.; Li, L.; Mao, G.; Zhou, Z.; Verani, C. N. Rectification in Nanoscale Devices based on an Asymmetric Five-Coordinate Iron(III)/Phenolate Complex. *Angew. Chem. Int. Ed.* **2013**, *52*, 13346-13350.

Presentations
1. "Isolation of Pentacoordinate Iron(III) and Manganese(III) Complexes for Nanoscale Devices" **Lanka D. Wickramasinghe**, Meeghage M. Perera, Li Li, Guangzhao Mao, Zhixian Zhou, and Cláudio N. Verani, **246th ACS National Meeting**, Indianapolis IN, September 8-12, **2013**, **Oral Presentation**.
2. "New Asymmetric Manganese(III) Species for Multi-Component Photo-Catalysis: Synthesis, Redox, Spectroscopic, and Amphiphilic Properties" **Lanka D. Wickramasinghe**, Li Li, Guangzhao Mao, and Cláudio N. Verani, **20th International Symposium on the Photophysics and Photochemistry of Coordination Compounds (ISPPCC)**, Traverse City MI, July 7-11, **2013**, **Poster Presentation**.
3. "Redox-active Trivalent Metal Complexes as Precursors for Langmuir-Blodgett Films" **Lanka D. Wickramasinghe** and Cláudio N. Verani, **244th ACS National Meeting**, Philadelphia PA, August 19-23, **2012**, **Oral Presentation**.
4. "Effect of Substituents on Redox and Amphiphilic Properties of Iron(III) Metallosurfactants" **Lanka D. Wickramasinghe** and Cláudio N. Verani, **43rd ACS CERM**, Dearborn MI, June 5-9, **2012**, **Poster Presentation**.
5. "Synthesis and Characterization of Redox-active Asymmetrical Iron(III) and Gallium(III) Metallosurfactants" **Lanka D. Wickramasinghe** and Cláudio N. Verani, **Ohio Inorganic Weekend**, Cincinnati OH, October 28-29, **2011**, **Poster Presentation**.

Technical Skills
Organic and inorganic synthesis, chromatography, spectroscopic techniques (FTIR, UV-visible, NMR, IRRAS), electrochemical measurements (CV, SWV, DPV, bulk electrolysis, spectroelectrochemistry), Langmuir-Blodgett methods, surface wetting experiments, device fabrication, and current-voltage measurements